New Directions in Quantum Simulation and Metrology via Contact and Photon-mediated Interactions

by

Anjun Chu

B.S., Tsinghua University, 2018

A thesis submitted to the

Faculty of the Graduate School of the

University of Colorado in partial fulfillment

of the requirements for the degree of

Doctor of Philosophy

Department of Physics

2024

Committee Members:

Ana Maria Rey, Chair

James K. Thompson

Jun Ye

Jose P. D'Incao

Joshua Combes

Chu, Anjun (Ph.D., Physics)

New Directions in Quantum Simulation and Metrology via Contact and Photon-mediated Interactions

Thesis directed by Prof. Ana Maria Rey

Highly controllable atomic, molecular, and optical systems have emerged as an increasingly powerful toolkit in advancing the frontiers of quantum simulation, metrology, computation, and fundamental physics. In this thesis, we present theoretical work on manipulation of contact and photon-mediated interactions in optical lattice clocks and cavity QED systems, as well as explorations of their possible applications on problems relevant for quantum simulation and metrology.

We start from an overview of the relevant theoretical background for this thesis, including optical lattices, contact interactions, spin systems, photon-mediated interactions and measurements, as well as metrological concepts. We then present research in three closely related directions.

Firstly, we discuss theory ideas for optimizing the performance of optical lattice clocks via Hamiltonian engineering. Based on the tunable delocalization of Wannier-Stark states in tilted lattices, we can fine-tune the relative strength of on-site p-wave and nearest-neighbor s-wave interactions, leading to a minimization of density shifts in a 1D optical lattice clock. We also discuss the tunability of nearest-neighbor interactions by lattice geometry. Considering the improved sensitivity of optical lattice clocks, we further analyze the manifestation of general relativistic effects in a quantum many-body optical lattice clock and discuss protocols for their near-term observation.

Additionally, we discuss theory ideas for exploring emergent collective behaviors and dynamical phases in interacting arrays. We utilize sideband transitions in trapped bosonic gases to engineer Lipkin-Meshkov-Glick model and identify dynamical phase transitions between ferromagnetic and paramagnetic phases. We also provide a theoretical proposal for correlated hopping processes facilitated by multilevel atoms in cavity QED systems, which features intriguing phenomena such as chiral transport and correlation spreading behaviors. We then consider protocols for the control and

amplification of atomic Bloch oscillations via cavity-mediated interactions. Moreover, we realize the Bardeen–Cooper–Schrieffer (BCS) model, an iconic model that describes the behavior of superfluids and superconductors, by photon-mediated spin exchange interactions using the Anderson pseudospin mapping, and for the first time observe a dynamical phase with persistent oscillations of the BCS order parameter.

Finally, we discuss theory ideas for entanglement generation via photon-mediated interactions and measurements. We provide a theory proposal for implementing homogeneous one-axis twisting interactions in a lattice-based atom interferometer using partial delocalized Wannier-Stark states in tilted lattices, which suppresses inhomogeneities in atom-light couplings at a magic lattice depth. We also compare two common approaches experimentally used to generate spin squeezing in cavity QED systems, quantum nondemolition measurements and unitary one-axis twisting dynamics. We derived simple criteria to determine the best protocol based on the detector's quantum efficiency.

Dedication

To my family.

Acknowledgements

My life at JILA and CU Boulder was a fantastic journey because of the many wonderful people I interacting with. First and foremost, I would like to thank my brilliant advisor Prof. Ana Maria Rey. Her profound insight and incredible passion for science have inspired and guided me to become a better researcher. I was mainly working as an experimentalist during my undergrad and I'm very grateful that she discovered my capability in theoretical research and provided a chance for me to work in her group even though I didn't have too much relevant experience. I am immensely thankful for her amazing support of meeting with me (each of her students) multiple times a week, as well as for her remarkable ability to create collaborative environment between theory and experiment. I cannot imagine a better advisor I can have during the past six years.

In addition, I would like to thank my excellent colleagues and friends in the Rey group: Peiru He, Asier Piñeiro Orioli, Diego Barberena, Robert Lewis-Swan, David Wellnitz, Bhuvanesh Sundar, Haoqing Zhang, Tianrui Xu, Mikhail Mamaev, Chunlei Qu, Thomas Bilitewski, Itamar Kimchi, Michael Perlin, Sean Muleady, Jeremy Young, Miskeen Khan, Raphael Kaubruegger, Sanaa Agarwal, Kris Tucker, Edwin Chaparro, Yongju Hai and Conall McCabe. It is a great pleasure to work together, have lunch together, and enjoy science together with all of you.

My sincere thanks also go to Prof. James Thompson, Prof. Jun Ye and for their help and inspiration as my experimental collaborators at JILA. I would also like to acknowledge their group members I have great scientific discussions with, including Dylan Young, Eric Song, Chengyi Luo, Chitose Maruko, Zhijing Niu, Vera Schäfer, Alexander Aeppli, Tobias Bothwell, Colin Kennedy, Kyungtae Kim, Maya Miklos, William Milner, Stefan Lannig, Lingfeng Yan and Ross Hutson. I

really enjoy the amazing experience of walking down into the lab for discussing theoretical protocols and witnessing the immediate implementation in experiments. I would also like to thank other excellent collaborators within and outside JILA: Prof. Carsten Klempt and Prof. Jan Arlt for my first project on sideband transitions in trapped bosonic gases, John Wilson and Prof. Murray Holland for momentum-exchange interactions, as well as Prof. Peter Zoller, Prof. Klemens Hammerer, and Victor Martínez-Lahuerta for understanding general relativistic effects in a quantum many-body optical lattice clock.

Last but not least, I cannot thank my family enough for their endless love and encouragement. To my parents, thank you for your constant support and love in my life. I really miss you since we have not seen each other since the beginning of my grad school. To my best friend, partner and fiancée, Minyan, this thesis would not have been possible without your love, company, understanding and belief in me. You have brought so much laughter and joy along this journey, and I am forever grateful for your presence in my life.

Contents

Chapter

1 Introduction **1**

1.1 Quantum technology in modern science 1

1.2 AMO toolboxes for modern science 3

1.2.1 Optical lattice clocks 4

1.2.2 Cavity QED systems 6

1.3 Outline of this thesis 7

2 Theoretical background **11**

2.1 Optical lattices 11

2.1.1 AC Stark effect 11

2.1.2 Band structure of 1D lattice 15

2.1.3 Effects of radial modes in a 1D lattice 20

2.1.4 Linearly tilted 1D lattice 22

2.2 Contact interactions 28

2.2.1 Partial wave expansion 28

2.2.2 Huang-Yang pseudopotential 30

2.2.3 Semiclassical approximation of scattering lengths 35

2.2.4 SU(n) symmetry 37

2.2.5 Approximations for many-body dynamics 40

2.3 Spin systems . . . 42
2.3.1 Boson representation of spins . . . 43
2.3.2 Phase space representation of spins . . . 45
2.3.3 Tensor product of spin-1/2 systems . . . 48
2.4 Photon-mediated interactions and measurements . . . 50
2.4.1 Open quantum system and Lindblad master equation . . . 51
2.4.2 Unitary and dissipative physics in cavity QED . . . 53
2.4.3 Derivation of spin exchange interactions . . . 58
2.4.4 Derivation of one-axis twisting interactions . . . 60
2.4.5 Continuous quantum measurements . . . 62
2.5 Quantum metrology . . . 67
2.5.1 Quantum Fisher information . . . 67
2.5.2 Standard quantum limit and Heisenberg limit . . . 71
2.5.3 Spin squeezing and one-axis twisting . . . 73

3 Improving optical lattice clocks via Hamiltonian engineering 78

3.1 Overview . . . 78
3.2 Hamiltonian engineering of spin-orbit coupled fermions in a Wannier-Stark optical lattice clock . . . 79
3.2.1 Introduction . . . 79
3.2.2 Experimental system and theoretical model . . . 80
3.2.3 Density shifts in the carrier transition . . . 84
3.2.4 Dynamical phase transition in the Wannier-Stark sidebands . . . 88
3.2.5 Conclusion and outlook . . . 91
3.2.6 Supplemental Materials: Spin model for the carrier transition . . . 92
3.2.7 Supplemental Materials: Spin model for the Wannier-Stark sidebands . . . 98
3.2.8 Supplemental Materials: Details in theory-experiment comparison . . . 105

3.3 Coherent evolution of superexchange interaction in seconds long optical clock spectroscopy . . . 109
3.3.1 Introduction . . . 110
3.3.2 System . . . 112
3.3.3 Weak transverse confinement regime . . . 118
3.3.4 Strong transverse confinement regime . . . 119
3.3.5 Conclusion and outlook . . . 124
3.3.6 Supplemental Materials: Two-well Fermi-Hubbard Hamiltonian . . . 124
3.3.7 Supplemental Materials: Superexchange contrast dynamics . . . 127
3.3.8 Supplemental Materials: 1D large-spin Hamiltonian . . . 130
3.3.9 Supplemental Materials: Spin wave analysis for 1D spin model . . . 133
3.4 Exploring the interplay between mass-energy equivalence, interactions and entanglement in an optical lattice clock . . . 136
3.4.1 Introduction . . . 136
3.4.2 Mass-energy equivalence in optical lattice clocks . . . 138
3.4.3 Tuning and distinguishing GR effects . . . 140
3.4.4 Interplay with many-body dynamics . . . 142
3.4.5 Conclusion and outlook . . . 146
3.4.6 Supplemental Materials: Post-Newtonian corrections . . . 147
3.4.7 Supplemental Materials: Dressing Protocol . . . 158
3.4.8 Supplemental Matertials: Additional numerical results . . . 164
3.4.9 Supplemental Materials: Analytic results for frequency synchronization . . . 166

4 Emergent collective behaviors and dynamical phases in interacting arrays 174
4.1 Overview . . . 174
4.2 Simulation of XXZ spin models using sideband transitions in trapped bosonic gases . 174
4.2.1 Introduction . . . 175

4.2.2 Theoretical model . . . 176
4.2.3 Experimental results . . . 181
4.2.4 Conclusion and outlook . . . 184
4.2.5 Supplemental Materials: Experimental realization . . . 184
4.2.6 Supplemental Materials: Spin model and mean-field dynamics . . . 187
4.2.7 Supplemental Materials: Dynamical phase diagram and critical behavior . . . 192
4.2.8 Supplemental Materials: Discussion of spin squeezing . . . 196
4.3 Photon-mediated correlated hopping in a synthetic ladder . . . 199
4.3.1 Introduction . . . 199
4.3.2 System . . . 201
4.3.3 Examples of correlated hopping . . . 204
4.3.4 Conclusion and outlook . . . 209
4.3.5 Supplemental Materials: Theory model . . . 210
4.3.6 Supplemental Materials: Schwinger bosons and undepleted pump approximation . . . 215
4.3.7 Supplemental Materials: Numerical results for dynamical phase transition . . . 221
4.3.8 Supplemental Materials: Experimental considerations . . . 222
4.4 Control and amplification of Bloch oscillations via photon-mediated interactions . . . 225
4.4.1 Introduction . . . 226
4.4.2 Model and single-particle dynamics . . . 227
4.4.3 Deep lattice regime . . . 232
4.4.4 Shallow lattice regime . . . 233
4.4.5 Experimental consideration . . . 235
4.4.6 Conclusion and outlook . . . 236
4.4.7 Supplemental Materials: Cavity QED with Wannier-Stark state . . . 236
4.4.8 Supplemental Materials: Dynamical phase transition with Wannier-Stark states 242

4.4.9 Supplemental Materials: Schwinger bosons and undepleted pump approximation . . . 245
4.4.10 Supplemental Materials: Experimental considerations . . . 247
4.5 Observing dynamical phases of BCS superconductors in a cavity QED simulator . . 253
4.5.1 Introduction . . . 253
4.5.2 Experimental setup and model system . . . 256
4.5.3 Phase I to phase II . . . 260
4.5.4 Phase II to phase III . . . 263
4.5.5 Scan across three dynamical phases . . . 264
4.5.6 Conclusion . . . 266
4.5.7 Methods: Experimental setup . . . 266
4.5.8 Methods: Dynamical phase diagram . . . 269
4.5.9 Methods: Phase III dynamics in the case of a continuous single-particle dispersion . . . 272
4.5.10 Methods: Numerical simulations . . . 274
4.5.11 Methods: Higgs-like behaviour in short-time phase II dynamics . . . 275
4.5.12 Supplemental Materials: Dynamical phase diagram . . . 277
4.5.13 Supplemental Materials: Short-time signatures of dynamical phases . . . 284
4.5.14 Supplemental Materials: Axial motion . . . 290

5 Entanglement generation via photon-mediated interactions and measurements 294
5.1 Overview . . . 294
5.2 Quantum enhanced cavity QED interferometer with partially delocalized atoms in lattices . . . 294
5.2.1 Introduction . . . 295
5.2.2 Engineering homogeneous couplings . . . 296
5.2.3 Quantum enhanced interferometric protocol . . . 300

5.2.4 Experimental considerations . . . 303
5.2.5 Conclusion and outlook . . . 304
5.2.6 Supplemental Materials: Cavity QED on Wannier-Stark states . . . 304
5.2.7 Supplemental Materials: Validity of spin model and homogeneous couplings . 308
5.2.8 Supplemental Materials: Analytic results of OAT model with time reversal . 314
5.3 Trade-offs between unitary and measurement induced spin squeezing in cavity QED 325
5.3.1 Introduction . . . 325
5.3.2 Model . . . 326
5.3.3 Analysis of spin squeezing . . . 329
5.3.4 Summary and conclusions . . . 334
5.3.5 Supplemental Materials: Effective evolution equation . . . 336
5.3.6 Supplemental Materials: Large N equations for first and second order correlators . . . 341
5.3.7 Supplemental Materials: Spin squeezing from second order correlators . . . 344
5.3.8 Supplemental Materials: Examples of experimental system . . . 350

6 Conclusion and outlook **355**

Bibliography **358**

Appendix

A Second order perturbation theory **384**

B Spherical tensor operators **387**

C Mathieu function **390**

D Phase space representation of bosons **392**

Tables

Table

2.1 Analytic solutions of 1D optical lattice 17

3.1 ^{87}Sr s-wave and p-wave scattering lengths 108

4.1 Summary of approximations in theory model and the required parameter regimes . . 223

4.2 Summary of conditions for different atom species 250

5.1 Squeezing in experiments 354

Figures

Figure

2.1 Magic wavelength for Sr clock transition 15

2.2 Band structure and Wannier functions 17

2.3 Wannier-Stark states 23

2.4 Examples of Husimi Q-representation and Wigner representation 47

2.5 Schematic of photon-mediated interactions 57

2.6 Schematic of homodyne detection 64

2.7 Spin squeezing and quantum Fisher information under one-axis twisting 77

3.1 Schematic of the Wannier-Stark optical lattice clock 81

3.2 Engineering s-wave and p-wave interactions via Wannier-Stark states 85

3.3 Density shift cancellation in experiment 86

3.4 Dynamical phase transition in Wannier-Stark sidebands 89

3.5 Spin model parameters for Wannier-Stark optical lattice clock 99

3.6 Supplemental plot of dynamical phase transition in Wannier-Stark sidebands 103

3.7 Radial temperature fit 105

3.8 Many-body decoherence in Wannier-Stark sidebands 107

3.9 Experimental setup and interaction model 113

3.10 Coherence time measurement 116

3.11 Weak transverse confinement regime 118

3.12 Observing superexchange interactions . . . 120
3.13 Controlling superexchange interactions . . . 123
3.14 Impact of spin wave growth on coherence times in the 1D limit . . . 134
3.15 Schematic of an optical lattice clock (OLC) embedded in the curved spacetime . . . 137
3.16 Tuning mass-energy equivalence via dressed states . . . 141
3.17 Interplay between photon-mediated interactions and redshift . . . 144
3.18 Interplay between entanglement and redshift . . . 145
3.19 Schematic of optical lattice clock and relativistic corrections . . . 153
3.20 Schematic of the dressing protocol . . . 158
3.21 Interplay between contact interactions and redshift . . . 163
3.22 Evolution of total spin . . . 164
3.23 Scaling of synchronization time . . . 170
3.24 Comparison between numerical simulations and analytic results . . . 173

4.1 Simulation of XXZ spin model using sideband transition in trapped bosonic gases . . . 177
4.2 Dynamical phase transition in LMG model . . . 179
4.3 Dynamical phase transition using sideband transition in trapped bosonic gases . . . 182
4.4 Mean-field dynamics of XXZ model in harmonic trap . . . 183
4.5 Setup of Rb sideband experiment . . . 185
4.6 Calibration of Rb mean density . . . 187
4.7 Theory-experimental comparison of red sideband Rabi lineshapes . . . 188
4.8 Supplemental plot of dynamical phase transition in LMG model . . . 194
4.9 Spin squeezing via motional sidebands . . . 197
4.10 Finite-size scaling of optimal spin squeezing in XXZ model achieved by motional sidebands . . . 197
4.11 Effective ground state dynamics in a multilevel cavity QED system . . . 201
4.12 Pair production dynamics in a synthetic 4-level ladder . . . 205

4.13 Chiral transport in a synthetic 6-level ladder 206
4.14 Correlation spreading in a synthetic 10-level ladder 208
4.15 Numerical benchmarking of adiabatic elimination of atomic excited states 212
4.16 Perturbative ground-ground processes 214
4.17 Dynamical phase boundary in the six-level system 219
4.18 Finite size scaling of DPT 222
4.19 Effect of a finite magnetic field 224
4.20 Setup for Bloch oscillations in cavity QED systems 228
4.21 Dynamical phase transition in the deep lattice regime 231
4.22 Cavity-mediated amplification of Bloch oscillations in the shallow lattice regime . . . 234
4.23 The coupling coefficient $J_{m,n}$ for ^{87}Rb atoms 238
4.24 Benchmarks of the atom-cavity Hamiltonian with the effective atom-only Hamiltonian 241
4.25 Number of roots for the effective potential 245
4.26 Different schemes of single-particle Bloch oscillation 248
4.27 Experimental considerations 251
4.28 Engineering BCS dynamical phases 255
4.29 Phase I to phase II transition 258
4.30 Phase II to phase III transition 261
4.31 Scan across three dynamical phases 265
4.32 Experimental configuration 270
4.33 Dynamical phase diagram 270
4.34 Alternative approach for phase III 273
4.35 Collective scaling in damped phase II oscillations 276
4.36 Dynamical phase diagrams 281
4.37 Experimental control of dynamical phases 283
4.38 Relation between oscillation frequency and averaged order parameter in Higgs oscillations 285

4.39 Frequency dip as a signature of the phase II to phase III transition 287

4.40 Axial motion effects 292

5.1 Schematic of cavity QED interferometer using Wannier-Stark states 297

5.2 Engineering homogeneous atom-cavity couplings via Wannier-Stark states 299

5.3 Schematic of the quantum-enhanced gravimetry using Wannier-Stark states 301

5.4 Sensitivity of Wannier-Stark interferometer 304

5.5 Corrections due to radial modes 310

5.6 Validity check for theoretical approximations 312

5.7 Schematic for spin squeezing in cavity QED systems 326

5.8 QND squeezing 331

5.9 OAT Squeezing and comparison 332

5.10 Summary of results 335

5.11 OAT squeezing and state area 350

Chapter 1

Introduction

1.1 Quantum technology in modern science

> Nature isn't classical, dammit, and if you want to make a simulation of nature, you'd better make it quantum mechanical, and by golly it's a wonderful problem, because it doesn't look so easy.
>
> —— Richard P. Feynman

Forty years ago, Richard Feynman delivered his seminal lecture "*Simulating Physics with Computers*" [1], in which he proposed the idea of harnessing quantum physics to build a more powerful computer and perform large scale simulation of nature. Richard Feynman's vision stemmed from the unique properties of quantum mechanics, such as superposition and entanglement. Superposition means particles can exist in multiple states simultaneously until measured, and entanglement means the quantum state of each particle cannot be described independently of the state of other particles, even when separating them by a large distance. Taking advantage of these properties, one can in principle handle certain types of problems with a substantial improvement compared to using the classical counterparts. Over the pass few decades, we have seen an explosion of theoretical and experimental advances in this direction. The key efforts can be divided into two aspects that are closely related with each other: 1) Deepening the understanding and improving the controllability of quantum many-body systems, which should enable physical realizations of such a quantum device; 2) Developing practical applications for controllable quantum systems including computation, simulation, metrology, communication, as well as fundamental studies of the mystery of the universe [2–9].

While quantum technology holds immense promise, several key challenges must be addressed to realize its full potential. Quantum systems are extremely sensitive to their environment, and inevitable decoherence effects can easily destroy the delicate entangled states required for quantum advantages. The pursue of a large-scale quantum device to surpass its classical counterpart also leads to significant challenges in scalability and complexity. In light of these challenges, further theoretical understanding of the complex many-body phenomena present in these systems can shed light on new experimental designs to suppress and mitigate undesired effects. Additionally, the theoretical exploration of robust quantum protocols against experimental noise would be very helpful for near-term application of quantum technology. In this thesis, we mainly focus on the problems related to quantum simulation and quantum metrology, so we provide a general overview of these two concepts below.

Quantum simulation [2, 3] aims to utilize a highly controllable quantum system as a proxy to explore other quantum systems that are difficult to probe directly or calculate numerically. For example, strongly correlated quantum systems feature exponential growth of the relevant Hilbert space dimension with system size, which is beyond the reach of classical simulation algorithms. The complexity in real physical systems in the field of condensed matter or high energy might also prevent a clean observation for certain types of phenomena. There is also great interest for exploring novel many-body phenomena that has never been seen in nature, such as certain classes of non-equilibrium quantum many-body dynamics. In all these directions, quantum simulation is believed to exhibit a form of quantum advantage compared to classical approaches, and has started to play a significant role for enriching our physical understandings in recent years. There are different approaches for the realization of quantum simulation, including highly tunable analog simulators that naturally feature the same Hamiltonian as the physics problem of interest, or fully programmable digital simulators that produce Hamiltonian evolution via quantum circuits. The former approach is straightforward to implement experimentally, while it is restricted to specific types of models in a given experimental platform and the relevant error sources in analog simulators are not completely understood. The latter approach can be applied to a wide range of many-body

phenomena, while it is limited by the system size and the circuit depth in the current generation of digital simulators. In this thesis, we describe our efforts in broadening the range of physics problems one can target in certain types of analog simulators, in the collaboration with experiment efforts towards the implementation of the desired protocols.

Quantum metrology [6, 7] aims to develop quantum enhanced techniques to improve the measurement precision of physical quantities to an unprecedented level and surpass the precision of classical counterparts. This is one of the most promising applications of quantum science in the near term. At the heart of quantum metrology is the use of quantum entanglement, which allows for correlations between particles that are not possible classically, leading to a reduction of measurement uncertainty below quantum projection noise. Quantum enhancement in state-of-the-art practical sensors is already demonstrated in gravitational wave detection in LIGO and Virgo [10, 11], as well as dark matter search in optomechanical systems [12,13]. Proof of principle experiments have also been achieved in optical clocks and atom interferometers [14–16]. However, maintaining quantum coherence and entanglement over long periods, which is crucial for a precise measurement, still remains technically challenging. The utility of quantum metrology under certain types of environmental noise might be limited [17]. In this thesis, we describe our efforts in developing optimal quantum enhanced protocols robust against decoherence effects, as well as furthering the understanding of experimental noise sources for improved design of experiments.

1.2 AMO toolboxes for modern science

> When we get to the very, very small world — say circuits of seven atoms — we have a lot of new things that would happen that represent completely new opportunities for design. Atoms on a small scale behave like nothing on a large scale, for they satisfy the laws of quantum mechanics.
>
> —— Richard P. Feynman

In Richard Feynman's famous lecture "*There's Plenty of Room at the Bottom*" [18], he described the prospect of great opportunities for manipulating matter down to the level of individual atoms, which have significant influence on a wide range of fields in modern science. In the field of

atomic, molecular, and optical (AMO) physics, the laser cooling and trapping techniques [19] allows for precise control of the quantum properties for individual or small groups of atoms at ultracold temperatures. These highly controllable AMO systems has already become a toolbox not only for practical applications of quantum technologies but also for the fundamental understanding of many-body physics. Here we provide a general overview of the two leading AMO platforms studied in this thesis: optical lattice clocks and cavity quantum electrodynamics (QED) systems.

1.2.1 Optical lattice clocks

Timekeeping has been one of the most important tasks since the beginning of civilization [20, 21]. The devices used for timekeeping, known as clocks, are oscillators that vibrate at a particular frequency ν. The unit of time can be defined as the oscillation period, and timekeeping is done by counting the number of oscillations. Since 1967, the SI unit of time, the second, has been defined as the duration of 9192631770 oscillations in the unperturbed ground state hyperfine transition of the ^{133}Cs atom [22]. The advantage of atomic clocks is ensured by the nature of quantum mechanics, since all atoms (or ions) of the same element and isotope are identical and thus feature exactly the same transitions between internal states.

Optical clocks are a new generation of atomic clocks built by replacing the microwave transition ($\nu \sim 9.2$ GHz) between hyperfine levels by an optical transition ($\nu \sim 10^2 - 10^3$ THz) between electronic levels with ultranarrow linewidth ($\Delta\nu \sim 1 - 10$ mHz). The enhancement of quality factor $Q = \nu/\Delta\nu$ can in principle lead to an improvement of clock precision. There are mainly two different designs of optical clocks: 1) Optical lattice clocks, based on alkaline earth atoms (e.g. Sr, Yb), i.e. atoms with two valence electrons, trapped in an optical lattice, i.e. a periodic standing wave potential generated by laser beams; 2) Ion clocks, based on ions with two valence electrons (e.g. Al^+), trapped in an ion trap. These atoms (or ions) feature an ultranarrow optical transition between $^1S_0$ and $^3P_0$ states.

Here we mainly focus on optical lattice clocks. Up to date (June 2024), the lowest frequency instability of optical clocks has reached 7.6×10^{-21} [23], and the lowest systematic uncertainty is

now at 8.1×10^{-19} [24], both in fractional frequency unit. These results have been achieved at JILA in the so called Wannier-Stark 1D optical lattice clock [23, 25], where atoms are trapped in a shallow lattice along the direction of gravity. The tilt on the optical lattice generated by gravity can not only lead to localized atomic wave functions known as Wannier-Stark states, but also enhances the tunability of the system significantly. In this thesis, we describe theoretical efforts on modeling the Wannier-Stark optical lattice clock and our understanding of the suppression of dominant systematic effects.

One of the key systematic effects in optical clocks is the so-called density shift, i.e. frequency shift due to atomic collisions. Since packing more atoms is the easiest way to improve the frequency stability in a given system, the density shift proportional to atom number N and therefore is an inevitable process when scaling up the clock. Note that atomic collisions at ultralow temperature can be understood based on a partial wave expansion, and the leading contributions includes s-wave interactions (spatially symmetric) and p-wave interactions (spatially antisymmetric). In order to suppress the density shift, researchers are focusing on fermionic alkaline earth atoms (e.g. ^{87}Sr, ^{171}Yb), since s-wave contributions are forbidden for identical fermionic particles (here we mean particles within the same lattice site) due to quantum statistics. However, even the weak on-site p-wave interactions or off-site s-wave interactions in the 1D lattice setting can lead to non-negligible effects on the clock operation. We propose the use of Wannier-Stark states to tune the relative strength of s-wave and p-wave interactions, leading to a cancellation of density shift at a magic lattice depth.

Apart from timekeeping applications, optical lattice clocks provide exciting new opportunities to explore the frontiers of quantum simulation, quantum metrology and fundamental physics. For example, the long atomic coherence time and the high spectroscopic resolution in optical lattice clocks can lead to new probing techniques for the iconic Fermi Hubbard model relevant for high T_c superconductors. Another example is the gravitational redshift, which is a general relativistic effect describing time dilation due to the earth's gravity. The resolution of the gravitational redshift within a single atomic ensemble has already been achieved at JILA [23]. This observation is a push

forward to witness the simultaneous interplay between general relativity and quantum mechanics. My PhD research includes theoretical analysis in all these directions for optical lattice clocks.

1.2.2 Cavity QED systems

Understanding and controlling the quantum nature of light-matter interactions is a key pursuit of modern quantum science. One of the most important experimental platforms in this pursuit is the so-called cavity QED system [26–28]. The term "cavity" refers to a system that confines electromagnetic (EM) fields using highly reflective mirrors, and "QED" emphasizes the quantum nature of interaction between atoms and photons, i.e. quantized EM fields, inside the cavity. Cavity QED systems have long been a central paradigm for the study of open quantum systems and a resource to illuminate the fundamental aspects of coherence and decoherence in quantum mechanics. At the heart of the physics is the interplay between coherent atom-photon couplings and dissipative effects such as cavity decay and atomic spontaneous emission. The early stage developments of this field were recognized by the 2012 Nobel Prize for physics [29].

In recent years, cavity QED systems have become a novel platform to manipulate atom-atom interactions. Neutral atoms typically interact via atomic collisions (short-range van der Waals interactions), but inside a cavity, atoms can have long-range or all-to-all interactions via exchanging virtual cavity photons. One example of photon-mediated interactions is the so-called spin exchange interaction, where an excited state atom emits a photon into the cavity mode and transitions into the ground state, and the same photon is reabsorbed by a ground state atom that transitions into the excited state. Such type of interactions are very suitable for simulating long-range interacting models in condensed matter physics, as well as for the implementation of synthetic quantum materials never seen in nature. An important part of my PhD research was dedicated to explore the mapping between spin exchange interactions and the Bardeen–Cooper–Schrieffer (BCS) model in condensed matter physics. I collaborated with experimentalists to observe a dynamical phase with persistent oscillations of the BCS order parameter for the first time. We also extended our exploration of spin exchange interactions to the case when the excited and ground manifold

contain multiple hyperfine levels.

Apart from near resonant couplings to atomic excited states, another focus was on the dispersive atom-light couplings in the atomic ground manifold. Based on the dispersive coupling, the frequency of cavity resonance is shifted depending on the atomic magnetization, and its feedback to atom dynamics can be interpreted as an infinite range Ising interaction known as one-axis twisting (OAT), an iconic model for generating spin squeezed states [30]. On the other hand, dispersive coupling allows for quantum non-demolition (QND) measurement of atomic magnetization via continuously monitoring the light leaking out of the cavity [7]. Without destroying the atomic state, such type of measurement can gradually decrease the quantum noise along the magnetization axis, leading to spin squeezing. Spin squeezing [31] is a type of quantum entanglement with a reduction of spin variance in some directions (increasing variance in other directions), which is a powerful and robust technique to enhance measurement precision compared to the classical counterparts. These techniques can also combine with practical sensors such as optical lattice clocks and atom interferometers to achieve quantum enhanced measurements. In this thesis, we discuss the optimal protocol for spin squeezing generation by comparing QND and OAT protocols, and also develop quantum enhanced protocols for lattice-based atom interferometers with Wannier-Stark states.

1.3 Outline of this thesis

In Chapter 2, we provide an overview of the relevant theoretical background for this thesis, including optical lattices, contact interactions, spin systems, photon-mediated interaction and measurements, as well as metrological concepts.

In Chapter 3, we discuss theoretical protocols and experimental collaborations on improving optical lattice clocks via Hamiltonian engineering, as well as the new possibilities on exploring the interplay between GR effects and many-body physics in optical clocks. This chapter is based on the following publications [25, 32, 33]:

- Alexander Aeppli*, **Anjun Chu***, Tobias Bothwell*, Colin J. Kennedy, Dhruv Kedar, Peiru

He, Ana Maria Rey, Jun Ye, *Hamiltonian engineering of spin-orbit coupled fermions in a Wannier-Stark optical lattice clock*, Science Advances 8, eadc9242 (2022)

- William R. Milner, Stefan Lannig, Mikhail Mamaev, Lingfeng Yan, **Anjun Chu**, Ben Lewis, Max N. Frankel, Ross B. Hutson, Ana Maria Rey, Jun Ye, *Coherent evolution of superexchange interaction in seconds long optical clock spectroscopy*, arXiv:2402.13398 (2024)

- **Anjun Chu**, Victor J. Martínez-Lahuerta, Maya Miklos, Kyungtae Kim, Peter Zoller, Klemens Hammerer, Jun Ye, and Ana Maria Rey, *Exploring the interplay between mass-energy equivalence, interactions and entanglement in an optical lattice clock*, arXiv:2406.03804 (2024)

In Chapter 4, we discuss theoretical protocols and experimental collaborations on emergent collective behaviors and dynamical phases in interacting arrays, such as cavity QED systems and trapped bosonic gases. This chapter is based on the following publications [34–37]:

- **Anjun Chu**, Johannes Will, Jan Arlt, Carsten Klempt, Ana Maria Rey, *Simulation of XXZ spin models using sideband transitions in trapped bosonic gases*, Physical Review Letters 125, 240504 (2020)

- **Anjun Chu**, Asier Piñeiro Orioli, Diego Barberena, James K. Thompson, Ana Maria Rey, *Photon-mediated correlated hopping in a synthetic ladder*, Physical Review Research 5, L022034 (2023)

- Haoqing Zhang, **Anjun Chu**, Chengyi Luo, James K. Thompson, Ana Maria Rey, *Control and amplification of Bloch oscillations via photon-mediated interactions*, Physical Review Research 5, L032039 (2023)

- Dylan J. Young*, **Anjun Chu***, Eric Yilun Song, Diego Barberena, David Wellnitz, Zhijing Niu, Vera M. Schäfer, Robert J. Lewis-Swan, Ana Maria Rey, James K. Thompson,

Observing dynamical phases of BCS superconductors in a cavity QED simulator, Nature 625, 679 (2024)

In Chapter 5, we discuss theoretical protocols in entanglement generation via photon-mediated interactions and measurements. This chapter is based on the following publications [38, 39]:

- **Anjun Chu**, Peiru He, James K. Thompson, Ana Maria Rey, *Quantum enhanced cavity QED interferometer with partially delocalized atoms in lattices*, Physical Review Letters 127, 210401 (2021)

- Diego Barberena, **Anjun Chu**, James K. Thompson, Ana Maria Rey, *Trade-offs between unitary and measurement induced spin squeezing in cavity QED*, Physical Review Research, in press (2024) [arXiv:2309.15353]

In Chapter 6, we provide a summary of the thesis, and discuss on-going projects as well as possible future research directions.

For the sake of brevity and cohesion, we don't include the following publications [40–43] in the thesis, although they are equally important parts of my PhD work.

- Bhuvanesh Sundar, Diego Barberena, Asier Piñeiro Orioli, **Anjun Chu**, James K. Thompson, Ana Maria Rey, Robert J. Lewis-Swan, *Bosonic pair production and squeezing for optical phase measurements in long-lived dipoles coupled to a cavity*, Physical Review Letters 130, 113202 (2023)

- Chengyi Luo, Haoqing Zhang, Vanessa P. W. Koh, John D. Wilson, **Anjun Chu**, Murray J. Holland, Ana Maria Rey, James K. Thompson, *Momentum-exchange interactions in a Bragg atom interferometer suppress Doppler dephasing*, Science 384, 551 (2024)

- Chengyi Luo, Haoqing Zhang, **Anjun Chu**, Chitose Maruko, Ana Maria Rey, James K. Thompson, *Hamiltonian engineering of collective XYZ spin models in an optical cavity: From one-axis twisting to two-axis counter twisting models*, arXiv:2402.19429 (2024)

- John D. Wilson, Jarrod T. Reilly, Haoqing Zhang, Chengyi Luo, **Anjun Chu**, James K. Thompson, Ana Maria Rey, Murray J. Holland, *Entangled matter-waves for quantum enhanced sensing*, arXiv:2406.13616 (2024)

Chapter 2

Theoretical background

2.1 Optical lattices

In this section, we introduce the concept of an optical lattice. We start from the AC Stark effect, which is the key physical mechanism for engineering optical lattice. Then we focus on the single-particle Hamiltonian and its wave functions within a 1D geometry, including the definition of the Bloch function, the Wannier function, as well as the tight-binding Hamiltonian. After that, we analyze the role of radial modes in a 1D lattice. Finally, we discuss the effects induced by an additional linear tilt applied to the optical lattice, which can lead to Bloch oscillation and Wannier-Stark localization.

2.1.1 AC Stark effect

We consider the interaction of an atom with a classical light field $\mathbf{E}$,

$$\mathbf{E}(\mathbf{R}) = \frac{1}{2}E_0(\mathbf{R})\vec{\varepsilon}e^{-i\omega t} + \text{c.c.}, \tag{2.1}$$

where $\vec{\varepsilon} = \cos(\theta)\vec{\varepsilon}_1 + i\sin(\theta)\vec{\varepsilon}_2$ labels the direction of polarization, with $\vec{\varepsilon}_1$ and $\vec{\varepsilon}_2$ orthogonal unit vectors. Here θ is the ellipticity angle, and we define the light propagation direction as $\vec{k} = \vec{\varepsilon}_1 \times \vec{\varepsilon}_2$. Under electric dipole approximation, the atom-light coupling is described by the following Hamiltonian,

$$\hat{H}_{AL} = -\hat{\mathbf{d}} \cdot \mathbf{E}, \tag{2.2}$$

where $\hat{\mathbf{d}}$ is the electric dipole moment.

We first discuss the simplest case of a two-level atom. The transition frequency between ground ($|g\rangle$) and excited ($|e\rangle$) states is given by $\omega_0 = \omega_e - \omega_g$. Assuming the light field is far from resonance with the atomic transition, the effective Hamiltonian for the $|g\rangle$ state can be estimated based on second order perturbation theory (see Appendix A),

$$\hat{H}_{AL,\text{eff}} = \Big(-\frac{1}{4}\alpha_g(\omega)|E_0(\mathbf{R})|^2 \Big)|g\rangle\langle g|, \tag{2.3}$$

where $\alpha_g(\omega)$ is the electric dipole polarizability,

$$\alpha_g(\omega) = \frac{|\langle e|\hat{\mathbf{d}}\cdot\vec{\varepsilon}|g\rangle|^2}{\hbar(\omega_0-\omega)} + \frac{|\langle e|\hat{\mathbf{d}}\cdot\vec{\varepsilon}^*|g\rangle|^2}{\hbar(\omega_0+\omega)}. \tag{2.4}$$

Here we have included the contribution from both rotating ($\omega_0 - \omega$) and counter-rotating ($\omega_0 + \omega$) terms. Usually $\alpha_g(\omega)$ is dominated by the rotating term. In this case, when the light field is red detuned ($\omega < \omega_0$), we have $\alpha_g(\omega) > 0$, which means atoms are trapped in the intensity maximum points of the light field; When the light field is blue detuned ($\omega > \omega_0$), we have $\alpha_g(\omega) < 0$, which means atoms are trapped in the intensity minimum points. Optical lattices are used to trap atoms in a periodic structure of intensity extremum points, which is generated by interfering laser beams. For example, $E_0(\mathbf{R}) \propto \cos(k_L X)$ can lead to a 1D optical lattice along $\vec{X}$, with k_L the wave number of the lattice beam.

Now we generalize the discussion to the case when the atomic ground and excited states have angular momentum F and F_n respectively, where n is the index for excited states. We denote the transition frequency by $\omega_n = \omega_{e_n} - \omega_g$. For simplicity, we assume the quantization axis $\vec{z}$ is set by a strong external magnetic field, which implies the couplings between different Zeeman levels due to AC Stark effects are suppressed. Similar to Eq. (2.4), we get

$$\alpha_g(F, m_F; \omega) = \sum_n \sum_{ij} \langle F m_F|\hat{T}_{ij}(F_n)|F m_F\rangle \left(\frac{\varepsilon_i^* \varepsilon_j}{\hbar(\omega_n - \omega)} + \frac{\varepsilon_i \varepsilon_j^*}{\hbar(\omega_n + \omega)} \right). \tag{2.5}$$

Here, $\hat{T}_{ij}(F_n)$ is a rank-2 Cartesian tensor operator,

$$\hat{T}_{ij}(F_n) = \hat{d}_i \Big(\sum_{m_{F_n}} |F_n m_{F_n}\rangle\langle F_n m_{F_n}| \Big) \hat{d}_j, \tag{2.6}$$

which can be decomposed in terms of spherical tensors $\hat{T}_q^{(k)}(F_n)$, with the rank $k = 0, 1, 2$ indicating scalar, vector and tensor contributions, and $q = -k, -k+1 \cdots, k$ (see Appendix B). This generates the so-called scalar, vector and tensor shifts correspondingly. In the following, we sketch the key steps of the derivation (see Ref. [44]).

Based on the Wigner-Eckart theorem (see Eq. (B.3)), the expectation value of a spherical tensor in angular momentum basis is proportional to the corresponding Clebsch-Gordan coefficients. As a result, only the spherical tensors $\hat{T}_0^{(0)}(F_n)$, $\hat{T}_0^{(1)}(F_n)$, $\hat{T}_0^{(2)}(F_n)$ have non-zero matrix element,

$$\langle Fm_F|\hat{T}_0^{(0)}|Fm_F\rangle \propto \langle Fm_F; 00|Fm_F\rangle = 1, \tag{2.7}$$

$$\langle Fm_F|\hat{T}_1^{(0)}|Fm_F\rangle \propto \langle Fm_F; 10|Fm_F\rangle = \frac{m_F}{\sqrt{F(F+1)}}, \tag{2.8}$$

$$\langle Fm_F|\hat{T}_0^{(2)}|Fm_F\rangle \propto \langle Fm_F; 20|Fm_F\rangle = \frac{3m_F^2 - F(F+1)}{\sqrt{F(F+1)(2F-1)(2F+3)}}, \tag{2.9}$$

where $\langle jm; kq|j'm'\rangle$ are Clebsch-Gordan coefficients. In terms of the spherical tensors, we have

$$\begin{aligned}\alpha_g(F, m_F; \omega) = \sum_{nF'} &-\frac{1}{\sqrt{3}}\frac{2\omega_n\langle Fm_F|\hat{T}_0^{(0)}(F_n)|Fm_F\rangle}{\hbar(\omega_n^2 - \omega^2)} + \sqrt{2}\mathrm{Im}(\varepsilon_x^*\varepsilon_y)\frac{2\omega\langle Fm_F|\hat{T}_0^{(1)}(F_n)|Fm_F\rangle}{\hbar(\omega_n^2 - \omega^2)} \\ &+ \frac{3\varepsilon_z^*\varepsilon_z - 1}{\sqrt{6}}\frac{2\omega_n\langle Fm_F|\hat{T}_2^{(0)}(F_n)|Fm_F\rangle}{\hbar(\omega_n^2 - \omega^2)}.\end{aligned} \tag{2.10}$$

One can further rewrite Eq. (2.10) in terms of reduced dipole matrix elements $\langle F||\hat{\mathbf{d}}||F_n\rangle$ (see Appendix B). Finally, we get

$$\alpha_g(F, m_F; \omega) = \alpha_g^s(F; \omega) + \alpha_g^v(F; \omega)\sin(2\theta)k_z\frac{m_F}{F} + \alpha_g^t(F; \omega)\frac{3|\varepsilon_z|^2 - 1}{2}\frac{3m_F^2 - F(F+1)}{F(2F-1)}. \tag{2.11}$$

Here, $\alpha_g^s(F; \omega)$ is the scalar polarizability,

$$\alpha_g^s(F; \omega) = \sum_n \frac{2}{3(2F+1)}\frac{\omega_n|\langle F||\hat{\mathbf{d}}||F_n\rangle|^2}{\hbar(\omega_n^2 - \omega^2)}, \tag{2.12}$$

$\alpha_g^v(F; \omega)$ is the vector polarizability,

$$\alpha_g^v(F; \omega) = -\sum_n (-1)^{F+F_n}\sqrt{\frac{6F}{(F+1)(2F+1)}}\begin{Bmatrix} 1 & 1 & 1 \\ F & F & F_n \end{Bmatrix}\frac{\omega|\langle F||\hat{\mathbf{d}}||F_n\rangle|^2}{\hbar(\omega_n^2 - \omega^2)}, \tag{2.13}$$

and $\alpha_g^t(F;\omega)$ is the tensor polarizability,

$$\alpha_g^t(F;\omega) = \sum_n (-1)^{F+F_n} \sqrt{\frac{40F(2F-1)}{3(F+1)(2F+1)(2F+3)}} \begin{Bmatrix} 1 & 1 & 2 \\ F & F & F_n \end{Bmatrix} \frac{\omega_n |\langle F||\hat{\mathbf{d}}||F_n\rangle|^2}{\hbar(\omega_n^2-\omega^2)}, \tag{2.14}$$

where the curly bracket marks the Wigner-6j symbol [45]. Note that the scalar shift is uniform for all m_F, the vector shift is similar to a magnetic field acting linearly on m_F, and the tensor shift is acting quadratically on m_F. The vector shift vanishes for linear polarized light. Due to the factor $(-1)^{F+F_n}$ in the summation, both vector and tensor shifts are usually smaller compared to the scalar shift.

The derivation above can be directly generalized to the case when the couplings between Zeeman levels are not negligible, which leads to the following effective Hamiltonian in the ground manifold [44],

$$\hat{H}_{AL,\text{eff}} = -\frac{1}{4}|E_0(\mathbf{R})|^2 \left(\alpha_g^s(F;\omega)\hat{I} - i\alpha_g^v(F;\omega)\frac{(\vec{\varepsilon}^* \times \vec{\varepsilon})\cdot \hat{\mathbf{F}}}{F} + \alpha_g^t(F;\omega)\frac{3\{\vec{\varepsilon}^*\cdot\hat{\mathbf{F}}, \vec{\varepsilon}\cdot\hat{\mathbf{F}}\} - 2\hat{\mathbf{F}}^2}{2F(2F-1)} \right), \tag{2.15}$$

where $\hat{I}$ is the identity matrix, $\hat{\mathbf{F}}$ are the spin-F operators, and $\{\hat{A},\hat{B}\} = \hat{A}\hat{B} + \hat{B}\hat{A}$. In the case of vanishing external magnetic field, the vector or tensor contributions also play the role of defining the quantization axis (choice of spin basis to make the Hamiltonian diagonal). When the vector contribution dominates, the quantization axis is along $\vec{k}$; When the tensor contribution dominates (assuming linear polarization), the quantization axis is along $\vec{\varepsilon}$.

In an optical lattice clock, we consider the clock transition between $^1S_0$ $|Fm_F\rangle$ and $^3P_0$ $|F'm_{F'}\rangle$ states. The magic wavelength lattice is defined at the wavelength at which the two clock states share the same lattice potential, ensuring by the following condition of electric dipole polarizability,

$$\alpha_{^1S_0}(F, m_F;\omega) = \alpha_{^3P_0}(F', m_{F'};\omega). \tag{2.16}$$

For Sr atoms, one can obtain a magic wavelength lattice near 813 nm (red detuned) or 390 nm (blue detuned), as shown in Fig. 2.1. The value of reduced dipole matrix elements and transition frequencies are listed in Ref. [24, 46]. Since both $^1S_0$ and $^3P_0$ states have $J = 0$, vector shift and

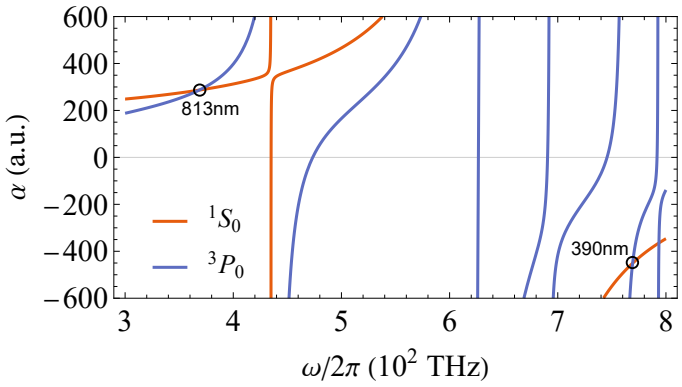

Figure 2.1: Scalar polarizability of $^1S_0$ and $^3P_0$ states of Sr atom. The calculation is based on the reduced dipole matrix elements and transition frequencies listed in Ref. [24, 46]. The atom unit of polarizability is given by $4\pi\epsilon_0 a_0^3$, where ϵ_0 is the vacuum permittivity, and a_0 is the Bohr radius. The intersections of the two polarizability curves (marked by black circles) indicate the magic wavelengths.

tensor shift are highly suppressed [47]. The magic wavelength lattice is a key technique to minimize the frequency shift of the clock transition induced by the lattice beams.

2.1.2 Band structure of 1D lattice

We consider the single-particle physics in an optical lattice described by the trapping potential

$$V(X) = V_0 \sin^2(k_L X), \tag{2.17}$$

where V_0 is the lattice depth, $k_L = 2\pi/\lambda_L$ is the wave number of the lattice beam, with λ_L the lattice wavelength. The lattice spacing is given by $a_L = \lambda_L/2$. So the single-particle Hamiltonian for atoms trapped in this optical lattice is given by the following second-quantized form,

$$\hat{H}_0 = \int dX \hat{\psi}^\dagger(X) \left[\frac{\hat{P}^2}{2M} + V(X) \right] \hat{\psi}(X), \tag{2.18}$$

where $\hat{\psi}(X)$ is the annihilation field operator for an atom at position X.

Notice that $V(X)$ is a periodic potential with $V(X + a_L) = V(X)$. Based on Bloch's theorem, H_0 has a set of eigenstates (known as Bloch functions) $\phi_{nk}(X)$ with eigenvalues $E_n(k)$, where n is the band index and k is the quasi-momentum restricted in the first Brillouin zone, $k \in [-k_L, k_L)$.

The Bloch functions satisfy $\phi_{nk}(X + a_L) = \mathrm{e}^{ika_L}\phi_{nk}(X)$. For $V(X)$ described by Eq. (2.17), it is possible to obtain analytic solutions for the Bloch functions using Mathieu functions [45]. The key idea is to rewrite the single-particle Hamiltonian in the following way,

$$\hat{H}_0 = \frac{\hat{P}^2}{2M} + V_0 \sin^2(k_L X) = \frac{\hat{P}^2}{2M} - \frac{V_0}{2}\cos(2k_L X) + \frac{V_0}{2}. \tag{2.19}$$

Without the constant term $V_0/2$, the time-independent Schrodigner equation $\hat{H}_0\phi = E\phi$ is equivalent to the Mathieu's differential equation as follow,

$$\frac{\mathrm{d}^2\phi}{\mathrm{d}\xi^2} + \Big(\lambda - 2q\cos(2\xi)\Big)\phi = 0, \tag{2.20}$$

where

$$\xi = k_L X \pm \frac{\pi}{2}, \quad \lambda = \frac{E}{E_R}, \quad q = \frac{V_0}{4E_R}, \quad E_R = \frac{\hbar^2 k_L^2}{2M}. \tag{2.21}$$

The eigenfunctions of Eq. (2.20) are denoted by Mathieu functions $\mathrm{me}_\nu(\xi, q)$ with eigenvalues $\lambda = \lambda_\nu(q)$, where ν can be any real numbers. Mathieu functions satisfy $\mathrm{me}_\nu(\xi+\pi, q) = \mathrm{e}^{i\pi\nu}\mathrm{me}_\nu(\xi, q)$. One can express me_ν using real-valued Mathieu functions ce_ν and se_ν (see Appendix C), and then map the Mathieu functions with $\nu \in [-n-1, -n)\cup[n, n+1)$ to Bloch functions with band index n, and the lowest band is denoted by $n = 0$. The results are summarized in Table. 2.1 and Fig. 2.2(a), where $a_n(q)$ and $b_n(q)$ are Mathieu characteristic values. Similar to plane waves, the normalization of the Bloch function $\phi_{nk}(X)$ is obtained by assuming a system with L lattice sites,

$$\int_0^{La_L} dX|\phi_{nk}(X)|^2 = 1. \tag{2.22}$$

We can define Wannier functions $w_{nj}(X)$ centered at lattice site j as a Fourier transform of Bloch functions $\phi_{nk}(X)$,

$$w_{nj}(X) = \frac{1}{\sqrt{L}}\sum_k \mathrm{e}^{-ikja_L}\phi_{nk}(X). \tag{2.23}$$

We focus on the Wannier functions at lattice site $j = 0$,

$$w_n(X) = \frac{1}{\sqrt{L}}\sum_k \phi_{nk}(X), \tag{2.24}$$

Table 2.1: Analytic solutions of 1D optical lattice

n	k	$\phi_{nk}(X) = (1/\sqrt{L\pi}) \times$	$E_n(k)/E_R =$
Even	0	$\sqrt{2}\,\mathrm{ce}_n(\xi, q)$	$a_n(q) + 2q$
Even	$-k_L$	$-\sqrt{2}i\,\mathrm{se}_{n+1}(\xi, q)$	$b_{n+1}(q) + 2q$
Even	$(0, k_L)$	$\mathrm{ce}_{n+k/k_L}(\xi, q) + i\,\mathrm{se}_{n+k/k_L}(\xi, q)$	$\lambda_{n+k/k_L}(q) + 2q$
Even	$(-k_L, 0)$	$\mathrm{ce}_{-n+k/k_L}(\xi, q) + i\,\mathrm{se}_{-n+k/k_L}(\xi, q)$	$\lambda_{-n+k/k_L}(q) + 2q$
Odd	0	$-\sqrt{2}i\,\mathrm{se}_{n+1}(\xi, q)$	$b_{n+1}(q) + 2q$
Odd	$-k_L$	$\sqrt{2}\,\mathrm{ce}_n(\xi, q)$	$a_n(q) + 2q$
Odd	$(0, k_L)$	$\mathrm{ce}_{-n-1+k/k_L}(\xi, q) + i\,\mathrm{se}_{-n-1+k/k_L}(\xi, q)$	$\lambda_{-n-1+k/k_L}(q) + 2q$
Odd	$(-k_L, 0)$	$\mathrm{ce}_{n+1+k/k_L}(\xi, q) + i\,\mathrm{se}_{n+1+k/k_L}(\xi, q)$	$\lambda_{n+1+k/k_L}(q) + 2q$

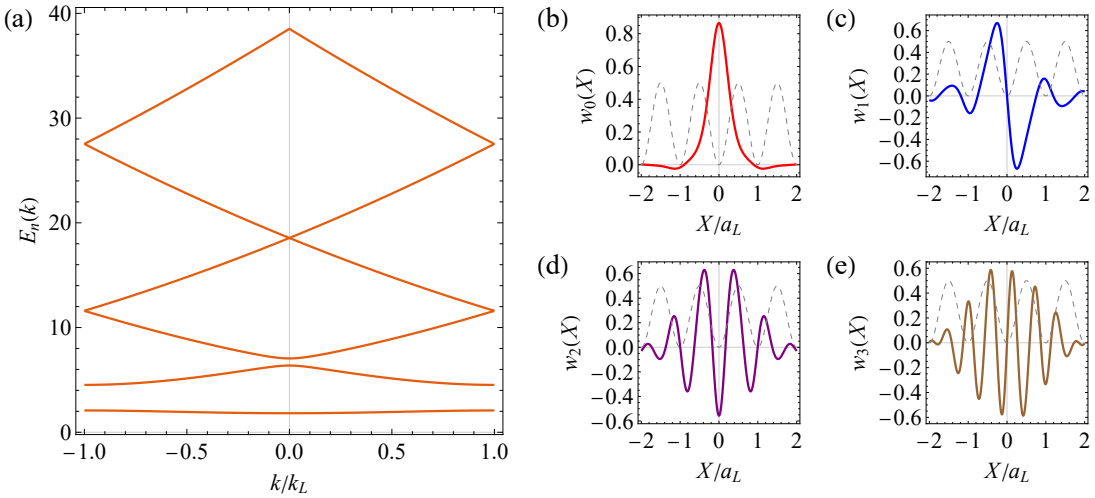

Figure 2.2: (a) Band structure for lattice depth $V_0 = 5E_R$. (b-e) Wannier functions for lattice depth $V_0 = 5E_R$ at (b) band $n = 0$; (c) band $n = 1$; (d) band $n = 2$; (e) band $n = 3$. The gray dashed line indicates the lattice potential.

since the other Wannier functions can be obtained via translation, $w_{nj}(X) = w_n(X - ja_L)$. However, the choice of Wannier function is still up to a gauge freedom in the definition of the Bloch function $\phi_{nk}(X)$,

$$\tilde{\phi}_{nk}(X) = e^{i\varphi_n(k)}\phi_{nk}(X). \tag{2.25}$$

A convenient gauge choice is the so-called maximally localized Wannier function [48], which leads to an exponentially localized wave function in a lattice site. For a general form of lattices, maximally localized Wannier function can only be obtained via numerical calculations. However, Ref. [49] showed that there is a simple gauge choice for 1D system as follows:

- If $\phi_{n,k=0}(0) \neq 0$ and $\phi_{n,k=-k_L}(0) \neq 0$, which is satisfied by even n in our case (see Table. 2.1), one can choose the phase $\varphi_n(k)$ such that $\phi_{n,k}(0)$ is real. Here we set

$$\varphi_n(k) = -\frac{ka_L}{2}. \tag{2.26}$$

  One can show that the Wannier function under this gauge choice is real and symmetric about $X = 0$ (see Fig. 2.2(b,d)).

- If $\phi_{n,k=0}(0) = 0$ and $\phi_{n,k=-k_L}(0) = 0$, which is satisfied by odd n in our case (see Table. 2.1), one can choose the phase $\varphi_n(k)$ such that $\phi_{n,k}(0)$ is purely imaginary. Here we set

$$\varphi_n(k) = \begin{cases} -\dfrac{ka_L}{2} - \dfrac{\pi}{2} & k \in [-k_L, 0) \\ -\dfrac{ka_L}{2} + \dfrac{\pi}{2} & k \in [0, k_L) \end{cases}. \tag{2.27}$$

  One can show that the Wannier function under this gauge choice is real and antisymmetric about $X = 0$ (see Fig. 2.2(c,e)).

We expand the field operator $\hat{\psi}(X)$ in terms of the maximally localized Wannier function,

$$\hat{\psi}(X) = \sum_{nj} \hat{c}_{nj} w_{nj}(X), \tag{2.28}$$

and the single-particle Hamiltonian becomes

$$\hat{H}_0 = -\sum_{njl} \tau_{n,l-j} \hat{c}^\dagger_{nj} \hat{c}_{nl}, \tag{2.29}$$

where

$$\tau_{n,l-j} = -\int dX w_{nj}^*(X)\left[\frac{\hat{P}^2}{2M} + V(X)\right] w_{nl}(X) = -\frac{1}{L}\sum_k \mathrm{e}^{-ik(l-j)a_L} E_n(k). \tag{2.30}$$

Note that $E_n(k) = E_n(-k)$, we have $\tau_{n,l-j} = \tau_{n,j-l}$ is a real number. Since $E_n(k)$ is a periodic function of k with period $2\pi/a_L$, we can interpret $\tau_{n,m}$ as the coefficients of the Fourier series of $E_n(k)$, which gives

$$E_n(k) = E_{n,0} - \sum_{m=1}^{\infty} 2\tau_{n,m}\cos(kma_L), \tag{2.31}$$

where $E_{n,0}$ is the average energy of band n,

$$E_{n,0} = \frac{1}{L}\sum_k E_n(k). \tag{2.32}$$

In the case where the Wannier functions are localized in a single lattice site, then we can only consider the nearest-neighbor tunneling terms, $\tau_n \equiv \tau_{n,1}$. In this situation we get the so-called tight-binding Hamiltonian,

$$\hat{H}_{\mathrm{TB}} = \sum_{nj} E_{n,0}\hat{c}_{nj}^\dagger \hat{c}_{nj} - \sum_{nj}\tau_n(\hat{c}_{n,j+1}^\dagger \hat{c}_{nj} + \mathrm{H.c.}). \tag{2.33}$$

Based on the properties of Mathieu functions (see Appendix C), we can provide an estimation of $E_{n,0}$ and τ_n in the tight-binding limit ($V_0/E_R \gg 1$). For the average band energy, we have

$$\frac{E_{n,0}}{E_R} \approx (2n+1)\sqrt{\frac{V_0}{E_R}} - \frac{2n^2+2n+1}{4}, \tag{2.34}$$

and the band gap is given by

$$\frac{\Delta E_n}{E_R} = \frac{E_{n+1,0} - E_{n,0}}{E_R} = 2\sqrt{\frac{V_0}{E_R}} - (n+1). \tag{2.35}$$

For the nearest-neighbor tunneling rate, one can truncate Eq. (2.31) to $m = 1$, which gives

$$\tau_n = \frac{E_n(k=-k_L) - E_n(k=0)}{4}. \tag{2.36}$$

This formula relates the nearest-neighbor tunneling rate to the width of the energy band. For the ground band $n = 0$, we have

$$\frac{\tau_0}{E_R} = \frac{b_1(q) - a_0(q)}{4} \approx \frac{4}{\sqrt{\pi}}\left(\frac{V_0}{E_R}\right)^{3/4}\exp\left[-2\sqrt{\frac{V_0}{E_R}}\right], \tag{2.37}$$

For the first excited band $n = 1$, we have

$$\frac{\tau_1}{E_R} = -\frac{b_2(q) - a_1(q)}{4} \approx -\frac{32}{\sqrt{\pi}}\left(\frac{V_0}{E_R}\right)^{5/4} \exp\left[-2\sqrt{\frac{V_0}{E_R}}\right]. \tag{2.38}$$

2.1.3 Effects of radial modes in a 1D lattice

In the previous subsection, we provide an exact solution of the energy spectrum and single-particle wave functions in a 1D optical lattice. In the tight-binding limit, we notice that the average band energy (see Eq. (2.34)) is similar to the one of a nonlinear harmonic oscillator. So we can approximate the lattice potential for each site as a harmonic potential plus extra correction terms. This approach allows us to go beyond the pure 1D regime and include the effects of radial modes in a 1D optical lattice.

In experiments, a 1D optical lattice is typically engineered by a pair of counter-propagating Gaussian beams, and described by the following trapping potential,

$$V(\mathbf{R}) = V_0 - V_0 \exp\left(-\frac{2r^2}{w_0^2}\right)\cos^2(k_L Z), \tag{2.39}$$

where w_0 is the beam waist, and $r^2 = X^2 + Y^2$. Notice that $V(\mathbf{R})$ is a non-separable potential, which couples the axial degrees of freedom Z and the radial degrees of freedom r. If one expands the potential near the lattice site at $Z = 0$ to the fourth order of Z and the second order of r (assuming the radial trapping is relatively weak and higher order terms can be ignored), we have

$$V(\mathbf{R}) \approx V_{\text{harm}}(\mathbf{R}) + V_{\text{corr}}(\mathbf{R}), \tag{2.40}$$

where $V_{\text{harm}}(\mathbf{R})$ is a harmonic potential,

$$V_{\text{harm}}(\mathbf{R}) = V_0 k_L^2 Z^2 + \frac{2V_0}{w_0^2} r^2 = \frac{1}{2}M\omega_Z^2 Z^2 + \frac{1}{2}M\omega_r^2 r^2. \tag{2.41}$$

Here, $\omega_Z = \sqrt{4V_0 E_R}/\hbar$ is the axial trapping frequency, and $\omega_r = \sqrt{4V_0/Mw_0^2}$ is the radial trapping frequency. The eigenenergy of an atom trapped in $V_{\text{harm}}(\mathbf{R})$ is given by $(n_X + n_Y + 1)\hbar\omega_r + (n_Z + 1/2)\hbar\omega_Z$, where n_X, n_Y label the radial harmonic oscillator modes, and n_Z labels the axial harmonic oscillator modes. We then consider the correction of anharmonicity,

$$V_{\text{corr}}(\mathbf{R}) = -\frac{V_0 k_L^4}{3} Z^4 - \frac{2V_0 k_L^2}{w_0^2} r^2 Z^2. \tag{2.42}$$

Based on first-order perturbation theory, one can obtain energy corrections to harmonic oscillator modes,

$$\langle n_X, n_Y, n_Z|V_{\rm corr}|n_X, n_Y, n_Z\rangle = -\frac{E_R}{4}(2n_Z^2+2n_Z+1) - E_R\frac{\omega_r}{\omega_Z}(n_X+n_Y+1)\left(n_Z+\frac{1}{2}\right). \quad (2.43)$$

Combining them with the harmonic oscillator part, we have

$$\frac{E(n_X,n_Y,n_Z)}{E_R} \approx (2n_Z+1)\sqrt{\frac{V_0}{E_R}} - \frac{2n_Z^2+2n_Z+1}{4} + (n_X+n_Y+1)\frac{\hbar\omega_r}{E_R} - \frac{\omega_r}{\omega_Z}(n_X+n_Y+1)\left(n_Z+\frac{1}{2}\right), \quad (2.44)$$

which agrees with Eq. (2.34) for $\omega_r \to 0$. So the band gap (axial sideband transition energy), $\Delta E_{n_Z}(n_X, n_Y) \equiv E(n_X, n_Y, n_Z+1) - E(n_X, n_Y, n_Z)$, is given by

$$\frac{\Delta E_{n_Z}(n_X,n_Y)}{E_R} \approx 2\sqrt{\frac{V_0}{E_R}} - (n_Z+1) - \frac{\omega_r}{\omega_Z}(n_X+n_Y+1). \quad (2.45)$$

Notice that the axial sideband frequency varies for different radial modes, due to the coupling between axial and radial degrees of freedom generated by the Gaussian beams. In experiments, if the radial modes are populated by atoms with a thermal distribution of radial temperature T_r, which gives $\hbar\omega_r(n_X+n_Y) \sim 2k_BT_r$, one should observe a shift of axial sideband frequency as well as broadening of the axial sideband linewidth.

Moreover, the coupling between axial and radial degrees of freedom can also lead to modifications of the nearest-neighbor tunneling rate. In this case we only expand r up to the second order and keep all the terms of Z. This gives

$$V(\mathbf{R}) \approx \frac{1}{2}M\omega_r^2r^2 + \left(V_0 - \frac{1}{2}M\omega_r^2r^2\right)\sin^2(k_LZ). \quad (2.46)$$

From Eq. 2.46, one can see that the radial modes can lead to a effective lowering of the lattice depth, $V_0 \to V_0 - M\omega_r^2r^2/2$. Here we assume the radial motion are much slower compared to the tunneling process such that the atoms tunnel with a fixed radial mode. We also assume weak coupling between axial and radial degrees of freedom such that we can still approximate the radial energy as $E_{n_X,n_Y} = (n_x+n_Y+1)\hbar\omega_r$. The correction to tunneling rate τ is given by

$$\Delta\tau \approx \left(\frac{\partial\tau}{\partial V_0}\right)\Delta V_0 = -\frac{1}{2}\left(\frac{\partial\tau}{\partial V_0}\right)E_{n_X,n_Y}. \quad (2.47)$$

Note that the factor 1/2 is because the radial potential energy is 1/2 of the radial energy E_{n_X,n_Y}.

It is worth to mention that all the calculations in this subsection approximate the radial modes as harmonic oscillator modes. For a more precise result, one can perform numerical calculation based on the so-called Born-Oppenheimer approximation, assuming the radial motion are typically much slower compared to the axial motion. Such type of calculations are discussed in Ref. [50].

2.1.4 Linearly tilted 1D lattice

In this subsection, we discuss the single-particle physics in a 1D optical lattice with linear tilt, which is described by the following Hamiltonian,

$$\hat{H} = \frac{\hat{P}^2}{2m} + V_0 \sin^2(k_L X) + FX, \tag{2.48}$$

where F is an external constant force generating a linear potential along the lattice direction. For example, if the 1D lattice is in the vertical direction aligned with gravity, we have $F = Mg$, with g the gravitational acceleration. In the semiclassical picture, the existence of a force F along the lattice direction induces Bloch oscillations. The quasi-momentum k of the particle satisfies

$$\hbar \frac{\mathrm{d}k}{\mathrm{d}t} = -F \quad \Rightarrow \quad k(t) = k_0 - \frac{Ft}{\hbar}, \tag{2.49}$$

Notice that $k \in [-\pi/a_L, \pi/a_L)$, where $a_L = \pi/k_L$ is the lattice spacing, so the Bloch oscillation frequency is given by

$$\omega_B = \frac{Fa_L}{\hbar}. \tag{2.50}$$

Note that the group velocity v_g can be determined by the dispersion relation $E(k) \approx \epsilon_0 - 2\tau\cos(ka_L)$, with ϵ_0 the average band energy and τ the nearest-neighbor tunneling rate,

$$v_g(t) = \frac{1}{\hbar}\frac{dE(k)}{dk} = \frac{2\tau a_L}{\hbar}\sin\Big(k(t)a_L\Big) = \frac{2\tau a_L}{\hbar}\sin(k_0 a_L - \omega_B t), \tag{2.51}$$

so the center-of-mass oscillation is given by

$$X(t) = \int dt v_g(t) = \frac{2\tau}{F}\Big(\cos(k_0 a_L - \omega_B t) - \cos(k_0 a_L)\Big), \tag{2.52}$$

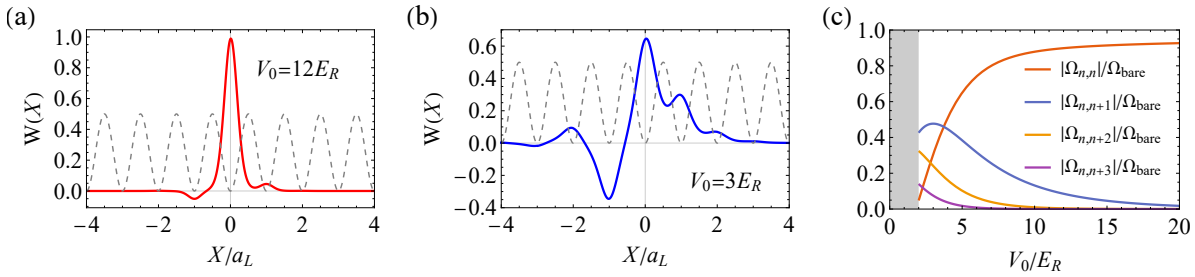

Figure 2.3: (a,b) Wave functions of Wannier-Stark states at lattice depth (a) $V_0 = 12E_R$ and (b) $V_0 = 3E_R$. $W(X)$ is a shorthand notation for the wave function of Wannier-Stark states centered at $X = 0$. (c) Rabi frequencies of carrier transitions and Wannier-Stark sidebands as a function of lattice depth. The gray shadow marks the region where the Wannier-Stark states becomes unstable due to Landau-Zener tunneling. For the numerical evaluation of wave functions and Rabi frequencies, we consider ^{87}Sr atoms trapped in a vertical 1D lattice tilted by gravity.

in which we assume $X(0) = 0$. The semiclassical picture for Bloch oscillation above is well-known in solid state physics. Here we would like to make a step further using a full quantum treatment.

We assume an atom is trapped in the ground band of the lattice, and the linear tilt is not strong enough to make the single-band approximation invalid. In the Wannier basis, one can write down the following tight-binding Hamiltonian,

$$\hat{H} = \sum_j (\epsilon_0 + Fa_L j)\hat{c}_j^\dagger \hat{c}_j - \sum_j \tau(\hat{c}_{j+1}^\dagger \hat{c}_j + \text{H.c.}). \tag{2.53}$$

We assume the single-particle eigenstates take the following form,

$$|\psi\rangle = \sum_l C_l |l\rangle, \tag{2.54}$$

where $|l\rangle = \hat{c}_l^\dagger |\text{vac}\rangle$. Plugging it in the equation $H|\psi\rangle = E|\psi\rangle$, we get

$$(\epsilon_0 + Fa_L l - E)C_l - \tau C_{l+1} - \tau C_{l-1} = 0. \tag{2.55}$$

Recall the following recurrence relation of Bessel function,

$$\frac{2\alpha}{x} J_\alpha(x) = J_{\alpha-1}(x) + J_{\alpha+1}(x), \tag{2.56}$$

by comparison we have

$$E_n = \epsilon_0 + Fa_L n, \quad \alpha = l - n, \quad x = \frac{2\tau}{Fa_L}. \tag{2.57}$$

Therefore, we get the eigenstates $|W_n\rangle$ (known as Wannier-Stark states) and corresponding eigenenergies E_n (known as Wannier-Stark ladder) for Eq. (2.53) as follow:

$$E_n = \epsilon_0 + Fa_L n, \quad n = 0, \pm 1, \pm 2, \cdots, \tag{2.58}$$

$$|W_n\rangle = \sum_l J_{l-n}\left(\frac{2\tau}{Fa_L}\right)|l\rangle. \tag{2.59}$$

By tuning the lattice depth V_0, one can control the tunneling rate τ and thus the width of Wannier-Stark wave functions (see Fig. 2.3(a,b)). An important part of my research is to apply this idea to control atomic contact interactions (see Chapter 3.2) and cavity-mediated interactions (see Chapter 5.2).

Considering a Rabi drive along the lattice direction, one can obtain the Rabi frequencies in the Wannier-Stark basis,

$$\begin{aligned}\Omega_{nm} &= \Omega_0 \int dX e^{ik_d X} W_n(X) W_m(X) \\ &\approx \sum_l J_{l-n}\left(\frac{2\tau}{Fa_L}\right) J_{l-m}\left(\frac{2\tau}{Fa_L}\right) e^{ik_d l a_L} \int dX e^{ik_d X} [w(z)]^2,\end{aligned} \tag{2.60}$$

where Ω_0 is the bare Rabi frequency, k_d is the wave number of the drive, and we assume the ground band Wannier function $w(z)$ is localized in a single lattice site. Using the Graf's addition theorem for Bessel functions [45],

$$\sum_{k=-\infty}^{\infty} J_{\nu+k}(u) J_k(v) e^{ik\alpha} = J_\nu(w) e^{i\nu\chi}, \tag{2.61}$$

where $w = \sqrt{u^2 + v^2 - 2uv\cos\alpha}$, $u - v\cos\alpha = w\cos\chi$, $v\sin\alpha = w\sin\chi$. Focusing mainly on the case when $u = v$, we obtain

$$\sum_{k=-\infty}^{\infty} J_{\nu+k}(u) J_k(u) e^{ik\alpha} = J_\nu\Big(2u\sin(\alpha/2)\Big) e^{i\nu(\pi-\alpha)/2}. \tag{2.62}$$

Therefore,

$$\Omega_{nm} \approx J_{n-m}\left(\frac{4\tau}{Fa_L}\sin(\varphi/2)\right) e^{i(n-m)(\pi-\varphi)/2} e^{im\varphi} \int dX e^{ik_d X} [w(z)]^2, \tag{2.63}$$

where $\varphi = k_d a_L$ is the laser phase difference between nearest-neighbor lattice sites. One can also approximate $w(z)$ as the harmonic oscillator ground state wave function (trapping frequency

$\omega = \sqrt{4V_0 E_R}/\hbar$), which gives

$$\int dX e^{ik_d X}[w(z)]^2 \approx e^{-\eta^2/2}, \quad \eta = k_d\sqrt{\frac{\hbar}{2M\omega}} = \frac{k_d}{k_L}\left(\frac{4V_0}{E_R}\right)^{-1/4}. \tag{2.64}$$

Here η is called the Lamb-Dicke parameter. Eq. (2.63) marks a key feature of the Wannier-Stark optical lattice clock described in Chapter 3: one can drive not only carrier transitions with $n = m$, but also Wannier-Stark sidebands with $n \neq m$. The relative strength of the Rabi frequencies can be controlled by the lattice depth V_0 (see Fig. 2.3(c)).

Now we discuss Bloch oscillations in a full quantum treatment. Generally speaking, Bloch oscillations are center-of-mass oscillations or coherent breathing experienced by independent particles in a periodic lattice potential in the presence of a constant force [51]. The case of coherent breathing can be easily understood using Wannier-Stark states. We consider the initial state as a Wannier state localized in a single lattice site ($l = 0$),

$$|\psi(t=0)\rangle = |0\rangle. \tag{2.65}$$

The time evolution of the wave function is given by

$$\begin{aligned} |\psi(t)\rangle &= e^{-i\epsilon_0 t}\sum_n J_{-n}\left(\frac{2\tau}{Fa_L}\right)e^{-i\omega_B nt}|W_n\rangle \\ &= e^{-i\epsilon_0 t}\sum_{nl} J_{-n}\left(\frac{2\tau}{Fa_L}\right)e^{-i\omega_B nt}J_{l-n}\left(\frac{2\tau}{Fa_L}\right)|l\rangle. \end{aligned} \tag{2.66}$$

Based on Eq. (2.62), we get

$$|\psi(t)\rangle = e^{-i\epsilon_0 t}\sum_l e^{il(\pi-\omega_B t)/2}J_l\left(\frac{4\tau}{Fa_L}\sin(\omega_B t/2)\right)|l\rangle. \tag{2.67}$$

The sinusoidal oscillations in the argument of the Bessel function generates the coherent breathing, as we shown in Eq. (2.67). One can characterize the coherent breathing using the position operator $\hat{X} = \sum_l a_L l|l\rangle\langle l|$, which gives $\langle\psi(t)|\hat{X}|\psi(t)\rangle = 0$, and

$$\langle\psi(t)|\hat{X}^2|\psi(t)\rangle = a_L^2\sum_l l^2\left[J_l\left(\frac{4\tau}{Fa_L}\sin(\omega_B t/2)\right)\right]^2. \tag{2.68}$$

Since the width of the atomic wave function is given by $2\sqrt{\langle\psi(t)|\hat{X}^2|\psi(t)\rangle}$, we can conclude that in this case, the wave function width oscillates with the Bloch oscillation frequency ω_B, while the wave function position remains unchanged.

For center-of-mass oscillations, we initialize a Gaussian wavepacket as follows,

$$|\psi(t=0)\rangle = \sum_s f(s)|s\rangle, \tag{2.69}$$

where

$$f(s) = \mathcal{N}^{-1/2} \exp\Big(- \frac{s^2}{4\sigma^2}\Big), \tag{2.70}$$

where $\mathcal{N}$ is the normalization factor. Here we assume the wavepacket is broad enough, so we can replace the summation by integration, $\int ds|f(s)|^2 = 1$. Similar to Eq. (2.67), we have

$$|\psi(t)\rangle = e^{-i\epsilon_0 t} \sum_l e^{il(\pi-\omega_B t)/2} A_l |l\rangle, \tag{2.71}$$

where

$$A_l = \sum_s f(s) e^{-is(\pi+\omega_B t)/2} J_{l-s}(z) \approx \int ds f(s) e^{-is(\pi+\omega_B t)/2} J_{l-s}(z). \tag{2.72}$$

where we have set $z = 4\tau \sin(\omega_B t/2)/Fa_L$. Using the integral representation of Bessel function,

$$J_n(z) = \frac{1}{2\pi} \int_{-\pi}^{\pi} d\zeta e^{i(n\zeta - z\sin\zeta)}, \tag{2.73}$$

we have

$$A_l \approx \frac{1}{2\pi} \int_{-\pi}^{\pi} d\zeta e^{il\zeta - iz\sin\zeta} \int ds f(s) e^{-is(\zeta-\zeta_0)} = \frac{\mathcal{N}^{-1/2}}{2\pi} \int_{-\pi}^{\pi} d\zeta e^{il\zeta - iz\sin\zeta} 2\sqrt{\pi\sigma^2} e^{-(\zeta-\zeta_0)^2\sigma^2}, \tag{2.74}$$

where we define $\zeta_0 = -(\pi + \omega_B t)/2$. Notice that σ is a large value due to the broad wavepacket in consideration, we define $\tilde{\zeta} = \zeta - \zeta_0$ and expand to in linear order of $\tilde{\zeta}$ in $e^{il\zeta - iz\sin\zeta}$, which gives

$$\begin{aligned} A_l &\approx e^{il\zeta_0 - iz\sin\zeta_0} \frac{\mathcal{N}^{-1/2}}{2\pi} \int_{-\pi}^{\pi} d\tilde{\zeta} e^{i(l - z\cos\zeta_0)\tilde{\zeta}} 2\sqrt{\pi\sigma^2} e^{-\tilde{\zeta}^2\sigma^2} \\ &\approx \mathcal{N}^{-1/2} e^{il\zeta_0 - iz\sin\zeta_0} \exp\Big(- \frac{(l - z\cos\zeta_0)^2}{4\sigma^2}\Big). \end{aligned} \tag{2.75}$$

Therefore, the wave function position is given by

$$\langle\psi(t)|\hat{X}|\psi(t)\rangle = a_L z\cos\zeta_0 = -\frac{4\tau}{F}\sin^2(\omega_B t/2), \tag{2.76}$$

indicating center-of-mass oscillations with frequency ω_B. Note that in this case the width of the wave packet is roughly unchanged. This formula agrees with the semiclassical picture with $k_0 = 0$ (see Eq. (2.52)).

So far we have assumed the atoms always stay in the ground band. However, based on the semiclassical picture, the role of the external force F is to scan the quasimomentum in the ground band, so the probability of an atom in the ground band tunnel into higher bands can be approximately described by the Landau-Zener tunneling probability,

$$P = \exp\left(-\frac{\pi\Delta^2}{2\alpha}\right). \tag{2.77}$$

In our case, Δ is the band gap, and α is the scanning rate of the energy difference, which can be estimated by $2(dE/dt)$ at $k = -\pi/a_L$ (the position of the band gap) in free particle case,

$$\alpha \approx \frac{2}{\hbar}\cdot\frac{dE}{dk}\cdot\frac{dk}{dt} = \frac{2}{\hbar}\cdot\frac{\hbar^2(-\pi/a)}{M}\cdot -\frac{F}{\hbar} = \frac{2\pi F}{Ma_L}. \tag{2.78}$$

So the probability of an interband transition per Bloch oscillation period $T_B = 2\pi/\omega_B$ can be approximated as

$$P \approx \exp\left(-\frac{Ma_L\Delta^2}{4F}\right). \tag{2.79}$$

Notice that $1 - P \approx \mathrm{e}^{-T_B/T_{\mathrm{decay}}}$, where T_{decay} is the decay time of ground band atoms. So we can approximate the decay time as

$$T_{\mathrm{decay}} \approx -\frac{T_B}{\ln(1-P)} \approx \frac{T_B}{P} = \frac{2\pi\hbar}{Fa_L}\exp\left(\frac{Ma_L\Delta^2}{4F}\right). \tag{2.80}$$

For ^{87}Sr atoms trapped in a 813 nm lattice along the vertical direction, one can estimate $T_{\mathrm{decay}} \sim 0.15$ s for $2E_R$ lattice in the ground band, while $T_{\mathrm{decay}} > 10^6$ s for lattice depths larger than $4E_R$. Therefore, Landau-Zener tunneling can limit the capability to trap atoms for low enough lattice depths along the vertical direction.

As for higher bands with band index n, the decay time T_{decay} can be estimated in a similar way, while we need to estimate α at $k = -n\pi/a_L$ in the free particle case. This can lead to an exponentially larger T_{decay} for higher bands. For ^{87}Sr atoms in the same condition, we have $T_{\mathrm{decay}} \sim 0.28$ s for $8E_R$ lattice in the first excited band, so only the ground band remains trapped below $8E_R$ along the vertical direction.

2.2 Contact interactions

In this section, we introduce the theory of atomic collisions under ultracold temperature. We start from the partial wave expansion of the two-body wave function. This is a useful expansion at ultracold temperatures since the centrifugal barriers strongly suppresses the contributions of higher partial waves. Then we discuss the technique known as pseudopotential, which approximates short-range interactions as contact interactions. In this way, it is very convenient to write down the many-body Hamiltonian in the second quantized form, and the description of atomic collisions can be simplified to a single parameter known as scattering length for each partial wave. We also provide an example for calculation of the scattering length under van der Waals interactions. After that, we discuss the concept of SU(n) symmetry, which plays a key role in ultracold collisions of fermionic alkaline earth atoms. Finally, we discuss the approximations we used in this thesis for analyzing many-body dynamics, depending on the regime where the interaction strength is weak or strong compared to the single-particle energy.

2.2.1 Partial wave expansion

We consider the following Hamiltonian for general two-body interactions,

$$\hat{H} = -\frac{\hbar^2}{2M_1}\nabla^2_{\mathbf{r}_1} - \frac{\hbar^2}{2M_2}\nabla^2_{\mathbf{r}_2} + V(\mathbf{r}_1 - \mathbf{r}_2). \tag{2.81}$$

If we define the center-of-mass coordinate $\mathbf{R}$ and the relative coordinate $\mathbf{r}$ as

$$\mathbf{R} = \frac{M_1\mathbf{r}_1 + M_2\mathbf{r}_2}{M_1 + M_2}, \quad \mathbf{r} = \mathbf{r}_1 - \mathbf{r}_2, \tag{2.82}$$

the Hamiltonian can be transformed into

$$\hat{H} = -\frac{\hbar^2}{2M_{\mathrm{tot}}}\nabla^2_{\mathbf{R}} - \frac{\hbar^2}{2\mu}\nabla^2_{\mathbf{r}} + V(\mathbf{r}), \tag{2.83}$$

where $M_{\mathrm{tot}} = M_1 + M_2$ is the total mass, and $\mu = M_1M_2/(M_1 + M_2)$ is the reduced mass. In this way, we can express the wave function of the two particles as

$$\psi(\mathbf{r}_1, \mathbf{r}_2) = \psi_{\mathrm{com}}(\mathbf{R})\psi_{\mathrm{rel}}(\mathbf{r}), \tag{2.84}$$

where ψ_{com} is the wave function in the center-of-mass degrees of freedom, and $\psi_{\text{rel}}(\mathbf{r})$ is the wave function in the relative coordinates. Notice that the two-body interaction term only affects $\psi_{\text{rel}}(\mathbf{r})$, so we reduce the two-body problem to an effective one-body problem in relative coordinates. In the following discussion, we use $\psi(\mathbf{r})$ as a simplified notation for $\psi_{\text{rel}}(\mathbf{r})$.

The two-body Schrödinger equation in the relative coordinates is given as follows,

$$\frac{\hbar^2}{2\mu}(\nabla^2 + k^2)\psi(\mathbf{r}) = V(r)\psi(\mathbf{r}), \tag{2.85}$$

where $k^2 = 2\mu E/\hbar^2$, and for simplicity we assume $V(r)$ is a central and finite-range potential which is non-zero in the regime $r < r_0$, with $r = |\mathbf{r}|$. Using a partial wave expansion, we can expand the wave function $\psi(\mathbf{r})$ in terms of the spherical harmonics $Y_{lm}(\theta, \phi)$,

$$\psi(\mathbf{r}) = \sum_{lm} R_{lm}(r) Y_{lm}(\theta, \phi). \tag{2.86}$$

The label l marks the l-partial wave. For $l = 0, 1, 2$, we call the partial waves as s-wave, p-wave, and d-wave. One can interpret l as the orbital angular momentum of the two-body wave function. Plugging Eq. (2.86) into Eq. (2.85) outside the range of the potential ($r > r_0$), we get the following differential equation for the radial part of the wave function,

$$\frac{1}{r^2}\frac{d}{dr}\left(r^2 \frac{dR_{lm}}{dr}\right) + \left(k^2 - \frac{l(l+1)}{r^2}\right) R_{lm} = 0. \tag{2.87}$$

Here, $l(l+1)/r^2$ is the centrifugal barrier, which increases with increasing partial wave label l. In the case of ultracold temperatures ($k \to 0$), the centrifugal barrier suppresses the contributions of higher partial waves, so we are able to truncate the partial wave expansion to a few values of l. The general solution of Eq. (2.87) is given by

$$R_{lm}(r) = A_{lm} j_l(kr) + B_{lm} n_l(kr), \tag{2.88}$$

where $j_l(r)$ and $n_l(r)$ are the spherical Bessel functions, and A_{lm} and B_{lm} are coefficients depending on the detail of the finite-range potential $V(r)$. In principle A_{lm} and B_{lm} can be estimated by matching the wave functions inside and outside the range of the potential at $r = r_0$. The asymptotic

behavior of $R_{lm}(r)$ for $kr \to \infty$ is given by

$$R_{lm}(r) \to \frac{1}{kr}\left[A_{lm}\sin\left(kr-\frac{l\pi}{2}\right)-B_{lm}\cos\left(kr-\frac{l\pi}{2}\right)\right] \propto \frac{1}{kr}\sin\left(kr-\frac{l\pi}{2}+\delta_l\right), \tag{2.89}$$

where δ_l is defined as the scattering phase shift of the l-partial wave,

$$\tan\delta_l = -\frac{B_{lm}}{A_{lm}}. \tag{2.90}$$

Since $V(r)$ is a central potential, there should be no m-dependence in the phase shift. In terms of phase shift δ_l, we can rewrite $R_{lm}(r)$ as follows,

$$R_{lm}(r) = A_{lm}[j_l(kr) - \tan\delta_l\, n_l(kr)] \quad (r > r_0). \tag{2.91}$$

In the following discussions, we call the wave function in the regime $r > r_0$ as $\psi_>(\mathbf{r})$.

It is worth to mention that we assumed $V(r)$ a finite-range potential with a hard cutoff at $r = r_0$ in the discussion above. As discussed in Ref. [52], the finite-range assumption is still partially valid for potentials with power-law decay $V(r) \propto 1/r^\alpha$: Eq. (2.87) is valid for the l-partial wave if $\alpha > 2l+3$. For van der Waals interactions ($\alpha = 6$), our strategy is valid for s-wave and p-wave. For higher partial waves, we cannot ignore $V(r)$ in Eq. (2.87).

2.2.2 Huang-Yang pseudopotential

The idea of Huang-Yang pseudopotential [53–57] is to replace the potential $V(r)$ in Eq. (2.85) by a contact potential $V_{ps}(\mathbf{r})$, which acts only at $\mathbf{r} = 0$ and gives the same wave function $\psi_>(\mathbf{r})$ outside the range of the potential at the low-energy threshold ($k \to 0$). Notice that the asymptotic behavior of $R_{lm}(r)$ for $kr \to 0$ is given by

$$R_{lm}(kr) \to A_{lm}\left[\frac{(kr)^l}{(2l+1)!!} + \tan\delta_l \frac{(2l-1)!!}{(kr)^{l+1}}\right], \tag{2.92}$$

the Huang-Yang pseudopotential $V_{ps}(\mathbf{r})$ can be constructed as

$$\begin{aligned} V_{ps}(\mathbf{r})\psi_>(\mathbf{r}) &= \frac{\hbar^2}{2\mu}\nabla^2\psi_>(kr\to 0) \\ &= \frac{\hbar^2}{2\mu}\sum_{lm} A_{lm}Y_{lm}(\theta,\phi)\left(\nabla^2 - \frac{l(l+1)}{r^2}\right)\left[\frac{(kr)^l}{(2l+1)!!} + \tan\delta_l\frac{(2l-1)!!}{(kr)^{l+1}}\right]. \end{aligned} \tag{2.93}$$

Using the fact that

$$\nabla^2(r^l) = \frac{l(l+1)}{r^2} r^l, \tag{2.94}$$

$$\begin{aligned}\left(\nabla^2 - \frac{l(l+1)}{r^2}\right)\frac{1}{r^{l+1}} &= \frac{1}{r^l}\left[r^l\nabla^2\left(\frac{1}{r^{l+1}}\right) - \frac{1}{r^{l+1}}\nabla^2(r^l)\right] = \frac{1}{r^l}\nabla\cdot\left[r^l\nabla\left(\frac{1}{r^{l+1}}\right) - \frac{1}{r^{l+1}}\nabla(r^l)\right] \\ &= -\frac{2l+1}{r^l}\nabla\cdot\left(\frac{\hat{r}}{r^2}\right) = -\frac{2l+1}{r^l}4\pi\delta(\mathbf{r}),\end{aligned} \tag{2.95}$$

with $\hat{r} = \mathbf{r}/r$, we have

$$V_{ps}(\mathbf{r})\psi_>(\mathbf{r}) = -\frac{\hbar^2}{2\mu}\sum_{lm} A_{lm}\tan\delta_l \frac{(2l+1)!!}{k^{l+1}}\frac{\delta(r)}{r^{l+2}}Y_{lm}(\theta,\phi), \tag{2.96}$$

where $\delta(r) = 4\pi r^2\delta(\mathbf{r})$. Based on Eq. (2.92), we can also express A_{lm} as follows,

$$A_{lm} = \frac{1}{k^l(2l)!!}\left[\left(\frac{d}{dr}\right)^{2l+1} r^{l+1}R_{lm}(kr)\right]\Big|_{r=0} = \frac{1}{k^l(2l)!!}\left[\left(\frac{\partial}{\partial r}\right)^{2l+1} r^{l+1}\int d\Omega Y^*_{lm}\psi_>(\mathbf{r})\right]\Big|_{r=0}, \tag{2.97}$$

where $d\Omega = \sin\theta d\theta d\phi/4\pi$. Plugging Eq. (2.97) into Eq. (2.96), we have

$$V_{ps}(\mathbf{r})\psi_>(\mathbf{r}) = \sum_{lm}\frac{\hbar^2 a_l^{2l+1}}{2\mu}\frac{(2l+1)!!}{(2l)!!}\frac{\delta(r)}{r^{l+2}}Y_{lm}(\theta,\phi)\left[\left(\frac{\partial}{\partial r}\right)^{2l+1} r^{l+1}\int d\Omega Y^*_{lm}\psi_>(\mathbf{r})\right]\Big|_{r=0}, \tag{2.98}$$

where we defined the scattering length for the l-partial wave as

$$a_l^{2l+1} = -\lim_{k\to 0}\frac{\tan\delta_l}{k^{2l+1}}. \tag{2.99}$$

Now we calculate the form of Huang-Yang pseudopotential in momentum space. Consider the plane wave basis,

$$\langle\mathbf{r}|\mathbf{k}\rangle = \frac{1}{\sqrt{V}}\mathrm{e}^{i\mathbf{k}\cdot\mathbf{r}}, \tag{2.100}$$

and

$$\langle\mathbf{k}|V_{ps}|\mathbf{k}'\rangle = \frac{1}{V}\int d^3\mathbf{r}\,\mathrm{e}^{-i\mathbf{k}\cdot\mathbf{r}}V_{ps}(\mathbf{r})\mathrm{e}^{i\mathbf{k}'\cdot\mathbf{r}}, \tag{2.101}$$

we have

$$\begin{aligned}\langle\mathbf{k}|V_{ps}|\mathbf{k}'\rangle = \sum_{lm}\frac{\hbar^2 a_l^{2l+1}}{2\mu V}\frac{(2l+1)!!}{(2l)!!}&\left[\int d^3\mathbf{r}\,\mathrm{e}^{-i\mathbf{k}\cdot\mathbf{r}}\frac{\delta(r)}{r^{l+2}}Y_{lm}(\theta,\phi)\right] \\ &\times\left[\left(\frac{\partial}{\partial r}\right)^{2l+1} r^{l+1}\int d\Omega Y^*_{lm}\mathrm{e}^{i\mathbf{k}'\cdot\mathbf{r}}\right]\Big|_{r=0}.\end{aligned} \tag{2.102}$$

Using the fact that

$$\mathrm{e}^{i\mathbf{k}\cdot\mathbf{r}} = 4\pi \sum_{lm} i^l j_l(kr) Y^*_{lm}(\hat{k}) Y_{lm}(\hat{r}), \tag{2.103}$$

where the notation $Y_{lm}(\hat{r})$ means $Y_{lm}(\theta,\phi)$ with θ and ϕ set to the direction of $\hat{r}$. We have

$$\begin{aligned}\int d^3\mathbf{r}\, \mathrm{e}^{-i\mathbf{k}\cdot\mathbf{r}} \frac{\delta(r)}{r^{l+2}} Y_{lm}(\theta,\phi) &= 4\pi \sum_{l'm'} (-i)^{l'} Y_{l'm'}(\hat{k}) \int r^2 dr\, j_{l'}(kr) \frac{\delta(r)}{r^{l+2}} \cdot \int d\Omega\, Y^*_{l'm'} Y_{lm} \\ &= 4\pi (-i)^l Y_{lm}(\hat{k}) \int r^2 dr\, j_l(kr) \frac{\delta(r)}{r^{l+2}} = \frac{4\pi(-i)^l Y_{lm}(\hat{k}) k^l}{(2l+1)!!},\end{aligned} \tag{2.104}$$

$$\begin{aligned}&\left[\left(\frac{\partial}{\partial r}\right)^{2l+1} r^{l+1} \int d\Omega Y^*_{lm}(\Omega) \mathrm{e}^{i\mathbf{k}'\cdot\mathbf{r}}\right]\Bigg|_{r=0} \\ &= 4\pi \sum_{l'm'} i^{l'} Y^*_{l'm'}(\hat{k}') \left[\left(\frac{\partial}{\partial r}\right)^{2l+1} r^{l+1} j_{l'}(k'r) \int d\Omega Y^*_{lm} Y_{l'm'}\right]\Bigg|_{r=0} \\ &= 4\pi\, i^l Y^*_{lm}(\hat{k}') \left[\left(\frac{\partial}{\partial r}\right)^{2l+1} r^{l+1} j_l(k'r)\right]\Bigg|_{r=0} \\ &= 4\pi\, i^l Y^*_{lm}(\hat{k}') (k')^l (2l)!!,\end{aligned} \tag{2.105}$$

which gives

$$\langle \mathbf{k}|V_{ps}|\mathbf{k}'\rangle = \frac{8\hbar^2\pi^2}{\mu V} \sum_{lm} a_l^{2l+1} (k')^l k^l Y^*_{lm}(\hat{k}') Y_{lm}(\hat{k}). \tag{2.106}$$

Recall the addition theorem for spherical harmonics,

$$P_l(\hat{k}\cdot\hat{k}') = \frac{4\pi}{2l+1} \sum_m Y_{lm}(\hat{k}) Y^*_{lm}(\hat{k}'), \tag{2.107}$$

where $P_l(x)$ is the Legendre polynomial. We then have

$$\langle \mathbf{k}|V_{ps}|\mathbf{k}'\rangle = \frac{2\hbar^2\pi}{\mu V} \sum_l (2l+1) a_l^{2l+1} (k')^l k^l P_l(\hat{k}\cdot\hat{k}'). \tag{2.108}$$

For s-wave ($l=0$), we have

$$\langle \mathbf{k}|V_{ps}|\mathbf{k}'\rangle = \frac{2\hbar^2\pi}{\mu V} a_0. \tag{2.109}$$

For p-wave ($l=1$), we have

$$\langle \mathbf{k}|V_{ps}|\mathbf{k}'\rangle = \frac{6\hbar^2\pi}{\mu V} a_1^3 (\mathbf{k}\cdot\mathbf{k}'). \tag{2.110}$$

Based on the Huang-Yang pseudopotential, it is convenient to express the many-body Hamiltonian for identical particles ($\mu = M/2$, with $M \equiv M_1 = M_2$) in the second quantized form as

follows,

$$\begin{aligned}\hat{H} &= \hat{H}_0 + \hat{H}_1,\\ \hat{H}_0 &= \sum_\alpha \int d^3\mathbf{r}\, \hat{\psi}^\dagger_\alpha(\mathbf{r})\Big[-\frac{\hbar^2}{2M}\nabla^2\Big]\hat{\psi}_\alpha(\mathbf{r}),\\ \hat{H}_1 &= \frac{1}{2}\sum_{\alpha\beta}\int d^3\mathbf{r}_1 d^3\mathbf{r}_2\, \hat{\psi}^\dagger_\alpha(\mathbf{r}_1)\hat{\psi}^\dagger_\beta(\mathbf{r}_2)V_{ps}^{\alpha\beta}(\mathbf{r}_1-\mathbf{r}_2)\hat{\psi}_\beta(\mathbf{r}_2)\hat{\psi}_\alpha(\mathbf{r}_1),\end{aligned} \tag{2.111}$$

in which $V_{ps}^{\alpha\beta}(\mathbf{r}_1-\mathbf{r}_2)$ is the pseudopotential for two-body interaction, α,β denote the internal levels of the particles, and we use $a_{\alpha\beta}$ ($b^3_{\alpha\beta}$) to denote the s-wave scattering length (p-wave scattering volume) between particles in internal levels α and β. In momentum space, the field operator can be expressed as

$$\hat{\psi}_\alpha(\mathbf{r}) = \frac{1}{\sqrt{V}}\sum_{\mathbf{k}} \mathrm{e}^{i\mathbf{k}\cdot\mathbf{r}}\hat{a}_{\mathbf{k}\alpha}, \tag{2.112}$$

so the interaction term can be written as

$$\begin{aligned}\hat{H}_1 &= \frac{1}{2V^2}\sum_{\alpha\beta}\sum_{\mathbf{k}_1\mathbf{k}_2\mathbf{k}_3\mathbf{k}_4}\hat{a}^\dagger_{\mathbf{k}_1\alpha}\hat{a}^\dagger_{\mathbf{k}_2\beta}\hat{a}_{\mathbf{k}_3\beta}\hat{a}_{\mathbf{k}_4\alpha}\int d^3\mathbf{r}_1 d^3\mathbf{r}_2\, \mathrm{e}^{-i\mathbf{k}_1\cdot\mathbf{r}_1}\mathrm{e}^{-i\mathbf{k}_2\cdot\mathbf{r}_2}V_{ps}^{\alpha\beta}(\mathbf{r}_1-\mathbf{r}_2)\mathrm{e}^{i\mathbf{k}_3\cdot\mathbf{r}_2}\mathrm{e}^{i\mathbf{k}_4\cdot\mathbf{r}_1}\\ &= \frac{1}{2V^2}\sum_{\alpha\beta}\sum_{\mathbf{k}_1\mathbf{k}_2\mathbf{k}_3\mathbf{k}_4}\hat{a}^\dagger_{\mathbf{k}_1\alpha}\hat{a}^\dagger_{\mathbf{k}_2\beta}\hat{a}_{\mathbf{k}_3\beta}\hat{a}_{\mathbf{k}_4\alpha}\int d^3\mathbf{R}\, \mathrm{e}^{-i(\mathbf{k}_1+\mathbf{k}_2-\mathbf{k}_3-\mathbf{k}_4)\cdot\mathbf{R}}\\ &\qquad\qquad\times\int d^3\mathbf{r}\, \mathrm{e}^{-i\frac{\mathbf{k}_1-\mathbf{k}_2}{2}\cdot\mathbf{r}}V_{ps}^{\alpha\beta}(\mathbf{r}_1-\mathbf{r}_2)\mathrm{e}^{i\frac{\mathbf{k}_4-\mathbf{k}_3}{2}\cdot\mathbf{r}}\\ &= \frac{1}{2}\sum_{\alpha\beta}\sum_{\mathbf{k}_1\mathbf{k}_2\mathbf{k}_3\mathbf{k}_4}\hat{a}^\dagger_{\mathbf{k}_1\alpha}\hat{a}^\dagger_{\mathbf{k}_2\beta}\hat{a}_{\mathbf{k}_3\beta}\hat{a}_{\mathbf{k}_4\alpha}\left\langle\frac{\mathbf{k}_1-\mathbf{k}_2}{2}\middle|V_{ps}^{\alpha\beta}\middle|\frac{\mathbf{k}_4-\mathbf{k}_3}{2}\right\rangle\delta_{\mathbf{k}_1+\mathbf{k}_2,\mathbf{k}_3+\mathbf{k}_4},\end{aligned} \tag{2.113}$$

where $\mathbf{R}=(\mathbf{r}_1+\mathbf{r}_2)/2$, and $\mathbf{r}=\mathbf{r}_1-\mathbf{r}_2$. For s-wave interactions, using Eq. (2.109), we have

$$\begin{aligned}\hat{H}_1 &= \frac{1}{2}\sum_{\alpha\beta}\frac{4\pi\hbar^2 a_{\alpha\beta}}{MV}\sum_{\mathbf{k}_1\mathbf{k}_2\mathbf{k}_3\mathbf{k}_4}\hat{a}^\dagger_{\mathbf{k}_1\alpha}\hat{a}^\dagger_{\mathbf{k}_2\beta}\hat{a}_{\mathbf{k}_3\beta}\hat{a}_{\mathbf{k}_4\alpha}\,\delta_{\mathbf{k}_1+\mathbf{k}_2,\mathbf{k}_3+\mathbf{k}_4}\\ &= \frac{1}{2}\sum_{\alpha\beta}\frac{4\pi\hbar^2 a_{\alpha\beta}}{MV^2}\sum_{\mathbf{k}_1\mathbf{k}_2\mathbf{k}_3\mathbf{k}_4}\hat{a}^\dagger_{\mathbf{k}_1\alpha}\hat{a}^\dagger_{\mathbf{k}_2\beta}\hat{a}_{\mathbf{k}_3\beta}\hat{a}_{\mathbf{k}_4\alpha}\int d^3\mathbf{r}\, \mathrm{e}^{-i(\mathbf{k}_1+\mathbf{k}_2-\mathbf{k}_3-\mathbf{k}_4)\cdot\mathbf{r}}\\ &= \frac{1}{2}\sum_{\alpha\beta}\frac{4\pi\hbar^2 a_{\alpha\beta}}{M}\int d^3\mathbf{r}\,\hat{\psi}^\dagger_\alpha(\mathbf{r})\hat{\psi}^\dagger_\beta(\mathbf{r})\hat{\psi}_\beta(\mathbf{r})\hat{\psi}_\alpha(\mathbf{r}).\end{aligned} \tag{2.114}$$

For p-wave interactions, using Eq. (2.110), we have

$$\begin{aligned}\hat{H}_1 &= \frac{1}{2}\sum_{\alpha\beta}\frac{3\pi\hbar^2 b_{\alpha\beta}^3}{MV}\sum_{\mathbf{k}_1\mathbf{k}_2\mathbf{k}_3\mathbf{k}_4}\hat{a}_{\mathbf{k}_1\alpha}^\dagger\hat{a}_{\mathbf{k}_2\beta}^\dagger\hat{a}_{\mathbf{k}_3\beta}\hat{a}_{\mathbf{k}_4\alpha}[(\mathbf{k}_1-\mathbf{k}_2)\cdot(\mathbf{k}_4-\mathbf{k}_3)]\,\delta_{\mathbf{k}_1+\mathbf{k}_2,\mathbf{k}_3+\mathbf{k}_4}\\ &= \frac{1}{2}\sum_{\alpha\beta}\frac{3\pi\hbar^2 b_{\alpha\beta}^3}{MV^2}\sum_{\mathbf{k}_1\mathbf{k}_2\mathbf{k}_3\mathbf{k}_4}\hat{a}_{\mathbf{k}_1\alpha}^\dagger\hat{a}_{\mathbf{k}_2\beta}^\dagger\hat{a}_{\mathbf{k}_3\beta}\hat{a}_{\mathbf{k}_4\alpha}\int d^3\mathbf{r}\,[(\mathbf{k}_1-\mathbf{k}_2)\cdot(\mathbf{k}_4-\mathbf{k}_3)]\mathrm{e}^{-i(\mathbf{k}_1+\mathbf{k}_2-\mathbf{k}_3-\mathbf{k}_4)\cdot\mathbf{r}}\\ &= \frac{1}{2}\sum_{\alpha\beta}\frac{3\pi\hbar^2 b_{\alpha\beta}^3}{M}\int d^3\mathbf{r}\,[(\nabla\hat{\psi}_\alpha^\dagger)\hat{\psi}_\beta^\dagger-\hat{\psi}_\alpha^\dagger(\nabla\hat{\psi}_\beta^\dagger)]\cdot[\hat{\psi}_\beta(\nabla\hat{\psi}_\alpha)-(\nabla\hat{\psi}_\beta)\hat{\psi}_\alpha].\end{aligned} \tag{2.115}$$

It is worth to mention that the contact potential for s-wave and p-wave interaction above might lead to ultraviolet divergence in some type of calculations, where proper regularization techniques would be in need to eliminate the divergence (see Ref. [58]). For all the calculations in this thesis, we have never encountered the divergence problem.

Now we use the many-body Hamiltonian for two-level atoms as an example to illustrate the s-wave and p-wave interaction. For a two-component Fermi gas with internal levels $|g\rangle$ and $|e\rangle$, since the total wave function for two fermionic atoms needs to be antisymmetric, the spatial wave function related to the spin state $(|ge\rangle-|eg\rangle)/\sqrt{2}$ is symmetric (s-wave interaction with scattering length a_{eg}), while the spatial wave functions related to spin states $|gg\rangle, (|ge\rangle+|eg\rangle)/\sqrt{2}, |ee\rangle$ are antisymmetric (p-wave interaction with scattering volumes $b_{gg}^3, b_{eg}^3, b_{ee}^3$ respectively). So the two-body interaction term $\hat{H}_1$ takes the following form,

$$\begin{aligned}\hat{H}_1 = &\frac{4\pi\hbar^2 a_{eg}}{M}\int d^3\mathbf{r}\,\hat{\psi}_e^\dagger(\mathbf{r})\hat{\psi}_g^\dagger(\mathbf{r})\hat{\psi}_g(\mathbf{r})\hat{\psi}_e(\mathbf{r})\\ &+\sum_{\alpha\beta}\frac{3\pi\hbar^2 b_{\alpha\beta}^3}{2M}\int d^3\mathbf{r}\,[(\nabla\hat{\psi}_\alpha^\dagger)\hat{\psi}_\beta^\dagger-\hat{\psi}_\alpha^\dagger(\nabla\hat{\psi}_\beta^\dagger)]\cdot[\hat{\psi}_\beta(\nabla\hat{\psi}_\alpha)-(\nabla\hat{\psi}_\beta)\hat{\psi}_\alpha].\end{aligned} \tag{2.116}$$

For a two-component Bose gas with internal levels $|g\rangle$ and $|e\rangle$, since the total wave function for two bosonic atoms must be symmetric, the spatial wave functions related to spin states $|gg\rangle, (|ge\rangle+|eg\rangle)/\sqrt{2}, |ee\rangle$ are symmetric (s-wave interaction with scattering lengths a_{gg}, a_{eg}, a_{ee} respectively), while the spatial wave function related to the spin state $(|ge\rangle-|eg\rangle)/\sqrt{2}$ is antisymmetric (p-wave interaction with scattering volume b_{eg}^3). So the two-body interaction term $\hat{H}_1$ takes the following

form,

$$\begin{aligned}\hat{H}_1 = &\sum_{\alpha\beta}\frac{2\pi\hbar^2 a_{\alpha\beta}}{M}\int d^3\mathbf{r}\,\hat{\psi}^\dagger_\alpha(\mathbf{r})\hat{\psi}^\dagger_\beta(\mathbf{r})\hat{\psi}_\beta(\mathbf{r})\hat{\psi}_\alpha(\mathbf{r})\\ &+\frac{3\pi\hbar^2 b^3_{eg}}{M}\int d^3\mathbf{r}\,[(\nabla\hat{\psi}^\dagger_e)\hat{\psi}^\dagger_g-\hat{\psi}^\dagger_e(\nabla\hat{\psi}^\dagger_g)]\cdot[\hat{\psi}_g(\nabla\hat{\psi}_e)-(\nabla\hat{\psi}_g)\hat{\psi}_e].\end{aligned} \tag{2.117}$$

2.2.3 Semiclassical approximation of scattering lengths

In the previous subsection, we derive the many-body Hamiltonian based on a single parameter known as scattering length (see Eq. (2.99)) for each partial wave. In general, the interactions between two neutral atoms can be described by the so-called Lennard-Jones potential,

$$V(r) = -\frac{C_6}{r^6}\Big(1-(\sigma/r)^6\Big). \tag{2.118}$$

In the long range, $V(r)\approx -C_6/r^6$ describes the van der Waals interaction characterized by the C_6 coefficient. In the short range, σ is a fitting parameter describing the repulsive core.

Here we would like to discuss the key idea of evaluating the scattering lengths based on $V(r)$, following the procedure in Ref. [59]. We define $\chi(r) = rR_{lm}(r)$, so the radial part of the two-body Schrödinger equation (see Eq. (2.85)) becomes

$$\frac{d^2\chi}{dr^2}+\left(k^2-\frac{2\mu V(r)}{\hbar^2}-\frac{l(l+1)}{r^2}\right)\chi = 0. \tag{2.119}$$

We separate the solution of $\chi(r)$ in three different regions:

(1) $r < r_1$: The physics is dominated by the short-range part of $V(r)$, and we can ignore the terms with k^2 and $l(l+1)/r^2$. In this region, we solve Eq. (2.119) using WKB approximation,

$$\chi(r)\propto\frac{1}{\sqrt{\mathcal{P}(r)}}\cos\left(\frac{1}{\hbar}\int_{r_*}^{r}\mathcal{P}(r)dr-\frac{\pi}{4}\right),\quad \mathcal{P}(r)=\sqrt{-2\mu V(r)}, \tag{2.120}$$

where r^* is the classical turning point satisfying $V(r^*)=0$, and the phase $-\pi/4$ originates from the WKB connection condition.

(2) $r_1 < r < r_0$: The physics is dominated by van der Waals interaction $V(r)\approx -C_6/r^6$ as well as the centrifugal barrier $l(l+1)/r^2$, and we can still ignore k^2. Thus Eq. (2.119) becomes

$$\frac{d^2\chi}{dr^2}+\left(\frac{\gamma^2}{r^6}-\frac{l(l+1)}{r^2}\right)\chi = 0, \tag{2.121}$$

where $\gamma = \sqrt{2\mu C_6}/\hbar$. The general solution of this differential equation is given by

$$\chi(r) = \sqrt{r}\left[c_1 \mathcal{J}_{\frac{2l+1}{4}}\left(\frac{\gamma}{2r^2}\right) - c_2 \mathcal{N}_{\frac{2l+1}{4}}\left(\frac{\gamma}{2r^2}\right)\right], \tag{2.122}$$

where $\mathcal{J}_\alpha(x)$ is the Bessel function of the first kind, $\mathcal{N}_\alpha(x)$ is the Bessel function of the second kind, and $\Gamma(x)$ is the gamma function.

(3) $r > r_0$: The physics is dominated by k^2 and $l(l+1)/r^2$, and we can drop $V(r)$. This region is already discussed in the subsection of partial wave expansion, and the general solution for $\chi(r)$ is given by

$$\chi(r) = r\Big[Aj_l(kr) + Bn_l(kr)\Big], \quad \tan\delta_l = -\frac{B}{A}, \tag{2.123}$$

where $j_l(r)$ and $n_l(r)$ are the spherical Bessel functions, and δ_l is the phase shift for the l-partial wave.

Then we consider wave function matching at $r = r_0$ and $r = r_1$, which is to match the logarithmic derivatives $\chi^{-1}(d\chi/dr)$. We assume $r \to \infty$ in Eq. (2.122) and $kr \to 0$ in Eq. (2.123) for matching the logarithmic derivatives at $r = r_0$, which relates the s-wave scattering length ($l = 0$) and the p-wave scattering volume ($l = 1$) with coefficients c_1 and c_2,

$$a = \frac{2\pi\gamma^{1/2}}{[\Gamma(1/4)]^2}\left(1 - \frac{c_{1,l=0}}{c_{2,l=0}}\right), \quad b^3 = -\frac{\gamma^{3/2}\pi}{18[\Gamma(3/4)]^2}\left(1 + \frac{c_{1,l=1}}{c_{2,l=1}}\right). \tag{2.124}$$

We also assume $r \to 0$ in Eq. (2.122) and $V(r) \approx -C_6/r^6$ in Eq. (2.120) for matching the logarithmic derivatives at $r = r_1$, which gives

$$\frac{c_{1,l}}{c_{2,l}} = \tan\left(\Phi - \frac{2l+1}{8}\pi\right), \tag{2.125}$$

where the semiclassical phase Φ is given by

$$\Phi = \frac{1}{\hbar}\int_{r^*}^{\infty} \sqrt{-2\mu V(r)}dr. \tag{2.126}$$

Therefore, one can finally arrive the formula for s-wave scattering length ($l = 0$),

$$a = \bar{a}\left(1 - \tan\left(\Phi - \frac{\pi}{8}\right)\right), \quad \bar{a} = \frac{2\pi}{[\Gamma(1/4)]^2}\left(\frac{2\mu C_6}{\hbar^2}\right)^{1/4}, \tag{2.127}$$

and the formula for the p-wave scattering volume ($l = 1$),

$$b^3 = -\bar{a}^3 \frac{[\Gamma(1/4)]^6}{144\pi^4[\Gamma(3/4)]^2}\left(1 + \tan\left(\Phi - \frac{3\pi}{8}\right)\right). \tag{2.128}$$

Eliminating the semiclassical phase Φ, one can achieve a universal relation between s-wave scattering length and p-wave scattering volume [60],

$$a/\bar{a} = 1 + \frac{b^3/\bar{a}^3}{b^3/\bar{a}^3 + \eta}, \quad \eta = \frac{[\Gamma(1/4)]^6}{72\pi^4[\Gamma(3/4)]^2} \approx 2.12856, \tag{2.129}$$

if they are generated by the same van der Waals interaction.

2.2.4 SU(n) symmetry

Fermionic ^{87}Sr atoms have two long-lived electronic orbitals, the $^1S_0$ and $^3P_0$ clock states, as well as a nuclear spin degree of freedom with $I = 9/2$. We denote the electronic states as $|g\rangle$ and $|e\rangle$ respectively and the $n = 2I + 1$ nuclear spin levels as $m = -I, -I + 1, \cdots, I$. Due to the lack of hyperfine coupling between the nuclear and electronic degrees of freedom, the scattering parameters that describe two-body interactions are independent of the nuclear spin states. This property gives rise to an interaction Hamiltonian invariant under SU(n) rotations [61, 62].

It is easy to show that the permutation of nuclear spin states between two particles,

$$\hat{\mathcal{P}}_{12} = \sum_{m,m'=\{-I,\cdots,I\}} |m\rangle_1\langle m'| \otimes |m'\rangle_2\langle m|, \tag{2.130}$$

commute with the single-particle SU(n) rotations. So we consider two possible interaction channels, permutation-symmetric (denoted by projection operator $\hat{\mathcal{P}}_+$) and permutation-antisymmetric (denoted by projection operator $\hat{\mathcal{P}}_-$), and the interaction potential can be written as

$$\hat{V}(\mathbf{r}_{12}) = V_+(\mathbf{r}_{12})\hat{\mathcal{P}}_+ + V_-(\mathbf{r}_{12})\hat{\mathcal{P}}_-, \quad \hat{\mathcal{P}}_\pm = \frac{\hat{\mathcal{I}} \pm \hat{\mathcal{P}}_{12}}{2}. \tag{2.131}$$

For the construction of the many-body Hamiltonian, it is more convenient to rewrite the interaction potential into the following form,

$$\hat{V}(\mathbf{r}_{12}) = \frac{V_+(\mathbf{r}_{12}) + V_-(\mathbf{r}_{12})}{2}\hat{\mathcal{I}} + \frac{V_+(\mathbf{r}_{12}) - V_-(\mathbf{r}_{12})}{2}\hat{\mathcal{P}}_{12}. \tag{2.132}$$

The s-wave interactions occur under spatially symmetric collisions. Due to the requirement for fermionic atoms to feature a fully antisymmetric total wave function, to collide under the s-wave channel, symmetric nuclear spin states require their electronic orbitals to be antisymmetric. Therefore, the state $(|ge\rangle - |eg\rangle)/\sqrt{2}$ is the only one that can feature s-wave interactions, characterized by the s-wave scattering length a_{eg}^{-}. Similarly, to collide via s-wave interactions, antisymmetric nuclear spin states require their electronic orbitals to be symmetric. So there are three possible combination of electronic states $|gg\rangle$, $|ee\rangle$, $(|ge\rangle + |eg\rangle)/\sqrt{2}$ that can collide via s-wave. Their interactions are characterized by the s-wave scattering lengths a_{gg}, a_{ee} and a_{eg}^{+} respectively. The resulting s-wave pseudopotential for SU(n) interaction takes the following form: $\hat{V}_s^{gg}(\mathbf{r}_{12}) \propto a_{gg}\hat{\mathcal{P}}_{-}$, $\hat{V}_s^{ee}(\mathbf{r}_{12}) \propto a_{ee}\hat{\mathcal{P}}_{-}$, $\hat{V}_s^{eg}(\mathbf{r}_{12}) \propto (a_{eg}^{-} + a_{eg}^{+})\hat{\mathcal{I}}/2 + (a_{eg}^{-} - a_{eg}^{+})\hat{\mathcal{P}}_{12}/2$. Thus the s-wave interaction Hamiltonian in the second quantized form,

$$\begin{aligned}
\hat{H}_s = &\frac{2\pi\hbar^2 a_{gg}}{M} \sum_{\substack{mm' \\ (m\neq m')}} \int d^3\mathbf{r}\, \hat{\psi}_{gm}^{\dagger}(\mathbf{r})\hat{\psi}_{gm'}^{\dagger}(\mathbf{r})\hat{\psi}_{gm'}(\mathbf{r})\hat{\psi}_{gm}(\mathbf{r}) \\
&+ \frac{2\pi\hbar^2 a_{ee}}{M} \sum_{\substack{mm' \\ (m\neq m')}} \int d^3\mathbf{r}\, \hat{\psi}_{em}^{\dagger}(\mathbf{r})\hat{\psi}_{em'}^{\dagger}(\mathbf{r})\hat{\psi}_{em'}(\mathbf{r})\hat{\psi}_{em}(\mathbf{r}) \\
&+ \frac{2\pi\hbar^2 (a_{eg}^{-} + a_{eg}^{+})}{M} \sum_{mm'} \int d^3\mathbf{r}\, \hat{\psi}_{gm}^{\dagger}(\mathbf{r})\hat{\psi}_{em'}^{\dagger}(\mathbf{r})\hat{\psi}_{em'}(\mathbf{r})\hat{\psi}_{gm}(\mathbf{r}) \\
&+ \frac{2\pi\hbar^2 (a_{eg}^{-} - a_{eg}^{+})}{M} \sum_{mm'} \int d^3\mathbf{r}\, \hat{\psi}_{gm}^{\dagger}(\mathbf{r})\hat{\psi}_{em'}^{\dagger}(\mathbf{r})\hat{\psi}_{em}(\mathbf{r})\hat{\psi}_{gm'}(\mathbf{r}),
\end{aligned} \tag{2.133}$$

where M is the mass of a ^{87}Sr atom, $\hat{\psi}_{gm}(\mathbf{r})$ and $\hat{\psi}_{em'}(\mathbf{r})$ are fermionic annihilation field operators of nuclear spin m in the ground manifold and nuclear spin m' in the excited manifold respectively.

For spatially antisymmetric p-wave interactions, antisymmetric nuclear spin states require their electronic orbitals to be antisymmetric for an antisymmetric total wavefunction, so the only possible electronic state is $(|ge\rangle - |eg\rangle)/\sqrt{2}$, which interacts via the p-wave scattering volume $(b_{eg}^{-})^3$. Symmetric nuclear spin states require their electronic orbitals to be symmetric, so the three possible electronic states are $|gg\rangle$, $|ee\rangle$, $(|ge\rangle + |eg\rangle)/\sqrt{2}$, which interact via the p-wave scattering volumes b_{gg}^3, b_{ee}^3 and $(b_{eg}^{+})^3$ respectively. The p-wave pseudopotential for SU(n) interactions takes the following form: $\hat{V}_p^{gg}(\mathbf{r}_{12}) \propto b_{gg}^3\hat{\mathcal{P}}_{+}$, $\hat{V}_p^{ee}(\mathbf{r}_{12}) \propto b_{ee}^3\hat{\mathcal{P}}_{+}$, $\hat{V}_p^{eg}(\mathbf{r}_{12}) \propto [(b_{eg}^{+})^3 + (b_{eg}^{-})^3]\hat{\mathcal{I}}/2 + [(b_{eg}^{+})^3 - (b_{eg}^{-})^3]\hat{\mathcal{P}}_{12}/2$.

This leads to the p-wave interaction Hamiltonian in the second quantized form,

$$\begin{aligned}\hat{H}_p = &\frac{3\pi\hbar^2 b_{gg}^3}{2M}\sum_{mm'}\int d^3\mathbf{r}\,[(\nabla\hat{\psi}^\dagger_{gm})\hat{\psi}^\dagger_{gm'} - \hat{\psi}^\dagger_{gm}(\nabla\hat{\psi}^\dagger_{gm'})]\cdot[\hat{\psi}_{gm'}(\nabla\hat{\psi}_{gm}) - (\nabla\hat{\psi}_{gm'})\hat{\psi}_{gm}]\\
&+\frac{3\pi\hbar^2 b_{ee}^3}{2M}\sum_{mm'}\int d^3\mathbf{r}\,[(\nabla\hat{\psi}^\dagger_{em})\hat{\psi}^\dagger_{em'} - \hat{\psi}^\dagger_{em}(\nabla\hat{\psi}^\dagger_{em'})]\cdot[\hat{\psi}_{em'}(\nabla\hat{\psi}_{em}) - (\nabla\hat{\psi}_{em'})\hat{\psi}_{em}]\\
&+\frac{3\pi\hbar^2[(b_{eg}^+)^3 + (b_{eg}^-)^3]}{2M}\sum_{mm'}\int d^3\mathbf{r}\,[(\nabla\hat{\psi}^\dagger_{gm})\hat{\psi}^\dagger_{em'} - \hat{\psi}^\dagger_{gm}(\nabla\hat{\psi}^\dagger_{em'})]\cdot[\hat{\psi}_{em'}(\nabla\hat{\psi}_{gm}) - (\nabla\hat{\psi}_{em'})\hat{\psi}_{gm}]\\
&+\frac{3\pi\hbar^2[(b_{eg}^+)^3 - (b_{eg}^-)^3]}{2M}\sum_{mm'}\int d^3\mathbf{r}\,[(\nabla\hat{\psi}^\dagger_{gm})\hat{\psi}^\dagger_{em'} - \hat{\psi}^\dagger_{gm}(\nabla\hat{\psi}^\dagger_{em'})]\cdot[\hat{\psi}_{em}(\nabla\hat{\psi}_{gm'}) - (\nabla\hat{\psi}_{em})\hat{\psi}_{gm'}].\end{aligned} \tag{2.134}$$

In an optical lattice clock experiment, we consider the least magnetically sensitive clock transition in ^{87}Sr, $|^1S_0, m_F = \pm 5/2\rangle \to |^3P_0, m_F = \pm 3/2\rangle$, denoted by $|\tilde{g}\rangle$ and $|\tilde{e}\rangle$ respectively. In a large magnetic field, the flip-flop process of nuclear spin states in Eq. (2.133) and Eq. (2.134) can be ignored, so the interaction Hamiltonian including s-wave and p-wave contributions can be restricted to these two states,

$$\begin{aligned}\hat{H}_{\text{int}} = &\frac{2\pi\hbar^2(a_{eg}^- + a_{eg}^+)}{M}\int d^3\mathbf{r}\,\hat{\psi}^\dagger_{\tilde{e}}(\mathbf{r})\hat{\psi}^\dagger_{\tilde{g}}(\mathbf{r})\hat{\psi}_{\tilde{g}}(\mathbf{r})\hat{\psi}_{\tilde{e}}(\mathbf{r})\\
&+\frac{3\pi\hbar^2 b_{gg}^3}{2M}\int d^3\mathbf{r}\,[(\nabla\hat{\psi}^\dagger_{\tilde{g}})\hat{\psi}^\dagger_{\tilde{g}} - \hat{\psi}^\dagger_{\tilde{g}}(\nabla\hat{\psi}^\dagger_{\tilde{g}})]\cdot[\hat{\psi}_{\tilde{g}}(\nabla\hat{\psi}_{\tilde{g}}) - (\nabla\hat{\psi}_{\tilde{g}})\hat{\psi}_{\tilde{g}}]\\
&+\frac{3\pi\hbar^2 b_{ee}^3}{2M}\int d^3\mathbf{r}\,[(\nabla\hat{\psi}^\dagger_{\tilde{e}})\hat{\psi}^\dagger_{\tilde{e}} - \hat{\psi}^\dagger_{\tilde{e}}(\nabla\hat{\psi}^\dagger_{\tilde{e}})]\cdot[\hat{\psi}_{\tilde{e}}(\nabla\hat{\psi}_{\tilde{e}}) - (\nabla\hat{\psi}_{\tilde{e}})\hat{\psi}_{\tilde{e}}]\\
&+\frac{3\pi\hbar^2[(b_{eg}^+)^3 + (b_{eg}^-)^3]}{2M}\int d^3\mathbf{r}\,[(\nabla\hat{\psi}^\dagger_{\tilde{g}})\hat{\psi}^\dagger_{\tilde{e}} - \hat{\psi}^\dagger_{\tilde{g}}(\nabla\hat{\psi}^\dagger_{\tilde{e}})]\cdot[\hat{\psi}_{\tilde{e}}(\nabla\hat{\psi}_{\tilde{g}}) - (\nabla\hat{\psi}_{\tilde{e}})\hat{\psi}_{\tilde{g}}].\end{aligned} \tag{2.135}$$

Another convenient choice of clock transition in ^{87}Sr is $|^1S_0, m_F = \pm 9/2\rangle \to |^3P_0, m_F = \pm 9/2\rangle$, also denoted by $|\tilde{g}\rangle$ and $|\tilde{e}\rangle$ respectively. In this case with the same nuclear spin state, the eg collision is described by a_{eg}^- for s-wave and $(b_{eg}^+)^3$ for p-wave, so the interaction Hamiltonian within these two states is given by

$$\begin{aligned}\hat{H}_{\text{int}} = &\frac{4\pi\hbar^2 a_{eg}^-}{M}\int d^3\mathbf{r}\,\hat{\psi}^\dagger_{\tilde{e}}(\mathbf{r})\hat{\psi}^\dagger_{\tilde{g}}(\mathbf{r})\hat{\psi}_{\tilde{g}}(\mathbf{r})\hat{\psi}_{\tilde{e}}(\mathbf{r})\\
&+\frac{3\pi\hbar^2 b_{gg}^3}{2M}\int d^3\mathbf{r}\,[(\nabla\hat{\psi}^\dagger_{\tilde{g}})\hat{\psi}^\dagger_{\tilde{g}} - \hat{\psi}^\dagger_{\tilde{g}}(\nabla\hat{\psi}^\dagger_{\tilde{g}})]\cdot[\hat{\psi}_{\tilde{g}}(\nabla\hat{\psi}_{\tilde{g}}) - (\nabla\hat{\psi}_{\tilde{g}})\hat{\psi}_{\tilde{g}}]\\
&+\frac{3\pi\hbar^2 b_{ee}^3}{2M}\int d^3\mathbf{r}\,[(\nabla\hat{\psi}^\dagger_{\tilde{e}})\hat{\psi}^\dagger_{\tilde{e}} - \hat{\psi}^\dagger_{\tilde{e}}(\nabla\hat{\psi}^\dagger_{\tilde{e}})]\cdot[\hat{\psi}_{\tilde{e}}(\nabla\hat{\psi}_{\tilde{e}}) - (\nabla\hat{\psi}_{\tilde{e}})\hat{\psi}_{\tilde{e}}]\\
&+\frac{3\pi\hbar^2 (b_{eg}^+)^3}{M}\int d^3\mathbf{r}\,[(\nabla\hat{\psi}^\dagger_{\tilde{g}})\hat{\psi}^\dagger_{\tilde{e}} - \hat{\psi}^\dagger_{\tilde{g}}(\nabla\hat{\psi}^\dagger_{\tilde{e}})]\cdot[\hat{\psi}_{\tilde{e}}(\nabla\hat{\psi}_{\tilde{g}}) - (\nabla\hat{\psi}_{\tilde{e}})\hat{\psi}_{\tilde{g}}].\end{aligned} \tag{2.136}$$

2.2.5 Approximations for many-body dynamics

Here we use the following Hamiltonian $\hat{H}$ containing the single-particle Hamiltonian $\hat{H}_0$ and the s-wave interaction for fermions $\hat{H}_s$,

$$\begin{aligned} \hat{H} &= \hat{H}_0 + \hat{H}_s, \\ \hat{H}_0 &= \sum_{\alpha=\{e,g\}} \int d^3\mathbf{r}\, \hat{\psi}_\alpha^\dagger(\mathbf{r}) \Big[-\frac{\hbar^2}{2M}\nabla^2 + V(\mathbf{r}) \Big] \hat{\psi}_\alpha(\mathbf{r}), \\ \hat{H}_s &= \frac{4\pi\hbar^2 a_{eg}}{M} \int d^3\mathbf{r}\, \hat{\psi}_e^\dagger(\mathbf{r}) \hat{\psi}_g^\dagger(\mathbf{r}) \hat{\psi}_g(\mathbf{r}) \hat{\psi}_e(\mathbf{r}), \end{aligned} \tag{2.137}$$

to illustrate the key ideas of the approximations we made in this thesis for analyzing many-body dynamics. We typically assume the single-particle Hamiltonian $\hat{H}_0$ has eigenstates $\phi_j(\mathbf{r})$ with corresponding eigenenergies E_j, with j the eigenstate index.

When the interaction strength is weak compared to the single-particle energy gap ($\Delta E = \min(E_{j+1} - E_j)$), we prefer to expand the field operators using the eigenbasis of $\hat{H}_0$,

$$\hat{\psi}_\alpha(\mathbf{r}) = \sum_{j\alpha} \hat{c}_{j\alpha} \phi_j(\mathbf{r}), \tag{2.138}$$

where $\hat{c}_{j\alpha}$ is the fermonic annihilation operator for state $|\alpha; j\rangle$. The interaction Hamiltonian becomes

$$\hat{H}_s = \sum_{ijkl} U_{ijkl} \hat{c}_{ie}^\dagger \hat{c}_{jg}^\dagger \hat{c}_{kg} \hat{c}_{le}, \quad U_{ijkl} = \frac{4\pi\hbar^2 a_{eg}}{M} \int d^3\mathbf{r} \phi_i^*(\mathbf{r}) \phi_j^*(\mathbf{r}) \phi_k(\mathbf{r}) \phi_l(\mathbf{r}). \tag{2.139}$$

Then we only keep the interaction processes conserving the total single-particle energy, since the other processes would be off-resonant due to the energy penalty. Typically there are two types of processes conserving the total single-particle energy:

- Direct coupling U_{ijji}, i.e. $|e; i\rangle|g; j\rangle \to |e; i\rangle|g; j\rangle$,
- Exchange coupling U_{ijij}, i.e. $|e; i\rangle|g; j\rangle \to |g; i\rangle|e; j\rangle$.

In these two types of processes, atoms are frozen in the single-particle eigenmodes and only feature spin dynamics between e and g states, thus this procedure is called frozen-mode approximation.

Under this approximation, $\hat{H}_0$ becomes a constant, and

$$\begin{aligned}\hat{H}_s &\approx \sum_{ij}(U_{ijji}\hat{c}_{ie}^\dagger\hat{c}_{jg}^\dagger\hat{c}_{jg}\hat{c}_{ie} + U_{ijij}\hat{c}_{ie}^\dagger\hat{c}_{jg}^\dagger\hat{c}_{ig}\hat{c}_{je}) \\ &\approx \frac{1}{2}\sum_{ij} J_{ij}(\hat{c}_{ie}^\dagger\hat{c}_{ie}\hat{c}_{jg}^\dagger\hat{c}_{jg} + \hat{c}_{ig}^\dagger\hat{c}_{ig}\hat{c}_{je}^\dagger\hat{c}_{je} - \hat{c}_{ie}^\dagger\hat{c}_{ig}\hat{c}_{jg}^\dagger\hat{c}_{je} - \hat{c}_{je}^\dagger\hat{c}_{jg}\hat{c}_{ig}^\dagger\hat{c}_{ie}),\end{aligned} \tag{2.140}$$

where $J_{ij} = U_{ijji} = U_{ijij}$, and we also assume no double occupancy in a single eigenmode. For fermions, this condition is strictly ensured by Pauli blocking if we initialize all the atoms in the same internal state. Similar idea can also apply to non-degenerate bosons, and this condition is ensured by low double occupancy probability under thermal distribution.

Now we define spin operators as

$$\begin{aligned}\hat{S}_j^x = \frac{1}{2}(\hat{c}_{je}^\dagger\hat{c}_{jg} + \hat{c}_{jg}^\dagger\hat{c}_{je}), \quad \hat{S}_j^y = -\frac{i}{2}(\hat{c}_{je}^\dagger\hat{c}_{jg} - \hat{c}_{jg}^\dagger\hat{c}_{je}), \\ \hat{S}_j^z = \frac{1}{2}(\hat{c}_{je}^\dagger\hat{c}_{je} - \hat{c}_{jg}^\dagger\hat{c}_{jg}), \quad \hat{N}_j = \hat{c}_{je}^\dagger\hat{c}_{je} + \hat{c}_{jg}^\dagger\hat{c}_{jg}.\end{aligned} \tag{2.141}$$

The interaction Hamiltonian $\hat{H}_s$ can be rewritten as

$$\begin{aligned}\hat{H}_s &\approx \frac{1}{2}\sum_{ij} J_{ij}\Big((\hat{N}_i/2 + \hat{S}_i^z)(\hat{N}_j/2 - \hat{S}_j^z) + (\hat{N}_i/2 - \hat{S}_i^z)(\hat{N}_j/2 + \hat{S}_j^z) - 2(\hat{S}_i^x\hat{S}_j^x + \hat{S}_i^y\hat{S}_j^y)\Big) \\ &= -\sum_{ij} J_{ij}\hat{\mathbf{S}}_i\cdot\hat{\mathbf{S}}_j,\end{aligned} \tag{2.142}$$

in which we drop the constant term $\hat{N}_i\hat{N}_j$. In this way, we approximate $\hat{H}_s$ as Heisenberg spin-spin interactions. In this thesis, we generalize this result to the case when the eigenmodes for e and g states are different, labelled by $\phi_{j\alpha}(\mathbf{r})$. In this case, we have $U_{ijji} \neq U_{ijij}$, which allows us to add anisotropy to the Heisenberg interactions. It is worth to mention that there might be mode-changing collisions $|e;j_1\rangle|g;j_2\rangle \to |e;j_3\rangle|g;j_4\rangle$ accidentally satisfying $E_{j_1} + E_{j_2} \approx E_{j_3} + E_{j_4}$, especially in harmonic oscillator potential with equally spacing energy levels. Since there is no initial coherence for the mode-changing processes (start from vacuum), it is still safe to ignore mode-changing processes for short-time dynamics, while for a longer time scale these processes can lead to decoherence of the spin dynamics.

On the other hand, when the interaction strength is strong compared to the single-particle energy gap, we prefer to expand the field operators using the a maximally localized basis, e.g. the

maximally localized Wannier states in an optical lattice. Here we denote the wave function in the maximally localized basis by $w_j(\mathbf{r})$, where j is the position index. In this case we can ignore the processes with non-local interactions due to the negligible wave function overlap, so the interaction Hamiltonian becomes

$$\hat{H}_s \approx \sum_j U_j \hat{c}^\dagger_{je}\hat{c}_{je}\hat{c}^\dagger_{jg}\hat{c}_{jg}, \quad U_j = \frac{4\pi\hbar^2 a_{eg}}{M}\int d^3\mathbf{r}|w_j(\mathbf{r})|^4. \tag{2.143}$$

Note that in this basis $\hat{H}_0$ is not a diagonal matrix, and the leading order off-diagonal term is the nearest neighbor tunneling due to the maximally localized basis. So the system Hamiltonian can be approximated as

$$\hat{H} \approx -\sum_{\langle ij\rangle\alpha}(\tau_{ij}\hat{c}^\dagger_{i\alpha}\hat{c}_{j\alpha} + \text{H.c.}) + \sum_j U_j \hat{c}^\dagger_{je}\hat{c}_{je}\hat{c}^\dagger_{jg}\hat{c}_{jg}, \tag{2.144}$$

where $\tau_{ij} = -\int d^3\mathbf{r} w_i^*(\mathbf{r})\hat{H}_0 w_j(\mathbf{r})$ are tunneling rates, $\langle ij\rangle$ means the nearest neighbor pairs. The Hamiltonian above with τ_{ij} and U_j translational invariant is the so-called Fermi Hubbard model, which is an iconic model for understanding strongly correlated materials.

Here we show the Fermi-Hubbard Hamiltonian in 1D to simplify the discussions,

$$\hat{H}_{\text{FH}} = -\tau\sum_j(\hat{c}^\dagger_{j\alpha}\hat{c}_{j+1,\alpha} + \text{H.c.}) + U\sum_j \hat{c}^\dagger_{je}\hat{c}_{je}\hat{c}^\dagger_{jg}\hat{c}_{jg}. \tag{2.145}$$

In this thesis, we typically focus on the Mott insulator regime with $U \gg \tau$, where the double-occupied states are separated by a large energy gap $\sim U$, allowing us to restrict of dynamics in the single-occupied states via second-order perturbation theory (see Appendix A). In the case of half filling, we get an effective Hamiltonian describing superexchange interactions,

$$\hat{H}_{\text{eff}} = J_{\text{SE}}\sum_j\left(\hat{\mathbf{S}}_j\cdot\hat{\mathbf{S}}_{j+1} - \frac{1}{4}\right), \quad J_{\text{SE}} = \frac{4\tau^2}{U}. \tag{2.146}$$

The spin operators are defined as Eq. (2.141), while the j means 1D lattice site index here.

2.3 Spin systems

In this section, we introduce a variety of tools for the theory treatment of spin systems. Firstly we discuss the boson representation of spins, including Holstein-Primakoff bosons and Schwinger

bosons. Then we focus on the phase space representation of spins, including the Wigner function, the Glauber-P function and the Husimi-Q function. Finally we discuss the tensor product space of spin-1/2 operators and its subspaces including the Dicke manifold and the spin-wave manifold.

2.3.1 Boson representation of spins

The spin operators (SU(2) generators) are vector operators obeying the following commutation relations,

$$[\hat{S}^\alpha, \hat{S}^\beta] = i\epsilon_{\alpha\beta\gamma}\hat{S}^\gamma, \tag{2.147}$$

where α, β, γ run over x, y, z. We also define $\hat{S}^\pm = \hat{S}^x \pm i\hat{S}^y$, and the commutation relation becomes

$$[\hat{S}^z, \hat{S}^\pm] = \pm\hat{S}^\pm, \quad [\hat{S}^+, \hat{S}^-] = 2\hat{S}^z. \tag{2.148}$$

The idea of the Holstein-Primakoff representation is to introduce a bosonic operator $\hat{b}$ to represent the spin operators as follows [63]:

$$\hat{S}^+ = (2S - \hat{b}^\dagger\hat{b})^{1/2}\,\hat{b}, \quad \hat{S}^- = \hat{b}^\dagger\,(2S - \hat{b}^\dagger\hat{b})^{1/2}, \quad \hat{S}^z = S - \hat{b}^\dagger\hat{b}. \tag{2.149}$$

Here we consider spin-S operators satisfying $\hat{\mathbf{S}}\cdot\hat{\mathbf{S}} = \hat{S}^x\hat{S}^x + \hat{S}^y\hat{S}^y + \hat{S}^z\hat{S}^z = S(S+1)$, with S integers or half-integers. Using the commutation relation $[\hat{b}, \hat{b}^\dagger] = 1$, one can check that the Holstein-Primakoff representation above agrees with the spin commutation relations (see Eq. (2.148)). The spin-wave theory is based on Holstein-Primakoff representation assuming $2S \gg \langle\hat{b}^\dagger\hat{b}\rangle$. So we can insert Eq. (2.149) into the spin Hamiltonian and keep the terms up to quadratic order of bosonic operators. Note that Eq. (2.148) is a special case when the spin-wave expansion is near the $|S^z = S\rangle$ state. In general, one can perform arbitrary rotation to the LHS of Eq. (2.148) and consider spin-wave expansion near any spin coherent states (see definition in the next subsection).

The idea of the Schwinger representation is to introduce bosonic operators $\hat{a}$ and $\hat{b}$ to represent the spin operators as follows [63]:

$$\hat{S}^+ = \hat{a}^\dagger\hat{b}, \quad \hat{S}^- = \hat{b}^\dagger\hat{a}, \quad \hat{S}^z = \frac{1}{2}(\hat{a}^\dagger\hat{a} - \hat{b}^\dagger\hat{b}). \tag{2.150}$$

For spin-S operators satisfying $\hat{\mathbf{S}} \cdot \hat{\mathbf{S}} = S(S+1)$, we have a constraint $\hat{a}^\dagger \hat{a} + \hat{b}^\dagger \hat{b} = 2S$. One can check that the Schwinger representation above agrees with the spin commutation relations (see Eq. (2.148)). In terms of Schwinger bosons, we can represent the spin states as

$$|S, m\rangle = \frac{(\hat{a}^\dagger)^{S+m}}{\sqrt{(S+m)!}} \frac{(\hat{b}^\dagger)^{S-m}}{\sqrt{(S-m)!}} |\text{vac}\rangle. \tag{2.151}$$

Since the spin operators are generators of the SU(2) group, we can parametrize the SU(2) group members by three Euler angles ϕ, θ, χ,

$$\hat{\mathcal{R}}(\chi, \theta, \phi) = e^{i\phi \hat{S}^z} e^{i\theta \hat{S}^y} e^{i\chi \hat{S}^z}. \tag{2.152}$$

Using the Baker–Campbell–Hausdorff formula,

$$e^X Y e^{-X} = Y + [X, Y] + \frac{[X, [X, Y]]}{2!} + \frac{[X, [X, [X, Y]]]}{3!} + \cdots, \tag{2.153}$$

we get the transformation rules for Schwinger bosons,

$$\begin{pmatrix} \hat{\tilde{a}}^\dagger \\ \hat{\tilde{b}}^\dagger \end{pmatrix} = \hat{\mathcal{R}} \begin{pmatrix} \hat{a}^\dagger \\ \hat{b}^\dagger \end{pmatrix} \hat{\mathcal{R}}^{-1} = \begin{pmatrix} u e^{i\chi/2} & v e^{i\chi/2} \\ -v^* e^{-i\chi/2} & u^* e^{-i\chi/2} \end{pmatrix} \begin{pmatrix} \hat{a}^\dagger \\ \hat{b}^\dagger \end{pmatrix}, \tag{2.154}$$

where

$$u = \cos(\theta/2) e^{i\phi/2}, \quad v = \sin(\theta/2) e^{-i\phi/2}. \tag{2.155}$$

The Schwinger boson representation can be easily generalized to the case of SU(n) generators by increasing the number of Schwinger boson flavors from 2 to n, $(\hat{a}, \hat{b}) \to (\hat{a}_1, \hat{a}_2, \cdots, \hat{a}_n)$. The SU($n$) generators can be expressed as [63]

$$\hat{S}^{mm'} = \hat{a}_m^\dagger \hat{a}_{m'}, \tag{2.156}$$

which satisfying the SU(n) commutation relation,

$$[\hat{S}^{mm'}, \hat{S}^{\mu\mu'}] = \delta_{m'\mu} \hat{S}^{m\mu'} - \delta_{m\mu'} \hat{S}^{\mu m'}. \tag{2.157}$$

Similar to the constraint in SU(2) case, the SU(n) Schwinger bosons have the constraint

$$\sum_{m=1}^{n} \hat{a}_m^\dagger \hat{a}_m = 0, 1, 2, \cdots. \tag{2.158}$$

2.3.2 Phase space representation of spins

The phase space representation of spins is based on spin coherent states, which is an analogy of the phase space representation of bosons based on bosonic coherent states (see Appendix D). A spin coherent state is defined by applying the rotation operator $\hat{R}(\theta,\phi) \equiv \hat{R}(\chi=0,\theta,\phi)$ to the maximally polarized state $|S,S\rangle$ (see Eq. (2.152)) [63],

$$|\theta,\phi\rangle = \hat{R}(\theta,\phi)|S,S\rangle = \sum_{m=-S}^{S} \sqrt{\binom{2S}{S+m}} u^{S+m} v^{S-m} |S,m\rangle. \tag{2.159}$$

where $\binom{n}{k}$ are binomial coefficients, and u, v are given by Eq. (2.155). Note that different spin coherent states are not orthogonal,

$$\langle\theta,\phi|\theta',\phi'\rangle = (u^* u' + v^* v')^{2S}, \tag{2.160}$$

and thus form an overcomplete basis,

$$\frac{2S+1}{4\pi} \int \sin\theta d\theta d\phi |\theta,\phi\rangle\langle\theta,\phi| = \hat{I}. \tag{2.161}$$

We then introduce the concept of the multipole operators [64],

$$\hat{T}_{kq} = \sum_{mm'} (-1)^{S-m} \sqrt{2k+1} \begin{pmatrix} S & k & S \\ -m & q & m' \end{pmatrix} |S,m\rangle\langle S,m'|, \tag{2.162}$$

where the matrix in round brackets is the Wigner-3j symbol. Note that $\hat{T}_{kq}$ are spherical tensor operators (see Appendix B). The multipole operators satisfies the following orthogonality property:

$$\mathrm{Tr}[\hat{T}^\dagger_{k_1 q_1} \hat{T}_{k_2 q_2}] = \delta_{k_1 k_2} \delta_{q_1 q_2}, \quad \hat{T}^\dagger_{kq} = (-1)^q \hat{T}_{k,-q}. \tag{2.163}$$

Thus any operators acting on the spin Hilbert space can be expanded in terms of the multipole operators,

$$\hat{O} = \sum_{k=0}^{2S} \sum_{q=-k}^{k} O_{kq} \hat{T}_{kq}, \quad O_{kq} = \mathrm{Tr}[\hat{O}\hat{T}^\dagger_{kq}]. \tag{2.164}$$

As discussed in Ref. [64], one can define the kernel operator

$$\hat{\Delta}^{(\Omega)}(\theta,\phi) = \sum_{kq} \Omega_{kq} Y^*_{kq}(\theta,\phi) \hat{T}_{kq}, \tag{2.165}$$

as well as the inverse kernel operator

$$\hat{\Delta}^{(\tilde{\Omega})}(\theta,\phi)=\sum_{kq}\tilde{\Omega}_{kq}Y_{kq}^{*}(\theta,\phi)\hat{T}_{kq}, \tag{2.166}$$

where $\tilde{\Omega}_{kq}=[\Omega_{k,-q}]^{-1}$, and $Y_{kq}(\theta,\phi)$ are spherical harmonics. Different choice of filter function Ω_{kq} leads to different types of phase space representation as we will discuss later. Based on the orthogonality property of multipole operators, one can prove that

$$\mathrm{Tr}[\hat{\Delta}^{(\Omega)}(\theta_1,\phi_1)\hat{\Delta}^{(\tilde{\Omega})}(\theta_2,\phi_2)]=\delta(\cos\theta_1-\cos\theta_2)\delta(\phi_1-\phi_2). \tag{2.167}$$

Based on Eq. (2.167), one can establish a mapping between the operator $\hat{O}$ and the c-number function $F^{(\Omega)}(\theta,\phi)$ using the kernel operators,

$$\hat{O}=\int\sin\theta d\theta d\phi F^{(\Omega)}(\theta,\phi)\hat{\Delta}^{(\Omega)}(\theta,\phi), \tag{2.168}$$

$$F^{(\Omega)}(\theta,\phi)=\mathrm{Tr}[\hat{O}\hat{\Delta}^{(\tilde{\Omega})}(\theta,\phi)]. \tag{2.169}$$

We call the c-number function $F^{(\Omega)}(\theta,\phi)$ as phase space representation of operator $\hat{O}$. A special case is that the operator $\hat{O}$ is the density matrix $\hat{\rho}$, and in this case the c-number function $F_{\rho}^{(\Omega)}(\theta,\phi)$ is called phase space representation of a quantum state. Since $\mathrm{Tr}[\hat{\rho}]=1$, we have

$$\sqrt{\frac{2S+1}{4\pi}}\Omega_{0,0}\int\sin\theta d\theta d\phi F_{\rho}^{(\Omega)}(\theta,\phi)=1. \tag{2.170}$$

So one can interpret $F^{(\Omega)}(\theta,\phi)$ under proper normalization as a quasi-probability distribution in phase space. Also based on Eq. (2.167), it is clear that

$$\mathrm{Tr}[\hat{O}_1\hat{O}_2]=\int\sin\theta d\theta d\phi F^{(\Omega)}(\theta,\phi)F^{(\tilde{\Omega})}(\theta,\phi). \tag{2.171}$$

Here we introduce some examples of the filter function Ω_{kq}:

- Wigner representation

$$\Omega_{kq}=\tilde{\Omega}_{kq}=1. \tag{2.172}$$

  Here we use $W(\theta,\phi)$ to represent the c-number function $F_{\rho}^{(W)}(\theta,\phi)$ for density matrix $\hat{\rho}$. In this case we have

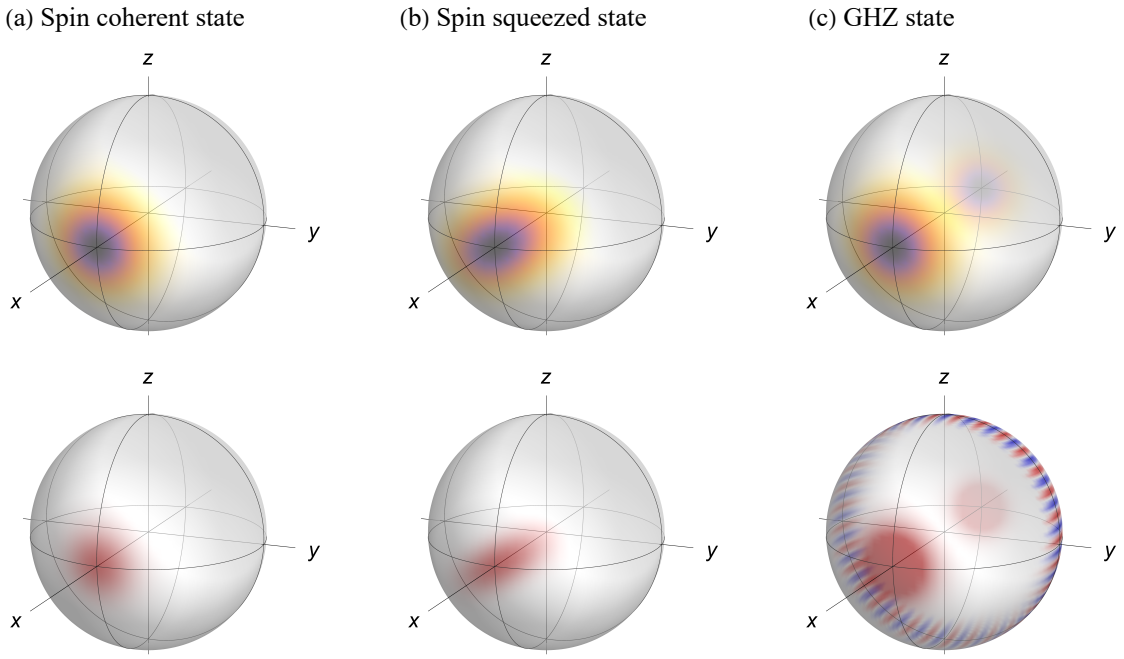

Figure 2.4: Examples of the Husimi Q-representation (above) and the Wigner representation (below) for collective spin states with 32 atoms, including (a) spin coherent state, (b) spin squeezed state, and (c) GHZ state. See Chapter 2.5 for definitions of the spin squeezed state and the GHZ state. For the Wigner representation, the red/blue color means the positive/negative sign.

$$\hat{\Delta}^{(W)}(\theta,\phi) = \sum_{kq} Y^*_{kq}(\theta,\phi)\hat{T}_{kq}, \tag{2.173}$$

$$W(\theta,\phi) = \sum_{kq} \rho_{kq} Y_{kq}(\theta,\phi), \quad \rho_{kq} = \mathrm{Tr}[\hat{\rho}\hat{T}^\dagger_{kq}]. \tag{2.174}$$

- Glauber P-representation (Ω_{kq}), Husimi Q-representation ($\tilde{\Omega}_{kq}$)

$$\Omega_{kq} = (-1)^{k-q}\frac{1}{\sqrt{4\pi}}\frac{(2S+1)!}{[(2S-k)!\,(2S+k+1)!\,]^{1/2}}. \tag{2.175}$$

Here we use $P(\theta,\phi)$ to represent the c-number function $F^{(P)}_\rho(\theta,\phi)$, and $Q(\theta,\phi)$ to represent the c-number function $F^{(Q)}_\rho(\theta,\phi)$. Using the fact that

$$\langle\theta,\phi|\hat{T}^\dagger_{kq}|\theta,\phi\rangle = Y^*_{kq}(\theta,\phi)(-1)^{k-q}\sqrt{4\pi}\frac{(2S)!}{[(2S-k)!\,(2S+k+1)!\,]^{1/2}}, \tag{2.176}$$

we have

$$\hat{\Delta}^{(P)}(\theta,\phi) = |\theta,\phi\rangle\langle\theta,\phi|, \tag{2.177}$$

which gives

$$\hat{\rho} = \int \sin\theta d\theta d\phi P(\theta,\phi)|\theta,\phi\rangle\langle\theta,\phi|. \tag{2.178}$$

On the other hand, we have

$$\langle\theta',\phi'|\hat{\Delta}^{(Q)}(\theta,\phi)|\theta',\phi'\rangle = \frac{4\pi}{2S+1}\delta(\cos\theta-\cos\theta')\delta(\phi-\phi'), \tag{2.179}$$

which gives

$$Q(\theta,\phi) = \frac{2S+1}{4\pi}\langle\theta,\phi|\hat{\rho}|\theta,\phi\rangle. \tag{2.180}$$

Notice that

$$\int \sin\theta d\theta d\phi Q(\theta,\phi) = 1. \tag{2.181}$$

In Fig. 2.4, we show examples of the Husimi Q-representation and the Wigner representation for different kinds of collective spin states.

2.3.3 Tensor product of spin-1/2 systems

Here we focus on the spin system with N spin-1/2 particles. Based on the addition of angular momentum, one can decompose the Hilbert space into subspaces of total spin $S = N/2, N/2-1, \cdots, N/2-\lfloor N/2\rfloor$. If we use $(\mathbf{2S+1})$ to label the Hilbert space of a spin-S particle (dimension $2S+1$), one can prove that

$$\mathbf{2}^{\otimes N} = \bigoplus_{k=0}^{\lfloor N/2\rfloor} \eta_k(\mathbf{N+1-2k}), \quad \eta_k = \frac{N-2k+1}{N-k+1}\binom{N}{k}, \tag{2.182}$$

where $\binom{N}{k}$ is binomial coefficients, $\otimes$ represents tensor product, and $\oplus$ represents direct sum. For clarification, we multiply the dimensions of Hilbert spaces for tensor product, while we sum the dimensions of Hilbert spaces for direct sum. The coefficients η_k means direct sum of η_k copies of Hilbert spaces. Here we briefly discuss the key idea of calculating η_k: Following the addition of angular momentum, η_k is the number of ways to construct a sequence with $n-k$ copies of $+1$

and k copies of -1 such that the partial sums of the sequence are always non-negative. Based on Ref. [65], we can describe η_k by Catalan's triangle, which gives rise to Eq. (2.182). For example, we have $\eta_0 = 1$ for $S = N/2$, $\eta_1 = N - 1$ for $S = N/2 - 1$, and $\eta_{N/2} = \binom{N}{N/2}/(N/2+1)$ for $S = 0$ (assuming N is a even number).

The subspace with $S = N/2$ is the so-called Dicke manifold, which contains all the permutationally symmetric states,

$$|\psi\rangle \propto \sum_{\mathcal{P}} |\psi_{\mathcal{P}(1)}\rangle_1 \otimes |\psi_{\mathcal{P}(2)}\rangle_2 \otimes \cdots \otimes |\psi_{\mathcal{P}(N)}\rangle_N, \tag{2.183}$$

where $\mathcal{P}$ is a permutation operation mapping particle indices $j \to \mathcal{P}(j)$, and we sum over all the possible permutations. The proof of the statement is straightforward: We start from the state with all the particles in the $|\downarrow\rangle$ state, which is the state $|S = N/2, m = -N/2\rangle$. Then we apply the operator $\hat{S}^+ = \sum_j \hat{S}_j^+$ multiple times to the state $|N/2, -N/2\rangle$ to get the other basis states of $S = N/2$. Since the operator $\hat{S}^+$ is permutationally symmetric, all the basis states (Dicke states) $|N/2, m\rangle$ should be permutationally symmetric. The states in the Dicke manifold are the ground state of the infinite-range ferromagnetic Heisenberg model, $\hat{H} = -J\hat{\mathbf{S}} \cdot \hat{\mathbf{S}}$ with $J > 0$.

The subspace with $S = N/2 - 1$ is the so-called spin-wave manifold, since the states in this subspace are spin-wave excitations of the ferromagnetic Heisenberg model. We typically construct the states based on Dicke states. First we can prove that a single spin flip on the Dicke state, $\hat{S}_j^+|N/2, m-1\rangle$, should be a superposition of states in the Dicke manifold ($S = N/2$) and spin-wave manifold ($S = N/2-1$) with the same magnetization m_S. This is because we can consider the addition of angular momentum for particle j ($S_j = 1/2$) and the other particles ($S_{\text{other}} = (N-1)/2$ with permutation symmetry), which gives $S = N/2$ or $S = N/2 - 1$. Therefore, $\hat{S}_j^+|N/2, m-1\rangle$ states with $j = 0, \cdots, N-1$ form a linear independent (not orthogonal) basis for the states with m_S in the Dicke manifold and spin-wave manifold. So we can diagonalize the following matrix,

$$A_{jl} = \langle N/2, m-1|\hat{S}_j^- \hat{S}_l^+|N/2, m-1\rangle, \tag{2.184}$$

to obtain a orthonormal basis of these states. Based on the permutation symmetry of Dicke state

$|N/2, m-1\rangle$, we have

$$A_{jj} = \frac{N/2-m+1}{N}, \quad A_{jl} = \frac{(N/2-m+1)(N/2+m-1)}{N(N-1)} \quad (j \neq l). \tag{2.185}$$

Note that the matrix A_{jl} is a circulant matrix, whose eigenvectors are the Fourier modes $v_k = (1, e^{i2\pi\, k/N}, e^{i2\pi\, 2k/N}, \cdots, e^{i2\pi\,(N-1)k/N})$, with $k = 0, \cdots, N-1$. Since permutation symmetry ensures there is only one Dicke state $|N/2, m\rangle$ with $k = 0$,

$$|N/2, m\rangle = \frac{1}{\sqrt{(N/2+m)(N/2-m+1)}} \sum_j \hat{S}_j^+ |N/2, m-1\rangle, \tag{2.186}$$

the other $N-1$ states lie in the spin-wave manifold with $k = 1, \cdots, N-1$,

$$|N/2-1, m, k\rangle = \sqrt{\frac{N-1}{(N/2-m)(N/2-m+1)}} \sum_j e^{i2\pi kj/N} \hat{S}_j^+ |N/2, m-1\rangle. \tag{2.187}$$

The following matrix elements are useful for perturbative calculations (note that there are typos in the formula of $\langle N/2, m|\hat{S}_j^+|N/2-1, m-1, k\rangle$ in Ref. [66]),

$$\langle N/2, m|\hat{S}_j^z|N/2, m\rangle = \frac{m}{N}, \tag{2.188}$$

$$\langle N/2, m|\hat{S}_j^z|N/2-1, m, k\rangle = e^{i2\pi kj/N} \sqrt{\frac{(N/2)^2-m^2}{N^2(N-1)}}, \tag{2.189}$$

$$\langle N/2, m|\hat{S}_j^+|N/2, m-1\rangle = \sqrt{\frac{(N/2+m)(N/2-m+1)}{N^2}}, \tag{2.190}$$

$$\langle N/2, m|\hat{S}_j^+|N/2-1, m-1, k\rangle = -e^{i2\pi kj/N} \sqrt{\frac{(N/2+m)(N/2+m-1)}{N^2(N-1)}}, \tag{2.191}$$

$$\langle N/2, m|\hat{S}_j^-|N/2-1, m+1, k\rangle = e^{i2\pi kj/N} \sqrt{\frac{(N/2-m)(N/2-m-1)}{N^2(N-1)}}. \tag{2.192}$$

2.4 Photon-mediated interactions and measurements

In this section, we first introduce the concepts of open quantum systems and derive the Lindblad master equation using the Markovian approximation, since the cavity QED system is an important example of an open quantum system. We then briefly discuss the quantization of electromagnetic fields in cavity QED systems, and list out the unitary evolution and dissipation terms in the Lindblad master equation for cavity QED systems. After that, we show the derivation

for two examples of photon-mediated interactions: spin exchange interactions and one-axis twisting interactions. Finally, we discuss continuous quantum measurements in cavity QED systems, which is easy to achieve in experiments by tracking the light leaking out of the cavity.

2.4.1 Open quantum system and Lindblad master equation

Here we would like to introduce theory tools for open quantum systems, which are quantum systems that interact with an external quantum system known as environment. The cavity QED system discussed in this thesis is an important example of an open quantum system. Here we provide a short review for the origin of the Lindblad master equation in open quantum systems, using a quantum information oriented way (see Ref. [67]) for the derivation. One can also refer to Ref. [68] for the traditional way of derivation in quantum optics.

The first step for understanding open quantum systems is to employ the existing theory tools in close quantum systems. Here we assume the environment is a quantum system with orthonormal basis $\{|a\rangle, a = 0, 1, \cdots, n-1\}$, and then consider a joint system including the physical system A and environment B. The physics of open quantum systems should be captured by unitary dynamics and projective measurements in the joint system. For example, we consider the system A and environment B are initially in a product state, and then apply a unitary transformation $\hat{U}$ to the joint system. Expanding $\hat{U}$ in the orthonormal basis of B, we have

$$\hat{U}|\tilde{\psi}\rangle_{AB} = \hat{U}(|\psi\rangle_A \otimes |0\rangle_B) = \sum_a \hat{M}_a|\psi\rangle_A \otimes |a\rangle_B. \tag{2.193}$$

Since $\hat{U}$ is a unitary operator, we have

$$\langle\tilde{\psi}|\hat{U}^\dagger\hat{U}|\tilde{\psi}\rangle_{AB} = 1 \quad \Rightarrow \quad \sum_a \langle\psi|\hat{M}_a^\dagger\hat{M}_a|\psi\rangle_A = 1. \tag{2.194}$$

Note that $|\psi\rangle_A$ is an arbitrary state in A, hence

$$\sum_a \hat{M}_a^\dagger\hat{M}_a = \hat{I}. \tag{2.195}$$

Consider projective measurements in the orthonormal basis of B (projection operator $\hat{I} \otimes$

$|a\rangle\langle a|$), the probability of outcome a and the post-measurement state of the system are given by

$$\text{Prob}(a) = \text{Tr}[\hat{M}_a \hat{\rho} \hat{M}_a^\dagger], \quad \hat{\rho}_a = \frac{\hat{M}_a \hat{\rho} \hat{M}_a^\dagger}{\sqrt{\text{Prob}(a)}}. \tag{2.196}$$

Here we only prove for pure states $\hat{\rho} = |\psi\rangle\langle\psi|$, and it is easy to show that the same formula also works for mixed states. Such type of measurement (satisfying Eq. (2.195)) is the most general form of measurement for system A, which is called a positive operator-valued measure (POVM), and $\hat{M}_a$ is a measurement operator.

We can also consider the evolution of the joint state under $\hat{U}$, and then trace out environment B to get the state in A. We have

$$\hat{\rho} \to \mathcal{E}(\hat{\rho}) = \sum_a \hat{M}_a \hat{\rho} \hat{M}_a^\dagger. \tag{2.197}$$

The linear map $\mathcal{E}(\hat{\rho})$ (satisfying Eq. (2.195)) is called a quantum channel, which is a general form of density matrix evolution in system A. This is equivalent to projective measurements in environment B while losing records of the measurement outcome, leading to a mixed state $\sum_a \text{Prob}(a)\hat{\rho}_a$. One can also consider the Heisenberg picture of the quantum channel, where the linear map is applied to operator $\hat{O}$ and $\hat{\rho}$ remains unchanged. One may write

$$\hat{O} \to \mathcal{E}^*(\hat{O}) = \sum_a \hat{M}_a^\dagger \hat{O} \hat{M}_a, \tag{2.198}$$

which leads to the same expectation value $\langle\hat{O}\rangle = \text{Tr}[\hat{\rho}\hat{O}]$ as the Schrödinger picture.

In most cases, the evolution of the density matrix can be described by a differential equation known as Lindblad master equation. This is based on the Markovian approximation, which assumes $\hat{\rho}(t+dt)$ is completely determined by $\hat{\rho}(t)$. The Markovian approximation is valid if the relaxation time scale of the environment B is much faster than the evolution time scale of the system A, and this is a reasonably good approximation for cavity QED systems. In the following, we will show that the Lindblad master equation is a direct consequence of the Markovian approximation. The Markovian evolution for a infinitesimal time step dt can be written as

$$\hat{\rho}(t+dt) = \mathcal{E}_{dt}(\hat{\rho}(t)) = \sum_a \hat{M}_a \hat{\rho}(t) \hat{M}_a^\dagger = \hat{\rho}(t) + O(dt). \tag{2.199}$$

Without loss of generality, we may assume $\hat{M}_0 = \hat{I} + O(dt)$, and $\hat{M}_a = O(\sqrt{dt})$ for $a > 0$. $\hat{M}_0$ smoothly connects to identity and describes how the system evolves when no quantum jump occurs, while $\hat{M}_a$ describes a possible quantum jump in the system. We may write

$$\hat{M}_0 = \hat{I} + \Big(-\frac{i}{\hbar}\hat{H} + \hat{K} \Big) dt, \quad \hat{M}_a = \sqrt{dt}\hat{L}_a \ (a > 0), \tag{2.200}$$

where $\hat{H}$ and $\hat{K}$ are both Hermitian matrices. Based on Eq. (2.195), we have

$$\hat{I} = \sum_a \hat{M}_a^\dagger \hat{M}_a = \hat{I} + dt\Big(2\hat{K} + \sum_{a>0} \hat{L}_a^\dagger \hat{L}_a\Big) + \cdots \quad \Rightarrow \quad \hat{K} = -\frac{1}{2}\sum_{a>0} \hat{L}_a^\dagger \hat{L}_a. \tag{2.201}$$

Plug in Eq. (2.199), one can obtain the so-call Lindblad master equation,

$$\begin{aligned} \frac{d}{dt}\hat{\rho} &= -\frac{i}{\hbar}[\hat{H}, \hat{\rho}] + \sum_{a>0}\left(\hat{L}_a \hat{\rho} \hat{L}_a^\dagger - \frac{1}{2}\hat{L}_a^\dagger \hat{L}_a \hat{\rho} - \frac{1}{2}\hat{\rho}\hat{L}_a^\dagger \hat{L}_a \right) \\ &= -\frac{i}{\hbar}[\hat{H}, \hat{\rho}] + \sum_{a>0} \mathcal{L}[\hat{L}_a]\hat{\rho}, \end{aligned} \tag{2.202}$$

where $\hat{H}$ is the Hamiltonian, $\hat{L}_a$ are Lindblad jump operators, and $\mathcal{L}[\hat{L}_a]\hat{\rho}$ is a shorthand notation for the dissipation part of the Lindblad master equation. We can also derive the equation of motion for operator $\hat{O}$ in the Heisenberg picture, where the Markovian evolution becomes

$$\hat{O}(t + dt) = \mathcal{E}_{dt}^*(\hat{O}(t)) = \sum_a \hat{M}_a^\dagger \hat{O}(t) \hat{M}_a, \tag{2.203}$$

so the Heisenberg equation of motion would be

$$\frac{d}{dt}\hat{O} = \frac{i}{\hbar}[\hat{H}, \hat{O}] + \sum_{a>0}\left(\hat{L}_a^\dagger \hat{O} \hat{L}_a - \frac{1}{2}\hat{L}_a^\dagger \hat{L}_a \hat{O} - \frac{1}{2}\hat{O}\hat{L}_a^\dagger \hat{L}_a \right). \tag{2.204}$$

2.4.2 Unitary and dissipative physics in cavity QED

The physics of cavity QED systems is based on the interaction between atoms and quantized electromagnetic (EM) fields inside the cavity. First we would like to briefly introduce the quantization of single-mode EM fields. Based on the Maxwell equations, the electric field $\mathbf{E}(\mathbf{r}, t)$ satisfies the wave equation,

$$\nabla^2 \mathbf{E} - \frac{1}{c^2}\frac{\partial^2 \mathbf{E}}{\partial t^2} = 0. \tag{2.205}$$

Here we consider $\mathbf{E}(\mathbf{r},t) = \alpha_E(t)\mathbf{f}(\mathbf{r}) + \text{c.c.}$, where $\alpha_E(t) = E_0 e^{-i\omega t}$ containing the temporal dependence, $\mathbf{f}(\mathbf{r})$ is the mode function containing all the spatial dependence, with normalization

$$\int d^3\mathbf{r}|\mathbf{f}(\mathbf{r})|^2 = 1. \tag{2.206}$$

By plugging the above relation into the wave equation, we find that the mode function $\mathbf{f}(\mathbf{r})$ satisfies the Helmholtz equation,

$$(\nabla^2 + k^2)\mathbf{f}(\mathbf{r}) = 0. \tag{2.207}$$

where $k = \omega/c$. Considering $\nabla \cdot \mathbf{E} = 0$, we have $\nabla \cdot \mathbf{f}(\mathbf{r}) = 0$. Considering $\nabla \times \mathbf{E} = -\partial_t \mathbf{B}$, we have $\mathbf{B}(\mathbf{r},t) = \alpha_B(t)(\nabla \times \mathbf{f}(\mathbf{r})) + \text{c.c.}$, where $\alpha_B(t) = -\frac{i}{\omega}E_0 e^{-i\omega t}$. Notice that $\alpha_E(t) = -\partial_t \alpha_B(t)$, and therefore we can define $p(t) = \epsilon_0(-i\alpha_E(t) + \text{c.c.})$, $q(t) = (i\alpha_B(t) + \text{c.c.})$. Using the fact that

$$\int d^3\mathbf{r}(\nabla \times \mathbf{f}^*) \cdot (\nabla \times \mathbf{f}) = \int d^3\mathbf{r}\ \mathbf{f}^* \cdot (\nabla \times (\nabla \times \mathbf{f})) = -\int d^3\mathbf{r}\ \mathbf{f}^* \cdot (\nabla^2 \mathbf{f}) = k^2 \int d^3\mathbf{r}\ |\mathbf{f}|^2, \tag{2.208}$$

we can rewrite the total energy of the EM field as

$$\begin{aligned} H &= \frac{\epsilon_0}{2}\int d^3\mathbf{r}\Big(|\mathbf{E}|^2 + c^2|\mathbf{B}|^2\Big) = \epsilon_0\Big(|\alpha_E(t)|^2 + \omega^2|\alpha_B(t)|^2\Big) \\ &= \frac{p^2}{2\epsilon_0} + \frac{1}{2}\epsilon_0\omega^2 q^2, \end{aligned} \tag{2.209}$$

which is the same as an harmonic oscillator Hamiltonian with mass $m = \epsilon_0$. Following the quantization of an harmonic oscillator Hamiltonian, one can express $\hat{q}$ and $\hat{p}$ in terms of creation and annihilation operators,

$$\hat{q} = \sqrt{\frac{\hbar}{2m\omega}}(\hat{a} + \hat{a}^\dagger), \quad \hat{p} = i\sqrt{\frac{\hbar m\omega}{2}}(\hat{a}^\dagger - \hat{a}). \tag{2.210}$$

In this way we can replace $\alpha_E \to \sqrt{\frac{\hbar\omega}{2\epsilon_0}}\hat{a}$, $\alpha_B \to -i\sqrt{\frac{\hbar}{2\omega\epsilon_0}}\hat{a}$. By plugging these expressions into the expressions of EM fields, we get

$$\hat{\mathbf{E}} = \sqrt{\frac{\hbar\omega}{2\epsilon_0}}\mathbf{f}(\mathbf{r})\hat{a} + \text{H.c.}, \quad \hat{\mathbf{B}} = -i\sqrt{\frac{\hbar}{2\omega\epsilon_0}}(\nabla \times \mathbf{f}(\mathbf{r}))\hat{a} + \text{H.c.}, \tag{2.211}$$

and the quantum Hamiltonian,

$$\hat{H} = \hbar\omega\left(\hat{a}^\dagger\hat{a} + \frac{1}{2}\right). \tag{2.212}$$

This Hamiltonian is consistent with each photon carrying energy $\hbar\omega$, where $\hat{a}^\dagger$ and $\hat{a}$ are photon creation and annihilation operators respectively. $\hat{a}^\dagger\hat{a}$ can be interpreted as the photon number in the system. The constant $\hbar\omega/2$ is the zero-point energy of the EM field.

Now we list some examples of running-wave mode functions $\mathbf{f}(\mathbf{r})$. Standing-wave mode functions can be constructed by superposition of two counter-propagating running-wave modes ($\mathbf{r} \leftrightarrow -\mathbf{r}$).

- Free space:

$$\mathbf{f}(\mathbf{r}) = \frac{1}{\sqrt{V}}\vec{\varepsilon}e^{i\mathbf{k}\cdot\mathbf{r}}, \tag{2.213}$$

  where $\vec{\varepsilon}$ is the polarization vector with $\vec{\varepsilon} \perp \mathbf{k}$.

- Paraxial approximation:

$$\mathbf{f}(\mathbf{r}) = f(x, y, z)\vec{\varepsilon}e^{ikz}, \tag{2.214}$$

  where $f(x, y, z)$ is a slowly varying function. Considering $|\frac{\partial^2 f}{\partial z^2}| \ll |k\frac{\partial f}{\partial z}|$, the Helmholtz equation can be approximated by

$$\frac{\partial^2 f}{\partial x^2} + \frac{\partial^2 f}{\partial y^2} + 2ik\frac{\partial f}{\partial z} = 0. \tag{2.215}$$

  Solutions of this equation are known as Hermite-Gaussian modes or Laguerre-Gaussian modes. We mainly focus on the lowest order mode (Gaussian beam) given by the following formula,

$$f(x, y, z) = \frac{1}{\sqrt{V}}\frac{w_0}{w(z)}\exp\left(-\frac{x^2+y^2}{[w(z)]^2}\right)\exp\left(ik\frac{x^2+y^2}{2R(z)} - i\Phi_{\text{Gouy}}(z)\right), \tag{2.216}$$

  where w_0 is the beam waist, $w(z) = w_0\sqrt{1+(z/z_R)^2}$ is the beam radius at position z, $R(z) = z[1+(z_R/z)^2]$ is the radius of curvature, $\Phi_{\text{Gouy}}(z) = \arctan(z/z_R)$ is the Gouy phase, with $z_R = kw_0^2/2$ the Rayleigh range. The mode volume $V = \pi w_0^2 L/2$ is the normalization factor for $\mathbf{f}(\mathbf{r})$ if we restrict the range of $z \in [-L/2, L/2]$.

After quantizing the EM fields, we now use the electric dipole approximation of the atom-light

coupling, $\hat{H}_{AL} = -\hat{\mathbf{d}} \cdot \hat{\mathbf{E}}$, leading to the following Hamiltonian for an array of two-level atoms,

$$\hat{H}_{AL}/\hbar = \sum_i (\mathcal{G}_i \hat{a} \hat{S}_i^+ + \text{H.c.}), \tag{2.217}$$

where we dropped the counter-rotating terms. Here the atom-light coupling strength is given by

$$\mathcal{G}_i = -\sqrt{\frac{\hbar\omega}{2\epsilon_0}} \frac{\langle e|\hat{\mathbf{d}} \cdot \vec{\varepsilon}|g\rangle}{\hbar} \int d^3\mathbf{r} \phi_{i,e}^*(\mathbf{r}) f(\mathbf{r}) \phi_{i,g}(\mathbf{r}), \tag{2.218}$$

where $\mathbf{f}(\mathbf{r}) = f(\mathbf{r})\vec{\varepsilon}$, $\phi_{i,e}(\mathbf{r})$ and $\phi_{i,g}(\mathbf{r})$ are the spatial wave functions for the i-th atom.

For simplicity, here we consider the case with homogeneous couplings, $\mathcal{G}_i = \mathcal{G}$. We also assume $\mathcal{G}$ is a real number. Combining with the Hamiltonian for EM field energy and atomic internal energy, one can obtain the so-called Tavis-Cumming model,

$$\hat{H}_{\text{TC}}/\hbar = \omega_c \hat{a}^\dagger \hat{a} + \omega_a \hat{S}^z + \mathcal{G}(\hat{a}\hat{S}^+ + \text{H.c.}), \tag{2.219}$$

where ω_c is the frequency of cavity resonance, and ω_a is the atomic transition frequency. Now we would like to discuss the single-photon dressed states in the Tavis-Cumming model. We use $|n\rangle$ to label the photon number in the cavity, and $|S, m\rangle$ to label the collective atomic states. When we restrict to the subspace form by $|1\rangle|N/2, -N/2\rangle$ and $|0\rangle|N/2, -N/2+1\rangle$, with N the total atom number, we have

$$\hat{H}_{\text{subspace}}/\hbar = \begin{pmatrix} \omega_c & \mathcal{G}\sqrt{N} \\ \mathcal{G}\sqrt{N} & \omega_a \end{pmatrix}. \tag{2.220}$$

The eigenenergies of $\hat{H}_{\text{subspace}}$ are as follows,

$$\begin{aligned} |+\rangle &= C_1|1\rangle|N/2, -N/2\rangle + C_2|0\rangle|N/2, -N/2+1\rangle, \quad E_+/\hbar = \frac{\omega_c + \omega_a}{2} + \frac{1}{2}\sqrt{(\omega_c - \omega_a)^2 + 4\mathcal{G}^2 N}, \\ |-\rangle &= -C_2|1\rangle|N/2, -N/2\rangle + C_1|0\rangle|N/2, -N/2+1\rangle, \quad E_-/\hbar = \frac{\omega_c + \omega_a}{2} - \frac{1}{2}\sqrt{(\omega_c - \omega_a)^2 + 4\mathcal{G}^2 N}. \end{aligned} \tag{2.221}$$

where

$$C_1 = \frac{1}{\sqrt{2}}\left(1 + \frac{\omega_c - \omega_a}{\sqrt{(\omega_c - \omega_a)^2 + 4\mathcal{G}^2 N}}\right)^{1/2}, \quad C_2 = \frac{1}{\sqrt{2}}\left(1 - \frac{\omega_c - \omega_a}{\sqrt{(\omega_c - \omega_a)^2 + 4\mathcal{G}^2 N}}\right)^{1/2}. \tag{2.222}$$

When $\omega_c = \omega_a$, we have $E_+ - E_- = 2\mathcal{G}\sqrt{N}$, which gives the vacuum Rabi splitting for N atoms. When $|\omega_c - \omega_a| \gg \mathcal{G}\sqrt{N}$, the two vacuum Rabi splitting peak will reduce to cavity-like and atom-like peak: $E_+ \to \omega_c$, $E_- \to \omega_a$ if $\omega_c > \omega_a$; $E_+ \to \omega_a$, $E_- \to \omega_c$ if $\omega_c < \omega_a$.

Apart from unitary dynamics, cavity QED systems intrinsically feature dissipative processes such as cavity decay and atom spontaneous emission. Cavity decay can be described by a Lindblad jump operator $\hat{L} = \sqrt{\kappa}\hat{a}$, which corresponds a photon leaking out of the cavity and never coming back. Atom spontaneous emission can be described by Lindblad jump operators $\hat{L}_i = \sqrt{\gamma}\hat{S}_i^-$, which are single-direction decays from the atomic excited state to the ground state. Therefore, the Lindblad master equation can be written as

$$\frac{d}{dt}\hat{\rho} = -\frac{i}{\hbar}[\hat{H}_{\mathrm{TC}}, \hat{\rho}] + \kappa\mathcal{L}[\hat{a}]\hat{\rho} + \gamma\sum_j \mathcal{L}[\hat{S}_j^-]\hat{\rho}. \tag{2.223}$$

We define a dimensionless parameter $\mathcal{C}$ known as cooperativity to characterize the competition of elastic vs. inelastic processes,

$$\mathcal{C} = \frac{4\mathcal{G}^2}{\kappa\gamma}. \tag{2.224}$$

The regime with $\mathcal{C} < 1$ is called weak coupling regime, where an excited atom is more likely to scatter a photon into free space. While in the regime with $\mathcal{C} > 1$, an excited atom is more likely to scatter a photon into the cavity. Note that $\mathcal{C}$ only depends on cavity parameters, since the dependence on the atomic dipole matrix element cancels out in the formula above. For the case of an atomic ensemble with N atoms, we can define the collective cooperativity as $N\mathcal{C}$. The quantity $N\mathcal{C}$ is fundamental to characterize many-body cavity QED processes such as superradiance and spin squeezing, which are key topics of my PhD research (see chapter 5).

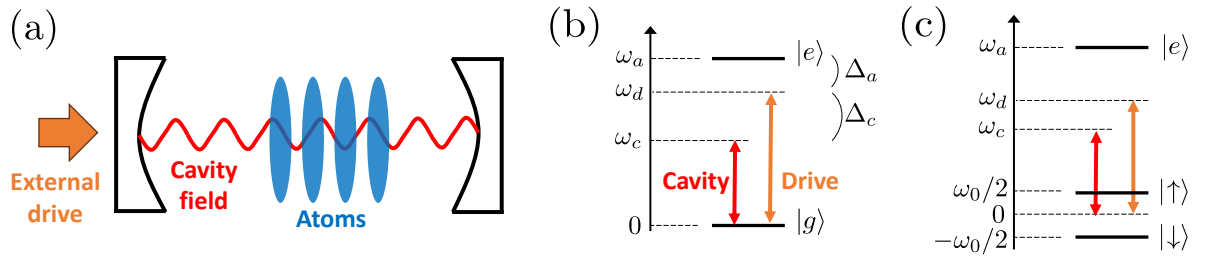

Figure 2.5: (a) Schematic of a cavity QED system. (b) Energy level diagram for spin exchange interactions, ω_a is the frequency of the atomic transition, ω_d is the frequency of the external drive, and ω_c is the frequency of cavity resonance. (c) Energy level diagram for one-axis twisting interactions. ω_0 is the frequency splitting of the ground state hyperfine spin.

2.4.3 Derivation of spin exchange interactions

In this subsection, we focus on the regime $|\omega_c - \omega_a| \gg \mathcal{G}\sqrt{N}$, where the cavity resonance is far detuned from the atomic transition. In this case, an atom in the excited state can virtually emit a photon into the cavity mode and flip to the ground state, while another atom in the ground state can absorb the same photon and flip to the excited state. This process is known as spin exchange interactions.

Since the preparation of atomic excited states requires an external laser, the appropriate theory discussion should lie in the laser rotating frame. Here we add an external drive to the cavity mode in $\hat{H}_{\mathrm{TC}}$, which gives (see Fig. 2.5(a,b))

$$\hat{H}/\hbar = \omega_c \hat{a}^\dagger \hat{a} + \omega_a \hat{S}^z + (\epsilon\, \mathrm{e}^{-i\omega_d t}\hat{a}^\dagger + \epsilon^*\, \mathrm{e}^{i\omega_d t}\hat{a}) + \mathcal{G}(\hat{a}\hat{S}^+ + \hat{a}^\dagger \hat{S}^-), \tag{2.225}$$

where ϵ is the intracavity drive amplitude. The whole system can now be described by the Lindblad master equation,

$$\frac{d}{dt}\hat{\rho} = -\frac{i}{\hbar}[\hat{H}, \hat{\rho}] + \kappa \mathcal{L}[\hat{a}]\hat{\rho} + \gamma \sum_j \mathcal{L}[\hat{S}_j^-]\hat{\rho}. \tag{2.226}$$

If we introduce a time-dependent unitary transformation $\hat{U}(t)$, the new Lindblad master equation for $\hat{\rho}' = \hat{U}\hat{\rho}\hat{U}^\dagger$ has a new effective Hamiltonian given by

$$\hat{H}' = \hat{U}\hat{H}\hat{U}^\dagger + i\hbar \frac{d\hat{U}}{dt}\hat{U}^\dagger, \tag{2.227}$$

and the Lindblad jump operators becomes $\hat{L}'_j = \hat{U}\hat{L}_j\hat{U}^\dagger$.

For the case when the unitary transformation is to move to the rotating frame of the driving laser, $\hat{U}(t)$ is a time-dependent unitary transformation as follows,

$$\hat{U} = \exp\Big(i\omega_d t(\hat{S}^z + \hat{a}^\dagger \hat{a})\Big), \tag{2.228}$$

under which the Hamiltonian becomes

$$\hat{H}'/\hbar = -\Delta_c \hat{a}^\dagger \hat{a} - \Delta_a \hat{S}^z + (\epsilon\, \hat{a}^\dagger + \epsilon^*\, \hat{a}) + \mathcal{G}(\hat{a}\hat{S}^+ + \hat{a}^\dagger \hat{S}^-). \tag{2.229}$$

Here, $\Delta_c = \omega_d - \omega_c$ is the detuning between the laser frequency and the cavity resonance, and $\Delta_a = \omega_d - \omega_a$ is the detuning between the laser frequency and the atomic transition frequency. The other parts of Lindblad master equation remains unchanged.

With no atoms in the cavity, the steady state of the system in the presense of an external drive and cavity decay, is a coherent state $|\alpha\rangle$. By plugging in $\hat{\rho} = |\alpha\rangle\langle\alpha|$ and setting $\partial_t \hat{\rho} = 0$. we get

$$\alpha = \frac{\epsilon}{\Delta_c + i\kappa/2}. \tag{2.230}$$

When adding atoms to the cavity, we can rewrite the cavity field operator as $\hat{a} = \alpha + \hat{b}$, where $\hat{b}$ describes the quantum fluctuations of the coherent state. In terms of $\hat{b}$, the Lindblad master equation becomes

$$\begin{aligned} \frac{d}{dt}\hat{\rho} &= -\frac{i}{\hbar}[\hat{H}', \hat{\rho}] + \kappa\mathcal{L}[\hat{b}]\hat{\rho} + \gamma\sum_j \mathcal{L}[\hat{S}_j^-]\hat{\rho}, \\ \hat{H}'/\hbar &= -\Delta_c \hat{b}^\dagger\hat{b} - \Delta_a\hat{S}^z + \frac{1}{2}(\Omega\hat{S}^+ + \Omega^*\hat{S}^-) + \mathcal{G}(\hat{b}\hat{S}^+ + \hat{b}^\dagger\hat{S}^-), \end{aligned} \tag{2.231}$$

where $\Omega = 2\mathcal{G}\alpha$ is the Rabi frequency. We assume Δ_c or κ is the largest frequency scale compared to $\mathcal{G}\sqrt{N}, \Delta_a, \Omega, \gamma$ (we estimate the validity at the end of this subsection), which allows us to consider the ground manifold as states with no photons in field $\hat{b}$, and the excited manifold as states with a single photon excitation. The effective atom-only master equation can be calculated based on second-order perturbation theory described in Appendix A,

$$\begin{aligned} \frac{d}{dt}\hat{\rho} &= -\frac{i}{\hbar}[\hat{H}_{\text{eff}}, \hat{\rho}] + \Gamma\mathcal{L}[\hat{S}^-]\hat{\rho} + \gamma\sum_j \mathcal{L}[\hat{S}_j^-]\hat{\rho}, \\ \hat{H}_{\text{eff}}/\hbar &= \chi\hat{S}^+\hat{S}^- - \Delta_a\hat{S}^z + \frac{1}{2}(\Omega\hat{S}^+ + \Omega^*\hat{S}^-). \end{aligned} \tag{2.232}$$

Here χN is the spin exchange interaction strength, and ΓN is the superradiant decay rate, which are given by

$$\chi = \frac{\mathcal{G}^2\Delta_c}{\Delta_c^2 + \kappa^2/4}, \quad \Gamma = \frac{\mathcal{G}^2\kappa}{\Delta_c^2 + \kappa^2/4}. \tag{2.233}$$

Now we explain why $\mathcal{G}\sqrt{N}$ is a good estimation for the strength of atom-light coupling,

$$\hat{H}_{AL}/\hbar = \mathcal{G}(\hat{b}\hat{S}^+ + \hat{b}^\dagger\hat{S}^-). \tag{2.234}$$

We consider the mean-field dynamics of $\hat{H}_{AL}$, which gives

$$\frac{d}{dt}\langle\hat{b}\rangle = -i\mathcal{G}\langle\hat{S}^{-}\rangle, \quad \frac{d}{dt}\langle\hat{S}^{-}\rangle = 2i\mathcal{G}\langle\hat{S}^{z}\rangle\langle\hat{b}\rangle, \quad \frac{d}{dt}\langle\hat{S}^{z}\rangle = i\mathcal{G}(\langle\hat{b}^{\dagger}\rangle - \langle\hat{b}\rangle). \tag{2.235}$$

Without loss of generality, we assume $\langle\hat{S}^{+}\rangle$ is a real number, which gives $\langle\hat{b}\rangle$ is pure imaginary. So we can define $i\langle\hat{b}\rangle = i\langle\hat{b}^{\dagger}\rangle = \beta$, $\langle\hat{S}^{+}\rangle = \langle\hat{S}^{-}\rangle = N\sin\theta/2$, $\langle\hat{S}^{z}\rangle = N\cos\theta/2$. Based on the two conserved quantities: $\langle\hat{S}^{+}\rangle\langle\hat{S}^{-}\rangle + \langle\hat{S}^{z}\rangle\langle\hat{S}^{z}\rangle = N^2/4$, $\langle\hat{b}^{\dagger}\rangle\langle\hat{b}\rangle + \langle\hat{S}^{z}\rangle = C$, with C a constant depending on initial state, we have

$$\frac{d}{dt}\theta = 2\mathcal{G}\beta, \quad \frac{d}{dt}\beta = \frac{\mathcal{G}N}{2}\sin\theta \quad \Rightarrow \quad \frac{d^2}{dt^2}\theta = \mathcal{G}^2 N\sin\theta. \tag{2.236}$$

Note that this is the differential equation of a pendulum, and the oscillation frequency is at the order of $\mathcal{G}\sqrt{N}$.

2.4.4 Derivation of one-axis twisting interactions

So far we have discussed the case that atomic spins are directly coupled by cavity photons. Now we focus on another type of photon-mediated interactions based on dispersive coupling between cavity photons and atomic spins. In this case, the atomic spins are maintained in their atomic ground states. Cavity photons can lead to differential AC Stark shifts on the atomic spins, while the atom dynamics also shifts the frequency of the cavity resonance. The overall effect of the atom dynamics due to the feedback of cavity photons can be interpreted as an infinite range Ising interaction known as one-axis twisting.

Here we consider atomic internal levels $|\downarrow\rangle$, $|\uparrow\rangle$ and $|e\rangle$. The transition $|\downarrow\rangle \to |e\rangle$ and $|\uparrow\rangle \to |e\rangle$ are off-resonantly coupled by a single cavity mode (we use the same Clebsch-Gordan coefficient for both transition for simplicity), which gives the following Hamiltonian (see Fig. 2.5(a,c)),

$$\hat{H}/\hbar = \omega_a\hat{P}_e + \omega_c\hat{a}^{\dagger}\hat{a} + \omega_0\hat{S}^{z} + (\epsilon\,\mathrm{e}^{-i\omega_d t}\hat{a}^{\dagger} + \epsilon^{*}\,\mathrm{e}^{i\omega_d t}\hat{a}) + \frac{\mathcal{G}}{\sqrt{2}}(\hat{a}\hat{S}^{+}_{\uparrow e} + \hat{a}\hat{S}^{+}_{\downarrow e} + \text{H.c.}), \tag{2.237}$$

where $\hat{P}_e = \sum_j |e\rangle_j\langle e|$, $\hat{S}^{+}_{\uparrow e} = \sum_j |e\rangle_j\langle\uparrow|$, and $\hat{S}^{+}_{\downarrow e} = \sum_j |e\rangle_j\langle\downarrow|$. Here, ω_0 is the frequency difference between $|\downarrow\rangle$, $|\uparrow\rangle$ states, which is much smaller compared to ω_a and ω_c. Similar to the previous

subsection, we move to the rotating frame of the driving laser using the following time-dependent unitary transformation,

$$\hat{U} = \exp\Big(i\omega_d t(\hat{P}_e + \hat{a}^\dagger\hat{a})\Big), \tag{2.238}$$

which gives

$$\hat{H}'/\hbar = -\Delta_a\hat{P}_e - \Delta_c\hat{a}^\dagger\hat{a} + \omega_0\hat{S}^z + (\epsilon\,\hat{a}^\dagger + \epsilon^*\,\hat{a}) + \frac{\mathcal{G}}{\sqrt{2}}(\hat{a}\hat{S}^+_{\uparrow e} + \hat{a}\hat{S}^+_{\downarrow e} + \text{H.c.}), \tag{2.239}$$

where $\Delta_c = \omega_d - \omega_c$ is the cavity detuning, and $\Delta_a = \omega_d - \omega_a$ is the atomic detuning. Combining with cavity decay and atomic spontaneous emission, one can obtain the following Lindblad master equation,

$$\frac{d}{dt}\hat{\rho} = -\frac{i}{\hbar}[\hat{H}', \hat{\rho}] + \kappa\mathcal{L}[\hat{a}]\hat{\rho} + \frac{\gamma}{2}\sum_j \mathcal{L}[\hat{S}^-_{j,\uparrow e}]\hat{\rho} + \frac{\gamma}{2}\sum_j \mathcal{L}[\hat{S}^-_{j,\downarrow e}]\hat{\rho}. \tag{2.240}$$

We assume $\Delta_a \pm \omega_0/2$ is much larger compared to $\mathcal{G}\langle\hat{a}\rangle, \gamma$, which allows us to consider the ground manifold as all the atoms in $|\downarrow\rangle$ and $|\uparrow\rangle$ states, and the excited manifold as only one atom in excited states. The effective master equation can be calculated based on the second-order perturbation theory described in Appendix A,

$$\begin{aligned}\frac{d}{dt}\hat{\rho} = &-\frac{i}{\hbar}[\hat{H}'', \hat{\rho}] + \kappa\mathcal{L}[\hat{a}]\hat{\rho} + \frac{\mathcal{G}^2\gamma}{2(\Delta_a + \omega_0/2)^2}\sum_j(\mathcal{L}[\hat{a}\hat{P}_{j,\uparrow}]\hat{\rho} + \mathcal{L}[\hat{a}\hat{S}^-_j]\hat{\rho}) \\ &+ \frac{\mathcal{G}^2\gamma}{2(\Delta_a - \omega_0/2)^2}\sum_j(\mathcal{L}[\hat{a}\hat{P}_{j,\downarrow}]\hat{\rho} + \mathcal{L}[\hat{a}\hat{S}^+_j]\hat{\rho}),\end{aligned} \tag{2.241}$$

where

$$\hat{H}'' = -\tilde{\Delta}_c\hat{a}^\dagger\hat{a} + \omega_0\hat{S}^z + (\epsilon\,\hat{a}^\dagger + \epsilon^*\,\hat{a}) + \tilde{\mathcal{G}}\hat{a}^\dagger\hat{a}\hat{S}^z. \tag{2.242}$$

Here the effective cavity detuning $\tilde{\Delta}_c$ and dispersive atom-light coupling strength $\tilde{\mathcal{G}}$ are given by

$$\tilde{\Delta}_c = \Delta_c + \frac{\mathcal{G}^2 N\Delta_a}{2(\omega_0^2/4 - \Delta_a^2)}, \quad \tilde{\mathcal{G}} = \frac{\mathcal{G}^2\omega_0}{2(\omega_0^2/4 - \Delta_a^2)}. \tag{2.243}$$

We also assume ω_0 is the largest frequency scale in the effective master equation, which allows us to rotate out all the crossed coupling terms, such as $\hat{S}^+$ terms in Hamiltonian part and $\hat{S}^+_j\hat{\rho}\hat{P}_{j,\uparrow}$, $\hat{S}^+_j\hat{\rho}$ terms is the dissipation part.

Similar to the previous subsection, we can rewrite the cavity field operator as $\hat{a} = \alpha + \hat{b}$, where $\alpha = \epsilon/(\tilde{\Delta}_c + i\kappa/2)$, $\hat{b}$ describes the quantum fluctuations of the coherent state. We neglect

the terms $\hat{b}^\dagger\hat{b}\hat{S}^z$ in the Hamiltonian and the terms containing $\hat{b}$ in the Lindblad jump operators, since they are higher order quantum fluctuation terms. The Lindblad master equation becomes

$$\frac{d}{dt}\hat{\rho} = -\frac{i}{\hbar}[\hat{H}'', \hat{\rho}] + \kappa\mathcal{L}[\hat{a}]\hat{\rho} + \gamma_+\sum_j \mathcal{L}[\hat{S}_j^+]\hat{\rho} + \gamma_-\sum_j \mathcal{L}[\hat{S}_j^-]\hat{\rho} + \gamma_z\sum_j \mathcal{L}[\hat{S}_j^z]\hat{\rho}, \tag{2.244}$$

where

$$\hat{H}'' = -\tilde{\Delta}_c\hat{b}^\dagger\hat{b} + (\omega_0 + \tilde{\mathcal{G}}|\alpha|^2)\hat{S}^z + \tilde{\mathcal{G}}(\alpha^*\hat{b} + \alpha\hat{b}^\dagger)\hat{S}^z. \tag{2.245}$$

Here we have defined

$$\gamma_+ = \frac{\mathcal{G}^2|\alpha|^2\gamma}{2(\Delta_a - \omega_0/2)^2}, \quad \gamma_- = \frac{\mathcal{G}^2|\alpha|^2\gamma}{2(\Delta_a + \omega_0/2)^2}, \quad \gamma_z = \gamma_+ + \gamma_-. \tag{2.246}$$

Then we assume $\tilde{\Delta}_c$ or κ is much larger than $\tilde{\mathcal{G}}\alpha\sqrt{N}, \gamma_+, \gamma_-$, which allows us to consider the ground manifold with no photons in field $\hat{b}$, and the excited manifold as a single photon excitation. The effective atom-only master equation can be calculated based on second-order perturbation theory described in Appendix A,

$$\frac{d}{dt}\hat{\rho} = -\frac{i}{\hbar}[\hat{H}_{\text{eff}}, \hat{\rho}] + \Gamma_z\mathcal{L}[\hat{S}^z]\hat{\rho} + \gamma_+\sum_j \mathcal{L}[\hat{S}_j^+]\hat{\rho} + \gamma_-\sum_j \mathcal{L}[\hat{S}_j^-]\hat{\rho} + \gamma_z\sum_j \mathcal{L}[\hat{S}_j^z]\hat{\rho}, \tag{2.247}$$

where

$$\hat{H}_{\text{eff}} = \chi\hat{S}^z\hat{S}^z + (\omega_0 + \tilde{\mathcal{G}}|\alpha|^2)\hat{S}^z. \tag{2.248}$$

Here χN is the one-axis twisting interaction strength, $\Gamma_z N$ is the collective dephasing rate, which are given by

$$\chi = \frac{\tilde{\mathcal{G}}^2|\alpha|^2\tilde{\Delta}_c}{\tilde{\Delta}_c^2 + \kappa^2/4}, \quad \Gamma_z = \frac{\tilde{\mathcal{G}}^2|\alpha|^2\kappa}{\tilde{\Delta}_c^2 + \kappa^2/4}. \tag{2.249}$$

2.4.5 Continuous quantum measurements

The concept of continuous quantum measurements originates from the derivation of the Lindblad master equation. As discussed in section 2.5.1, one interpretation of the Lindblad master equation is to perform POVM measurements $\hat{M}_a$ for infinitesimal time steps, and then losing the record of the measurement outcome. If we keep track of all the measurement outcome, for each time step, the system will have random quantum jumps or no jump to the post-measurement

state depending on the probability of the measurement outcome. In this case, we are performing continuous quantum measurements to the system, and the measurement outcome uniquely defines a quantum trajectory. Here we will mainly focus on the special case of cavity QED systems, and one can refer to Ref. [69] for a more general discussion.

We start from the Lindblad master equation for cavity decay,

$$\frac{d}{dt}\hat{\rho} = -\frac{i}{\hbar}[\hat{H},\hat{\rho}] + \kappa\left(\hat{a}\hat{\rho}\hat{a}^\dagger - \frac{1}{2}\hat{a}^\dagger\hat{a}\hat{\rho} - \frac{1}{2}\hat{\rho}\hat{a}^\dagger\hat{a}\right), \tag{2.250}$$

which is equivalent to the following measurement operators,

$$\hat{M}_0 = \hat{I} + \left(-\frac{i}{\hbar}\hat{H} - \frac{\kappa}{2}a^\dagger\hat{a}\right)dt, \quad \hat{M}_1 = \sqrt{\kappa dt}\,\hat{a}. \tag{2.251}$$

If we put a single-photon detector to keep track of the measurement outcome, i.e. the detected photon number $N(t)$ increases by 1 if a photon leaks out of the cavity and reaches the detector (described by annihilation operator $\hat{a}$). For simplicity, we first assume all the photons leaking out will be collected by the detector. We consider an infinitesimal time step such that $dN(t) = N(t+dt) - N(t)$ is a random integer 0 or 1, with expectation value $E[dN] = \kappa\langle\hat{a}^\dagger\hat{a}\rangle dt$. Based on the random number dN, we can describe the system dynamics in the following way,

$$\hat{\rho}(t+dt) = \frac{\hat{M}_0\hat{\rho}(t)\hat{M}_0^\dagger}{1-\mathrm{Tr}[\hat{M}_1\hat{\rho}(t)\hat{M}_1^\dagger]}(1-dN) + \frac{\hat{M}_1\hat{\rho}(t)\hat{M}_1^\dagger}{\mathrm{Tr}[\hat{M}_1\hat{\rho}(t)\hat{M}_1^\dagger]}dN. \tag{2.252}$$

Dropping the terms at the order of $O(dt^2)$ and $O(dN\,dt)$, we have

$$d\hat{\rho} = -\frac{i}{\hbar}[\hat{H},\hat{\rho}]dt - \frac{\kappa}{2}(\hat{a}^\dagger\hat{a}\hat{\rho} - \hat{\rho}\hat{a}^\dagger\hat{a})dt + \kappa\langle\hat{a}^\dagger\hat{a}\rangle\hat{\rho}dt + \left(\frac{\hat{a}\hat{\rho}\hat{a}^\dagger}{\langle\hat{a}^\dagger\hat{a}\rangle} - \hat{\rho}\right)dN. \tag{2.253}$$

In a cavity QED system, a key example of continuous quantum measurements is the homodyne detection of cavity field (see Fig. 2.6). This is to mix the cavity output field ($\hat{b}_1$) with a local oscillator field ($\hat{b}_2$) by a 50:50 beamsplitter, so the two output fields of the beamsplitter would be

$$\hat{c}_1 = \frac{1}{\sqrt{2}}(\hat{b}_1 + i\hat{b}_2), \quad \hat{c}_2 = \frac{1}{\sqrt{2}}(i\hat{b}_1 + \hat{b}_2). \tag{2.254}$$

Then we use two single-photon detectors to keep track of the two output fields of the beamsplitter, with detected photon number $N_1(t)$ and $N_2(t)$. So we can define measurement operators

$$\hat{M}_1 = \sqrt{\kappa dt}\,\frac{\hat{a}+i\beta}{\sqrt{2}}, \quad \hat{M}_2 = \sqrt{\kappa dt}\,\frac{i\hat{a}+\beta}{\sqrt{2}}, \tag{2.255}$$

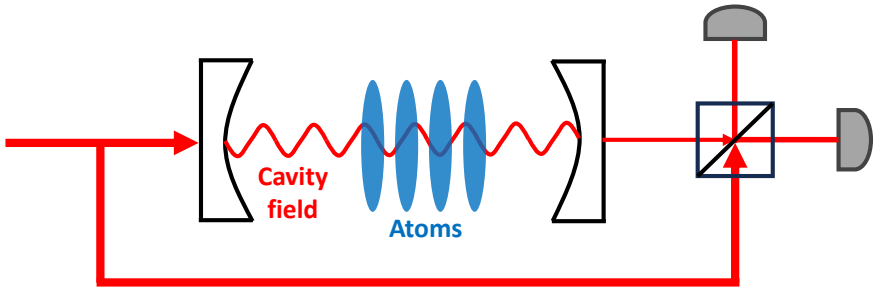

Figure 2.6: Schematic of the homodyne detection of the cavity field. We mix the cavity output field with a local oscillator field by a 50:50 beamsplitter, and use single-photon detectors to keep track of the two output paths of the beamsplitter.

where β is a c-number describing the coherent state of a local oscillator. As for $\hat{M}_0$, we consider the restriction $\hat{M}_0^\dagger \hat{M}_0 + \hat{M}_1^\dagger \hat{M}_1 + \hat{M}_2^\dagger \hat{M}_2 = \hat{I}$, as well as the Lindblad master equation (Eq. (2.250)) remains unchanged if losing all the measurement record, which gives

$$\hat{M}_0 = \hat{I} + \left(-\frac{i}{\hbar}\hat{H} - \frac{\kappa}{2}(\hat{a}^\dagger \hat{a} + |\beta|^2) \right) dt. \tag{2.256}$$

Similarly, we consider an infinitesimal time step such that $dN_1(t) = N_1(t+dt) - N_1(t)$ and $dN_2(t) = N_2(t+dt) - N_2(t)$ are random integers 0 or 1 (negligible probability for simultaneously reaching 1), with expectation values $E[dN_1] = \kappa \langle (\hat{a}^\dagger - i\beta^*)(\hat{a} + i\beta) \rangle dt/2$, $E[dN_2] = \kappa \langle (-i\hat{a}^\dagger + \beta^*)(i\hat{a} + \beta) \rangle dt/2$. Based on the random number dN_1 and dN_2, we can describe the system dynamics in the following way,

$$\begin{aligned} \hat{\rho}(t+dt) = & \frac{\hat{M}_0 \hat{\rho}(t) \hat{M}_0^\dagger}{1 - \mathrm{Tr}[\hat{M}_1 \hat{\rho}(t) \hat{M}_1^\dagger] - \mathrm{Tr}[\hat{M}_2 \hat{\rho}(t) \hat{M}_2^\dagger]} (1 - dN_1)(1 - dN_2) \\ & + \frac{\hat{M}_1 \hat{\rho}(t) \hat{M}_1^\dagger}{\mathrm{Tr}[\hat{M}_1 \hat{\rho}(t) \hat{M}_1^\dagger]} dN_1 + \frac{\hat{M}_2 \hat{\rho}(t) \hat{M}_2^\dagger}{\mathrm{Tr}[\hat{M}_2 \hat{\rho}(t) \hat{M}_2^\dagger]} dN_2. \end{aligned} \tag{2.257}$$

Dropping the terms at the order of $O(dt^2)$, $O(dN_1\, dt)$, $O(dN_2\, dt)$ and $O(dN_1\, dN_2)$, we have

$$\begin{aligned} d\hat{\rho} = & -\frac{i}{\hbar}[\hat{H}, \hat{\rho}]dt - \frac{\kappa}{2}(\hat{a}^\dagger \hat{a} \hat{\rho} - \hat{\rho} \hat{a}^\dagger \hat{a}) dt + \kappa \langle \hat{a}^\dagger \hat{a} \rangle \hat{\rho} dt + \left(\frac{(\hat{a} + i\beta)\hat{\rho}(\hat{a}^\dagger - i\beta^*)}{\langle (\hat{a}^\dagger - i\beta^*)(\hat{a} + i\beta) \rangle} - \hat{\rho} \right) dN_1 \\ & + \left(\frac{(i\hat{a} + \beta)\hat{\rho}(-i\hat{a}^\dagger + \beta^*)}{\langle (-i\hat{a}^\dagger + \beta^*)(i\hat{a} + \beta) \rangle} - \hat{\rho} \right) dN_2. \end{aligned} \tag{2.258}$$

Since the the two output fields of the beamsplitter are dominated by the local oscillator field, $N_1(t)$ and $N_2(t)$ are well described by Poisson processes with large detected photon num-

bers. In this case, we can approximate a Poisson distribution with expectation λ by a Gaussian distribution $\mathcal{N}(\mu = \lambda, \sigma^2 = \lambda)$, which gives $dN_1 \sim \mathcal{N}(E[dN_1/dt]dt, E[dN_1/dt]dt)$ and $dN_1 \sim \mathcal{N}(E[dN_2/dt]dt, E[dN_2/dt]dt)$. Here we define a Wiener process as the continuous limit of a random walk, such that $W(0) = 0$, $dW = W(t + dt) - W(t) \sim \mathcal{N}(0, dt)$ are independent Gaussian random numbers, and $dW^2 = dt$ is a fixed number without randomness. In order to reach the standard form of Itô stochastic differential equations, we can rewrite dN_1 and dN_2 in terms of Wiener processes,

$$dN_1 = E[dN_1/dt]\ dt + \sqrt{E[dN_1/dt]}\ dW_1, \quad dN_2 = E[dN_2/dt]\ dt + \sqrt{E[dN_2/dt]}\ dW_2. \tag{2.259}$$

Defining $\beta/|\beta| = -ie^{i\phi}$, and taking the limit of $|\beta| \to \infty$, we have

$$\begin{aligned} d\hat{\rho} = &-\frac{i}{\hbar}[\hat{H}, \hat{\rho}]dt - \frac{\kappa}{2}(\hat{a}^\dagger\hat{a}\hat{\rho} - \hat{\rho}\hat{a}^\dagger\hat{a})dt + \kappa\langle\hat{a}^\dagger\hat{a}\rangle\hat{\rho}dt + \kappa\left(\hat{a}\hat{\rho}\hat{a}^\dagger - \langle\hat{a}^\dagger\hat{a}\rangle\hat{\rho}\right)dt \\ &+ \sqrt{\frac{\kappa}{2}}\left(\hat{\rho}\hat{a}^\dagger e^{i\phi} + \hat{a}e^{-i\phi}\hat{\rho} - \langle\hat{a}^\dagger e^{i\phi} + \hat{a}e^{-i\phi}\rangle\hat{\rho}\right)(dW_1 - dW_2). \end{aligned} \tag{2.260}$$

Since the sum of independent Gaussian random variables is still a Gaussian random variable with a summed expectation value and variance, we have $dW = (dW_1 - dW_2)/\sqrt{2}$. Therefore, we get

$$\begin{aligned} d\hat{\rho} = &-\frac{i}{\hbar}[\hat{H}, \hat{\rho}]dt + \kappa\left(\hat{a}\hat{\rho}\hat{a}^\dagger - \frac{1}{2}\hat{a}^\dagger\hat{a}\hat{\rho} - \frac{1}{2}\hat{\rho}\hat{a}^\dagger\hat{a}\right) \\ &+ \sqrt{\kappa}\left(\hat{\rho}\hat{a}^\dagger e^{i\phi} + \hat{a}e^{-i\phi}\hat{\rho} - \langle\hat{a}^\dagger e^{i\phi} + \hat{a}e^{-i\phi}\rangle\hat{\rho}\right)dW. \end{aligned} \tag{2.261}$$

The measurement record for the homodyne detection is the difference between the signals of the two photon detectors,

$$I_{\text{det}}dt = dN_1 - dN_2 = |\beta|\left(\kappa\langle\hat{a}^\dagger e^{i\phi} + \hat{a}e^{-i\phi}\rangle dt + \sqrt{\kappa}dW\right). \tag{2.262}$$

In an experiment, it is not possible to collect all the photons leaking out from the cavity. Here we define the quantum efficiency $\eta \in [0, 1]$ to describe the case that we only detect ηN photons from the N photons leaking out. In this case, the system dynamics under homodyne detection

becomes

$$\begin{aligned}\hat{\rho}(t+dt) = &\frac{\hat{M}_0\hat{\rho}(t)\hat{M}_0^\dagger}{1-\mathrm{Tr}[\hat{M}_1\hat{\rho}(t)\hat{M}_1^\dagger]-\mathrm{Tr}[\hat{M}_2\hat{\rho}(t)\hat{M}_2^\dagger]}(1-dN_1)(1-dN_2)\\ &+(1-\eta)\left(\frac{\hat{M}_1\hat{\rho}(t)\hat{M}_1^\dagger}{\mathrm{Tr}[\hat{M}_1\hat{\rho}(t)\hat{M}_1^\dagger]}+\frac{\hat{M}_2\hat{\rho}(t)\hat{M}_2^\dagger}{\mathrm{Tr}[\hat{M}_2\hat{\rho}(t)\hat{M}_2^\dagger]}\right)(1-dN_1)(1-dN_2)\\ &+\eta\frac{\hat{M}_1\hat{\rho}(t)\hat{M}_1^\dagger}{\mathrm{Tr}[\hat{M}_1\hat{\rho}(t)\hat{M}_1^\dagger]}dN_1+\eta\frac{\hat{M}_2\hat{\rho}(t)\hat{M}_2^\dagger}{\mathrm{Tr}[\hat{M}_2\hat{\rho}(t)\hat{M}_2^\dagger]}dN_2.\end{aligned} \tag{2.263}$$

Using the same calculation procedure, one can obtain the following stochastic master equation,

$$\begin{aligned}d\hat{\rho} = &-\frac{i}{\hbar}[\hat{H},\hat{\rho}]dt+\kappa\left(\hat{a}\hat{\rho}\hat{a}^\dagger-\frac{1}{2}\hat{a}^\dagger\hat{a}\hat{\rho}-\frac{1}{2}\hat{\rho}\hat{a}^\dagger\hat{a}\right)\\ &+\sqrt{\kappa\eta}\left(\hat{\rho}\hat{a}^\dagger e^{i\phi}+\hat{a}e^{-i\phi}\hat{\rho}-\langle\hat{a}^\dagger e^{i\phi}+\hat{a}e^{-i\phi}\rangle\hat{\rho}\right)dW.\end{aligned} \tag{2.264}$$

as well as the measurement record,

$$I_{\mathrm{det}}dt = dN_1-dN_2 = |\beta|\Big(\kappa\eta\langle\hat{a}^\dagger e^{i\phi}+\hat{a}e^{-i\phi}\rangle dt+\sqrt{\kappa\eta}\,dW\Big). \tag{2.265}$$

Following a similar derivation to the one we did for the one-axis twisting interaction, for the dispersive atom-light coupling Hamiltonian (see Eq. (2.242)), we can rewrite the cavity field operator as $\hat{a} = \alpha+\hat{b}$, where $\alpha = \epsilon/(\tilde{\Delta}_c+i\kappa/2)$, $\hat{b}$ describes the quantum fluctuations near the coherent state. In the regime with $\tilde{\Delta}_c$ or κ the largest frequency scale, one can eliminate the photon field by replacing

$$\hat{b}\to\frac{\tilde{\mathcal{G}}\alpha\hat{S}^z}{\tilde{\Delta}_c+i\kappa/2}, \tag{2.266}$$

and obtain the atom-only stochastic master equation (dropping single-particle rotation terms),

$$\begin{aligned}d\hat{\rho} = &-i[\chi\hat{S}^z\hat{S}^z,\hat{\rho}]dt+\Gamma_z\left(\hat{S}^z\hat{\rho}\hat{S}^z-\frac{1}{2}\hat{S}^z\hat{S}^z\hat{\rho}-\frac{1}{2}\hat{\rho}\hat{S}^z\hat{S}^z\right)\\ &+\sqrt{\Gamma_z\eta}\left(\hat{\rho}\hat{S}^z+\hat{S}^z\hat{\rho}-2\langle\hat{S}^z\rangle\hat{\rho}\right)dW.\end{aligned} \tag{2.267}$$

with χ and Γ_z given by Eq. (2.249), as well as the measurement record,

$$I_{\mathrm{det}}dt\propto\Big(2\sqrt{\Gamma_z\eta}\langle\hat{S}^z\rangle dt+\,dW\Big). \tag{2.268}$$

Here we choose the homodyne angle $\phi = 2\arctan\Big(2\tilde{\Delta}_c/\kappa\Big)$ to maximize the average measurement record $E[I_{\mathrm{det}}]$, if we assume the intracavity pump ϵ is a real number. Since the measurement observable $\hat{S}^z$ commutes with the system Hamiltonian, such type of measurement is known as a quantum nondemolition (QND) measurement.

2.5 Quantum metrology

In this section, we introduce the theory tools for quantum metrology. We start from a brief review of the concepts of quantum Fisher information and quantum Cramér–Rao bound, and then discuss the standard quantum limit and Heisenberg limit in phase shift measurements widely used in atomic clocks and atom interferometers. We then introduce the concept of spin squeezing arise from phase shift measurements, and discuss an analytic solvable model known as one-axis twisting model for spin squeezing and quantum Fisher information.

2.5.1 Quantum Fisher information

Here we introduce the concept of quantum Fisher information, which is a key concept for understanding the precision of quantum measurements. Instead of providing a direct definition that comes out of nowhere, we prefer to first explain the context of evaluation of the precision of a measurement, and one could see the idea of quantum Fisher information comes out naturally when exploring the precision limit. For simplicity, here we discuss the case of measuring a single parameter ϕ.

A general measurement procedure is to prepare an initial state described by density matrix $\hat{\rho}_0$, then let the system evolve based on the unknown parameter ϕ which transforms the density matrix into $\hat{\rho}_\phi$, and finally measure an observable to obtain outcome x. The measurement outcome x can be described by a conditional probability $p(x|\phi)$. Based on our knowledge of the system dynamics, we can construct an estimator function $\phi_{\text{est}}(x)$ to infer the parameter from measurement outcome x. The measurement precision is characterized by the mean square error between the infer parameter $\phi_{\text{est}}(x)$ and the actual parameter ϕ,

$$(\Delta\phi)^2 = \int dx[\phi - \phi_{\text{est}}(x)]^2 p(x|\phi). \tag{2.269}$$

We also assume the estimator is unbiased such that the expectation of the estimator equals the actual parameter ϕ, i.e.

$$\int dx[\phi - \phi_{\text{est}}(x)]p(x|\phi) = 0. \tag{2.270}$$

Different types of estimators are discussed in Ref. [7]. Here we only discuss one example of estimator widely used in experiments, which is based on the expectation value of the measurement outcome, $\bar{x}(\phi) = \int dx\, x\, p(x|\phi)$. If we consider the actual parameter is near a constant value ϕ_0, $\phi = \phi_0 + d\phi$, Taylor expansion of $\bar{x}(\phi)$ gives $\bar{x}(\phi) \simeq \bar{x}(\phi_0) + \frac{d\bar{x}}{d\phi}|_{\phi_0} d\phi$, so the estimator function is given by

$$\phi_{\text{est}}(x) \simeq \phi_0 + \frac{x - \bar{x}(\phi_0)}{\frac{d\bar{x}}{d\phi}|_{\phi_0}}. \tag{2.271}$$

The mean square error is this case is given by the error propagation formula,

$$(\Delta\phi)^2 \simeq \frac{(\Delta x)^2|_{\phi_0}}{(\frac{d\bar{x}}{d\phi}|_{\phi_0})^2}, \tag{2.272}$$

where $(\Delta x)^2 = \int dx [x - \bar{x}(\phi)]^2 p(x|\phi)$.

The first step is to analyze a lower bound of $(\Delta\phi)^2$ regardless of the choice of estimator function $\phi_{\text{est}}(x)$. Taking derivative to Eq. (2.270) with respect to ϕ, we have

$$\int dx\, [\phi_{\text{est}}(x) - \phi]\, p(x|\phi)\, \frac{\partial \ln p(x|\phi)}{\partial \phi} = 1. \tag{2.273}$$

We consider the LHS of the equation above is the inner product of a function $f = [\phi_{\text{est}}(x) - \phi]\sqrt{p(x|\phi)}$ and another function $g = \sqrt{p(x|\phi)}\frac{\partial \ln p(x|\phi)}{\partial \phi}$. Based on the Cauchy-Schwarz inequality, $(\int dx\, fg)^2 \leq (\int dx\, f^2)(\int dx\, g^2)$, which gives

$$(\Delta\phi)^2 \geq \frac{1}{F_\phi}, \quad F_\phi = \int dx\, p(x|\phi) \left(\frac{\partial \ln p(x|\phi)}{\partial \phi}\right)^2. \tag{2.274}$$

This is the so-called classical Cramér–Rao bound, and F_ϕ is the so-called classical Fisher information.

Note that classical Fisher information F_ϕ depends on the conditional probability $p(x|\phi)$, which is determined by the details of measurement procedure. So the second step is to analyze a lower bound of F_ϕ regardless of the choice of measurement. The most general form of quantum measurement is described by a positive operator valued measure (POVM), which is a set $\{\hat{\Pi}_x\}$ of positive Hermitian operators such that $\int dx \hat{\Pi}_x = \hat{I}$. Based on POVM, we have $p(x|\phi) = \text{Tr}[\hat{\rho}_\phi \hat{\Pi}_x]$. If we define the symmetric logarithmic derivative (SLD) $\hat{L}_\phi$ as a Hermitian operator satisfying the

equation

$$\frac{\partial\hat{\rho}_\phi}{\partial\phi}=\frac{1}{2}(\hat{L}_\phi\hat{\rho}_\phi+\hat{\rho}_\phi\hat{L}_\phi), \tag{2.275}$$

which gives $\partial_\phi p(x|\phi)=\mathrm{Re}(\mathrm{Tr}[\hat{\rho}_\phi\hat{\Pi}_x\hat{L}_\phi])$. Plugging this in Eq. (2.274), we have

$$F_\phi=\int dx\frac{\mathrm{Re}(\mathrm{Tr}[\hat{\rho}_\phi\hat{\Pi}_x\hat{L}_\phi])^2}{\mathrm{Tr}[\hat{\rho}_\phi\hat{\Pi}_x]}. \tag{2.276}$$

The lower bound of F_ϕ can be calculated in the following way [70]:

$$\begin{aligned}F_\phi&\leq\int dx\left|\frac{\mathrm{Tr}[\hat{\rho}_\phi\hat{\Pi}_x\hat{L}_\phi]}{\sqrt{\mathrm{Tr}[\hat{\rho}_\phi\hat{\Pi}_x]}}\right|^2=\int dx\left|\mathrm{Tr}\left[\frac{\sqrt{\hat{\rho}_\phi}\sqrt{\hat{\Pi}_x}}{\sqrt{\mathrm{Tr}[\hat{\rho}_\phi\hat{\Pi}_x]}}\sqrt{\hat{\Pi}_x}\hat{L}_\phi\sqrt{\hat{\rho}_\phi}\right]\right|^2\\&\leq\int dx\mathrm{Tr}[\hat{\Pi}_x\hat{L}_\phi\hat{\rho}_\phi\hat{L}_\phi]=\mathrm{Tr}[\hat{\rho}_\phi\hat{L}_\phi^2].\end{aligned} \tag{2.277}$$

Between the first and the second line, we used the Cauchy-Schwarz inequality for Frobenius inner product of matrices, $|\mathrm{Tr}[\hat{A}^\dagger\hat{B}]|^2\leq\mathrm{Tr}[\hat{A}^\dagger\hat{A}]\mathrm{Tr}[\hat{B}^\dagger\hat{B}]$. So we reach the quantum Cramér–Rao bound, with $\mathcal{F}_\phi$ the quantum Fisher information,

$$(\Delta\phi)^2\geq\frac{1}{\mathcal{F}_\phi},\quad\mathcal{F}_\phi=\mathrm{Tr}[\hat{\rho}_\phi\hat{L}_\phi^2]=\mathrm{Tr}[\hat{L}_\phi(\partial_\phi\hat{\rho}_\phi)]. \tag{2.278}$$

Note that quantum Fisher information $\mathcal{F}_\phi$ still depends on the initial state of the system and the ways to encode ϕ into the system evolution. We discuss the further optimization of $\mathcal{F}_\phi$ in the next subsection.

The discussion above can be easily generalized to the case of measuring multiple parameters $\boldsymbol{\phi}=(\phi_1,\phi_2,\cdots,\phi_n)$. In this case we can define the quantum Fisher information matrix (QFIM) $\mathcal{F}$, whose matrix elements are given by

$$\mathcal{F}_{\mu\nu}=\frac{1}{2}\mathrm{Tr}[\hat{\rho}(\hat{L}_\mu\hat{L}_\nu+\hat{L}_\nu\hat{L}_\mu)]=\mathrm{Tr}[\hat{L}_\mu(\partial_\nu\hat{\rho})], \tag{2.279}$$

where $\hat{L}_\mu$ is the SLD defined by Eq. (2.275) with respect to ϕ_μ, $\partial_\nu\equiv\partial_{\phi_\nu}$, and $\hat{\rho}\equiv\hat{\rho}_{\boldsymbol{\phi}}$. In this case the quantum Cramér–Rao bound becomes [71]

$$\mathrm{Cov}(\boldsymbol{\phi})\geq\mathcal{F}^{-1}. \tag{2.280}$$

Here the matrix inequality means $\mathrm{Cov}(\boldsymbol{\phi}) - \mathcal{F}^{-1}$ is a positive semi-definite matrix. Since the diagonal element of a positive semi-definite matrix is non-negative, the matrix inequality can be converted into n different quantum Cramér–Rao bounds for measurements in the eigenbasis of $\mathcal{F}$.

Explicit expressions for the QFIM [71] can be obtained via formal integration of Eq. (2.275),

$$\hat{L}_\mu = 2\int_0^\infty ds e^{-\hat{\rho}s}(\partial_\mu\hat{\rho})e^{-\hat{\rho}s}, \tag{2.281}$$

which leads to

$$\mathcal{F}_{\mu\nu} = 2\int_0^\infty ds \mathrm{Tr}[e^{-\hat{\rho}s}(\partial_\mu\hat{\rho})e^{-\hat{\rho}s}(\partial_\nu\hat{\rho})]. \tag{2.282}$$

If we expand the density matrix $\hat{\rho}$ in its eigendecomposition $\hat{\rho} = \sum_j \lambda_j|\lambda_j\rangle\langle\lambda_j|$, plug in Eq. (2.282) we get

$$\mathcal{F}_{\mu\nu} = 2\sum_{\substack{jk \\ (\lambda_j+\lambda_k>0)}} \frac{\mathrm{Re}(\langle\lambda_j|\partial_\mu\hat{\rho}|\lambda_k\rangle\langle\lambda_k|\partial_\nu\hat{\rho}|\lambda_j\rangle)}{\lambda_j+\lambda_k}. \tag{2.283}$$

In the case of a pure state parametrized by $\boldsymbol{\phi}$, $|\psi\rangle \equiv |\psi(\boldsymbol{\phi})\rangle$, we can plug in $\hat{\rho} = |\psi\rangle\langle\psi|$, which gives

$$\mathcal{F}_{\mu\nu} = 4\,\mathrm{Re}\Big(\langle\partial_\mu\psi|\partial_\nu\psi\rangle - \langle\partial_\mu\psi|\psi\rangle\langle\psi|\partial_\nu\psi\rangle\Big). \tag{2.284}$$

Note that the calculation above is based on the fact that $\partial_\mu\langle\psi|\psi\rangle = \langle\partial_\mu\psi|\psi\rangle + \langle\psi|\partial_\mu\psi\rangle = 0$.

In the following we would like to discuss the physical meaning of the QFIM. Since a more precise measurement of a parameter $\boldsymbol{\phi}$ is equivalent to a larger distance between $|\psi(\boldsymbol{\phi})\rangle$ and $|\psi(\boldsymbol{\phi}+d\boldsymbol{\phi})\rangle$ states with an infinitesimal change of parameter $d\boldsymbol{\phi}$, we can interpret QFIM as a measure for the distance between these two states. The Bures distance between quantum states are defined by the reduction of fidelity [72], which gives

$$\begin{aligned} D_B^2 &= 2 - 2|\langle\psi(\boldsymbol{\phi})|\psi(\boldsymbol{\phi}+d\boldsymbol{\phi})\rangle| \\ &= -\Big(\langle\partial_\mu\psi|\psi\rangle\langle\psi|\partial_\nu\psi\rangle + \langle\psi|\partial_\mu\partial_\nu\psi\rangle + \langle\partial_\mu\partial_\nu\psi|\psi\rangle\Big)d\phi_\mu d\phi_\nu. \end{aligned} \tag{2.285}$$

Since we require $\langle\psi(\boldsymbol{\phi}+d\boldsymbol{\phi})|\psi(\boldsymbol{\phi}+d\boldsymbol{\phi})\rangle = 1$, which is equivalent to $\langle\partial_\mu\psi|\partial_\nu\psi\rangle + \langle\partial_\nu\psi|\partial_\mu\psi\rangle + \langle\psi|\partial_\mu\partial_\nu\psi\rangle + \langle\partial_\mu\partial_\nu\psi|\psi\rangle = 0$. So we have

$$D_B^2 = \Big(\langle\partial_\mu\psi|\partial_\nu\psi\rangle + \langle\partial_\nu\psi|\partial_\mu\psi\rangle - \langle\partial_\mu\psi|\psi\rangle\langle\psi|\partial_\nu\psi\rangle\Big)d\phi_\mu d\phi_\nu = \frac{1}{4}\mathcal{F}_{\mu\nu}d\phi_\mu d\phi_\nu, \tag{2.286}$$

where we used the fact that $\langle\partial_\mu\psi|\psi\rangle$ is pure imaginary, hence $\langle\partial_\mu\psi|\psi\rangle\langle\psi|\partial_\nu\psi\rangle$ is a real number. Note that this relation also holds for mixed states if we replace the definition of fidelity $|\langle\psi_1|\psi_2\rangle|^2$ by the miexed state fidelity $\left(\mathrm{Tr}[\sqrt{\sqrt{\hat{\rho}_1}\hat{\rho}_2\sqrt{\hat{\rho}_1}}]\right)^2$.

It is also worth to mention a interesting connection between QFIM and Berry curvature in the case of pure states. Here we define a quantum geometry tensor [72],

$$Q_{\mu\nu} = \langle\partial_\mu\psi|\partial_\nu\psi\rangle - \langle\partial_\mu\psi|\psi\rangle\langle\psi|\partial_\nu\psi\rangle. \tag{2.287}$$

The real part of $Q_{\mu\nu}$ is related to QFIM by

$$\mathrm{Re}(Q_{\mu\nu}) = \frac{1}{4}\mathcal{F}_{\mu\nu}, \tag{2.288}$$

while the imaginary part of $Q_{\mu\nu}$ is related to Berry curvature $\Omega_{\mu\nu}$ by

$$\mathrm{Im}(Q_{\mu\nu}) = \mathrm{Im}(\langle\partial_\mu\psi|\partial_\nu\psi\rangle) = -\frac{1}{2}\Omega_{\mu\nu}. \tag{2.289}$$

Note that $\Omega_{\mu\nu} = \partial_\mu\mathcal{A}_\nu - \partial_\nu\mathcal{A}_\mu$, where $\mathcal{A}_\mu = i\langle\psi|\partial_\mu\psi\rangle$ is the Berry connection. The geometric phase γ for a close loop can be obtained by

$$\gamma = \oint_{\partial S}\mathcal{A}_\mu d\phi_\mu = \frac{1}{2}\int_S \Omega_{\mu\nu}d\phi_\mu\wedge d\phi_\nu, \tag{2.290}$$

where ∂S is a close loop around the surface S, and $\wedge$ means the exterior product satisfying $d\phi_\mu\wedge d\phi_\nu = -d\phi_\nu\wedge d\phi_\mu$. We understand the connection between QFIM and Berry curvature in the following way: The Berry connection originates from the phase difference $d\varphi$ between two wave functions $|\psi(\boldsymbol{\phi})\rangle$ and $|\psi(\boldsymbol{\phi}+d\boldsymbol{\phi})\rangle$ with an infinitesimal change of parameter $d\boldsymbol{\phi}$,

$$e^{-i(d\varphi)} = \frac{\langle\psi(\boldsymbol{\phi})|\psi(\boldsymbol{\phi}+d\boldsymbol{\phi})\rangle}{|\langle\psi(\boldsymbol{\phi})|\psi(\boldsymbol{\phi}+d\boldsymbol{\phi})\rangle|} \quad\Rightarrow\quad d\varphi = \mathcal{A}_\mu d\phi_\mu. \tag{2.291}$$

As we discussed in Eq. (2.286), QFIM measures the distance between $|\psi(\boldsymbol{\phi})\rangle$ and $|\psi(\boldsymbol{\phi}+d\boldsymbol{\phi})\rangle$. So one can unify QFIM and Berry curvature when discussing the difference between these two states.

2.5.2 Standard quantum limit and Heisenberg limit

Here we are considering the upper bound of the quantum Fisher information for a system with N two-level spins, which gives a lower bound of measurement precision. We focus on the

phase shift measurement widely used in atomic clocks and atom interferometers, where the phase ϕ is encoded into the density matrix in the following way,

$$\hat{\rho}_\phi = e^{-i\phi\hat{S}^z}\,\hat{\rho}_0\,e^{i\phi\hat{S}^z}, \tag{2.292}$$

so the quantum Fisher information becomes

$$\mathcal{F}_\phi = 2\sum_{\substack{jk\\(\lambda_j+\lambda_k>0)}}\frac{(\lambda_j-\lambda_k)^2}{\lambda_j+\lambda_k}|\langle\lambda_j|\hat{S}^z|\lambda_k\rangle|^2. \tag{2.293}$$

In the case of pure state, we have

$$\mathcal{F}_\phi = 4\Big(\langle\psi|\hat{S}^z\hat{S}^z|\psi\rangle - \langle\psi|\hat{S}^z|\psi\rangle^2\Big). \tag{2.294}$$

Based on the convexity of quantum Fisher information, $\mathcal{F}_\phi[p\hat{\rho}_1+(1-p)\hat{\rho}_2] \le p\mathcal{F}_\phi[\hat{\rho}_1]+(1-p)\mathcal{F}_\phi[\hat{\rho}_2]$, the upper bound of quantum Fisher information should be achieved by pure states.

First we consider product states with $|\psi\rangle = |\psi_1\rangle\otimes|\psi_2\rangle\otimes\cdots\otimes|\psi_N\rangle$, so the quantum Fisher information becomes

$$\mathcal{F}_\phi = \sum_j 4\Big(\langle\psi_j|\hat{S}_j^z\hat{S}_j^z|\psi_j\rangle - \langle\psi_j|\hat{S}_j^z|\psi_j\rangle^2\Big) = \sum_j\Big(1-\langle\psi_j|\hat{S}_j^z|\psi_j\rangle^2\Big) \le N. \tag{2.295}$$

The equal sign can be reached for product states on the equator, $\langle\psi_j|\hat{S}_j^z|\psi_j\rangle = 0$. This leads to the standard quantum limit (SQL) restricted to product states [73]

$$(\Delta\phi)^2 \ge \frac{1}{N}. \tag{2.296}$$

Then we consider the case with all possible quantum states, and in this case we have

$$\mathcal{F}_\phi \le 4\langle\psi|\hat{S}^z\hat{S}^z|\psi\rangle \le N^2. \tag{2.297}$$

The equal sign can be achieved by a GHZ state,

$$|\psi_{\rm GHZ}\rangle = \frac{1}{\sqrt{2}}\Big(|N/2,N/2\rangle + e^{-i\varphi}|N/2,-N/2\rangle\Big). \tag{2.298}$$

This leads to the Heisenberg limit (for all possible quantum states) [73]

$$(\Delta\phi)^2 \ge \frac{1}{N^2}. \tag{2.299}$$

2.5.3 Spin squeezing and one-axis twisting

For the phase accumulation described by Eq. (2.292), suppose the initial state is along the x direction of the Bloch sphere, i.e. $\langle \hat{S}^x \rangle_{\phi=0} \neq 0$, $\langle \hat{S}^y \rangle_{\phi=0} = \langle \hat{S}^z \rangle_{\phi=0} = 0$, and we perform a projective measurement $\hat{S}^y$ after phase accumulation. Since $\langle \hat{S}^y \rangle = \sin\phi \langle \hat{S}^x \rangle_{\phi=0}$, we can calculate the phase sensitivity for small ϕ based on the error propagation formula (see Eq. (2.272)),

$$(\Delta\phi)^2 = \frac{(\Delta S^y)^2}{(\partial_\phi \langle \hat{S}^y \rangle)^2} \simeq \frac{(\Delta S^y)^2_{\phi=0}}{|\langle \hat{S}^x \rangle_{\phi=0}|^2}, \tag{2.300}$$

where $(\Delta S^y)^2 = \langle \hat{S}^y \hat{S}^y \rangle - \langle \hat{S}^y \rangle^2$. Generalizing to the case of arbitrary spin orientation, the phase sensitivity is given by (we drop the subscript $\phi = 0$ for simplicity)

$$(\Delta\phi)^2 = \min_\theta \frac{(\Delta S^\perp_\theta)^2}{|\langle \hat{\mathbf{S}} \rangle|^2}, \tag{2.301}$$

where $(\Delta S^\perp_\theta)^2$ is the spin variance perpendicular to the spin orientation parametrized by θ. In the case of product states, if we assume all the spins pointing to the same direction, we get $|\langle \hat{\mathbf{S}} \rangle| = N/2$, $(\Delta S^\perp_\theta)^2 = N/4$, which leads to $(\Delta\phi)^2 = 1/N$, which is the standard quantum limit (SQL). Spin squeezing is referred to the reduction of the spin variance $(\Delta S^\perp_\theta)^2$ for some choices of θ, which leads to a enhancement of phase sensitivity beyond the SQL. Based on the Heisenberg uncertainty principle, $(\Delta S^\perp_\theta)^2 (\Delta S^\perp_{\theta+\pi/2})^2 \geq |\langle \hat{\mathbf{S}} \rangle|^2/4$, which gives $(\Delta\phi)^2 \geq 1/[4 \max_\theta (\Delta S^\perp_\theta)^2]$. Similar to the discussions in the previous subsection, this leads to the Heisenberg limit $(\Delta\phi)^2 \geq 1/N^2$.

Comparing the phase sensitivity with the SQL, one can obtain the Wineland spin squeezing parameter [74],

$$\xi^2 = \frac{(\Delta\phi)^2}{(\Delta\phi)^2_{\mathrm{SQL}}} = \min_\theta \frac{N(\Delta S^\perp_\theta)^2}{|\langle \hat{\mathbf{S}} \rangle|^2}. \tag{2.302}$$

Note that we have $\xi^2 = 1$ for SQL, $\xi^2 < 1$ when spin squeezing occurs, with a lower bound $\xi^2 \geq 1/N$ set by the Heisenberg limit. Usually the spin squeezing parameter is reported in terms of decibel (dB), i.e. $10 \log_{10} \xi^2$.

As proposed by Ref. [30], an iconic model for spin squeezing generation is known as the one-axis twisting (OAT) model,

$$\hat{H}_{\mathrm{OAT}} = \chi \hat{S}^z \hat{S}^z. \tag{2.303}$$

This model features an analytical solution for the expectation value of all possible combinations of spin operators as we discuss below. We consider the Heisenberg equation of motion under one-axis twisting (OAT),

$$\frac{d}{dt}\hat{O} = i\Big[\frac{\chi}{2}\sum_{j<k}\hat{\sigma}_j^z\hat{\sigma}_k^z, \hat{O}\Big], \tag{2.304}$$

where $\hat{\sigma}_j^{x,y,z}$ are Pauli matrices for the j-th spin. A general form of operator $\hat{O}$ up to permutation symmetry can be written as

$$\hat{O}(n_1, n_2, n_3) = \prod_{j_1=1}^{n_1+n_2}\hat{\sigma}_{j_1}^{+}\prod_{j_2=n_1+n_2+1}^{n_1+2n_2}\hat{\sigma}_{j_2}^{-}\prod_{j_3=n_1+2n_2+1}^{n_1+2n_2+n_3}\hat{\sigma}_{j_3}^{z}, \tag{2.305}$$

where $n_1+2n_2+n_3 \leq N$. We focus on the initial state with all the spin aligned to the $+x$ direction. Note that in the case of $n_1 = 0$, $\hat{O}$ commutes with the OAT Hamiltonian, so we can directly evaluate the expectation value using the initial state,

$$\langle\hat{O}(0, n_2, 0)\rangle = \frac{1}{2^{2n_2}}, \quad \langle\hat{O}(0, n_2, n_3 > 0)\rangle = 0. \tag{2.306}$$

Then we consider the case when $n_1 > 0$. The Heisenberg equations of motion can now be written as a set of coupled differential equations based on permutation symmetry of the spin indices,

$$\frac{\mathrm{d}}{\mathrm{d}t}\langle\hat{O}(n_1, n_2, j)\rangle = i\chi\sum_k A_{jk}\langle\hat{O}(n_1, n_2, k)\rangle, \quad j, k = 0, 1, \cdots, N - n_1 - 2n_2. \tag{2.307}$$

where the non-zero matrix elements of A_{jk} are

$$A_{j,j+1} = (N - n_1 - 2n_2 - j)n_1, \quad A_{j,j-1} = jn_1. \tag{2.308}$$

We solve the differential equations above via a trial solution as follows,

$$\langle\hat{O}(n_1, n_2, j)\rangle = \frac{1}{2^{n_1+2n_2}}[f(t)]^{N-n_1-2n_2-j}\left(\frac{f'(t)}{in_1\chi}\right)^j. \tag{2.309}$$

This trial solution simplifies the coupled differential equations into the following form,

$$f''(t) + \chi^2 n_1^2 f(t) = 0, \tag{2.310}$$

with initial condition $f(0) = 1, f'(0) = 0$, which gives

$$f(t) = \cos(n_1\chi t), \quad \frac{f'(t)}{in_1\chi} = i\sin(n_1\chi t). \tag{2.311}$$

Therefore, we have a single expression for all choices of n_1, n_2, n_3 (define $0^0 = 1$),

$$\langle \hat{O}(n_1, n_2, n_3) \rangle = \frac{i^{n_3}}{2^{n_1+2n_2}} [\cos(n_1 \chi t)]^{N-n_1-2n_2-n_3} [\sin(n_1 \chi t)]^{n_3}. \tag{2.312}$$

Based on the analytical solution above, one can obtain the following list of expectation values of collective spin operators:

$$\begin{gathered}
\langle S^x \rangle = \frac{N}{2} \cos^{N-1}(\chi t), \quad \langle \hat{S}^z \rangle = \langle \hat{S}^y \rangle = \langle \hat{S}^x \hat{S}^y + \hat{S}^y \hat{S}^x \rangle = \langle \hat{S}^x \hat{S}^z + \hat{S}^z \hat{S}^x \rangle = 0, \\
\langle \hat{S}^x \hat{S}^x \rangle = \frac{N}{4} + \frac{N(N-1)}{8} \Big[1 + \cos^{N-2}(2\chi t) \Big], \quad \langle \hat{S}^y \hat{S}^y \rangle = \frac{N}{4} + \frac{N(N-1)}{8} \Big[1 - \cos^{N-2}(2\chi t) \Big], \\
\langle \hat{S}^z \hat{S}^z \rangle = \frac{N}{4}, \quad \langle \hat{S}^y \hat{S}^z + \hat{S}^z \hat{S}^y \rangle = \frac{N(N-1)}{2} \sin(\chi t) \cos^{N-2}(\chi t).
\end{gathered} \tag{2.313}$$

This approach can be easily generalized to the cases including dissipations (see Chapter 5.2).

If we only focus on the unitary dynamics, these formula are also possible to achieve in the collective spin basis $|S, m\rangle$. Here we use the collective spin basis $|S, m\rangle$ to discuss the resulting state at $\chi t = \pi/2$ (assuming S is an integer or equivalently N is even). Considering an initial state

$$|\psi_0\rangle = \sum_m c_m |S, m\rangle, \tag{2.314}$$

the time evolution under the OAT model leads to

$$|\psi(t)\rangle = \sum_m c_m e^{-i\chi m^2 t} |S, m\rangle. \tag{2.315}$$

Note that $m^2 \mod 4 \equiv 0$ for even m and $m^2 \mod 4 \equiv 1$ for odd m. For $\chi t = \pi/2$, we have

$$|\psi(\chi t = \pi/2)\rangle = \sum_{m \in \text{even}} c_m |S, m\rangle - i \sum_{m \in \text{odd}} c_m |S, m\rangle. \tag{2.316}$$

Based on the definition of spin coherent state (see Eq. (2.159)), we have

$$|+x\rangle = \frac{1}{2^S} \sum_{m=-S}^{S} \sqrt{\binom{2S}{S+m}} |S, m\rangle, \quad |-x\rangle = \frac{1}{2^S} \sum_{m=-S}^{S} \sqrt{\binom{2S}{S+m}} (-1)^m |S, m\rangle. \tag{2.317}$$

Considering $|\psi_0\rangle = |+x\rangle$, one can obtain $\sum_{m \in \text{even}} c_m |S, m\rangle = (|+x\rangle + |-x\rangle)/2$, $\sum_{m \in \text{odd}} c_m |S, m\rangle = (|+x\rangle - |-x\rangle)/2$, leading to

$$|\psi(\chi t = \pi/2)\rangle = \frac{1-i}{2} |+x\rangle + \frac{1+i}{2} |-x\rangle = \frac{1}{\sqrt{2}} \Big(|+x\rangle + i |-x\rangle \Big). \tag{2.318}$$

Here we removed a global phase in the last step. Therefore, the time evolution with $\chi t = \pi/2$ under OAT model leads to a GHZ state.

In the following, we analyze several metrological properties of the OAT model using Eq. (2.313):

- Optimal spin squeezing

  In this case we have $\langle \hat{\mathbf{S}} \rangle = \langle \hat{S}^x \rangle$, and $(\Delta S_\theta^\perp)^2 = \mathcal{A}\cos^2\theta + \mathcal{B}\sin^2\theta + \mathcal{C}\cos\theta\sin\theta$, where $\mathcal{A} = \langle \hat{S}^z\hat{S}^z \rangle$, $\mathcal{B} = \langle \hat{S}^y\hat{S}^y \rangle$, $\mathcal{C} = \langle \hat{S}^y\hat{S}^z + \hat{S}^z\hat{S}^y \rangle$. Minimizing over θ, we have

  $$\min_\theta (\Delta S_\theta^\perp)^2 = \frac{\mathcal{A}+\mathcal{B}}{2} - \frac{1}{2}\sqrt{(\mathcal{B}-\mathcal{A})^2 + \mathcal{C}^2}, \tag{2.319}$$

  and it is convenient to consider the following approximation for intermediate time ($\mathcal{B} \gg \mathcal{A}, \mathcal{C}$)

  $$\min_\theta (\Delta S_\theta^\perp)^2 = \frac{1}{2}\frac{4\mathcal{A}\mathcal{B}-\mathcal{C}^2}{\mathcal{A}+\mathcal{B}+\sqrt{(\mathcal{B}-\mathcal{A})^2+\mathcal{C}^2}} \approx \frac{4\mathcal{A}\mathcal{B}-\mathcal{C}^2}{4\mathcal{B}}. \tag{2.320}$$

  Notice that intermediate time means $\beta = S(\chi t)^2 \ll 1$ and $S\beta \gg 1$, with $S = N/2$, we have $4\mathcal{A}\mathcal{B} - \mathcal{C}^2 \approx S^2 + \frac{8}{3}S^3\beta^3$, and $\mathcal{B} \approx 2S^2\beta$. Also plugging in $\langle \hat{S}^x \rangle \approx S$, we get (see Fig. 2.7(a))

  $$\xi^2 \approx \frac{1}{2N\beta} + \frac{2}{3}\beta^2 \quad \Rightarrow \quad \xi^2_{\text{opt}} \approx \frac{3^{2/3}}{2}\frac{1}{N^{2/3}}. \tag{2.321}$$

  Therefore, we have shown that the scaling of optimal spin squeezing parameter for the OAT model $\xi^2_{\text{opt}} \sim N^{-2/3}$, which leads to the scaling of phase sensitivity $\Delta\phi \sim N^{-5/6}$.

- Maximal quantum Fisher information

  Here we consider phase accumulation parametrized by $\hat{U} = e^{-i\phi_\mu \hat{S}^\mu}$, with $\mu = x, y, z$. In this case, QFIM becomes

  $$\mathcal{F}_{\mu\nu} = 4\left(\frac{1}{2}\langle\psi|\hat{S}^\mu\hat{S}^\nu + \hat{S}^\nu\hat{S}^\mu|\psi\rangle - \langle\psi|\hat{S}^\mu|\psi\rangle\langle\psi|\hat{S}^\nu|\psi\rangle\right). \tag{2.322}$$

  We then diagonalize the QFIM to find the optimal axis (eigenvector) associated with the maximal eigenvalue of the QFIM. If the phase accumulation is along the optimal axis, the maximal eigenvalue is the corresponding quantum Fisher information, and this is the largest quantum Fisher information for phase accumulation with state $|\psi\rangle$.

Based on the analytical solution of the OAT model, the 3 eigenvalues of $\mathcal{F}_{\mu\nu}$ is given by $4\min_\theta(\Delta S_\theta^\perp)^2$, $4\max_\theta(\Delta S_\theta^\perp)^2$, $4(\Delta S^x)^2$, where

$$\max_\theta(\Delta S_\theta^\perp)^2 = \frac{\mathcal{A}+\mathcal{B}}{2} + \frac{1}{2}\sqrt{(\mathcal{B}-\mathcal{A})^2+\mathcal{C}^2}. \tag{2.323}$$

The maximal quantum Fisher information (see Fig. 2.7(b)) would be the maximal eigenvalue, which indicating the phase sensitivity if choosing the optimal rotation axis,

$$\mathcal{F}_{\max} = 4\max\{\max_\theta(\Delta S_\theta^\perp)^2, (\Delta S^x)^2\}. \tag{2.324}$$

One can check that in the time scale relevant for spin squeezing, we always have $\mathcal{F}_{\max} = 4\max_\theta(\Delta S_\theta^\perp)^2$, and $\xi^2 \approx N/\mathcal{F}_{\max}$. While for $\chi t = \pi/2$, we have $\mathcal{F}_{\max} = N^2$, since the system evolves into a GHZ state.

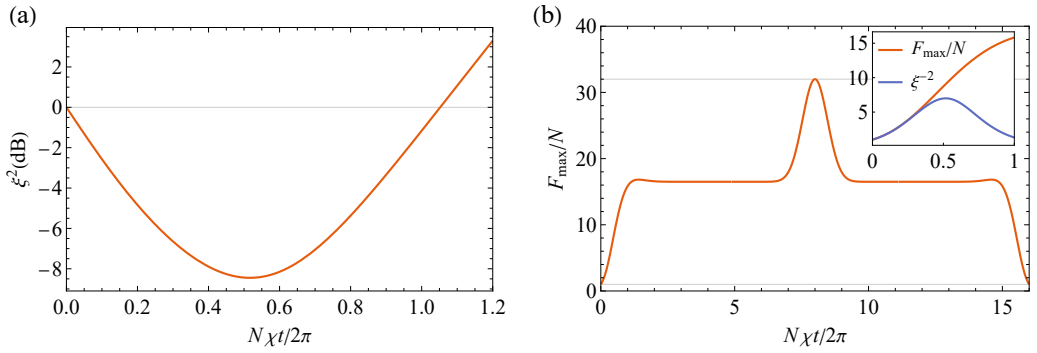

Figure 2.7: (a) Spin squeezing parameter ξ^2 under OAT evolution (32 atoms). (b) Maximal quantum Fisher information $\mathcal{F}_{\max}$ under OAT evolution. The inset is the comparison of $\mathcal{F}_{\max}/N$ and ξ^{-2} in the time scale relevant for spin squeezing.

Chapter 3

Improving optical lattice clocks via Hamiltonian engineering

3.1 Overview

The recent generation of optical lattice clocks, known as the Wannier-Stark optical lattice clocks, have led to a significant enhancement of precision and accuracy [23–25, 75]. Wannier-Stark optical lattice clock uses a vertically oriented lattice to trap the atoms. Since the linear tilt generated by gravity imposes an energy penalty to hop between lattice sites, one can achieve localized atomic wave functions even in shallow lattice depths, which is known as the Wannier-Stark localization. Operating at shallower lattice depths allows for a reduction of the decoherence effects and frequency shifts generated by the lattice potential, while the motional dephasing effects are still under controlled due to the Wannier-Stark localization. Most importantly, as we discussed in this chapter, Wannier-Stark optical lattice clocks also allow for a suppression of density shifts and an enhancement of coherence time by balancing the s-wave and p-wave contributions via Hamiltonian engineering. We applied Hamiltonian engineering tools to explore dynamical phase transitions and coherent superexchange interactions. Moreover, we have shown that the development of Wannier-Stark optical lattice clocks could enable the exploration of the interplay between general relativity and quantum many-body dynamics.

3.2 Hamiltonian engineering of spin-orbit coupled fermions in a Wannier-Stark optical lattice clock

This section is adapted from: Alexander Aeppli*, **Anjun Chu***, Tobias Bothwell*, Colin J. Kennedy, Dhruv Kedar, Peiru He, Ana Maria Rey, Jun Ye, *Hamiltonian engineering of spin-orbit coupled fermions in a Wannier-Stark optical lattice clock*, Science Advances 8, eadc9242 (2022).

3.2.1 Introduction

The joint advance of quantum metrology and quantum simulation provides exciting new opportunities to explore the frontiers of measurement science and the emergence of many-body complexity. An outstanding example has been the development of optical lattice clocks (OLCs) where excellent quantum coherence and exquisite quantum control of many atoms have enabled rapid advances in metrological capabilities [20,23,76–80], culminating in the recent demonstration of clock measurement precision at 7.6×10^{-21} and near minute-long atomic coherence [23]. To achieve this level of performance, we use a shallow, vertically aligned optical lattice. The acceleration due to local gravity lifts the degeneracy of neighboring sites, supporting partially delocalized Wannier-Stark eigenstates. This trapping scheme, first suggested in 2005 [81], allows us to operate the clock at substantially smaller lattice depths, greatly suppressing detrimental motional, light scattering, and atomic density induced decoherence.

The use of tilted optical lattices to manipulate motional degrees of freedom in ultracold gases has been widely reported. They have been used to suppress direct tunneling but not spin transport and realize new types of spin Hamiltonians [82–84], generate spin-orbit coupling via laser-assisted tunneling [85–88], emulate magnetic models in spinless bosons [89, 90], probe non-ergodicity due to kinetic constraints [91] and subdiffusive transport [92] in Fermi-Hubbard chains and many-body localization in trapped ions [93], as well as measure gravity in Raman interferometers [94–96]. In this work, we demonstrate how a tilted optical lattice combined with pristine quantum coherence and exquisite spectral resolution offer new capabilities to engineer, drive, and understand many-

body systems.

As we continue to push the OLC to new levels of precision, a key remaining issue for clock accuracy is related to frequency shifts associated with atomic interactions. Quantum statistics dictates that identical fermions experience only odd partial wave interactions that are suppressed at ultralow temperatures [66,97–101]. Yet, even the weak elastic and inelastic p-wave collisions were found to significantly affect clock operation and limit the number of interrogated atoms at deep lattice depths. As atoms delocalize along neighboring sites in the shallow lattice, p-wave collisions are reduced but s-wave interactions can emerge from the spin-orbit coupling (SOC) generated by the differential clock laser phase [102–104]. The superior quantum coherence obtained in our gravity-tilted optical lattice clock stems from better control over motional and internal degrees of freedom [23], allowing the engineering of s- and p-wave interactions in driven spin-orbit coupled fermionic atoms. By operating at the 'magic' lattice depth where s-wave interactions precisely cancel residual p-wave interactions, we reduce atomic-interaction induced shifts in our 1D lattice clock to a fractional frequency shift of $5.0(1.7) \times 10^{-21}$ per atom at a single site.

We further explore the tunability of atomic interactions by driving a site-changing Wannier-Stark transition. This leads to an atomic superposition that not only carries a distinct internal label but also features different motional orbitals. As a consequence, s-wave interactions are significantly enhanced. This gives rise to a many-body dynamical phase transition between dynamical ferromagnetic and paramagnetic states controlled by the interplay between the clock drive and atomic interactions. Although similar dynamical phase transitions have been observed in trapped ions [105], superconducting qubits [106], and atoms in cavities [107] and optical traps [34], here we use in situ imaging to locally resolve the emergence of a non-linear excitation lineshape as a function of atom number.

3.2.2 Experimental system and theoretical model

Several hundred thousand nuclear-spin-polarized fermionic ^{87}Sr atoms are cooled via standard techniques and loaded into a vertical one-dimensional optical lattice that defines the $\hat{Z}$ axis [23].

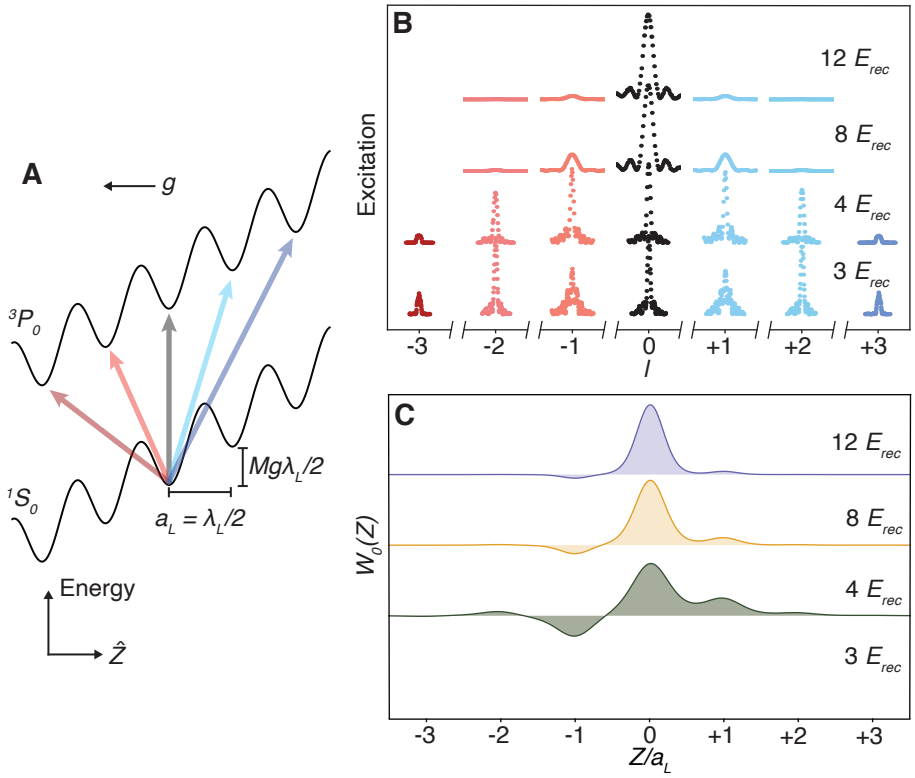

Figure 3.1: **The Wannier-Stark Clock.** (**A**) We trap ^{87}Sr atoms in a $1D$ optical lattice along the $\hat{Z}$ direction aligned with local gravitational acceleration g. This type of external confinement realizes Wannier-Stark states, eigenstates of the joint lattice plus gravitational potential. The n^{th} Wannier state $W_n(Z)$ is centered at lattice site n and has energy Mga_Ln, where M is the mass of ^{87}Sr and $a_L = \lambda_L/2$ is the lattice spacing with lattice wavelength λ_L. The Wannier-Stark ladder creates a set of transitions from the ground ($|g\rangle \equiv |^1S_0, m_F = \pm 5/2\rangle$) to clock ($|e\rangle \equiv |^3P_0, m_F = \pm 3/2\rangle$) state at different lattice sites accessible by the differential clock laser phase between them. The black line indicates a carrier $|g\,;W_n\rangle \rightarrow |e\,;W_n\rangle$ transition. At shallow lattice depths, a set of off-site transitions $|g\,;W_n\rangle \rightarrow |e\,;W_{n\pm l}\rangle$ for integer l are indicated by blue and red lines. (**B**) At shallow lattice depths, the atomic wavefunction becomes delocalized, allowing $|g\,;W_n\rangle \rightarrow |e\,;W_{n\pm l}\rangle$ transition for a range of l to be addressed. Here we show Rabi scans of these transitions at four different lattice depths, given in lattice photon recoil energy (E_{rec}). As the depth decreases, the Rabi frequency on the carrier transition decreases. We correspondingly lengthen the pulse time to maintain a π pulse on the carrier leading to narrower lineshapes at shallow depths. (**C**) The wavefunction $W_0(Z)$ for the four corresponding lattice depths, illustrating the tunable delocalization due to the interplay between lattice and gravitational potential.

We load the lattice at a depth of 300 lattice photon recoil energies (E_{rec}) with atoms in the lowest motional band along the $\hat{Z}$ axis. Perpendicular to the lattice axis, the atoms are weakly confined and thermally populate the resultant radial modes with a temperature of 800 nK. We then adiabatically reduce the lattice depth to a much lower operational depth with a correspondingly reduced radial temperature measured with Doppler spectroscopy.

The gravitational potential with local acceleration g adds a linear energy gradient across the lattice, with the combined single-particle Hamiltonian supporting Wannier-Stark (WS) eigenstates. The WS state $W_n(Z)$ is centered at lattice site n and has eigenenergy Mga_Ln, where M is the mass of ^{87}Sr and $a_L = \lambda_L/2$ is the lattice site spacing (Fig. 3.1(A)). Here, we use the strontium 'magic' wavelength $\lambda_L = 813$ nm, guaranteeing identical confinement for both clock states.

The clock laser $\lambda_c = 698$ nm, aligned along the lattice, drives the ultranarrow $|^1S_0, m_F = \pm 5/2\rangle \rightarrow |^3P_0, m_F = \pm 3/2\rangle$ ($|g\rangle \rightarrow |e\rangle$) clock transition, where m_F is the nuclear Zeeman level. This σ-polarized transition is the least magnetically sensitive clock transition in ^{87}Sr. Because the clock laser wavelength differs from the lattice spacing, adjacent lattice sites see a different clock phase $\varphi = \pi\lambda_L/\lambda_c \approx 7\pi/6$. This phase difference generates SOC when the lattice depth is sufficiently low for atoms to tunnel during the course of the experiment. Thus, when tuned to appropriate frequencies, the clock laser effectively couples Wannier-Stark states between different lattice sites, i.e. $|g\,;\, W_n\rangle \rightarrow |e\,;\, W_{n+l}\rangle$, for a range of integer l. The corresponding Rabi frequency Ω_l set by the wavefunction overlap is

$$\Omega_l \propto \exp\left(-\frac{\lambda_L^2}{4\lambda_c^2\sqrt{V_0}}\right)\mathcal{J}_l\left(\frac{4J_0}{Mga_L}\sin(\varphi/2)\right). \tag{3.1}$$

Here, $\mathcal{J}_l$ is a Bessel function, J_0 is the nearest neighbor tunneling energy of the ground band, and V_0 is the lattice depth in E_{rec}.

We utilize Rabi spectroscopy in a dilute ensemble to demonstrate the partially delocalized nature of the single-particle wavefunctions in shallow, tilted lattices of four different values of V_0, shown in Fig. 3.1(B). The corresponding WS wavefunctions $W_0(Z)$ are shown in Fig. 3.1(C). For each V_0, we optimize the transition probability on the carrier transition, $|g\,;\, W_n\rangle \rightarrow |e\,;\, W_n\rangle$. For

$V_0 = 12\ E_{rec}$, the atoms are still well localized, and thus the $|g\,;W_n\rangle \rightarrow |e\,;W_{n\pm1}\rangle$ transition amplitudes are significantly suppressed in comparison to the carrier. As V_0 is reduced, we resolve a set of Rabi lines spectrally separated by $Mga_L/h = 867$ Hz, where h is Planck's constant. At 4 E_{rec}, the Rabi frequency for the carrier and $|g\,;W_n\rangle \rightarrow |e\,;W_{n\pm1}\rangle$ transitions are roughly equivalent. At 3 E_{rec}, the carrier and $|g\,;W_n\rangle \rightarrow |e\,;W_{n\pm2}\rangle$ have similar Rabi frequencies, while the $|g\,;W_n\rangle \rightarrow |e\,;W_{n\pm1}\rangle$ transition has the greatest Rabi frequency and is thus overdriven. At low atomic density, we observe coherence times well past 10 s on $|g\,;W_n\rangle \rightarrow |e\,;W_{n+1}\rangle$.

Under our operating conditions, where the collisional rate for motional relaxation is smaller than the internal spin dynamics and trap frequencies, atoms remain effectively frozen in single-particle eigenstates during clock interrogation. Since all atoms are initially prepared in a single internal state, Fermi statistics forbids double occupancy of motional states. Under these conditions, the quantum dynamics can be described with a spin Hamiltonian in energy space spanned by the appropriate single-particle trap eigenmodes [34,62,100,101,108]. We identify a two level system for an atom in mode $\mathbf{n}$ as $|\uparrow_{\mathbf{n}}\rangle \equiv |e;n_X,n_Y,W_n\rangle$ and $|\downarrow_{\mathbf{n}}\rangle \equiv |g;n_X,n_Y,W_n\rangle$. Here, n_X and n_Y label the radial harmonic oscillator modes.

Two dominant types of interatomic interactions determine the coupling constants in the spin model: local interactions between atoms within a single lattice site and nearest-neighbour interactions between atoms in adjacent sites. Next to nearest-neighbor interactions are on the order of 10^{-2} of nearest-neighbor interactions or smaller for the operating conditions in our system and are neglected. The couplings between radial harmonic oscillator modes are highly collective as shown in prior experiments [62, 100, 101]. Therefore, to an excellent approximation, we define collective spin operators at each lattice site after summing over occupied harmonic oscillator modes, $\hat{S}_n^{x,y,z} = \sum_{n_X,n_Y} \hat{S}_{\mathbf{n}}^{x,y,z}$. The dynamics of the collective spin vector $\langle\hat{\mathbf{S}}_n\rangle = \{\langle\hat{S}_n^x\rangle, \langle\hat{S}_n^y\rangle, \langle\hat{S}_n^z\rangle\}$ are described by the following mean-field equation of motion written in a gauge frame where the laser drive is homogeneous (see SOM):

$$\frac{\mathrm{d}}{\mathrm{d}t}\langle\hat{\mathbf{S}}_n\rangle = \mathbf{B}^{\perp} \times \langle\hat{\mathbf{S}}_n\rangle. \tag{3.2}$$

The synthetic magnetic field $\mathbf{B}^{\perp}$ contains contributions of the laser drive with detuning δ from the bare transition and the self-generated interactions terms:

$$\mathbf{B}^{\perp} = \{\Omega_0, 0, -\delta + 2(\chi_0 + \chi_1)\langle \hat{S}^z \rangle + C_0 N_{\mathrm{loc}}\}. \tag{3.3}$$

Here $\langle \hat{S}^z \rangle = \frac{1}{2L+1} \sum_{m=-L}^{L} \langle \hat{S}^z_{n+m} \rangle$ is the average magnetization over a region of $2L+1 \sim 15$ lattice sites (corresponding to 1 camera pixel or 6 μm in our imaging spectroscopy) centered around n. N_{loc} is the number of atoms per lattice site averaged over the same region. The couplings, $\chi_0 = \eta_0(V_{ee}+V_{gg}-2V_{eg})/2, C_0 = \eta_0(V_{ee}-V_{gg})/2$, and $\chi_1 = -\eta_1 U_{eg}(1-\cos\varphi)$, respectively describe thermally averaged p-wave and s-wave interaction parameters between internal clock states, as well as on the on-site (η_0) and nearest-neighbour (η_1) overlap matrix elements along the lattice. In the absence of SOC, $\varphi = 0$, the s-wave interactions vanish.

Without interactions, the collective spin features a characteristic Rabi lineshape profile when driven during a pulse area $\Omega_0 T = \pi$ with excitation fraction $n_{\uparrow}(t) = \langle \hat{S}^z(t) \rangle / N_{\mathrm{loc}} + 1/2$, symmetric and centered around $\delta = 0$. With interactions the time evolution takes place in the presence of an additional self-generated axial magnetic field-like term that induces a non-linear response, resulting in an asymmetric lineshape. A simple estimation of the density shift can be obtained by setting it to be the value of δ at which $\mathbf{B}^{\perp}_z = 0$:

$$\Delta\nu_{\alpha\to\beta} = \Delta\nu^{s}_{\alpha\to\beta} + \Delta\nu^{p}_{\alpha\to\beta}, \tag{3.4}$$

$$2\pi\Delta\nu^{p}_{\alpha\to\beta} \approx 2\chi_0 \varsigma^{z}_{\alpha\to\beta} + C_0, \qquad 2\pi\Delta\nu^{s}_{\alpha\to\beta} \approx 2\chi_1 \varsigma^{z}_{\alpha\to\beta}. \tag{3.5}$$

Here, $\Delta\nu^{s,p}_{\alpha\to\beta}$ are the s-wave and p-wave contributions to the density shift, α and β indicate initial and final states, $|g\rangle$ or $|e\rangle$. $\varsigma^{z}_{\alpha\to\beta}$ is a fitting parameter that accounts for the time evolution of $\langle \hat{S}^z \rangle / N_{\mathrm{loc}}$ during the Rabi dynamics, which depends on the details of the Rabi drive such as the pulse area, excitation fraction, and initial conditions used in the experiment (see SOM).

3.2.3 Density shifts in the carrier transition

To measure the effect of collisional shifts on the clock transition, we perform extended measurements using a 'clock lock' to track the drift of the laser. Each clock lock consists of a set of

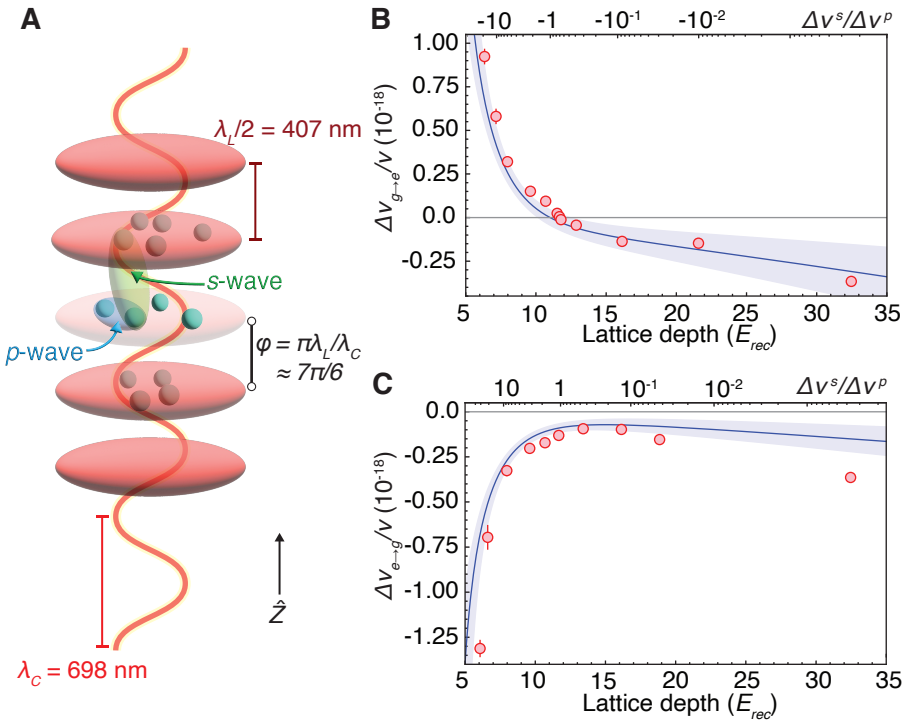

Figure 3.2: **Engineering Interactions.** (**A**) By varying the lattice depth during clock spectroscopy, we modify the ratio of off-site s-wave to on-site p-wave collisional shifts, $\Delta\nu^s_{\alpha\to\beta}/\Delta\nu^p_{\alpha\to\beta}$, where α and β indicate clock states. Atoms are trapped in an optical lattice with wavelength λ_L and probed by clock light with wavelength λ_C. Each antinode of the lattice light traps a number of atoms which interact via p-wave collisions. The 698 nm clock wavelength is incommensurate with the lattice spacing, so atoms in neighboring lattice sites see different clock phases, $\varphi = \pi\lambda_L/\lambda_C \approx 7\pi/6$, allowing s-wave interactions at low lattice depths. (**B**) The fractional frequency density shift $\Delta\nu_{g\to e}/\nu$ over a range of lattice depths. Red points and error bars indicate experimental data and corresponding uncertainty in density shift and lattice depth. The theoretical density shift is shown as a solid blue line with the shaded blue region accounting for uncertainties in the s-wave scattering length and p-wave scattering volumes [62, 109], as well as 10 nK temperature uncertainty. (**C**) The density shift $\Delta\nu_{e\to g}/\nu$ over a range of lattice depths.

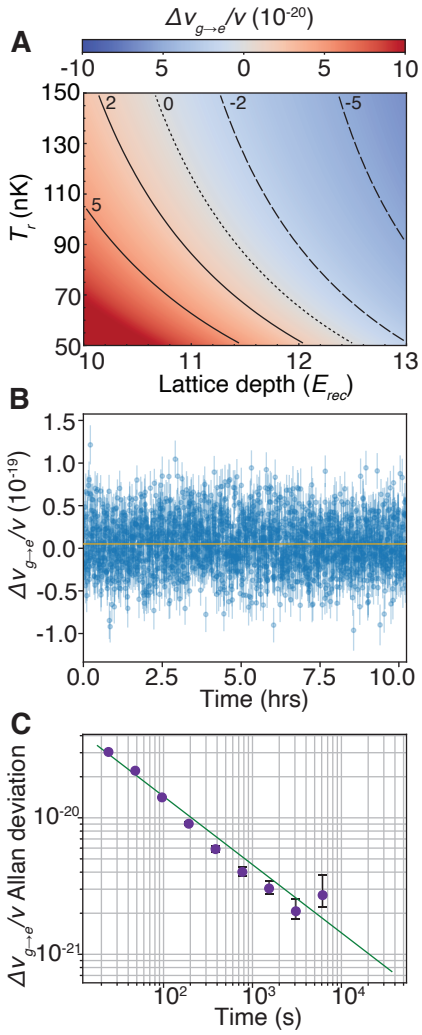

Figure 3.3: **Density Shift Cancellation.** (**A**) At 11.7(0.1) E_{rec}, the contributions from p-wave and s-wave interactions balance, allowing clock operation with a density shift many orders lower than previous regimes. The heat map and contours show the calculated fractional frequency shift coefficient $\Delta\nu_{g\to e}/\nu$ for a range of radial temperatures T_r and lattice depths in our system. (**B**) Over a 10 hour measurement, we report a mean coefficient $\Delta\nu_{g\to e}/\nu = 5.0(1.7) \times 10^{-21}$. For each set of four lock points, we extract a density shift coefficient, shown with corresponding uncertainty in blue. The weighted mean over the duration of the run is in gold. (**C**) Allan deviation of the density shift coefficient (purple dots) with corresponding uncertainty reported in error bars. The green line is an instability fit with slope $1.3 \times 10^{-19}/\sqrt{\tau}$ for averaging time τ.

four lock points, a standard interleaved sequence probing opposite sign m_F states to reject first order Zeeman shifts. As reported in [23], we employ in situ imaging to construct a microscopic frequency map throughout the extended sample, fitting a linear slope to the relationship between frequency and number of atoms per site at each lock point. We define a linear density shift coefficient $\Delta\nu_{\alpha\to\beta}/\nu$ such that the total fractional frequency shift is the product of this coefficient and N_{loc}, calibrated using quantum projection noise techniques. The reported values of $\Delta\nu_{\alpha\to\beta}/\nu$ are the weighted mean of $\Delta\nu_{\alpha\to\beta}/\nu$ at every lock point during an extended clock lock measurement campaign. The statistical uncertainty is given by the Allan deviation fit at 1/6 total measuring time.

In Fig. 3.2 we plot the measured coefficients over a range of V_0 for both the $|g\rangle \to |e\rangle$ and $|e\rangle \to |g\rangle$ transition. We typically utilize a 3.2 s π pulse duration. To account for increased delocalization and reduced Rabi frequencies at the shallowest depths we lengthen the pulse time. The effect of s-wave collisions at low lattice depths is readily apparent, with a dramatic increase in density shift between 12 E_{rec} and 5 E_{rec}, consistent with the growth of the off-site matrix element η_1 as V_0 is reduced. For the $|g\rangle \to |e\rangle$ transition presented in Fig. 3.2(B), the s-wave frequency shift has an opposite sign compared to that of the p-wave. At the magic lattice depth, the s-wave and p-wave shifts have the same magnitude, resulting in a nearly perfect cancellation for a vanishingly small collisional frequency shift. In the $|e\rangle \to |g\rangle$ case presented in Fig. 3.2(C), the s-wave frequency shift has the same sign as that of the p-wave, and thus the density shift remains negative over all lattice depths. This behavior is well described by the mean-field solution from Eq. (3.2), represented by the solid blue lines in Fig. 3.2(B) and Fig. 3.2(C). The disagreement at a large V_0 of 32 E_{rec}, as shown in Fig. 3.2(C), likely arises from lattice photon assisted excited state decay to other spin states, leading to background s-wave interactions not included in our theoretical model.

In Fig. 3.3(A), we model the fractional frequency shift over a range of experimentally relevant lattice depths and radial temperatures near this magic point. The density shift is sensitive to ensemble temperature, lattice depth, and excitation fraction. Experimentally, the lattice depth is maintained through a precise and large bandwidth lattice intensity servo, and our clock lock tracks

the laser drift to ensure a similar excitation fraction throughout the measurement duration. The atomic temperature is less precisely controlled, with small drifts in the cooling laser frequency and stray magnetic fields contributing to reduced cooling reproducibility and observed 10 nK variation. To evaluate the robustness of operating at the magic lattice depth, we demonstrate a 10 hour clock lock using a 3.2 s Rabi probe near the magic depth and report a $5.0(1.7) \times 10^{-21}$ fractional frequency shift per atom, as shown in Fig. 3.3(B). There is no apparent long term trend in the density shift, and the coefficient seems to reach a flicker beyond ∼1000 s, as shown by the Allan deviation in Fig. 3.3(C).

The data presented in Fig. 3.3 was collected with an average of 51 atoms per site in the studied region. For comparison, the synchronous measurement presented in [23] with single clock instability of 3.1×10^{-18} at 1 s utilized 0.5 mm length samples with an average of 38 atoms per site. Operating in the density shift regime near the magic lattice depth presented here, the average density shift magnitude would be approximately $1.9(0.6) \times 10^{-19}$.

3.2.4 Dynamical phase transition in the Wannier-Stark sidebands

By addressing a transition to a different WS state, we further modify the atomic interactions. We can still define an interaction spin model by identifying the states $|\uparrow_{\mathbf{n}}\rangle \equiv |e; n_X, n_Y, W_{n+l}\rangle$ and $|\downarrow_{\mathbf{n}}\rangle \equiv |g; n_X, n_Y, W_n\rangle$ as the spin-1/2 internal levels. In particular, we interrogate the $l = 1$ transition. The many-body dynamics are then described by the same mean field equation of motion, Eq. (3.2), but with a different effective magnetic field (see SOM):

$$\mathbf{B}^{\perp}_{l=1} \approx \{\Omega_1, 0, -\delta_1 + 2\chi_1^{l=1}\langle \hat{S}^z \rangle\}, \tag{3.6}$$

where $\chi_1^{l=1} = -\eta_0 U_{eg}/2$ and δ_1 is the detuning of the laser to the $l = 1$ transition. Note that because the wavefunction of the excited state is displaced by one lattice site (see Fig. 3.4(B)), the overlap matrix element that characterizes the s-wave interactions is proportional to η_0. Therefore atomic interactions are significantly enhanced in this case and increase with higher trap depth. Although the SOC phase does not enter directly in $\chi_1^{l=1}$, SOC still plays a key role by allowing the transition to

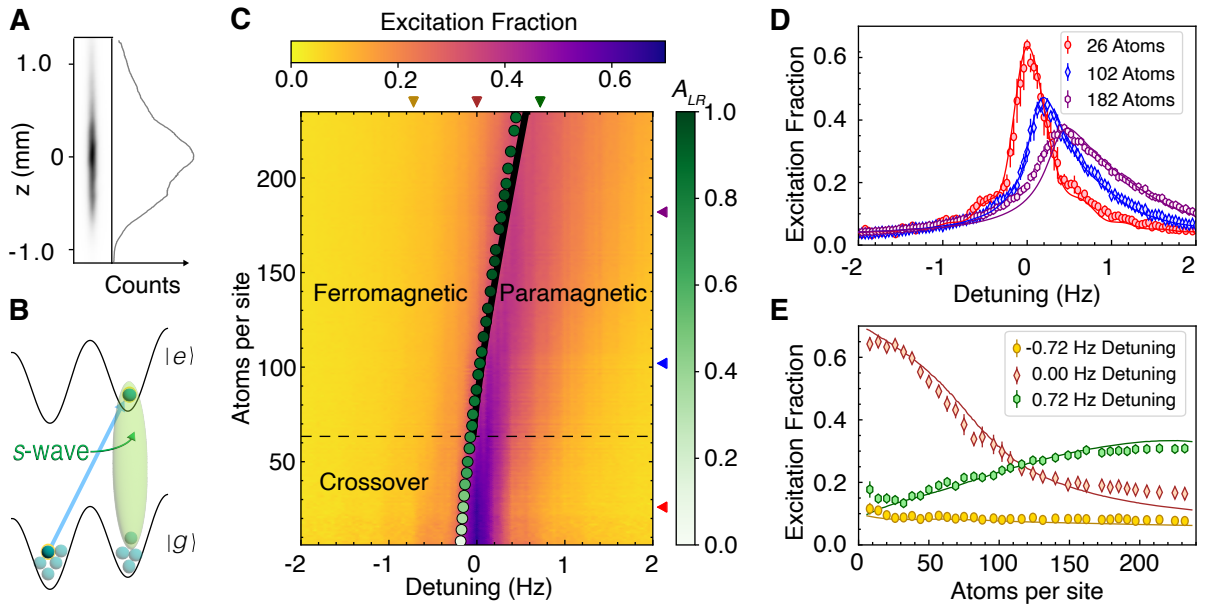

Figure 3.4: **Dynamical Phase Transition.** (**A**) An image of lattice trapped atoms, indicating a spatial extent over a millimeter in length. Within a single image we can study lattice site density regimes ranging over two orders of magnitude, shown here as camera counts. (**B**) Addressing the $|g\,;W_n\rangle \rightarrow |e\,;W_{n+1}\rangle$ transition, s-wave interactions effectively become on-site, leading to a strong collisional shift. (**C**) The excitation fraction as a function of detuning and atom number on the $|g\,;W_m\rangle \rightarrow |e\,;W_{m+1}\rangle$ transition at 22 E_{rec}. Above ~ 63 atoms per site, denoted by the dashed black line, the system features a dynamical phase transition between ferromagnetic and paramagnetic phases when varying the laser detuning and atomic density. The phase boundary is denoted by a solid black line from theoretical calculations and green points from the experimental data. The normalized asymmetry of the lineshape A_{LR} is indicated by the shade of these points. Arrows on the right and top axis indicate data plotted in **D** and **E** at constant atom number and detuning. (**D**) Excitation fraction as a function of detuning at different atom numbers demonstrates the significant distortion and asymmetry that arises in the strongly interacting regime. (**E**) Excitation fraction as a function of atom number in the ferromagnetic phase (-0.72 Hz), across the phase transition (0 Hz), and in the paramagnetic phase (0.72 Hz). Solid lines in **D** and **E** indicate theoretical calculations.

be driven, see Eq. (3.1). The stronger interactions modify the spin dynamics more dramatically and give rise to a dynamical phase transition (DPT) between dynamical ferromagnetic and paramagnetic phases (see SOM). The DPT appears as a sharp change in behavior of the long-time average excitation fraction for an initial state prepared with all atoms in $|g\rangle$, $\overline{n_\uparrow} = \lim_{T\to\infty} \frac{1}{T}\int_0^T n_\uparrow(t)\mathrm{d}t$. In the dynamical ferromagnetic phase, interactions dominate and the system features small oscillations near a single pole of the Bloch sphere, with $\overline{n_\uparrow} \approx 0$. In the dynamical paramagnetic phase, the system exhibits large excursions around the Bloch sphere and $\overline{n_\uparrow}$ dynamically adjusts itself as δ_1 is varied. In the interaction dominant regime, the DPT generates a second order critical line that distinguishes the two dynamical phases. The transition evolves into a smooth crossover region in the weakly interacting regime, where the dynamics are dominated by single-particle Rabi flopping.

Similar to other DPT experiments, instead of direct measurements of $\overline{n_\uparrow}$, the order parameter is estimated by measuring the excitation fraction at a fixed probe time. We use a 2.3 s Rabi π pulse with lattice depth $V_0 = 22\ E_{rec}$ and radial temperature $T_r = 190$ nK. Within a single image we observe a density range spanning over two orders of magnitude (Fig. 3.4(A)). We spatially resolve the excitation fraction within the sample and construct the dynamical phase diagram shown in Fig. 3.4(C).

For a given N_{loc} we extract the lineshape asymmetry A_{LR} defined as $(n_R - n_L)/(n_R + n_L)$ from experimental data, and normalize by the maximum value of A_{LR}. Here, $n_R = \int_{\delta_{max}}^{\delta_{max}+f} n_\uparrow(\delta)\mathrm{d}\delta$, $n_L = \int_{\delta_{max}-f}^{\delta_{max}} n_\uparrow(\delta)\mathrm{d}\delta$, where δ_{max} is the detuning for the peak value of the Rabi lineshape, and $f/2\pi = 1$ Hz covers almost the entire frequency range of the Rabi lineshape. The lineshape asymmetry allows us to characterize the dynamical phases. For $N_{loc} < 63$, below the dashed black line in Fig. 3.4(C), the system is in a crossover regime featuring a linear density shift and asymmetry A_{LR} that becomes more pronounced as the atom number increases. Over 63 atoms per site, the lineshape is near maximally asymmetric, and distinct ferromagnetic and paramagnetic dynamical phases are identified. The phase boundary is experimentally determined by finding the maximum derivative of the lineshape as a function of detuning, plotted as green points in Fig. 3.4(C), with A_{LR} indicated by the shade. The points lie very close to the theoretically calculated phase boundary

shown as a solid black line.

The asymmetry in the lineshape becomes apparent by viewing the excitation at a constant atom number, as in Fig. 3.4(D). At densities well below the crossover boundary, the lineshape is only slightly distorted from that of an ideal Rabi response. Above the crossover density, the excitation displays very different behaviors for the two opposite signs of detuning, and the excitation becomes highly insensitive to changes of detuning deep in the ferromagnetic phase. The constant detuning profiles presented in Fig. 3.4(E) further illustrate this dynamical phase transition. At $\delta_1/2\pi = 0$ Hz, the laser drive is on resonance with the non-interacting transition. Above the crossover regime, the ensemble features both dynamical phases, evolving from a dynamical paramagnet to a dynamical ferromagnet for $N_{loc} > 82$. At $\delta_1/2\pi = -0.72$ Hz the system is in the dynamical ferromagnetic phase above the crossover region. However, with $\delta_1/2\pi = 0.72$ Hz detuning, the excitation fraction initially rises with atom number when the system is in the paramagnetic phase and saturates close to the phase boundary. In both panels D and E the solid lines are theoretical predictions from the mean field spin model with an additional dephasing term accounting for mode-changing collisions (see SOM).

3.2.5 Conclusion and outlook

Operating in the Wannier-Stark regime has realized a new and optimized platform for optical lattice clocks, with record coherence time and clock precision [23]. The work here highlights the use of Hamiltonian engineering and control of atomic interactions to remove the compromise between increased precision and reduced systematic uncertainties. Operating with hundreds of thousands of atoms we still limit the density-related frequency shift well below the current state of the art, and further reduction in density shift is readily attainable. Importantly, this work utilizes precise tuning of interactions to explore rich many-body behavior. With selective Wannier-Stark interrogation and in situ imaging, we efficiently map out a dynamical phase transition over a range of density of more than two orders of magnitude.

So far we operate in a regime where a mean-field model is sufficient to describe the many-

body dynamics. Driving the system with more sophisticated pulse sequences will allow us to further explore quantum correlation and beyond mean-field effects. This will open a path for the generation of spin squeezed states with a net quantum metrological advantage for state-of-the-art quantum sensors.

3.2.6 Supplemental Materials: Spin model for the carrier transition

As described in the main text, our experimental system is a vertical 1D lattice with magic wavelength ($\lambda_L = 813$ nm), so the external trapping potential $V_{\text{ext}}(\mathbf{R})$ is the same for $|g\rangle$ and $|e\rangle$ states. To the leading order, we have

$$V_{\text{ext}}(\mathbf{R}) \approx V_0 \sin^2(k_L Z) + MgZ + \frac{1}{2}M\omega_R^2(X^2 + Y^2). \tag{3.7}$$

Here, $k_L = 2\pi/\lambda_L$ is the wavenumber of the lattice that sets the atomic recoil energy $E_{rec} = \hbar^2 k_L^2/2M$, g is the gravitational acceleration, and ω_R is the radial trapping frequency. In addition, the clock laser ($\lambda_c = 698$ nm), aligned with the lattice direction, drives the transitions between $|g\rangle$ and $|e\rangle$ states with bare Rabi frequency Ω and detuning δ. In the rotating frame of the clock laser, the second quantized Hamiltonian take the following form,

$$\hat{H} = \hat{H}_0 + \hat{H}_{\text{int}} + \hat{H}_{\text{laser}}, \tag{3.8}$$

where

$$\hat{H}_0 = \sum_{\alpha=\{g,e\}} \int \mathrm{d}^3\mathbf{R}\, \hat{\psi}_\alpha^\dagger(\mathbf{R}) \Big[-\frac{\hbar^2}{2M}\nabla^2 + V_{\text{ext}}(\mathbf{R}) \Big] \hat{\psi}_\alpha(\mathbf{R}), \tag{3.9}$$

$$\begin{aligned}
\hat{H}_{\text{int}} = {} & \frac{2\pi\hbar^2(a_{eg}^- + a_{eg}^+)}{M} \int d^3\mathbf{r}\, \hat{\psi}_e^\dagger(\mathbf{r})\hat{\psi}_g^\dagger(\mathbf{r})\hat{\psi}_g(\mathbf{r})\hat{\psi}_e(\mathbf{r}) \\
& + \frac{3\pi\hbar^2 b_{gg}^3}{2M} \int d^3\mathbf{r}\, [(\nabla\hat{\psi}_g^\dagger)\hat{\psi}_g^\dagger - \hat{\psi}_g^\dagger(\nabla\hat{\psi}_g^\dagger)] \cdot [\hat{\psi}_g(\nabla\hat{\psi}_g) - (\nabla\hat{\psi}_g)\hat{\psi}_g] \\
& + \frac{3\pi\hbar^2 b_{ee}^3}{2M} \int d^3\mathbf{r}\, [(\nabla\hat{\psi}_e^\dagger)\hat{\psi}_e^\dagger - \hat{\psi}_e^\dagger(\nabla\hat{\psi}_e^\dagger)] \cdot [\hat{\psi}_e(\nabla\hat{\psi}_e) - (\nabla\hat{\psi}_e)\hat{\psi}_e] \\
& + \frac{3\pi\hbar^2[(b_{eg}^+)^3 + (b_{eg}^-)^3]}{2M} \int d^3\mathbf{r}\, [(\nabla\hat{\psi}_g^\dagger)\hat{\psi}_e^\dagger - \hat{\psi}_g^\dagger(\nabla\hat{\psi}_e^\dagger)] \cdot [\hat{\psi}_e(\nabla\hat{\psi}_g) - (\nabla\hat{\psi}_e)\hat{\psi}_g],
\end{aligned} \tag{3.10}$$

$$\hat{H}_{\text{laser}} = \frac{\hbar\Omega}{2} \int \mathrm{d}^3\mathbf{R} \Big[\mathrm{e}^{ik_c Z} \hat{\psi}_e^\dagger(\mathbf{R})\hat{\psi}_g(\mathbf{R}) + \text{h.c.} \Big] - \frac{\hbar\delta}{2} \int \mathrm{d}^3\mathbf{R} \Big[\hat{\psi}_e^\dagger(\mathbf{R})\hat{\psi}_e(\mathbf{R}) - \hat{\psi}_g^\dagger(\mathbf{R})\hat{\psi}_g(\mathbf{R}) \Big]. \tag{3.11}$$

Here, $k_c = 2\pi/\lambda_c$ is the wave number of the clock laser, and $\psi_\alpha(\mathbf{R})$ is the annihilation field operator for a fermionic atom of internal state α. One can refer to chapter 2.3 for the derivation of the interaction Hamiltonian in the case of nuclear spin changing clock transition, with $a_{\alpha\beta}$ the s-wave scattering lengths and $b^3_{\alpha\beta}$ the p-wave scattering volumes.

Our experiment operates in the regime where the collisional rate of relaxation for motional degrees of freedom is slower than internal spin dynamics and trapping frequencies [34, 62, 100, 101, 108]. This condition ensures only internal levels evolve while atoms remain frozen in their single-particle eigenstates during the dynamics. We first focus on the case of the carrier transition, where the clock laser couples the following two single particle states: $|\uparrow_{\mathbf{n}}\rangle \equiv |e; n_X, n_Y, W_n\rangle$ and $|\downarrow_{\mathbf{n}}\rangle \equiv |g; n_X, n_Y, W_n\rangle$, where $\mathbf{n} = \{n_X, n_Y, n\}$, with n_X, n_Y denoting the radial harmonic oscillator modes and n the lattice site index of the center of the Wannier-Stark state $|W_n\rangle$. We expand the field operator $\hat{\psi}_\alpha(\mathbf{R})$ in terms of single-particle eigenstates as follows,

$$\hat{\psi}_e(\mathbf{R}) = \sum_{\mathbf{n}} \phi_{n_X}(X)\phi_{n_Y}(Y)W_n(Z)\hat{c}_{\mathbf{n}\uparrow}, \quad \hat{\psi}_g(\mathbf{R}) = \sum_{\mathbf{n}} \phi_{n_X}(X)\phi_{n_Y}(Y)W_n(Z)\hat{c}_{\mathbf{n}\downarrow}, \tag{3.12}$$

where $\hat{c}_{\mathbf{n}\uparrow}$ and $\hat{c}_{\mathbf{n}\downarrow}$ are fermionic annihilation operators for $|\uparrow_{\mathbf{n}}\rangle$ and $|\downarrow_{\mathbf{n}}\rangle$ states respectively. Here, the harmonic oscillator wave function is

$$\phi_{n_X}(X) = \frac{1}{\sqrt{2^{n_X} n_X!}} \left(\frac{M\omega_R}{\pi\hbar}\right)^{1/4} \mathrm{e}^{-M\omega_R X^2/2\hbar} H_{n_X}\left(\sqrt{\frac{M\omega_r}{\hbar}} X\right), \tag{3.13}$$

where $H_{n_X}(X)$ are Hermite polynomials. The wave function for the Wannier-Stark state is

$$W_n(Z) = \sum_m \mathcal{J}_{m-n}\left(\frac{2J_0}{Mga_l}\right) w(Z - ma_L), \tag{3.14}$$

where $\mathcal{J}_n(x)$ are Bessel functions, $J_0 \approx (4/\sqrt{\pi}) E_{rec}^{1/4} V_0^{3/4} \exp\left[-2\sqrt{V_0/E_{rec}}\right]$ is the ground band nearest-neighbor tunneling energy, $a_L = \lambda_L/2$ is the lattice spacing, and $w(Z)$ is the ground band Wannier function centering at $Z = 0$.

Under the frozen mode approximation, we treat each atom as a spin-1/2 system spanned by $|\uparrow_{\mathbf{n}}\rangle$ and $|\downarrow_{\mathbf{n}}\rangle$ states. Therefore, we define the spin operators,

$$\begin{aligned} \hat{S}^x_{\mathbf{n}} &= \frac{1}{2}(\hat{c}^\dagger_{\mathbf{n}\uparrow}\hat{c}_{\mathbf{n}\downarrow} + \hat{c}^\dagger_{\mathbf{n}\downarrow}\hat{c}_{\mathbf{n}\uparrow}), \quad \hat{S}^y_{\mathbf{n}} = -\frac{i}{2}(\hat{c}^\dagger_{\mathbf{n}\uparrow}\hat{c}_{\mathbf{n}\downarrow} - \hat{c}^\dagger_{\mathbf{n}\downarrow}\hat{c}_{\mathbf{n}\uparrow}), \\ \hat{S}^z_{\mathbf{n}} &= \frac{1}{2}(\hat{c}^\dagger_{\mathbf{n}\uparrow}\hat{c}_{\mathbf{n}\uparrow} - \hat{c}^\dagger_{\mathbf{n}\downarrow}\hat{c}_{\mathbf{n}\downarrow}), \quad \hat{N}_{\mathbf{n}} = \hat{c}^\dagger_{\mathbf{n}\uparrow}\hat{c}_{\mathbf{n}\uparrow} + \hat{c}^\dagger_{\mathbf{n}\downarrow}\hat{c}_{\mathbf{n}\downarrow}, \end{aligned} \tag{3.15}$$

and rewrite the interaction Hamiltonian,

$$\hat{H}_{\rm int}/\hbar = \sum_{\substack{\mathbf{nm}\\(\mathbf{n}\neq\mathbf{m})}} \left[J^{\perp}_{\mathbf{nm}} \hat{\mathbf{S}}_{\mathbf{n}} \cdot \hat{\mathbf{S}}_{\mathbf{m}} + \chi_{\mathbf{nm}} \hat{S}^z_{\mathbf{n}} \hat{S}^z_{\mathbf{m}} + \frac{C_{\mathbf{nm}}}{2} (\hat{S}^z_{\mathbf{n}} \hat{N}_{\mathbf{m}} + \hat{N}_{\mathbf{n}} \hat{S}^z_{\mathbf{m}}) \right], \tag{3.16}$$

where

$$\begin{gathered} J^{\perp}_{\mathbf{nm}} = \eta_{|n-m|}(V^{eg}_{\mathbf{nm}} - U^{eg}_{\mathbf{nm}})/2, \quad \chi_{\mathbf{nm}} = \eta_{|n-m|}(V^{ee}_{\mathbf{nm}} + V^{gg}_{\mathbf{nm}} - 2V^{eg}_{\mathbf{nm}})/2, \\ C_{\mathbf{nm}} = \eta_{|n-m|}(V^{ee}_{\mathbf{nm}} - V^{gg}_{\mathbf{nm}})/2. \end{gathered} \tag{3.17}$$

Here, $\eta_{|n-m|}$ is a dimensionless overlap integral of Wannier-Stark states defined as

$$\eta_{|n-m|} = \frac{\lambda_L}{\sqrt{2\pi}} \left(\frac{V_0}{E_{rec}} \right)^{-1/4} \int \mathrm{d}Z \, [W_n(Z)]^2 [W_m(Z)]^2. \tag{3.18}$$

$U^{\alpha\beta}_{\mathbf{nm}}$ and $V^{\alpha\beta}_{\mathbf{nm}}$ are s-wave and p-wave interaction parameters respectively ($\alpha, \beta = \{g, e\}$),

$$\begin{aligned} U^{\alpha\beta}_{\mathbf{nm}} &= \frac{8\pi\hbar a_{\alpha\beta}}{M} s_{n_x m_x} s_{n_y m_y} \frac{k_L}{\sqrt{2\pi}} \left(\frac{V_0}{E_{rec}} \right)^{1/4}, \\ V^{\alpha\beta}_{\mathbf{nm}} &= \frac{6\pi\hbar b^3_{\alpha\beta}}{M} (p_{n_x m_x} s_{n_y m_y} + s_{n_x m_x} p_{n_y m_y}) \frac{k_L}{\sqrt{2\pi}} \left(\frac{V_0}{E_{rec}} \right)^{1/4}, \end{aligned} \tag{3.19}$$

where $a_{eg} \equiv (a^+_{eg} + a^-_{eg})/2$, $b^3_{eg} \equiv [(b^+_{eg})^3 + (b^-_{eg})^3]/2$, $s_{nm} = \int \mathrm{d}X \, [\phi_n(X)]^2 [\phi_m(X)]^2$, and $p_{nm} = \int \mathrm{d}X \, [(\partial_X \phi_n(X))\phi_m(X) - \phi_n(X)(\partial_X \phi_m(X))]^2$. Note that in $V^{\alpha\beta}_{\mathbf{nm}}$ we ignore the p-wave contributions in the $\hat{Z}$ direction, because its leading order terms are overlap matrix elements of gradients of Wannier functions in nearest-neighbor lattice sites based on the expansion in Eq. (3.14). These matrix elements are small for parameters used in the experiment.

On the carrier transition, $\hat{H}_{\rm laser}$ becomes

$$\hat{H}_{\rm laser}/\hbar = \frac{1}{2} \sum_{\mathbf{n}} (\Omega_{\mathbf{n}} \hat{S}^+_{\mathbf{n}} + \text{h.c.}) - \delta \sum_{\mathbf{n}} \hat{S}^z_{\mathbf{n}}, \tag{3.20}$$

where

$$\Omega_{\mathbf{n}} = \Omega \int \mathrm{d}Z \, \mathrm{e}^{ik_c Z} [W_n(Z)]^2 = \Omega_0 \mathrm{e}^{in\varphi}. \tag{3.21}$$

Here, $\varphi = k_c a_L = \pi\lambda_L/\lambda_c$ is the clock laser phase difference between nearest-neighbor Wannier-Stark states, generating spin-orbit coupling. The Rabi frequency for carrier transition is

$$\Omega_0 = \Omega \cdot \mathcal{C} \mathcal{J}_0 \left(\frac{4J_0}{Mga_L} \sin(\varphi/2) \right), \tag{3.22}$$

where $\mathcal{C} = \int \mathrm{d}Z\, \mathrm{e}^{ik_c Z}[w(Z)]^2 \approx \exp\left[-\lambda_L^2/4\lambda_c^2\sqrt{V_0/E_{rec}}\right]$. The dependence of Ω_0 on lattice depth V_0 is shown in Fig. 3.5(A). In the following discussions, it is convenient to remove the phase dependence on lattice sites in the $\hat{H}_{\text{laser}}$ term by a gauge transformation $\hat{\tilde{c}}_{\mathbf{n}\uparrow} = \mathrm{e}^{-in\varphi}\hat{c}_{\mathbf{n}\uparrow}$, $\hat{\tilde{c}}_{\mathbf{n}\downarrow} = \hat{c}_{\mathbf{n}\downarrow}$. Under the gauge transformation the spin operators become:

$$\begin{gathered}\hat{\tilde{S}}^x_{\mathbf{n}} = \cos(n\varphi)\hat{S}^x_{\mathbf{n}} - \sin(n\varphi)\hat{S}^y_{\mathbf{n}}, \quad \hat{\tilde{S}}^y_{\mathbf{n}} = \sin(n\varphi)\hat{S}^x_{\mathbf{n}} + \cos(n\varphi)\hat{S}^y_{\mathbf{n}}, \\ \hat{\tilde{S}}^z_{\mathbf{n}} = \hat{S}^z_{\mathbf{n}}, \quad \hat{\tilde{N}}_{\mathbf{n}} = \hat{N}_{\mathbf{n}}.\end{gathered} \tag{3.23}$$

Combining the discussions above, the effective Hamiltonian in the gauged frame becomes

$$\begin{aligned}\hat{H}/\hbar = &\sum_{\substack{\mathbf{nm}\\(\mathbf{n}\neq\mathbf{m})}}\left[\tilde{J}^{\perp}_{\mathbf{nm}}\hat{\tilde{\mathbf{S}}}_{\mathbf{n}}\cdot\hat{\tilde{\mathbf{S}}}_{\mathbf{m}} + \tilde{\chi}_{\mathbf{nm}}\hat{\tilde{S}}^z_{\mathbf{n}}\hat{\tilde{S}}^z_{\mathbf{m}} + D_{\mathbf{nm}}(\hat{\tilde{S}}^x_{\mathbf{n}}\hat{\tilde{S}}^y_{\mathbf{m}} - \hat{\tilde{S}}^y_{\mathbf{n}}\hat{\tilde{S}}^x_{\mathbf{m}}) + \frac{C_{\mathbf{nm}}}{2}(\hat{\tilde{S}}^z_{\mathbf{n}}\hat{\tilde{N}}_{\mathbf{m}} + \hat{\tilde{N}}_{\mathbf{n}}\hat{\tilde{S}}^z_{\mathbf{m}})\right] \\ &- \hbar\delta\sum_{\mathbf{n}}\hat{\tilde{S}}^z_{\mathbf{n}} + \hbar\Omega_0\sum_{\mathbf{n}}\hat{\tilde{S}}^x_{\mathbf{n}},\end{aligned} \tag{3.24}$$

where $\tilde{J}^{\perp}_{\mathbf{nm}} = \cos[(n-m)\varphi]J^{\perp}_{\mathbf{nm}}$, $\tilde{\chi}_{\mathbf{nm}} = \chi_{\mathbf{nm}} + J^{\perp}_{\mathbf{nm}} - \tilde{J}^{\perp}_{\mathbf{nm}}$, and $D_{\mathbf{nm}} = -\sin[(n-m)\varphi]J^{\perp}_{\mathbf{nm}}$.

Now we discuss the dependence of interaction parameters $\tilde{J}^{\perp}_{\mathbf{nm}}$, $\tilde{\chi}_{\mathbf{nm}}$ and $D_{\mathbf{nm}}$ on radial harmonic oscillator modes (n_X, n_Y, m_X, m_Y) and the distance along lattice direction $(|n-m|)$. As reported in [34, 62, 100], the overlap integrals are not overly sensitive to the radial modes in consideration, allowing us to simplify the Hamiltonian dynamics in terms of collective spin operators at each lattice site, $\hat{S}^{x,y,z}_n = \sum_{n_X n_Y}\hat{\tilde{S}}^{x,y,z}_{\mathbf{n}}$, $\hat{N}_n = \sum_{n_X n_Y}\hat{\tilde{N}}_{\mathbf{n}}$. Due to the partial delocalization of the Wannier-Stark states along the lattice direction, the dominant terms are on-site and nearest-neighbor interactions. Since the characteristic s-wave interaction strength is much larger than p-wave interaction strength at ultracold temperatures (~ 100 nK in our case), we include p-wave interaction only for on-site terms. All these approximations simplify Eq. (3.24) into a large-spin Hamiltonian in a 1D lattice,

$$\begin{aligned}\hat{H} &= \hat{H}_{\text{on-site}} + \hat{H}_{\text{off-site}} + \hat{H}_{\text{laser}}, \\ \hat{H}_{\text{on-site}}/\hbar &= \sum_n\Big[J^{\perp}_0\hat{\mathbf{S}}_n\cdot\hat{\mathbf{S}}_n + \chi_0\hat{S}^z_n\hat{S}^z_n + C_0\hat{N}_n\hat{S}^z_n\Big], \\ \hat{H}_{\text{off-site}}/\hbar &= \sum_n\Big[J^{\perp}_1\hat{\mathbf{S}}_n\cdot\hat{\mathbf{S}}_{n+1} + \chi_1\hat{S}^z_n\hat{S}^z_{n+1} + D_1(\hat{S}^x_n\hat{S}^y_{n+1} - \hat{S}^y_n\hat{S}^x_{n+1})\Big], \\ \hat{H}_{\text{laser}}/\hbar &= \sum_n\Big[-\delta\hat{S}^z_n + \Omega_0\hat{S}^x_n\Big].\end{aligned} \tag{3.25}$$

The interaction parameters for these collective spin operators are calculated by performing a thermal average over radial harmonic oscillator modes,

$$\begin{gathered} J_0^{\perp} = \eta_0(V_{eg} - U_{eg})/2, \quad \chi_0 = \eta_0(V_{ee} + V_{gg} - 2V_{eg})/2, \quad C_0 = \eta_0(V_{ee} - V_{gg})/2, \\ J_1^{\perp} = -\eta_1 U_{eg}\cos\varphi, \quad \chi_1 = -\eta_1 U_{eg}(1-\cos\varphi), \quad D_1 = -\eta_1 U_{eg}\sin\varphi. \end{gathered} \tag{3.26}$$

Here, η_0 and η_1 are dimensionless overlap integrals for on-site and nearest-neighbor interaction respectively [defined in Eq. (3.18)], and the thermal average for s-wave ($U_{\alpha\beta}$) and p-wave ($V_{\alpha\beta}$) interaction strengths are

$$U_{\alpha\beta} = \frac{8\pi\hbar a_{\alpha\beta}}{M}\frac{M\omega_R^2}{4\pi k_B T}\frac{k_L}{\sqrt{2\pi}}\left(\frac{V_0}{E_{rec}}\right)^{1/4}, \quad V_{\alpha\beta} = \frac{6\pi\hbar b_{\alpha\beta}^3}{M}\frac{1}{\pi}\left(\frac{M\omega_R}{\hbar}\right)^2\frac{k_L}{\sqrt{2\pi}}\left(\frac{V_0}{E_{rec}}\right)^{1/4}. \tag{3.27}$$

The dependence of interaction parameters χ_0, χ_1, C_0 on lattice depth V_0 is shown in Fig. 3.5(B).

As described in the main text, we measure the density shift of the carrier transition in Rabi spectroscopy. Note that the clock transition frequency is obtained by the average of two frequencies with the same excitation fraction on the positive and negative detuned side of the π-pulse Rabi spectrum, typically with an excitation fraction near 0.45 (the maximum excitation fraction is near 0.9). The density shift per atom

$$\Delta\nu = \frac{\delta_{\text{left}} + \delta_{\text{right}}}{4\pi N_{\text{loc}}}, \tag{3.28}$$

where δ_{left} and δ_{right} are the laser detuning from clock transition resonance for the excitation fraction we set on the positive and negative detuned side of the Rabi spectrum, and $N_{\text{loc}} = \frac{1}{2L+1}\sum_{m=-L}^{L} N_{n+m}$ is the averaged atom number per site in a local region centered around site n. The local region is $2L+1 \sim 15$ lattice sites, corresponding to our 6 μm imaging resolution.

To calculate the density shift, we apply a mean-field approximation to Eq. (3.25),

$$\hat{H}_{\text{MF}}/\hbar = \sum_n \hat{\mathbf{S}}_n \cdot \mathbf{B}_n, \tag{3.29}$$

where

$$\begin{aligned} B_n^x &= \Omega_0 + J_1^{\perp}(\langle\hat{S}_{n-1}^x\rangle + \langle\hat{S}_{n+1}^x\rangle) + D_1(\langle\hat{S}_{n+1}^y\rangle - \langle\hat{S}_{n-1}^y\rangle), \\ B_n^y &= J_1^{\perp}(\langle\hat{S}_{n-1}^y\rangle + \langle\hat{S}_{n+1}^y\rangle) - D_1(\langle\hat{S}_{n+1}^x\rangle - \langle\hat{S}_{n-1}^x\rangle), \\ B_n^z &= -\delta + 2\chi_0\langle\hat{S}_n^z\rangle + C_0 N_n + J_1^{\perp}(\langle\hat{S}_{n-1}^z\rangle + \langle\hat{S}_{n+1}^z\rangle) + \chi_1(\langle\hat{S}_{n-1}^z\rangle + \langle\hat{S}_{n+1}^z\rangle). \end{aligned} \tag{3.30}$$

Note that we drop the $J_0^{\perp}$ term in Eq. (3.25) because this term is a constant for any collective state at each lattice site.

We further simplify Eq. (3.29) by assuming all lattice sites share the same atom number N_{loc} in a local region (15 lattice sites). We calculate the spin dynamics in this local region by assuming translationally invariant conditions $\langle \hat{S}_n^{x,y,z} \rangle = \langle \hat{S}^{x,y,z} \rangle$ to Eq. (3.30), where $\langle \hat{S}^{x,y,z} \rangle = \frac{1}{2L+1} \sum_{m=-L}^{L} \langle \hat{S}_{n+m}^{x,y,z} \rangle$. In this way, we have a homogeneous field on each site, $\mathbf{B}_n = \mathbf{B}$. The mean-field Hamiltonian becomes

$$\hat{H}_{\mathrm{MF}}/\hbar = \sum_n \hat{\mathbf{S}}_n \cdot \mathbf{B}^{\perp}, \tag{3.31}$$

where $\mathbf{B}^{\perp} \perp \langle \mathbf{S} \rangle$ is the perpendicular component of $\mathbf{B}$, with

$$\mathbf{B}^{\perp} = \{\Omega_0, 0, -\delta + 2(\chi_0 + \chi_1)\langle \hat{S}^z \rangle + C_0 N_{\mathrm{loc}}\}. \tag{3.32}$$

Dropping the parallel component of $\mathbf{B}$ because it does not contribute to the mean-field dynamics,

$$\frac{\mathrm{d}}{\mathrm{d}t} \langle \hat{\mathbf{S}}_n \rangle = \mathbf{B}^{\perp} \times \langle \hat{\mathbf{S}}_n \rangle. \tag{3.33}$$

Using the mean-field equations above, we simulate the experimental protocol and obtain theoretical predictions for the density shift. In Rabi spectroscopy, we initialize all the atoms in the ground state ($\langle \hat{S}_n^z \rangle = -N_{\mathrm{loc}}/2$) for $g \to e$ case, and all the atoms in the excited state ($\langle \hat{S}_n^z \rangle = N_{\mathrm{loc}}/2$) for $e \to g$ case.

From Eq. (3.32), we obtain a simple expression for the density shift by setting it to be the value of δ at which $\mathbf{B}_z^{\perp} = 0$:

$$\begin{gathered} \Delta\nu_{\alpha\to\beta} = \Delta\nu^s_{\alpha\to\beta} + \Delta\nu^p_{\alpha\to\beta}, \\ 2\pi\Delta\nu^p_{\alpha\to\beta} \approx 2\chi_0\varsigma^z_{\alpha\to\beta} + C_0, \qquad 2\pi\Delta\nu^s_{\alpha\to\beta} \approx 2\chi_1\varsigma^z_{\alpha\to\beta}. \end{gathered} \tag{3.34}$$

Here, $\Delta\nu^{s,p}_{\alpha\to\beta}$ are the s-wave and p-wave contributions to the density shift, $\varsigma^z_{\alpha\to\beta}$ is a fitting parameter that accounts for the time evolution of $\langle \hat{S}^z \rangle / N_{\mathrm{loc}}$ during the Rabi dynamics, which depends on the details of the Rabi drive such as the pulse area, excitation fraction, and initial conditions used in the experiment, $g \to e$ or $e \to g$. Based on our experimental condition in the carrier transition, we find $\varsigma^z_{g\to e} = -0.12$ and $\varsigma^z_{e\to g} = 0.095$ [see Fig. 3.5(C)]. Note that $\Delta\nu^p_{\alpha\to\beta}$ are generated

by on-site p-wave interactions, while $\Delta\nu^{s}_{\alpha\to\beta}$ are generated by nearest-neighbor s-wave interaction. This dependence allows us to control the density shift by adjusting the spatial extension of the Wannier-Stark states, which is tunable by varying the lattice depth, the key idea to eliminating the density shift presented in the main text.

3.2.7 Supplemental Materials: Spin model for the Wannier-Stark sidebands

Apart from the carrier transition, we can also drive transitions to other Wannier-Stark states by using the clock laser to couple two different internal and motional states of an atom, $|\uparrow_{\mathbf{n}}\rangle \equiv |e; n_X, n_Y, W_{n+l}\rangle$ and $|\downarrow_{\mathbf{n}}\rangle \equiv |g; n_X, n_Y, W_n\rangle$, with $l = \pm1, \pm2, \cdots$. Compared to the carrier transition, the subscript $\mathbf{n}$ labels different motional states for $|\uparrow_{\mathbf{n}}\rangle$ and $|\downarrow_{\mathbf{n}}\rangle$ states in off-site Wannier-Stark transitions. In this case, we expand the field operator $\hat{\psi}_\alpha(\mathbf{r})$ in terms of single-particle eigenstates,

$$\hat{\psi}_e(\mathbf{R}) = \sum_{\mathbf{n}} \phi_{n_X}(X)\phi_{n_Y}(Y)W_{n+l}(Z)\hat{c}_{\mathbf{n}\uparrow}, \quad \hat{\psi}_g(\mathbf{R}) = \sum_{\mathbf{n}} \phi_{n_X}(X)\phi_{n_Y}(Y)W_n(Z)\hat{c}_{\mathbf{n}\downarrow}. \tag{3.35}$$

Similar to the frozen-mode approximation used for the carrier transition, we treat each atom as a spin-1/2 system spanned by the $|\uparrow_{\mathbf{n}}\rangle$ and $|\downarrow_{\mathbf{n}}\rangle$ states defined for the specific Wannier-Stark states coupled by the laser, and rewrite the interaction Hamiltonian in terms of the corresponding spin operators,

$$\hat{H}_{\rm int}/\hbar = \sum_{\substack{\mathbf{nm}\\(\mathbf{n}\neq\mathbf{m})}} \left[J^{\perp,l}_{\mathbf{nm}} \hat{\mathbf{S}}_{\mathbf{n}}\cdot\hat{\mathbf{S}}_{\mathbf{m}} + \chi^{l}_{\mathbf{nm}}\hat{S}^z_{\mathbf{n}}\hat{S}^z_{\mathbf{m}} + \frac{C_{\mathbf{nm}}}{2}(\hat{S}^z_{\mathbf{n}}\hat{N}_{\mathbf{m}} + \hat{N}_{\mathbf{n}}\hat{S}^z_{\mathbf{m}}) + \frac{K^l_{\mathbf{nm}}}{2}(\hat{S}^z_{\mathbf{n}}\hat{N}_{\mathbf{m}} - \hat{N}_{\mathbf{n}}\hat{S}^z_{\mathbf{m}}) \right], \tag{3.36}$$

where

$$\begin{aligned}
J^{\perp,l}_{\mathbf{nm}} &= \eta^{\mathrm{ex},l}_{|n-m|}(V^{\mathrm{eg}}_{\mathbf{nm}} - U^{\mathrm{eg}}_{\mathbf{nm}})/2,\\
\chi^{l}_{\mathbf{nm}} &= \eta_{|n-m|}(V^{ee}_{\mathbf{nm}} + V^{gg}_{\mathbf{nm}})/2 - \eta^{\mathrm{dir},l}_{|n-m|}(V^{eg}_{\mathbf{nm}} + U^{eg}_{\mathbf{nm}})/2 - \eta^{\mathrm{ex},l}_{|n-m|}(V^{\mathrm{eg}}_{\mathbf{nm}} - U^{\mathrm{eg}}_{\mathbf{nm}})/2,\\
C_{\mathbf{nm}} &= \eta_{|n-m|}(V^{ee}_{\mathbf{nm}} - V^{gg}_{\mathbf{nm}})/2,\\
K^{l}_{\mathbf{nm}} &= \eta^{\mathrm{diff},l}_{nm}(V^{eg}_{\mathbf{nm}} + U^{eg}_{\mathbf{nm}})/2.
\end{aligned} \tag{3.37}$$

Here, $\eta_{|n-m|}$, $U^{\alpha\beta}_{\mathbf{nm}}$, $V^{\alpha\beta}_{\mathbf{nm}}$ have the same definition as the ones used for the carrier transition [see

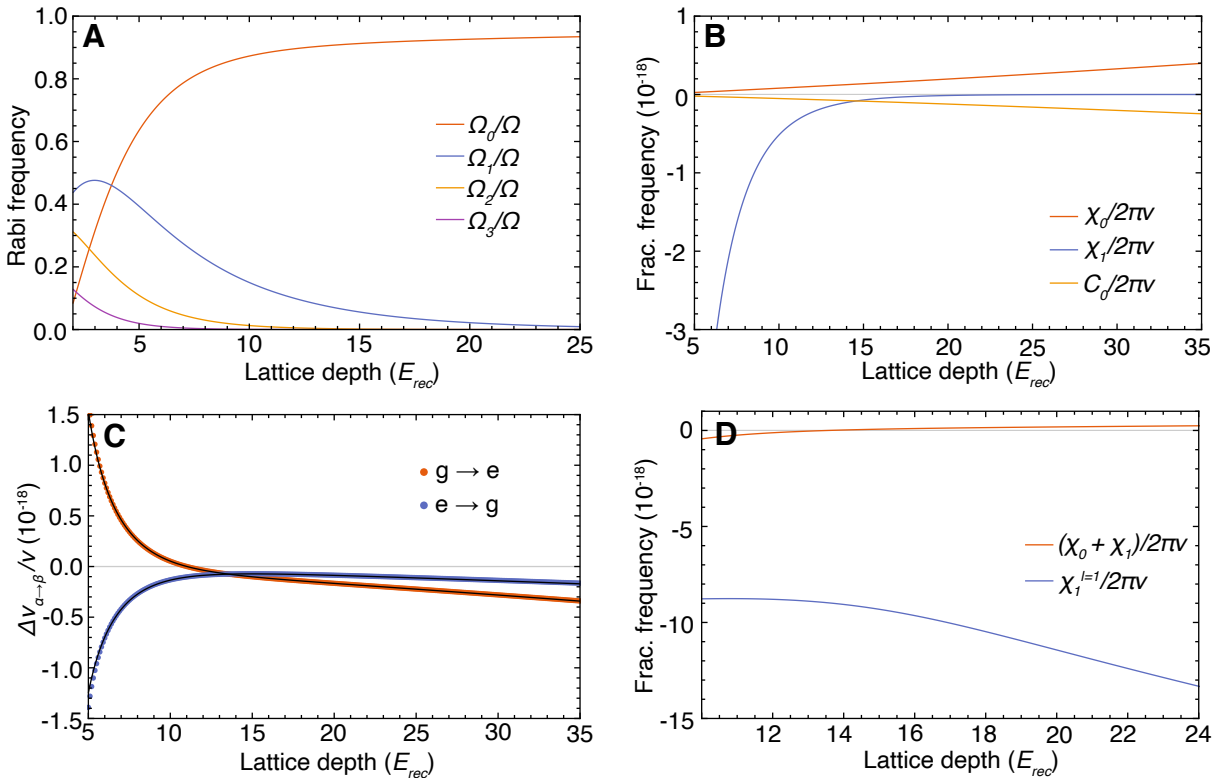

Figure 3.5: **Spin Model Parameters.** (**A**) Rabi frequency for the carrier transition (Ω_0) and $l = 1, 2, 3$ Wannier-Stark sidebands ($\Omega_1, \Omega_2, \Omega_3$) as a function of lattice depth. (**B**) Spin model parameters for the carrier transition as a function of lattice depth. The radial temperature at each lattice depth used is the reported experimental value (See Fig. 3.7). (**C**) Theoretical predictions of the fractional frequency shift per atom (orange points for $g \to e$ case, blue points for $e \to g$ case) and numerical fits based on Eq. (3.34) shown as black lines. The fitting parameter used are $\varsigma^z_{g\to e} = -0.12$ and $\varsigma^z_{e\to g} = 0.095$. (**D**) Wannier-Stark sideband interaction parameter ($\chi_1^{l=1}$) compared to the carrier transition parameter ($\chi_0 + \chi_1$), with the former significantly enhanced compared to the latter. In this case as well the radial temperature at each lattice depth is the reported experimental value in subsection 3.2.8.

Eq. (3.18) and Eq. (3.19)], and the definitions for the extra dimensionless overlap intergrals are

$$\begin{aligned}\eta^{\mathrm{dir},l}_{|n-m|} &= \frac{1}{2}(\eta_{|n-m+l|} + \eta_{|n-m-l|}),\\ \eta^{\mathrm{diff},l}_{nm} &= \frac{1}{2}(\eta_{|n-m+l|} - \eta_{|n-m-l|}),\\ \eta^{\mathrm{ex},l}_{|n-m|} &= \frac{\lambda_L}{\sqrt{2\pi}}\left(\frac{V_0}{E_{rec}}\right)^{-1/4}\int \mathrm{d}Z\, W_n(Z)W_m(Z)W_{n+l}(Z)W_{m+l}(Z).\end{aligned} \tag{3.38}$$

Note that the Rabi frequency for the Wannier-Stark sidebands experiences the same spin-orbit coupling phase as the carrier transition. We use the gauge transformation as in the carrier transition to redefine the spin operators [see Eq. (3.23)], and the effective Hamiltonian in the gauged frame becomes

$$\begin{aligned}\hat{H}/\hbar = \sum_{\substack{\mathbf{nm}\\(\mathbf{n}\neq\mathbf{m})}} \Big[&\tilde{J}^{\perp,l}_{\mathbf{nm}}\hat{\tilde{\mathbf{S}}}_{\mathbf{n}}\cdot\hat{\tilde{\mathbf{S}}}_{\mathbf{m}} + \tilde{\chi}^{l}_{\mathbf{nm}}\hat{\tilde{S}}^{z}_{\mathbf{n}}\hat{\tilde{S}}^{z}_{\mathbf{m}} + D^{l}_{\mathbf{nm}}(\hat{\tilde{S}}^{x}_{\mathbf{n}}\hat{\tilde{S}}^{y}_{\mathbf{m}} - \hat{\tilde{S}}^{y}_{\mathbf{n}}\hat{\tilde{S}}^{x}_{\mathbf{m}}) + \frac{C_{\mathbf{nm}}}{2}(\hat{\tilde{S}}^{z}_{\mathbf{n}}\hat{\tilde{N}}_{\mathbf{m}} + \hat{\tilde{N}}_{\mathbf{n}}\hat{\tilde{S}}^{z}_{\mathbf{m}})\\ &\frac{K^{l}_{\mathbf{nm}}}{2}(\hat{\tilde{S}}^{z}_{\mathbf{n}}\hat{\tilde{N}}_{\mathbf{m}} - \hat{\tilde{N}}_{\mathbf{n}}\hat{\tilde{S}}^{z}_{\mathbf{m}})\Big] - \hbar\delta_l\sum_{\mathbf{n}}\hat{\tilde{S}}^{z}_{\mathbf{n}} + \hbar\Omega_l\sum_{\mathbf{n}}\hat{\tilde{S}}^{x}_{\mathbf{n}},\end{aligned} \tag{3.39}$$

where $\tilde{J}^{\perp,l}_{\mathbf{nm}} = \cos[(n-m)\varphi]J^{\perp}_{\mathbf{nm}}$, $\tilde{\chi}^{l}_{\mathbf{nm}} = \chi^{l}_{\mathbf{nm}} + J^{\perp,l}_{\mathbf{nm}} - \tilde{J}^{\perp,l}_{\mathbf{nm}}$, $D^{l}_{\mathbf{nm}} = -\sin[(n-m)\varphi]J^{\perp,l}_{\mathbf{nm}}$, $\delta_l = \delta - lMga_L/\hbar$, and

$$\Omega_l = \Omega\cdot\mathcal{C}\mathcal{J}_l\left(\frac{4J_0}{Mga_L}\sin(\varphi/2)\right). \tag{3.40}$$

The dependence of Ω_l ($l = 1, 2, 3$) on lattice depth V_0 is shown in Fig. 3.5(A).

In the following discussions, we focus on the $l = 1$ Wannier-Stark transition. Following the same procedure we used for the carrier transition, we can express the Hamiltonian dynamics in terms of collective spin operators, $\hat{S}^{x,y,z}_{n} = \sum_{n_x n_y}\hat{\tilde{S}}^{x,y,z}_{\mathbf{n}}$, $\hat{N}_n = \sum_{n_x n_y}\hat{\tilde{N}}_{\mathbf{n}}$. Recall that for the carrier transition we discussed in previous sections, on-site s-wave interactions only gave rise to a constant term ($J^{\perp}_0$ term) which does not play any role in the mean-field dynamics. The dominant interaction comes from on-site p-wave interactions and nearest-neighbor s-wave interactions. However, in the case of the $l = 1$ site-changing Wannier-Stark transition, a ground state atom in $|W_n\rangle$ acquires a non-zero admixture of the excited state in $|W_{n+1}\rangle$. This component can interact with a ground state atom in $|W_{n+1}\rangle$ via s-wave interactions. Since the on-site s-wave interactions play a significant role in this case, we drop all the interaction terms smaller than such on-site s-wave interactions.

We can also drop the $K^{l}_{\mathbf{nm}}$ term due to the uniform atom population for lattice sites in a local regime. These approximations lead to the following large-spin Hamiltonian in a 1D lattice,

$$\hat{H}/\hbar = \sum_{n} \left[\chi_1^{l=1}\hat{S}_n^z\hat{S}_{n+1}^z - \delta_1\hat{S}_n^z + \Omega_1\hat{S}_n^x\right], \tag{3.41}$$

where

$$\chi_1^{l=1} = -\eta_0 U_{eg}/2. \tag{3.42}$$

In Fig. 3.5(D), we compare $\chi_1^{l=1}$ with its counterpart $\chi_0 + \chi_1$ in the carrier transition. It is clear that the interaction is significantly enhanced due to site-changing Wannier-Stark transitions.

In the main text we presented theoretical and experimental results on the ferromagnetic to paramagentic dynamical phase transition (DPT) when we address the $l = 1$ Wannier-Stark transition. Given that Eq. (3.41) is a large-spin Hamiltonian, its dynamical phase diagram is well captured by a mean-field approximation. Similar to the carrier transition, we apply the translationally invariant condition $\langle\hat{S}_n^{x,y,z}\rangle = \langle\hat{S}^{x,y,z}\rangle$ in a local regime (15 lattice sites), where $\langle\hat{S}^{x,y,z}\rangle = \frac{1}{2L+1}\sum_{m=-L}^{L}\langle\hat{S}_{n+m}^{x,y,z}\rangle$. This leads to the following mean-field Hamiltonian,

$$\hat{H}_{\mathrm{MF}}/\hbar = \sum_{n} \hat{\mathbf{S}}_n \cdot \mathbf{B}, \tag{3.43}$$

where

$$\mathbf{B} = \{\Omega_1, 0, -\delta_1 + 2\chi_1^{l=1}\langle\hat{S}^z\rangle\}. \tag{3.44}$$

Writing mean-field equations can be written in terms of normalized expectation value of collective spin operators on a single site $s^{x,y,z} = 2\langle\hat{S}^{x,y,z}\rangle/N_{\mathrm{loc}}$,

$$\begin{aligned} \frac{\mathrm{d}}{\mathrm{d}t}s^x &= -N_{\mathrm{loc}}\chi_1^{l=1}s^z s^y + \delta_1 s^y, \\ \frac{\mathrm{d}}{\mathrm{d}t}s^y &= N_{\mathrm{loc}}\chi_1^{l=1}s^z s^x - \delta_1 s^x - \Omega_1 s^z, \\ \frac{\mathrm{d}}{\mathrm{d}t}s^z &= \Omega_1 s^y. \end{aligned} \tag{3.45}$$

Note that Eq. (3.45) takes the same form as the mean-field equations obtained in [34, 107], which predicted a DPT between ferromagnetic and paramagnetic phases.

In general terms, a DPT is characterized by the existence of a critical point separating phases with distinct dynamical properties in many-body systems after a sudden quench. The analog of

thermodynamic order parameters is found in long-time average observables, which have a non-analytic dependence on system parameters. We initialize all the atoms in the $|\downarrow\rangle$ state, the ground state of our model when $\delta_1 \to -\infty$, and then perform a sudden quench of the longitudinal field to its final value δ_1. The DPT is signaled by a sharp change in behavior of the long-time average excitation fraction $\overline{n_\uparrow} = (\overline{s^z} + 1)/2$, where $\overline{s^z} = \lim_{T\to\infty} \frac{1}{T} \int_0^T s^z(t)\mathrm{d}t$. In the dynamical ferromagnetic phase, $\overline{n_\uparrow} \approx 0$ persists even when the final longitudinal field δ_1 is varied. In the dynamical paramagnetic phase, $\overline{n_\uparrow}$ dynamically adjusts itself following the change of final longitudinal field δ_1 [See Fig. 3.6(C)].

In the following, we analyze the critical points for the DPT in our system based on the procedure described in [34, 107]. Using energy conservation in H_{MF} for an initial state with $s^z = -1$, $s^x = s^y = 0$,

$$\frac{N_{\mathrm{loc}}\chi_1^{l=1}}{2} s^z s^z - \delta_1 s^z + \Omega_1 s_x = \frac{N_{\mathrm{loc}}\chi_1^{l=1}}{2} + \delta_1, \tag{3.46}$$

as well as the identity,

$$(s^x)^2 + (s^y)^2 + (s^z)^2 = 1. \tag{3.47}$$

In the large-N_{loc} limit, we can eliminate s^x and s^y, and obtain the following differential equation for s^z,

$$\frac{1}{2}\left(\frac{\mathrm{d}}{\mathrm{d}t} s^z\right)^2 + V(s^z) = 0, \tag{3.48}$$

where

$$\begin{aligned} V(s^z) = (s^z+1)\Bigg\{ & \frac{(N_{\mathrm{loc}}\chi_1^{l=1})^2}{8}(s^z)^3 - \left[\frac{(N_{\mathrm{loc}}\chi_1^{l=1})^2}{8} + \frac{N_{\mathrm{loc}}\chi_1^{l=1}\delta_1}{2}\right](s^z)^2 \\ & + \left[\frac{\delta_1^2+\Omega_1^2}{2} - \frac{(N_{\mathrm{loc}}\chi_1^{l=1})^2}{8}\right] s^z + \left[\frac{\delta_1^2-\Omega_1^2}{2} + \frac{N_{\mathrm{loc}}\chi_1^{l=1}\delta_1}{2} + \frac{(N_{\mathrm{loc}}\chi_1^{l=1})^2}{8}\right]\Bigg\}. \end{aligned} \tag{3.49}$$

Our experimental conditions lie in the parameter regime where $N_{\mathrm{loc}}\chi_1^{l=1} < 0$ with a fixed positive Ω_1.

We interpret Eq. (3.48) as the Hamiltonian of a classical particle with position s^z moving in the effective potential $V(s^z)$, which is shown in Fig. 3.6(A). The condition $V(s^z) = 0$ determines the physical turnover points of s^z. Since $V(-1) = 0$, $V'(-1) = -1$, $V(1) = 2\delta_1^2$, this effective potential

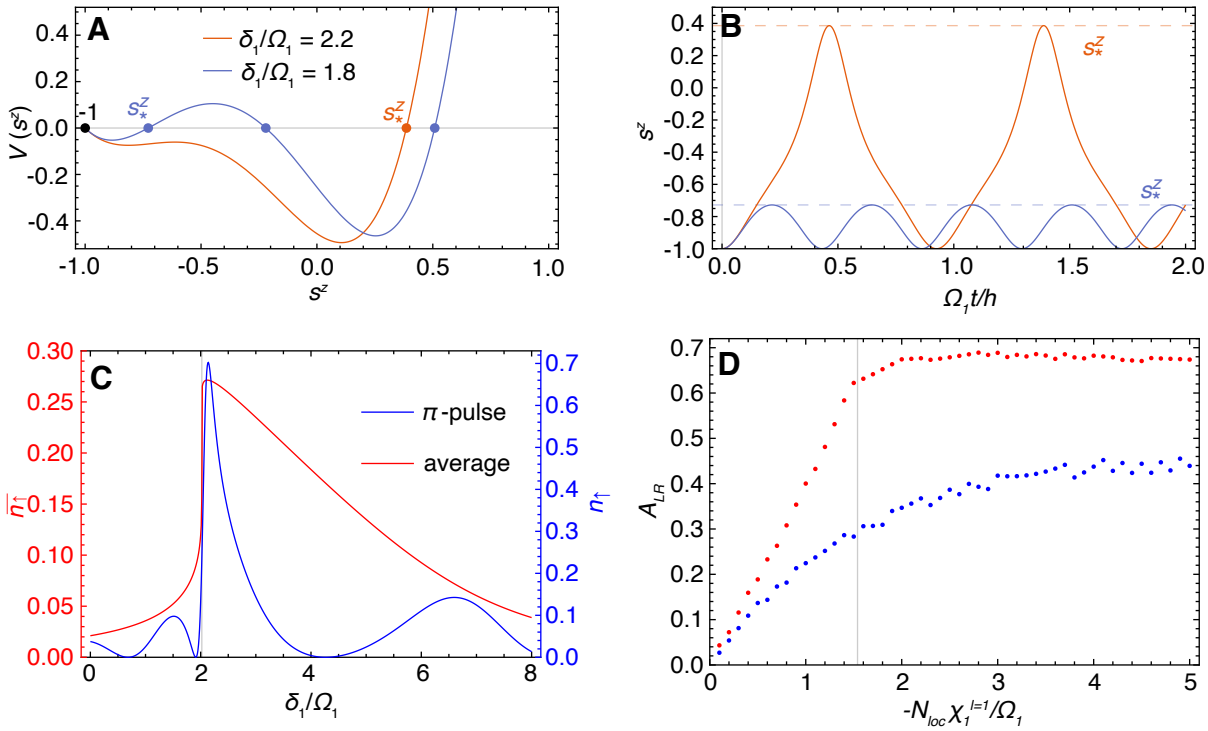

Figure 3.6: **Dynamical Phase Transition.** (**A**) The effective potential $V(s^z)$ with $N_{\rm loc}\chi_1^{l=1}/\Omega_1 = -5$. In the case of $\delta_1/\Omega_1 = 2.2$, $V(s^z)$ has two real roots; In the case of $\delta_1/\Omega_1 = 1.8$, $V(s^z)$ has four real roots. The nearest turnover point is labelled by s_*^z, and the jump of s_*^z indicates the DPT. (**B**) The mean-field dynamics of our model with $N_{\rm loc}\chi_1^{l=1}/\Omega_1 = -5$ and $\delta_1/\Omega_1 = 2.2, 1.8$, which shows a sharp change of mean-field dynamical behavior. The choice of color for the lines is the same as (**A**). (**C**) The long-time average excitation fraction $\overline{n_\uparrow}$ (red line) and the Rabi lineshape after a π-pulse (blue line) with $N_{\rm loc}\chi_1^{l=1}/\Omega_1 = -5$. The critical point (marked by gray line) that separates the ferromagnetic phase (left) and paramagnetic phase (right) is captured by the maximum derivative in both of the curves. (**D**) Asymmetry of the long-time averaged excitation fraction and Rabi lineshape in (**C**) with the same choice of color. The gray line separates the crossover regime (left) and DPT regime (right).

has at least two real roots in $[-1, 1]$. The dynamics of s^z can be understood as the oscillations between -1 and the nearest turnover point s^z_* [see Fig. 3.6(B)]. Suppose we start from a $V(s^z)$ with two real roots, and continuously tune the parameters of $V(s^z)$ so that two new real roots appear in between. Then a jump of the nearest turnover point s^z_* should occur in this process. This abrupt change in behavior is what sets the dynamical phase transition [see Fig. 3.6(A,B)].

To count the number of roots in $V(s^z)$, we factor out the known root $s^z = -1$, and then consider the discriminant $\Delta = 18abcd - 4b^3d + b^2c^2 - 4ac^3 - 27a^2d^2$ of cubic equation $ax^3 + bx^2 + cx + d = 0$. If $\Delta > 0$, the cubic equation has three distinct real roots; if $\Delta < 0$, the cubic equation has one real root. So $\Delta = 0$ sets the critical points of the DPT, presented as the black solid line in Fig. 3.4(C) of the main text. As shown in Fig. 3.6(C), the critical points can be captured by the divergence of the first derivative of $\overline{n_\uparrow}$. Similar to [34,107], our experiment measures the excitation fraction at a finite time (after a π pulse) instead of the long-time averaged excitation fraction. Although the derivative does not diverge in experiment, the maximum derivative can still be used to capture the critical point as shown in Fig. 3.6(C)]. In Fig. 3.4(C) of the main text, we construct the phase boundary of the DPT with the maximum derivative of the experimental Rabi lineshapes. We find that the many-body decoherence discussed in the next section has negligible effect on the position of the critical points, nevertheless it obscures the sharp features at the DPT expected from Eq. (3.43).

Moreover, based on the existence of real roots in equation $\Delta = 0$, we can also differentiate the DPT regime ($N_{\rm loc}\chi_1^{l=1}/\Omega_1 < -8\sqrt{3}/9$) dominated by interactions and the smooth crossover regime ($-8\sqrt{3}/9 < N_{\rm loc}\chi_1^{l=1}/\Omega_1 < 0$) dominated by single-particle Rabi flopping where no DPT takes place. Based on our experimental condition ($22E_{rec}$, 190nK and 2.3s π-pulse), the boundary of these two regimes $N_{\rm loc}\chi_1^{l=1}/\Omega_1 = -8\sqrt{3}/9$ is equivalent to $N_{\rm loc} = 63.4$, indicated by the black dashed line in Fig. 3.4(C) of the main text. These two regimes can also be determined by the asymmetry of the long-time averaged excitation fraction or Rabi lineshape, defined as $A_{LR} = (n_R - n_L)/(n_R + n_L)$. Here, $n_R = \int_{\delta_{max}}^{\delta_{max}+f} n_\uparrow(\delta)\mathrm{d}\delta$, $n_L = \int_{\delta_{max}-f}^{\delta_{max}} n_\uparrow(\delta)\mathrm{d}\delta$, where δ_{max} is the detuning at which the peak value of $n_\uparrow$ is reached, and we choose f to cover almost the entire frequency range of non-vanishing

$n_\uparrow$. In Fig. 3.6(D), we compare the A_{LR} obtained from the long-time averaged excitation fraction and the the one obtained from the Rabi lineshape after a π pulse. In both cases, the asymmetry A_{LR} becomes more pronounced as the atom number increases in the crossover regime, while A_{LR} saturates near the maximum value in the DPT regime. Note that the many-body decoherence discussed in the next section generally reduces the asymmetry. Nevertheless the saturation behavior observed in the DPT regime is maintained. For convenience, in Fig. 3.4(C) of the main text we normalize the maximum value of A_{LR} obtained from experimental lineshapes to 1.

3.2.8 Supplemental Materials: Details in theory-experiment comparison

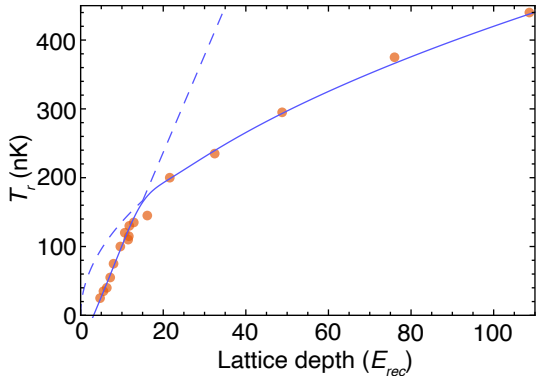

Figure 3.7: **Radial Temperature.** Radial temperature T_r measured over a range of operational lattice depths V_0 in units of lattice photon recoil energies, E_{rec}. The red points indicate experimental data, and the solid blue lines show the piecewise fit of Eq. (3.50).

Here we would like to discuss additional details in theory-experiment comparison:

- Determination of radial temperature

  In experiment, we prepare a nuclear spin polarized, cold sample of ^{87}Sr at a high lattice depth of 300 E_{rec} and then adiabatically reduce the lattice depth. We measure the radial temperature T_r of the ensemble before each density shift measurement by driving the narrow clock transition with a beam oriented perpendicular to the lattice direction and extracting a Doppler absorption profile. Our camera based imaging spectroscopy technique provides a spatial map of the temperature throughout the mm length cloud. We observe temperature

variations of up to 10 nK over the entire sample. The temperature over the range of operational lattice depths V_0 is well described by:

$$T_r(nK) = \begin{cases} -45.2 + 14.1 V_0/E_{rec} & (V_0 < 15 E_{rec}), \\ 42\sqrt{V_0/E_{rec}} & (V_0 > 15 E_{rec}). \end{cases} \tag{3.50}$$

For $V_0 > 15\ E_{rec}$, the trend of T_r matches that expected from an adiabatic lowering of the trap depth. At sufficiently low lattice depths, the anharmonic radial trap behavior leads to a deviation from adiabatic temperatures. For the lowest values of T_r approaching 20 nK, our Doppler spectroscopy technique also reaches its limit of reliability. The radial temperature T_r over a range of lattice depths is shown in Fig. 3.7. The piecewise function Eq. (3.50) is plotted alongside the red experimental data points.

- Many-body decoherence in off-site Wannier-Stark transitions

  Our theoretical model is based on the frozen-mode approximation, which restricts the accessible Hilbert space of each atom into a spin-1/2 degree of freedom spanned by the $|\uparrow_{\mathbf{n}}\rangle$ and $|\downarrow_{\mathbf{n}}\rangle$ states. Our spin model is valid in the collisionless regime, breaking down at long times or at high enough densities where mode relaxation is not negligible. Since the interaction strength is significantly enhanced when interrogating site-changing WS transitions, as discussed in previous sections, the mode relaxation rate is expected to be more significant. We take into account the mode-changing collisions phenomenologically by adding a density-dependent dephasing term (γ_z) into our mean-field equations for the $l = 1$ Wannier-Stark sideband [see Eq. (3.45)],

$$\begin{aligned} \frac{\mathrm{d}}{\mathrm{d}t} s^x &= -N_{\mathrm{loc}} \chi_1^{l=1} s^z s^y + \delta_1 s^y - \gamma_z s^x, \\ \frac{\mathrm{d}}{\mathrm{d}t} s^y &= N_{\mathrm{loc}} \chi_1^{l=1} s^z s^x - \delta_1 s^x - \Omega_1 s^z - \gamma_z s^y, \\ \frac{\mathrm{d}}{\mathrm{d}t} s^z &= \Omega_1 s^y, \end{aligned} \tag{3.51}$$

  We use γ_z as a fitting parameter and find it has a linear dependence on N_{loc} as expected from mode changing decoherence. In Fig. 3.8, we compare our theoretical predictions with

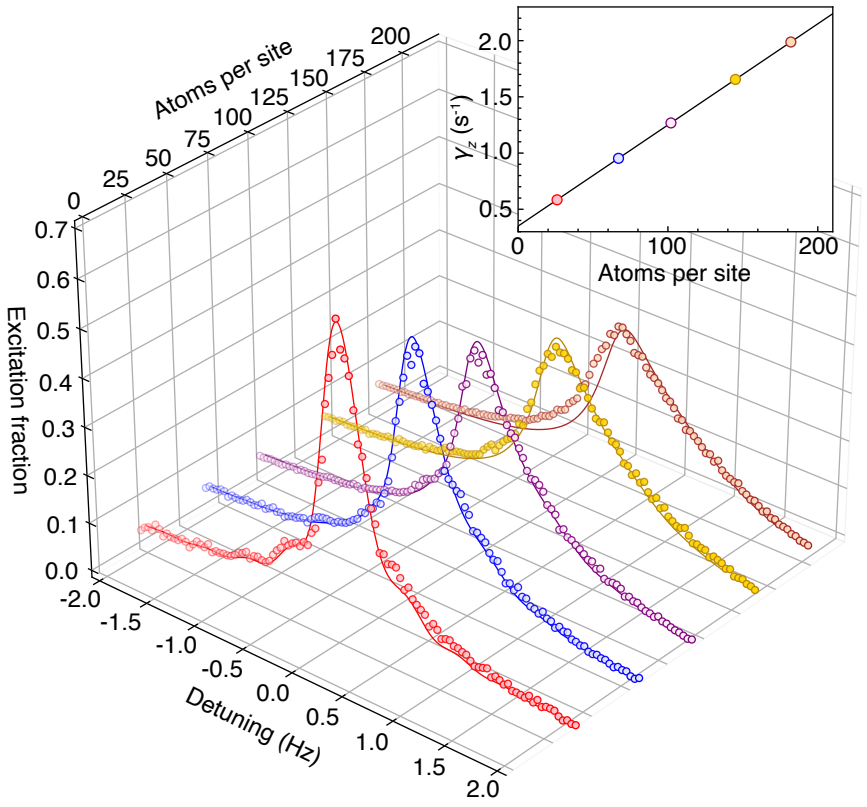

Figure 3.8: **Many-body Decoherence.** Rabi lineshapes for the $l = 1$ Wannier-Stark $l = 1$ transition and corresponding theoretical fits at different N_{loc}. The dephasing rate γ_z is the only fitting parameter, which is shown in the inset using the same color as the Rabi lineshapes. The linear dependence of γ_z on atom number per site ($\gamma_z = 0.35 + 0.009 N_{\mathrm{loc}}$) confirms that the dephasing effect is generated by mode-changing collisions.

the Rabi lineshapes observed in experiment at different N_{loc}, with good agreement by setting the dephasing rate $\gamma_z = 0.35 + 0.009 N_{\mathrm{loc}}$. Small deviations are observed at the highest densities approaching 200 atoms per site.

- Scattering parameters

  In Ref. [62, 100], the relation between the p-wave interaction and p-wave scattering length was missing a factor of 1/2, with the correct coefficient being $3\pi\hbar^2 b_{\alpha\beta}^3/2M$. Using the past notation, in Ref. [62] the p-wave scattering lengths were found to be: $\tilde{b}_{eg}^{+} = (-169 \pm 23)a_0$, $\tilde{b}_{ee} = (-119 \pm 18)a_0$. These values can be corrected by solving: $b_{ee}^3 - b_{gg}^3 = 2(\tilde{b}_{ee}^3 - b_{gg}^3)$ and $(b_{eg}^{+})^3 - b_{gg}^3 = 2((\tilde{b}_{eg}^{+})^3 - b_{gg}^3)$, which gives $b_{eg}^{+} = (-215.9 \pm 28.2)a_0$ and $b_{ee} = (-155.8 \pm 21.1)a_0$. For p-wave inelastic scattering length β_{ee}, one can multiply the factor $2^{1/3}$ to the value in Ref. [62], which gives $\beta_{ee} = (152.5 \pm 16.4)a_0$. Using these corrected values of the p-wave parameters, combined with the measured s-wave scattering lengths in Ref. [109], as well as the universal relation between the complex s-wave scattering length $A = a - i\alpha$ and the complex p-wave scattering volume $B^3 = b^3 - i\beta^3$ for a single van der Waals potential [60,62], one can finally obtain Table 3.1 that includes the updated s-wave and p-wave scattering lengths that are used in this work.

Table 3.1: ^{87}Sr s-wave and p-wave scattering lengths in Bohr radius (a_0)

Channel	s-wave	p-wave
gg	96.2 ± 0.1	74.5 ± 0.3
eg^+	161.3 ± 2.5	-215.9 ± 28.2
eg^-	69.1 ± 0.9	-41.3 ± 2.7
ee (elastic)	176.3 ± 9.5	-155.8 ± 21.1
ee (inelastic)	17.3^{+14}_{-8}	152.5 ± 16.4

- Corrections in the tunneling rate from Gaussian beam geometry

  In previous sections, we assume a separable confinement potential and tunneling only along

the direction of gravity. However in the experimental system, the Gaussian geometry of the laser beams inevitably couple the axial and radial wave functions. This coupling leads to corrections in the nearest-neighbor tunneling rate which now depends on the thermal distribution of the radial modes. Notice that the Gaussian beam profile of a 1D lattice leads to the following trapping potential,

$$V(X,Y,Z) = V_0 - V_0 \cos^2(k_L Z) \exp\big[-2(X^2+Y^2)/w_L^2\big], \tag{3.52}$$

where $k_L = 2\pi/\lambda_L$ is the lattice wave number, w_L is the beam waist, and $V_0 > 0$ is the lattice depth. Based on Eq. (2.46) and Eq. (2.47), an atomic gas with radial temperature T_r feels an effective lattice depth given by $V_0 - k_B T_r$. Although $k_B T_r \ll V_0$, it may still lead to non-negligible corrections to the nearest-neighbor tunneling rate, which shows exponential dependence on lattice depth. Note that in the large-spin Hamiltonian discussed in previous subsections, the interaction parameters are determined by thermal average over radial modes. To take into account the leading order effects of the thermal distribution, we replace the ground band tunnel coupling by

$$J_0(T_r) \approx \frac{4}{\sqrt{\pi}} E_{rec}^{1/4} (V_0 - k_B T_r)^{3/4} \exp\left[-2\sqrt{\frac{V_0 - k_B T_r}{E_{rec}}} \right]. \tag{3.53}$$

This correction leads to $\sim 40\%$ increase of nearest-neighbor s-wave interaction strength near the zero-crossing point.

3.3 Coherent evolution of superexchange interaction in seconds long optical clock spectroscopy

This section is adapted from: William R. Milner, Stefan Lannig, Mikhail Mamaev, Lingfeng Yan, **Anjun Chu**, Ben Lewis, Max N. Frankel, Ross B. Hutson, Ana Maria Rey, Jun Ye, *Coherent evolution of superexchange interaction in seconds long optical clock spectroscopy*, arXiv:2402.13398 (2024).

3.3.1 Introduction

Optical lattice clocks are advancing studies of fundamental physics, metrology, and quantum simulation [23,79,110–113]. By controlling all external perturbations to the ground and metastable "clock" state, each one of the confined atoms becomes a pristine, two-level system. With clock precision limited fundamentally by quantum projection noise [114], a natural approach for improving clock performance is to probe the largest possible number of atoms combined with the longest possible coherence time. However, given a densely packed sample of atoms, we must address outstanding challenges including maintaining a maximum coherence time for clock precision and evaluating systematic effects for clock accuracy. Often it is desirable to minimize atomic interactions to enhance single-particle coherence and control systematic effects. At the same time, as the level of understanding of these interactions becomes more mature and sophisticated, we can engineer a large, coherent spin ensemble with interaction precisely controlled to introduce and optimize quantum coherence, correlation, and entanglement to advance the frontier of quantum metrology [14,16,115,116]. With the ease of geometry tunability, optical lattices provide a versatile platform to confine large numbers of atoms and control their interactions and motion. Over the past two decades, progress in clock precision [20, 77] has been largely advanced by the study and control of interactions in one-dimensional (1D) optical lattice clocks. The corresponding interaction dynamics are well described by a collective spin model [62, 100] that includes both on-site p-wave interactions between atoms in different radial modes and off-site s-wave interactions. The latter are induced by the spin-orbit coupling (SOC), arising from a difference in wavelength between the clock probe and the lattice laser [102, 103], which lifts the indistinguishability between spin-polarized fermions on neighboring lattice layers along the clock k-vector. Systematic exploration of this 1D spin model identified a confinement depth at which the combination of s and p-wave interactions suppressed detrimental mean-field density shifts [23, 25]. These advances based on precise experimental control motivates quantum simulation investigations of the comparatively less-studied three-dimensional (3D) lattice spin model [76].

In a 3D lattice filled with a degenerate Fermi gas of spin-polarized ^{87}Sr atoms in the motional ground state [117], the system can be modelled with the Fermi-Hubbard Hamitonian where ground and excited state atoms on the same lattice site interact via the Hubbard interaction parameter U, and motion is captured by a tunneling parameter t. In the unity filled limit a Mott-insulating regime emerges at $U \gg t$, atomic motion is restricted, and atoms interact only via virtual second order tunneling processes that induce spin-exchange couplings between nearest neighbour atomic spins known as superexchange [84, 118, 119]. The physics of superexchange is central in describing magnetic phenomena such as antiferromagnetism [63, 120] and is believed to play a role in superconductivity [121]. Several ultracold atom experiments have employed optical lattices to explore low-temperature bosonic ferromagnetic and fermionic antiferromagnetic correlations induced by superexchange [122–129], as well as some non-equilibrium superexchange-driven quantum dynamics in local density probes [83, 130, 131]. With the goal of achieving optimal and scalable clock performance at a unity filled 3D lattice, understanding and controlling the effects of superexchange on collective spin dynamics becomes necessary [76, 109]. The current work employing seconds long Ramsey spectroscopy on tens of thousands of atoms directly probes the coherent nature of superexchange interaction, thus strengthening our understanding of interaction regimes that are favorable for robust quantum coherence and entanglement.

In the current experiment we independently vary the lattice confinement to explore the 1D and 3D lattice spin models, including the crossover between the two regimes for the first time. To do so we load a degenerate Fermi gas of ^{87}Sr atoms into a 3D lattice with tunable confinement, allowing us to vary the interaction strength and tunneling rates. The interaction effects on spin coherence between the ground and metastable clock state are directly recorded on Ramsey fringes. In a vertical 1D lattice, we achieve coherence times of $\sim$20 s when minimizing the contribution of s and p-wave interactions. As a weak transverse confinement is turned on, s-wave interactions are increased by orders of magnitude and very fast dephasing is observed. At deep transverse confinement, favorable coherence times are partially recovered, and coherent superexchange interactions are manifested directly in oscillations of the Ramsey fringe contrast persisting over a timescale of

multiple seconds. These experimental observations are well captured by an anisotropic lattice spin model (XXZ plus antisymmetric exchange terms), which breaks the Heisenberg SU(2) symmetry of the Fermi-Hubbard physics due to the spin-orbital coupling phase [102,103,132,133]. Realization of anisotropic spin interactions in controlled cold atomic systems has only recently seen exploration, and is highly relevant to studies of spin magnetism [127] and transport [134]. In clocks, such interactions can also be directly employed for the generation of large scale quantum entanglement over the entire 3D lattice system [135–137].

3.3.2 System

The experimental schematic is depicted in Fig. 3.9(a). After evaporation, we confine the atoms in a retroreflected, cubic lattice operating at the magic wavelength of $\lambda_{magic} = 813$ nm with lattice constant $a \approx 407$ nm [76]. Beginning with a nuclear-spin polarized Fermi gas with a temperature $T/T_F \approx 0.2$, the atoms are adiabatically loaded into the ground band of the 3D lattice [76, 117]. In the deep lattice, the initial state is nearly a band insulator with a peak filling of one atom per lattice site [111, 139]. The lattice depth ($V_\perp$) of the transverse (horizontal with respect to gravity) confinement is tuned independently from the depth of the vertical confinement (V_z) by adjusting the optical power in the corresponding lattice beams. Our two-level spin system is established between the ground $^1S_0$ ($|g\rangle$) and metastable electronic "clock" state $^3P_0$ ($|e\rangle$). We coherently drive the clock transition $|g, m_F = -9/2\rangle \leftrightarrow |e, m_F = -9/2\rangle$ at $\lambda_{clk} \approx 698$ nm with a vertical laser beam using an optical local oscillator locked to an ultrastable silicon cavity [140].

After loading the lattice, we put the atoms into a superposition of $|g\rangle$ and $|e\rangle$ and perform Ramsey spectroscopy. For detection, *in situ* absorption imaging along the vertical direction is employed and approximately 100 photons per atom are scattered over a 1 μs pulse duration with minimal blurring compared to the diffraction-limited point-spread function of 1.3 μm [111, 139]. Two images of the ground and clock state atoms, their numbers denoted N_g and N_e, are taken to determine the excitation fraction $p_e = N_e/(N_e + N_g)$. For a chosen region-of-interest P_A of our imaged density distribution, we record the local excitation fraction $p_e^A = N_e^A/(N_e^A + N_g^A)$. This is

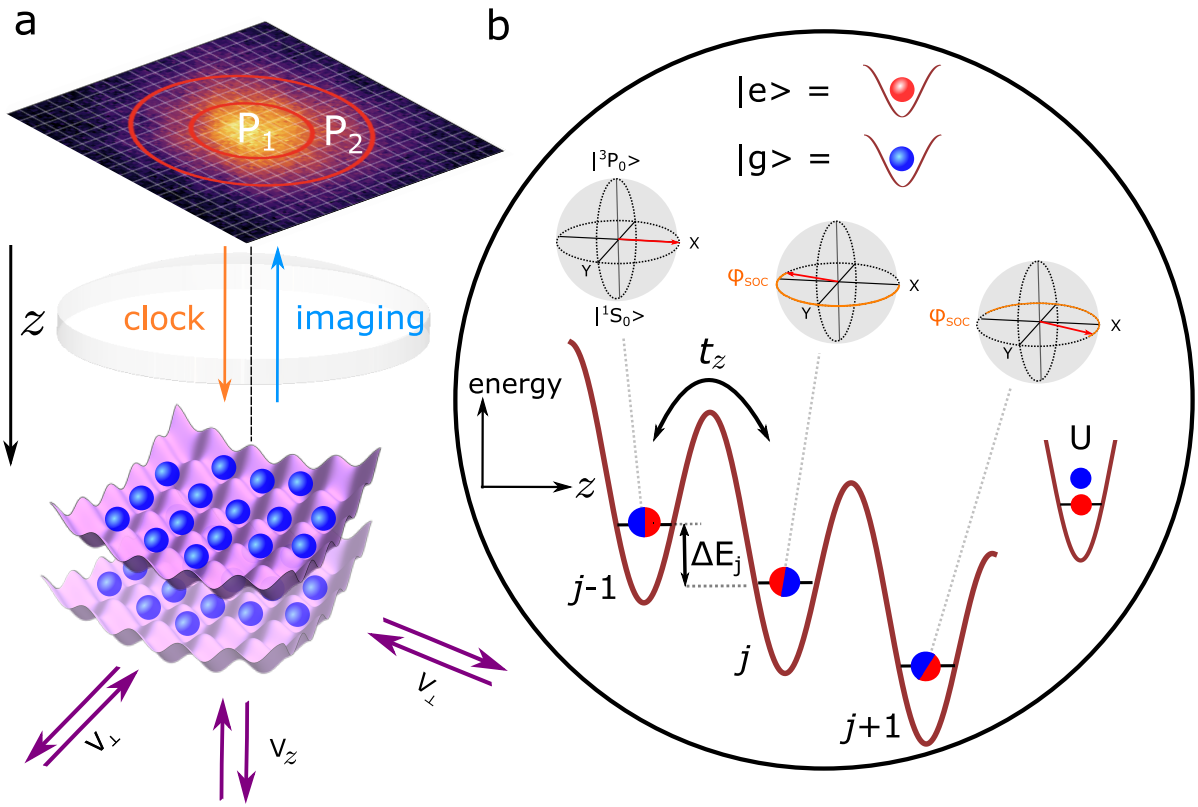

Figure 3.9: **Experimental setup and interaction model**. **a,** Ultracold fermions are confined in the ground band of a three-dimensional optical lattice with tunable confinement. Lattice depths can be independently varied by changing the optical power of retro-reflected beams in the transverse $V_\perp$ or vertical direction V_z. *In situ* imaging allows to spatially resolve interactions and dephasing via imaging spectroscopy [138]. **b,** Dynamics are described via the Fermi-Hubbard model with tunneling t_z, interaction energy U, and a site-to-site energy shift ΔE_j from the lattice Gaussian confinement. Atoms along the z axis on sites indexed $j-1, j$ are initialized in a superposition state of the ground state $|g = {}^1S_0\rangle$ and the metastable electronic state ("clock" state) $|e = {}^3P_0\rangle$, where the clock laser imprints local phase shift φ due to spin-orbit coupling. Dephasing of the coherence is proportion to an effective superexchange rate: $4t_z^2U/(U^2 - \Delta E_j^2)$

shown in Fig. 3.9(a), where the excitation fractions are evaluated in spatially separate regions P_1 and P_2 to determine both the Ramsey fringe contrast and relative atomic coherence using imaging spectroscopy [138].

During the Ramsey interrogation time the atoms interact via the Fermi-Hubbard model presented in Fig. 3.9(b) [141]. The on-site interaction $U = \frac{4\pi\hbar^2}{m} a_{eg-} \int |W(\mathbf{r})|^4 d^3\mathbf{r}$ is determined by the anti-symmetric scattering length $a_{eg-} = 69.1(0.9)a_B$ [62, 109] and the 3D, single-particle Wannier function $W(\mathbf{r})$ is determined by the lattice confinement. Along the vertical direction, z, the atoms on neighboring sites are coupled with the tunneling rate t_z, and also experience both the linear gravitational potential and the confinement from the Gaussian transverse lattice beams, leading to an energy offset ΔE_j between adjacent vertical lattice planes indexed by j [81]. The clock laser is also launched along the vertical direction imprinting a spin-orbit-coupling (SOC) phase $\varphi = 2\pi a/\lambda_{clk} \approx 7\pi/6$ between neighboring vertical lattice planes [102, 142] as depicted in Fig. 3.9(b).

The superexchange oscillations, observed in the deep 3D confinement regime of our experiment, can be understood from a simple double-well model describing two atoms (spin $s = \frac{1}{2}$) on two adjacent lattice sites $j = 0, 1$ along the z lattice direction. The Ramsey spectroscopy protocol initializes the atoms in a superposition state $|\psi_{\text{init}}\rangle = (|g\rangle_0 + |e\rangle_0)/\sqrt{2} \otimes (e^{-i\varphi/2}|g\rangle_1 + e^{+i\varphi/2}|e\rangle_1)/\sqrt{2}$. Crucially, due to the site-dependent, spin-orbit coupling phase φ, aside from a global phase this initial state is an admixture of the spin triplet and singlet states, with $|\psi_{\text{init}}\rangle \sim e^{-i\varphi/2}|g,g\rangle + e^{i\varphi/2}|e,e\rangle + \cos(\varphi/2)(|g,e\rangle + |e,g\rangle) + i\sin(\varphi/2)(|g,e\rangle - |e,g\rangle)$. At half-filling and in the strongly interacting limit, $U \gg t_z$, superexchange interactions arising between neighboring spins, $J_{\text{SE}}\hat{\tilde{\mathbf{s}}}_0 \cdot \hat{\tilde{\mathbf{s}}}_1$, introduce an energy shift for the singlet state, which translates to a phase difference $J_{\text{SE}}T$ compared to the triplet states during the coherent evolution time T. Here $\hat{\tilde{s}}_j^\alpha$ for $\alpha \in \{X, Y, Z\}$ refers to spin-1/2 matrices describing atoms on sites j in the lab frame.

More formally, we rotate into a "spiral" frame where the initial state is uniform (all atoms in the same superposition state) and the site-dependent laser phase φ is absorbed into the spin operators across the lattice, $\hat{s}_j^\pm = \hat{\tilde{s}}_j^\pm e^{\pm ij\varphi}$, $\hat{s}_j^Z = \hat{\tilde{s}}_j^Z$. Thus, we obtain a superexchange spin

Hamiltonian in the spiral frame (see SOM)

$$\hat{H}_{\mathrm{SE}} = \sum_j J_{\mathrm{SE}}(j)\Big[\frac{1}{2}\left(e^{i\varphi}\hat{s}_j^+\hat{s}_{j+1}^- + H.c.\right) + \hat{s}_j^Z\hat{s}_{j+1}^Z\Big]. \tag{3.54}$$

The superexchange interaction strength is $J_{\mathrm{SE}}(j) = 4t_z^2U/(U^2 - \Delta E_j^2)$, which is inhomogeneous due to the local potential difference between adjacent sites ΔE_j, including gravity and the lattice Gaussian confinement. Furthermore, the spiral phase makes this spin Hamiltonian go beyond conventional superexchange interactions in optical lattices, as it exhibits exchange-symmetric XXZ-style anisotropy and an antisymmetric spin exchange term (see SOM). Observables such as atomic coherence reveal collective quantum dynamics on timescales of the averaged $\bar{J}_{\mathrm{SE}}$ over the ensemble, which is tuned by controlling the inhomogeneity and the lattice depth.

The above theoretical description is valid in the regime $V_z \ll V_\perp$, for which the system acts as individual vertical tubes and each site with an atom acts as a spin-1/2 particle. Prior work [25] has also shown that in the 1D lattice confinement along z ($V_\perp = 0$), each lattice site holds many atoms. In this 1D limit, on-site interactions favor spin alignment between atoms, locking them into large collective spins of Wannier-Stark level n along gravity (see SOM), $\hat{S}_n^\alpha$, whose dynamics is described by the same type of spin Hamiltonian as superexchange but with modified couplings and an additional onsite term. $\hat{H}_{\mathrm{LS}} = \hat{H}_{\mathrm{on-site}} + \hat{H}_{\mathrm{off-site}}$. Here, $\hat{H}_{\mathrm{on-site}} \sim \sum_n \hat{S}_n^Z\hat{S}_n^Z$ describes the on-site p-wave interactions (see Fig. 3.11(a)), and $\hat{H}_{\mathrm{off-site}}$ includes the off-site s-wave interactions and takes the same form as $\hat{H}_{\mathrm{SE}}$ by replacing the spin-1/2 operators with large-spin operators. In this work, we bridge these two regimes by varying the transverse lattice confinement $V_\perp$. We extend the theoretical description of Ref. [25] to the regime $V_z \gg V_\perp$, where in each pancake the weak transverse lattice defines a new set of transverse eigenmodes with renormalized spin couplings (see SOM).

To evaluate atomic coherence that is related to clock performance at different lattice confinement, we measure the Ramsey fringe contrast for varying dark time T. An XY8 sequence consisting of eight π pulses along the two orthogonal rotation axes in the equatorial place of the Bloch sphere is used to remove single particle dephasing as depicted in Fig. 3.10(a) [143, 144]. To decouple the

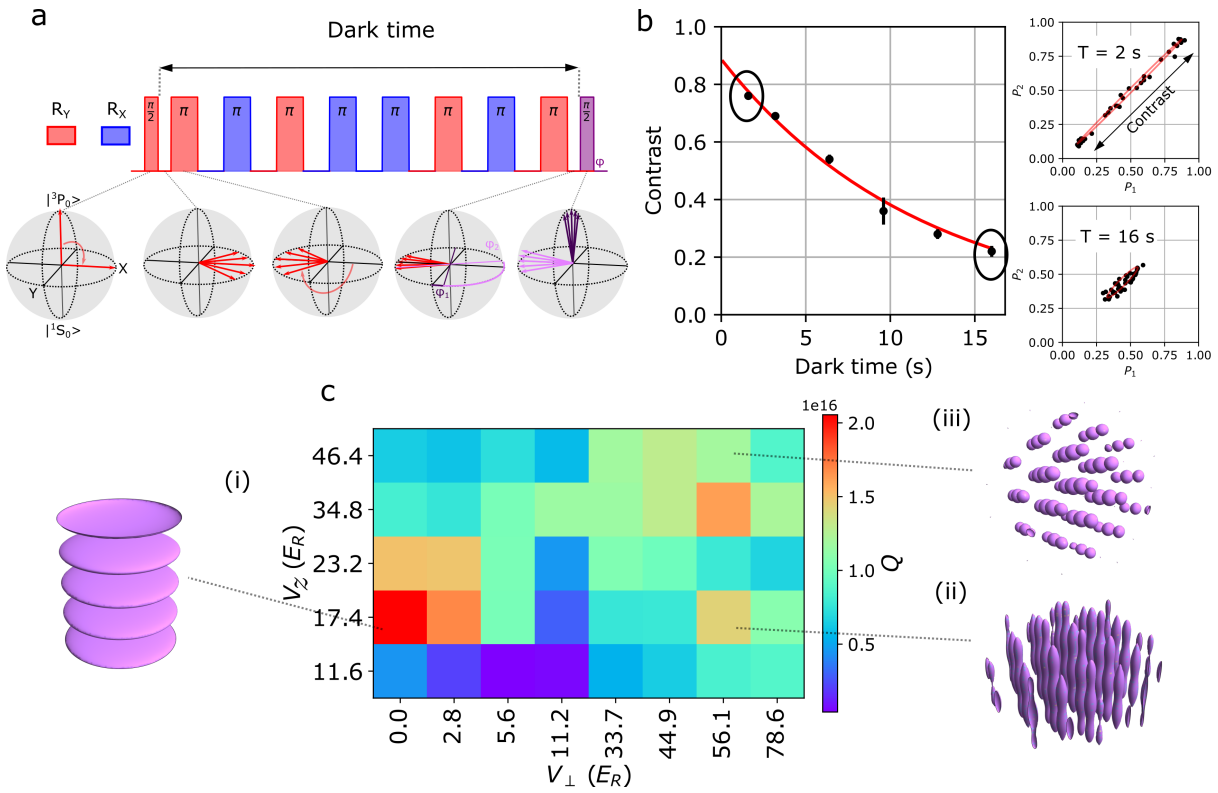

Figure 3.10: **Coherence time measurement**. **a**, Ramsey spectroscopy is employed to study the coherence time. An XY8 pulse sequence is used to mitigate single-particle dephasing. The dephasing and rephasing of individual spins is depicted on the Bloch sphere during the echo sequence. For the final $\pi/2$ pulse two choices of the randomized phase $\varphi_{1,2}$ are shown (light and dark purple) to illustrate the spread of resulting excitation fractions in individual realizations. **b**, To determine the coherence time T_2, the contrast decay is fit to a stretched exponential $C(T) = C_0 e^{-(T/T_2)^\alpha}$ as a function of dark time T. The contrast is determined via parametric plots of excitation fractions in regions P_1 and P_2 of the ensemble as depicted in Fig. 1. Error bars are 1σ (standard deviation) obtained from jackknifing (see SOM). **c**, The quality factor $Q = \pi C_0 T_2 \nu$ where $\nu \approx 429$ THz is plotted over a wide range of transverse and vertical confinement. Two candidate regimes are identified to investigate further. The weak or zero transverse confinement regime (i), where the longest optical lattice clock T_2 times have been reported [23]. Regime (ii), where fast initial contrast decay is observed due to superexchange interactions. The deep 3D lattice regime (iii) was studied on this platform in [142] where the coherence time is limited by Raman scattering of lattice photons.

atomic coherence measurement from the finite atom-light coherence time (∼3 s) [140], the phase of the final Ramsey $\pi/2$ pulse is randomized. Parametric plots of the excitation fractions from concentric regions P_1 and P_2 ($P_1 < 6\mu$m and $6\ \mu\text{m} < P_2 < 12\mu$m with respect to the trap center) are used to determine the contrast as shown in Fig. 3.10(b). These parametric plots show ellipses, where a maximum likelihood estimator determines the ellipse contrast and jackknifing is used to extract 1σ (standard deviation) errorbars for all Ramsey contrast measurements [138]. The system is sufficiently homogeneous in the spatial regions P_1 and P_2 that the contrast C is approximately the same (see SOM). No statistically significant phase shift between P_1 and P_2 is measured, indicating that the XY8 pulse sequence largely removes any spatially varying frequency shift.

As a function of dark time T, a stretched exponential function $C_0 e^{-(T/T_2)^\alpha}$ is fit to the Ramsey contrast to extract a T_2 coherence time for $T > 1$ s. For $V_\perp = 0$, we expect intra-site, all-to-all p-wave interactions to lead to Gaussian decoherence. We extract a single value $\alpha = 1.38$ by minimizing the combined χ^2 for all measurements for $V_\perp = 0$. For all other measurements with $V_\perp > 0$, we set $\alpha = 1$ when fitting T_2. The extracted quality factor $Q = \pi C_0 T_2 \nu$ is plotted in Fig. 3.10(c), where ν is the clock transition frequency ≈ 429 THz. We identify two interesting regimes to investigate further: (1) In the 1D lattice regime with no transverse confinement the longest coherence times are observed; (2) With deep transverse confinement where the average $\bar{J}_{\text{SE}}/h \gtrsim 1$ Hz, coherent superexchange dynamics are observed on the Ramsey fringe contrast over a timescale of seconds. As previously reported [142], the deep 3D lattice regime (3) where $\bar{J}_{\text{SE}}/h \ll 1$ Hz reveals a limit on the coherence time primarily due to Raman scattering of lattice photons on $|e\rangle$ atoms. The dark times in this study ($T < 16$ s) are short compared to both the $^1S_0$ lattice lifetime and vacuum lifetime (see SOM).

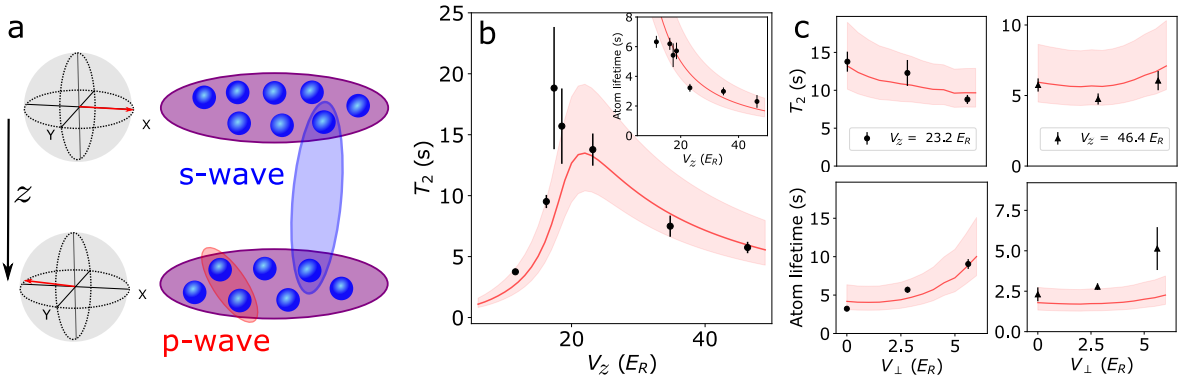

Figure 3.11: **Weak transverse confinement regime**. **a**, In the weak transverse confinement regime, both off-site s-wave interactions, induced by the SOC phase between lattice sites, and on-site p-wave interactions between atoms contribute to dephasing [25]. Their strength is controlled by the vertical confinement V_z and transverse confinement $V_\perp$, strongly influencing the observed coherence time T_2. **b**, T_2 is measured without transverse confinement ($V_\perp = 0$). In the inset the atom lifetime τ, limited by inelastic p-wave loss, is plotted as a function of V_z (see SOM). Theory modeling Ramsey contrast decay based on the 1D spin Hamiltonian using experimental measured parameters is overlaid in red. The error bands are based on the uncertanties of the experimental parameters (see SOM). Error bars are 1σ (standard deviation) uncertainty of the fitted T_2 and τ values. **c**, A weak transverse confinement $V_\perp$ is applied. This leads to increased τ, as well as a reduction of T_2 at intermediate $V_z = 23.2E_R$ and a enhancement of T_2 at deep $V_z = 46.4E_R$.

3.3.3 Weak transverse confinement regime

Intrigued by the results in Fig. 3.10(c), we compare the 1D and 3D confinement regimes (1) and (2). In 1D ($V_\perp = 0$), both on-site p-wave and off-site s-wave interactions contribute to the contrast decay (see Fig. 3.11(a)). The observed T_2 coherence time and atom lifetime are plotted as a function of V_z in Fig. 3.11(b). Varying V_z provides two distinct regimes to probe the physics of contrast decay. At large V_z, atoms become localized in Wannier orbitals along the z-lattice and interact predominantly via on-site Ising-type p-wave interactions that contribute to slow contrast decay with $T_2 \sim 1/\sqrt{N_s}$ (N_s is the atom number per pancake, see SOM), as

observed in previous studies [100]. As V_z decreases, the reduced p-wave interaction leads to slower decoherence rate. However, the Wannier-Stark states become increasingly delocalized along z and atoms experience progressively stronger off-site s-wave interactions. The interplay between s-wave and p-wave interactions leads to spin wave instabilities that contribute to fast contrast decay with $T_2 \sim 1/N_s$ (see SOM). With increasing s-wave interaction strength, this instability rate increases as V_z decreases. The crossover between these two mechanisms occurs around $V_z = 17.4E_R$, where $E_R = h^2/8ma^2 \approx h \times 3.5$ kHz is the lattice photon recoil energy, with a correspondingly longest coherence time of 19(5) s. While experiment and theory largely agree with each other, the discrepancy at long coherence times could arise from unexpected reduction of the s-wave interaction strength from re-thermalization processes neglected in the theory. The 1D lattice employed in this study operates with a much higher density than previous studies [23, 25]. Thus, the atom lifetimes (see Fig. 3.11(b) inset), limited by inelastic p-wave loss are correspondingly much shorter [23].

Upon introduction of a weak transverse confinement ($V_\perp \ll V_z$), the increasing localization of the transverse modes in the x-y plane leads to enhancement of s-wave interactions. Additionally, due to decreased overlap of transverse modes, p-wave interactions are suppressed, which in turn substantially improves atom lifetimes as shown in Fig. 3.11(c). Meanwhile, different trends in the coherence time are observed between the intermediate $V_z = 23.2E_R$ and deep $V_z = 46.4E_R$ lattices. For $V_z = 23.2E_R$, the weak transverse confinement increases s-wave interactions within pancakes, enhancing the population of unstable spin wave modes, and a subsequent decrease of T_2. For $V_z = 46.4E_R$, the system remains in the quasi-stable Ising dominated regime and T_2 increases as p-wave interactions decrease.

3.3.4 Strong transverse confinement regime

As the transverse confinement is increased further, only s-wave interactions remain relevant. When the system enters the strongly interacting regime doubly occupied lattice sites across the whole array are suppressed and coherent superexchange interactions dominate the quantum dynamics. In Figs. 3.12(a), 3.12(b) we show the contrast decay as a function of dark time for

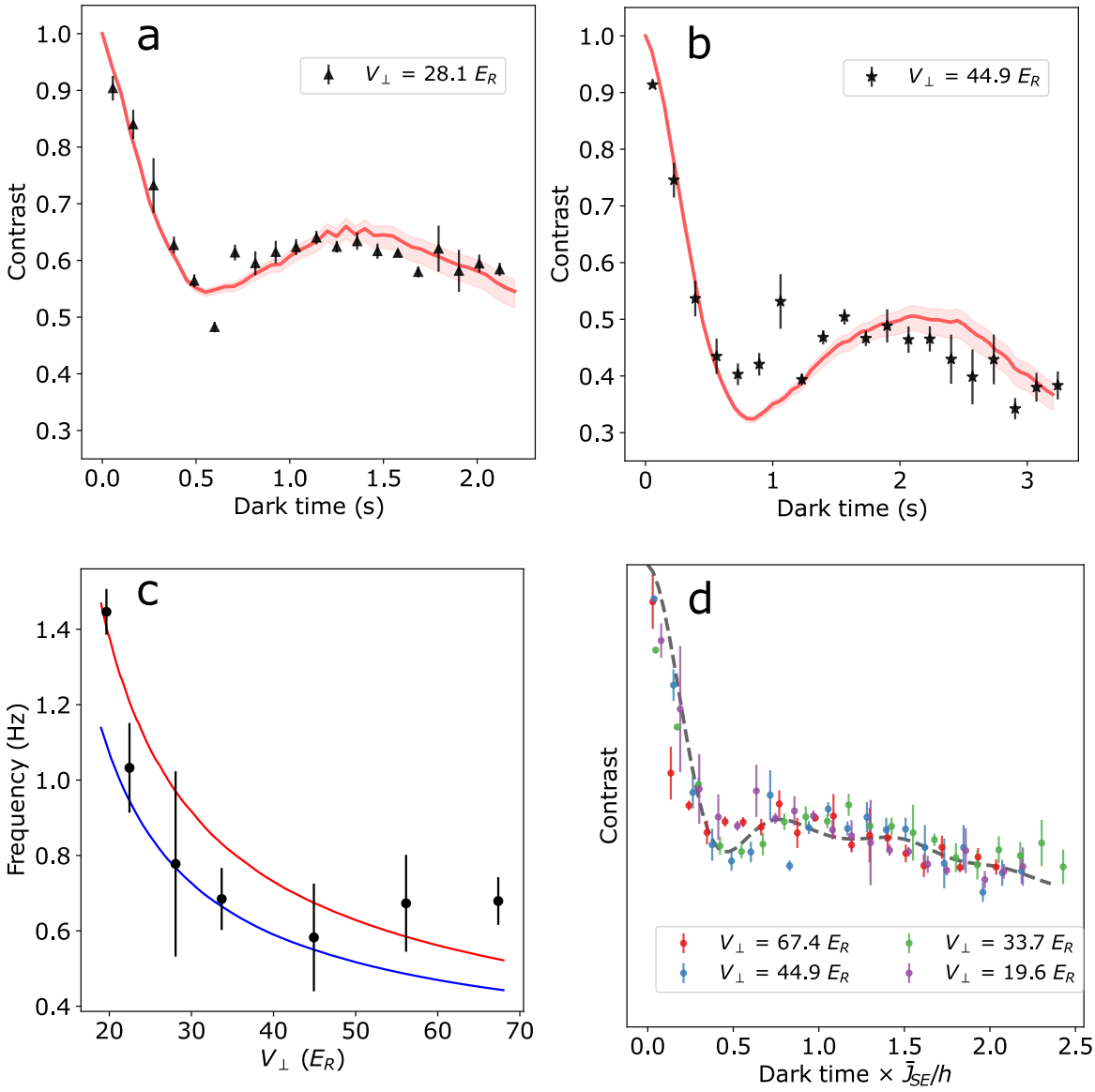

Figure 3.12: **Observing superexchange interactions**. Ramsey contrast decay is studied in a 3D lattice at fixed $V_z = 17.4\ E_R$ and thus t_z, while $V_\perp$ is varied between approximately 70 and 20 E_R primarily modifying U. Decay curves at $V_\perp = 28.1\ E_R$ **a**, and 44.9 E_R **b**, are plotted. Error bars are 1σ (standard deviation). Red lines are theory, averaging contrast decay in 1D chains initialized from a thermal distribution of the 3D cloud including error bands stemming from T_2 uncertainties (see SOM). **c**, Fitted contrast oscillation frequencies (black points) are compared to the calculated superexchange frequency (blue line) including bond-charge corrections to t_z (see SOM), which averages the expected oscillations with local ΔE_j and U along the imaging direction. Contrast oscillation frequencies are also fit to the function $\kappa \times \bar{J}_{SE}$ (red line), with $\bar{J}_{SE}$ including no corrections to t_z, finding $\kappa = 1.42(7)$. Error bars are 1σ (standard deviation) uncertainty of the fitted frequency f. **d**, Contrast curves approximately collapse when dark times are rescaled by the fitted oscillation frequency (red line) in Fig. 3.12(c). A simple simulation sampling spin chains with different lengths and coupling strengths (gray dashed line) is overlaid.

$V_\perp > V_z$, finding a clear oscillatory feature on timescales of the superexchange rate $\bar{J}_{\mathrm{SE}}$. For these measurements V_z is fixed to $17.4E_R$ at which $t_z \approx 14.2$ Hz. $\bar{J}_{\mathrm{SE}}$ is tuned by varying $V_\perp$ between 19.7 and $67.4E_R$, thus varying U from 1.2 to 2.3 kHz. In the $V_\perp \gg V_z$ regime, the system is comprised of isolated vertical tubes along z as shown in Fig. 3.10(c). We assume all atoms within each tube are pinned in place even for non-unit filling, since the local potential difference is much stronger than tunneling ($\Delta E_j \gg t_z$). We further assume that every uninterrupted chain of neighbouring atoms within a given tube undergoes evolution under the superexchange Hamiltonian $\hat{H}_{\mathrm{SE}}$. Their evolution is independent of other chains, and the contrast is an average over all chains. The curves in Figs. 3.12(a), 3.12(b) show numerical predictions averaging over the full 3D system using calibrated experimental parameters except entropy-per-particle in the lattice (see SOM), which find good agreement when the overall slow decay in contrast reported in Fig. 3.10(c) is factored in.

To extract the measured superexchange rates, we vary $V_\perp$ and fit the experimentally measured contrast decay to the function $C_{\mathrm{SE}}(T) = Ae^{-T/T_2} + B\cos(2\pi fT)e^{-T/T_{\mathrm{osc}}} + D$. The measured oscillation frequencies f are compared to a theoretically modelled superexchange frequency (blue line) accounting for the lattice inhomogeneity and bond-charge corrections (see SOM) of t_z in Fig. 3.12(c). To mitigate uncertainties of higher order corrections to Hubbard parameters like t_z, the contrast oscillation frequencies are also fit to the function $\kappa \times \bar{J}_{\mathrm{SE}}$ (red line), where we determine $\kappa = 1.42(7)$. The simplified model for calculating $\bar{J}_{\mathrm{SE}}$ assigns individual U and ΔE_j to localized atom pairs and averages the resulting local contrast oscillations in vertical direction to extract an oscillation frequency (see SOM for more details). The agreement is good for all but the deepest $V_\perp$, for which the experimentally measured rate appears to be higher-frequency. Numerical calculations suggest this could arise from additional interaction inhomogeneity that favors higher frequency contributions. In Fig. 3.12(d), the dark times of the contrast decay data are rescaled by the fitted superexchange rate $\kappa \times \bar{J}_{\mathrm{SE}}$ from Fig. 3.12(c). The rescaled data collapse to a single curve, reflecting the underlying superexchange dynamics in all measurements. This is also in agreement with a theoretical model with randomly sampled spin chains of different lengths and coupling strengths to capture the effects of finite temperature and trap inhomogeneity without

invoking explicit parameters (see discussion of Fig. 3.13(c-e) and SOM for more detail). We note that the lattice curvature is changing as a function of $V_\perp$, thus increasing $J_{\mathrm{SE}}(j)$ inhomogeneity which prevents rescaling surpassing the measurement errors.

In order to study the properties of the interactions further, we vary the lattice filling and the energy offsets ΔE_j of the local lattice tilt in Fig. 3.13. First, the fraction of atoms participating in superexchange is reduced by imprinting holes in the lattice. Beginning with maximum filling, before Ramsey spectroscopy a variable clock laser pulse duration is used to shelve atoms in $|e\rangle$ with spatially uniform probability, and subsequently the remaining $|g\rangle$ atoms are removed with resonant light at 461 nm (see Fig. 3.13(a)). The ensuing contrast decay as a function of the total atom number N is plotted in Fig. 3.13(b). The oscillation amplitude, reflecting the fraction of atoms participating in superexchange, is strongly decreased as N is reduced due to the increasing number of holes. Due to the reduced filling fraction at the wings of the atom cloud, this effect is also observed when choosing the region of interest to be an annulus and increasing its radius compared to P_2 (see SOM).

As the position of the atoms in the combined potential of gravity and the lattice confinement is shifted vertically the site-to-site energy shift ΔE_j, and consequently the superexchange interaction strength, is strongly modified. We precisely move the cloud position at the μm scale (see SOM). Figure 3.13(d) displays these oscillations as a function of cloud position z. We compare the oscillation frequency with a heuristic simulation analogous to Fig. 3.12(c) of the Ramsey contrast in Fig. 3.13(e) (red line). Averaging the Ramsey signal along the z-direction during imaging strongly suppresses the effect of locally enhanced $J_{\mathrm{SE}}(j)$ where $U = \Delta E_j$. The asymmetry of the background trap gradient around $z = 0$ leads to a reduction of the oscillation frequency at large z where $\Delta E_j > U$. The frequency of the simulation shows qualitative agreement with the measured oscillation.

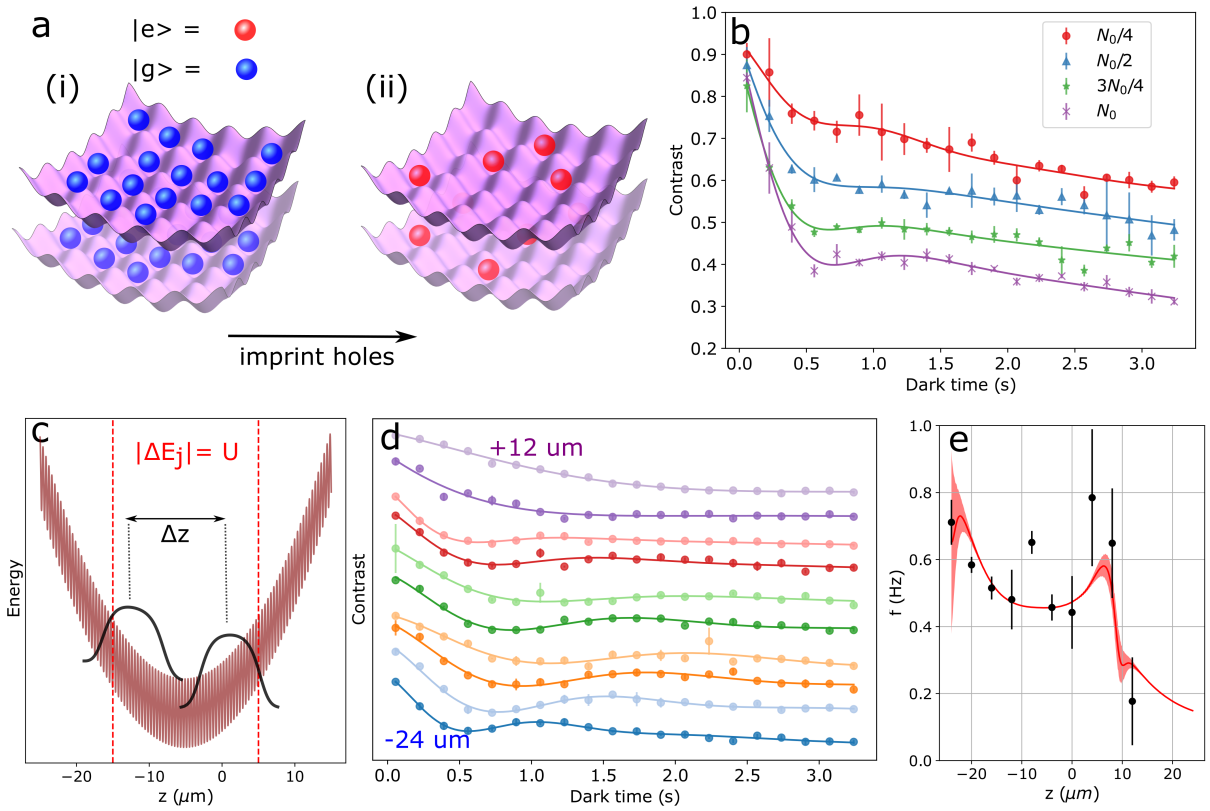

Figure 3.13: **Controlling superexchange interactions**. All measurements presented here are performed at trap depths $V_z = 17.4\ E_R$ and $V_\perp = 44.9\ E_R$. The fraction of atoms participating in superexchange is modified by reducing the filling fraction via uniformly adding holes as depicted in panel **a**. In (i), the initial state is a near unity filled sample of ground state atoms. Next, atoms are placed in a superposition state with tunable pulse area. Light resonant with $|^1S_0\rangle$ is turned on to imprint holes, with the remaining atoms in $|^3P_0\rangle$ as shown in (ii). The contrast decay is plotted in **b** as the clock pulse area and thus total atom number N is reduced compared to the initial atom number N_0. The solid lines shown in panels **b**, **d** are fits using the model $C_{\mathrm{SE}}(T)$ provided in the main text. Error bars are 1σ (standard deviation). In panel **c**, the superexchange coupling is modified by changing the position of the atoms in the lattice potential varying the site-to-site energy shift ΔE_j. At the positions indicated by vertical red lines tunneling becomes resonant and strongly enhances the local $J_{\mathrm{SE}}(j)$. However, averaged over the whole cloud this only slightly modifies the oscillation frequencies. Oscillations in contrast at different vertical positions z are shown in panel **d**; curves are shifted vertically according to z position. These measured oscillation frequencies are compared with a heuristic superexchange simulation (red line) of the Ramsey contrast in panel **e** (see SOM).

3.3.5 Conclusion and outlook

In conclusion, we have used our degenerate Fermi gas 3D optical lattice clock with anisotropic and tunable tunneling rates in the presence of spin-orbit coupling to directly probe different regimes of interaction effects described by the Fermi-Hubbard Hamiltonian. Superexchange interactions are identified as an important systematic effect that degrade the precision of optical lattice clocks operating with high filling at timescales $h/\bar{J}_{\mathrm{SE}}$. We demonstrate that we can both microscopically model and control these interactions in the 3D optical lattice.

For clock metrology, we can either reduce the magnitude or control the form of the superexchange interactions to enhance clock performance. For example, we can increase the lattice constant a sufficiently large to reduce the tunneling rate to a negligible value [142]. Alternatively, a variable lattice spacing can be used to make a commensurate with λ_{clk} to achieve $\varphi \bmod 2\pi = 0$. Without SOC ($\varphi \bmod 2\pi = 0$) the isotropic Heisenberg Hamiltonian $\sum_j J_{\mathrm{SE}}(j)\hat{\mathbf{s}}_j \cdot \hat{\mathbf{s}}_{j+1}$ is recovered, and any coherent spin state becomes an eigenstate accumulating only a trivial global phase. On the other hand, collective superexchange interactions can be used to produce spin entanglement for quantum enhanced sensing [145]. At intermediate in-plane tunnelling rates, these isotropic, Heisenberg interactions couple the single particles within each plane to collective spins [137]. Thus, by reducing single-particle inhomogeneities via potential shaping or layer selection [146], the collective spins across all planes can be squeezed by SOC-induced XXZ interactions investigated here.

3.3.6 Supplemental Materials: Two-well Fermi-Hubbard Hamiltonian

To understand the superexchange dynamics, we start from the two-well Fermi-Hubbard Hamiltonian with a energy tilt ΔE between sites,

$$\hat{H}_{\mathrm{FH}} = -t_z \sum_{\sigma\in\{g,e\}} (\hat{\tilde{c}}^{\dagger}_{0,\sigma}\hat{\tilde{c}}_{1,\sigma} + H.c.) + U \sum_{j\in\{0,1\}} \hat{n}_{j,e}\hat{n}_{j,g} + \frac{\Delta E}{2}(\hat{n}_1 - \hat{n}_0), \tag{3.55}$$

Here, $\hat{\tilde{c}}^{\dagger}_{j,\sigma}(\hat{\tilde{c}}_{j,\sigma})$ creates (annihilates) a fermion on site j with spin σ in the lab frame. We define $\hat{n}_{j,\sigma} = \hat{\tilde{c}}^{\dagger}_{j,\sigma}\hat{\tilde{c}}_{j,\sigma}$, and $\hat{n}_j = \hat{n}_{j,e} + \hat{n}_{j,g}$. In the Mott-insulating limit $U \gg t_z$, the double-occupied states are separated by a large energy gap $\sim U$, which allows for restriction of dynamics in the

single-occupied states via second-order perturbation theory. We get the effective Hamiltonian for superexchange interaction,

$$\hat{H}_{\text{eff}} = J_{\text{SE}}\left(\hat{\tilde{\mathbf{s}}}_0 \cdot \hat{\tilde{\mathbf{s}}}_1 - \frac{1}{4}\right), \tag{3.56}$$

where

$$J_{\text{SE}} = \frac{4t_z^2 U}{U^2 - \Delta E^2}. \tag{3.57}$$

Here the spin operators are defined as $\hat{\tilde{\mathbf{s}}}_j = \sum_{\alpha\beta=\{e,g\}} \hat{\tilde{c}}^{\dagger}_{j,\alpha} \boldsymbol{\sigma}_{\alpha\beta} \hat{\tilde{c}}_{j,\beta}/2$, where $\boldsymbol{\sigma}_{\alpha\beta}$ are Pauli matrices. Expanding $\hat{\tilde{\mathbf{s}}}_0 \cdot \hat{\tilde{\mathbf{s}}}_1 = (\hat{\tilde{\mathbf{s}}}_0 + \hat{\tilde{\mathbf{s}}}_1)^2/2 - 3/4$, we obtain triplet states ($|d\rangle \equiv |g,g\rangle$, $|u\rangle \equiv |e,e\rangle$,$|t\rangle \equiv (|g,e\rangle + |e,g\rangle)/\sqrt{2}$) with zero energy, and the singlet state ($|s\rangle \equiv (|g,e\rangle - |e,g\rangle)/\sqrt{2}$) with energy $-J_{\text{SE}}$ with respect to the triplet states.

The oscillation of the Ramsey contrast can be understood based on the time evolution of the initial state generated by the first Ramsey pulse. This state has a spiral phase $e^{ij\varphi}$ imprinted by the clock laser with Rabi frequency Ω, $\hat{H}_{\text{clock}}(\theta)/\hbar = \frac{1}{2}\sum_j (|\Omega| e^{i\theta} \times \hat{\tilde{s}}_j^{+} e^{ij\varphi} + H.c.)$, where θ controls the rotation axis. We consider the initial state generated by the first Ramsey pulse with $|\Omega| T_1 = \pi/2$,

$$\begin{aligned} |\psi_{\text{init}}\rangle &= e^{-i\hat{H}_{\text{clock}}(\theta=\pi/2)T_1/\hbar} |g\rangle_0 \otimes |g\rangle_1 \\ &= \frac{1}{\sqrt{2}}(|g\rangle_0 + |e\rangle_0) \otimes \frac{1}{\sqrt{2}}(e^{-i\varphi/2}|g\rangle_1 + e^{i\varphi/2}|e\rangle_1) \\ &= \frac{1}{2}\left[e^{-i\varphi/2}|d\rangle + e^{i\varphi/2}|u\rangle + \sqrt{2}\cos(\varphi/2)|t\rangle + i\sqrt{2}\sin(\varphi/2)|s\rangle\right]. \end{aligned} \tag{3.58}$$

For simplicity, we ignore all the echo pulses during the dark time. So the dynamics in the dark time can be described by the singlet state $|s\rangle$ acquiring a phase $e^{iJ_{\text{SE}}T/\hbar}$. Then we apply the second Ramsey pulse with $|\Omega| T_2 = \pi/2$ with the same θ, and get the final state

$$\begin{aligned} |\psi_f\rangle = -ie^{i\varphi/2}\sin(J_{\text{SE}}T/2\hbar)\sin^2(\varphi/2)|d\rangle + \frac{1}{4}e^{-i\varphi/2}\Big(3e^{-iJ_{\text{SE}}T/2\hbar} + (1-\cos(\varphi))e^{iJ_{\text{SE}}T/2\hbar} \\ + \cos(\varphi)\Big)|u\rangle + \frac{i}{\sqrt{2}}\sin(J_{\text{SE}}T/2\hbar)\sin(\varphi/2)\sin(\varphi)|t\rangle - \frac{1}{\sqrt{2}}\sin(J_{\text{SE}}T/2\hbar)\cos(\varphi/2)\sin(\varphi)|s\rangle. \end{aligned} \tag{3.59}$$

In this case the Ramsey contrast is given by $C = 2|\langle\psi_f|\hat{\tilde{s}}^z|\psi_f\rangle|/N$, where $\hat{\tilde{s}}^z = \hat{\tilde{s}}_1^z + \hat{\tilde{s}}_2^z$. The Ramsey contrast will thus undergo oscillatory dynamics,

$$C(T) = \left|\cos^2\left(\frac{\varphi}{2}\right) + \sin^2\left(\frac{\varphi}{2}\right)\cos(J_{\text{SE}}T/\hbar)\right|. \tag{3.60}$$

In our experiment operating under the conditions $V_z \ll V_\perp$, we ignore tunneling in the transverse directions and consider superexchange dynamics only along the z direction. To capture the superexchange dynamics, we need to include a spatially varying superexchange rate $J_{\mathrm{SE}}(j)$, due to the tilt generated by gravity and the confinement generated by the Gaussian profile of the lattice beam. In addition to the site-to-site energy shift ΔE_j, the reduction of the transverse lattice power at $|j - j_{\mathrm{s}}| \gtrsim w/a$ (with lattice constant a) also decreases the on-site interactions U_j and therefore induces a weak j-dependence. Instead of applying Eq. (3.57), to avoid artifacts from the divergence present in this approximation, we obtain $J_{\mathrm{SE}}(j)$ from an independent diagonalization of Eq. (3.55) at each lattice site j. For simplicity, we focus on the region with uniform density in the x-y plane and therefore consider the variation of J_{SE} only in vertical direction.

Here we assume the oscillatory dynamics are mainly generated by two-atom chains. So we can heuristically generalize Eq. (3.60) to average over all possible local one-atom and two-atom chains in our system. We define $n(j)$ as the local filling fraction of lattice sites labelled by j, such that the total atom number in each vertical tube is $N_{\mathrm{tube}} = \sum_j n(j)$. In the following, two adjacent lattice sites along z direction are considered but all quantities are given with respect to individual lattice sites. The probability to have only one atom in these two lattice sites is $p^{(1)}(j) = n(j)[1 - n(j)]$, and the probability to have two atoms is $p^{(2)}(j) = [n(j)]^2$. Here, the magnetization of a one-atom chain is $\langle \tilde{s}^{z,(1)}(j)\rangle = \langle \psi_f | \hat{\tilde{s}}^z | \psi_f \rangle = 1/2$, and in a local two-atom chain $\langle \tilde{s}^{z,(2)}(j)\rangle = \{\cos^2(\varphi/2) + \sin^2(\varphi/2)\cos[J_{\mathrm{SE}}(j)T/\hbar]\}/2$ (see Eq. (3.60)) and thus the average magnetization per size is $\langle \tilde{s}^z(j)\rangle = \sum_k p^{(k)} \langle \tilde{s}^{z,(k)}\rangle$. We then average over all spatial positions to obtain the Ramsey contrast

$$\begin{aligned} C(T) &= \frac{1}{N_{\mathrm{tube}}} \left| \sum_j 2\langle \tilde{s}^z(j)\rangle \right| \\ &= \left| 1 - \sum_j \frac{[n(j)]^2}{N_{\mathrm{tube}}} \sin^2\left(\frac{\varphi}{2}\right) + \sum_j \frac{[n(j)]^2}{N_{\mathrm{tube}}} \sin^2\left(\frac{\varphi}{2}\right) \cos(J_{\mathrm{SE}}(j)T/\hbar) \right|. \end{aligned} \tag{3.61}$$

By fitting a function of the from $Ae^{-T/\tau_{\mathrm{osc}}} \cos\left(\bar{J}_{\mathrm{SE}} T/\hbar\right)$ to the oscillatory term in $C(T)$ we obtain the oscillation frequency $\bar{J}_{\mathrm{SE}}/h$, which is the basis for the solid red lines in Figs. 3.12(c) and 3.13(e). The bond-charge corrections Δt_z taken into account for the blue line in Fig. 3.12(c) are scaled with

U_j to account for the inhomogeneity across the atom cloud. The error bands are derived from the uncertainty of this fit parameter. We choose a temperature of ~ 370nK to roughly match the peak-to-peak oscillation amplitude of $2\sin^2(\varphi/2)\sum_j[n(j)]^2/N_{\text{tube}} \sim 0.7$ observed in most measurements (cf. Figs. 3.13(d) or 3.12(b)).

We note that this approach of estimating the oscillation frequency does not provide a comprehensive and quantitative model for the coherence as it neglects effects from longer chains and the dynamical decoupling pulse sequence. These are taken into account in the following discussion.

3.3.7 Supplemental Materials: Superexchange contrast dynamics

Now we generalize Eq. (3.56) to the case of many-atoms. Here we work in a "spiral" frame where the initial state is uniform (all atoms in the same superposition state) and the site-dependent laser phase φ is absorbed into the spin operators across the lattice, $\hat{s}_j^{\pm} = \hat{\tilde{s}}_j^{\pm} e^{\pm ij\varphi}$, $\hat{s}_j^Z = \hat{\tilde{s}}_j^Z$, where j is the lattice index along z direction. This transformation lead to the following 1D spin-spin interaction Hamiltonian [132],

$$\begin{aligned} \hat{H}_{\text{SE}} &= \sum_{j=1}^{L-1} J_{\text{SE}}(j)\left[\cos(\varphi)\left(\hat{s}_j^X\hat{s}_{j+1}^X + \hat{s}_j^Y\hat{s}_{j+1}^Y\right) + \hat{s}_j^Z\hat{s}_{j+1}^Z + \sin(\varphi)\left(\hat{s}_j^X\hat{s}_{j+1}^Y - \hat{s}_j^Y\hat{s}_{j+1}^X\right)\right], \\ J_{\text{SE}}(j) &= \frac{4t_z^2U}{U^2 - \Delta E_j^2}, \end{aligned} \tag{3.62}$$

where L is the number of sites, and $J_{\text{SE}}(j)$ the superexchange interaction strength. The latter depends on both the on-site Hubbard interactions and the local potential difference $\Delta E_j = \frac{1}{2}m\omega_{lat}^2a^2[(j+1-j_0)^2 - (j-j_0)^2]$, where j_0 is the bottom of the lattice confining potential.

The first three terms act as an XXZ Hamiltonian with spin anisotropy $\sim \sec(\varphi)$, which induces contrast decay. The last two terms are a Dzyaloshinskii-Moriya (DM) type interaction, which breaks exchange symmetry due to the chirality of the imprinted clock laser phase. The latter has been studied in the context of exotic chiral properties such as skyrmions. At the collective mean-field level such an interaction has no effect. In our case since the interaction strengths $J_{\text{SE}}(j)$ are inhomogeneous, the DM interaction will also generate contrast decay, as each atom will feel an unequal force from its left and right neighbours due to the lack of exchange symmetry.

The Ramsey decay dynamics are modeled by initializing a product state of all spins in a uniform superposition state following the first Ramsey pulse as written above,

$$|\psi_{\text{init}}\rangle = e^{-i\frac{\pi}{2}\sum_j \hat{s}_j^Y} \bigotimes_j |\downarrow\rangle_j \,. \tag{3.63}$$

The chain then undergoes time-evolution under the Hamiltonian, interspersed with echo pulses during the XY8 sequence. For a sequence including a single echo pulse we write,

$$|\psi_f(t)\rangle = e^{-i\hat{H}_{\text{SE}}t/2} e^{-i\pi\sum_j \hat{s}_j^X} e^{-i\hat{H}_{\text{SE}}t/2} |\psi_{\text{init}}\rangle \,. \tag{3.64}$$

An XY8 sequence instead applies eight pulses about different axes as depicted in the main text Fig. 3.10(a). After time-evolving the state, a final Ramsey pulse with an arbitrary phase θ is performed,

$$|\psi_{f,\theta}(t)\rangle = e^{-i\frac{\pi}{2}\sum_j \left[\cos(\theta)\hat{s}_j^Y + \sin(\theta)\hat{s}_j^X\right]} |\psi_f(t)\rangle \,. \tag{3.65}$$

The contrast of the uninterrupted chain is obtained by measuring the excited state fraction,

$$N_\theta(t) = \langle\psi_{f,\theta}(t)| \left[\sum_j \left(\hat{s}_j^Z + \frac{1}{2}\right)\right] |\psi_{f,\theta}(t)\rangle \,. \tag{3.66}$$

For a single independent chain, contrast is obtained via,

$$C(t) = \frac{1}{L}\left[\max_\theta N_\theta(t) - \min_\theta N_\theta(t)\right]. \tag{3.67}$$

If there are multiple independent chains, their contributions to the excited state fraction $N_\theta(t)$ must be summed together for each angle θ before performing the maximization and minimization above.

A single site $L = 1$ has unity contrast $C = 1$ at all times. Chains with few sites will exhibit persistent oscillations of contrast, whereas chains with many sites will undergo decay, with revivals only occuring on timescales $\sim 1/L$. Inhomogeneity in the superexchange couplings $J_{\text{SE}}(j)$ will also wash out revivals or oscillatory dynamics at longer times. The contrast dynamics from many summed, disordered chains thus generally exhibits only one or two oscillations before saturating to a constant value determined by how many of the chains had isolated single sites.

We compare this theory to the experiment by using specific lattice parameters, interaction coupling coefficients, and averaging over the 3D distribution, as detailed in the Supplementary Material, which yields a theoretically predicted contrast $C(T)$. Since the experiment also finds a slower decay on timescale $\sim 1/T_2$ measured in Fig. 3.10(c), we normalize the resulting contrast obtained from numerical simulation of the superexchange Hamiltonian by a further factor $C(T) \to C(T)e^{-T/T_2}$. The resulting theoretically predicted contrast is shown as solid lines in Figs. 3.12(a), 3.12(b) of the main text, which is in good agreement with the measurements. The shaded region on the theory curves corresponds to an uncertainty of ± 2 s for the T_2 in this adjustment factor (in line with the T_2 measurement uncertainty).

In addition, we provide a more simple theoretical prediction without invoking explicit experimental conditions. We randomly sample a large number of chains with lengths L drawn from a Poisson distribution $P(\lambda)$ with low Poisson parameter $\lambda < 1$, appropriate for an initial thermal distribution. The coupling strengths V_j in each chain are drawn from a Gaussian distribution of mean $J_{\mathrm{SE}}(j)$ and standard deviation $\epsilon J_{\mathrm{SE}}(j)$, with ϵ meant to capture inhomogeneity in the superexchange interactions. As ϵ increases, the contrast oscillations reduce in amplitude to the profile observed in the experiment. The curve in Fig. 3.12(d) of the main text shows the prediction for Poisson parameter $\lambda = 0.25$ and $\epsilon = 0.4$. This curve is also adjusted by a factor of $e^{-\frac{1}{5}T\overline{J}_{\mathrm{SE}}/h}$ to account for slower atomic decay, using an effective lifetime of five superexchange cycles, which is in line with the experimental lifetimes and yields good agreement with all measured data.

Due to wavefunction overlap with adjacent sites, additional interaction and tunneling terms are present in the Fermi-Hubbard Hamiltonian. We identify the main contributions to be bond-charge type effects [147] and an admixture of higher bands due to the gravitational tilt.

Bond-charge interactions are those with interactions between adjacent sites and additionally an exchange of the particles. This can be cast into the form of a tunneling term, thus directly correcting the tunneling energy $t_z' = t_z + \Delta t_z$ for single-occupied sites with

$$\Delta t_z = -\frac{4\pi\hbar^2 a_{eg}^-}{m} \int d^3x \, \psi_0^3 \psi_1, \tag{3.68}$$

where $\psi_j = \psi(x, y, z - ja)$ describes the ground band Wannier function ψ at lattice site j. For lattice depths of $V_z = 17.4\ E_R$ and $V_\perp = 44.9\ E_R$ we obtain $\Delta t \approx h \times 1.2$Hz, which corresponds to an increase of about 8% with respect to the bare value of $t_z \approx h \times 14.2$Hz.

A direct calculation of the Wannier-Stark wavefunction suggests an additional correction to the tunneling energy on the order of $\sim 10\%$. However, the exact calculation of the full contribution remains challenging because we estimate that all higher bands would be needed to be taken into account for a faithful quantification [109]. Because these effects are barely above our experimental uncertainty we are mostly neglecting these corrections in this work.

3.3.8 Supplemental Materials: 1D large-spin Hamiltonian

To model the contrast decay in Fig. 3.11 we describe the $V_z \gg V_\perp$ regime in 3D optical lattice clocks using the assumption that the spins in each pancake are locking into a large spin based on Ref. [25, 100], which leads to the following 1D large-spin Hamiltonian:

$$\begin{aligned} \hat{H}_{\mathrm{LS}} &= \hat{H}_{\mathrm{on-site}} + \hat{H}_{\mathrm{off-site}}, \\ \hat{H}_{\mathrm{on-site}}/\hbar &= \sum_n \Big[J_{0,n} \hat{\mathbf{S}}_n \cdot \hat{\mathbf{S}}_n + \chi_{0,n} \hat{S}_n^Z \hat{S}_n^Z + C_{0,n} \hat{N}_n \hat{S}_n^Z \Big], \\ \hat{H}_{\mathrm{off-site}}/\hbar &= \sum_n \Big[J_{1,n} \hat{\mathbf{S}}_n \cdot \hat{\mathbf{S}}_{n+1} + \chi_{1,n} \hat{S}_n^Z \hat{S}_{n+1}^Z + D_{1,n} (\hat{S}_n^X \hat{S}_{n+1}^Y - \hat{S}_n^Y \hat{S}_{n+1}^X) \Big]. \end{aligned} \tag{3.69}$$

The collective spin operators are defined as $\hat{\tilde{\mathbf{S}}}_n = \sum_{n_x n_y} \sum_{\alpha\beta=\{e,g\}} \hat{\tilde{c}}^\dagger_{n_x n_y n,\alpha} \boldsymbol{\sigma}_{\alpha\beta} \hat{\tilde{c}}_{n_x n_y n,\beta}/2$ in the lab frame, where $\boldsymbol{\sigma}_{\alpha\beta}$ are Pauli matrices, $\hat{\tilde{c}}_{n_x n_y n,\alpha}$ are fermionic annihilation operators for radial mode labelled by (n_x, n_y) assuming separable potential in pancakes, Wannier-Stark level n along gravity and internal state α. $\hat{N}_n$ is the atom number operator for Wannier-Stark level n. We transform into the "spiral" frame by unitary transformation $\hat{S}_n^\pm = e^{\pm i n \varphi} \hat{\tilde{S}}_n^\pm$ and $\hat{S}_n^z = \hat{\tilde{S}}_n^z$. The interaction parameters are

$$\begin{aligned} J_{0,n} &= \eta_0 (V_{eg}^{n,n} - U_{eg}^{n,n})/2, \quad \chi_{0,n} = \eta_0 (V_{ee}^{n,n} + V_{gg}^{n,n} - 2V_{eg}^{n,n})/2, \\ C_{0,n} &= \eta_0 (V_{ee}^{n,n} - V_{gg}^{n,n})/2, \quad J_{1,n} = -\eta_1 U_{eg}^{n,n+1} \cos\varphi, \\ \chi_{1,n} &= -\eta_1 U_{eg}^{n,n+1} (1 - \cos\varphi), \quad D_{1,n} = -\eta_1 U_{eg}^{n,n+1} \sin\varphi. \end{aligned} \tag{3.70}$$

where $\varphi = 2\pi a/\lambda_{clk}$ is the spin-orbit-coupled clock phase between nearest-neighbor sites of the lattice, with a the lattice spacing. η_0 and η_1 are dimensionless overlap integrals for on-site and nearest-neighbor interaction respectively,

$$\eta_{|n-m|} = \frac{\sqrt{2\pi}}{k_L}\left(\frac{V_z}{E_R}\right)^{-1/4}\int \mathrm{d}z\,[W_n(z)]^2[W_m(z)]^2, \tag{3.71}$$

where $E_R = \hbar^2 k_L^2/2m$ is the lattice recoil energy, with wave number $k_L = \pi/a$, and $W_n(z)$ is the wave function of a Wannier-Stark state centered at site n.

The s-wave ($U_{\alpha\beta}$) and p-wave ($V_{\alpha\beta}$) interaction strengths ($\alpha, \beta = \{g, e\}$) are calculated by averaging a Fermi-Dirac distribution over radial modes,

$$\begin{aligned} U_{\alpha\beta}^{n,m} &= \frac{8\pi\hbar a_{\alpha\beta}}{m}\frac{k_L}{\sqrt{2\pi}}\left(\frac{V_z}{E_R}\right)^{1/4}\sum_{n_x m_x n_y m_y} s_{n_x m_x} s_{n_y m_y}\frac{N_{n_x n_y n}}{N_{n,\mathrm{init}}}\frac{N_{m_x m_y m}}{N_{m,\mathrm{init}}}, \\ V_{\alpha\beta}^{n,m} &= \frac{6\pi\hbar b_{\alpha\beta}^3}{m}\frac{k_L}{\sqrt{2\pi}}\left(\frac{V_z}{E_R}\right)^{1/4}\sum_{n_x m_x n_y m_y} (p_{n_x m_x} s_{n_y m_y} + s_{n_x m_x} p_{n_y m_y})\frac{N_{n_x n_y n}}{N_{n,\mathrm{init}}}\frac{N_{m_x m_y m}}{N_{m,\mathrm{init}}}, \end{aligned} \tag{3.72}$$

where $a_{\alpha\beta}$ is the elastic s-wave scattering length, and $b_{\alpha\beta}^3$ is the elastic p-wave scattering volume. As the atoms are nuclear-spin polarized ($m_F = \pm 9/2 \to m_F' = \pm 9/2$ transition between $^1S_0$ and $^3P_0$ states), to fully anti-symmeterize the wavefunction the following scattering lengths are required $a_{eg} = a_{eg}^-$, $b_{eg}^3 = (b_{eg}^+)^3$ [25, 62]. Defining the wave function for a radial mode (n_x, n_y) is $\phi_{n_x}\phi_{n_y}$, we have $s_{nm} = \int \mathrm{d}x\,[\phi_n(x)]^2[\phi_m(x)]^2$, $p_{nm} = \int \mathrm{d}x\,[(\partial_x\phi_n(x))\phi_m(x) - \phi_n(x)(\partial_x\phi_m(x))]^2$. Here $N_{n_x n_y n}$ are the initial population in radial mode (n_x, n_y) and lattice site n under a Fermi-Dirac distribution, $N_{n_x n_y n} = \left[\exp\left[(\epsilon_{n_x n_y} - \mu_n)/k_B T_R\right] + 1\right]^{-1}$, where the chemical potential for each lattice site μ_n is chosen to match the initial atom number for each Wannier-Stark level $N_{n,\mathrm{init}} = \sum_{n_x n_y} N_{n_x n_y n}$, and T_R is the radial temperature. Errorbands in Fig. 3.11 include the uncertainty of s-wave and p-wave scattering parameters, $0.5E_R$ uncertainty of lattice depth, as well as 20% uncertainty in radial temperature.

Apart from unitary evolution under $\hat{H}_{\mathrm{LS}}$, inelastic on-site p-wave e-e collision can lead to two-body loss of the atom number as observed in previous studies [62, 100]. We describe the atom loss based on the following Lindblad master equation,

$$\hbar\frac{d}{dT}\hat{\rho} = -i[\hat{H}_{\mathrm{LS}}, \hat{\rho}] + \sum_n \Gamma_{0,n}\mathcal{L}_n(\hat{\rho}), \tag{3.73}$$

where $\hat{H}_{\rm LS}$ is the Hamiltonian given in Eq. (3.69). The Liouvillian for e-e loss is given by

$$\mathcal{L}_n(\hat{\rho}) = \sum_{n_x n_y m_x m_y} \left[\hat{L}_{n_x n_y m_x m_y} \hat{\rho} \hat{L}^\dagger_{n_x n_y m_x m_y} - \frac{1}{2} \{ \hat{L}^\dagger_{n_x n_y m_x m_y} \hat{L}_{n_x n_y m_x m_y}, \hat{\rho} \} \right], \tag{3.74}$$

where $\hat{L}_{n_x n_y m_x m_y} = \hat{\tilde{c}}_{n_x n_y n, e} \hat{\tilde{c}}_{m_x m_y n, e}$. We use the averaged e-e loss rate over the radial modes to maintain the large-spin description,

$$\Gamma_{0,n} = \eta_0 \tilde{V}^{n,n}_{ee}/4, \tag{3.75}$$

where we replace the elastic p-wave scattering volume b^3_{ee} in $V^{n,m}_{ee}$ by inelastic p-wave scattering volume β^3_{ee} to get $\tilde{V}^{n,m}_{ee}$. For simplicity, we assume $U^{n,m}_{\alpha\beta}$, $V^{n,m}_{\alpha\beta}$ and $\tilde{V}^{n,m}_{ee}$ approximately unchanged under atom loss. Due to the XY8 pulse sequence, one can assume the atom loss for ground and excited states is symmetric, and obtain the following equation for atom loss,

$$\frac{d}{dT} N_n = -\frac{\Gamma_{0,n}}{2} N_n^2, \tag{3.76}$$

which gives an exact solution

$$N_n(T) = \frac{N_{n,\rm init}}{1 + \Gamma_{0,n} N_{n,\rm init} T/2}. \tag{3.77}$$

We fit the total atom number measured in the experiment integrating through all lattice layers with the fitting function $A/(1+BT)$ using fitting parameters A, B to extract the atom loss rate, and then compare with the analytic solution above.

We perform numerical simulation based on truncated Wigner approximation (TWA) [148]. The key idea is to solve the mean-field equations of Eq. (3.73) with random sampling of initial conditions. For the initial state ("spiral" frame) with all the spins pointing towards $+X$ direction, we set $S^X_n(0) = N_{n,\rm init}/2$, $N_n(0) = N_{n,\rm init}$, and sample $S^Y_n(0)$ and $S^Z_n(0)$ using a Gaussian distribution $\mathcal{N}(\mu = 0, \sigma^2 = N_{n,\rm init}/2)$.

In the case of $V_\perp = 0$, we consider the radial modes as harmonic oscillator modes with trapping frequency $\omega_R = \sqrt{4V_z/m w_L^2}$, where w_L is the Gaussian beam waist of the vertical lattice. We determine the radial temperature T_R by comparing the density distribution projected to the x-y plane between theory and experiment at $17.4E_R$, which leads to $T_R = 250$nK at this lattice

depth. Since the lattice depth is ramping up adiabatically, the ratio $k_B T_R/\hbar\omega_R$ should be roughly a constant, we use $T_R(\mathrm{nK}) = 60 \times \sqrt{V_z/E_R}$ to generate atom distribution in radial modes.

In the case of $V_\perp > 0$, the radial modes are generated by the potential of a 2D lattice with lattice depth $V_\perp$ plus harmonic oscillator with trapping frequency $\omega_R = \sqrt{4(V_z + V_\perp)/mw_L^2}$, where we assume the Gaussian beam waist is nearly the same for all lattice beams, i.e. $w_L \approx w$. The compression step in the loading sequence leads to a lower temperature compared to the case of $V_\perp = 0$, and we use radial temperature $T_R(V_\perp > 0) = 0.42 \times T_R(V_\perp = 0)$ to generate atom distribution in radial modes.

The validity of the 1D spin model is based on the frozen-mode approximation [25, 100], which is to assume all the atoms are fixed in their single-particle eigenstates due to negligible effects of interaction on the single-particle energy spectrum, ensured by $N_{n,\mathrm{init}} J_{0,n} \ll \hbar\omega_R$ and $N_{n,\mathrm{init}} J_{0,n} \ll mga$. We restrict our calculation within $V_\perp \leq 6E_R$ to avoid the breakdown of this approximation.

3.3.9 Supplemental Materials: Spin wave analysis for 1D spin model

Here we perform a spin wave analysis to $\hat{H}_{\mathrm{LS}}$ (see Eq. (3.69)) to have a further understanding of Ramsey contrast decay beyond numerical simulations. We assume the same atom number N_s for each lattice site, periodic boundary conditions, and no atom loss. We drop the terms proportional to $\hat{S}_n^Z$ since it is suppressed by the XY8 pulses. Considering the initial state with all the spins pointing to $+X$ direction, we perform a Holstein–Primakoff transformation to the large-spin operators, $\hat{S}_n^X = N_s/2 - \hat{a}_n^\dagger \hat{a}_n$, $\hat{S}_n^Y \approx \sqrt{N_s}(\hat{a}_n + \hat{a}_n^\dagger)/2$, $\hat{S}_n^Z \approx \sqrt{N_s}(\hat{a}_n - \hat{a}_n^\dagger)/(2i)$. In this way, the initial state becomes the vacuum state of the bosonic operators. We keep the terms up to quadratic order of bosonic operators, and then apply a Fourier transform to obtain the bosonic operators for spin waves ($k \in (-\pi, \pi]$), $\hat{a}_n = \sum_k e^{ikn} \hat{a}_k/\sqrt{L}$, with L the number of lattice sites.

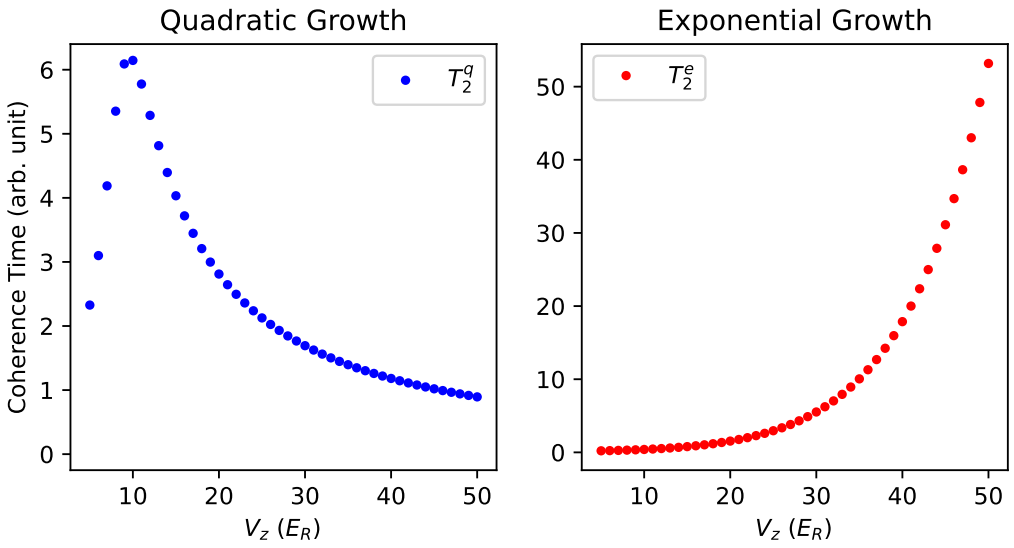

Figure 3.14: **Impact of spin wave growth on coherence times in the 1D limit**. The plots show the qualitative impact of the quadratically and exponentially growing spin wave modes on the coherence time T_2 according to Eqs. (3.82) and (3.83). At large lattice depths the T_2 time is limited by the quadratically growing modes while the coherence in a shallow lattice is dominated by the exponential instability around $k = \pi$. Here we present the coherence time in arbitrary unit since Eqs. (3.82) and (3.83) are only order-of-magnitude estimations up to unknown constant factors of order 1.

We get

$$\hat{H}_{\mathrm{LS}} \approx \frac{1}{2}\sum_k c_1(\hat{a}_k^\dagger \hat{a}_k + \hat{a}_k^\dagger \hat{a}_k) - c_2(\hat{a}_k^\dagger \hat{a}_{-k}^\dagger + \hat{a}_{-k}\hat{a}_k), \tag{3.78}$$

where

$$c_1 = c_2 - N_s J_1\Big(1 - \cos(k)\Big), \quad c_2 = \frac{N_s\chi_0}{2} + \frac{N_s\chi_1}{2}\cos(k). \tag{3.79}$$

Here, J_1, χ_0, χ_1 are the mean values of $J_{1,n}$, $\chi_{0,n}$, $\chi_{1,n}$. So the excitation numbers for spin waves is given by

$$n_{\pm k}(T) = \langle \mathrm{vac}|\hat{a}_k^\dagger(T)\hat{a}_k(T)|\mathrm{vac}\rangle = \langle \mathrm{vac}|\hat{a}_{-k}^\dagger(T)\hat{a}_{-k}(T)|\mathrm{vac}\rangle = c_2^2\left[\frac{\sin\left(T\sqrt{c_1^2 - |c_2|^2}\right)}{\sqrt{c_1^2 - |c_2|^2}}\right]^2. \tag{3.80}$$

We can express the Ramsey contrast at short time in terms of the excitation numbers for spin waves,

$$C(T) = 1 - \frac{2}{N_s L} \sum_k n_k(T). \tag{3.81}$$

Now we discuss the physics of spin-wave excitations for spin-wave modes $k = 0$ (minimizing the difference between c_1 and c_2) and $k = \pi$ (maximizing the difference between c_1 and c_2). In the case of $k = 0$, we have $n_{k=0} = N_s^2(\chi_0 + \chi_1)^2 T^2/4$, which leads to quadratic growth of the $k = 0$ mode. In the case of $k = \pi$, we have $n_{k=\pi} = N_s^2(\chi_0 - \chi_1)^2 \sinh^2(KT)/(4K^2)$, where $K = N_s\sqrt{2J_1(\chi_0 - \chi_1 - 2J_1)}$. Experimental values of the interaction strengths ensure K is a real number. It seems we always have exponential growth of the $k = \pi$ mode. However, the spin wave analysis breaks down for $n_k \sim N_s$. If K is small enough such that we reach $n_{k=\pi} \sim N_s$ at a time $KT \ll 1$, we can approximate $n_{k=\pi} \approx N_s^2(\chi_0 - \chi_1)^2 T^2/4$, which returns to quadratic growth. Therefore, exponential growth only occurs in the regime $N_s(\chi_0 - \chi_1)^2 \ll K^2$.

Based on the discussions above, we can separate the system dynamics considering quadratic or exponential growth for the $k = \pi$ mode. As discussed in [25], s-wave and p-wave interaction strengths in the 1D lattice have different dependence on the lattice depth V_z. When increasing V_z, p-wave interaction strength increases, $\chi_0 \propto V_z^{5/4}$, while s-wave interaction strength decreases, $J_1, \chi_1 \propto e^{-4\sqrt{V_z/E_R}}$. So we can access these two regimes at different V_z.

In the regime of large V_z, the system dynamics can be described by quadratic growth for all the spin wave modes. So we obtain the Ramsey contrast by summing over all the spin wave modes, $C(T) = 1 - N_s(\chi_0^2 + \chi_1^2/2)T^2/2$, which agrees with the short-time expansion under Ising-type interactions by setting $J_1 = 0$. We can estimate the T_2 coherence time for quadratic growth,

$$T_2^q \sim \frac{1}{\sqrt{N_s}} \frac{1}{\sqrt{\chi_0^2 + \chi_1^2/2}}. \tag{3.82}$$

Since this regime is mainly dominated by p-wave interactions, the coherence time decreases as we increase V_z (see Fig. S5).

In the regime of small V_z, the system dynamics is dominated by exponential growth near the $k = \pi$ mode. To obtain the Ramsey contrast we only consider the spin wave modes near $k = \pi$,

which leads to $1 - C(T) \sim N_s(\chi_0 - \chi_1)^2 e^{2KT}/K^2$. We can estimate the T_2 coherence time for exponential growth,

$$T_2^e \sim \frac{1}{K} = \frac{1}{N_s} \frac{1}{\sqrt{2J_1(\chi_0 - \chi_1 - 2J_1)}}. \tag{3.83}$$

Since this regime requires the existence of s-wave interaction, the coherence time increases as we increase V_z (see Fig. 3.14).

The crossover between these two regimes occurs when T_2^q is comparable with T_2^e. Due to the different dependence of the atom number per site N_s in these two regimes, the crossover point depends on N_s, i.e. $N_s J_1/\chi_0 \sim 1$. Note that at the crossover point the p-wave interaction strength is already much larger than the s-wave interaction strength. This explains why the crossover point occurs at a larger lattice depth V_z compared to the cancellation of density shift in [25].

3.4 Exploring the interplay between mass-energy equivalence, interactions and entanglement in an optical lattice clock

This section is adapted from: **Anjun Chu**, Victor J. Martínez-Lahuerta, Maya Miklos, Kyungtae Kim, Peter Zoller, Klemens Hammerer, Jun Ye, and Ana Maria Rey, *Exploring the interplay between mass-energy equivalence, interactions and entanglement in an optical lattice clock*, arXiv:2406.03804 (2024)

3.4.1 Introduction

Understanding the interplay between quantum mechanics (QM) and general relativity (GR) is a fundamental quest for modern science. Nevertheless up to date, measurements capable to genuinely witness this simultaneous interplay have not been realized in tabletop experiments. A push forward towards this milestone is becoming feasible thanks to recent improvements in sensitivity, precision, and accuracy in atomic clocks and interferometers, including matter-wave tests of GR [95, 149–154], the resolution of the gravitational redshift using spatially separated clocks [155, 156] and more recently within a millimeter-scale sample [23, 157]. These developments [9, 95] open up unique opportunities to search for new physics that could help reconcile the

seemingly contradictory predictions of QM and GR.

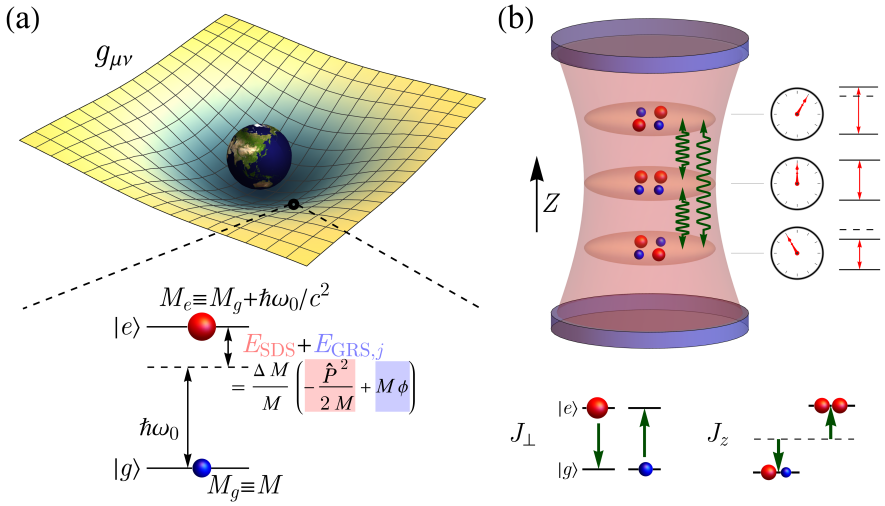

Figure 3.15: (a) Schematic of an optical lattice clock (OLC) embedded in the curved spacetime (metric $g_{\mu\nu}$) formed by the earth's gravity. Mass-energy equivalence is the leading order GR correction that translates internal energy difference $\hbar\omega_0$ between $|e\rangle$ and $|g\rangle$ states into a difference in the rest mass of an atom $\hbar\omega_0/c^2$. Such type of correction generates second-order Doppler shift $E_{\rm SDS}$ and gravitational redshift $E_{{\rm GRS},j}$ to the clock transition (see Eq. (3.86) and Eq. (3.87)). (b) Schematic of the interplay between gravitational redshift and collective cavity-mediated interactions (see Eq. (3.88)), with $J_\perp$ and J_z collective exchange and Ising couplings.

Experimental developments have in parallel driven a great deal of theoretical effort towards the understanding of quantum dynamics with GR corrections. These progresses encompass analyses of relativistic corrections to Hamiltonians considered specifically in the context of neutral-atom and trapped-ion systems [158–171], tests of mass-energy equivalence with atoms in internal superposition states including predictions of energy-dependent phase shifts, loss of coherence and spin-motion coupling induced by gravitational time dilation [172–177], among others [178–184]. However, understanding the direct consequence of GR effects in more complex scenarios such as many-body systems, where particles can interact over the entire array, remains an outstanding problem.

In this work, we provide a first step in this direction by proposing near-term protocols to explore the manifestations of the leading order single-atom GR corrections in quantum many-body dynamics, taking advantage of the state-of-the-art Wannier-Stark OLCs with an array of fully controllable interacting particles under gravity [23, 25]. We perform detailed analysis of the effects of mass-energy equivalence in a clock transition, i.e. net change in relativistic rest mass due to internal energy, including the gravitational redshift and the second-order Doppler shift. We devise a dressing protocol using an additional nuclear spin state that can be used to tune and uniquely distinguish mass-energy equivalence in an OLC. Taking advantage of the dressing protocol, we further analyze the interplay between photon-mediated interactions and the gravitational redshift acting on individual atoms. While gravitational redshift is akin to a mere level shift due to a magnetic field gradient, the observation in future OLCs will provide a direct test of GR effects acting on a many-body system. Depending on the relative strength of the redshift to a many-body energy gap induced by interactions, the system can feature local or global synchronization, as well as entanglement generation for both cases. For the latter case, we show that the synchronization time depends on the entanglement of the initial state and can be used as a proxy for the state's metrological utility.

3.4.2 Mass-energy equivalence in optical lattice clocks

We consider a single atom in earth's gravity described by a curved spacetime metric $g_{\mu\nu}$ (see Fig. 3.15(a)). We perform post-Newtonian expansion of $g_{\mu\nu}$ in power series of ϕ/c^2 (see Ref. [185] and SOM), with $\phi \approx gZ$ the Newtonian gravitational potential near the earth's surface and g the local gravitational acceleration. Following the treatment in Ref. [158, 161, 163, 168], one can obtain a single-atom Hamiltonian $\hat{H}_A$ accounting for the leading relativistic corrections:

$$\hat{H}_A = \hat{H}_{\text{point}}\left(M + \frac{\hat{H}_I}{c^2}\right) + O(c^{-4}). \tag{3.84}$$

Here, $\hat{H}_{\text{point}}(M) = Mc^2 + \hat{H}_0(M) + \hat{H}_{\text{other}}$ is the Hamiltonian of a point particle with mass M, $\hat{H}_0(M) = \hat{\mathbf{P}}^2/(2M) + M\phi$ contains the non-relativistic terms, and $\hat{H}_{\text{other}}$ contains other GR correc-

tions arising from motion and metric geometry corrections (see SOM). The key idea of Eq. (3.84) can be understood as the mass-energy equivalence, summarized by the replacement $M \to M + \hat{H}_I/c^2$ in $\hat{H}_{\text{point}}$. OLCs feature an ultranarrow optical transition (clock transition) between two long-lived electronic states (excited state $|e\rangle$, ground state $|g\rangle$), which is described by the internal Hamiltonian $\hat{H}_I = \hbar\omega_0|e\rangle\langle e|$, with ω_0 the clock transition frequency measured at the lab position $Z = 0$ (see Fig. 3.15(a)). Since in an OLC $\hat{H}_I$ contains the largest frequency scale compared to other degrees of freedom, the mass-energy equivalence is the leading order GR correction. It translates into a difference in the rest mass of an atom in states $|e\rangle$ and $|g\rangle$: $M_g = M$, $\Delta M = M_e - M_g = \hbar\omega_0/c^2$. Note that the mass defect ΔM is not simply a fixed number, and its tunability (see Fig. 3.16) is an important tool to determine the relativistic origin of the mass defect.

We assume that in OLCs atoms are trapped in a magic-wavelength 1D lattice along the gravitational potential (Z axis), where $|e\rangle$ and $|g\rangle$ states experience the same potential, $V(Z) = V_Z \sin^2(k_L Z) + M\phi$ [23,25]. Here V_Z is the lattice depth, k_L is the wave number of the lattice that sets the atomic recoil energy $E_R = \hbar^2 k_L^2/2M$ and lattice spacing $a_L = \pi/k_L$. Metric geometry can also lead to corrections to optical lattices [171], which are negligible in our case. In a tilted 1D lattice described by $V(Z)$, the motional eigenstates in the ground band are the so-called Wannier-Stark (WS) states $|W_j\rangle$, with j the Z-lattice site index where the WS state is centered at. Assuming the radial degrees of freedom are also confined to the lowest ground state by an additional 2D lattice, with lattice depths $V_{X,Y}$, the eigenenergies of WS states are given by $E_j = Mga_L j + E_{\text{band}}$, where $E_{\text{band}} \approx \sum_{\alpha=X,Y,Z} E_R(\sqrt{V_\alpha/E_R} - 1/4)$ is the ground band zero-point energy. The GR corrections due to mass-energy equivalence is given by

$$\hat{H}_{\text{corr}} = \sum_j (E_{\text{GRS},j} + E_{\text{SDS}})|e, W_j\rangle\langle e, W_j|, \tag{3.85}$$

with $E_{\text{GRS},j}$ the gravitational redshift (GRS) and E_{SDS} the second-order Doppler shift (SDS). Their orders of magnitude are discussed below for ^{87}Sr atoms.

Applying the mass-energy equivalence to the gravitational potential energy $M\phi$, we get the

so-called GRS (or gravitational time dilation),

$$E_{\mathrm{GRS},j} = \frac{\Delta M}{M}\langle W_j|M\phi|W_j\rangle = \hbar\omega_0 \frac{g a_L j}{c^2}. \tag{3.86}$$

The GRS leads to a gradient of frequency shift across the lattice. For example, the fractional frequency difference for nearest-neighbor lattice sites is just 4.4×10^{-23}, while it is at the order of 10^{-19} for 1 mm spatial separation as recently observed [23, 157].

The contribution of mass-energy equivalence in the kinetic energy leads to a local modification of the zero-point energy known as SDS (or motional time dilation),

$$E_{\mathrm{SDS}} = -\frac{\Delta M}{M}\frac{\langle W_j|\hat{\mathbf{P}}^2|W_j\rangle}{2M} = -\frac{\hbar\omega_0}{2Mc^2}E_{\mathrm{band}}. \tag{3.87}$$

The magnitude of E_{SDS} increases with the lattice depth. For example, a deep lattice with $V_{X,Y,Z} = 300E_R$ leads to fractional frequency shift -4.5×10^{-21}. Corrections in the kinetic energy can also lead to a modification of the WS wave functions for $|e\rangle$ atoms, while they play a negligible role compared to $E_{\mathrm{GRS},j}$ and E_{SDS}.

3.4.3 Tuning and distinguishing GR effects

In standard OLCs, the effects of GRS might be mimicked by a weak magnetic field gradient. To observe genuine GR effects, one approach is to simultaneously observe $E_{\mathrm{GRS},j}$ and E_{SDS} in the same system. This should be possible in next-term OLCs by populating higher motional bands if the systematic uncertainty of lattice Stark shifts [75] is suppressed below 10^{-20}.

We propose an alternative approach to use dressed states as means to tune the mass defect ΔM and with it simultaneously change $E_{\mathrm{GRS},j}$ and E_{SDS}. As shown in Fig. 3.16(a), we make use of the intrinsic multilevel structure in fermionic alkaline earth atoms with nuclear spin F. We apply a dressing beam with Rabi frequency Ω and detuning δ connecting $|e, m_F\rangle$ with $|g, m_F - 1\rangle$ states, leading to the dressed states, $|+\rangle = C_1|e, m_F\rangle + C_2|g, m_F - 1\rangle$, $|-\rangle = -C_2|e, m_F\rangle + C_1|g, m_F - 1\rangle$, where $C_1 = (1 - \delta/\sqrt{\Omega^2 + \delta^2})^{1/2}/\sqrt{2}$, $C_2 = (1 + \delta/\sqrt{\Omega^2 + \delta^2})^{1/2}/\sqrt{2}$ in the rotating frame of the dressing laser. By addressing transition between the $|\uparrow\rangle \equiv |-\rangle$ state and $|\downarrow\rangle \equiv |g, m_F\rangle$ with a

clock laser for $\Delta m_F = 0$ transition, one can therefore get a tunable mass defect $\Delta M = |C_2|^2 \Delta M_0$ in the dressed clock transition via scanning the dressing parameter δ/Ω (see Fig. 3.16(b)), where $\Delta M_0 = \hbar\omega_0/c^2$ is the mass defect without the dressing laser. Since the nuclear spin states in the ground manifold share the same mass M but different Zeeman shifts (see SOM), the dressing allows us to differentiate between a gravitational redshift and a magnetic field gradient.

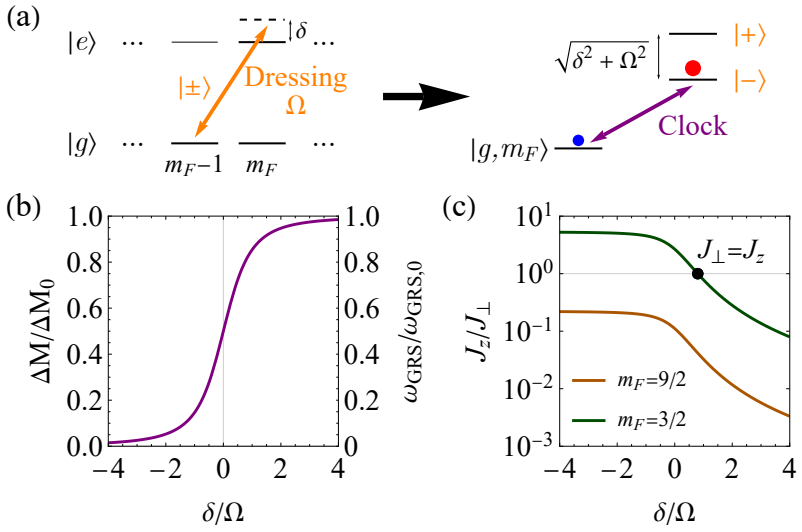

Figure 3.16: Tuning mass-energy equivalence via dressed states. (a) Schematic of dressing the clock transition with another nuclear spin. The left panel show the application of the dressing laser, and the right panel show the new clock transition in the dressed basis. (b) The tunability of the mass defect ΔM and gravitational redshift ω_{GRS} as a function of dressing parameter δ/Ω. ΔM_0 and $\omega_{\mathrm{GRS},0}$ are the corresponding values without dressing. (c) The tunability of cavity-mediated interactions (see $\hat{H}_{\mathrm{cav}}$ in Eq. (3.88)) as a function of dressing parameters δ/Ω and nuclear spin level m_F. Heisenberg interaction ($J_\perp = J_z$) can be reached with $m_F = 3/2$.

In the lab frame, we can understand the tunability of the mass-energy equivalence achieved by the dressing scheme by noticing that the state $|-\rangle$ has a probability $|C_2|^2$ to be in the excited optical level and therefore an average internal energy of $|C_2|^2\hbar\omega_0$. This protocol is feasible thanks to the fact that due to magnetic Zeeman shifts, the clock transitions between different nuclear

spins are frequency resolved. We also assume all other dynamical frequencies are smaller than the dressed state energy gap $\sqrt{\Omega^2+\delta^2}$ and the Zeeman shifts between nuclear spins.

To guarantee the matching of laser phases for each atom, the dressing beam and the clock beam should be co-propagating. Moreover, spatial inhomogeneities in atomic detunings δ and in the dressing laser Rabi frequency Ω need to be controlled to avoid obscuring the effects of gravitational redshift. For a mHz gravitational redshift arising from a cm-scale spatial separation, it would be required to suppress the absolute variations of δ and Ω below 10^{-4} Hz. For the case of atomic detunings δ, such level has been already achieved [23]. As for the Rabi frequency Ω, the requirement could be achievable using a cavity to stabilize the spatial mode of the dressing laser. One can also circumvent the stringent requirement by averaging the transition frequency of $|g,m_F\rangle \leftrightarrow |-\rangle$ and $|g,m_F\rangle \leftrightarrow |+\rangle$ (see SOM), while sacrificing the tunability of mass defect ($\Delta M = \Delta M_0/2$).

3.4.4 Interplay with many-body dynamics

After providing a recipe to distinguish genuine GR effects in OLCs, we further explore their manifestations in quantum many-body dynamics. We consider photon-mediated interactions generated by placing the atoms in an optical cavity [16,186], in a regime where atomic contact interactions are controlled to be much weaker. The interplay between photon-mediated interactions and the GRS is described by the following Hamiltonian (see Fig. 3.15(b)):

$$\hat{H}_{\mathrm{cav}}/\hbar = J_\perp \hat{\mathbf{S}}\cdot\hat{\mathbf{S}} + (J_z - J_\perp)\hat{S}^z\hat{S}^z + \omega_{\mathrm{GRS}}\sum_j j\hat{\mathcal{S}}_j^z, \tag{3.88}$$

where $\hbar\omega_{\mathrm{GRS}} = (\Delta M)ga_L$ is the GRS between nearest neighbor sites, $J_\perp$ and J_z are the collective exchange and Ising couplings. Here $\hat{\mathcal{S}}_j^{x,y,z}$ are collective spin operators summed over all atoms at the same height ja_L, and $\hat{S}^{x,y,z} = \sum_j \hat{\mathcal{S}}_j^{x,y,z}$. Based on Eq. (3.88), a magnetic field gradient will in principle give rise to similar single-atom inhomogeneities in the Hamiltonian. We drop the GR corrections for interaction terms since they are negligible in our case (see SOM). While the use of a single nuclear spin state restricts the cavity exchange interactions to a single polarization mode ($J_z = 0$ only), the dressing to another nuclear spin allows for coupling two polarization modes

of the cavity (see SOM), which enhances the tunability of $\hat{H}_{\rm cav}$ and realizes collective Heisenberg interactions ($J_\perp = J_z$) as shown in Fig. 3.16(c). In the following, we mainly focus on the case of $J_\perp = J_z$, since the $\hat{\mathbf{S}} \cdot \hat{\mathbf{S}}$ term becomes a constant and does not alter entanglement in the fully symmetric manifold. This requirement is unnecessary for observing frequency synchronization.

We propose to initialize all the atoms in the state $(|g\rangle + |e\rangle)/\sqrt{2}$, perform time evolution under Hamiltonian $\hat{H}_{\rm cav}$ (Eq. (3.88)), and then measure the phase shift of $\langle \hat{\mathcal{S}}_j^+ \rangle$ for every Z-lattice site, resulting in frequency shift $\omega_j(t) = \tan^{-1}\left[\langle \hat{\mathcal{S}}_j^y \rangle / \langle \hat{\mathcal{S}}_j^x \rangle\right]/t$ as a function of evolution time (see Fig. 3.17(a)). It can be observed by the application of a $\pi/2$ pulse followed by local population measurements. Without interactions or in the case of short interrogation times, one expects to observe the GRS, $\omega_j = j\omega_{\rm GRS}$, as reported in Ref. [23]. In the interaction dominated regime, the GRS persists only for a time scale shorter than the atomic interaction time scale. Beyond this period, the frequencies become synchronized due to interaction locking and reach $\omega_j \approx 0$ at synchronization time $t_{\rm syn}$ (see Fig. 3.17(b)). Without loss of generality, the numerical simulations in Fig. 3.17 and Fig. 3.18 are based on exact diagonalization for $N = 16$ atoms with one atom per Z-lattice site.

The emergent synchronization is the result of many-body gap protection also observed in prior experiments [37, 108, 186–189], which arises when $\omega_{\rm split} \ll \Delta E$. Here $\omega_{\rm split} = (N_s - 1)\omega_{\rm GRS}$ is the maximum redshift in the array, with N_s the number of lattice sites, and ΔE is the many-body gap due to Heisenberg couplings. On the contrary, in the regime $\omega_{\rm split} \sim \Delta E$, the gap cannot maintain global synchronization (see Fig. 3.17(c)). Using a spin wave analysis one obtains $\Delta E = NJ_\perp$ and $NJ_\perp t_{\rm syn} = \pi$ for $J_\perp = J_z$, where N corresponds to the total atom number in the array. For $N \sim 10^4 - 10^5$ ^{87}Sr atoms [186], one can achieve $NJ_\perp/2\pi \sim$ Hz ($\omega_{\rm split}/NJ_\perp \sim 10^{-3}$ for cm-scale separation), leading to an achievable synchronization time scale in experiment.

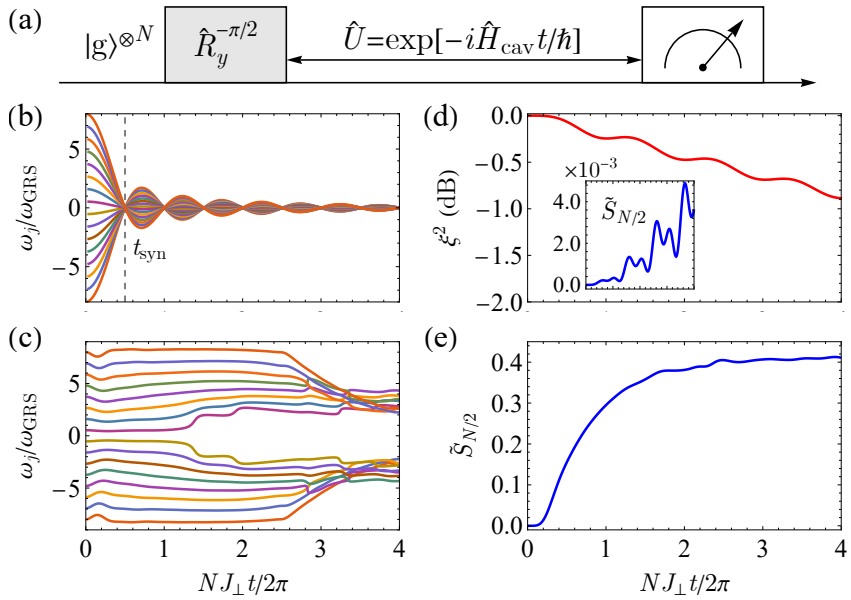

Figure 3.17: Interplay between photon-mediated interactions and GRS. (a) We prepare a product state with all atoms in $|g\rangle$ state and apply a laser pulse $\hat{R}_y^{-\pi/2} = \exp\left(i\frac{\pi}{2}\hat{S}^y\right)$ to start the dynamics. We focus on a single chain with $N = 16$ atoms under the Hamiltonian $\hat{H}_{\rm cav}$ (Eq. (3.88)) with $J_\perp = J_z$. (b) Individual atomic frequency shift ω_j with $\omega_{\rm split}/NJ_\perp = 0.3125$. Synchronization of atomic frequencies can be reach at time $t_{\rm syn}$. (c) Individual atomic frequency shift ω_j with $\omega_{\rm split}/NJ_\perp = 3.125$. Global synchronization fails to occur in this regime. (d) Spin squeezing parameter ξ^2 and normalized Rényi entropy $\tilde{S}_{N/2}$ (inset) in the case of (b). (e) Normalized Rényi entropy $\tilde{S}_{N/2}$ in the case of (c).

Furthermore, we find that the simultaneous presence of single-atom GRS and photon-mediated interactions can lead to quantum entanglement as shown in Fig. 3.17(d,e). In fact, in the regime $\omega_{\rm split} \ll \Delta E$, the projection of the wave function into the fully symmetric manifold imposed by the many-body gap transforms the single-particle term into an effective one-axis twisting (OAT) [30,31] interaction term $\chi\hat{S}^z\hat{S}^z$, with $\chi \sim \omega_{\rm split}^2/[N(\Delta E)]$ (see Ref. [135] where the splitting is generated by a different mechanism). In this case, entanglement builds up for $t > t_{\rm syn}$, as witnessed by a squeezing parameter [31], $\xi^2 \equiv \min_\varphi N(\Delta S_\varphi^\perp)^2/|\langle\hat{\mathbf{S}}\rangle|^2 < 1$ (see Fig. 3.17(d)). Here, $(\Delta S_\varphi^\perp)^2$ is the variance of spin noise along an axis perpendicular to the collective spin $\langle\hat{\mathbf{S}}\rangle$. A faster growth of

entanglement can be seen in the regime $\omega_{\rm split} \sim \Delta E$ (see Fig. 3.17(e)), while it is not captured by the spin squeezing parameter. Instead we characterize the entanglement by the normalized Rényi entropy $\tilde{S}_{N/2} = -2\log_2(\mathrm{tr}(\rho_{N/2}^2))/N$, where $\rho_{N/2}$ is the reduced density matrix by taking partial trace over half of the system. The entanglement builds up for $\omega_{\rm split}t/2\pi > 1$ in this case, which might be due to population transfer to highly entangled states in manifolds of lower total spin (see SOM). For the implementation of entanglement generation, $\omega_{\rm split}/NJ_\perp \sim 0.1 - 1$ is achievable for 10 cm $-$ 1 m separation and $NJ_\perp/2\pi \sim 0.1$ Hz.

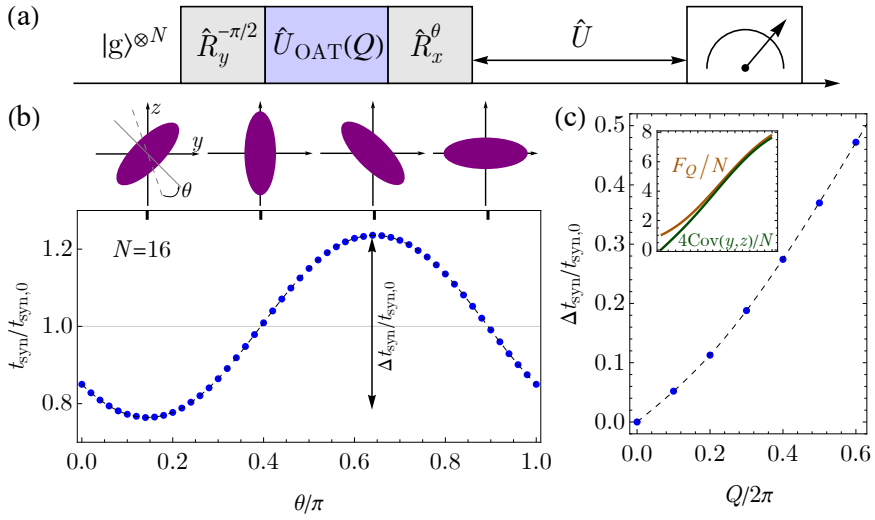

Figure 3.18: Interplay between entanglement and GRS. (a) One-axis twisting (OAT) interactions $\hat{U}_{\rm OAT}(Q) = \exp\left(-iQ\hat{S}^z\hat{S}^z/N\right)$ and rotations $\hat{R}_x^{\theta} = \exp\left(-i\theta\hat{S}^x\right)$ are first applied to generate a spin squeezed initial state (at $Q/2\pi = 0.6$), followed by unitary evolution(b)The synchronization time, $t_{\rm syn}$ depends on the orientation of the spin squeezed state determined by θ. (c) $\Delta t_{\rm syn}$ (marked in (b)) as a function of OAT shearing strength Q. We show $4\mathrm{Cov}(y,z)$ is approaching the quantum Fisher information F_Q for spin squeezed states (inset). We compare the numerical simulations (blue points) for $N = 16$ atoms under $\hat{H}_{\rm cav}$ ($J_\perp = J_z$) with Eq. (3.89) (black dashed lines).

To study the effects of the GRS on quantum entanglement, we consider the scenario with entangled initial states, such as the ones generated using cavity induced OAT interactions [14,190],

$\hat{U}_{\mathrm{OAT}}(Q) = \exp\Big(-iQ\hat{S}^z\hat{S}^z/N\Big)$, where Q is the shearing strength (Fig. 3.18(a)). The squeezing direction corresponds to the direction with minimum value of $(\Delta S_{\varphi}^{\perp})^2$, which can be controlled by performing a rotation $\hat{R}_x^{\theta} = \exp\Big(-i\theta\hat{S}^x\Big)$ as shown in Fig. 3.18. We use $|\psi_0\rangle$ to denote the state after OAT interactions, and $|\psi(\theta)\rangle$ for the state after the $\hat{R}_x^{\theta}$ rotation.

In Fig. 3.18(b), we show that it is possible to control t_{syn} below or above the value of a product initial state $t_{\mathrm{syn},0}$ (obtained in Fig. 3.17) depending on the rotation $\hat{R}_x^{\theta}$. The ratio $t_{\mathrm{syn}}/t_{\mathrm{syn},0}$ under $\hat{H}_{\mathrm{cav}}$ ($J_{\perp} = J_z$) can be understood using the following analytic result (see SOM),

$$\frac{t_{\mathrm{syn}}}{t_{\mathrm{syn},0}} = 1 - \frac{2}{\pi}\arctan\left[\frac{\mathrm{Cov}(y,z)}{(N-1)\langle\psi_0|\hat{S}^x|\psi_0\rangle}\right], \tag{3.89}$$

where $\mathrm{Cov}(\alpha,\beta) \equiv \langle\psi(\theta)|(\hat{S}^{\alpha}\hat{S}^{\beta}+\hat{S}^{\beta}\hat{S}^{\alpha})|\psi(\theta)\rangle - 2\langle\psi(\theta)|\hat{S}^{\alpha}|\psi(\theta)\rangle\langle\psi(\theta)|\hat{S}^{\beta}|\psi(\theta)\rangle$, with $\alpha,\beta = x,y,z$. The tunability of t_{syn} is due to the θ-dependence of $\mathrm{Cov}(y,z)$. The tunable range $\Delta t_{\mathrm{syn}} \equiv \max_{\theta} t_{\mathrm{syn}} - \min_{\theta} t_{\mathrm{syn}}$ can be used as a measure of entanglement (see Fig. 3.18(c)), since $4\mathrm{Cov}(y,z)$ is approaching the quantum Fisher information F_Q [31], which corresponds to the maximal eigenvalue of the matrix $F_{Q,\alpha\beta} = 2\mathrm{Cov}(\alpha,\beta)$.

3.4.5 Conclusion and outlook

We discussed protocols accessible in OLCs that explore how the single-atom GR effects modify many-body dynamics generated by photon-mediated interactions. A similar interplay should be observable with atomic superexchange interactions (see SOM). While so far we have mostly focused on highly localized atomic arrays, generalizations to the case of itinerant particles where motion also and other GR corrections become relevant, will open unique opportunities for testing the basic tenets of GR when extended into the complex quantum domain.

3.4.6 Supplemental Materials: Post-Newtonian corrections

3.4.6.1 Post-Newtonian metric in the lab frame

Our starting point to include relativistic corrections is the parametrized post-Newtonian metric [163, 168, 171, 185] in the isotropic coordinates (ct, x, y, z),

$$ds^2 = g_{\mu\nu}dx^\mu dx^\nu = -\left(1 + 2\frac{\bar{\phi}}{c^2} + 2\beta\frac{\bar{\phi}^2}{c^4}\right)c^2dt^2 + \left(1 - 2\gamma\frac{\bar{\phi}}{c^2}\right)(dx^2 + dy^2 + dz^2) + O\left(\frac{1}{c^4}\right), \quad (3.90)$$

where $\bar{\phi}(R) = -GM_\oplus/R$ is the Newtonian gravitational potential of the earth, with $M_\oplus$ the mass of the earth and $R = \sqrt{x^2 + y^2 + z^2}$. This metric agrees with the post-Newtonian expansion of Schwarzschild metric if $\beta = \gamma = 1$. Note that Eq. (3.90) is reduced to Minkowski metric $(ds^2 = \eta_{\mu\nu}dx^\mu dx^\nu = -c^2dt^2 + dx^2 + dy^2 + dz^2)$ when $x, y, z \to \infty$.

Now we would like to define the lab frame, a reference frame which can be reduced to Minkowski metric at the lab position. First, we replace z by $R_\oplus + z$, with $R_\oplus$ the earth's radius, so the lab position at the earth's surface is described by $x = y = z = 0$, where the radial direction is along the z axis. In this step, Eq. (3.90) remains unchanged, and we can rewrite the gravitational potential as $\bar{\phi} = \phi_0 + \phi$, where $\phi_0 = \bar{\phi}(R_\oplus)$ is the gravitational potential at the earth's surface. Following Ref. [171], we consider the following coordinate transformation,

$$T = \left(1 + \frac{\phi_0}{c^2} + \frac{2\beta - 1}{2}\frac{\phi_0^2}{c^4}\right)t, \quad X = \left(1 - \gamma\frac{\phi_0}{c^2}\right)x, \quad Y = \left(1 - \gamma\frac{\phi_0}{c^2}\right)y, \quad Z = \left(1 - \gamma\frac{\phi_0}{c^2}\right)z. \quad (3.91)$$

The lab frame can be described in terms of the new coordinates (cT, X, Y, Z),

$$ds^2 = -\left(1 + 2\frac{\phi}{c^2} + 2\beta\frac{\phi^2}{c^4} + 4(\beta - 1)\phi_0\frac{\phi}{c^4}\right)c^2dT^2 + \left(1 - 2\gamma\frac{\phi}{c^2}\right)(dX^2 + dY^2 + dZ^2) + O\left(\frac{1}{c^4}\right). \quad (3.92)$$

Note that ϕ can be expanded as

$$\phi(Z) = gZ + O(Z^2), \quad (3.93)$$

where g is the gravitational acceleration. In the case of GR theory ($\beta = \gamma = 1$), the post-Newtonian metric in the two reference frames (see Eq. (3.90) and Eq. (3.92)) takes the same form, and this is the metric we used in the main text.

As a general remark, the gravitational redshift originates from the difference in the proper time $d\tau_p = ds/c$ for clocks at rest at different spatial coordinates due to the metric (see Eq. (3.92)). If there is a single observer at a fixed position, the way to measure gravitational redshift is to send out laser beams with a unique frequency to different position, and the observer should find the difference of atomic transition frequency (clock) at different positions. If there are several observers at different positions, the way to measure gravitational redshift is to measure the frequency of the same laser beam at different positions assuming they have the same atomic transition frequency (clock), and they should observe different frequency for the light field. It is worth to mention that all the following discussions are based on the lab frame (see Eq. (3.92)) defined here with a single observer at rest at the lab position.

3.4.6.2 Post-Newtonian single-atom quantum Hamiltonian

Key steps towards mass-energy equivalence

Post-Newtonian corrections for a quantum Hamiltonian can be determined in the following way [163, 168]: Write down the classical action/Lagrangian in the lab frame consistent with GR, perform Legendre transformation to achieve the classical Hamiltonian, and then perform canonical quantization to achieve the quantum Hamiltonian. In the following, we will discuss the key idea of how mass-energy equivalence can be interpreted from the post-Newtonian corrections, and much more details can be found in Ref. [163].

First we consider the post-Newtonian quantum Hamiltonian for a single free point particle with mass M. We start from the following classical action,

$$\mathcal{S}_{\text{point}} = -Mc \int dT \sqrt{g_{\mu\nu}\dot{x}^{\mu}\dot{x}^{\nu}}, \tag{3.94}$$

and the classical Lagrangian L_{point} is given by $\mathcal{S}_{\text{point}} = \int L_{\text{point}} dT$ in the lab frame (cT, X, Y, Z).

We have

$$\begin{aligned} L_{\text{point}} &= -Mc^2\sqrt{-g_{\mu\nu}\dot{x}^\mu\dot{x}^\nu/c^2} \\ &= -Mc^2 + \frac{M\dot{\mathbf{X}}^2}{2}\left(1+\frac{\dot{\mathbf{X}}^2}{4c^2}\right) - M\phi\left(1+\frac{2\beta-1}{2}\frac{\phi}{c^2}+2(\beta-1)\frac{\phi_0}{c^2}\right) \\ &- \frac{2\gamma+1}{2}\frac{M\phi}{c^2}\dot{\mathbf{X}}^2 + O\left(\frac{1}{c^4}\right), \end{aligned} \tag{3.95}$$

where $\dot{\mathbf{X}}^2 = \dot{X}^2+\dot{Y}^2+\dot{Z}^2$. The momentum $\mathbf{P}$ is given by

$$\mathbf{P} = \frac{\partial L_{\text{point}}}{\partial \dot{\mathbf{X}}} = M\dot{\mathbf{X}}\left(1+\frac{\dot{\mathbf{X}}^2}{2c^2}-(2\gamma+1)\frac{\phi}{c^2}\right)+O\left(\frac{1}{c^4}\right). \tag{3.96}$$

We use Legendre transformation to get the classical Hamiltonian, $H_{\text{point}} = \mathbf{P}\cdot\dot{\mathbf{X}} - L_{\text{point}}$, and then perform canonical quantization to achieve the quantum Hamiltonian,

$$\hat{H}_{\text{point}}(\hat{\mathbf{X}},\hat{\mathbf{P}},M) = Mc^2 + \hat{H}_0 + \hat{H}_{\text{other}}, \tag{3.97}$$

where $\hat{H}_0$ is the nonrelativistic Hamiltonian,

$$\hat{H}_0 = \frac{\hat{\mathbf{P}}^2}{2M} + M\phi, \tag{3.98}$$

and $\hat{H}_{\text{other}}$ contains the relativistic corrections,

$$\hat{H}_{\text{other}} = -\frac{\hat{\mathbf{P}}^4}{8M^3c^2} + M\phi\left(\frac{2\beta-1}{2}\frac{\phi}{c^2}+2(\beta-1)\frac{\phi_0}{c^2}\right)+\frac{2\gamma+1}{2}\frac{\hat{\mathbf{P}}\cdot\phi\hat{\mathbf{P}}}{Mc^2}+O\left(\frac{1}{c^4}\right). \tag{3.99}$$

For simplicity, we then consider the atom is formed by two charged particles interacting via EM fields, and there are no external EM fields coupled to the system. We also assume that the atom is a localized object such that the gravitational potential ϕ remains unchanged within the size of an atom. In the Coulomb gauge, one can finally reach the following atomic Hamiltonian [163,168],

$$\begin{aligned} \hat{H}_A = &\Big(\sum_{n=1,2} M_n\Big)c^2 + \sum_{n=1,2}\left[\frac{\hat{\mathbf{P}}_n^2}{2M_n} - \frac{\hat{\mathbf{P}}_n^4}{8M_n^3c^2} + M_n\phi\left(1+\frac{2\beta-1}{2}\frac{\phi}{c^2}+2(\beta-1)\frac{\phi_0}{c^2}\right)\right. \\ &\left.+\frac{2\gamma+1}{2}\frac{\hat{\mathbf{P}}_n\cdot\phi\hat{\mathbf{P}}_n}{M_nc^2}\right] + \left(1+(\gamma+1)\frac{\phi}{c^2}\right)\frac{e_1e_2}{4\pi\epsilon_0|\hat{\mathbf{X}}_{12}|} - \frac{e_1e_2}{16\pi\epsilon_0M_1M_2c^2}\left[\hat{\mathbf{P}}_1\cdot\frac{1}{|\hat{\mathbf{X}}_{12}|}\hat{\mathbf{P}}_2\right. \\ &\left.+\hat{\mathbf{P}}_1\cdot\frac{(\hat{\mathbf{X}}_{12})(\hat{\mathbf{X}}_{12})}{|\hat{\mathbf{X}}_{12}|^3}\cdot\hat{\mathbf{P}}_2+\text{h.c.}\right]+O\left(\frac{1}{c^4}\right), \end{aligned} \tag{3.100}$$

where $\hat{\mathbf{X}}_{12} = \hat{\mathbf{X}}_1 - \hat{\mathbf{X}}_2$. This Hamiltonian is the so-called Darwin Hamiltonian which includes relativistic corrections except the terms related to the electron spin. Here we would like to use this

Hamiltonian as a toy model to discuss the relativistic corrections to the center-of-mass frame and the connection to the Hamiltonian of a point particle (see Eq.(3.97)).

In the non-relativistic case, we define center-of-mass (COM) coordinates ($\hat{\mathbf{X}}'$, $\hat{\mathbf{P}}'$) and internal coordinates ($\hat{\mathbf{x}}'$, $\hat{\mathbf{p}}'$) in the following way,

$$\hat{\mathbf{X}}' = \frac{1}{M}(M_1\hat{\mathbf{X}}_1 + M_2\hat{\mathbf{X}}_2), \quad \hat{\mathbf{P}}' = \hat{\mathbf{P}}_1 + \hat{\mathbf{P}}_2, \quad \hat{\mathbf{x}}' = \hat{\mathbf{X}}_2 - \hat{\mathbf{X}}_1, \quad \hat{\mathbf{p}}' = \frac{M_1}{M}\hat{\mathbf{P}}_2 - \frac{M_2}{M}\hat{\mathbf{P}}_1, \tag{3.101}$$

where $M = M_1 + M_2$ is the total mass, and $\mu = M_1M_2/M$ is the reduced mass. However, if applying the coordinate transformation above to $\hat{H}_A$ (see Eq. (3.100)), one can easily find that it fails to separate the Hamiltonian into COM and internal degrees of freedom without crossed couplings. As proposed by Ref. [158], one can apply relativistic corrections to the COM and internal coordinates using the following unitary transformation,

$$\hat{\mathbf{X}} = \hat{U}^\dagger\hat{\mathbf{X}}'\hat{U}, \quad \hat{\mathbf{P}} = \hat{U}^\dagger\hat{\mathbf{P}}'\hat{U}, \quad \hat{\mathbf{x}} = \hat{U}^\dagger\hat{\mathbf{x}}'\hat{U}, \quad \hat{\mathbf{p}} = \hat{U}^\dagger\hat{\mathbf{p}}'\hat{U}, \tag{3.102}$$

where

$$\begin{aligned}\hat{U} = \exp\Bigg[& i\frac{1}{4M^2c^2}\Big((\hat{\mathbf{P}}'\cdot\hat{\mathbf{p}}')(\hat{\mathbf{P}}'\cdot\hat{\mathbf{x}}') + (\hat{\mathbf{P}}'\cdot\hat{\mathbf{x}}')(\hat{\mathbf{P}}'\cdot\hat{\mathbf{p}}')\Big) \\ & + i\frac{M_1 - M_2}{4\mu M^2c^2}\Big((\hat{\mathbf{p}}'\cdot\hat{\mathbf{p}}')(\hat{\mathbf{P}}'\cdot\hat{\mathbf{x}}') + (\hat{\mathbf{P}}'\cdot\hat{\mathbf{x}}')(\hat{\mathbf{p}}'\cdot\hat{\mathbf{p}}')\Big) \\ & + i\frac{e_1e_2(M_1 - M_2)}{8\pi\epsilon_0 M^2c^2}\frac{\hat{\mathbf{P}}'\cdot\hat{\mathbf{x}}'}{|\hat{\mathbf{x}}'|}\Bigg].\end{aligned} \tag{3.103}$$

Using these new coordinates in Hamiltonian $\hat{H}_A$ (see Eq. (3.100)), we get

$$\hat{H}_A = \hat{H}_{\text{point}}\left(\hat{\mathbf{X}}, \hat{\mathbf{P}}, M + \frac{\hat{H}_I}{c^2}\right) + O(c^{-4}). \tag{3.104}$$

This is the so-called mass-energy equivalence since the atom Hamiltonian $\hat{H}_A$ can be generated by replacing mass M by $M + \hat{H}_I/c^2$ in the point-particle Hamiltonian $\hat{H}_{\text{point}}$. In other words, the mass of a composite particle comprises the rest masses of the constituent particles as well as the internal energy. Here the internal Hamiltonian $\hat{H}_I$ is given by

$$\hat{H}_I = \hat{H}_{I,0} + \hat{H}_{I,\text{SR}} + \hat{H}_{I,\text{GR}}, \tag{3.105}$$

where $\hat{H}_{I,0}$ is the non-relativistic internal Hamiltonian,

$$\hat{H}_{I,0} = \frac{\hat{\mathbf{p}}^2}{2\mu} + \frac{e_1e_2}{4\pi\epsilon_0|\hat{\mathbf{x}}|}, \tag{3.106}$$

$\hat{H}_{I,\mathrm{SR}}$ contains the corrections due to special relativity,

$$\hat{H}_{I,\mathrm{SR}} = -\frac{\hat{\mathbf{p}}^4}{8\mu^3 c^2}\frac{M_1^3+M_2^3}{M^3} - \frac{e_1 e_2}{8\pi\epsilon_0 \mu M c^2}\left(\hat{\mathbf{p}}\cdot\frac{1}{|\hat{\mathbf{x}}|}\hat{\mathbf{p}} + \hat{\mathbf{p}}\cdot\frac{\hat{\mathbf{x}}\hat{\mathbf{x}}}{|\hat{\mathbf{x}}|^3}\cdot\hat{\mathbf{p}}\right) + O\left(\frac{1}{c^4}\right), \tag{3.107}$$

$\hat{H}_{I,\mathrm{GR}}$ contains the corrections due to metric geometry,

$$\hat{H}_{I,\mathrm{GR}} = \gamma\frac{\phi(\hat{\mathbf{X}})}{c^2}\left(\frac{\hat{\mathbf{p}}^2}{\mu} + \frac{e_1 e_2}{4\pi\epsilon_0|\hat{\mathbf{x}}|}\right) + O\left(\frac{1}{c^4}\right). \tag{3.108}$$

List of relevant post-Newtonian correction terms

Here we list all the relevant post-Newtonian corrections terms for the single-atom Hamiltonian (see Fig. 3.19),

$$\hat{H}_{\mathrm{sp}} = \hat{H}_A + \hat{H}_{AL}. \tag{3.109}$$

- $\hat{H}_A$ is the atom Hamiltonian including center of mass and internal degrees of freedom. To the leading order of post-Newtonian expansion, we have $\hat{H}_A$ given by Eq. (3.104), with internal Hamiltonian $\hat{H}_I$ (the case of two charged particles) given by Eq. (3.105) and point-particle Hamiltonian $\hat{H}_{\mathrm{point}}$ given by Eq. (3.97). To clearly indicate the post-Newtonian corrections, one can rewrite $\hat{H}_A$ in the following form,

$$\hat{H}_A = Mc^2 + \hat{H}_0 + \hat{H}_I + \hat{H}_{\mathrm{SDS}} + \hat{H}_{\mathrm{GRS}} + \hat{H}_{\mathrm{other}}. \tag{3.110}$$

  We understand these corrections in the following way:

  (1) Mass-energy equivalence. This is to replace M by $M + \hat{H}_I/c^2$ in $\hat{H}_0$ (see Fig. 3.19(a)). The replacement in the kinetic energy term of $\hat{H}_0$ can lead to second-order Doppler shift,

$$\hat{H}_{\mathrm{SDS}} = -\frac{\hat{\mathbf{P}}^2}{2M}\frac{\hat{H}_I}{Mc^2}. \tag{3.111}$$

  The replacement in the gravitational potential energy term of $\hat{H}_0$ can lead to gravitational redshift,

$$\hat{H}_{\mathrm{GRS}} = \frac{\phi}{c^2}\hat{H}_I. \tag{3.112}$$

We have discussed these two types of corrections in the main text, since they are the dominant GR corrections for optical lattice clocks. Here we list their order of magnitudes in Fig. 3.19(b).

(2) $\hat{H}_{\text{other}}$ (see Eq. (3.99)). Compared to mass-energy equivalence, $\hat{H}_{\text{other}}$ only acts on motional degrees of freedom and does not lead to frequency shifts of the clock transition. For comparison, we still list their orders of magnitude in terms of fractional frequency in Fig. 3.19(b). The first term of $\hat{H}_{\text{other}}$ represents the corrections to the kinetic energy in $\hat{H}_0$ due to relativistic COM motion, which is at the order of fractional frequency 10^{-29} assuming MHz scale of kinetic energy. The rest of the terms are metric geometry corrections to the kinetic energy and potential energy terms in $\hat{H}_0$, which is at the order of 10^{-25} for 1 cm spatial separation. It is worth to mention that the term $M\phi^2/c^2$ in metric geometry corrections depends quadratically on the spatial separation ($\sim Z^2$), and this term will become relevant in the case of larger spatial separations such as atom interferometers.

(3) Corrections in $\hat{H}_I$ (see Eq. (3.105)). The special relativistic corrections $\hat{H}_{I,\text{SR}}$, as well as the terms related to electron spin, can give rise to atomic fine structure, which has already been taken into account in standard AMO experiments. As for the metric geometry corrections $\hat{H}_{I,\text{GR}}$, Ref. [168] points out that $\hat{H}_{I,\text{GR}}$ is off-diagonal in the unperturbed eigenbasis of internal states, so the corrections to internal energy is negligible. Here, we typically assume $\hat{H}_I$ is the same as the internal Hamiltonian used in standard AMO experiments including atomic fine structure and hyperfine structure. On the other hand, $\hat{H}_{I,\text{GR}}$ might lead to corrections to the internal wave function, so the dipole matrix elements might need to be corrected in $\hat{H}_{AL}$, although it is suppressed due to the small spatial separation in optical clocks.

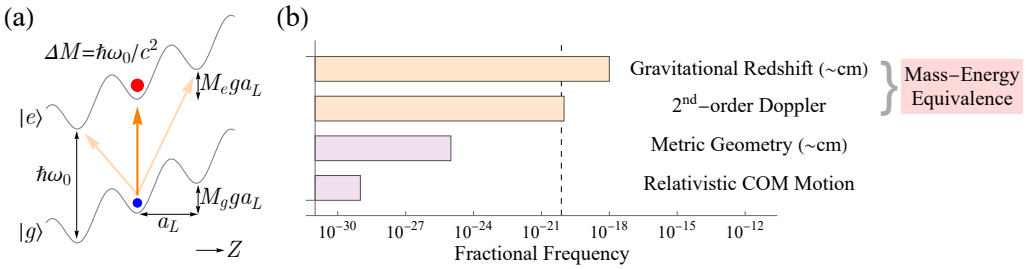

Figure 3.19: (a) Schematic of an optical lattice clock with atoms trapped in a lattice tilted by gravity. Internal energy difference $\hbar\omega_0$ between $|e\rangle$ and $|g\rangle$ states can lead to mass difference ΔM in the Newtonian gravitational potential and generate gravitational redshift. It is possible to tune the frequency of laser beams to excite either on-site (orange arrow) or off-site (light orange arrows) transitions [23, 25]. (b) Order of magnitude of the GR corrections for $\hat{H}_A$ in fractional frequency of the clock transition (^{87}Sr). The light orange color marks the corrections due to mass-energy equivalence (see Eq. (3.111) and Eq. (3.112)), and the light purple color marks the other source of corrections (see Eq. (3.99)). We assume MHz scale of kinetic energy and cm scale spatial separation of gravitational potential. The dashed line shows the current record of optical clock stability, 7.6×10^{-21} [23].

- $\hat{H}_{AL}$ describes the couplings to external electromagnetic field, which is relevant for the optical lattice beam as well as the clock laser beam. Although the higher order terms in multipolar expansion can play a more important role compared to the post-Newtonian corrections, here we only focus on the post-Newtonian corrections to the leading order electric dipole terms. Under electric dipole approximation, we have [161, 163]

$$\hat{H}_{AL} = -\hat{\mathbf{d}} \cdot \mathbf{E} + \frac{1}{2M}\left[\hat{\mathbf{P}} \cdot (\hat{\mathbf{d}} \times \mathbf{B}) + (\hat{\mathbf{d}} \times \mathbf{B}) \cdot \hat{\mathbf{P}}\right], \tag{3.113}$$

where $\hat{\mathbf{d}}$ is the electric dipole moment. In Eq. (3.113), the first term is the standard electric dipole couplings, and the second term is relativistic correction term known as the Röntgen term, which describes the coupling between a moving dipole and magnetic field generated by Lorentz transformation of electric field $\mathbf{E}$ due to relativistic COM motion. We consider

monochromatic light field in the following form, $\mathbf{E} = \mathbf{E}^{(+)}e^{-i\omega t}$+H.c., $\mathbf{B} = \mathbf{B}^{(+)}e^{-i\omega t}$+H.c., where ω is the laser frequency. First we focus on the post-Newtonian corrections to the optical lattice beam:

(1) Röntgen term. For simplicity, we assume the lattice AC Stark shifts are dominated by a single dipole-allowed transition $|a\rangle \to |b\rangle$, so the AC Stark shifts for internal state $|a\rangle$ is given by second-order perturbation theory,

$$\hat{H}_{\mathrm{ac}} \approx -\frac{\langle a|\hat{H}_{AL}|b\rangle\langle b|\hat{H}_{AL}|a\rangle}{E_b - E_a - \hbar\omega_L}, \tag{3.114}$$

where ω_L is the frequency of the lattice beam, E_a, E_b are the energy of states $|a\rangle$ and $|b\rangle$ respectively. Here we assume linear polarization of the lattice beam, with $\mathbf{E}^{(+)} = \mathcal{E}\cos(k_L Z)\vec{X}$, $\mathbf{B}^{(+)} = (i\mathcal{E}/c)\sin(k_L Z)\vec{Y}$ and propagation direction $\vec{Z}$. Here the vector symbol $\vec{X}$ means a unit vector along X direction. Plug in Eq. (3.114), we have

$$\hat{H}_{\mathrm{ac}} \approx -\alpha_{\mathrm{E1}}\mathcal{E}^2\cos^2(k_L Z) + \alpha_{\mathrm{E1}}\mathcal{E}^2\frac{\hbar\omega_L}{Mc^2}\sin^2(k_L Z), \tag{3.115}$$

where $\alpha_{\mathrm{E1}} = \langle a|\hat{\mathbf{d}}\cdot\vec{X}|b\rangle\langle b|\hat{\mathbf{d}}\cdot\vec{X}|a\rangle/(E_b - E_a - \hbar\omega)$ is the electric dipole polarizability. Here, the first term is the standard optical lattice potential, and the second term is the corrections due to the Röntgen term. This leads to a correction of the lattice depth at the order of $\hbar\omega_L/Mc^2 \sim 10^{-11}$, which is equivalent to a fractional frequency of 10^{-20} for a MHz trapping potential. However, this term does not lead to frequency shifts of the clock transition in a magic wavelength lattice, which means the same α_{E1} for the ground and excited states of the clock transition.

(2) Metric geometry corrections to electromagnetic plane waves. As pointed out in Ref. [171], the calculation of the electromagnetic field is based on solving Maxwell equations under the post-Newtonian metric. For example, the plane wave propagating along $\hat{Z}$ direction (electric field polarized along $\hat{X}$ direction) should be corrected in

the following way,

$$\mathbf{E} \propto \left(\left(1 - (\gamma+1)\frac{\phi}{c^2} \right) \exp\left[-i\omega T \pm \left(1 - \frac{\gamma+1}{2}\frac{\phi}{c^2} \right) ikZ \right] + \text{c.c.}, 0, 0 \right), \quad (3.116)$$

where $k = \omega/c$. As shown in Eq. (3.116), we have ϕ/c^2 corrections in the amplitude and phase of the electric field. Note that this term does not lead to differential AC Stark shifts, while it leads to spatial dependent lattice depth and lattice spacing. Such type of correction has negligible effects in optical clocks due to small spatial separation (fractional frequency 10^{-27} or smaller for 1 cm separation), while it will become relevant in the case of larger spatial separations such as atom interferometers.

We then focus on the post-Newtonian corrections to the clock laser beam. We consider the case of the carrier transition without changing the motional degrees of freedom (motional wave function $\psi_e \approx \psi_g$). Similar to the discussion of the lattice beam, the ϕ/c^2 corrections due to metric geometry are suppressed due to the small spatial separation of the optical clocks. For simplicity, we consider the clock laser beam propagating along $\vec{X}$ direction, with $\mathbf{E}^{(+)} = \mathcal{E} e^{ik_L X}\vec{Z}$, $\mathbf{B}^{(+)} = -(\mathcal{E}/c)e^{ik_L X}\vec{Y}$, the Rabi frequency is given by

$$\Omega_{\text{clk}} = -\frac{\langle e|\hat{\mathbf{d}}\cdot\vec{Z}|g\rangle\mathcal{E}}{\hbar}\left[\int \mathrm{d}^3\mathbf{R}\ \psi_e^* e^{ik_L X}\psi_g - \frac{1}{2Mc}\int \mathrm{d}^3\mathbf{R}\ \psi_e^*(\hat{P}_X e^{ik_L X} + e^{ik_L X}\hat{P}_X)\psi_g \right]. \quad (3.117)$$

If we assume the motional states of the atoms are approximately harmonic oscillator states, since $\hat{P}_X e^{ik_L X} + e^{ik_L X}\hat{P}_X$ is off-diagonal in the harmonic oscillator basis, the effects of Röntgen term are significantly suppressed for the carrier transition. On the other hand, $\hat{H}_{\text{SDS}}$ due to mass-energy equivalence couples the ground band Wannier function to high bands, which gives perturbative corrections to ψ_e at the order of 10^{-11}. Therefore, the relativistic corrections should be at the order of 10^{-11} for Ω_{clk}, which is equivalent to $10^{-26} - 10^{-25}$ in fractional frequency unit assuming Ω_{clk} in the range of $1 - 10$ Hz.

3.4.6.3 Intuitive discussion of post-Newtonian atomic interactions

Here we would like to briefly discuss our intuition for post-Newtonian corrections on atomic interactions. As for the cavity-mediated interactions, post-Newtonian corrections lie in the atom-light couplings and the analysis is similar to the discussion of Ω_{clk} in the previous subsection, thus we can reasonably assume 10^{-11} corrections to the cavity-mediated interactions. As we discuss in the main text, $NJ_\perp$ can be of the order of $1-10$ Hz for clock transition [186], so the post-Newtonian corrections are at the order of fractional frequency $10^{-26}-10^{-25}$, which is negligible for current experiments.

As for the contact interaction, we consider the major source of corrections is the mass-energy equivalence, as we discussed below. Our analysis is based on the s-wave interaction Hamiltonian,

$$\hat{H}_s = \frac{2\pi\hbar^2 a_{eg}^-}{\mu}\int \mathrm{d}^3\mathbf{R}\,\hat{\psi}_e^\dagger(\mathbf{R})\hat{\psi}_g^\dagger(\mathbf{R})\hat{\psi}_g(\mathbf{R})\hat{\psi}_e(\mathbf{R}), \tag{3.118}$$

where $\mu = M_e M_g/(M_e+M_g)$ is the reduced mass, and $a_{eg}^- = 69.1a_0$ is the s-wave scattering length [25, 62]. Here we will simply assume the C_6 coefficient remains unchanged. The effects of mass-energy equivalence on the s-wave interaction are as follows:

- Correction of the s-wave scattering length and the reduced mass. Based on Ref. [59], the s-wave scattering length can be estimated by

$$a_{eg}^- = \bar{a}_{eg}\left(1-\tan\left(\Phi-\frac{\pi}{8}\right)\right), \quad \bar{a}_{eg} = \frac{2\pi}{[\Gamma(1/4)]^2}\left(\frac{2\mu C_{6,eg}}{\hbar^2}\right)^{1/4}, \tag{3.119}$$

  where $\Phi = \int_{r_0}^{\infty} dr\sqrt{2\mu[-V(r)]}/\hbar$ is the WKB phase, with r_0 the classical turning point and $V(r)$ the molecular potential. To remove the modπ ambiguity of Φ, here we note that Φ/π is directly related to the number of bound states N_b in the molecular potential,

$$N_b = \left\lfloor \frac{\Phi}{\pi} - \frac{5}{8}\right\rfloor + 1. \tag{3.120}$$

  In the formula above, $C_{6,eg} = 3880E_h a_0^6$ is the C_6 coefficient for eg channel of ^{87}Sr atoms [62], with E_h the Hartree energy and a_0 the Bohr radius, which leads to $\bar{a}_{eg} = 75.4a_0$. Now

we apply the mass-energy equivalence, which gives

$$\mu = \frac{M}{2}\left(1 + \frac{\hbar\omega_0}{2Mc^2}\right), \tag{3.121}$$

$$\tilde{a}_{eg}^{-} = a_{eg}^{-}\left(1 + \frac{\hbar\omega_0}{8Mc^2}\right)\left(1 - 1.099\Phi\frac{\hbar\omega_0}{4Mc^2}\right). \tag{3.122}$$

- Correction of the single-atom wave function. Since $\hat{H}_{\mathrm{SDS}}$ couples the ground band Wannier function to high bands, we have perturbative corrections to the ground band Wannier function of $|e\rangle$ state. If we approximate the Wannier functions as the harmonic oscillator states, we get

$$\psi_g(X) \approx \psi_0(X), \quad \psi_e(X) \approx \psi_0(X) - \frac{\sqrt{2}\hbar\omega_0}{8Mc^2}\psi_2(X), \tag{3.123}$$

where ψ_n is the wave function of harmonic oscillator level n. The same formula can apply to Y and Z direction.

Combining all the corrections in Eq. (3.121-3.123), we can estimate the on-site interaction U by

$$\begin{aligned} U &= \frac{2\pi\hbar^2\tilde{a}_{eg}^{-}}{\mu}\int \mathrm{d}X\,[\psi_e(X)]^2[\psi_g(X)]^2\int \mathrm{d}Y\,[\psi_e(Y)]^2[\psi_g(Y)]^2\int \mathrm{d}Z\,[\psi_e(Z)]^2[\psi_g(Z)]^2 \\ &\approx U_0\left(1 - 1.099\Phi\frac{\hbar\omega_0}{4Mc^2}\right), \end{aligned} \tag{3.124}$$

where $U_0 = \sqrt{8/\pi}(k_L a_{eg}^{-})(E_R V_X V_Y V_Z)^{1/4}$. This calculation shows that the main contribution comes from the WKB phase. Up to date there are no experimental measurements for the number of bound states in the eg channel of ^{87}Sr atoms. If we assume Φ/π falls into the range of $10^1 - 10^2$, this leads to $10^{-10} - 10^{-9}$ corrections to U, which is equivalent to fractional frequency $10^{-22} - 10^{-21}$ for U at kHz scale. We note that this correction is much smaller than the modification of bare scattering length due to the lattice potential itself [109, 191], and therefore can be ignored for current experiments.

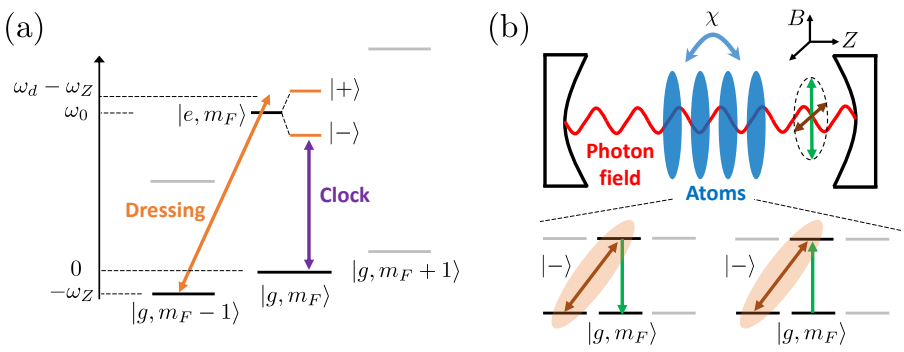

Figure 3.20: (a) Schematic of the dressing protocol. We apply dressing laser connecting $|e, m_F\rangle$ with $|g, m_F - 1\rangle$ states, which leads to the dressed basis $|+\rangle$ and $|-\rangle$. We then define the new clock qubit based on the transition between $|g, m_F\rangle$ and $|-\rangle$ states. (b) Schematic of the cavity-mediated interactions in the dressed basis. The cavity axis is along Z and the quantization axis is along magnetic field B labeled in the plot. The additional nuclear spin state in the dressing protocol allows for coupling to two polarization modes in the cavity and enhancing the tunability of the cavity-mediated interactions.

3.4.7 Supplemental Materials: Dressing Protocol

3.4.7.1 Derivation

In Fig. 2 of the main text, we discussed state dressing protocol proposed to tune and distinguish the mass-energy equivalence from other effects. We explain the protocol in more detail. We consider three internal levels $|e, m_F\rangle$, $|g, m_F\rangle$ and $|g, m_F - 1\rangle$. A dressing laser (with Rabi frequency Ω, laser frequency ω_d) is used to couple $|e, m_F\rangle$ with $|g, m_F - 1\rangle$ states (see Fig. 3.20(a)). Due to magnetic Zeeman shifts, the clock transitions between different nuclear spins are frequency resolved, thus we assume the modification on other states are typically small. In the rotating frame of the dressing laser, the Hamiltonian of internal levels plus dressing laser becomes

$$\hat{H}_{I+D} = \hbar\omega_0|e, m_F\rangle + \hbar(\omega_0 + \delta)|g, m_F - 1\rangle + \frac{\hbar\Omega}{2}(|e, m_F\rangle\langle g, m_F - 1| + \text{H.c.}), \tag{3.125}$$

where $\delta = \omega_d - \omega_0 - \omega_Z$ is the detuning of the dressing laser, and ω_Z the Zeeman shift between $|g, m_F\rangle$ and $|g, m_F - 1\rangle$ states. We set the energy of $|g, m_F\rangle$ state to 0. The eigenstates of this Hamiltonian are given by

$$|+\rangle = C_1|e, m_F\rangle + C_2|g, m_F - 1\rangle, \quad E_+/\hbar = \omega_0 + \frac{\delta}{2} + \frac{1}{2}\sqrt{\Omega^2 + \delta^2}, \tag{3.126}$$

$$|-\rangle = -C_2|e, m_F\rangle + C_1|g, m_F - 1\rangle, \quad E_-/\hbar = \omega_0 + \frac{\delta}{2} - \frac{1}{2}\sqrt{\Omega^2 + \delta^2}, \tag{3.127}$$

where

$$C_1 = \frac{1}{\sqrt{2}}\left(1 - \frac{\delta}{\sqrt{\Omega^2 + \delta^2}}\right)^{1/2}, \quad C_2 = \frac{1}{\sqrt{2}}\left(1 + \frac{\delta}{\sqrt{\Omega^2 + \delta^2}}\right)^{1/2}. \tag{3.128}$$

Since $\omega_Z \ll \omega_0$, we can ignore the mass difference between $|g, m_F\rangle$ and $|g, m_F - 1\rangle$ states. The corrections from the second order Doppler shift $\hat{H}_{\mathrm{SDS}}$ and gravitational redshift $\hat{H}_{\mathrm{GRS}}$ take the following form,

$$\hat{H}_{\mathrm{SDS}} = -\hbar\omega_0 \frac{\hat{\mathbf{P}}^2}{2M^2c^2}|e\rangle\langle e|, \quad \hat{H}_{\mathrm{GRS}} = \hbar\omega_0 \frac{gZ}{c^2}|e\rangle\langle e|. \tag{3.129}$$

Since $\hat{H}_{\mathrm{SDS}}$ and $\hat{H}_{\mathrm{GRS}}$ are much smaller than the energy gap $\sqrt{\Omega^2 + \delta^2}$, we can restrict the dynamics within the effective two level system formed by $|g, m_F\rangle$ and $|-\rangle$ states if tuning the clock laser frequency resonant with this transition. In this case we define the projection operator

$$\hat{\mathcal{P}} = |-\rangle\langle -| + |g, m_F\rangle\langle g, m_F|. \tag{3.130}$$

Using the projection operator, $\hat{H}_{\mathrm{SDS}}$ and $\hat{H}_{\mathrm{GRS}}$ become

$$\hat{\mathcal{P}}\hat{H}_{\mathrm{SDS}}\hat{\mathcal{P}} = -\hbar\omega_0 \frac{\hat{\mathbf{P}}^2}{2M^2c^2}|C_2|^2|-\rangle\langle -|, \quad \hat{\mathcal{P}}\hat{H}_{\mathrm{GRS}}\hat{\mathcal{P}} = \hbar\omega_0 \frac{gZ}{c^2}|C_2|^2|-\rangle\langle -|, \tag{3.131}$$

which is equivalent to a modification of the mass defect,

$$\Delta M = |C_2|^2 \Delta M_0, \tag{3.132}$$

where $\Delta M_0 = \hbar\omega_0/c^2$ is the mass defect without the dressing protocol. The GRS leads to a position-dependent correction of the dressed state energy E_- (we do not include the second order Doppler shift for simplicity),

$$E_-(Z) = E_- + \frac{\hbar\omega_0 g}{c^2}|C_2|^2 Z. \tag{3.133}$$

which can be resolved via clock spectroscopy in the effective two level system formed by $|g, m_F\rangle$ and $|-\rangle$ states.

All the discussion above is in the rotating frame of the dressing laser. When an atom is in the state $|-\rangle$, the probability to populate the excited clock state is $|C_2|^2$ and therefore in the lab frame it has an average energy $\approx |C_2|^2\hbar\omega_0$. This is another way to understand how the dressing laser enables the tunability of the mass defect ΔM.

3.4.7.2 Technical considerations

Due to experimental imperfection, spatial inhomogeneities exist for the atomic frequency and the parameters δ and Ω in E_-. The effects of gravitational redshiftthe GRS will be washed out if the inhomogeneities are much larger than the redshift value. For 1 cm spatial separation, the GRS is at the order of mHz, thus one needs to control the inhomogeneities below 10^{-4} Hz for direct observation of the GRS.

Relating the single atom energies, the leading order contribution are from position-dependent Zeeman shifts due to spatial inhomogeneties is the magnetic field. One can suppress first order Zeeman shifts by probing opposite nuclear spin states and calculating the averaged frequency, which has been already demonstrated in Ref. [23]. The same idea also works for the dressing protocol. One can average the transition frequency of $|g, m_F\rangle \leftrightarrow (-C_2|e, m_F\rangle + C_1|g, m_F - 1\rangle)$ and $|g, -m_F\rangle \leftrightarrow (-C_2|e, -m_F\rangle + C_1|g, -m_F + 1\rangle)$. Without shot-to-shot fluctuations, this approach allows for exact cancellation of the effects from magnetic field gradients.

Since the GRS behaves like a magnetic field gradient across the atomic sample in the case of two-level systems, it is important to distinguish it from any residual magnetic field gradient. Suppose there is no gravitational redshift in the system, and there is a small magnetic field gradient term adding on top of a constant magnetic field, then we have $\omega_0(Z) = \omega_0 + (\eta_e - \eta_g)m_F Z$, $\omega_Z(Z) = \omega_Z + \eta_g Z$, where $\eta_e = -\mathcal{G}_{^3P_0}\mu_B\partial_Z B$, $\eta_g = -\mathcal{G}_{^1S_0}\mu_B\partial_Z B$, with $\mathcal{G}_{^3P_0}$ and $\mathcal{G}_{^1S_0}$ representing the Landé g-factors, and μ_B is the Bohr magneton. So the first-order perturbation correction of the energy of the $|-\rangle$ state is given by

$$E_-(Z) = E_- + \left[|C_2|^2(\eta_e - \eta_g)m_F - |C_1|^2\eta_g\right]Z. \tag{3.134}$$

Since $\eta_g \neq 0$, we find different dependence by varying δ compared to the gravitational redshift (see Eq. (3.133)). The reason is that different ground-state nuclear spins have the same mass but different Zeeman shifts.

As for the dressing laser Rabi frequency Ω, the leading order contributions are from the spatial profile of the laser beam. If we denote the modification of Ω as $\Delta\Omega$, the change of E_- is

given by

$$\Delta E_-/\hbar = -\frac{1}{2}\sqrt{\Omega^2+\delta^2}\left(1+\frac{(\Delta\Omega)\Omega}{\Omega^2+\delta^2}\right). \tag{3.135}$$

For ^{87}Sr atoms, the Zeeman shifts between nuclear spin states are at the order of 10^2 Hz, in order to frequency resolve a single transition between nuclear spin states, we have $\Omega/2\pi \sim 10$ Hz. So the requirement $\Delta\Omega/2\pi < 10^{-4}$ Hz is equivalent to $\Delta\Omega/\Omega < 10^{-5}$. In principle, this requirement is achievable using an ultrastable cavity, which allows for precise control of the spatial mode of the dressing laser. An alternative approach is to reduce this requirement is to notice that the change of E_+ due to $\Delta\Omega$ as the opposite sign,

$$\Delta E_+/\hbar = \frac{1}{2}\sqrt{\Omega^2+\delta^2}\left(1+\frac{(\Delta\Omega)\Omega}{\Omega^2+\delta^2}\right). \tag{3.136}$$

If we average the transition frequency of $|g,m_F\rangle \leftrightarrow |-\rangle$ and $|g,m_F\rangle \leftrightarrow |+\rangle$, we get

$$\frac{E_-(Z)+E_+(Z)}{2} = \hbar\omega_0 + \frac{\hbar\delta}{2} + \frac{1}{2}\frac{\hbar\omega_0 g}{c^2}Z. \tag{3.137}$$

In this way, the averaged transition frequency becomes independent of Ω. Even though one sacrifices the full tunability of gravitational redshift, it is still changed to half of its value without dressing.

3.4.7.3 Contact interactions

Here we analyze the effects of the dressing protocol on the interatomic s-wave interactions. We start from the following second quantized Hamiltonian describing the s-wave interaction of alkaline earth atoms due to SU(n) symmetry [25],

$$\begin{aligned}
\hat{H}_s = &\frac{2\pi\hbar^2 a_{gg}}{M}\sum_{\substack{mm'\\(m\neq m')}}\int \mathrm{d}^3\mathbf{R}\,\hat{\psi}^\dagger_{gm}(\mathbf{R})\hat{\psi}^\dagger_{gm'}(\mathbf{R})\hat{\psi}_{gm'}(\mathbf{R})\hat{\psi}_{gm}(\mathbf{R})\\
&+\frac{2\pi\hbar^2 a_{ee}}{M}\sum_{\substack{mm'\\(m\neq m')}}\int \mathrm{d}^3\mathbf{R}\,\hat{\psi}^\dagger_{em}(\mathbf{R})\hat{\psi}^\dagger_{em'}(\mathbf{R})\hat{\psi}_{em'}(\mathbf{R})\hat{\psi}_{em}(\mathbf{R})\\
&+\frac{2\pi\hbar^2(a^-_{eg}+a^+_{eg})}{M}\sum_{mm'}\int \mathrm{d}^3\mathbf{R}\,\hat{\psi}^\dagger_{gm}(\mathbf{R})\hat{\psi}^\dagger_{em'}(\mathbf{R})\hat{\psi}_{em'}(\mathbf{R})\hat{\psi}_{gm}(\mathbf{R})\\
&+\frac{2\pi\hbar^2(a^-_{eg}-a^+_{eg})}{M}\sum_{mm'}\int \mathrm{d}^3\mathbf{R}\,\hat{\psi}^\dagger_{gm}(\mathbf{R})\hat{\psi}^\dagger_{em'}(\mathbf{R})\hat{\psi}_{em}(\mathbf{R})\hat{\psi}_{gm'}(\mathbf{R}).
\end{aligned} \tag{3.138}$$

Here m is the label of nuclear spins $-F, -F+1, \cdots, F$, and a_{gg}, a_{ee}, a_{eg}^{-} and a_{eg}^{+} are the s-wave scattering lengths.

Assuming the frequency difference between nuclear spins (Zeeman shifts) and energy gap $\sqrt{\Omega^2+\delta^2}$ between two dressed states are typically larger than the interaction strength, one can restrict the dynamics within two levels, $|\downarrow\rangle \equiv |g, m_F\rangle$ and $|\uparrow\rangle \equiv |-\rangle$. Projecting the interaction Hamiltonian into these two states (see Eq. (3.130)), we have

$$\hat{\mathcal{P}}\hat{H}_s\hat{\mathcal{P}} = \frac{4\pi\hbar^2}{M}\left(|C_1|^2 a_{gg} + |C_2|^2 a_{eg}^{-}\right)\int \mathrm{d}^3\mathbf{R}\,\hat{\psi}_{\uparrow}^{\dagger}(\mathbf{R})\hat{\psi}_{\downarrow}^{\dagger}(\mathbf{R})\hat{\psi}_{\downarrow}(\mathbf{R})\hat{\psi}_{\uparrow}(\mathbf{R}). \tag{3.139}$$

In this way, we modify the on-site interaction strength U by

$$\frac{U}{U_0} = \frac{|C_1|^2 a_{gg} + |C_2|^2 a_{eg}^{-}}{a_{eg}^{-}}. \tag{3.140}$$

3.4.7.4 Cavity-mediated interactions

Here we analyze the effects of the dressing protocol on the cavity-mediated interactions. Refs. [35, 192] provide a detailed discussion of cavity-mediated interactions for multilevel alkaline earth atoms. Here we focus on the case that the quantization axis for nuclear spins is perpendicular to the cavity axis (see Fig. 3.20(b)). In this case, the two polarization modes supported by the cavity can drive the π transition and the linear combination of σ^+ and σ^- transitions, so we can define the multilevel raising operators for these two polarization modes,

$$\hat{\Pi}^{+} = \sum_{jm} C_m^0 |e_m\rangle_j\langle g_m|, \quad \hat{\Sigma}^{+} = \sum_{jm}\frac{i}{\sqrt{2}}(C_m^{-1}|e_{m-1}\rangle_j\langle g_m| + C_m^{+1}|e_{m+1}\rangle_j\langle g_m|), \tag{3.141}$$

where j is the label of atoms, m is the label of nuclear spins, and $C_m^{\sigma} \equiv \langle F, m; 1, \sigma | F, m+\sigma\rangle$ are the Clebsch-Gordan coefficients. Based on Ref. [192], the multilevel exchange interactions take the following form,

$$\hat{H}_c/\hbar = \chi(\hat{\Pi}^{+}\hat{\Pi}^{-} + \hat{\Sigma}^{+}\hat{\Sigma}^{-}), \tag{3.142}$$

with $\hat{\Pi}^{-} = (\hat{\Pi}^{-})^{\dagger}$ and $\hat{\Sigma}^{-} = (\hat{\Sigma}^{-})^{\dagger}$.

Assuming the frequency difference between nuclear spins (Zeeman shifts) and energy gap $\sqrt{\Omega^2+\delta^2}$ between two dressed states are typically larger than the interaction strength χN, one

can restrict the dynamics within two levels, $|\downarrow\rangle \equiv |g, m_F\rangle$ and $|\uparrow\rangle \equiv |-\rangle$. In this two-level system, one can define collective spin operators, $\hat{S}^+ = \sum_j |\uparrow\rangle_j\langle\downarrow|$, $\hat{S}^- = (\hat{S}^+)^\dagger$, and $\hat{S}^z = \sum_j (|\uparrow\rangle_j\langle\uparrow| - |\downarrow\rangle_j\langle\downarrow|)/2$. Projecting $\hat{H}_c$ into this two-level system (see Eq. (3.130)), we get

$$\hat{\mathcal{P}}\hat{H}_c\hat{\mathcal{P}} = \chi(C^0_{m_F})^2|C_2|^2\hat{S}^+\hat{S}^- + \chi\frac{(C^{+1}_{m_F-1})^2}{2}|C_1|^2|C_2|^2\left(\frac{N}{2} + \hat{S}^z\right)^2. \tag{3.143}$$

In this way, we modify $J_\perp$ and J_z by

$$J_\perp = \chi(C^0_{m_F})^2|C_2|^2, \quad J_z = \chi\frac{(C^{+1}_{m_F-1})^2}{2}|C_1|^2|C_2|^2. \tag{3.144}$$

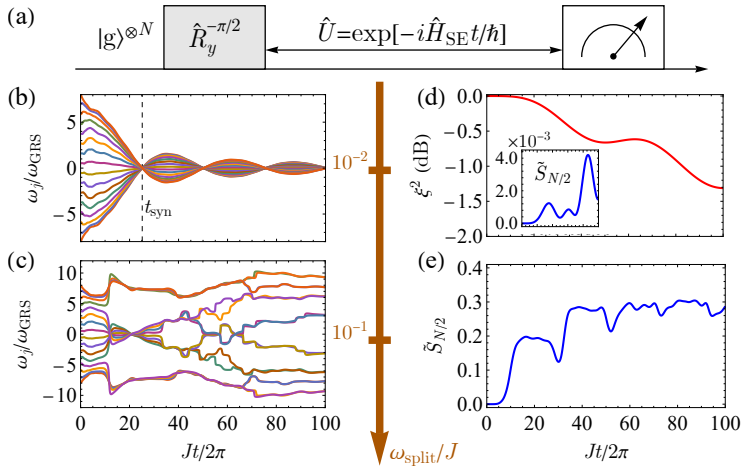

Figure 3.21: Interplay between contact interactions and redshift. (a) We prepare a product state with all atoms in $|g\rangle$ state and apply a laser pulse $\hat{R}_y^{-\pi/2} = \exp\left(i\frac{\pi}{2}\hat{S}^y\right)$ to start the dynamics. We focus on a single tube with $N = 16$ atoms evolving under the Hamiltonian $\hat{H}_{\rm SE}$ (Eq. (3.145)), and then perform measurements for each atom. (b) Individual atomic frequency shift ω_j with $\omega_{\rm split}/NJ_\perp = 10^{-2}$. Synchronization of atomic frequencies can be reach at time $t_{\rm syn}$. (c) Individual atomic frequency shift ω_j with $\omega_{\rm split}/NJ_\perp = 10^{-1}$. Global synchronization fails to occur in this regime. (d) Spin squeezing parameter ξ^2 and normalized Rényi entropy $\tilde{S}_{N/2}$ in the case of (b). (e) Normalized Rényi entropy $\tilde{S}_{N/2}$ in the case of (c). The interplay between cavity-meditated interactions and gravitational redshift can lead to entanglement generation for both cases.

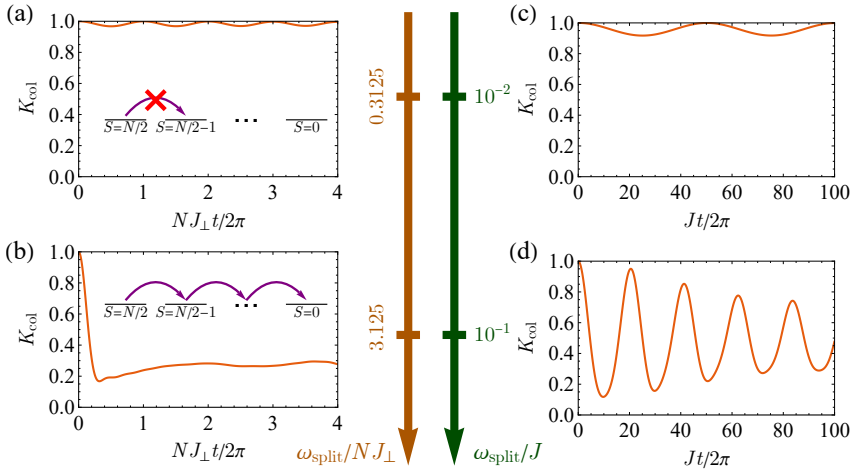

Figure 3.22: We evolve the system based on the time sequence in Fig. 3 in the main text and calculate the expectation value $K_{\rm col} = \langle \hat{\mathbf{S}} \cdot \hat{\mathbf{S}} \rangle / [\frac{N}{2}(\frac{N}{2}+1)]$ as a function of evolution time. (a,b) We consider Hamiltonian of cavity-mediated interactions $\hat{H}_{\rm cav}$ with $J_\perp = J_z$ (Eq. (5) in the main text). The choice of parameters is the same as Fig. 3.21. (c,d) We consider Hamiltonian of nearest-neighbor superexchange interaction $\hat{H}_{\rm SE}$ (Eq. (3.145)). The choice of parameters is the same as Fig. 3 in the main text.

3.4.8 Supplemental Matertials: Additional numerical results

In the main text, we have shown that frequency synchronization and entanglement generation can be achieved due to the interplay between cavity-mediated interactions and gravitational redshift. Here we show that similar phenomena can be achieved if we replace cavity-mediated interactions by superexchange interactions. For simplicity, we consider the case $V_Z \ll V_X = V_Y$ for a 3D lattice with ^{87}Sr atoms in the ground band, so the system behaves as an array of independent tubes along the gravitational potential (Z axis). We assume the system is in the Mott insulator regime with one atom per lattice site, where the leading dynamics can be described by superexchange interactions mediated by motion between nearest neighbor sites [32]. The Hamiltonian within a tube can be written in terms of spin-1/2 operators $\hat{s}_j^{x,y,z} = \hat{c}_{j\beta}^\dagger \sigma_{\beta\beta'}^{x,y,z} \hat{c}_{j\beta'}$ in the two-level system defined by the dressing scheme, where $\sigma^{x,y,z}$ are Pauli matrices, $\hat{c}_{j\beta}$ is the fermionic annihilation

operator for lattice site index j and spin label $\beta = \{\uparrow, \downarrow\}$. We get

$$\hat{H}_{\mathrm{SE}}/\hbar = J \sum_j \hat{\mathbf{s}}_j \cdot \hat{\mathbf{s}}_{j+1} + \omega_{\mathrm{GRS}} \sum_j j \hat{s}_j^z, \tag{3.145}$$

where $\hbar\omega_{\mathrm{GRS}} = (\Delta M) g a_L$ is the gravitational redshift between nearest neighbor sites, and $\hbar J = 4\tau^2/U_{\mathrm{eff}}$ is the superexchange interaction strength. Here $U_{\mathrm{eff}} = (U^2 - (Mga_L)^2)/U$, with U the on-site interaction strength. Based on Eq. (3.145), a magnetic field gradient will in principle give rise to similar single-atom inhomogeneities in the Hamiltonian. The combination of the dressed states allows us to tune the value of U by coupling to different atomic collision channels (see previous sections). This assumes all the interaction strengths are smaller than dressed state energy gap $\sqrt{\Omega^2 + \delta^2}$ and Zeeman shifts between nuclear spins, to restrict dynamics within two levels. Note that mass-energy equivalence might also lead to corrections of U via modifying scattering lengths (see previous sections), while they are smaller than the current uncertainty of interaction parameters [109].

In Fig. 3.21, we perform the same analysis as Fig. 3 in the main text, while replacing cavity-mediated interactions $\hat{H}_{\mathrm{cav}}$ (Eq. (5) in the main text) by the nearest-neighbor superexchange interaction $\hat{H}_{\mathrm{SE}}$ (see Eq. (3.145)). Since the initial state is an eigenstate of the interaction terms, and the interplay between interaction and gravitational redshift can lead to quantum dynamics away from this eigenstate and generate quantum entanglement, similar to the phenomena discussed in Fig. 3 in the main text. In the interaction dominant regime, we find frequency synchronization and spin squeezing generation due to many-body gap protection. While in the regime where the interaction strength is comparable with the gravitational redshift, frequency synchronization fails to occur, and we find a faster growth of normalized Rényi entropy.

In contrast to the cavity-mediated interactions discussed in the main text, the spin wave analysis (see the next section) of superexchange interaction shows a scaling of $\Delta E \propto J/N^2$ for the many-body gap and $Jt_{\mathrm{syn}} \propto N^2$ for the synchronization time. For the typical OLC setup [32], the frequency synchronization can be reached within 1 s for a tube with $N = 16$. Considering the 3D lattice with an array of independent tubes, the total atom number would be $16^3 = 4096$, which is

at the same order of magnitude as the atom number in Ref. [32].

In Fig. 3.22, we use the same time sequence as Fig. 3 in the main text, and calculate the expectation value $\langle \hat{\mathbf{S}} \cdot \hat{\mathbf{S}} \rangle$ as a function of the evolution time. Note that in a given total spin-S manifold, we have $\langle \hat{\mathbf{S}} \cdot \hat{\mathbf{S}} \rangle = S(S+1)$. So $\langle \hat{\mathbf{S}} \cdot \hat{\mathbf{S}} \rangle$ can serve as a measure of population in the collective manifold ($S = N/2$), spin-wave manifold ($S = N/2 - 1$), as well as the manifolds with lower total spin. We consider both nearest-neighbor superexchange interaction $\hat{H}_{\mathrm{SE}}$ (Eq. (3.145)) and cavity-mediated interaction $\hat{H}_{\mathrm{cav}}$ with $J_\perp = J_z$ (Eq. (5) in the main text). In the interaction dominant regime where frequency synchronization can occur, we find undamped oscillations between the collective manifold ($S = N/2$) and the spin-wave manifold ($S = N/2 - 1$). In the other regime where frequency synchronization fails to occur, the system can evolve to manifolds with lower total spin.

3.4.9 Supplemental Materials: Analytic results for frequency synchronization

In the main text, we discuss the interplay between atomic interactions (contact interaction or cavity mediated interactions) and gravitational redshift. Here we would like to provide analytic spin-wave calculations based on two different approaches, including Holstein–Primakoff approximation and restriction of dynamics within collective and spin-wave manifold. We focus on the single chain of N atoms and consider each atom as a spin-1/2 particle with operators $\hat{s}_n^{x,y,z}$, and in this case we also use N to label the number of lattice sites. Based on our protocol in Fig. 3 and Fig. 4 in the main text, the frequency of each atom $\omega_n(t)$ can be estimated by

$$\omega_n(t) = \frac{1}{t} \arctan\left(\frac{\langle \hat{s}_n^y(t) \rangle}{\langle \hat{s}_n^x(t) \rangle} \right). \tag{3.146}$$

The rigorous definition of the synchronization time t_{syn} is the time for the first minimum in the variance of atomic frequencies. In fact, we can approximately reach the zero crossing of $\omega_n(t)$ for all the n at t_{syn}, as demonstrated by the analytic results below and by numerical evidences.

3.4.9.1 Holstein–Primakoff approximation

We would like to use Holstein–Primakoff approximation to describe the case with an unentangled initial state (see Fig. 3 in the main text). Considering the initial state with all N spins pointing to $+x$ direction, we can approximate the spin-1/2 operators as

$$\hat{s}_n^x = \frac{1}{2} - \hat{a}_n^\dagger \hat{a}_n, \quad \hat{s}_n^y \approx \frac{\hat{a}_n + \hat{a}_n^\dagger}{2}, \quad \hat{s}_n^z \approx \frac{\hat{a}_n - \hat{a}_n^\dagger}{2i}. \tag{3.147}$$

In this way, the initial state becomes the vacuum state of all these bosonic operators. In the following, we will plug these bosonic operators into the Hamiltonian and keep the terms up to quadratic order of bosonic operators. We then apply Fourier transform to obtain the bosonic operators for spin waves $k = 2\pi m/N$ with $m = 0, 1, 2, \cdots, N-1$,

$$\hat{a}_n = \frac{1}{\sqrt{N}} \sum_k e^{ikn} \hat{a}_k, \quad \hat{a}_n^\dagger = \frac{1}{\sqrt{N}} \sum_k e^{-ikn} \hat{a}_k^\dagger, \tag{3.148}$$

and rewrite the Hamiltonian accordingly. The validity of Holstein–Primakoff approximation requires $\langle \hat{a}_n \rangle \ll 1$ for all n. If we define η as the ratio between the maximum redshift in the array ($\omega_{\text{split}} = (N-1)\omega_{\text{GRS}}$) and the smallest spin wave excitation gap (discussed below), the typical condition for validity would be $\eta \ll 1$. In this regime, the frequency of each atom $\omega_n(t)$ can be approximated as

$$\omega_n(t) \approx \frac{2\langle \hat{s}_n^y(t) \rangle}{t}. \tag{3.149}$$

Nearest-neighbor Heisenberg interactions

Here we consider the Hamiltonian for nearest-neighbor Heisenberg interactions,

$$\hat{H}_1/\hbar = J \sum_{n=0}^{N-2} \hat{\mathbf{s}}_n \cdot \hat{\mathbf{s}}_{n+1} + \omega_{\text{GRS}} \sum_{n=0}^{N-1} \left(n - \frac{N-1}{2} \right) \hat{s}_n^z, \tag{3.150}$$

in which we set the average value of gravitational redshift to 0, based on our convention. Applying the Holstein–Primakoff bosons and keeping the terms up to quadratic order, the Hamiltonian in terms of the spin-wave operators becomes

$$\hat{H}_1/\hbar \approx -J \sum_{k \neq 0} \Big(1 - \cos(k) \Big) \hat{a}_k^\dagger \hat{a}_k + \frac{\omega_{\text{GRS}}}{2i} \sqrt{N} \sum_{k \neq 0} \left(\frac{1}{e^{ik} - 1} \hat{a}_k - \frac{1}{e^{-ik} - 1} \hat{a}_k^\dagger \right). \tag{3.151}$$

For simplicity, we ignore the boundary effect in the formula above. Solving the Heisenberg equation of motion for $\hat{a}_k$ with $k \neq 0$, one can finally reach

$$\omega_n(t) \approx -\frac{\omega_{\mathrm{GRS}}}{2} \sum_{k\neq 0} \frac{\sin\Big(J(1-\cos(k))t\Big)}{J(1-\cos(k))t} \frac{\sin\Big(kn+k/2\Big)}{\sin(k/2)}. \tag{3.152}$$

In the limit of $t \to 0$, we have

$$\omega_n(0) = -\frac{\omega_{\mathrm{GRS}}}{2} \sum_{k\neq 0} \frac{\sin(kn+k/2)}{\sin(k/2)} = -\frac{\omega_{\mathrm{GRS}}}{2} \sum_{k\neq 0} \left(1 + 2\sum_{j=1}^{n} \cos(jk)\right) = \omega_{\mathrm{GRS}}\left(n - \frac{N-1}{2}\right), \tag{3.153}$$

which agrees with the gravitational redshift value without interactions.

Since the energy gap of spin wave excitation has the smallest value at $k = 2\pi/N$ and $k = 2\pi(N-1)/N$, so the system dynamics is dominated by these two spin wave modes. Therefore, one can conclude that the frequency synchronization occurs at $J(1-\cos(2\pi/N))t \approx Jt/2(2\pi/N)^2 = \pi$ which gives

$$Jt_{\mathrm{syn}} \approx \frac{N^2}{2\pi}. \tag{3.154}$$

In fact, the Jt_{syn} we found numerically is larger by nearly a factor of 4 compared to what we predicted here, since the boundary effect we ignored in the analytic calculation is equivalent to a reduction of spin wave gap. Nevertheless, we are able to capture the N-scaling of t_{syn} (see Fig. 3.23(a) for numerical calculations). To ensure the validity of the Holstein–Primakoff approximation, we have

$$\eta \sim \frac{\omega_{\mathrm{GRS}}}{J} N^3 \ll 1, \tag{3.155}$$

which in principle sets a limit for the largest possible system size.

Within the Holstein–Primakoff approximation, the deviation of $\omega_n(t_{\mathrm{syn}})$ from 0 originates from the non-vanishing contribution of other spin wave modes. Based on Eq. (3.152), we can estimate $\sin\left(J(1-\cos(k))t_{\mathrm{syn}}\right)/(J(1-\cos(k))t_{\mathrm{syn}}) \sim O(N^{-2})$, which gives

$$\frac{\omega_n(t_{\mathrm{syn}})}{\omega_n(0)} \sim O\left(\frac{1}{N^2}\right). \tag{3.156}$$

Collective Heisenberg interactions

Here we consider the Hamiltonian for collective Heisenberg interactions,

$$\hat{H}_2/\hbar = J_\perp \sum_{n=0}^{N-1}\sum_{m=0}^{N-1} \hat{\mathbf{s}}_n \cdot \hat{\mathbf{s}}_m + \omega_{\mathrm{GRS}} \sum_{n=0}^{N-1} \left(n - \frac{N-1}{2}\right)\hat{s}_n^z. \tag{3.157}$$

Applying the Holstein–Primakoff bosons and keeping the terms up to quadratic order, the Hamiltonian in terms of spin wave operators becomes

$$\hat{H}_2/\hbar \approx -NJ_\perp \sum_{k\neq 0} \hat{a}_k^\dagger \hat{a}_k + \frac{\omega_{\mathrm{GRS}}}{2i}\sqrt{N}\sum_{k\neq 0}\left(\frac{1}{e^{ik}-1}\hat{a}_k - \frac{1}{e^{-ik}-1}\hat{a}_k^\dagger\right). \tag{3.158}$$

Solving the Heisenberg equation of motion for $\hat{a}_k$ with $k \neq 0$, one can finally reach

$$\omega_n(t) \approx -\frac{\omega_{\mathrm{GRS}}}{2}\frac{\sin\left(NJ_\perp t\right)}{NJ_\perp t}\sum_{k\neq 0}\frac{\sin\left(kn + k/2\right)}{\sin(k/2)} = \omega_{\mathrm{GRS}}\frac{\sin\left(NJ_\perp t\right)}{NJ_\perp t}\left(n - \frac{N-1}{2}\right). \tag{3.159}$$

Similarly, $\omega_n(0)$ agrees with the gravitational redshift value without interactions. As for the frequency synchronization, it happens at $NJ_\perp t = \pi$, which gives

$$J_\perp t_{\mathrm{syn}} = \frac{\pi}{N}. \tag{3.160}$$

This analytic result agrees with the numerical simulations (see Fig. 3.23(b)). To ensure the validity of the Holstein–Primakoff approximation, we have

$$\eta \sim \frac{\omega_{\mathrm{GRS}}}{J_\perp} \ll 1, \tag{3.161}$$

which is independent of the system size. Within the Holstein–Primakoff approximation, there is no deviation of $\omega_n(t_{\mathrm{syn}})$ from 0.

3.4.9.2 Restriction within collective and spin-wave manifold for two large spins

For the case with an entangled initial state, it is not possible to use the Holstein–Primakoff approximation. Alternatively, we would like to simplify the Hamiltonian into two large spins ($S_1 = S_2 = N/4$) with effective Heisenberg interaction strength J_{eff} and effective redshift value ω_{eff},

$$\hat{H}_{\mathrm{eff}}/\hbar = 2J_{\mathrm{eff}}\hat{\mathbf{S}}_1 \cdot \hat{\mathbf{S}}_2 + \frac{\omega_{\mathrm{eff}}}{2}(\hat{S}_1^z - \hat{S}_2^z). \tag{3.162}$$

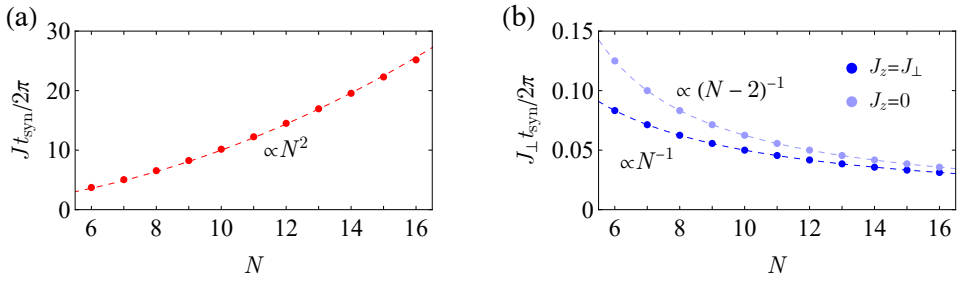

Figure 3.23: Scaling of synchronization time $t_{\rm syn}$ as a function of atom number N for (a) contact interactions and (b) cavity-medited interactions. In (b), we compare the $t_{\rm syn}$ between collective Heisenberg interactions ($J_z = J_\perp$) and spin exchange interactions ($J_z = 0$). All the calculations are based on an initial unentangled state with all the spins pointing to $+x$ direction. See the protocol in Fig. 3(a) in the main text.

In the regime $\omega_{\rm eff} \ll N J_{\rm eff}$, we can restrict the dynamics within the collective manifold with total spin $S = N/2$ as well as the spin-wave manifold with total spin $S = N/2 - 1$. Based on the Clebsch-Gordan coefficients, the states in the collective manifold ($S = N/2$) can be expressed as

$$|N/2, m\rangle = \sum_{m_1} \sqrt{\frac{\binom{N/2}{N/4+m_1}\binom{N/2}{N/4+m-m_1}}{\binom{N}{N/2+m}}} |N/4, m_1\rangle_1 |N/4, m-m_1\rangle_2, \tag{3.163}$$

and the states in the spin-wave manifold ($S = N/2 - 1$) can be expressed as

$$|N/2-1, m\rangle = \sum_{m_1} (2m_1 - m) \sqrt{\frac{\binom{N/2}{N/4+m_1}\binom{N/2}{N/4+m-m_1}}{N\binom{N-2}{N/2-1+m}}} |N/4, m_1\rangle_1 |N/4, m-m_1\rangle_2, \tag{3.164}$$

where $\binom{n}{k}$ are binomial coefficients. A key observation from Eq. (3.163) and Eq. (3.164) is that

$$(\hat{S}_1^z - \hat{S}_2^z)|N/2, m\rangle = \sqrt{\frac{(N/2+m)(N/2-m)}{N-1}} |N/2-1, m\rangle. \tag{3.165}$$

If we restrict the dynamics within the collective and spin-wave manifold, $\hat{H}_{\rm eff}$ can be reduced to 2×2 matrices in each m sector in the basis $\{|N/2, m\rangle, |N/2-1, m\rangle\}$,

$$\hat{H}_{{\rm eff},m}/\hbar = \begin{pmatrix} N J_{\rm eff} & \frac{\omega_{\rm eff}}{2}\sqrt{\frac{(N/2+m)(N/2-m)}{N-1}} \\ \frac{\omega_{\rm eff}}{2}\sqrt{\frac{(N/2+m)(N/2-m)}{N-1}} & 0 \end{pmatrix}. \tag{3.166}$$

Also based on Eq. (3.163) and Eq. (3.164), we have ($j = 1, 2$)

$$\begin{aligned} \hat{S}_j^+ |N/2, m\rangle = &\frac{1}{2}\sqrt{(N/2+m+1)(N/2-m)} |N/2, m+1\rangle \\ &- \frac{(-1)^j}{2}\sqrt{\frac{(N/2-m)(N/2-m-1)}{N-1}} |N/2-1, m+1\rangle, \end{aligned} \tag{3.167}$$

$$\begin{aligned}\hat{S}_j^-|N/2,m\rangle = &\frac{1}{2}\sqrt{(N/2-m+1)(N/2+m)}|N/2,m-1\rangle \\ &+\frac{(-1)^j}{2}\sqrt{\frac{(N/2+m)(N/2+m-1)}{N-1}}|N/2-1,m-1\rangle.\end{aligned} \tag{3.168}$$

Now we consider a general initial state in the collective manifold,

$$|\psi_0\rangle = \sum_m c_m|N/2,m\rangle, \tag{3.169}$$

with the constraint $\langle\psi_0|\hat{S}_n^y|\psi_0\rangle = 0$, $\langle\psi_0|\hat{S}_n^z|\psi_0\rangle = 0$. With time evolution under $\hat{H}_{\text{eff}}$, we have

$$\begin{aligned}|\psi(t)\rangle &= e^{-i\hat{H}_{\text{eff}}t/\hbar} \\ &\approx \sum_m c_m\left[e^{-iNJ_{\text{eff}}t/2}|N/2,m\rangle - i\frac{\omega_{\text{eff}}}{NJ_{\text{eff}}}\sqrt{\frac{(N/2)^2-m^2}{N-1}}\sin(NJ_{\text{eff}}t/2)|N/2-1,m\rangle\right],\end{aligned} \tag{3.170}$$

which gives

$$\begin{aligned}&\langle\psi(t)|\hat{S}_j^+|\psi(t)\rangle \\ &\approx \sum_m c_m c_{m+1}^*\Bigg[\langle N/2,m+1|\hat{S}_j^+|N/2,m\rangle \\ &- i\frac{\omega_{\text{eff}}}{NJ_{\text{eff}}}e^{iNJ_{\text{eff}}t/2}\sqrt{\frac{(N/2)^2-m^2}{N-1}}\sin(NJ_{\text{eff}}t/2)\langle N/2,m+1|\hat{S}_j^+|N/2-1,m\rangle \\ &+ i\frac{\omega_{\text{eff}}}{NJ_{\text{eff}}}e^{-iNJ_{\text{eff}}t/2}\sqrt{\frac{(N/2)^2-(m+1)^2}{N-1}}\sin(NJ_{\text{eff}}t/2)\langle N/2-1,m+1|\hat{S}_j^+|N/2,m\rangle\Bigg] \\ &= \sum_m c_m c_{m+1}^*\langle N/2,m+1|\hat{S}_j^+|N/2,m\rangle \\ &\qquad\times\left[1-(-1)^j\frac{\omega_{\text{eff}}}{NJ_{\text{eff}}}\left(i\frac{1}{2}\sin(NJ_{\text{eff}}t)-\frac{2m+1}{N-1}\sin^2(NJ_{\text{eff}}t/2)\right)\right] \\ &= \langle\psi_0|\hat{S}_j^+|\psi_0\rangle\left[1-i(-1)^j\frac{\omega_{\text{eff}}}{2}\frac{\sin(NJ_{\text{eff}}t)}{NJ_{\text{eff}}}\right]+\frac{\langle\psi_0|(\hat{S}_n^+\hat{S}^z+\hat{S}^z\hat{S}_n^+)|\psi_0\rangle}{N-1}(-1)^j\frac{\omega_{\text{eff}}}{NJ_{\text{eff}}}\sin^2(NJ_{\text{eff}}t/2).\end{aligned} \tag{3.171}$$

Therefore, we can obtain the frequency for each of the two large spins,

$$\omega_j(t) \approx (-1)^{j-1}\frac{\omega_{\text{eff}}}{2}\left(\frac{\sin(NJ_{\text{eff}}t)}{NJ_{\text{eff}}t}-2\frac{\langle\psi_0|(\hat{S}^y\hat{S}^z+\hat{S}^z\hat{S}^y)|\psi_0\rangle}{(N-1)\langle\psi_0|\hat{S}^x|\psi_0\rangle}\frac{\sin^2(NJ_{\text{eff}}t/2)}{NJ_{\text{eff}}t}\right), \tag{3.172}$$

leading to the synchronization time

$$NJ_{\text{eff}}t_{\text{syn}} = \pi - 2\arctan\left[\frac{\langle\psi_0|(\hat{S}^y\hat{S}^z+\hat{S}^z\hat{S}^y)|\psi_0\rangle}{(N-1)\langle\psi_0|\hat{S}^x|\psi_0\rangle}\right]. \tag{3.173}$$

In the following, we consider three different types of initial states:

- $|\psi_0\rangle = |+x\rangle^{\otimes N}$

  In this case we have $\langle\psi_0|(\hat{S}^y\hat{S}^z + \hat{S}^z\hat{S}^y)|\psi_0\rangle = 0$, which gives

  $$NJ_{\text{eff}}t_{\text{syn},0} = \pi. \tag{3.174}$$

  Here we use $t_{\text{syn},0}$ to label the synchronization time with this unentangled initial state. This result agrees with the prediction using the Holstein–Primakoff approximation in the previous subsection.

- $|\psi_0\rangle = e^{-iQ\hat{S}^z\hat{S}^z/N}|+x\rangle^{\otimes N}$

  In this case we have

  $$\langle\psi_0|(\hat{S}^y\hat{S}^z + \hat{S}^z\hat{S}^y)|\psi_0\rangle = \frac{N(N-1)}{2}\sin(Q/N)\cos^{N-2}(Q/N), \tag{3.175}$$

  $$\langle\psi_0|\hat{S}^x|\psi_0\rangle = \frac{N}{2}\cos^{N-1}(Q/N), \tag{3.176}$$

  which gives

  $$NJ_{\text{eff}}t_{\text{syn}} = \pi - 2Q/N. \tag{3.177}$$

  Note that the $\hat{S}^z\hat{S}^z$ term commutes with $\hat{H}_{\text{eff}}$, this result can also apply to the following Hamiltonian generated by cavity-mediated interactions,

  $$\hat{H}_{\text{cav}}/\hbar = J_\perp\hat{\mathbf{S}}\cdot\hat{\mathbf{S}} + (J_z - J_\perp)\hat{S}^z\hat{S}^z + \frac{\omega_{\text{eff}}}{2}(\hat{S}_1^z - \hat{S}_2^z), \tag{3.178}$$

  with initial state $|\psi_0\rangle = |+x\rangle^{\otimes N}$. Now we can replace J_{eff} by $J_\perp$, and Q/N by $(J_z - J_\perp)t_{\text{syn}}$, which gives

  $$\Big((N-2)J_\perp + 2J_z\Big)t_{\text{syn}} = \pi. \tag{3.179}$$

  We have shown numerical calculations for collective spin exchange interactions ($J_z = 0$) and collective Heisenberg interactions ($J_z = J_\perp$) for a 1D tube with N atoms in Fig. 3.23(b), which agrees well with the analytic results using two large spins.

- $|\psi_0\rangle = e^{-i\theta\hat{S}^x}e^{-iQ\hat{S}^z\hat{S}^z/N}|+x\rangle^{\otimes N}$

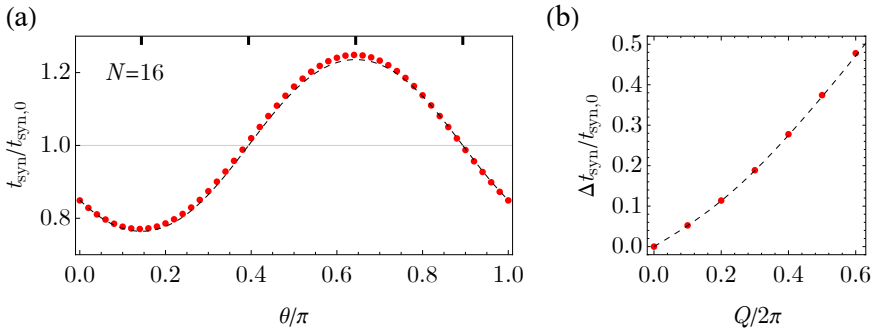

Figure 3.24: Comparison between numerical simulations of superexchange interactions $\hat{H}_{\rm SE}$ with $N = 16$ atoms in a single tube and analytic results Eq. (3.181) and Eq. (3.182). We use the same protocol as Fig. 4 in the main text. (a) The dependence of synchronization time on the rotation $\hat{R}_x^{\theta} = \exp\Big(-i\theta\hat{S}^x\Big)$ at $Q/2\pi = 0.6$. (b) The dependence of the tunable range of synchronization time on OAT shearing strength Q.

In this case we have

$$\begin{aligned}\langle\psi_0|(\hat{S}^y\hat{S}^z+\hat{S}^z\hat{S}^y)|\psi_0\rangle = \cos(2\theta)\frac{N(N-1)}{2}\sin(Q/N)\cos^{N-2}(Q/N)\\ +\sin(2\theta)\frac{N(N-1)}{8}\Big(1-\cos^{N-2}(2Q/N)\Big),\end{aligned} \tag{3.180}$$

and $\langle\psi_0|\hat{S}^x|\psi_0\rangle$ is still given by Eq. (3.176). So the tunability of synchronization time is due to the θ-rotation of $\langle\psi_0|(\hat{S}^y\hat{S}^z+\hat{S}^z\hat{S}^y)|\psi_0\rangle$. In Fig. 4 of the main text and Fig. 3.24, we find that the analytic results for two large spins can also explain the numerical simulations for collective or nearest-neighbor Heisenberg interactions, if we rewrite the formula of synchronization time $t_{\rm syn}$ and its tunable range $\Delta t_{\rm syn}$ into dimensionless form,

$$\frac{t_{\rm syn}}{t_{\rm syn,0}} = 1-\frac{2}{\pi}\arctan\left[\frac{\langle\psi_0|(\hat{S}^y\hat{S}^z+\hat{S}^z\hat{S}^y)|\psi_0\rangle}{(N-1)\langle\psi_0|\hat{S}^x|\psi_0\rangle}\right], \tag{3.181}$$

$$\frac{\Delta t_{\rm syn}}{t_{\rm syn,0}} = \frac{4}{\pi}\arctan\left[\frac{(\langle\psi_0|(\hat{S}^y\hat{S}^z+\hat{S}^z\hat{S}^y)|\psi_0\rangle_{\max}}{(N-1)\langle\psi_0|\hat{S}^x|\psi_0\rangle}\right]. \tag{3.182}$$

In the main text, we use $|\psi(\theta)\rangle$ instead of $|\psi_0\rangle$ in this case to emphasize the θ-dependence.

Chapter 4

Emergent collective behaviors and dynamical phases in interacting arrays

4.1 Overview

Understanding the non-equilibrium dynamics of a quantum many-body system is one of the most challenging problems in modern quantum science. In recent years, we have seen a tremendous progress in this direction, partly because of advances in quantum simulation which are enabling us to access fundamentally new regimes of coherent and highly excited dynamics previously inaccessible in conventional materials, such as the long-time dynamical behavior after a sudden quench (dynamical phases) [193–196], the existence and absence of thermalization [197–199], the quantum information and entanglement dynamics [200, 201], and the non-equilibrium transport [202, 203]. In this chapter, we mainly focus on the development of quantum simulation protocols for emergent collective behaviors and dynamical phases in different experimental platforms, including trapped bosonic gases and cavity QED systems. In cavity QED systems, we study a variety of problems, such as spin exchange interactions among two-level atomic spins, two-polarization couplings of multilevel atoms, as well as dispersive couplings of motional states.

4.2 Simulation of XXZ spin models using sideband transitions in trapped bosonic gases

This section is adapted from: **Anjun Chu**, Johannes Will, Jan Arlt, Carsten Klempt, Ana Maria Rey, *Simulation of XXZ spin models using sideband transitions in trapped bosonic gases*, Physical Review Letters 125, 240504 (2020).

4.2.1 Introduction

Quantum simulation of iconic models of quantum magnetism in highly controllable atomic systems is emerging as a promising way to gain new insights into fundamental many-body phenomena in condensed matter physics [63], and as a pathway to shed light onto exciting new phenomena in non-equilibrium many-body spin arrays [105, 107, 108, 204–206]. In recent years, rapid progress in the simulation of quantum spin models has been made by taking advantage of the diversity of interactions in ultracold quantum systems, including contact interactions in the motional ground state of ultracold atomic gases [3, 206], dipolar interactions in polar molecules [207], magnetic atoms [208–210] and Rydberg atoms [211], as well as photon/phonon-mediated long-range interactions in trapped ions [212] and cavity QED systems [107, 186, 213–215].

One promising avenue in this direction is the fact that non-degenerate thermal gases interacting via purely contact interactions, can emulate spin models by mapping the single-particle energy eigenstates onto a lattice in mode space [101, 108, 216, 217]. This mapping has been shown to be a powerful way to emulate long-range interacting spin models featuring large many-body energy gaps that have enabled significant enhancement of coherence time [188, 218, 219]. Nevertheless, the tunability of the spin model parameters has so far been mainly accomplished by the use of Feshbach resonances, and the atom loss associated with the latter imposes a trade-off between tunability and coherence time [108, 220].

In this work, we theoretically propose and experimentally demonstrate the use of motional sidebands in a thermal trapped gas of ^{87}Rb atoms to engineer long-range XXZ spin models with tunable spin couplings. We benchmark our simulator by probing a dynamical phase transition (DPT) between ferromagnetic and paramagnetic phases in the collective XXZ model plus additional transverse and longitudinal fields (also known as the Lipkin-Meshkov-Glick (LMG) model [105, 107, 221, 222]) via Rabi spectroscopy. We experimentally reconstruct the boundary of the dynamical phases by varying atom density and longitudinal field strength and show good agreement with mean-field theoretical predictions. At the end we also discuss the further applications of our scheme in

entanglement-enhanced metrology [30,31,74], as well as generalizations to a wide range of quantum systems.

4.2.2 Theoretical model

We consider an ensemble of thermal ^{87}Rb atoms confined in a 3D harmonic trap and prepared in the magnetically insensitive clock states $|\downarrow\rangle \equiv |F=1, m_F=0\rangle$ and $|\uparrow\rangle \equiv |F=2, m_F=0\rangle$. The contact interaction in this two-component bosonic gas can be written in the following second quantized form [224, 225],

$$\hat{H}_{\text{int}} = \sum_{\sigma\sigma'=\uparrow,\downarrow} \frac{U_{\sigma\sigma'}}{2} \int \mathrm{d}^3\mathbf{R}\, \hat{\psi}^\dagger_\sigma(\mathbf{R})\hat{\psi}^\dagger_{\sigma'}(\mathbf{R})\hat{\psi}_{\sigma'}(\mathbf{R})\hat{\psi}_\sigma(\mathbf{R}), \tag{4.1}$$

where $U_{\sigma\sigma'} = 4\pi\hbar^2 a_{\sigma\sigma'}/m$ is the interaction strength between atoms of spin σ and σ', parametrized by the s-wave scattering lengths, $a_{\uparrow\uparrow} = 94.55a_0$, $a_{\uparrow\downarrow} = 98.09a_0$, $a_{\downarrow\downarrow} = 100.76a_0$ [226]. The bosonic field operator $\hat{\psi}_\sigma(\mathbf{R})$, is expanded in the eigenmode basis of the 3D harmonic trap, $\hat{\psi}_\sigma(\mathbf{R}) = \sum_{\mathbf{n}} a_{\mathbf{n}\sigma}\phi_{\mathbf{n}}(\mathbf{R})$, where $a_{\mathbf{n}\sigma}$ annihilates a boson of spin σ in eigenmode $\mathbf{n} = \{n^X, n^Y, n^Z\}$ of the harmonic trap, with corresponding wave function $\phi_{\mathbf{n}}(\mathbf{R})$.

We understand and analyze the many-body dynamics through a mapping of the single-particle eigenstates of the 3D harmonic trap onto a 3D lattice in mode space, as depicted in Fig. 4.1(a). Notice that a blue sideband transition along the Z-direction couples the following two states in the harmonic trap, $|\Uparrow_i\rangle \equiv |\uparrow; n_i^X, n_i^Y, n_i^Z + 1\rangle$ and $|\Downarrow_i\rangle \equiv |\downarrow; n_i^X, n_i^Y, n_i^Z\rangle$. So we can visualize the states $|\Uparrow_i\rangle$ and $|\Downarrow_i\rangle$ as two spin states localized at site i in an effective 3D mode-space lattice. The wave functions associated with $|\Uparrow_i\rangle$ and $|\Downarrow_i\rangle$ states are denoted as $\phi_i^{\Uparrow}(\mathbf{R})$ and $\phi_i^{\Downarrow}(\mathbf{R})$ respectively. Similar treatments can apply to blue sideband transitions along other directions, carrier transitions as well as red sideband transitions (see SOM).

Since we are interested in the collisionless regime of a trapped atomic ensemble, where the trapping potential is much larger than the interaction strength, we assume that each atom is fixed in the mode-space lattice [101, 108, 216, 217], and that the only relevant process between two colliding atoms is to either remain in the same internal states or to exchange them. Furthermore,

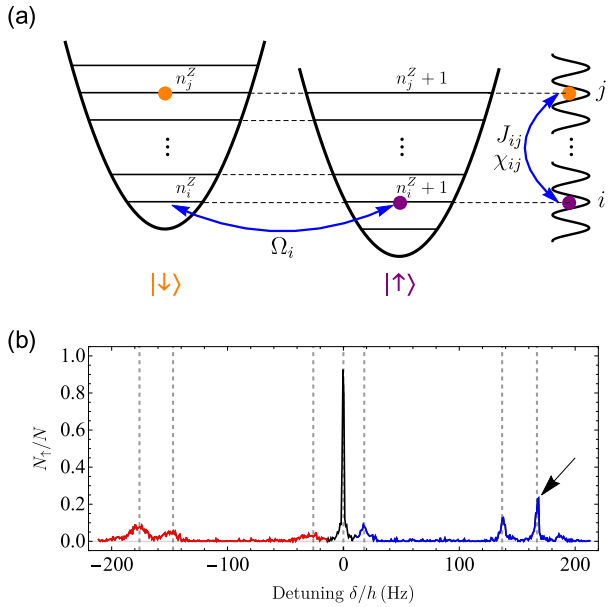

Figure 4.1: Simulating XXZ spin models using sideband transitions in a thermal bosonic gas confined in a 3D harmonic trap. (a) Schematic of the effective 3D mode-space lattice for blue Z-sideband (only the projection along the Z-direction is shown for simplicity). The states $|\Uparrow_i\rangle \equiv |\uparrow; n_i^X, n_i^Y, n_i^Z+1\rangle$ and $|\Downarrow_i\rangle \equiv |\downarrow; n_i^X, n_i^Y, n_i^Z\rangle$, which are the ones coupled by the Raman pulse with Rabi frequency Ω_i, can be regarded as the two spin states pinned at the i^{th} site of the effective 3D mode-space lattice. Contact interactions in bosonic gases generate long-range XXZ couplings J_{ij}, χ_{ij} between lattice sites i and j in mode space (see text). (b) Rabi spectrum in the resolved sideband limit for mean atom density $n = 2.0 \times 10^{12}\text{cm}^{-3}$. The black (blue, red) line represents carrier (blue sideband, red sideband) transitions. Our experiment focuses on the strongest sideband pointed out by the arrow. It is worth mentioning that the suppression of red sideband transitions is related to the anharmonic corrections in optical dipole traps, also observed in Ref. [223].

we can restrict our discussions to include either empty or singly-occupied lattice sites since the ^{87}Rb gas temperature is above quantum degeneracy (see SOM). These approximations map the contact interaction term in the Hamiltonian (see Eq.(4.1)) to a spin-1/2 long-range XXZ model in the mode-space lattice:

$$\hat{H}_{\text{int}} = \sum_{ij} J_{ij} \hat{\mathbf{S}}_i \cdot \hat{\mathbf{S}}_j + \sum_{ij} \chi_{ij} \hat{S}_i^z \hat{S}_j^z + \sum_i B_i \hat{S}_i^z. \tag{4.2}$$

Here, the spin operators can be written in terms of bosonic operators on each lattice site, $\hat{\mathbf{S}}_i = \sum_{\alpha\beta=\Uparrow,\Downarrow} \hat{a}_{i\alpha}^\dagger \boldsymbol{\sigma}_{\alpha\beta} \hat{a}_{i\beta}/2$, where $\boldsymbol{\sigma}_{\alpha\beta}$ are Pauli matrices, and $\hat{a}_{i\beta}$ annihilates a boson of spin β on lattice site i. The XXZ interaction parameters are given by $J_{ij} = V_{ij}^{\text{ex}} U_{\uparrow\downarrow}$, $\chi_{ij} = V_{ij}^{\Uparrow\Uparrow} U_{\uparrow\uparrow} + V_{ij}^{\Downarrow\Downarrow} U_{\downarrow\downarrow} - V_{ij}^{\Uparrow\Downarrow} U_{\uparrow\downarrow} - V_{ij}^{\text{ex}} U_{\uparrow\downarrow}$, and $B_i = \sum_{j\neq i} (V_{ij}^{\Uparrow\Uparrow} U_{\uparrow\uparrow} - V_{ij}^{\Downarrow\Downarrow} U_{\downarrow\downarrow})$, and are set by the overlap integral of the relevant 3D harmonic oscillator wave functions: $V_{ij}^{\alpha\beta} = \int \mathrm{d}^3\mathbf{R} [\phi_i^\alpha(\mathbf{R})]^2 [\phi_j^\beta(\mathbf{R})]^2$, and $V_{ij}^{\text{ex}} = \int \mathrm{d}^3\mathbf{R} \phi_i^\Uparrow(\mathbf{R}) \phi_i^\Downarrow(\mathbf{R}) \phi_j^\Uparrow(\mathbf{R}) \phi_j^\Downarrow(\mathbf{R})$. The tunability of spin-spin couplings depends on these overlap integrals. For carrier transitions we have $\phi_i^\Uparrow(\mathbf{R}) = \phi_i^\Downarrow(\mathbf{R}) = \langle \mathbf{R} | n_i^X, n_i^Y, n_i^Z \rangle$, and therefore $V_{ij}^{\alpha\beta} = V_{ij}^{\text{ex}}$, making the XXZ spin model equivalent to the isotropic Heisenberg model ($J_{ij} \gg \chi_{ij}$). For the sideband transitions, the wave functions are not the same for the two spin components (e.g. for the blue Z-sideband $\phi_i^\Downarrow(\mathbf{R}) = \langle \mathbf{R} | n_i^X, n_i^Y, n_i^Z \rangle$ and $\phi_i^\Uparrow(\mathbf{R}) = \langle \mathbf{R} | n_i^X, n_i^Y, n_i^Z + 1 \rangle$), and therefore the overlap integrals are no longer equal. This allows us to have larger Ising couplings χ_{ij}.

In addition to the interaction term, there are extra transverse and longitudinal fields generated by the interrogating laser. For blue sideband transitions, the single-particle Hamiltonian can be written as $\hat{H}_{\text{sp}} = \sum_i (\Omega_i \hat{S}_i^x - (\delta - \hbar\omega) \hat{S}_i^z)$, where Ω_i is the mode-dependent Rabi frequency, δ is the laser detuning from the carrier transition, and ω is the relevant trapping frequency. Both $\hat{H}_{\text{sp}}$ and $\hat{H}_{\text{int}}$ (see Eq.(4.2)) contribute to the dynamics in our XXZ simulator ($\hat{H}_{\text{XXZ}} = \hat{H}_{\text{sp}} + \hat{H}_{\text{int}}$), and the dynamics can be restricted to the fully symmetric Dicke manifold to the leading order. In this limit our model simplifies to the Lipkin-Meshkov-Glick (LMG) model [221],

$$\hat{H}_{\text{LMG}} = \chi \hat{S}^z \hat{S}^z + \Omega \hat{S}^x - \tilde{\delta} \hat{S}^z. \tag{4.3}$$

Here, $\tilde{\delta} = \delta - \hbar\omega - B$ is the effective longitudinal field, χ, Ω and B are the thermal-averaged value of χ_{ij}, Ω_i and B_i respectively, and $\hat{S}^{x,y,z} = \sum_i \hat{S}_i^{x,y,z}$ are the collective spin operators.

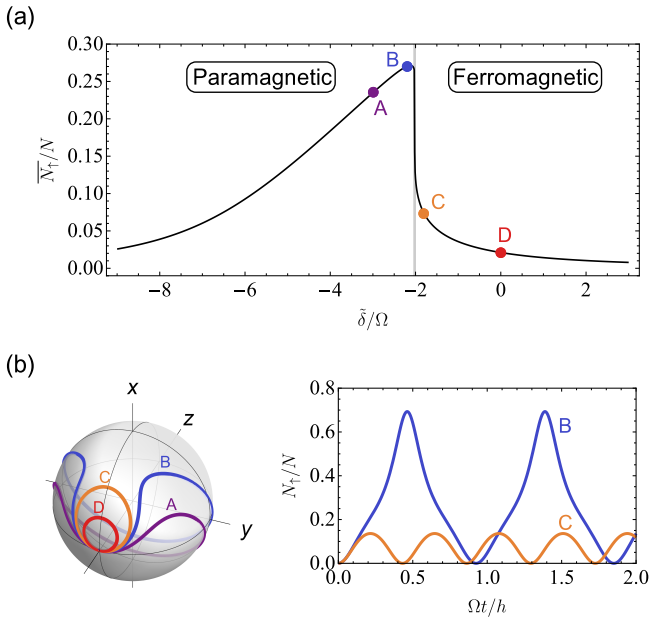

Figure 4.2: (a) Dynamical phase transition (DPT) in LMG model with $N\chi/\Omega = 5$, indicated by the sharp behavior in long-time average excitation fraction $\overline{N_\uparrow}/N$. The critical point is marked by the vertical gray line at $\tilde{\delta}/\Omega = -2.02$, separating the dynamical paramagnetic phase (left) and the dynamical ferromagnetic phase (right). (b) Mean-field dynamics of the LMG model with $\tilde{\delta}/\Omega = -3$(A), -2.2(B), -1.8(C), 0(D). The left panel shows the mean-field trajectories on the Bloch sphere, and the right panel presents the mean-field evolution of the excitation fraction for trajectory B and C. The sharp change in dynamics between trajectory B and C also signals the DPT.

The LMG model features interesting spin dynamics, including a ferromagnetic to paramagnetic dynamical phase transition (DPT) [105,107,222]. In general terms, a DPT is characterized by the existence of a critical point separating phases with distinct dynamical properties in many-body systems. The analog of thermodynamic order parameters is found in long-time average observables, which have a nonanalytic dependence on system parameters. To observe the DPT we initialize all the atoms in the $|\downarrow\rangle$ state, which is the ground state of LMG model when $\tilde{\delta} \to -\infty$, and then perform a sudden quench of the longitudinal field to its final value $\tilde{\delta}$.

In this case, the DPT is signaled by a sharp change in behavior of the long-time average excitation fraction, $\overline{N_\uparrow}/N = \lim_{T\to\infty} \frac{1}{T}\int_0^T N_\uparrow(t)/N$, which serves as an order parameter and distinguishes two dynamical phases (see Fig. 4.2(a)): A dynamical ferromagnetic phase characterized by $\overline{N_\uparrow}/N \approx 0$, where the vanishing excitation fraction persists even when the final longitudinal field $\tilde{\delta}$ is varied, and a dynamical paramagnetic phase, where $\overline{N_\uparrow}/N$ dynamically adjusts itself following the change of the final longitudinal field $\tilde{\delta}$.

To analyze the DPT we derive mean-field equations of motion for the collective spin operators. They are given by

$$\frac{\mathrm{d}}{\mathrm{d}t}\mathbf{s} = \mathbf{b}\times\mathbf{s}, \quad \mathbf{b} = \left(\Omega, 0, N\chi s^z - \tilde{\delta}\right), \tag{4.4}$$

where $s^{x,y,z} = 2\langle \hat{S}^{x,y,z}\rangle/N$ are the normalized expectation values of collective spin operators. As shown in SOM, Eq.(4.4) can be further reduced to $(\dot{s}^z)^2/2 + V(s^z) = 0$ by eliminating s^x and s^y, and we can relate the DPT with an abrupt change in the number of real roots of the effective potential $V(s^z)$ in this form. The abrupt change in $V(s^z)$ gives rise to distinct properties in spin dynamics shown in Fig. 4.2(b): The ferromagnetic phase features small oscillations near south pole (trajectory C), while the paramagnetic phase exhibits large excursions that precess around the x axis (trajectory B). The DPT can also be tuned by varying the interaction strength as shown in Fig. 4.3(d). In the interaction dominant regime ($N\chi/\Omega > 8\sqrt{3}/9$), the DPT generates a second order critical line (marked by the black solid line in Fig. 4.3(d)) that distinguishes the two dynamical phases. On the other hand, the transition evolves into a smooth crossover region in the weakly

interacting regime ($N\chi/\Omega < 8\sqrt{3}/9$, below the black dashed line in Fig. 4.3(d)), where instead the dynamics is dominated by single particle Rabi flopping.

4.2.3 Experimental results

We experimentally realize the XXZ spin model in a cloud of ^{87}Rb atoms, which is prepared at a temperature of 375(25) nK in a crossed-beam optical dipole trap with trapping frequencies of 143 Hz, 21.5 Hz and 171 Hz. This setting ensures the validity of the key approximations in our spin model, including the collisionless regime and a negligible number of doubly occupied modes (below 1.4% for 10^5 atoms). The atomic ensemble is initialized with a variable mean density n from 0.46 to $4.8 \times 10^{12}\mathrm{cm}^{-3}$ (atom number N from 0.33 to 3.4×10^5), and the atom densities are calibrated by the collisional frequency shift of the carrier transition ($-0.48\,\mathrm{Hz}/10^{12}\mathrm{cm}^{-3}$ [218]). To ensure an unperturbed cloud temperature for different atom densities, an adjustable spin rotation is performed, which partially transfers atoms from the $|\uparrow\rangle$ to the $|\downarrow\rangle$ state and a subsequent removal of the $|\uparrow\rangle$ atoms. The coherent drive between two clock states with resolved motional levels is realized by two copropagating Raman beams focused into the atomic cloud with a 39 μm beam waist. The beams are offset from the trap center in order to drive the first-order motional sidebands. The typical Rabi spectrum of our system is depicted in Fig. 4.1(b). Here we focus on the strongest blue sideband at $\omega/2\pi = 171$ Hz. Considering the mean Ising couplings ($N\chi/h \approx 4.63\,\mathrm{Hz}/10^{12}\mathrm{cm}^{-3}$) and the mean Rabi frequency ($\Omega/h \approx 0.56$ Hz) for this sideband, our XXZ simulator lies in the interaction dominant regime, where the mentioned DPT is predicted to occur. Instead of direct measurements of the long-time-averaged excitation fraction, which is inevitably limited by technical challenges (e.g. collisional dephasing and atom loss), the order parameter $\overline{N_\uparrow}/N$ is estimated by measuring the excitation fraction at a probe time $t_f = 0.5$s for fixed Rabi frequency. The entire phase diagram is then obtained by scanning the two-photon detuning δ in 0.8 Hz steps and by varying interactions using different atom densities.

The recorded asymmetric lineshapes for different atom densities are shown in Fig. 4.3(a-c, e-f), which is in good agreement with the mean-field theoretical predictions by $\hat{H}_{\mathrm{XXZ}}$ (see SOM

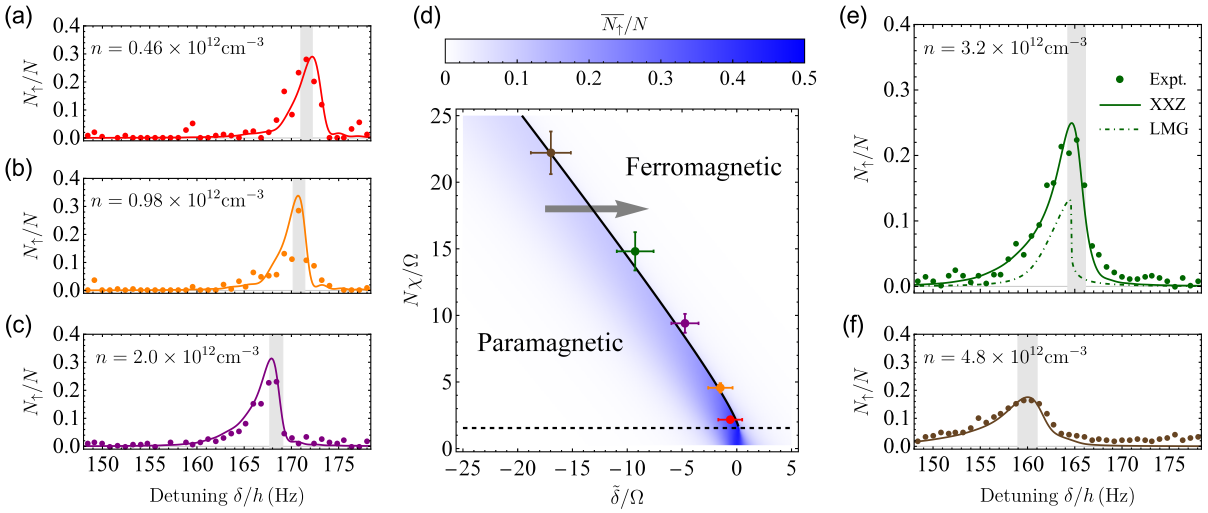

Figure 4.3: (a-c, e-f) Dynamical phase transition in the 171 Hz blue sideband with mean atom density $n = \{0.46, 0.98, 2.0, 3.2, 4.8\} \times 10^{12}\mathrm{cm}^{-3}$, indicated by the asymmetric lineshape after evolution time 0.5s. The shaded areas indicate the critical points, where the uncertainty is set by finite frequency step of detuning as well as fluctuations in atom density and Rabi frequency. The filled circles denote experimental data, the solid lines denote mean-field theoretical predictions by $\hat{H}_{\mathrm{XXZ}}$, and the green dot-dashed line in (e) denotes the order parameter $\overline{N_\uparrow}/N$ predicted by $\hat{H}_{\mathrm{LMG}}$ (see text). We do not directly add the experimental error bars to the lineshape data in (a-c, e-f) for visual reasons, and the typical statistical uncertainty in each figure is $\Delta N_\uparrow/N = \{0.038, 0.020, 0.013, 0.010, 0.011\}$ respectively. (d) Phase diagram for ferromagnetic to paramagnetic dynamical phase transition. The black solid line denotes the sharp phase boundary of DPT, the black dashed line separates the smooth crossover regime (below) with DPT regime (above), and the gray arrow illustrates the probing direction on phase diagram. The phase boundary is reconstructed from the critical points in (a-c, e-f) using the same choice of color to label data points.

for comparison in the red sideband). In Fig. 4.3(e), we also compare the experimental observation with the order parameter $\overline{N_\uparrow}/N$ (green dot-dashed line) predicted by $\hat{H}_{\mathrm{LMG}}$ (see Eq.(4.3)). We find that the recorded lineshape captures the two dynamical phases in the LMG model: if we increase the two-photon detuning δ, the slow increase of $N_\uparrow/N$ below resonance indicates the paramagnetic phase, while the sharp change back to $N_\uparrow/N \approx 0$ above resonance indicates the ferromagnetic phase. Compared to the critical behavior of $\overline{N_\uparrow}/N$ in the LMG model, the recorded lineshapes are broadened by the inhomogeneous couplings but retain the sharp features associated with the DPT. The inhomogeneities also lead to modifications of effective interaction strength in experiment compared to the LMG model, which can be accounted for by scaling χ by a factor of 0.56. By interpreting the experimentally observed resonant frequencies (obtained from maximal population transfer) as a signature of the critical point of the DPT, we reconstruct the phase boundary between these two dynamical phases (see Fig. 4.3(d)), which agrees with the theoretical prediction.

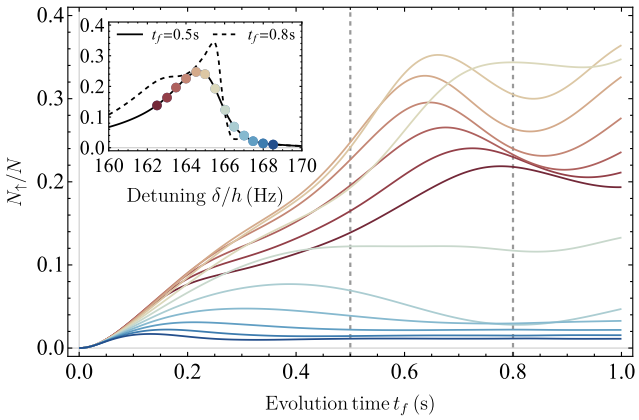

Figure 4.4: Numerical simulation of mean-field evolution under $\hat{H}_{\mathrm{XXZ}}$ with mean atom density $n = 3.2 \times 10^{12}\mathrm{cm}^{-3}$. The lines with a color gradient from red to blue show the dynamical behavior from red to blue detuning with 0.5 Hz frequency steps. A sharp change in the excited atom fraction can be observed as the system approaches the critical point. The inset compares two lineshapes taken at different evolution times.

To further verify the existence of a DPT with inhomogeneous couplings, we present numerical simulations of mean-field evolution under $\hat{H}_{\mathrm{XXZ}}$ with mean atom density $n = 3.2 \times 10^{12}\mathrm{cm}^{-3}$ in Fig. 4.4. As the detuning is scanned from below to above the critical point (marked by a color

gradient from red to blue), the excitation fraction $N_\uparrow(t)/N$ features a sharp change in dynamical behavior at the critical detuning, validating the existence of a DPT under our experimental conditions. Compared to the LMG model, we observe damping in the oscillation amplitude of excitation fraction for the inhomogeneous case. To understand the role of the damping, in the inset of Fig. 4.4 we compare the lineshapes at evolution times of $t_f = 0.5$s (see also Fig. 4.3) and $t_f = 0.8$s. Although we see variations in the lineshapes computed at these two evolution times (the latter is sharper than the former), both of them consistently display clear signatures of the DPT up to a 1 Hz shift in resonant frequency, which nevertheless lies within the experimental error bars. This analysis justifies the use of $N_\uparrow/N$ evaluated at $t_f = 0.5$s as a good proxy for the long-time-averaged order parameter.

4.2.4 Conclusion and outlook

In summary, we have demonstrated the use of motional sidebands in trapped bosonic gases as a tool to simulate long-range XXZ spin models. A practical application of the demonstrated sideband protocol is the dynamical generation of spin squeezing, a well known feature of the LMG model [31] which makes it useful for enhanced sensing. Although further control of inhomogeneties will be required to observe squeezing in the current setup, we expect spin squeezing can be in reach in the next generation of experiments (see SOM). Moreover, we expect our protocol can be feasibly implemented in a wide range of experiments, including atomic systems in optical lattices. In these systems the SU(2) symmetry of superexchange interactions could be broken into a XXZ spin model via motional sideband spectroscopy, thanks to the larger tunneling rates of excited bands.

4.2.5 Supplemental Materials: Experimental realization

To initiate our experiments, ultracold ^{87}Rb atoms are captured in a magneto-optical trap loaded from a background gas. The captured atoms are subsequently transported to a vacuum region with reduced pressure, where they are cooled by forced evaporative cooling. Initial cooling is performed in a hybrid trap that combines a magnetic quadrupole trap with an optical dipole

potential [227]. The final temperatures are achieved by evaporation in a pure optical dipole trap. This trap is formed by two laser beams at a wavelength of 1064 nm, which intersect at an angle of 18° as shown in Fig. 4.5(a). The two beams have waists of 60 and 75 μm, which provide a nearly harmonic trapping potential with trapping frequencies of 143 Hz, 21.5 Hz and 171 Hz at the chosen laser power.

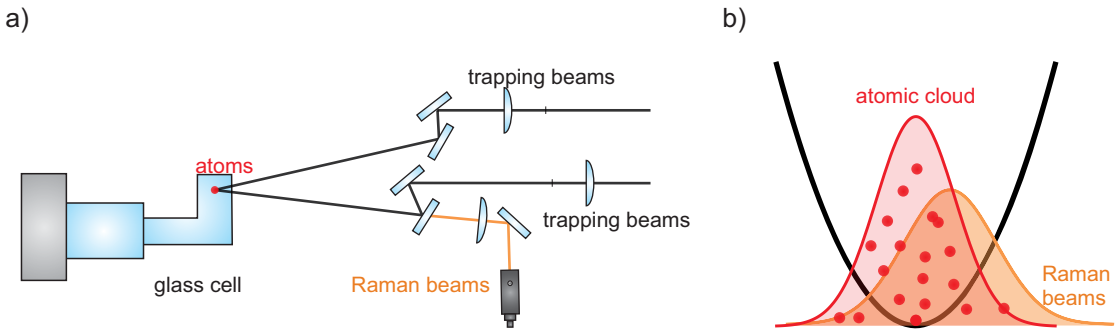

Figure 4.5: (a) Experimental implementation. The optical dipole potential is formed by two laser beams (black) which intersect with an angle of 18° in the experimental chamber. The Raman laser beams (orange) are directed onto the atomic cloud along one of these beams. (b) To address the motional sidebands an asymmetric coupling field is required, which is realized by introducing a small offset between the Raman laser focus and the atomic cloud.

The procedure outlined above results in an ensemble of 4×10^5 atoms in the $|F=2, m_F=2\rangle$ state at a temperature of 375(25) nK. Subsequently, the atoms are transferred to the $|\uparrow\rangle = |F=2, m_F=0\rangle$ state by a radio-frequency rapid adiabatic passage. In a final step, the atomic ensemble is initialized with a variable mean density n between 0.46 and $4.8 \times 10^{12}\mathrm{cm}^{-3}$ in the $|\downarrow\rangle = |F=1, m_F=0\rangle$ state by a microwave Rabi pulse of variable duration. The remaining atoms in the $|\uparrow\rangle$ state are removed with a resonant light pulse on an optical transition. Importantly, this method allows for the preparation of a variable density at constant temperature. The density of these ensembles is calibrated by performing microwave-based Ramsey interferometry on the clock transition (Fig. 4.6(b)) and by recording the density-dependent frequency shift of the carrier transition ($-0.48\,\mathrm{Hz}/10^{12}\mathrm{cm}^{-3}$ [218]). Here we provide a list that connects the mean atom density n and the corresponding atom number N we used in the DPT experiment:

Mean atom density n (cm^{-3})	0.46×10^{12}	0.98×10^{12}	2.0×10^{12}	3.2×10^{12}	4.8×10^{12}
Atom number N	0.33×10^{5}	0.69×10^{5}	1.4×10^{5}	2.2×10^{5}	3.4×10^{5}

The inhomogeneous coupling field between the two clock states $|\downarrow\rangle$ and $|\uparrow\rangle$ is realized by using two copropagating Raman beams which are derived from two phase-locked diode lasers. The Raman beams are focused onto the atomic cloud with a beam waist of 39 μm. In principle, these Raman beams can lead to a differential shift of the clock states and thus fluctuations in the Raman beam power may lead to a significant broadening of the spectroscopic signal. To avoid this effect, a specific relative intensity of the Raman beams can be chosen, which reduces the light shift [228]. Figure 4.6(a)) shows the experimental determination of the optimal relative intensity based on the comparison of spectroscopy on the clock transition with the Raman system and with microwave radiation. In the experiments a relative intensity $I_1/I_2 = 1.98$ was chosen to avoid differential shifts.

The first-order motional sidebands can only be addressed with a coupling field that is asymmetric with respect to the trapping potential. This asymmetry is realized by shifting the Raman beams compared to the center position of the atomic cloud as shown in Fig. 4.5(b) and leads to a spatial inhomogeneity of the coupling.

The spectroscopic signals shown in of Fig. 1 and Fig. 2 (main text) are obtained by applying Raman pulses with a duration of 500 ms for detunings between ≈ -200 Hz and $\approx +200$ Hz of the two Raman laser beams. In Fig. 1 (main text), the carrier and all six sidebands are well resolved and, in addition, a higher order sideband is visible at ≈ 192 Hz. Compared to previous work [229], the small Fourier width of these pulses allow for a full resolution of the sideband transitions.

At the end of each experimental sequence, the trap is switched off to allow for ballistic expansion and Stern-Gerlach separation of the atoms in the two clock states. The number of atoms in both states, $N_\uparrow$ and $N_\downarrow$, and their temperature are detected by simultaneous absorption imaging, calibrated according to Ref. [230].

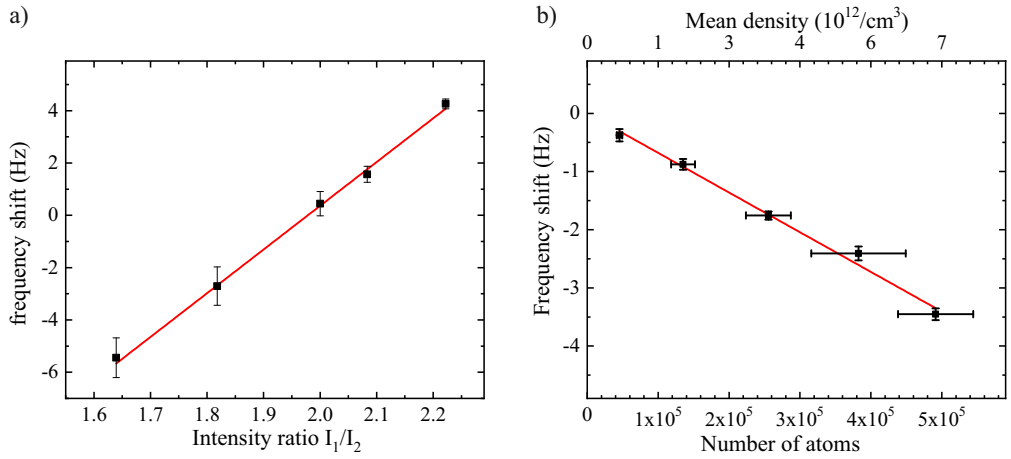

Figure 4.6: (a) Frequency shift observed using the Raman transition relative to the frequency obtained by using the corresponding microwave transition. The shift vanishes for an intensity ratio of $I_1/I_2 = 1.98$. (b) Calibration of the mean density. The measured frequency of the carrier transition is shown as a function of the recorded number of atoms. Based on the known density-dependent frequency shift for Rb atoms [218], the mean density of the ensemble is obtained.

4.2.6 Supplemental Materials: Spin model and mean-field dynamics

In the main text we show that long-range XXZ spin models describe trapped bosonic gases interacting via purely contact interactions. Here we discuss the various parameters of the XXZ spin models and derive the corresponding mean-field equations of motion. We use them to calculate associated Rabi lineshapes.

Recall the Hamiltonian H_{XXZ} defined in main text,

$$\hat{H}_{\mathrm{XXZ}} = \sum_{ij} J_{ij} \hat{\mathbf{S}}_i \cdot \hat{\mathbf{S}}_j + \sum_{ij} \chi_{ij} \hat{S}_i^z \hat{S}_j^z + \sum_i \Omega_i \hat{S}_i^x - \sum_i (\delta - B_i) \hat{S}_i^z. \tag{4.5}$$

This Hamiltonian describes the spin dynamics of thermal bosonic gases in the collisionless regime. By adequately mapping the harmonic trap eigenmodes to lattice sites in mode space, we can understand the spin dynamics for the carrier transition, the blue sideband transition, as well as the red sideband transition. The definitions of the two spin states in lattice site i for all these cases are as follows:

- Carrier transition: $|\Uparrow_i\rangle = |\uparrow; n_i^X, n_i^Y, n_i^Z\rangle$, $|\Downarrow_i\rangle = |\downarrow; n_i^X, n_i^Y, n_i^Z\rangle$
- Blue sideband transition ($\hat{Z}$ direction): $|\Uparrow_i\rangle = |\uparrow; n_i^X, n_i^Y, n_i^Z + 1\rangle$, $|\Downarrow_i\rangle = |\downarrow; n_i^X, n_i^Y, n_i^Z\rangle$

- Red sideband transition ($\hat{Z}$ direction): $|\Uparrow_i\rangle = |\uparrow; n_i^X, n_i^Y, n_i^Z - 1\rangle$, $|\Downarrow_i\rangle = |\downarrow; n_i^X, n_i^Y, n_i^Z\rangle$

Here we will use the convention of capital letters to denote spatial coordinates to distinguish them from coordinates in spin space denoted by lowercase letters. We denote the wave functions associated with $|\Uparrow_i\rangle$ and $|\Downarrow_i\rangle$ states respectively as $\phi_i^{\Uparrow}(\mathbf{R})$ and $\phi_i^{\Downarrow}(\mathbf{R})$. To avoid confusion, we define δ as the laser detuning from the carrier transition, and this convention is also used in the main text. For the blue sideband transition, we replace δ by $\delta - \hbar\omega$, where ω is the relevant trapping frequency; while for red sideband transition, we replace δ by $\delta + \hbar\omega$.

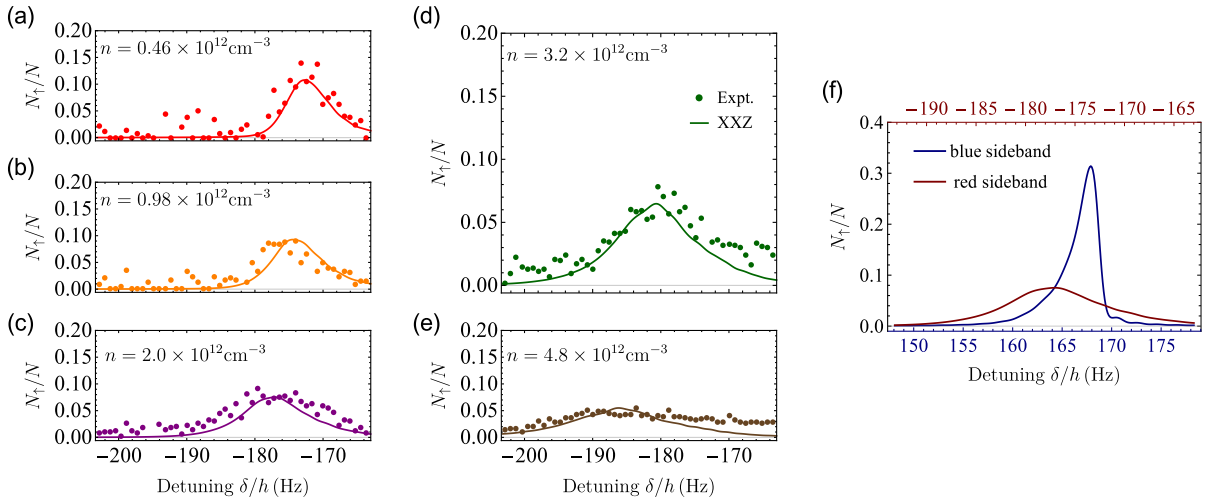

Figure 4.7: (a-e) The Rabi lineshapes for 171 Hz red sideband with mean atom density $n = \{0.46, 0.98, 2.0, 3.2, 4.8\} \times 10^{12}\text{cm}^{-3}$. The solid points denote experimental data, the solid lines denote mean-field theoretical predictions by H_{XXZ} (see text). (f) The comparison of theoretical Rabi lineshapes between blue sideband and red sideband with mean density $n = 2.0 \times 10^{12}\text{cm}^{-3}$, and the difference can be understood as the effect of the anharmonicity of the optical dipole trap (see text).

As we discuss in the main text, the key approximations in our spin model are the collisionless regime (trapping frequency is much larger than the interaction strength) as well as a negligible number of doubly occupied modes. Our experimental system is a thermal cloud of ^{87}Rb atoms prepared at a temperature $T = 375(25)$ nK in a 3D harmonic trap with trapping frequencies $\omega_X/2\pi = 143$ Hz, $\omega_Y/2\pi = 21.5$ Hz, $\omega_Z/2\pi = 171$ Hz. Based on the numerical calculation described below, we find $N\chi/h \approx 4.63\text{Hz}/10^{12}\text{cm}^{-3}$ for blue sideband transition in the $\hat{Z}$ direction,

which demonstrates the validity of collisionless regime. For the number of doubly occupied modes, we evaluate the quantity $\sum_i \langle \hat{n}_i(\hat{n}_i - 1)\rangle/2N$, where $\hat{n}_i = \hat{a}_i^\dagger \hat{a}_i$, and we are summing over all possible eigenmodes. This quantity is only non-zero when there is more than one atom per mode. Using Wick's theorem, we have

$$\frac{1}{2N}\sum_i \langle \hat{n}_i(\hat{n}_i - 1)\rangle = \frac{1}{2N}\sum_i \langle \hat{a}_i^\dagger \hat{a}_i^\dagger \hat{a}_i \hat{a}_i\rangle = \frac{1}{N}\sum_i \langle \hat{a}_i^\dagger \hat{a}_i\rangle\langle \hat{a}_i^\dagger \hat{a}_i\rangle = \frac{1}{N}\sum_i \langle \hat{n}_i\rangle^2 \tag{4.6}$$

Then we can estimate the average occupation number of each eigenmode by a Boltzmann distribution, $\langle \hat{n}_i\rangle/N = \exp\big[-(n^X\omega_X + n^Y\omega_Y + n^Z\omega_Z)\hbar/k_BT\big]/Z$, in which the partition function $Z \approx (k_BT/\hbar\bar{\omega})^3$. Then we get

$$\frac{1}{2N}\sum_i \langle \hat{n}_i(\hat{n}_i - 1)\rangle \approx N\left(\frac{\hbar\bar{\omega}}{2k_BT}\right)^3 \tag{4.7}$$

For $N = 1\times 10^5$ atoms, we obtain that the number of occupied eigenmodes with two atoms or more is $N(\hbar\bar{\omega}/2k_BT)^3 \sim 1.4\%$. This result leads to our conclusion that the number of lattice sites occupied by more than one atoms is very small in our experiment.

For the bosonic gas of interest, the Heisenberg couplings J_{ij} and the Ising couplings χ_{ij} are purely generated by contact interactions, and can be written in terms of the various scattering lengths and overlap integrals of harmonic trap eigenmodes,

$$J_{ij} = \frac{4\pi\hbar^2 a_{\uparrow\downarrow} V_{ij}^{\mathrm{ex}}}{m}, \quad \chi_{ij} = \frac{4\pi\hbar^2(V_{ij}^{\Uparrow\Uparrow} a_{\uparrow\uparrow} + V_{ij}^{\Downarrow\Downarrow} a_{\downarrow\downarrow} - V_{ij}^{\Uparrow\Downarrow} a_{\uparrow\downarrow} - V_{ij}^{\mathrm{ex}} a_{\uparrow\downarrow})}{m}, \tag{4.8}$$

where

$$V_{ij}^{\alpha\beta} = \int \mathrm{d}^3\mathbf{R}[\phi_i^\alpha(\mathbf{R})]^2[\phi_j^\beta(\mathbf{R})]^2, \quad V_{ij}^{\mathrm{ex}} = \int \mathrm{d}^3\mathbf{R}\phi_i^{\Uparrow}(\mathbf{R})\phi_i^{\Downarrow}(\mathbf{R})\phi_j^{\Uparrow}(\mathbf{R})\phi_j^{\Downarrow}(\mathbf{R}). \tag{4.9}$$

Besides spin-spin interaction, the Raman laser couples $|\Uparrow_i\rangle$ and $|\Downarrow_i\rangle$ states via a intermediate state, and the effective Rabi frequencies are given by

$$\Omega_i = \Omega_0 \int \mathrm{d}^3\mathbf{R}\exp\left[-\frac{2(\mathbf{R}_\perp - \mathbf{R}_{\perp,0})^2}{w^2}\right]\phi_i^{\Uparrow}(\mathbf{R})\phi_i^{\Downarrow}(\mathbf{R}). \tag{4.10}$$

Here, Ω_0 is the bare Rabi frequency determined by the Rabi couplings and detunings to the intermediate state of the two Raman beams, $\mathbf{R}_\perp$ is perpendicular to the propagating direction of Raman

beams, $\mathbf{R}_{\perp,0}$ is the offset from trap center, and w is the Gaussian beam radius at the position of atomic cloud. Due to the copropagating geometry of Raman beams used in the experiment, the momentum kicks of Raman beams can be ignored.

The different inhomogeneous longitudinal fields $B_i = B_i^{(1)} + B_i^{(2)} + B_i^{(3)}$ come from the interplay between contact interaction ($B_i^{(1)}$), the differential frequency shift generated by the optical trap and the magnetic curvature ($B_i^{(2)}$), and the anharmonicity in optical trap ($B_i^{(3)}$). We already discuss $B_i^{(1)}$ in the main text. It is given by

$$B_i^{(1)} = \frac{4\pi\hbar^2}{m}\sum_{j\neq i}(V_{ij}^{\Uparrow\Uparrow}a_{\uparrow\uparrow} - V_{ij}^{\Downarrow\Downarrow}a_{\downarrow\downarrow}). \tag{4.11}$$

The different trapping frequency experienced by the $|\uparrow\rangle$ and $|\downarrow\rangle$ atoms give an additional differential frequency shift in mode space. If we defined $\Delta\omega_{X,Y,Z} = \omega_{X,Y,Z}^{\uparrow} - \omega_{X,Y,Z}^{\downarrow}$, we can express $B_i^{(2)}$ as

$$B_i^{(2)} = \left(n_i^X + \frac{1}{2}\right)\hbar\Delta\omega_X + \left(n_i^Y + \frac{1}{2}\right)\hbar\Delta\omega_Y + \left(n_i^Z + \frac{1}{2}\right)\hbar\Delta\omega_Z. \tag{4.12}$$

Moreover, the actual Gaussian shape of the laser beams that make the dipole trap introduces corrections beyond the leading order harmonic trapping potential $U(\mathbf{R}) = \frac{1}{2}m(\omega_X^2X^2 + \omega_Y^2Y^2 + \omega_Z^2Z^2)$. These corrections generate an additional anharmonic potential $\Delta U(\mathbf{R}) = -\frac{1}{2}m(\gamma_{XX}^2X^4 + \gamma_{YY}^2Y^4 + \gamma_{ZZ}^2Z^4 + \gamma_{XY}^2X^2Y^2 + \gamma_{XZ}^2X^2Z^2 + \gamma_{YZ}^2Y^2Z^2)$. In first-order perturbation, this term gives rise to a shift of harmonic oscillator levels, which leads to a small change of atom density. As the shift generated by the anharmonicity is mode-dependent, it generates an extra longitudinal field that should be taken in consideration for sideband transitions. This field has a sign difference for the blue sideband ($B_i^{(3)b}$) and red sideband ($B_i^{(3)r}$). Here we use the sideband transitions in $\hat{Z}$ direction as an example,

$$B_i^{(3)b} = -\frac{\hbar}{2\omega_Z}\left[3\gamma_{ZZ}^2(a_{\text{ho}}^Z)^2(n_i^Z+1) + \gamma_{YZ}^2(a_{\text{ho}}^Y)^2(n_i^Y+1/2) + \gamma_{XZ}^2(a_{\text{ho}}^X)^2(n_i^X+1/2)\right], \tag{4.13}$$

$$B_i^{(3)r} = \frac{\hbar}{2\omega_Z}\left[3\gamma_{ZZ}^2(a_{\text{ho}}^Z)^2n_i^Z + \gamma_{YZ}^2(a_{\text{ho}}^Y)^2(n_i^Y+1/2) + \gamma_{XZ}^2(a_{\text{ho}}^X)^2(n_i^X+1/2)\right], \tag{4.14}$$

where $a_{\text{ho}}^{X,Y,Z} = \sqrt{\hbar/m\omega_{X,Y,Z}}$ is the harmonic oscillator length. Sideband transitions in other directions can be treated in a similar way.

For carrier transition, due to the negligible Ising couplings χ_{ij}, our XXZ spin model can be simplified to the Heisenberg model. Given that the transverse field Ω_i and longitudinal field B_i are small compared to the Heisenberg couplings J_{ij}, we can restrict the spin model in the Dicke manifold, which gives $\hat{H}_{\text{carrier}} \approx \Omega\hat{S}^x - (\delta - B)\hat{S}^z$, where Ω is the mean Rabi frequency for carrier transition, and B is the thermal-averaged value of B_i. We understand B as the frequency shift of carrier transition, which can be evaluated analytically in the large-N limit,

$$B = \frac{4\pi\hbar^2(a_{\uparrow\uparrow} - a_{\downarrow\downarrow})n}{m} + k_B T\left(\frac{\Delta\omega_X}{\omega_X} + \frac{\Delta\omega_Y}{\omega_Y} + \frac{\Delta\omega_Z}{\omega_Z}\right), \tag{4.15}$$

where $n = N(m\bar{\omega}^2/4\pi k_B T)^{3/2}$ is the mean atom density in harmonic trap with atom number N, and $\bar{\omega} = (\omega_X\omega_Y\omega_Z)^{1/3}$. The density-dependent part in B agrees with the density-dependent clock shift -0.48 Hz/10^{12}cm^{-3} observed in previous experiment [218]. In our experiment, we use this known value of density-dependent shift of the carrier transition to calibrate the atom density.

For sideband transitions, the Ising couplings χ_{ij} become larger. We use a mean-field approximation in the Heisenberg equations of $\hat{S}_i^{x,y,z}$ in our XXZ spin model (see Eq.(4.5)), which neglects the quantum correlation between different spins, $\langle\hat{S}_i^{\mu}\hat{S}_j^{\mu'}\rangle \approx \langle\hat{S}_i^{\mu}\rangle\langle\hat{S}_j^{\mu'}\rangle$ $(\mu, \mu' = x, y, z)$. The mean-field equations we get are the following ones:

$$\begin{aligned}
\frac{\mathrm{d}}{\mathrm{d}t}\langle\hat{S}_j^x\rangle &= 2\sum_i\left[J_{ij}\langle\hat{S}_i^y\rangle\langle\hat{S}_j^z\rangle - (J_{ij}+\chi_{ij})\langle\hat{S}_i^z\rangle\langle\hat{S}_j^y\rangle\right] + (\delta - B_j)\langle\hat{S}_j^y\rangle,\\
\frac{\mathrm{d}}{\mathrm{d}t}\langle\hat{S}_j^y\rangle &= 2\sum_i\left[(J_{ij}+\chi_{ij})\langle\hat{S}_i^z\rangle\langle\hat{S}_j^x\rangle - J_{ij}\langle\hat{S}_i^x\rangle\langle\hat{S}_j^z\rangle\right] - (\delta - B_j)\langle\hat{S}_j^x\rangle - \Omega_j\langle\hat{S}_j^z\rangle,\\
\frac{\mathrm{d}}{\mathrm{d}t}\langle\hat{S}_j^z\rangle &= 2\sum_i J_{ij}\left[\langle\hat{S}_i^x\rangle\langle\hat{S}_j^y\rangle - \langle\hat{S}_i^y\rangle\langle\hat{S}_j^x\rangle\right] + \Omega_j\langle\hat{S}_j^y\rangle.
\end{aligned} \tag{4.16}$$

We solve Eq.(4.16) numerically, with random sampling of motional states drawn from a Boltzmann distribution. As it is computationally difficult to solve the equations above for $\sim 10^5$ atoms, instead we use $N_{\text{th}} = 1000$ and scale the transverse and longitudinal field from the one in the experiment by a factor $N_{\text{th}}/N_{\text{exp}}$. We also allow an overall scaling factor η of the atomic density to take both finite-size effects and the anharmonicities into account. The thermal-averaged sideband spectrum agrees well with our experimental measurements, when the overall scaling factor is set to $\eta = 0.72$ for both blue sideband and red sideband. The Rabi spectrum of blue sideband transition is

discussed in the main text (see Fig. 3(a-c,e-f)), and the Rabi spectrum of red sideband transition is depicted in Fig. 4.7(a-e). We also compare the theoretical Rabi lineshapes for blue and red sideband for mean atom density $n = 2.0 \times 10^{12}\text{cm}^{-3}$ in Fig. 4.7(f), which shows a significant suppression of red sideband. As the temperature of our system is above quantum degeneracy, the ground state concentration is not a reasonable explanation. Instead, the difference between the blue and red sidebands comes from a sign difference between $B_i^{(3)b}$ and $B_i^{(3)r}$, generated by anharmonicity. Because of this sign difference, $B_i^{(3)b}$ partially cancels the inhomogeneity in the longitudinal fields, while $B_i^{(3)r}$ increases the inhomogeneity. Similar phenomenon was also observed in Ref. [223].

4.2.7 Supplemental Materials: Dynamical phase diagram and critical behavior

In the main text we discuss about the ferromagnetic to paramagentic dynamical phase transition (DPT) in the Lipkin-Meshkov-Glick (LMG) model (see Eq.(3) main text), a collective XXZ model plus additional transverse and longitudinal field. Here we elaborate on the calculation of the dynamical phase diagram and the associated critical points, following the procedure discussed in Ref. [107]. The mean-field equations of the LMG model can be written in terms of normalized expectation value of total spin operators $s^{x,y,z} = 2\langle \hat{S}^{x,y,z} \rangle / N$ as follows,

$$\begin{aligned} \frac{\mathrm{d}}{\mathrm{d}t} s^x &= -N\chi s^z s^y + \tilde{\delta} s^y, \\ \frac{\mathrm{d}}{\mathrm{d}t} s^y &= N\chi s^z s^x - \tilde{\delta} s^x - \Omega s^z, \\ \frac{\mathrm{d}}{\mathrm{d}t} s^z &= \Omega s^y. \end{aligned} \tag{4.17}$$

Using both energy conservation in H_{LMG}, for an initial state with $s^z = -1$, $s^x = s^y = 0$, as well as the identity $(\hat{S}^x)^2 + (\hat{S}^y)^2 + (\hat{S}^z)^2 = (\frac{N}{2}+1)\frac{N}{2}$, the mean-field variables satisfy the following two conservation relations in large-N limit:

$$\frac{N\chi}{2} s^z s^z - \tilde{\delta} s^z + \Omega s_x = \frac{N\chi}{2} + \tilde{\delta}, \tag{4.18}$$

$$(s^x)^2 + (s^y)^2 + (s^z)^2 = 1. \tag{4.19}$$

Combining these three equations (Eq.(4.17)-(4.19)), we can eliminate s^x and s^y, and obtain

the following differential equation for s^z,

$$\frac{1}{2}\left(\frac{\mathrm{d}}{\mathrm{d}t}s^z\right)^2 + V(s^z) = 0, \tag{4.20}$$

where

$$\begin{aligned} V(s^z) = (s^z+1)\Bigg\{ &\frac{(N\chi)^2}{8}(s^z)^3 - \left[\frac{(N\chi)^2}{8} + \frac{N\chi\tilde{\delta}}{2}\right](s^z)^2 + \left[\frac{\tilde{\delta}^2+\Omega^2}{2} - \frac{(N\chi)^2}{8}\right]s^z \\ &+ \left[\frac{\tilde{\delta}^2-\Omega^2}{2} + \frac{N\chi\tilde{\delta}}{2} + \frac{(N\chi)^2}{8}\right]\Bigg\}. \end{aligned} \tag{4.21}$$

We interpret Eq.(4.20) as the Hamiltonian of a classical particle with position s^z moving in the effective potential $V(s^z)$. The condition $V(s^z) = 0$ determines the turning points of s^z. Since $V(-1) = 0$, $V'(-1) = -1$, $V(1) = \tilde{\delta}^2$, this effective potential should have at least two real roots in $[-1, 1]$, and we consider these roots as physical turning points. So the dynamics of s^z can be understood as the oscillations between -1 and the nearest turnover point s^z_*. Imagine that we start from a $V(s^z)$ with two real roots, and continuously tune the parameters of $V(s^z)$ so that two new real roots appear in between, a jump of the nearest turning point s^z_* should occur in this process (see Fig. 4.8(a-b)). This abrupt change in behavior is what sets the dynamical phase transition.

To count the number of roots in $V(s^z)$, we can factor out the known root $s^z = -1$, and then consider the discriminant $\Delta = 18abcd - 4b^3d + b^2c^2 - 4ac^3 - 27a^2d^2$ of cubic equation $ax^3 + bx^2 + cx + d = 0$. If $\Delta > 0$, the cubic has three distinct real roots; if $\Delta < 0$, the cubic has one real root. So $\Delta = 0$ captures the critical point of the DPT. We focus on the parameter regime where $N\chi > 0$ with a fixed positive Ω, and define $y = N\chi/\Omega$, $x = \tilde{\delta}/\Omega$. In terms of these variables the phase boundary plotted in the main text (see Fig. 2(d)) is given by

$$\begin{aligned} y_* = \frac{1}{12x_*}\Bigg[1 - 12x_*^2 &- \left(5832x_*^4 + 540x_*^2 - 1 + 24x_*\sqrt{3(27x_*^2-1)^3}\right)^{1/3} \\ &- \left(5832x_*^4 + 540x_*^2 - 1 - 24x_*\sqrt{3(27x_*^2-1)^3}\right)^{1/3}\Bigg]. \end{aligned} \tag{4.22}$$

As this formula includes square root and cube root, we need to specify the argument of complex number to avoid the branch cut. Here we choose $\arg[3(27x_*^2-1)^3] = \{0, \pi\}$, $\arg[5832x_*^4 + 540x_*^2 - 1 + 24x_*\sqrt{3(27x_*^2-1)^3}] \in (-2\pi, 0]$, and $\arg[5832x_*^4 + 540x_*^2 - 1 - 24x_*\sqrt{3(27x_*^2-1)^3}] \in [0, 2\pi)$. And we can conclude that this phase boundary exists in the regime $x < \sqrt{3}/9$ and $y > 8\sqrt{3}/9$.

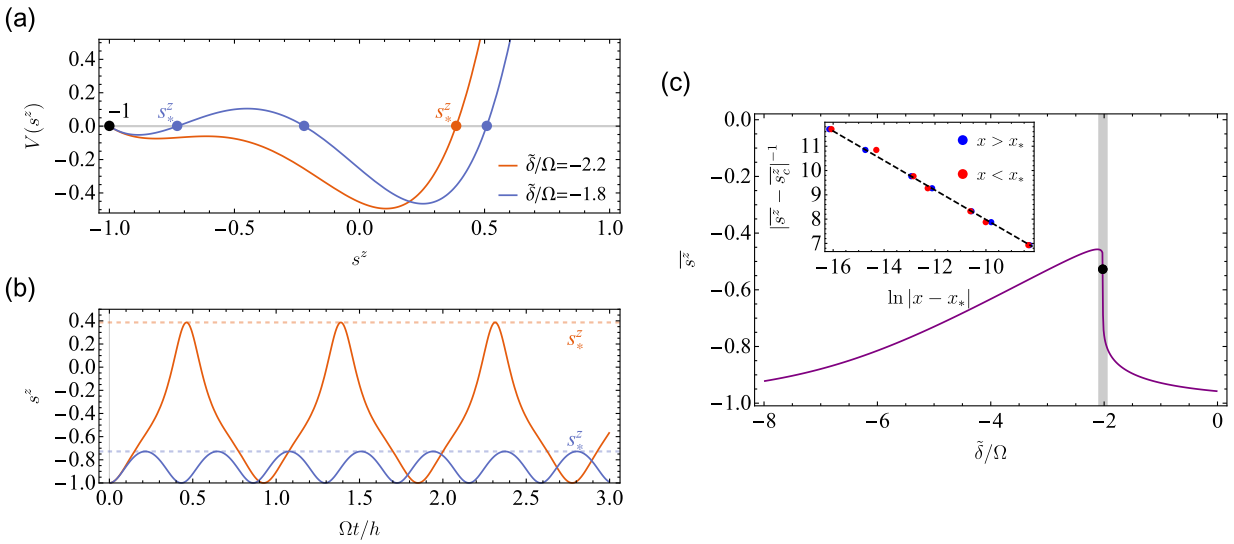

Figure 4.8: (a) The effective potential $V(s^z)$ with $N\chi/\Omega = 5$. In the case of $\tilde{\delta}/\Omega = -2.2$, $V(s^z)$ has two real roots; In the case of $\tilde{\delta}/\Omega = -1.8$, $V(s^z)$ has four real roots. The nearest turnover point is labelled by s^z_*, and the jump of s^z_* indicates dynamical phase transition (see text). (b) The mean-field dynamics of LMG model with $N\chi/\Omega = 5$ and $\tilde{\delta}/\Omega = -2.2, -1.8$, which shows a sharp change of mean-field dynamical behavior. The choice of color for the lines is the same as (a), and the dashed lines mark the nearest turnover point s^z_*. (c) The long-time average value $\overline{s^z}$ with $N\chi/\Omega = 5$, and the critical point is labelled by black circle. The shaded area is the region close to the critical point, which is shown in details in the inset with logarithmic non-analyticity at the critical point (see text).

Therefore, only when $N\chi/\Omega > 8\sqrt{3}/9$, the DPT occurs. Instead, if $N\chi/\Omega < 8\sqrt{3}/9$, there is a smooth crossover.

As we mentioned in the main text, our experiment always lie in the DPT regime, and we characterize the ferromagnetic and paramagentic phase using the long-time average of excitation fraction $\overline{N_\uparrow}/N$, which is possible to express in terms of s^z,

$$\frac{\overline{N_\uparrow}}{N} = \frac{1}{2}(\overline{s^z} + 1), \quad \overline{s^z} = \frac{1}{T}\int_0^T s^z(t)\mathrm{d}t, \tag{4.23}$$

where T is the oscillation period of s^z. This integral can be evaluated using Eq.(4.20), as

$$\int_0^T s^z(t)\mathrm{d}t = \int_{-1}^{s_*^z} \frac{2s^z \mathrm{d}s^z}{\sqrt{-2V(s^z)}}, \quad T = \int_{-1}^{s_*^z} \frac{2\,\mathrm{d}s^z}{\sqrt{-2V(s^z)}}. \tag{4.24}$$

All these integrals can be calculated analytically in terms of elliptic integrals. Considering the asymptotic behavior near the critical point, we find that instead of the sudden jump behavior of s_*^z, the long-time average $\overline{s^z}$ is continuous at the critical point, and the first derivative of $\overline{s^z}$ diverge logarithmically. The following formula describe the asymptotic behavior of $\overline{s^z}$ with fixed $N\chi/\Omega$,

$$\overline{s^z} \to \overline{s_c^z} + \frac{C}{\ln|x - x_*|}, \quad \overline{s_c^z} = \frac{1}{2} - \frac{1}{2}\sqrt{1 - \frac{8x_*}{y_*}}, \tag{4.25}$$

where C is a constant set by $N\chi/\Omega$. We can verify the asymptotic behavior predicted above numerically. This is plotted in Fig. 4.8(c) for the case $N\chi/\Omega = 5$. The continuous behavior of s_*^z at the critical point determines a second-order dynamical phase transition in our case.

Here we also discuss how to determine the critical point in experiment. Based on Fig. 4.8(c), the first derivative of the long-time average excitation fraction diverges at the critical point. However, in the analysis of experimental data, we have to use the finite difference as an approximation of the first derivative, which is limited by the precision of laser frequency and experimental fluctuation. To construct a stable phase boundary, instead we use the maximum transfer point as a signature of the critical point. Also, as we mentioned in the main text, we measure the Rabi spectrum at a fixed time instead of taking the long-time average excitation fraction due to technical challenges. All these systematic errors in determination of the critical point are smaller than the measurement error bars under current experimental conditions.

Finally we discuss the scaling factor in χ used in the main text to match the experimental critical points to the DPT in LMG model. This scaling factor originates from the inhomogeneities in the Ising coulings χ_{ij}, which couple the Dicke manifold to the states with different total spins. In this way, the effective Ising coupling should be modified by an overall factor from its value χ in Dicke manifold. We use the same scaling factor 0.56 for all the measurements with different atom densities, and the experimental critical points agrees very well with the phase boundary in LMG model.

4.2.8 Supplemental Materials: Discussion of spin squeezing

We proceed to study the role of quantum correlations and entanglement in our XXZ simulator by theoretical calculation of spin squeezing, since it provides a relevant entanglement witness and an important resource for quantum metrology [31]. We study the proposed Ramsey spectroscopy sequence depicted in Fig. 4.9(a). Initially all atoms are assumed to be in the $|\downarrow\rangle$ state and a $\pi/2$ blue-sideband pulse is applied to transfer the atoms to the $|S^x = N/2\rangle$ state. Then the system is allowed to evolve for $\tau/2$ under XXZ interaction (see Eq.(2) in the main text), followed by a blue-sideband spin echo pulse, and a further evolution time $\tau/2$. The additional spin echo pulse at half of the evolution suppresses the dephasing effect of inhomogeneous longitudinal fields. The squeezing is quantified by the Ramsey spin squeezing parameter [74], $\xi^2 = \min_\theta N(\Delta S_\theta^\perp)^2/|\langle\hat{\mathbf{S}}\rangle|^2$, which signals entanglement if $\xi^2 < 1$. Here, $(\Delta S_\theta^\perp)^2$ is the variance of the spin noise along an axis perpendicular to the collective spin $\langle\hat{\mathbf{S}}\rangle$, parametrized by an angle $\theta \in [0, 2\pi)$. This squeezing parameter can be extracted by an appropriate sequence of spin rotations at the end of the Ramsey protocol.

To estimate the achievable spin squeezing, we adopt the discrete truncated Wigner approximation (DTWA), which solves the mean-field equations of motion supplemented by Monte Carlo sampling of the initial conditions to account for quantum fluctuations [231]. We choose $N_{\rm th} = 1000$ and scale the longitudinal field from the one in the experiment by a factor $N_{\rm th}/N_{\rm exp}$. The theoretical prediction of spin squeezing is depicted in Fig. 4.9(b). We compare it to the spin squeezing in

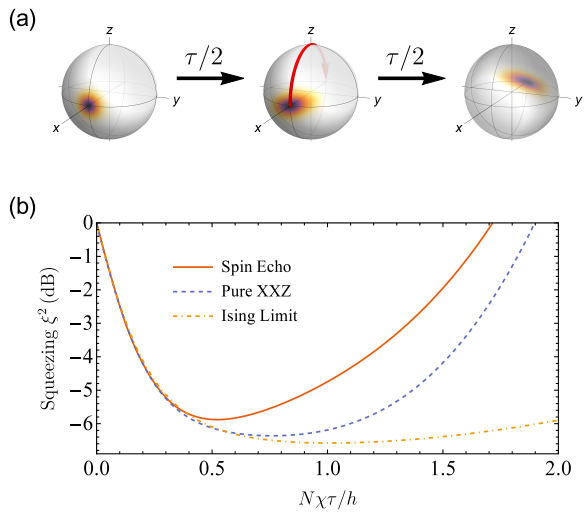

Figure 4.9: (a) Spin echo sequence for generation of squeezing using motional sidebands (see text). The total spin state $|\Psi(t)\rangle$ is illustrated using the Husimi-Q function [31]. (b) Comparison of the obtained spin squeezing for a spin echo sequence (DTWA method), the pure XXZ model (DTWA method) and the Ising limit (analytic solution). The spin squeezing parameter is expressed in terms of decibels (dB), i.e. $10\log_{10}\xi^2$.

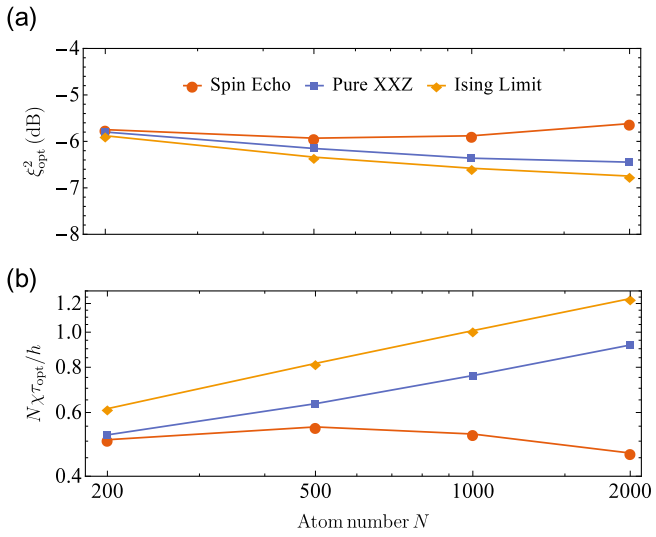

Figure 4.10: (a) Finite-size scaling of optimal spin squeezing in our XXZ simulator with spin echo sequence (DTWA method), compared to pure XXZ model (DTWA method) and Ising limit (analytic solution). (b) Finite-size scaling of optimal squeezed time in our XXZ simulator with spin echo sequence (DTWA method), compared to pure XXZ model (DTWA method) and Ising limit (analytic solution).

the pure XXZ model (ignoring longitudinal fields in Eq.(2) in the main text), and the Ising model ($\hat{H}_{\text{Ising}} = \sum_{ij} \chi_{ij} \hat{S}_i^z \hat{S}_j^z$) which allows for an exact solution as listed below,

$$\begin{aligned}
\langle \hat{S}^x \rangle &= \frac{1}{2} \sum_k \prod_j^{(k)} \cos(\chi_{kj} t), \quad \langle \hat{S}^z \hat{S}^z \rangle = \frac{N}{4}, \\
\langle \hat{S}^y \hat{S}^y \rangle &= \frac{N}{4} + \frac{1}{4} \sum_{k<l} \Big[\prod_j^{(k,l)} \cos\left[(\chi_{kj} - \chi_{lj})t\right] - \prod_j^{(k,l)} \cos\left[(\chi_{kj} + \chi_{lj})t\right] \Big], \\
\langle \hat{S}^z \hat{S}^y + \hat{S}^y \hat{S}^z \rangle &= \frac{1}{2} \sum_{k<l} \sin(\chi_{kl} t) \Big[\prod_j^{(k,l)} \cos(\chi_{kj} t) + \prod_j^{(k,l)} \cos(\chi_{lj} t) \Big],
\end{aligned} \tag{4.26}$$

where $\prod_j^{(k)}$ means multiplication without the term $j = k$. Based on all these expectation values, we can calculate the spin squeezing parameter ξ^2 by tuning θ to reach the minimum value of $(\Delta S_\theta^\perp)^2$.

We find that the beyond-mean-field dynamics in our simulator is similar to the Ising limit, with an additional small suppression arising from the inhomogeneties in the longitudinal fields. For $N_{\text{th}} = 1000$ atoms, near 6dB optimal squeezing can be achieved at $N\chi\tau/h \approx 0.5$, which translates under current experimental conditions to optimal squeezing times around 100ms. On this time scale we do not expect detrimental effects from the technical imperfections. The predicted squeezing emphasizes the metrological potential of motional sidebands.

In Fig. 4.9, we discuss the achievable spin squeezing in our XXZ simulator, with comparison to the pure XXZ model and the Ising limit. As it is hard to calculate spin squeezing for $\sim 10^5$ atoms in theory, we choose $N_{\text{th}} = 1000$ and scale the longitudinal field from the one in the experiment by a factor $N_{\text{th}}/N_{\text{exp}}$. The spin squeezing as a function of Ramsey dark time is depicted in the main text (see Fig. 4(b)). Here we use finite-size scaling as a way to predict the achievable spin squeezing under experimental conditions (see Fig. 4.9).

We extract the optimal spin squeezing (see Fig. 4.9(a)) and optimal squeezed time (see Fig. 4.9(b)) with $N_{\text{th}} = 200, 500, 1000, 2000$. We find that under current experimental conditions, the optimal squeezing saturates around 6dB when we increase the atom number in theory, and the optimal squeezed time stays near $N\chi\tau/h \approx 0.5$. Unfortunately the finite-size scaling curve for the current experiment condition is not monotonic, which means that our estimation of the optimal

spin squeezing is not necessarily accurate. The analysis nevertheless shows the detrimental effects caused by the inhomogeneities in longitudinal fields, which will lead to a non-negligible suppression of spin squeezing, compared to pure XXZ model and Ising limit. Therefore we predict that if it were possible to carefully control the longitudinal fields in experiment and reduce their size, one could get closer to the finite-size scaling curve of pure XXZ model, which increases monotonically when increasing atom number, although the improvement is not significant due to the thermal distribution. In this case, we predict an optimal spin squeezing set by $\xi^2_{\text{opt}} \propto N^{-0.067}$, and an optimal squeezed time by $\tau_{\text{opt}} \propto N^{-0.752}$. Ideally speaking, for 5×10^5 atoms, 8dB optimal squeezing can be achieved around 100ms.

4.3 Photon-mediated correlated hopping in a synthetic ladder

This section is adapted from: **Anjun Chu**, Asier Piñeiro Orioli, Diego Barberena, James K. Thompson, Ana Maria Rey, *Photon-mediated correlated hopping in a synthetic ladder*, Physical Review Research 5, L022034 (2023).

4.3.1 Introduction

Correlated hopping, a process whereby the hopping rate of a particle depends on the presence of other particles in an array, is believed to contribute to the complex behaviors seen in strongly correlated materials [232–234], and also to be a key requisite for the generation of dynamical gauge fields [235,236] and topological behaviors [237,238]. Regardless of its importance, correlated hopping is typically small and hard to manipulate in real materials, and ultracold atoms have been identified as a unique playground to study these processes under controllable conditions. However, the implementation so far has been mainly limited to isolated double-well arrays [235,236], indirect detection via spectroscopic measurements [239–242], or weak corrections due to dipolar interaction of magnetic atoms [209]. Experimentally accessible protocols to engineer correlated hopping processes in strongly interacting many-body systems are still lacking.

In this work, we propose the use of multilevel atoms in an optical cavity as a toolbox to

engineer different types of bosonic models featuring correlated hopping processes in a genuine unitary many-body system. Cavity QED systems have started to demonstrate their great potential as quantum simulators [28, 107, 186, 214, 243–251]. Important initial steps for correlated hopping have been achieved such as the engineering of pair production processes [214, 248] and dissipative dynamical tunneling [250]. Therefore, the time is ripe to explore the full power of cavity systems under accessible conditions.

A key idea behind our protocol is to treat the internal levels of the atoms as a synthetic dimension [252], where a notion of spatial locality can naturally emerge, even in the presence of infinite-range photon-mediated interactions. The use of internal levels as a synthetic spatial dimension has already lead to beautiful demonstrations of topological lattice models and chiral transport in non-interacting systems [102, 253–256], and very recently in interacting many-body systems [257]. Here, we propose a way to go beyond the single-particle paradigm by engineering interaction-induced hopping processes in the synthetic dimension spanned by the atomic ground state manifold. This is accomplished by weakly coupling it to a set of many-body excited states dressed by photon-mediated interactions.

The implementation uses two laser drives with appropriate detunings to suppress undesirable single-particle and collective shifts of the internal levels. In this way, we energetically favor only the desired hopping process where in a correlated manner one atom moves **two** internal levels up while another atom in the array moves **two** levels down. The correlated hopping processes we introduce split the ground state manifold into two sets of levels, which we visualize as a synthetic two-leg ladder. By doing that, we open up a variety of many-body phenomena that can be realized in this system, including dynamical phase transitions in pair production processes, chiral transport tunable via laser detunings and initial state preparation, and correlation spreading and emergent light-cone transport in the synthetic ladder. We also discuss a feasible experimental implementation using long-lived alkaline earth atoms.

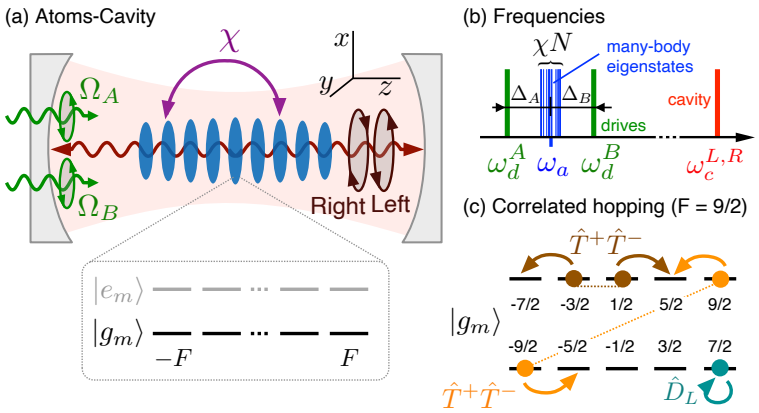

Figure 4.11: Effective ground state dynamics in a multilevel cavity QED system. (a) An ensemble of multilevel atoms (blue pancakes) with ground ($|g_m\rangle$) and excited ($|e_m\rangle$) manifold are trapped in an optical cavity with quantization axis ($\hat{z}$) along the cavity axis. The cavity photons (red curve) with left-handed (σ^-) and right-handed (σ^+) circular polarizations mediate collective interactions (χ) among the atoms. Two external drives are applied to the σ^- polarized mode with atomic Rabi frequency $\Omega_{A,B}$. (b) Frequencies of cavity resonance, two external drives, and atomic transition dressed by photon-mediated interactions. (c) Sketch of the correlated hopping ($\hat{T}^+\hat{T}^-$) and single-particle AC Stark shifts ($\hat{D}_L$) in the synthetic two-leg ladder spanned by the ground manifold ($|g_m\rangle$), using $F = 9/2$ case as an example.

4.3.2 System

Effective Hamiltonian

We consider an ensemble of N multilevel atoms confined in an optical cavity with quantization axis ($\hat{z}$) along the cavity axis, as depicted in Fig. 4.11(a,b). The internal level structure of each atom consists of a ground and an excited manifold with hyperfine spin F_g and F_e respectively. The excited state manifold decays with spontaneous emission rate γ. We consider a weak magnetic field limit such that all atomic transition frequencies can be approximated as a single ω_a (see SOM). Specifically, we label the ground states as $|g_m\rangle_i$, and the excited states as $|e_m\rangle_i$, where m is the magnetic quantum number, and i labels the atoms. Two degenerate cavity modes with left-handed (σ^-) and right-handed (σ^+) circular polarization at frequency $\omega_c \equiv \omega_c^{L,R}$ couple to the transition between ground and excited manifolds with coupling strength g_c and detuning $\Delta_c = \omega_c - \omega_a$. Two external σ^- polarized lasers with frequencies $\omega_d^{A,B}$, detuned from the atomic transition by $\Delta_{A,B} = \omega_d^{A,B} - \omega_a$, are used to drive the cavity with intracavity Rabi frequency $\Omega_{A,B}$ respectively.

We focus on the far-detuned regime of the cavity ($|\Delta_c| \gg |\Delta_{A,B}|$), where the frequencies of laser drives are closer to the atomic transition rather than the cavity resonance. In this regime, one can first adiabatically eliminate the injected light fields and intracavity fluctuations assuming $|\Delta_c| \gg g_c\sqrt{N}, \kappa$, with κ the cavity intensity decay rate. The system is thus well described by an atom-only Hamiltonian with photon-mediated elastic interactions (see Ref. [192] and SOM),

$$\hat{H}/\hbar = \omega_a \hat{N}_e + \chi(\hat{L}^+\hat{L}^- + \hat{R}^+\hat{R}^-) + \left[\left(\Omega_A e^{-i\omega_d^A t} + \Omega_B e^{-i\omega_d^B t}\right)\hat{L}^+ + h.c.\right], \tag{4.27}$$

where $\chi = -g_c^2/\Delta_c$ is the photon-mediated interaction strength. Here, $\hat{N}_e = \sum_{im} |e_m\rangle\langle e_m|_i$ is the atom number operator for the excited manifold, $\hat{L}^+ = \sum_{im} C_m^{-1} |e_{m-1}\rangle\langle g_m|_i$, $\hat{L}^- = (\hat{L}^+)^\dagger$ are multilevel dipole operators with σ^- polarization, and $\hat{R}^+ = \sum_{im} C_m^{+1} |e_{m+1}\rangle\langle g_m|_i$, $\hat{R}^- = (\hat{R}^+)^\dagger$ are multilevel dipole operators with σ^+ polarization, where $C_m^p \equiv \langle F_g, m; 1, p | F_e, m+p\rangle$ are the Clebsch-Gordan coefficients.

The photon-mediated interactions in $\hat{H}$ [Eq. (4.27)] exchange excitations among atoms and generate a rich many-body spectrum of collective states [see Fig. 4.11(b)], if $|\chi N| \gg \gamma$. In this regime and assuming weak driving fields ($|\Delta_{A,B}|, |\chi N| \gg |\Omega_{A,B}|$), as shown in SOM, the many-body excited states are only virtually populated and can be adiabatically eliminated, giving rise to net interactions in the atomic ground manifold described by the following effective ground-state Hamiltonian,

$$\hat{H}_{\text{eff}}/\hbar = \sum_{\nu=A,B} \frac{|\Omega_\nu|^2 \Delta_\nu}{\chi} \left[\Delta_\nu - \chi \hat{D}_L - \chi^2 \hat{T}^+ \hat{G}_R^\nu \hat{T}^-\right]^{-1}, \tag{4.28}$$

where $\hat{G}_R^\nu = (\Delta_\nu - \chi \hat{D}_R)^{-1}$. Here, $\hat{D}_L = \hat{P}_g \hat{L}^- \hat{L}^+ \hat{P}_g$, $\hat{D}_R = \hat{P}_g \hat{R}^- \hat{R}^+ \hat{P}_g$, $\hat{T}^+ = \hat{P}_g \hat{L}^- \hat{R}^+ \hat{P}_g$, and $\hat{T}^- = (\hat{T}^+)^\dagger$ are operators acting only on the ground manifold as ensured by $\hat{P}_g$, which is defined as the projection operator of the atomic ground states. In the case of $F_g = F_e = F$ as we explore in this paper, these operators can be expressed as $\hat{D}_{L,R} = \sum_i \hat{D}_i^{L,R}/\mathcal{N}_F$ and $\hat{T}^+ = \sum_i \hat{T}_i^+/\mathcal{N}_F$, where

$$\hat{D}_i^L = \hat{S}_i^+ \hat{S}_i^-, \quad \hat{D}_i^R = \hat{S}_i^- \hat{S}_i^+, \quad \hat{T}_i^+ = -\hat{S}_i^+ \hat{S}_i^+, \tag{4.29}$$

$\mathcal{N}_F = 2F(F+1)$ is the normalization factor and $\hat{S}_i^\pm$ are raising and lowering spin-F operators acting on atom i. Note that $\hat{H}_{\text{eff}}$ is fully collective and thus couples an atom i with any other atom

j in the ensemble. If the atoms start in the permutationally symmetric manifold, or on a direct product state of permutationally symmetric subsystems, they will remain there, and the scaling of Hilbert space dimension with atom number N is reduced from exponential to polynomial. Thanks to this simplification, we perform all the numerical calculations using Eq. (4.28). However, the underlying physics in $\hat{H}_{\text{eff}}$, which includes a sum over multi-body interactions, is still extremely complex even in these restricted Hilbert space.

Discussions

To gain physical intuition of the physical processes encapsulated in Eq. (4.28), first we discuss the simplest case with $F = 1/2$, which gives $\hat{T}^{\pm} = 0$, and $\hat{D}_L = 2(N/2 + \hat{S}_z)/3$. So the effective ground state Hamiltonian takes the following form,

$$H_{\text{eff}}/\hbar = \sum_{\nu=A,B} \frac{|\Omega_\nu|^2 \Delta_\nu/\chi}{\Delta_\nu - 2\chi(N/2 + \hat{S}_z)/3}. \tag{4.30}$$

In the off-resonant regime ($|\Delta_{A,B}| \gtrsim |\chi N|$), one can expand $\hat{H}_{\text{eff}}$ in a power series of the $\hat{S}_z$ operator. At the leading non-trivial order, this expansion recovers the well-known one-axis twisting interaction $\hat{S}_z\hat{S}_z$, a powerful resource for spin squeezing generation [7]. At higher orders it also generates non-negligible n-body interaction terms such as $(\hat{S}_z)^n$ when $\Delta_{A,B}$ is comparable with χN. Such multi-body operators, which emerge naturally in our system, can speed up the entanglement generation dynamics as recently suggested in trapped ion arrays [258].

In the presence of more levels ($F > 1/2$), the operators $\hat{T}^{\pm}$ cannot be ignored and they start to play a non-trivial role, leading to tunable multi-body interactions. Regardless of their complexity, one can gain physical insight by focusing on the leading order terms obtained in a power series in $\chi N/\Delta_{A,B}$. To leading order the effective Hamiltonian simplifies to

$$\hat{H}_{\text{eff}}/\hbar \approx \sum_{\nu=A,B} \frac{|\Omega_\nu|^2}{\Delta_\nu}\hat{D}_L + \frac{|\Omega_\nu|^2\chi}{\Delta_\nu^2}(\hat{D}_L\hat{D}_L + \hat{T}^{+}\hat{T}^{-}). \tag{4.31}$$

The first term in Eq. (4.31) describes single-particle AC Stark shifts generated by each light field injected into the cavity, and the second term describes the leading order interactions in the ground manifold generated by exchanging cavity photons. The exchange of σ^- polarized cavity photon leads

to the diagonal $\hat{D}_L\hat{D}_L$ term, a multilevel generalization of one-axis twisting interaction, generating population-dependent collective shifts on the ground state levels. In contrast, the exchange of σ^+ polarized cavity photon leads to the $\hat{T}^+\hat{T}^-$ term, a new term emerged in multilevel ground states, generating the processes where one atom moves two internal levels down ($\hat{T}^-$) while another atom moves two levels up ($\hat{T}^+$).

Assuming the hyperfine spin F is a half-integer, it is convenient to visualize the atomic ground manifold as a synthetic two-leg ladder, where the upper and lower legs are sets of internal states directly connected by the $\hat{T}^\pm$ operators [see Fig. 4.11(c)]. Under this concept, the $\hat{T}^+\hat{T}^-$ term is equivalent to correlated hopping in the synthetic ladder which can occur between atoms in the same leg or in different legs. These processes can generate strong correlations between the legs despite having no direct hopping processes. In order to better understand the Hamiltonian dynamics, it is useful to write the operators acting only on the ground manifold in terms of Schwinger bosons,

$$\begin{gathered}\hat{D}_L = \sum_m (C_m^{-1})^2 \hat{a}_m^\dagger \hat{a}_m, \quad \hat{D}_R = \sum_m (C_m^{+1})^2 \hat{a}_m^\dagger \hat{a}_m, \\ \hat{T}^+ = \sum_m C_m^{+1} C_{m+2}^{-1} \hat{a}_{m+2}^\dagger \hat{a}_m,\end{gathered} \tag{4.32}$$

where $\hat{a}_m$ is the bosonic annihilation operator for state $|g_m\rangle$. For simplicity, we also set the strength of the external drives to $\Omega \equiv \Omega_{A,B} = 0.05\chi N$, and analyze the unitary dynamics by varying the detunings $\Delta_{A,B}$ of the laser drives. By appropriate choices of $\Delta_{A,B}$, we can suppress the single-particle and collective shifts at $t = 0$, and make the correlated hopping terms as the dominant process in the synthetic ladder (see SOM).

4.3.3 Examples of correlated hopping

Pair production

One of the simplest cases to understand the correlated hopping process ($\hat{T}^+\hat{T}^-$) is a system with a 4-level $F = 3/2$ ground state manifold [see Fig. 4.12(a)]. Considering the initial state $|g_{-3/2}\rangle^{\otimes(N/2)}|g_{3/2}\rangle^{\otimes(N/2)}$, the role of the $\hat{T}^+\hat{T}^-$ term is to generate correlated atom pairs in the initially unoccupied states $|g_{-1/2}\rangle$ and $|g_{1/2}\rangle$. We show that $\hat{H}_{\text{eff}}$ [Eq. (4.28)] in this system features

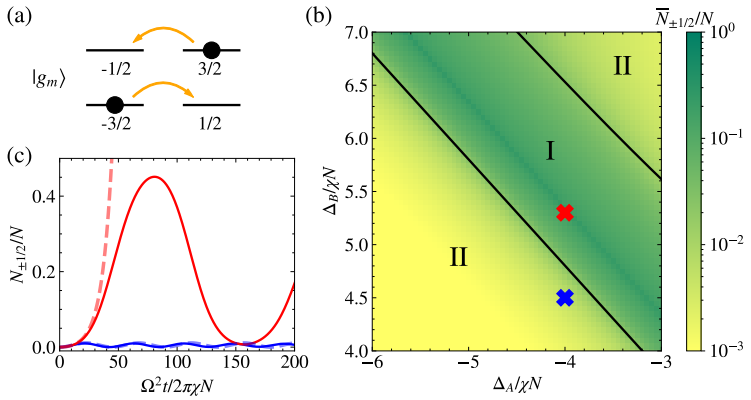

Figure 4.12: Pair production dynamics in a synthetic 4-level ladder. (a) The black dots show the initial state of the atoms and the orange arrows show the correlated hopping process. (b) Dynamical phase diagram of pair production process. The black lines are the phase boundary separating phase I (with pair production) and phase II (without pair production). (c) Short-time dynamics in phase I (red curves) and phase II (blue curves). The choices of detunings $\Delta_{A,B}$ are indicated by cross marks in (b) with corresponding color. The solid lines are calculated by exact diagnoalization (ED), while the dashed lines are based on undepleted pump approximation (UPA).

an abrupt change of dynamical behavior as we tune the system parameters, i.e. dynamical phase transition (DPT). This type of DPT generated by pair production processes can be analyzed at both short times and long times [206].

The short-time dynamics can be understood via undepleted pump approximation (UPA), where to the leading order one can replace the bosonic operators for macroscopically occupied states as c-numbers, $\hat{a}_{\pm3/2}, \hat{a}^\dagger_{\pm3/2} \sim \sqrt{N/2}$. Under UPA, $\hat{H}_{\rm eff}$ [Eq. (4.28)] becomes quadratic and therefore can be diagonalized analytically:

$$\hat{H}_{\rm eff}/\hbar \approx K_1 \hat{a}^\dagger_{-1/2}\hat{a}_{-1/2} + K_2 \hat{a}^\dagger_{1/2}\hat{a}_{1/2} + K_3(\hat{a}_{-1/2}\hat{a}_{1/2} + h.c.). \tag{4.33}$$

Here, K_1, K_2 and K_3 can be expressed as functions of $\Delta_{A,B}/\chi N$ (see SOM). The term proportional to K_3 is responsible for generating correlated atom pairs, while the terms proportional to $K_{1,2}$ impose an energy penalty for the pair production. Note that Eq. (4.33) is equivalent to the two-mode squeezing Hamiltonian well known in quantum optics [68] and spinor BEC systems [7, 259], and very recently achieved in cavity QED systems [214, 248]. At short times when UPA is valid [see Fig. 4.12(c)], one observes exponential growth of atom population $N_{\pm1/2}$ in the initially unoccupied

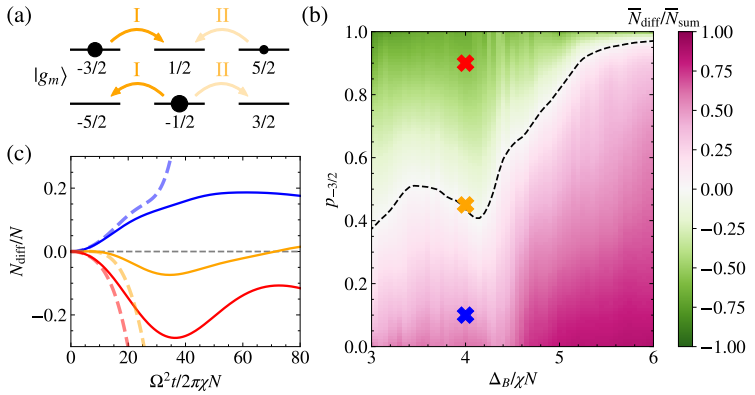

Figure 4.13: Chiral transport in a synthetic 6-level ladder. (a) The strength of the relevant correlated hopping processes (orange arrows) is indicated by the opacity of the arrows, which depends on the atom distribution in the upper leg (black dots). (b) Chiral transport behavior in the lower leg depends on the initial probability of occupying the state $|g_{-3/2}\rangle$ (y axis) and the detuning of the external drive B (x axis) for fixed drive A detuning which is set to $\Delta_A = -3\chi N$. The dashed line indicates balanced transport. (c) Short-time dynamics of population imbalance with parameters indicated by cross marks in (b) using the same color. The solid lines are calculated by ED, while the dashed lines are based on UPA.

states $|g_{\pm 1/2}\rangle$ (red curves) in phase I (with pair production), which is described by $(K_1 + K_2)^2 < 4K_3^2$. Instead in phase II (without pair production), described by $(K_1 + K_2)^2 > 4K_3^2$, one observes small oscillations of atom population (blue curves). The dynamical critical points are located at $(K_1 + K_2)^2 = 4K_3^2$ [see black lines in Fig. 4.12(b)].

To analyze the dynamics generated by $\hat{H}_{\rm eff}$ [Eq. (4.28)] at longer times, we use exact diagonalization (ED) with 100 atoms. At long times the DPT is signaled by a sharp change in behavior of the long-time average fractional population, $\overline{N}_{\pm 1/2}/N = \lim_{T\to\infty} \int_0^T dt\, N_{\pm 1/2}(t)/(NT)$, which serves as an order parameter and distinguishes the two dynamical phases [see Fig. 4.12(b)]. Phase I is characterized by non-zero $\overline{N}_{\pm 1/2}/N$, while phase II is characterized by $\overline{N}_{\pm 1/2}/N \approx 0$. We analyze the critical exponents of this DPT in (see SOM). Our discussions of the 4-level system can be generalized to larger synthetic ladders directly, and the detunings $\Delta_{A,B}$ serve as control knobs of the correlated hopping process.

Chiral transport

Including more levels in the dynamics opens up the possibility to engineer interaction-induced

chiral transport. As shown in Fig. 4.13(a), this can be achieved in a 6-level model ($F = 5/2$) by preparing atoms in the $|g_{-1/2}\rangle$ state, which is the center of the lower leg. The chiral transport in the lower leg can be characterized by the population difference between atoms hopping to the right side ($|g_{3/2}\rangle$) and the left side ($|g_{-5/2}\rangle$), $N_{\text{diff}} = N_{3/2} - N_{-5/2}$. The chiral transport is not a consequence of the external drive polarization. Suppose there are no atoms in the upper leg, the only relevant correlated hopping process will generate atom pairs in the state $|g_{-5/2}\rangle$ and $|g_{3/2}\rangle$, which leads to $N_{\text{diff}} = 0$. Nevertheless, adding atoms in the upper chain gives rise to extra correlated hopping processes, in which the process I and II shown in Fig. 4.13(a) become the dominant processes and break left-right symmetry at short time (see SOM). If process I is stronger than process II, we have chiral transport to the left side of the lower chain ($N_{\text{diff}} < 0$), and vice versa.

We analyze the chiral transport behavior via ED of $\hat{H}_{\text{eff}}$ [Eq. (4.28)] with 20 atoms. The initial state of this calculation is $[\sqrt{p_{-3/2}}|g_{-3/2}\rangle + \sqrt{1-p_{-3/2}}|g_{5/2}\rangle]^{\otimes(N/2)}|g_{-1/2}\rangle^{\otimes(N/2)}$, where $p_{-3/2}$ is the initial probability of occupying the state $|g_{-3/2}\rangle$ for the atoms in the upper leg. The normalized longtime average $\overline{N}_{\text{diff}}/\overline{N}_{\text{sum}}$ as a function of $p_{-3/2}$ and Δ_B, where $N_{\text{sum}} = N_{3/2} + N_{-5/2}$, is shown in Fig. 4.13(b) for fixed Δ_A. It can be seen that for different choices of Δ_B it is possible to turn on both processes (I and II) if $\Delta_B/\chi N \in (3, 4)$, or mainly turn on process II if $\Delta_B/\chi N \in (5, 6)$. Enforcing balanced transport [see the dashed line in Fig. 4.13(b)] requires equal weight of process I and II in the former case, or suppression of both processes in the latter case. In Fig. 4.13(c), we compare the short-time dynamics of chiral transport at $\Delta_B = 4\chi N$ with different choices of $p_{-3/2}$, indicating that the transport direction is fully tunable via initial state in this case. Unlike the 4-level system discussed above, UPA is not able to provide a qualitative description of chiral transport behavior at long times.

Correlation spreading

Regardless of the all-to-all nature of the cavity mediated interactions, in our synthetic ladder we can engineer light-cone spreading of quantum correlations analogous to the one observed in real lattices with short-range or power-law interactions [260–262]. In Fig. 4.14(a), we show a 10-level $F = 9/2$ ground state manifold visualized as a synthetic ladder. For an initial product state

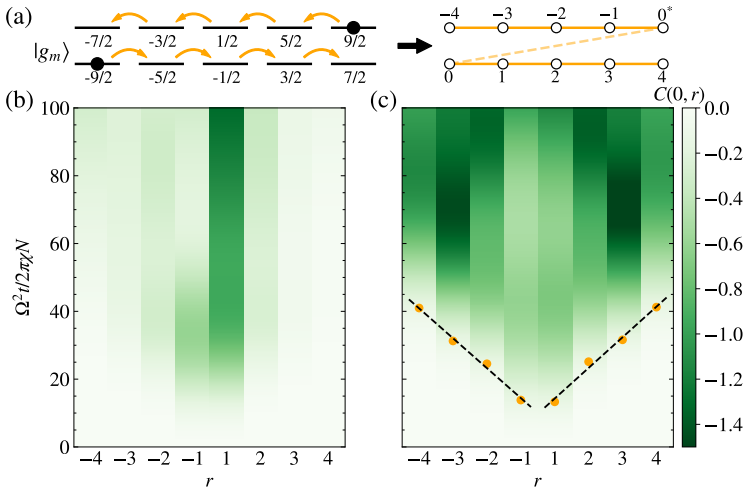

Figure 4.14: Correlation spreading in a synthetic 10-level ladder. (a) The correlated hopping processes (orange arrows) for the initial state (black dots) allow us to assign position indices based on the direction of hopping. The orange dashed line indicates the spread of correlations between legs without direct hopping processes. (b) The atom number two-point correlations (see text) are restricted to nearest-neighbor sites for $\Delta_A = -3\chi N$, $\Delta_B = 3.7\chi N$, (c) but can undergo light-cone spreading for $\Delta_A = -3\chi N$, $\Delta_B = 4.1\chi N$.

$|g_{-9/2}\rangle^{\otimes(N/2)}|g_{9/2}\rangle^{\otimes(N/2)}$, it is possible to visualize the correlation spreading from a concatenated set of hopping processes [see orange arrows in Fig. 4.14(a)] by assigning position indices for the synthetic lattice sites: 0 and 0^* for the initial sites, and site labels increasing to the right and decreasing to the left. Using this convention, we can analyze the correlation spreading in our synthetic ladder, in terms of the two-point correlators $C(i,j) = \langle \hat{N}_i \hat{N}_j \rangle - \langle \hat{N}_i \rangle \langle \hat{N}_j \rangle$.

For the case of a system of 10 atoms, ED of $\hat{H}_{\text{eff}}$ [Eq. (4.28)] shows two distinct behaviors of $C(0,r)$ depending on the choice of Δ_B for fixed Δ_A: In one parameter regime, differential energy shifts imposed by Δ_B favor localization and the correlation is restricted to nearest-neighbor sites [see Fig. 4.14(b)]; for another configuration, linear correlation spreading ($t \propto r$) to the whole system is energetically allowed [see Fig. 4.14(c)]. The spreading is signaled by the appearance of a symmetric light cone [orange points in Fig. 4.14(c)] in the two-point correlators, which is set at the time when $C(0,r)$ reaches -0.15 ($\sim 10\%$ of the maximum value).

Experimental implementation

Our protocol can be directly implemented using fermionic alkaline-earth atoms featuring

$F_g > 0$ in a cavity. The main advantage of these atoms is their unique atomic structure which offers simple ground ($^1S_0$) and long-lived excited state manifolds (e.g. $^3P_1$) where we can explicitly isolate a single $F_g \to F_e$ transition, such as $5/2 \to 5/2$ for ^{173}Yb and $9/2 \to 9/2$ for ^{87}Sr. Although it might be possible to engineer similar correlated hopping processes in the ground hyperfine levels of alkali atoms, the proposed implementation is less direct since in this system the condition $|\chi N| \gg \gamma$ requires to make χN comparable to the excited hyperfine splitting and as a consequence it is necessary to sum over the set of all excited hyperfine levels. For the particular case of ^{87}Sr as discussed in SOM, under current experimental conditions it is possible to operate in a regime where $|\chi N|/\gamma > 10^2$ using 2×10^5 atoms, so the dissipation during the time scale of interests can be ignored. Moreover, our protocol can be directly generalized to the case with inhomogeneous atom-cavity couplings, $g_i = g_c \eta_i$. The effective ground state Hamiltonian [Eq. (4.28)] still takes the same form if we redefine the operators in Eq. (4.29) as $\hat{D}_i^L = \eta_i^2 \hat{S}_i^+ \hat{S}_i^-$, $\hat{D}_i^R = \eta_i^2 \hat{S}_i^- \hat{S}_i^+$, $\hat{T}_i^+ = -\eta_i^2 \hat{S}_i^+ \hat{S}_i^+$ (see SOM).

The most common type of initial state required in our protocol, $|g_{-F}\rangle^{\otimes(N/2)} |g_F\rangle^{\otimes(N/2)}$, has already been demonstrated in previous experiments using ^{87}Sr atoms [186, 263]. It is achieved by targeting the $|g_{\pm F}\rangle$ states to be dark states of a laser cooling process. The generated state has roughly equal number of atoms in these two levels with no initial coherence, up to an statistical atom number imbalance in the order of $\sqrt{N}$. The small imbalance in the prepared state has negligible effects on the physical phenomena we are investigating, for the large ensemble situations relevant for current cavity QED experiments.

4.3.4 Conclusion and outlook

We have presented a protocol to explore correlated hopping processes using cavity mediated interactions and discussed a few examples in regimes tractable by current theoretical methods. However, even in the permutationally symmetric subspace, more generic initial conditions can lead to situations only explorable directly in experiments. Moreover, with additional tuning knobs currently accessible in experiments we open further opportunities for quantum simulation. For

example, using an additional transverse magnetic field, our protocol opens a path to engineer dynamical gauge fields, since the hopping phase in correlated hopping processes can be dynamically adjusted by the presence of other particles. Furthermore, even though here we assume a dilute gas and ignore contact interactions between atoms, by trapping atoms in 3D optical lattices, it is possible to make superexchange interactions comparable to the correlated hopping strength, opening a path for designing complex many-body Hamiltonians that are likely to display fast scrambling of quantum information and chaotic quantum behaviors [264].

4.3.5 Supplemental Materials: Theory model

Here we describe how to obtain Eq. (4.27) in the main text beginning with the fundamental interaction between atoms and light in a cavity. We work with ground and excited state manifolds of N atoms, which are assumed to have hyperfine spin F_g and F_e, respectively and are split by an energy ω_a. The ground and excited states of atom i are defined with respect to a quantization axis that is parallel to the cavity axis, and we label them as $|g_m\rangle_i$ and $|e_m\rangle_i$, respectively, where m is the magnetic quantum number. These atoms interact with two circularly polarized cavity modes at frequency ω_c, with strength g_i for atom i. These coupling constants are parameterized as $g_i = g_c\eta_i$, where η_i are dimensionless numbers of order 1 that describe the inhomogeneity in the couplings. The Hamiltonian describing this interaction is then [192]

$$\hat{H}_{\text{atom-light}}/\hbar = \omega_a\hat{N}_e + \omega_c(\hat{a}_L^\dagger\hat{a}_L + \hat{a}_R^\dagger\hat{a}_R) + g_c(\hat{a}_L\hat{L}^+ + \hat{a}_R\hat{R}^+ + h.c.), \tag{4.34}$$

where $\hat{a}_L(\hat{a}_R)$ are boson operators that annihilate a σ^- (σ^+) photon, $\hat{N}_e = \sum_{i,m}|e_m\rangle\langle e_m|_i$ is the number of atoms in the excited state, $\hat{L}^+ = \sum_{i,m}\eta_i C_m^{-1}|e_{m-1}\rangle\langle g_m|_i$ and $\hat{R}^+ = \sum_{i,m}\eta_i C_m^{+1}$ $|e_{m+1}\rangle\langle g_m|_i$ are multilevel collective dipole operators with σ^- and σ^+ polarization, and $C_m^p = \langle F_g, m; 1, p|F_e, m+p\rangle$ are Clebsch-Gordan coefficients. The interaction describes the absorption of a σ^- (σ^+) cavity photon by the atomic ensemble accompanied by an atomic excitation with σ^- (σ^+) light, together with the inverse process.

We consider the situation in which the cavity is far detuned from the atomic transition

$|\Delta_c| \gg g_c\sqrt{N}, \kappa$, where $\Delta_c = \omega_c - \omega_a$, and κ is the cavity decay rate. In addition to this, the cavity will be driven by two tones with frequencies close to ω_a, so they are far away from the cavity resonance frequency. Because of this, the number of intracavity photons is always very small, hence the light degrees of freedom can be adiabatically eliminated. The atom-light interaction, albeit weak, induces many-body splittings of the excited states, which the drives are designed to probe. The cavity-mediated atom-atom interactions are described by the following effective Hamiltonian [192]

$$\hat{H}_{\text{atom-atom}}/\hbar = \omega_a \hat{N}_e + \chi \hat{L}^+ \hat{L}^- + \chi \hat{R}^+ \hat{R}^-, \tag{4.35}$$

where $\hat{L}^- = (L^+)^\dagger$, $\hat{R}^- = (R^+)^\dagger$ and $\chi = -g_c^2/\Delta_c$ is the effective atom-atom interaction. The two injected driving fields (A, B) are assumed to be σ^- polarized, with frequencies $\omega_d^{A,B}$ and intensities outside the cavity of $|\alpha_{A,B}|^2$ photons per second. These injected fields establish a small intracavity field that induces Rabi flopping on the atoms with Rabi frequencies $\Omega_{A,B} = -\sqrt{\kappa}\alpha_{A,B} g_c/\Delta_c$. Adding these terms leads to Eq. (1) in the main text,

$$\hat{H}_{\text{aa+d}}/\hbar = \omega_a \hat{N}_e + \chi \hat{L}^+ \hat{L}^- + \chi \hat{R}^+ \hat{R}^- + \left[\left(\Omega_A e^{-i\omega_d^A t} + \Omega_B e^{-i\omega_d^B t}\right)\hat{L}^\dagger + h.c.\right]. \tag{4.36}$$

When the intracavity Rabi frequencies are small compare to $\max(\chi N, |\Delta_{A,B}|)$, with $\Delta_{A,B} = \omega_d^{A,B} - \omega_a$, the excited state will only be virtually populated and can thus be adiabatically eliminated. To make the discussion simple, we consider first the case of a single drive Ω_A, with associated Hamiltonian

$$\hat{H}_A/\hbar = \omega_a \hat{N}_e + \chi \hat{L}^+ \hat{L}^- + \chi \hat{R}^+ \hat{R}^- + \left(\Omega_A e^{-i\omega_d^A t}\hat{L}^+ + \Omega_A^* e^{i\omega_d^A t}\hat{L}^-\right). \tag{4.37}$$

In the rotating frame of the drive, this becomes

$$\hat{H}'_A/\hbar = \underbrace{-\Delta_A \hat{N}_e + \chi \hat{L}^+ \hat{L}^- + \chi \hat{R}^+ \hat{R}^-}_{\hat{H}_0} + \underbrace{\left(\Omega_A \hat{L}^+ + \Omega_A^* \hat{L}^-\right)}_{\text{perturbation}}. \tag{4.38}$$

Given that the Hamiltonian in this rotating frame is time-independent, the ground state effective description can be calculated using perturbation theory. First, notice that all the ground states are degenerate, with energy 0, in the absence of the perturbation. Furthermore, since the operator $\hat{L}^+$

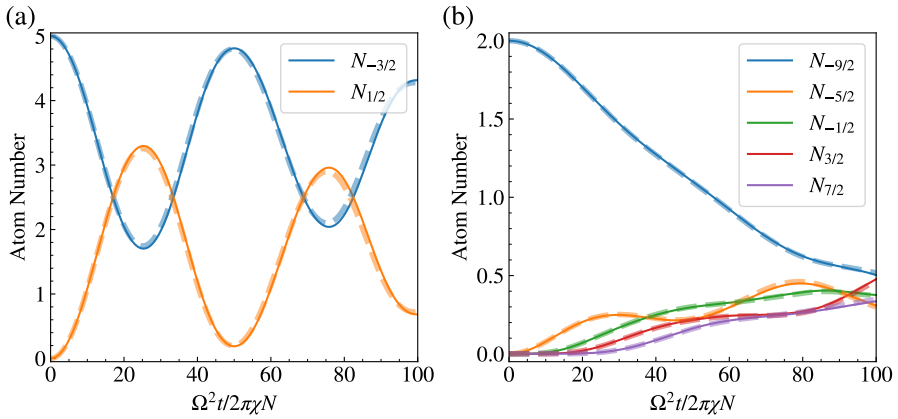

Figure 4.15: Numerical benchmarking of adiabatic elimination of atomic excited states. The Hamiltonian dynamics under Eq. (4.36) are shown in solid lines, while the Hamiltonian dynamics under Eq. (4.28) are shown in dashed lines. We set $\Delta_A = -3\chi N$, $\Delta_B = 4.1\chi N$, $\Omega_{A,B} = \Omega = 0.05\chi N$. We consider the following two cases: (a) 4-level system with initial state $|g_{-3/2}\rangle^{\otimes(N/2)}|g_{3/2}\rangle^{\otimes(N/2)}$, and atom number $N = 10$. (b) 10-level system with initial state $|g_{-9/2}\rangle^{\otimes(N/2)}|g_{9/2}\rangle^{\otimes(N/2)}$, and atom number $N = 4$.

maps the ground state manifold to single excitation states, the first order perturbative correction due to the drive is 0. The degeneracy of the ground states is lifted at second order using degenerate perturbation theory,

$$\hat{H}_{\text{eff},A}/\hbar \approx -\hat{P}_g\left(\Omega_A\hat{L}^+ + \Omega_A^*\hat{L}^-\right)\frac{1}{\hat{H}_0}\left(\Omega_A\hat{L}^+ + \Omega_A^*\hat{L}^-\right)\hat{P}_g = -|\Omega_A|^2\hat{P}_g\hat{L}^-\frac{1}{\hat{H}_0}\hat{L}^+\hat{P}_g, \tag{4.39}$$

where $\hat{P}_g$ are projectors onto the ground state manifold. The unperturbed Hamiltonian $\hat{H}_0$ includes not only the single particle term $\propto \hat{N}_e$ but also nonlinear contributions $\propto \hat{L}^+\hat{L}^-, \hat{R}^+\hat{R}^-$ and thus obtaining a simple expression for $\hat{H}_0^{-1}$ is not straightforward. Fortunately, $\hat{H}_0$ conserves the number of excitations, which is a strong enough symmetry to allow for an explicit calculation of $\hat{H}_0^{-1}$. To do this, consider the quantity

$$\hat{H}_0\hat{L}^+\hat{P}_g = -\Delta_A\hat{N}_e\hat{L}^+\hat{P}_g + \chi\hat{L}^+\hat{L}^-\hat{L}^+\hat{P}_g + \chi\hat{R}^+\hat{R}^-\hat{L}^+\hat{P}_g. \tag{4.40}$$

Due to the projectors, some parts of this expression can be simplified. First, $\hat{N}_e\hat{L}^+\hat{P}_g = \hat{L}^+\hat{P}_g$ since the image of the operator $\hat{L}^+\hat{P}_g$ is on the single excitation manifold. Second, the operators $\hat{L}^-\hat{L}^+\hat{P}_g$ and $\hat{R}^-\hat{L}^+\hat{P}_g$ preserve the ground state manifold and can thus be written as $\hat{L}^-\hat{L}^+\hat{P}_g \equiv$

$\hat{D}_L\hat{P}_g$ and $\hat{R}^-\hat{L}^+\hat{P}_g \equiv \hat{T}^-\hat{P}_g$ where

$$\begin{aligned}\hat{D}_L &\equiv \hat{P}_g\hat{L}^-\hat{L}^+\hat{P}_g = \sum_i \hat{D}_i^L, \quad \hat{D}_i^L = \sum_m \eta_i^2 (C_m^{-1})^2 |g_m\rangle\langle g_m|_i, \\ \hat{T}^- &\equiv \hat{P}_g\hat{R}^-\hat{L}^+\hat{P}_g = \sum_i \hat{T}_i^-, \quad \hat{T}_i^- = \sum_m \eta_i^2 C_{m-2}^{+1} C_m^{-1} |g_{m-2}\rangle\langle g_m|_i,\end{aligned} \tag{4.41}$$

are collective ground state operators only. Therefore

$$\boxed{\hat{H}_0\hat{L}^+\hat{P}_g = (\hat{L}^+\hat{P}_g)(-\Delta_A + \chi\hat{D}_L) + (\hat{R}^+\hat{P}_g)(\chi\hat{T}^-)}. \tag{4.42}$$

Note the ordering of the operators, which is important since $[\hat{L}^\pm, \hat{D}_L] \neq 0$ and $[\hat{R}^\pm, \hat{T}^-] \neq 0$. Similarly,

$$\boxed{\hat{H}_0\hat{R}^+\hat{P}_g = (\hat{R}^+\hat{P}_g)(-\Delta_A + \chi\hat{D}_R) + (\hat{L}^+\hat{P}_g)(\chi\hat{T}^+)}, \tag{4.43}$$

where

$$\begin{aligned}\hat{D}_R &\equiv \hat{P}_g\hat{R}^-\hat{R}^+\hat{P}_g = \sum_i \hat{D}_i^R, \quad \hat{D}_i^R = \sum_m \eta_i^2 (C_m^{+1})^2 |g_m\rangle\langle g_m|_i, \\ \hat{T}^+ &\equiv \hat{P}_g\hat{L}^-\hat{R}^+\hat{P}_g = \sum_i \hat{T}_i^+, \quad \hat{T}_i^+ = \sum_m \eta_i^2 C_m^{+1} C_{m+2}^{-1} |g_{m+2}\rangle\langle g_m|_i.\end{aligned} \tag{4.44}$$

Right multiplying Eq. (4.43) by $(-\Delta_A + \chi\hat{D}_R)^{-1}\chi\hat{T}^-$ and subtracting the result from Eq. (4.42) results in

$$\begin{aligned}&\hat{H}_0\Big[\hat{L}^+\hat{P}_g - \hat{R}^+\hat{P}_g(-\Delta_A + \chi\hat{D}_R)^{-1}\chi\hat{T}^-\Big] \\ &= (\hat{L}^+\hat{P}_g)\Big[(-\Delta_A + \chi\hat{D}_L) - \chi^2\hat{T}^+(-\Delta_A + \chi\hat{D}_R)^{-1}\hat{T}^-\Big].\end{aligned} \tag{4.45}$$

Left multiplying by $\hat{P}_g\hat{L}^-\hat{H}_0^{-1}$ leads to

$$\begin{aligned}&\hat{D}_L - \hat{T}^+(-\Delta_A + \chi\hat{D}_R)^{-1}\chi\hat{T}^- \\ &= (\hat{P}_g\hat{L}^-\hat{H}_0^{-1}\hat{L}^+\hat{P}_g)\Big[(-\Delta_A + \chi\hat{D}_L) - \chi^2\hat{T}^+(-\Delta_A + \chi\hat{D}_R)^{-1}\hat{T}^-\Big].\end{aligned} \tag{4.46}$$

Therefore

$$(\hat{P}_g\hat{L}^-\hat{H}_0^{-1}\hat{L}^+\hat{P}_g) = \frac{1}{\chi} - \frac{\Delta_A}{\chi}\left(\Delta_A - \chi\hat{D}_L - \chi^2\hat{T}^+\hat{G}_R^A\hat{T}^-\right)^{-1}, \tag{4.47}$$

where $\hat{G}_R^\nu = (\Delta_\nu - \chi\hat{D}_R)^{-1}$ and the effective ground state Hamiltonian due to drive A is

$$\boxed{\hat{H}_{\text{eff},A}/\hbar = -\frac{|\Omega_A|^2}{\chi} + \frac{|\Omega_A|^2\Delta_A}{\chi}\left(\Delta_A - \chi\hat{D}_L - \chi^2\hat{T}^+\hat{G}_R^A\hat{T}^-\right)^{-1}}. \tag{4.48}$$

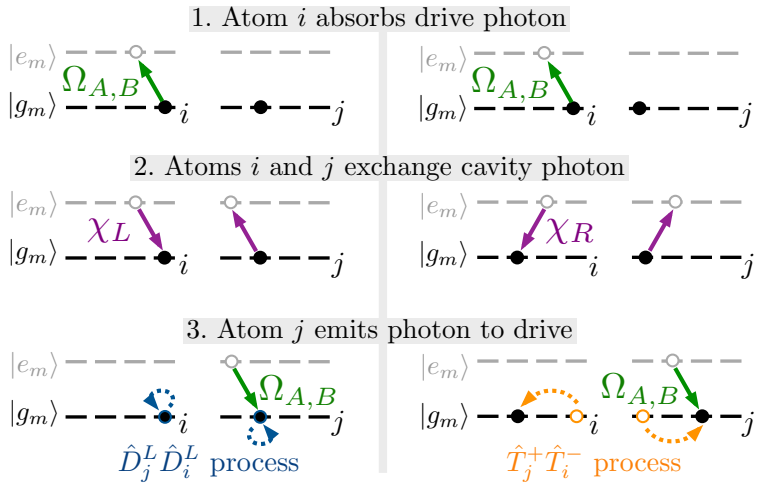

Figure 4.16: Perturbative ground-ground processes between atom i and j. (a) The $\hat{D}_L\hat{D}_L$ process exchanging left circular polarized photons. (b) The $\hat{T}^+\hat{T}^-$ process exchanging right circular polarized photons. Here we define $\chi_L = \chi_R = \chi$, with subscript L or R labelling photon polarizations.

Similarly, drive B will generate an analogous contribution to the effective ground state Hamiltonian. Since there are no possible interference pathways between the two drives (at second order) due to their different frequencies (we will take $\Delta_A\Delta_B < 0$), the full effective Hamiltonian will be the sum of both contributions

$$\boxed{\hat{H}_{\text{eff}}/\hbar = -\sum_{\nu=A,B}\frac{|\Omega_\nu|^2}{\chi} + \sum_{\nu=A,B}\frac{|\Omega_\nu|^2\Delta_\nu}{\chi}\left(\Delta_\nu - \chi\hat{D}_L - \chi^2\hat{T}^+\hat{G}_R^\nu\hat{T}^-\right)^{-1}}. \tag{4.49}$$

Omitting the c-number terms leads to Eq. (2) in the main text. We have numerically benchmarked the validity of $\hat{H}_{\text{eff}}$ [Eq. (4.49)] to capture the dynamics of the full atomic Hamiltonian $\hat{H}_{\text{aa+d}}$ [Eq. (4.36)]. Fig. 4.15 shows the excellent agreement between them.

Now we proceed to discuss the reason why we need two external drives. In the off-resonant regime ($|\Delta_{A,B}| \gtrsim |\chi N|$), one can expand $\hat{H}_{\text{eff}}$ in a power series of $\chi N/\Delta_{A,B}$, and keep only the leading order terms as an excellent approximation. It's worth to mention that we only use this approximation for a qualitative understanding of the dynamics in our system, while all the quantitative calculations are still based on Eq. (4.49). In this approximation, the effective Hamiltonian simplifies to

$$\hat{H}_{\text{eff}}/\hbar \approx \sum_{\nu=A,B}\frac{|\Omega_\nu|^2}{\Delta_\nu}\hat{D}_L + \frac{|\Omega_\nu|^2\chi}{\Delta_\nu^2}(\hat{D}_L\hat{D}_L + \hat{T}^+\hat{T}^-). \tag{4.50}$$

As we discussed in the main text, the first term describes the single-particle AC Stark shift, the second term describes the population dependent collective shift, and the third term describes correlated hopping. The microscopic mechanism of the second and the third term is shown in Fig. 4.16. If we have only one external drive, the single-particle AC Stark shift term always play dominant role. In order to observe correlated hopping, one can use two external drives with detunings in opposite sign to suppress the undesirable energy shifts generated by the first two terms. Considering an initial state $|i\rangle$ and a final state $|f\rangle$ connected by correlated hopping processes, $\langle f|\hat{T}^{+}\hat{T}^{-}|i\rangle \neq 0$, the condition of suppressing the first two terms can be written as

$$\left|\langle i|\hat{H}_{\text{eff}}|i\rangle - \langle f|\hat{H}_{\text{eff}}|f\rangle\right| \ll \left|\sum_{\nu=A,B} \frac{\hbar|\Omega_\nu|^2\chi}{\Delta_\nu^2}\langle f|\hat{T}^{+}\hat{T}^{-}|i\rangle\right|. \tag{4.51}$$

This condition can be satisfied by tuning $\Delta_{A,B}$. Even though it is only computed using the initial state and thus only guarantee to be satisfied at $t = 0$, we find that in a large parameter regime it allows to make the correlated hopping process to be dominant during a time window where they can give rise to non-trivial spreading through the synthetic ladder.

4.3.6 Supplemental Materials: Schwinger bosons and undepleted pump approximation

In the main text, we focused on the initial states as a direct product of a permutationally symmetric states of $N/2$ atoms on the upper leg of the synthetic ladder ($|\psi_{\text{up}}\rangle$) and a permutationally symmetric state of $N/2$ atoms on the lower leg ($|\psi_{\text{down}}\rangle$),

$$|\psi\rangle = |\psi_{\text{up}}\rangle \otimes |\psi_{\text{down}}\rangle. \tag{4.52}$$

Since the effective ground state Hamiltonian [Eq. (4.49)] forbids any direct hopping process between the legs of the synthetic ladder, the Hamiltonian dynamics with these initial states occurs in a reduced Hilbert space consisted of any $SU\left(\frac{2F_g+1}{2}\right) \times SU\left(\frac{2F_g+1}{2}\right)$ rotations on $|\psi\rangle$, where $SU(n)$ denotes special unitary group of $n \times n$ matrices. So we can assign one set of Schwinger bosons $\{\hat{a}_{-F_g+1}, \hat{a}_{-F_g+3}, \cdots, \hat{a}_{F_g}\}$ to the upper leg and another set of Schwinger bosons

$\{\hat{a}_{-F_g}, \hat{a}_{-F_g+2}, \cdots, \hat{a}_{F_g-1}\}$ to the lower leg. In this way, we can rewrite the operators acting only on the ground manifold as,

$$\hat{D}_L = \sum_m (C_m^{-1})^2 \hat{a}_m^\dagger \hat{a}_m, \quad \hat{D}_R = \sum_m (C_m^{+1})^2 \hat{a}_m^\dagger \hat{a}_m, \quad \hat{T}^+ = \sum_m C_m^{+1} C_{m+2}^{-1} \hat{a}_{m+2}^\dagger \hat{a}_m, \tag{4.53}$$

where $\hat{a}_m$ is the bosonic annihilation operator for state $|g_m\rangle$. In the following, we will apply undepleted pump approximation (UPA) to the four-level and the six-level system discussed in the main text. The cascaded correlated hopping process in the ten-level system is beyond the reach of UPA.

UPA for four-level system

We first consider the initial state $|g_{-3/2}\rangle^{\otimes(N/2)}|g_{3/2}\rangle^{\otimes(N/2)}$ for the four-level ($F_g = F_e = 3/2$) system discussed in the main text. The short time dynamics in this system can be understood via UPA, where to the leading order one can replace the bosonic operators of the initial macroscopically occupied states as c-numbers,

$$\hat{a}_{\pm 3/2} = \hat{a}_{\pm 3/2}^\dagger \approx \sqrt{\frac{N}{2}}, \quad \text{and} \quad \hat{a}_{\pm 3/2}^\dagger \hat{a}_{\pm 3/2} = \frac{N}{2} - \hat{a}_{\mp 1/2}^\dagger \hat{a}_{\mp 1/2}. \tag{4.54}$$

So the operators in Eq. (4.53) can be approximated as

$$\hat{D}_L \approx \frac{N}{5} + \frac{8}{15}\hat{a}_{1/2}^\dagger \hat{a}_{1/2}, \quad \hat{D}_R \approx \frac{N}{5} + \frac{8}{15}\hat{a}_{-1/2}^\dagger \hat{a}_{-1/2}, \quad \hat{T}^+ \approx -\frac{2\sqrt{6N}}{15}(\hat{a}_{1/2}^\dagger + \hat{a}_{-1/2}). \tag{4.55}$$

Plugging in this approximation in the effective ground state Hamiltonian [Eq. (4.49)], and keeping the terms with operators $\hat{a}_{\pm 1/2}, \hat{a}_{\pm 1/2}^\dagger$ up to second order, we obtain,

$$\begin{aligned}
\hat{H}_{\text{eff}}/\hbar &= \sum_{\nu=A,B} \frac{|\Omega_\nu|^2 \Delta_\nu}{\chi} \left[\Delta_\nu - \chi \hat{D}_L - \chi^2 \hat{T}^+ (\Delta_\nu - \chi \hat{D}_R)^{-1} \hat{T}^- \right]^{-1} \\
&\approx \sum_{\nu=A,B} \frac{|\Omega_\nu|^2 \Delta_\nu}{\chi} \Bigg[(\Delta_\nu - \chi N/5) - \frac{8\chi}{15}\hat{a}_{1/2}^\dagger \hat{a}_{1/2} \\
&\qquad\qquad - \frac{\chi^2}{\Delta_\nu - \chi N/5} \frac{8N}{75} (\hat{a}_{1/2}^\dagger + \hat{a}_{-1/2})(\hat{a}_{1/2} + \hat{a}_{-1/2}^\dagger) \Bigg]^{-1} \\
&\approx K_1 \hat{a}_{-1/2}^\dagger \hat{a}_{-1/2} + K_2 \hat{a}_{1/2}^\dagger \hat{a}_{1/2} + K_3 (\hat{a}_{-1/2}^\dagger \hat{a}_{1/2}^\dagger + \hat{a}_{-1/2} \hat{a}_{1/2}).
\end{aligned} \tag{4.56}$$

where

$$K_1 = K_3 = \sum_{\nu=A,B} \frac{8}{75} \frac{|\Omega_\nu|^2 \Delta_\nu \chi N}{(\Delta_\nu - \chi N/5)^3},$$
$$K_2 = \sum_{\nu=A,B} \frac{8}{15} \frac{|\Omega_\nu|^2 \Delta_\nu}{(\Delta_\nu - \chi N/5)^2} + \frac{8}{75} \frac{|\Omega_\nu|^2 \Delta_\nu \chi N}{(\Delta_\nu - \chi N/5)^3}. \tag{4.57}$$

The effective Hamiltonian under the UPA [Eq. (4.56)] can be exactly diagonalized using a Bogoliubov transformation. In this case the dynamics of the populations in the $|g_{\pm 1/2}\rangle$ states, labelled as $N_{\pm 1/2}$, is found to be given by the following analytic formula in different parameter regimes:

$$N_{\pm 1/2}(t) = \begin{cases} \dfrac{4K_3^2}{(K_1+K_2)^2 - 4K_3^2} \sin^2\left(\sqrt{(K_1+K_2)^2 - 4K_3^2}\, \dfrac{t}{2}\right) & \text{if } (K_1+K_2)^2 > 4K_3^2 \\ K_3^2 t^2 & \text{if } (K_1+K_2)^2 = 4K_3^2 \\ \dfrac{4K_3^2}{4K_3^2 - (K_1+K_2)^2} \sinh^2\left(\sqrt{4K_3^2 - (K_1+K_2)^2}\, \dfrac{t}{2}\right) & \text{if } (K_1+K_2)^2 < 4K_3^2 \end{cases}, \tag{4.58}$$

which are shown using dashed lines in Fig. 2(c) in the main text. Notice that $N_{\pm 1/2}(t)$ shows small sinusoidal oscillations in the regime $(K_1+K_2)^2 > 4K_3^2$, while it shows an exponential growth in the regime $(K_1+K_2)^2 < 4K_3^2$. This indicates a dynamical phase transition (DPT) at the critical point $(K_1+K_2)^2 = 4K_3^2$, which is equivalent to

$$\sum_{\nu=A,B} \frac{|\Omega_\nu|^2 \Delta_\nu}{(\Delta_\nu - \chi N/5)^2} = 0 \quad \text{or} \quad \sum_{\nu=A,B} \frac{|\Omega_\nu|^2 \Delta_\nu}{(\Delta_\nu - \chi N/5)^2} + \frac{4}{5} \frac{|\Omega_\nu|^2 \Delta_\nu \chi N}{(\Delta_\nu - \chi N/5)^3} = 0. \tag{4.59}$$

By solving these two equations, one can obtain the phase boundaries shown in Fig. 2(b) in the main text.

UPA for six-level system

In the main text, we consider the initial state $[\sqrt{p_{-3/2}}|g_{-3/2}\rangle + \sqrt{p_{5/2}}|g_{5/2}\rangle]^{\otimes(N/2)} |g_{-1/2}\rangle^{\otimes(N/2)}$ for the six-level ($F_g = F_e = 5/2$) system, where $p_{5/2} = 1 - p_{-3/2}$. Similar to the previous subsection, we use the UPA to analyze the short time dynamics in this system. We have 6 independent

Schwinger bosons in this problem,

$$\text{Empty}: \quad \hat{a}_{-5/2}, \quad \hat{a}_{3/2}, \quad \hat{a}_{1/2}, \quad \hat{a}_- = -\sqrt{p_{5/2}}\hat{a}_{-3/2} + \sqrt{p_{-3/2}}\hat{a}_{5/2}$$

$$\text{Occupied}: \quad \hat{a}_{-1/2}, \quad \hat{a}_+ = \sqrt{p_{-3/2}}\hat{a}_{-3/2} + \sqrt{p_{5/2}}\hat{a}_{5/2}$$

We would like to replace the occupied modes by c-numbers, and keep the empty modes up to second order. So we have

$$\begin{aligned}\hat{D}_L &= \frac{16}{35}\hat{a}^\dagger_{-1/2}\hat{a}_{-1/2} + \frac{16}{35}\hat{a}^\dagger_{3/2}\hat{a}_{3/2} + \frac{18}{35}\hat{a}^\dagger_{1/2}\hat{a}_{1/2} + \frac{2}{7}\hat{a}^\dagger_+\hat{a}_+ + \frac{2}{7}\hat{a}^\dagger_-\hat{a}_- \\ &\approx \frac{13}{35}N - \frac{16}{35}\hat{a}^\dagger_{-5/2}\hat{a}_{-5/2} + \frac{8}{35}\hat{a}^\dagger_{1/2}\hat{a}_{1/2},\end{aligned} \tag{4.60}$$

$$\begin{aligned}\hat{D}_R &= \frac{2}{7}\hat{a}^\dagger_{-5/2}\hat{a}_{-5/2} + \frac{2}{7}\hat{a}^\dagger_{3/2}\hat{a}_{3/2} + \frac{18}{35}\hat{a}^\dagger_{-1/2}\hat{a}_{-1/2} + \frac{16}{35}\hat{a}^\dagger_{1/2}\hat{a}_{1/2} \\ &\quad + \frac{16}{35}(\sqrt{p_{-3/2}}\hat{a}^\dagger_+ - \sqrt{p_{5/2}}\hat{a}^\dagger_-)(\sqrt{p_{-3/2}}\hat{a}_+ - \sqrt{p_{5/2}}\hat{a}_-) \\ &\approx \left(\frac{9}{35} + \frac{8}{35}p_{-3/2}\right)N - \frac{8}{35}\hat{a}^\dagger_{-5/2}\hat{a}_{-5/2} - \frac{8}{35}\hat{a}^\dagger_{3/2}\hat{a}_{3/2} + \frac{16}{35}(1-p_{-3/2})\hat{a}^\dagger_{1/2}\hat{a}_{1/2} \\ &\quad + \frac{16}{35}(p_{5/2}-p_{-3/2})\hat{a}^\dagger_-\hat{a}_- - \frac{16}{35}\sqrt{p_{-3/2}p_{5/2}}\sqrt{\frac{N}{2}}(\hat{a}^\dagger_- + \hat{a}_-),\end{aligned} \tag{4.61}$$

$$\begin{aligned}\hat{T}^+ &= -\left[\frac{4\sqrt{10}}{35}\hat{a}^\dagger_{-1/2}\hat{a}_{-5/2} + \frac{12\sqrt{2}}{35}\hat{a}^\dagger_{3/2}\hat{a}_{-1/2} + \frac{12\sqrt{2}}{35}\hat{a}^\dagger_{1/2}(\sqrt{p_{-3/2}}\hat{a}_+ - \sqrt{p_{5/2}}\hat{a}_-)\right. \\ &\quad \left. + \frac{4\sqrt{10}}{35}(\sqrt{p_{5/2}}\hat{a}^\dagger_+ + \sqrt{p_{-3/2}}\hat{a}^\dagger_-)\hat{a}_{1/2}\right] \\ &\approx -\left[\frac{4\sqrt{10}}{35}\sqrt{\frac{N}{2}}\hat{a}_{-5/2} + \frac{12\sqrt{2}}{35}\sqrt{\frac{N}{2}}\hat{a}^\dagger_{3/2} + \frac{12\sqrt{2}}{35}\sqrt{\frac{p_{-3/2}N}{2}}\hat{a}^\dagger_{1/2} + \frac{4\sqrt{10}}{35}\sqrt{\frac{p_{5/2}N}{2}}\hat{a}_{1/2}\right].\end{aligned} \tag{4.62}$$

In this way, the effective ground state Hamiltonian [see Eq. (4.49)] can be approximated into the following form,

$$\hat{H}_{\text{eff}}/\hbar \approx \sum_{ij}\left[\mathcal{L}_{ij}\hat{a}^\dagger_i\hat{a}_j + \frac{1}{2}\mathcal{M}_{ij}\hat{a}^\dagger_i\hat{a}^\dagger_j + \frac{1}{2}\mathcal{M}^*_{ij}\hat{a}_i\hat{a}_j\right], \tag{4.63}$$

where $i,j \in \{-5/2, 1/2, 3/2\}$, and $\hat{a}_-, \hat{a}^\dagger_-$ are not included because they only appear in the terms beyond the second order. Here, $\mathcal{L}$ is a Hermitian matrix, and $\mathcal{M}$ is a symmetric matrix. They take the following form:

$$\mathcal{L} = \begin{pmatrix} K_1 & K_4\sqrt{p_{5/2}} & 0 \\ K_4\sqrt{p_{5/2}} & K_2 & K_5\sqrt{p_{-3/2}} \\ 0 & K_5\sqrt{p_{-3/2}} & K_3 \end{pmatrix}, \quad \mathcal{M} = \begin{pmatrix} 0 & K_6\sqrt{p_{-3/2}} & K_6 \\ K_6\sqrt{p_{-3/2}} & 2K_6\sqrt{p_{-3/2}p_{5/2}} & K_6\sqrt{p_{5/2}} \\ K_6 & K_6\sqrt{p_{5/2}} & 0 \end{pmatrix}, \tag{4.64}$$

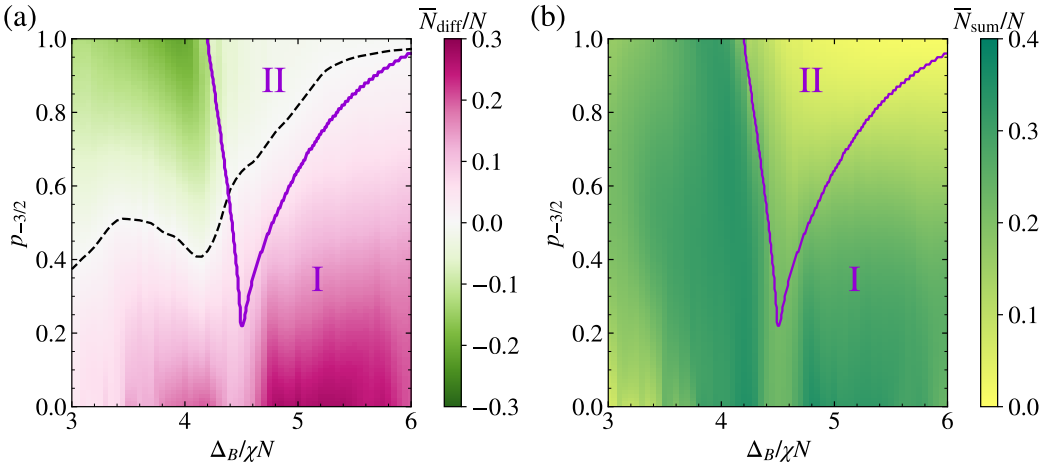

Figure 4.17: Dynamical phase boundary in the six-level system (purple line) calculated by UPA in comparison with (a) $\overline{N}_{\rm diff}/N$ and (b) $\overline{N}_{\rm sum}/N$ calculated by exact diagonalization with 20 atoms. We set $\Delta_A = -3\chi N$, and the same initial state for the six-level system as discussed in the main text. The black dashed line in (a) indicates balanced transport.

where

$$K_1 = -\frac{16}{35}C_1 + \frac{16}{245}C_2, \quad K_2 = \frac{8}{35}C_1 + \left(\frac{144}{1225}p_{-3/2} + \frac{16}{245}p_{5/2}\right)C_2,$$
$$K_3 = K_5 = \frac{144}{1225}C_2, \quad K_4 = \frac{16}{245}C_2, \quad K_6 = \frac{48\sqrt{5}}{1225}C_2, \tag{4.65}$$
$$C_1 = \sum_{\nu=A,B}\frac{|\Omega_\nu|^2\Delta_\nu}{(\Delta_\nu - 13\chi N/35)^2}, \quad C_2 = \sum_{\nu=A,B}\frac{|\Omega_\nu|^2\Delta_\nu\chi N}{(\Delta_\nu - 13\chi N/35)^2[\Delta_\nu - (9+8p_{-3/2}\chi N/35)]}.$$

The dynamics of an operator $\hat{O}$ under Eq. (4.63) can be solved exactly using the Heisenberg equations of motion $\partial_t\hat{O} = i[\hat{H},\hat{O}]/\hbar$, so we have the following set of equations for the bosonic creation and annilation operators,

$$\partial_t\begin{pmatrix}\hat{A}\\ \hat{A}^\dagger\end{pmatrix} = -i\begin{pmatrix}\mathcal{L} & \mathcal{M}\\ -\mathcal{M}^* & -\mathcal{L}^*\end{pmatrix}\begin{pmatrix}\hat{A}\\ \hat{A}^\dagger\end{pmatrix}, \tag{4.66}$$

where $\hat{A} = (\hat{a}_{-5/2}, \hat{a}_{1/2}, \hat{a}_{3/2})^T$. This allows us to reduce the problem into the calculation of right eigenvalues and right eigenvectors for a non-Hermitian matrix,

$$\begin{pmatrix}\mathcal{L} & \mathcal{M}\\ -\mathcal{M}^* & -\mathcal{L}^*\end{pmatrix}\begin{pmatrix}\vec{u}_p\\ \vec{v}_p\end{pmatrix} = \epsilon_p\begin{pmatrix}\vec{u}_p\\ \vec{v}_p\end{pmatrix}, \tag{4.67}$$

These are the so-called Bogoliubov-de Gennes (BdG) equations. By defining a matrix $\mathcal{T}$ whose column vectors are the right eigenvectors $(\vec{u}_p, \vec{v}_p)^T$, and a diagonal matrix $\mathcal{H}$ whose diagonal elements are the right eigenvalues ϵ_p, we have

$$\begin{pmatrix} \hat{A}(t) \\ \hat{A}^\dagger(t) \end{pmatrix} = \mathcal{U}_t \begin{pmatrix} \hat{A}(0) \\ \hat{A}^\dagger(0) \end{pmatrix}, \quad \mathcal{U}_t = \exp\left[-i \begin{pmatrix} \mathcal{L} & \mathcal{M} \\ -\mathcal{M}^* & -\mathcal{L}^* \end{pmatrix} t\right] = \mathcal{T} e^{-i\mathcal{H}t} \mathcal{T}^{-1}. \tag{4.68}$$

Since we are considering the initial state as the vacuum state, the expectation values of any quadratic form of bosonic operators are given by

$$\left\langle \text{vac} \left| \begin{pmatrix} \hat{A}(t) \\ \hat{A}^\dagger(t) \end{pmatrix} \begin{pmatrix} \hat{A}(t) & \hat{A}^\dagger(t) \end{pmatrix} \right| \text{vac} \right\rangle = \mathcal{U}_t \begin{pmatrix} 0 & \mathcal{I} \\ 0 & 0 \end{pmatrix} \mathcal{U}_t^T, \tag{4.69}$$

where $\mathcal{I}$ is the identity matrix. Using this method, we can calculate the short time dynamics of N_{diff}, which are shown with dashed lines in Fig. 3(c) in the main text.

Based on Eq. (4.68), one can separate between the exponential growth (Phase I) and the sinusoidal oscillation (Phase II): If all the right eigenvalues ϵ_p are real numbers, the system is in Phase II; If at least one of the right eigenvalues ϵ_p are complex numbers, the system is in Phase I. According to Eq. (4.67), if $(\vec{u}_p, \vec{v}_p)^T$ is a right eigenvector with right eigenvalue ϵ_p, $(\vec{v}_p^*, \vec{u}_p^*)^T$ is a right eigenvector with right eigenvalue $-\epsilon_p^*$. Since all the element of matrix $\mathcal{L}$ and $\mathcal{M}$ are real numbers, if ϵ_p is a right eigenvalue, ϵ_p^* is also a right eigenvalue. Therefore, if ϵ_p is a real number, we have a pair of right eigenvalues $\epsilon_p, -\epsilon_p$; if ϵ_p is a complex number, we have four right eigenvalues $\epsilon_p, -\epsilon_p, \epsilon_p^*, -\epsilon_p^*$. So we have two different cases for the six-level system discussed above: 2 real eigenvalues, 4 complex eigenvalues (Phase I); 6 real eigenvalues (Phase II). The phase boundary calculated by UPA generally agrees with the long-time averages $\overline{N}_{\text{diff}} = \overline{N}_{3/2} - \overline{N}_{-5/2}$ and $\overline{N}_{\text{sum}} = \overline{N}_{3/2} + \overline{N}_{-5/2}$ calculated by exact diagonalization with 20 atoms [see Fig. 4.17].

We can now explain the short-time behavior of chiral transport discussed in the main text based on the 4 pair creation processes described by matrix $\mathcal{M}$:

- Process I: $\hat{a}^\dagger_{-5/2}\hat{a}^\dagger_{1/2}$ with strength $K_6\sqrt{p_{-3/2}}$
- Process II: $\hat{a}^\dagger_{3/2}\hat{a}^\dagger_{1/2}$ with strength $K_6\sqrt{p_{5/2}}$

- Process III: $\hat{a}^{\dagger}_{-5/2}\hat{a}^{\dagger}_{3/2}$ with strength K_6
- Process IV: $\hat{a}^{\dagger}_{1/2}\hat{a}^{\dagger}_{1/2}$ with strength $K_6\sqrt{p_{-3/2}p_{5/2}}$

Notice that only process I and II change the value of $N_{\rm diff}$, and the relative strength between these two processes can be tuned by $p_{-3/2}$, while Δ_B is another control knob to determine whether these processes are on resonance or not. When these two processes are both on resonance, e.g. $\Delta_B/\chi N \in (3,4)$, the direction of chiral transport is fully tunable via $p_{-3/2}$ [see Fig. 4.17(a)]. When process I is off resonance, e.g. $\Delta_B/\chi N \in (5,6)$, we always find chiral transport to the right side in the exponential growth regime, and balanced transport is only possible to achieved by tuning the whole system to sinusoidal oscillation regime [see Fig. 4.17(a)].

4.3.7 Supplemental Materials: Numerical results for dynamical phase transition

Here we present additional numerical results using exact diagonalization that complements the discussion of the dynamical phase transition (DPT) discussed in Fig. 2 of the main text. Since exact diagonalization is only possible for a small atom number, we explore the properties of this DPT in the thermodynamic limit using finite size scaling. Given the collective nature of the cavity-mediated interactions, it is convenient to vary the atom number N while keeping χN fixed. As we described in the main text, we consider the initial state $|g_{-3/2}\rangle^{\otimes(N/2)}|g_{3/2}\rangle^{\otimes(N/2)}$, which is an eigenstate of this system when $\Delta_A, \Delta_B \to \infty$. We choose $\Omega_A = \Omega_B = \Omega = 0.05\chi N$, and then perform a sudden quench to $\Delta_A = -4\chi N$ and Δ_B between $4\chi N$ and $7\chi N$. The order parameter of this DPT is the long-time average of the fractional atom population of the $|g_{\pm 1/2}\rangle$ states,

$$\overline{n}_{\pm 1/2} = \lim_{T\to\infty} \frac{1}{T}\int_0^T \frac{N_{\pm 1/2}(t)}{N} dt, \tag{4.70}$$

shows a sharp change behavior as we varying Δ_B [see Fig. 4.18(a)]. Near the dynamical critical points ($\Delta_{B,1} = 4.80\chi N$, $\Delta_{B,2} = 6.53\chi N$), it is convenient to assume $\overline{n}_{\pm 1/2}$ as a homogeneous function,

$$\overline{n}_{\pm 1/2} = N^{-\beta_{1,2}/\nu} f(\tau_{1,2} N^{1/\nu}), \tag{4.71}$$

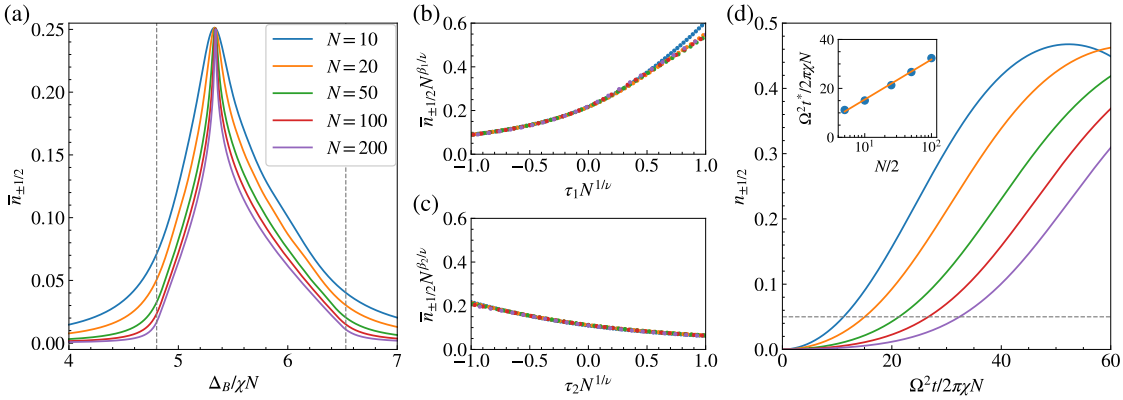

Figure 4.18: Finite size scaling of DPT by varying atom number N while keeping χN fixed. (a) The long-time average fractional atom population of $|g_{\pm1/2}\rangle$ states ($\overline{n}_{\pm1/2}$) at $\Delta_A = -4\chi N$. The dashed lines indicate the dynamical critical points predicted by UPA in the previous section. (b,c) Data collapse of finite-size calculations of $\overline{n}_{\pm1/2}$ near the critical points $\Delta_{B,1}$ and $\Delta_{B,2}$ (see text). (d) Short-time dynamics of $n_{\pm1/2}$ at $\Delta_A = -4\chi N$ and $\Delta_B = 5.3\chi N$. The dashed line marks $n_{\pm1/2} = 0.05$, which determines the typical time scale t^* for the obsevation of the DPT. The inset shows the logarithmic scaling of t^*.

where $\tau_1 = (\Delta_B - \Delta_{B,1})/\chi N$, $\tau_2 = (\Delta_B - \Delta_{B,2})/\chi N$. The data collapse of finite-size calculations are shown in Fig. 4.18(b,c), which gives $\beta_1 = 1.15$, $\beta_2 = 1.04$, $\nu = 2.38$. Based on the data collapse, one can conclude that

$$\begin{aligned} &\overline{n}_{\pm1/2} = 0 \ (\tau_1 < 0), \quad \overline{n}_{\pm1/2} \propto \tau_1^{\beta_1} \ (\tau_1 > 0), \\ &\overline{n}_{\pm1/2} \propto (-\tau_2)^{\beta_2} \ (\tau_2 < 0), \quad \overline{n}_{\pm1/2} = 0 \ (\tau_2 > 0), \end{aligned} \tag{4.72}$$

at thermodynamic limit with $\tau_{1,2} \to 0$.

In experiments, it is easier to explore the DPT using short-time dynamics instead of long-time averages. In phase I, the exponential growth of $n_{\pm1/2}$ is triggered by quantum fluctuations in the initial state, and therefore there is a delay time for $|g_{\pm1/2}\rangle$ states to accumulate a macroscopic population [see Fig. 4.18(d)]. The delay time increases as we increase the atom number N. A reasonable measure of the delay time would be the time t^* for $n_{\pm1/2}$ reaching 0.05 ($\sim$ 10% of maximum value). As shown in the inset of Fig. 4.18(d), we find $t^* \propto \ln(N/2)$.

4.3.8 Supplemental Materials: Experimental considerations

Experimental parameters

Here we discuss the specific case of the $^1S_0 \to {}^3P_1$ transition in ^{87}Sr using the experimental parameters described in Ref. [107]. We show that current experimental parameters lie in the regime where our theory predictions are valid and the dynamics is dominated by unitary evolution. The conditions are summarized in Table 4.1. In this system the typical atom-light coupling strength is $g_c \sim 2\pi \times 10$kHz, and the cavity intensity decay rate is $\kappa \sim 2\pi \times 100$kHz. Choosing atom number $N \sim 2 \times 10^5$, and cavity detuning $\Delta_c = 2\pi \times 20$MHz, we ensure the adiabatic elimination of the cavity photons and dominant unitary dynamics compared to cavity decay. As we discussed in the main text, setting $\Omega_{A,B} = \Omega = 0.05\chi N$, and $\Delta_{A,B}$ comparable or larger than χN satisfy the requirement of adiabatic elimination of atomic excited states. Note that the correlated hopping processes occur at a rate $\Omega^2\chi N/\Delta_{A,B}^2$, while the dissipation process in atomic ground manifold due to spontaneous emission from excited manifold occur at a rate $\Omega^2\gamma/\Delta_{A,B}^2$. Since for the above parameters $\chi N \sim 2\pi \times 1$MHz, is more than two orders of magnitude larger than the spontaneous emission rate $\gamma = 2\pi \times 7.5$kHz of $^3P_1$ states, we can ignore dissipation during the time scale of interests. As shown in Fig. 4 in the main text, the correlation spreading takes place at a time scale $\Omega^2 t/2\pi\chi N \sim 100$ for atom number $N = 10$, and the corresponding delay time is $\Omega^2 t^*/2\pi\chi N \sim 10$. For $N \sim 2 \times 10^5$, the delay time is expected to be 7 times longer, and the relevant experimental time scale to observe correlation spreading is $\Omega^2 t/2\pi\chi N \sim 200$, which corresponds to $t \sim 80$ms.

Table 4.1: Summary of approximations in theory model and the required parameter regimes (see text for details)

Theory approximations	Required parameter regimes
Adiabatic elimination of cavity photons	$\lvert\Delta_c\rvert \gg g_c\sqrt{N}$
Negligible cavity loss	$\lvert\Delta_c\rvert \gg \kappa$
Adiabatic elimination of atomic excited states	$\lvert\Delta_{A,B}\rvert, \lvert\chi N\rvert \gg \lvert\Omega_{A,B}\rvert$
Negligible spontaneous emission	$\lvert\chi N\rvert \gg \gamma$
Weak magnetic field limit	$\lvert\chi N\rvert \gg \delta_e F_e$

Although we have assumed a vanishing magnetic field in our discussions, our protocol is relatively robust against the magnetic field along the quantization axis ($\hat{z}$), because the effective

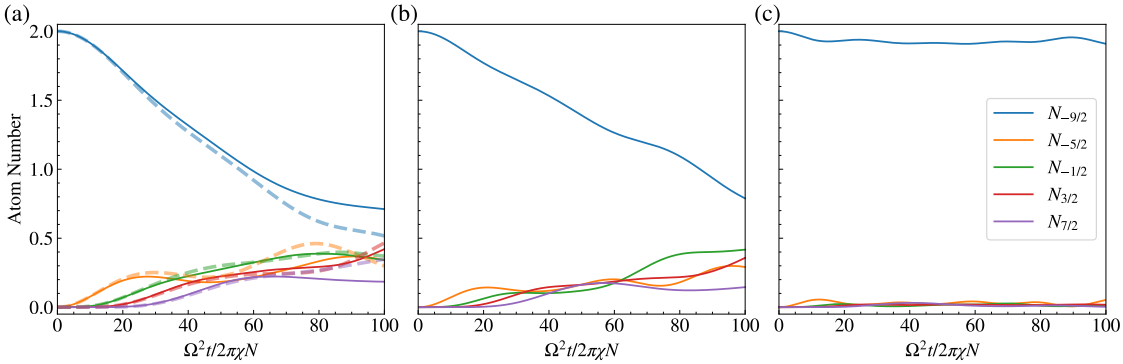

Figure 4.19: Effect of a finite magnetic field in the short-time dynamics for the case of ^{87}Sr atoms. The initial state is $|g_{-9/2}\rangle^{\otimes(N/2)}|g_{9/2}\rangle^{\otimes(N/2)}$, and $N = 4$. We set $\chi N = 2\pi \times 1$MHz, $\Delta_A = -3\chi N$, $\Delta_B = 4.1\chi N$. The solid lines are calculated based on Eq. (4.73), with magnetic field (a) $B = 0.12$G ($\delta_e = 0.01\chi N$), (b) $B = 0.59$G ($\delta_e = 0.05\chi N$), and (c) $B = 1.77$G ($\delta_e = 0.15\chi N$). The dashed lines in (a) are the ideal case with zero magnetic field.

ground state Hamiltonian [Eq. (4.49)] commutes with linear Zeeman shifts on the ground manifold. The only constraint for the maximum tolerable magnetic field is the Zeeman shifts of the excited manifold. They should be small compared to χN, otherwise the many-body structure of the atomic excited states will change and the Zeeman splitting must be included in the derivation of the effective Hamiltonian. We benchmark the effect of magnetic field using the following Hamiltonian,

$$\hat{H} = \hat{H}_{\text{aa+d}} + \hat{H}_Z, \quad \hat{H}_Z/\hbar = \delta_e \hat{F}_e^z + \delta_g \hat{F}_g^z, \tag{4.73}$$

where $\hat{H}_{\text{aa+d}}$ is defined in Eq. (4.36), $\delta_e = \mathcal{G}_{F=9/2,^3P_1}\mu_B B$, and $\delta_g = \mathcal{G}_{F=9/2,^1S_0}\mu_B B$ with μ_B the Bohr magneton, and B the magnetic field. Here, $\mathcal{G}_{F=9/2,^3P_1} = 2/33$, $\mathcal{G}_{F=9/2,^1S_0} = -1.3 \times 10^{-4}$ are the Landé g-factors for ^{87}Sr atoms [265]. We have calculated the exact short-time dynamics for 4 atoms using Trotterization, which are shown as solid lines in Fig. 4.19. For the case of 0.1G magnetic field [see Fig. 4.19(a)], the Hamiltonian dynamics agrees with the case of zero magnetic field at short time. Even with a 0.6G magnetic field [see Fig. 4.19(b)], it is still possible to observe similar dynamics generated by correlated hopping processes. A larger magnetic field can be problematic since it leads to a significant suppression of the correlated hopping processes [see Fig. 4.19(c)].

Initial state preparation

Here we discuss the experimental protocol for initial state preparation. The most common

type of initial state required in the main text is half of atoms in $m_F = -F$ state and half of atoms in $m_F = F$ state. Here we use ^{87}Sr atom ($F = 9/2$) as an example to explain how to prepare it via optical pumping during the laser cooling procedure. Such type of initial state preparation has already been demonstrated in previous experiments [186, 263]. Note that $^1S_0 \to {}^3P_1$ transition is a common choice for narrow-line cooling. If we use π-polarized light to interrogate the transition $^1S_0(F = 9/2) \to {}^3P_1(F' = 7/2)$, one can see that the $m_F = \pm 9/2$ states in the ground manifold are the dark states during the cooling process, and atoms will spontaneous decay and accumulate there at the end of cooling process. So one can prepare roughly $N/2$ atoms in $m_F = -9/2$ state, and $N/2$ atoms in $m_F = 9/2$ state due to the symmetric Clebsch-Gordan coefficients. Note that this process generates no coherence between $m_F = \pm 9/2$ states due to dissipation, which allows us to generate the state $|g_{-9/2}\rangle^{\otimes(N/2)}|g_{9/2}\rangle^{\otimes(N/2)}$, up to an statistical atom number imbalance of the order of $\sqrt{N}$. This small imbalance in the initial state has negligible effects on the physical phenomena we are investigating.

For the general initial states with half of atoms atoms on the upper leg and half of atoms atoms on the lower leg, $|\psi\rangle = |\psi_{\text{up}}\rangle \otimes |\psi_{\text{down}}\rangle$, one can first prepare half of atoms in $m_F = -F$ state and half of atoms in $m_F = F$ state as we discussed above, and then use the ultranarrow $^1S_0 \to {}^3P_0$ transition to perform coherent transfer. This ultranarrow transition allows us to energetically resolve each of the hyperfine levels even with a small magnetic field.

4.4 Control and amplification of Bloch oscillations via photon-mediated interactions

This section is adapted from: Haoqing Zhang, **Anjun Chu**, Chengyi Luo, James K. Thompson, Ana Maria Rey, *Control and amplification of Bloch oscillations via photon-mediated interactions*, Physical Review Research 5, L032039 (2023).

4.4.1 Introduction

Bloch oscillations (BO) [266] are center-of-mass oscillations or coherent breathing experienced by independent particles in a periodic lattice potential in the presence of a constant force (e.g. gravity). Although it has been hard to directly control BO in conventional electron systems, they have been observed in tailored semiconductor systems [267] as well as ultracold atom systems trapped in optical lattices [268, 269]. Nevertheless, for the latter, the lattice potential is by implementation rigid and therefore not a good test bed example of the underlying physics in real materials where the phonons of the crystal dynamically interact with the electron motion. Furthermore, inter-atomic interactions have always been a competing mechanism which damp the oscillations.

Here we propose a scheme to control and amplify atomic BO via photon-mediated interactions in a gravity-tilted optical lattice supported by a standing-wave optical cavity with incommensurate lattice and cavity wavelengths. In our case, photons can actively modify the periodic potential experienced by the atoms and therefore resemble the role of phonons in a real solid state environment. Even though experiments that track BO in optical cavities have been implemented before using a Bose Einstein Condensate (BEC) [270–274], here we propose to use inhomogeneous atom-light couplings to prepare an array of atoms on specific lattice sites and initialize the dynamics [275]. This can be achieved via position-dependent dispersive atom-light couplings to map the motion of the atoms under BO into the frequency shift of the cavity resonance. Our protocol not only avoids the ultracold degenerate initial states required in non-destructive measurements of BO, but also provides flexible self-tunability of the cavity-mediated long-range interactions by the atomic motion. Moreover, in contrast to prior experiments where the periodic potential was generated by the probe laser field itself [270–274] or separate probe field for site-independent atom-light coupling [276], we use an additional lattice potential that traps the atoms and controls the degree of delocalization of the underlying Wannier-Stark (WS) states [38] in our system. In this setting, different to the well-studied case of contact interactions [277–284], the photon-mediated interactions can modify BO depending on the position of other atoms in the array. Taking advantage of this

feature we show versatile many-body phenomena can be realized in different parameter regimes of this system: In the deep lattice region, we find dynamical phase transitions (DPT) related to the Lipkin-Meshkov-Glick (LMG) model [34, 107], which potentially enables rapid generation of spin-squeezed states [7, 31, 285] with WS states directly, bypassing the need for Raman transitions [38]; In the shallow lattice, we find the amplification of Bloch oscillation amplification originating from the pair production [248, 286–288] process from the central to adjacent WS states. We also discuss feasible implementations in state-of-the-art cavity QED experiments [42, 289].

4.4.2 Model and single-particle dynamics

We consider an ensemble of N ultracold atoms with mass M trapped in a standing-wave optical cavity along the vertical direction $\hat{z}$ as shown in Fig. 4.20(a). The atoms are confined in the lowest band of the one-dimensional (1D) optical lattice supported by the cavity, with local gravitational acceleration $\vec{g}$ generating an additional Mgz potential between sites separated by a vertical distance z. Here we consider the pure 1D model for simplicity and discuss the modification by the radial modes in SOM. A single internal level $|g\rangle$ in the atomic ground manifold, is coupled to an atomic excited state $|e\rangle$ with a transition energy $\hbar\omega_0$ via a single cavity mode $\hat{a}$ with frequency ω_c and wavelength λ_c. The atom-cavity coupling has spatial dependence $\mathcal{G}(z) = \mathcal{G}_0 \sin(k_c z)$, where $k_c = 2\pi/\lambda_c$ and $\mathcal{G}_0$ is proportional to single atom vacuum Rabi splitting. The cavity mode is coherently driven by an additional laser with frequency ω_p thus detuning $\Delta_c = \omega_p - \omega_c$ from the bare cavity mode, which generates a net injected field in the cavity with amplitude η_p. The cavity has a finite linewidth κ.

We work in the dispersive regime of the atom-light interaction, where both the cavity mode and the external drive are far detuned from the atomic resonance, i.e., $\Delta_0 \gg \mathcal{G}_0\sqrt{\langle \hat{a}^\dagger \hat{a}\rangle}$ with $\Delta_0 = \omega_p - \omega_0$. In such limit, we can adiabatically eliminate the excited state and only consider the atomic motion in the ground state, which results in the following second-quantized Hamiltonian,

$$\hat{H} = \hat{H}_0 + \int dz \hat{\psi}_g^\dagger(z) \frac{\hbar\,|\mathcal{G}(z)|^2}{\Delta_0} \hat{a}^\dagger \hat{a} \hat{\psi}_g(z) + \hat{H}_{\text{cav}}, \tag{4.74}$$

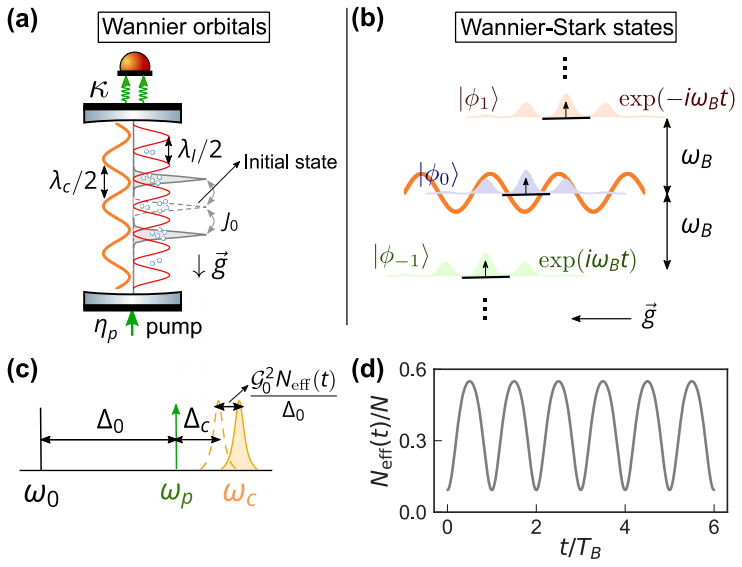

Figure 4.20: Model system. (a) An ensemble of N atoms are trapped in the lowest band of an optical lattice supported by an optical cavity aligned with gravitational acceleration $\vec{g}$. Considering the atoms are initially localized in a Wannier orbital (grey dashed line), hopping to the nearby sites (grey solid line) can lead to a change of atom-cavity coupling due to incommensurate lattice (λ_l) and cavity (λ_c) wavelengths. The cavity has a finite linewidth κ. (b) The initially localized Wannier orbitals can also be written as a superposition of partially delocalized Wannier-Stark states which accumulate different phases due to gravity. (c) Frequencies of atomic transition (ω_0), external pump (ω_p) and cavity resonance (ω_c). Due to atomic motion, the cavity resonance will be shifted by $\mathcal{G}_0^2 N_{\text{eff}}(t)/\Delta_0$, with $N_{\text{eff}}(t)$ defined in Eq. (4.76). (d) $N_{\text{eff}}(t)$ displays oscillatory behavior reflecting single-particle atomic BO, generated by a sudden quench on lattice depth from $15E_R$ to $8E_R$.

where $\hat{H}_0 = \int dz \hat{\psi}_g^\dagger (\hat{p}^2/2M + V_0 \sin^2(k_l z) + Mgz)\hat{\psi}_g$ includes the kinetic energy, lattice potential, and gravitational potential experienced by the atoms. Here, V_0 is the lattice depth, $k_l = 2\pi/\lambda_l$ is the wavenumber of the lattice beam that sets the atomic recoil energy $E_R = \hbar^2 k_l^2/2M$, where λ_l is the lattice wavelength. The field operator $\hat{\psi}_g(z)$ annihilates a ground state atom at position z. The second term in Eq. (4.74) describes the dispersive atom-light coupling after the adiabatic elimination of the excited state. The cavity Hamiltonian is given by $\hat{H}_{\text{cav}}/\hbar = -\Delta_c \hat{a}^\dagger \hat{a} + \eta_p \hat{a}^\dagger + \eta_p^* \hat{a}$.

The eigenstates of $\hat{H}_0$ are the so-called Wannier-Stark (WS) states. In the tight-binding limit, the wave function for a WS state centered at lattice site n takes the form of $\phi_n(z) = \sum_m \mathcal{J}_{m-n}(2J_0/Mga_l)\, w(z - ma_l)$ [38,290], which is a superposition of localized ground-band Wannier functions $w(z)$ [See Fig. 4.20(b)]. Here $\mathcal{J}_n$ is the Bessel function of the first kind, $J_0/\hbar$ is the nearest-neighbour tunneling rate, and $a_l = \lambda_l/2$ is the lattice spacing. The eigenenergy of $|\phi_n\rangle$ is $n\hbar\omega_B$, where $\omega_B = Mga_l/\hbar$ is the Bloch frequency and $T_B = 2\pi/\omega_B$ the corresponding Bloch period. We expand the field operator in the WS basis, $\hat{\psi}_g(z) = \sum_n \hat{c}_n \phi_n(z)$, where the operator $\hat{c}_n$ annihilates an atom in the WS state ϕ_n. In this basis, Eq. (4.74) can be rewritten as

$$\hat{H} = \hat{H}_{\text{cav}} + \frac{\hbar \mathcal{G}_0^2}{\Delta_0} \hat{a}^\dagger \hat{a} \hat{N}_{\text{eff}} + \hbar\omega_B \sum_n n \hat{c}_n^\dagger \hat{c}_n, \tag{4.75}$$

where

$$\hat{N}_{\text{eff}} = \sum_{m,n} J_{m,n} \hat{c}_m^\dagger \hat{c}_n. \tag{4.76}$$

Here, $J_{m,n} = \int dz \phi_m(z)\phi_n(z)\sin^2(k_c z)$ describes the overlap between the WS states ϕ_m, ϕ_n weighted by the cavity field mode function. $\hat{N}_{\text{eff}}$ can be understood as the effective number of atoms coupled to the cavity, which are responsible for generating a frequency shift $\mathcal{G}_0^2 N_{\text{eff}}/\Delta_0$ on the cavity resonance, where $N_{\text{eff}} = \langle \hat{N}_{\text{eff}} \rangle$. This dispersive term allows us to either perform non-destructive probing or many-body control of the atomic motion, depending on the operating parameter regime.

Assuming the cavity field adiabatically follows the atomic motion, which is valid since the cavity field dynamics ($\Delta_c \sim$ MHz) is much faster than the time evolution of the atomic field ($\omega_B \sim$ kHz), one can replace the cavity field operator by $\hat{a} \approx \eta_p/(\Delta_c - \mathcal{G}_0^2 \hat{N}_{\text{eff}}/\Delta_0)$. This leads to the

following effective atom-only Hamiltonian (see SOM),

$$\hat{H}_{\text{eff}}/\hbar = \omega_B \sum_n n\hat{c}_n^\dagger \hat{c}_n + \hat{V}_{\text{cav}}(\hat{N}_{\text{eff}}), \tag{4.77}$$

where $\hat{V}_{\text{cav}}(\hat{N}_{\text{eff}}) = -(VN/\beta)/(1+\beta\hat{N}_{\text{eff}}/N)$ is the cavity-induced potential depending on the atomic motion. Here, $V = \mathcal{G}_0^2|\eta_p|^2/(\Delta_c^2\Delta_0)$ is the maximum AC Stark shift on the atoms introduced by the bare cavity mode, $\beta = -N\mathcal{G}_0^2/(\Delta_0\Delta_c)$ is the ratio between the maximum cavity shift and the bare cavity detuning. We assume $\beta > 0$ (Δ_0 and Δ_c have opposite signs) to avoid hitting a cavity resonance.

First we consider the simplest case where the cavity is used as a probe and does not affect the single-particle dynamics set by $\hat{H}_0$, valid in the regimes $V \ll \omega_B$. We consider the case where atoms are initially loaded in an almost localized WS state in a deep lattice at sites n minimally coupled to the cavity ($k_c n a_l/\pi = r$ with $n, r \in \mathbb{Z}$). Then we suddenly quench the lattice depth to a shallow depth, and the atoms start hopping to the nearest-neighbour sites [see Fig. 4.20(a)]. Since the initially localized state corresponds to a superposition of WS states of the shallow lattice [see Fig. 4.20(b)], after the quench, each WS state acquires a phase that evolves at a rate set by ω_B. The interference of different WS states induces tunneling away from the initially populated site, resulting in coherent breathing behavior at the BO frequency ω_B.

To probe the BO, we use the fact that atoms at different sites coupled differently to the cavity. Therefore tunneling out and back into the initial site leads to a periodic oscillation in $N_{\text{eff}}(t)$ at frequency ω_B as shown in Fig. 4.20(d), which can be measured by tracking the cavity frequency shift $\mathcal{G}_0^2 N_{\text{eff}}(t)/\Delta_0$. Note that a technique to initially prepare atoms at lattice sites with low initial coupling to the cavity mode has been demonstrated in [275]. Instead of an initially localized state, we can also use amplitude modulation of the lattice depth [283] to prepare a superposition of WS states. In this case a similar behavior can be observed as detailed in SOM.

For the numerical simulations throughout this letter, we consider the case of ^{87}Rb atoms with cavity wavelength $\lambda_c = 780$ nm and lattice wavelength $\lambda_l = 532$ nm. However, the discussion can be easily adapted to other type of atoms discussed in SOM.

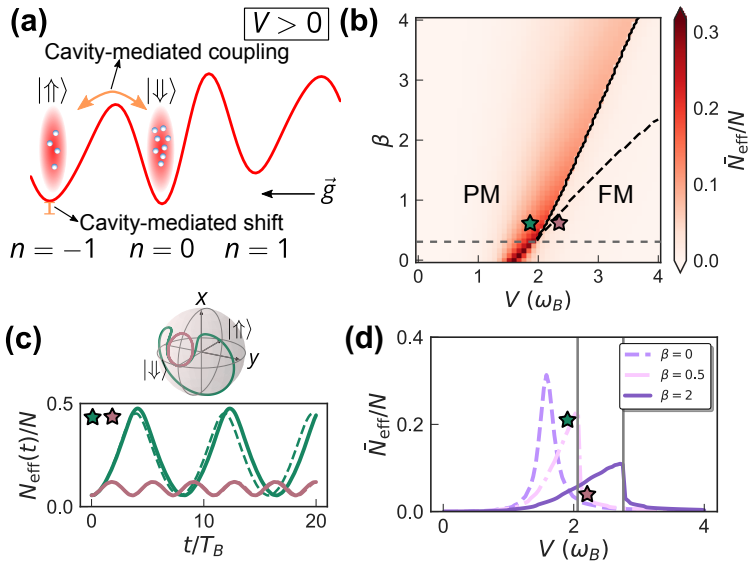

Figure 4.21: Dynamical Phase Transition (DPT) in the deep lattice regime ($V_0 = 20E_R$). (a) For the case of $V > 0$ we define an effective spin-1/2 degrees of freedom: $|\Uparrow\rangle$ ($|\phi_{-1}\rangle$) and $|\Downarrow\rangle$ ($|\phi_0\rangle$). The cavity-mediated interactions generate energy shifts to balance the potential energy of these two sites (red curve), as well as dynamical couplings between them (orange arrow). (b) Phase diagram of the DPT determined by the long-time average $\bar{N}_{\text{eff}}/N$. The phase boundary separating the paramagnetic (PM) and ferromagnetic (FM) phase is predicted by the full model (solid line) and LMG model (black dashed line). The smooth crossover regime is below the gray dashed line. (c) Mean-field dynamics with $V = 1.9\omega_B, \beta = 0.5$ (green) and $V = 2.2\omega_B, \beta = 0.5$ (red). The upper panel shows the mean-field trajectories on the Bloch sphere, and the lower panel displays the normalized signal $N_{\text{eff}}(t)/N$. The solid (dashed) line show predictions of the full (LMG) model respectively. (d) Horizontal cut of the phase diagram in (b) for $\beta = 0$ (solid), $\beta = 0.5$ (dashed), $\beta = 2$ (dot dashed).

4.4.3 Deep lattice regime

The interplay between single-particle atomic motion and cavity-mediated interactions occurs if $V \sim \omega_B$. Here we focus on the deep lattice regime ($V_0 = 20E_R$) where WS states are almost localized at individual lattice sites. If atoms are prepared at site $n = 0$, and $V > 0$, the differential cavity induced AC Stark shift (first order in β in the limit $\beta \ll 1$) between the $n = 0$ and $n = -1$ sites $\propto V(J_{0,0} - J_{-1,-1})$ can compensate for their energy difference $\hbar\omega_B$ as shown in Fig. 4.21(a), restoring tunnelling between these two sites. Since the atomic motion is restricted to take place between these two states, we map them to an effective spin 1/2 degree of freedom: $\hat{c}_{-1}$ as $\hat{c}_{\Uparrow}$, $\hat{c}_0$ as $\hat{c}_{\Downarrow}$ as well as the spin operators $\hat{S}_z = (\hat{c}^\dagger_{\Uparrow}\hat{c}_{\Uparrow} - \hat{c}^\dagger_{\Downarrow}\hat{c}_{\Downarrow})/2$, $\hat{S}_x = (\hat{c}^\dagger_{\Uparrow}\hat{c}_{\Downarrow} + \hat{c}^\dagger_{\Downarrow}\hat{c}_{\Uparrow})/2$. Thus we have $\hat{N}_{\text{eff}} = 2(\Delta_{-1}\hat{S}_z + \Omega_{-1}\hat{S}_x) + N\bar{\omega}$, where $\Delta_{-1} = (J_{-1,-1} - J_{0,0})/2$, $\Omega_{-1} = J_{-1,0}$, and $\bar{\omega} = (J_{-1,-1} + J_{0,0})/2$.

In the limit of $\beta \ll 1$, one can expand $\hat{H}_{\text{eff}}$ [Eq. (4.77)] in a power series of β, and keep only the leading order terms. The Hamiltonian simplifies to,

$$\hat{H}_{\text{eff}}/\hbar \approx -\omega_B\hat{S}_z + V\hat{N}_{\text{eff}} - \frac{V\beta}{N}\hat{N}^2_{\text{eff}}. \tag{4.78}$$

This approximated Hamiltonian [Eq. (4.78)] is equivalent to the LMG model (see Refs. [7, 25, 31, 34, 38, 107, 285] and SOM), $H_{\text{LMG}} = \chi\tilde{\hat{S}}_z^2 + \tilde{\Omega}\tilde{\hat{S}}_x - \tilde{\delta}\tilde{\hat{S}}_z$, by a rotation along the y-axis of the Bloch sphere, $\tilde{\hat{S}}_\alpha = \hat{R}^\dagger\hat{S}_\alpha\hat{R}$, where $\hat{R} = \exp\left(i\theta\hat{S}_y\right)$, and $\tan\theta = \Delta_{-1}/\Omega_{-1}$ (see SOM), which enables fast entanglement state generation under particular choice of $\chi, \tilde{\Omega}, \tilde{\delta}$ [7,31,285]. The LMG model features a DPT from a dynamical ferromagnetic (FM) to a dynamical paramagnetic phase (PM), signaled by a sharp change in the behavior of the long-time average of the excitation fraction [34, 107]. In our model [Eq. (4.77)], the long-time average of the signal $\overline{N}_{\text{eff}}/N = \lim_{T\to\infty}\int_0^T dt N_{\text{eff}}(t)/(TN)$ plays the role of the dynamical order parameter. We also show that the DPT exists in our model [Eq. (4.77)] even beyond the $\beta \ll 1$ limit as we discuss below.

To find the DPT, we solve the mean-field equations of motion for $s_{x,y,z} = 2\langle\hat{S}_{x,y,z}\rangle/N$. Such non-linear dynamics can be further reduced to $(\dot{N}_{\text{eff}}/N)^2 + f(N_{\text{eff}}/N) = 0$ with $f(J_{0,0}) = 0$, and we can associate the DPT with an abrupt change in the number of real roots of the effective potential

$f(N_{\text{eff}}/N)$ (see SOM). This leads to the distinct dynamical behaviors of N_{eff}/N tuned by varying V and β as shown in Fig. 4.21(b,c,d). When the dynamics are dominated by interaction effects, the system is in the FM phase where the Bloch vector features small oscillations around the south pole, also shown as small amplitude oscillations in $N_{\text{eff}}(t)/N$. This phase is separated by a DPT to a PM phase where the Bloch vector exhibits large excursions around the Bloch sphere, also shown as large amplitude oscillations in $N_{\text{eff}}(t)/N$. For $\beta < 0.32$ (see SOM), the DPT transforms into a smooth crossover and the dynamics becomes dominated by single-particle tunneling processes. The dynamical phase boundary is plotted in Fig. 4.21(b) with the full model (solid line) and the LMG model (dashed line). The LMG model is unable to capture the phase boundary beyond the $\beta \ll 1$ limit.

4.4.4 Shallow lattice regime

In a shallow lattice, the WS states extend over a few adjacent lattice sites. In this case, one can obtain a significant suppression of differential AC Stark shifts generated by the cavity by operating near the so-called magic lattice depth ($V_0 = 6E_R$ for the Rb parameters we use) [38], where $J_{n,n}$ is nearly a constant and the energy difference between nearest-neighbour WS states is roughly $\hbar\omega_B$ [see Fig. 4.22(a)]. Thus the dynamics features BO even in the presence of strong cavity-mediated interactions. In fact, after preparing the atoms in the WS state $|\phi_0\rangle$ and thus in an eigenstate of the single particle Hamiltonian, one can observe the generation and amplification of BO due to cavity-mediated interactions in a window around the magic depth as shown in Fig. 4.22(b,c,d). Since the short-time dynamics occurs mainly between the WS states centered at $n = 0, \pm 1$, we can concentrate only on these states and simplify the dynamics via the undepleted pump approximation (UPA): To the leading order, one can replace the operators for the initially occupied states as c-numbers, $\hat{c}_0, \hat{c}_0^\dagger \sim \sqrt{N}$, and keep the operators for unoccupied states ($\hat{c}_{\pm 1}, \hat{c}_{\pm 1}^\dagger$) to the second order while absorbing the linear term generated by single-particle tunneling via a displacement of a coherent state, $\hat{c}_{\pm 1} = \alpha_{\pm 1} + \hat{c}'_{\pm 1}$. In this way, $\hat{H}_{\text{eff}}$ [Eq. (4.77)] simplifies into a quadratic form (see

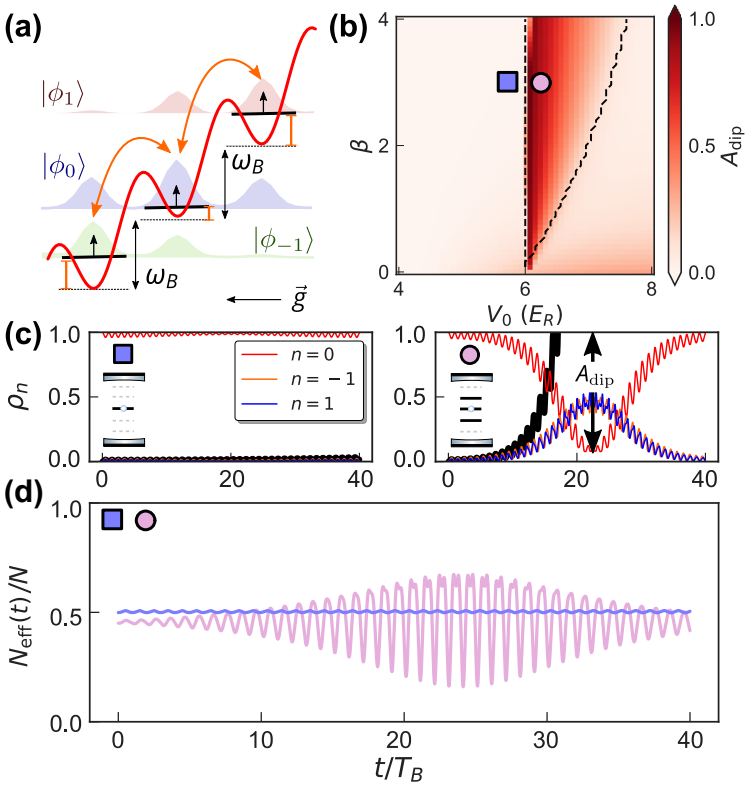

Figure 4.22: Cavity-mediated amplification of Bloch oscillations in the shallow lattice regime. (a) The red lines show the gravity plus optical lattice potential. Around $V_0 \approx 6E_R$, WS states can extend to the nearest-neighbour lattice sites. The orange vertical lines represent the cavity-induced onsite shift of the energy levels and the orange arrows illustrate the cavity-mediated tunneling process shown in Eq. (4.79). (b) Transition between amplification regime and normal regime indicated by $A_{\rm dip} = 1 - \min\{\rho_0\}$. V is fixed to be $2\omega_B$. The black dashed line shows the predicted boundary from UPA. (c) Mean-field dynamics of ρ_n with initial state $|\phi_0\rangle$ and $V = 2\omega_B, \beta = 3$. Nearly no dynamics happen in the left panel (purple square, $V_0 = 5.8E_R$) while large population transfer to $|\phi_1\rangle$ and $|\phi_{-1}\rangle$ (pink circle, $V_0 = 6.2E_R$) is observed in the right panel. (d) Mean-field simulations for the normalized signal $N_{\rm eff}(t)/N$ for the same parameters described in (c). The purple line stays almost constant while the pink line signals the cavity enhancement of the BO.

SOM),

$$\hat{H}_{\text{eff}}/\hbar \approx \omega_B(\hat{c}_1'^{\dagger}\hat{c}_1' - \hat{c}_{-1}'^{\dagger}\hat{c}_{-1}') + V_1\Delta(\hat{c}_1'^{\dagger}\hat{c}_1' + \hat{c}_{-1}'^{\dagger}\hat{c}_{-1}') + V_2N\Omega^2(\hat{c}_1'^{\dagger} + \hat{c}_1' - \hat{c}_{-1}'^{\dagger} - \hat{c}_{-1}')^2, \quad (4.79)$$

with the expansion coefficient V_1, V_2 in SOM and $\Delta = \Delta_1 \approx \Delta_{-1}$, $\Omega = \Omega_1 \approx -\Omega_{-1}$.

We analyze the exact dynamics of Eq. (4.79) via the Bogoliubov-de Gennes method, in which the Heisenberg equation of motion for operators $\hat{C} = (\hat{c}_1', \hat{c}_{-1}', \hat{c}_1'^{\dagger}, \hat{c}_{-1}'^{\dagger})^T$ takes the form $i\partial_t\hat{C} = \mathcal{H}_{\text{BdG}}\hat{C}$. The matrix $\mathcal{H}_{\text{BdG}}$ can have either real or complex eigenvalues, which leads to distinct dynamical behaviors as shown in Fig. 4.22(c). When all the eigenvalues are real (normal regime), the populations ρ_0 and $\rho_{\pm1}$, with $\rho_n = \langle\hat{c}_n^{\dagger}\hat{c}_n\rangle$, feature stable small amplitude oscillations; on the other hand when all the eigenvalues are complex, then $\rho_{\pm1}$ feature an exponential growth associated with the correlated pair production of atoms at WS centered at $n = \pm1$, which leads to the amplification of the BO signal until UPA breaks down. The transition between the real and complex eigenvalues of $\mathcal{H}_{\text{BdG}}$ is marked by dashed lines in Fig. 4.22(b).

To quantify the population transfer, we define $A_{\text{dip}} = 1 - \min\{\rho_0\}$ with $\min\{\rho_0\}$ as the minimum of ρ_0 during $t \in [0, 40T_B]$. A large A_{dip} signals efficient population transfer. In Fig. 4.22(b), we show A_{dip} as a function of the lattice depth V_0 and the cavity parameter β. The region of amplified BO lies within the two dashed boundaries. The left boundary is fixed at the magic lattice depth ($V_0 = 6E_R$) and the right boundary pushes to larger β as V_0 increases. Inside the amplification region $A_{\text{dip}} \neq 0$, while outside $A_{\text{dip}} \approx 0$. The evolution of $N_{\text{eff}}(t)/N$ is shown in Fig. 4.22(d), where the enhanced population transfer induced by the cavity-mediated interactions lead to the growth of the BO amplitude in the amplification regime.

4.4.5 Experimental consideration

The predicted behavior should be achievable in state-of-the-art cavity QED systems with $N \sim 10^4$ ^{87}Rb atoms. We focus on the unitary dynamics in this letter while the main decoherence sources come from cavity loss and spontaneous emission from the excited states. The cavity loss generates collective dephasing processes at a rate $V\beta\kappa/\Delta_c$ and spontaneous emission generates

off-resonant photon scattering processes at a rate $V\gamma/\Delta_0$, where γ is the spontaneous emission rate. For an optical cavity with cooperativity $C = 4\mathcal{G}_0^2/\gamma\kappa \sim 0.5$, $\kappa/\Delta_c \sim 0.05$, $\gamma/\Delta_0 \sim 0.01$, one obtains negligible dissipation within experimentally relevant time scales (~ 50 BO periods). Our scheme does not require BEC while utilizes site-selection to prepare the initial state, which is robust to the radial thermal noise up to $T \sim 1\mu$K (see SOM). Contact interactions between atoms can also be ignored for the dilute quantum gas used here (~ 50 atoms per site). Moreover, our model can be realized with other species of alkali atoms (D_2 transition) and alkaline earth atoms ($^1S_0 \rightarrow {}^3P_1$ transition) with appropriate choices of lattice wavelength (see SOM). In particular, contact interactions can be further suppressed using ^{88}Sr atoms featuring negligible scattering lengths or any type of fermionic atoms interacting only via the p-wave channel.

4.4.6 Conclusion and outlook

In summary, we proposed a scheme to perform many-body control of atomic BO in an optical cavity. Our work opens new possibilities for Hamiltonian engineering in many-body systems by taking advantage of the interplay between atomic motion, gravity and cavity-mediated interactions. For example, although so far we only focused on a single internal level, by including more levels and more cavity modes, it should be possible to engineer dynamical self-generated couplings between WS states via cavity-mediated interactions, which could be used to study dynamical gauge field [28, 250, 291] in a synthetic ladder without the overhead of Raman beams. Furthermore, although most of the calculations so far have been limited to regimes where the mean-field dynamics are a good description of the system, by loading the atoms in 2D or 3D lattice, one should be able to increase the role of beyond mean-field effects and enter the regimes where quantum correlations dominate the dynamics.

4.4.7 Supplemental Materials: Cavity QED with Wannier-Stark state

Dispersive coupling between atoms and cavity

In the main text, we considered N ultracold atoms trapped in a standing-wave optical cavity

along the vertical direction $\hat{z}$. The atoms are assumed to be confined in the ground band of the one-dimensional lattice with lattice depth V_0 and wave vector $k_l = 2\pi/\lambda_l$. A single internal level $|g\rangle$ in the atomic ground manifold is coupled to an atomic excited state $|e\rangle$ with a transition energy $\hbar\omega_0 = \hbar(\omega_e - \omega_g)$, via a single cavity mode $\hat{a}$ with angular frequency ω_c and wavelength λ_c. The atom-cavity coupling has spatial dependence $\mathcal{G}(z) = \mathcal{G}_0 \sin(k_c z)$, with $k_c = 2\pi/\lambda_c$. The cavity mode is coherently driven by an external light field with detuning $\Delta_c = \omega_p - \omega_c$ from the bare cavity mode, which generates a net injected field in the cavity with amplitude η_p. The full atom-cavity Hamiltonian is given as $H = \hat{H}_{\text{atom}} + \hat{H}_{\text{light}} + \hat{H}_{\text{int}}$. Each of the terms can be written as:

$$\hat{H}_{\text{light}} = \hbar\left(\eta_p \hat{a}^\dagger e^{-i\omega_p t} + \eta_p^* \hat{a} e^{i\omega_p t}\right) + \hbar\omega_c \hat{a}^\dagger \hat{a} \tag{4.80}$$

$$\hat{H}_{\text{atom}} = \sum_{\tau=g,e} \int dz\ \hat{\psi}_\tau^\dagger(z) \left[\frac{p^2}{2M} + V(z) + \hbar\omega_\tau\right] \hat{\psi}_\tau(z) \tag{4.81}$$

$$\hat{H}_{\text{int}} = \hbar \int dz\ \mathcal{G}_0 \sin k_c z \left[\hat{a}\hat{\psi}_e^\dagger(z)\hat{\psi}_g(z) + \hat{a}^\dagger \hat{\psi}_g^\dagger(z)\hat{\psi}_e(z)\right]. \tag{4.82}$$

Here $V(z) = Mgz + V_0 \sin^2 k_l z$ describes the external potentials experienced by the atoms. $\hat{\psi}_{e(g)}^\dagger(z)$ is the field operator that creates an atom in the state $e(g)$ at position z, $\omega_{e(g)}$. Under the rotating frame of the pump field (set by the Hamiltonian $H_0 = \hbar\omega_p \hat{a}^\dagger \hat{a} + \hbar\omega_p \int dz\ \hat{\psi}_e^\dagger(z)\hat{\psi}_e(z)$), the system's Hamiltonian takes the following form:

$$\begin{aligned}\hat{H} = {} & \hbar\left(\eta_p \hat{a}^\dagger + \eta_p^* \hat{a}\right) - \Delta_c \hbar \hat{a}^\dagger \hat{a} - \hbar\Delta_0 \int dz\ \hat{\psi}_e^\dagger(z)\hat{\psi}_e(z) + \sum_{\tau=g,e} \int dz\ \hat{\psi}_\tau^\dagger(z) \left[\frac{p^2}{2M} + V(z)\right] \hat{\psi}_\tau(z) \\ & + \hbar \int dz \mathcal{G}_0 \sin k_c z \left[\hat{a}\hat{\psi}_e^\dagger(z)\hat{\psi}_g(z) + \hat{a}^\dagger \hat{\psi}_g^\dagger(z)\hat{\psi}_e(z)\right],\end{aligned} \tag{4.83}$$

where we defined the detuning of the pump from the atomic transition as $\Delta_0 = \omega_p - \omega_0$.

Furthermore, under the assumption $\Delta_0 \gg \mathcal{G}_0\sqrt{\langle \hat{a}^\dagger \hat{a}\rangle}$ and $\Delta_0 \gg \gamma$ with γ the excited state spontaneous emission rate, the excited state population remains negligible during the relevant time scales. In this limit we can adiabatic eliminate the excited state $|e\rangle$ ($\hat{\psi}_e(z) \approx \mathcal{G}_0 \hat{a}\hat{\psi}_g(z) \sin k_c z/\Delta_0$), which leads to the following effective Hamiltonian acting on the ground state $|g\rangle$ manifold only,

$$\hat{H} = -\hbar\Delta_c \hat{a}^\dagger \hat{a} + \hbar\left(\eta_p \hat{a}^\dagger + \eta_p^* \hat{a}\right) + \int dz\ \hat{\psi}_g^\dagger(z) \left[\frac{\hbar(\mathcal{G}_0 \sin k_c z)^2}{\Delta_0} \hat{a}^\dagger \hat{a} + \frac{p^2}{2M} + V(z)\right] \hat{\psi}_g(z). \tag{4.84}$$

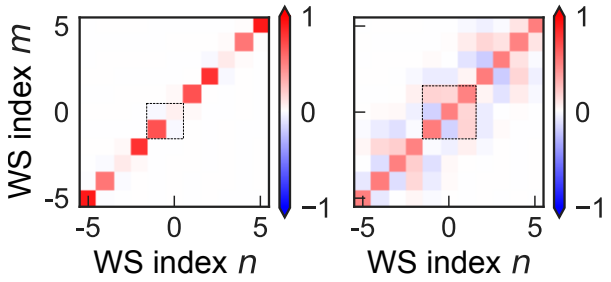

Figure 4.23: The coupling coefficient $J_{m,n}$ for ^{87}Rb atoms ($\lambda_l = 532$ nm, $\lambda_c = 780$ nm). Left: $V_0 = 20E_R$ and right: $V_0 = 6E_R$. Start from $|\phi_0\rangle$, the many-body dynamics mainly happens within the dashed square for either two-level model (left, deep lattice region for dynamical phase transitions) and three-level model (right, shallow lattice region for amplification of Bloch oscillations).

In the tight-binding limit, the resulting single-particle eigenstates of the Hamiltonian $p^2/2m + V(z)$ become the so-called Wannier-Stark (WS) states $|\phi_n\rangle$ ($n \in \mathbb{Z}$):

$$E_n = Mga_l n, \quad \phi_n(z) = \sum_m \mathcal{J}_{m-n}\left(\frac{2J_0}{Mga_l}\right) w(z - ma_l). \tag{4.85}$$

Here $\mathcal{J}_n$ denotes the Bessel function of the first kind, J_0 denotes the nearest-neighbor couplings in the ground band, $a_l = \lambda_l/2$ is the lattice spacing and $w(z)$ is the ground band Wannier function. We will also use $E_R = (\hbar k_l)^2/2M$ for the atomic recoil energy.

The field operator, when written in the WS basis takes the form, $\hat{\psi}_g(z) = \sum_n \hat{c}_n \phi_n(z)$, where $\hat{c}_n$ annihilates an atom in the state $|\phi_n\rangle$. In this basis we can rewrite the Hamiltonian [Eq. (4.84)] as:

$$\hat{H}/\hbar = -\Delta_c \hat{a}^\dagger \hat{a} + \eta_p \hat{a}^\dagger + \eta_p^* \hat{a} + \frac{\mathcal{G}_0^2}{\Delta_0} \hat{a}^\dagger \hat{a} \sum_{m,n} J_{m,n} \hat{c}_m^\dagger \hat{c}_n + \omega_B \sum_n n \hat{c}_n^\dagger \hat{c}_n, \tag{4.86}$$

where $J_{m,n} = \int dz \phi_m(z) \phi_n(z) \sin^2 k_c z$ describes the overlap between the WS states $|\phi_m\rangle$, $|\phi_n\rangle$ weighted by the cavity field mode function. In Fig. 4.23 we show the value of these couplings for the typical lattice depths we work in this paper. We define the effective particle number:

$$\hat{N}_{\text{eff}} = \sum_{m,n} J_{m,n} \hat{c}_m^\dagger \hat{c}_n, \tag{4.87}$$

as the effective number of atoms coupled to the cavity, which shifts the cavity resonance frequency by $\mathcal{G}_0^2 \left\langle \hat{N}_{\text{eff}} \right\rangle / \Delta_0$.

Adiabatic elimination of cavity field

Here we study the dynamics via Heisenberg equations of motion using a Markovian approximation. We adiabatic eliminate the cavity field using the fact that Δ_c sets the largest frequency scale and derive the effective atom-only Hamiltonian. To do that, we formally integrate the Heisenberg equation of motion of the cavity mode operator $\hat{a}$ and photon number operators $\hat{a}^\dagger\hat{a}$, then plug them back into the Hamiltonian [Eq. (4.86)]. We remove the fast rotating terms which relax much faster than the time it takes an atom to perform a BO.

The Heisenberg-Langevin equation of the motion for the cavity mode $\hat{a}$ is given by:

$$\frac{d}{dt}\hat{a} = i[\hat{H}/\hbar, \hat{a}] + (\frac{\kappa}{2}\hat{a}^\dagger + \hat{f}^\dagger)[\hat{a}, \hat{a}] - [\hat{a}, \hat{a}^\dagger](\frac{\kappa}{2}\hat{a} + \hat{f}) = i(\Delta_c - \frac{\mathcal{G}_0^2\hat{N}_{\text{eff}}}{\Delta_0})\hat{a} - i\eta_p - \frac{\kappa}{2}\hat{a} + \hat{f}, \quad (4.88)$$

with κ for the cavity decay rate. The above equation captures the dissipative dynamics generated by κ along with the quantum Langevin noise operator $\hat{f}$, which gives the formal solution for the cavity field operator:

$$\begin{aligned}\hat{a} &= -i\eta_p \exp\left[i\int_0^t d\tau \left(\hat{\Delta} + i\kappa/2\right)\right]\int_0^t dt' \exp\left[-i\int_0^{t'} d\tau \left(\hat{\Delta} + i\kappa/2\right)\right] + \hat{f}' \\ &\approx \frac{\eta_p}{\hat{\Delta} + i\kappa/2} + \hat{f}'\end{aligned} \quad (4.89)$$

with

$$\hat{\Delta} = \Delta_c - \frac{\mathcal{G}_0^2\hat{N}_{\text{eff}}}{\Delta_0}, \quad (4.90)$$

Here $\hat{f}'$ is another quantum Langevin noise operator. Below we consider the regime $\Delta_c, \kappa \gg \omega_B$ where the cavity-field dynamics evolve much faster than the atomic dynamics, thus it follows the latter adiabatically. As a result, we can obtain the formal solution for the cavity photon number operator:

$$\hat{a}^\dagger\hat{a} = \frac{|\eta_p|^2}{\hat{\Delta}^2 + (\kappa/2)^2} + \hat{g} \approx \frac{|\eta_p|^2}{\hat{\Delta}^2}. \quad (4.91)$$

One more time $\hat{g}$ represents a different quantum Langevin noise operator. For the last approximation above, we focus of the regime $\Delta_c \gg \kappa$ where the unitary dynamics dominates and we can ignore the dissipation process to leading order.

If we insert the above solution of the cavity field into Eq. (4.86), the effective atom-only Hamiltonian in the Schrodinger picture can be written as:

$$\begin{aligned}\hat{H}_{\text{eff}}/\hbar &= \omega_B \sum_n n\hat{c}_n^\dagger \hat{c}_n + \eta_p \frac{\eta_p^*}{\hat{\Delta}} + \eta_p^* \frac{\eta_p}{\hat{\Delta}} + \left(\mathcal{G}_0^2 \hat{N}_{\text{eff}}/\Delta_0 - \Delta_c\right) \frac{|\eta_p|^2}{\hat{\Delta}^2} \\ &= \omega_B \sum_n n\hat{c}_n^\dagger \hat{c}_n + 2\frac{|\eta_p|^2}{\hat{\Delta}} - \hat{\Delta}\frac{|\eta_p|^2}{\hat{\Delta}^2} \\ &= \omega_B \sum_n n\hat{c}_n^\dagger \hat{c}_n + \frac{|\eta_p|^2}{\Delta_c - \mathcal{G}_0^2 \hat{N}_{\text{eff}}/\Delta_0} \\ &\equiv \omega_B \sum_n n\hat{c}_n^\dagger \hat{c}_n + \hat{V}_{\text{cav}}(\hat{N}_{\text{eff}})\end{aligned} \tag{4.92}$$

where $\hat{V}_{\text{cav}}(\hat{N}_{\text{eff}}) = -(VN/\beta)/(1+\beta\hat{N}_{\text{eff}}/N)$ is the dynamical potential induced by the cavity which depends on the atomic motion. $\hat{V}_{\text{cav}}$ is parameterized by the maximum AC Stark shift introduced by the bare cavity mode, $V = \mathcal{G}_0^2|\eta_p|^2/(\Delta_c^2\Delta_0)$, as well as by the ratio between the maximum cavity shift and the bare cavity detuning, $\beta = -N\mathcal{G}_0^2/(\Delta_0\Delta_c)$. We assume $\beta > 0$ (Δ_0 and Δ_c have opposite signs) to avoid hitting a resonance.

As a benchmark for the effective atom-only Hamiltonian derived in Eq. (4.92), we compare the exact dynamics for 6 particles in 3 WS states under Eq. (4.86) and Eq. (4.92) in Fig. 4.24(a). In the simulation, we choose $\Delta_c = 400\omega_B$, $\kappa = 20\Delta_c$, $\eta_p = \Delta_c/10$ as well as $\mathcal{G}_0^2/\Delta_0 = -100\omega_B$ in the atom-cavity simulation (dashed lines), which corresponds to $V = \mathcal{G}_0^2|\eta_p|^2/(\Delta_c^2\Delta_0) = \omega_B$ and $\beta = -N\mathcal{G}_0^2/(\Delta_0\Delta_c) = 1.5$ in the atom-only simulation (solid lines). The simulation results match well with each other for the lattice depth in the normal regime (red curves) and amplification regime (blue curves), which verify the effectiveness of the atom-only Hamitlonian.

Equations of motion for atoms

To simulate the dynamics under Eq. (4.92), we can calculate the equations of motion for the field operators $\hat{c}_m$ as:

$$\begin{aligned}i\dot{\hat{c}}_m &= m\omega_B \hat{c}_m - \frac{VN}{\beta}\left[\hat{c}_m, \frac{1}{\left(1+\beta\hat{N}_{\text{eff}}/N\right)}\right] \\ &= m\omega_B \hat{c}_m - \frac{VN}{\beta}\left[\hat{c}_m, 1 - \frac{\beta}{N}\hat{N}_{\text{eff}} + (\frac{\beta}{N})^2\hat{N}_{\text{eff}}^2 - (\frac{\beta}{N})^3\hat{N}_{\text{eff}}^3 + \cdots\right],\end{aligned} \tag{4.93}$$

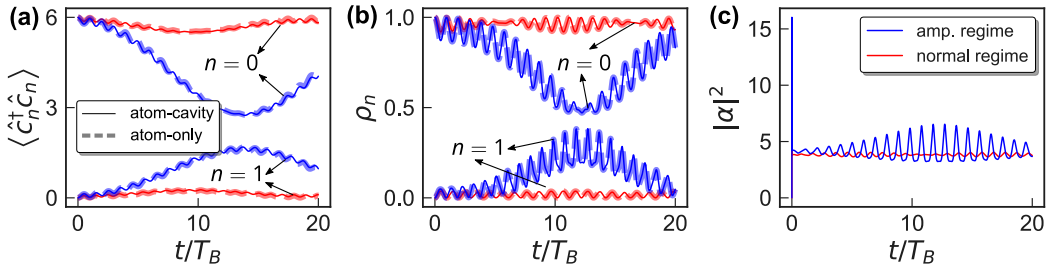

Figure 4.24: Benchmarks of the atom-cavity Hamiltonian [Eq. (4.86)] with the effective atom-only Hamiltonian [Eq. (4.92)]. The red curves for $V_0 = 5.8E_R$ (normal regime) and the blue curves for $V_0 = 6.2E_R$ (amplification regime) are used for all the simulations in the figure. (a) Exact Diagonalization (ED) simulation of the dynamics for 6 particles in 3 WS states with the initial state $(\hat{c}_0^\dagger)^6 |\text{vac}\rangle$. Populations $\left\langle \hat{c}_0^\dagger \hat{c}_0 \right\rangle$ (start from 6) as well as $\left\langle \hat{c}_1^\dagger \hat{c}_1 \right\rangle$ (start from 0) for these two lattice depths are plotted. The solid lines are the exact simulations under the Hamiltonian Eq. (4.86) (with the photon space $n_{\text{cut}} = 10$) and the dashed lines under the Hamiltonian Eq. (4.92). (b) Mean-field dynamics of ρ_n with initial state $|\phi_0\rangle$. The solid lines are simulated with the atom-cavity mean-field equations of motion [Eq. (4.96)] and the dashed lines are simulated with atom-only equations of motion [Eq. (4.95)]. Populations ρ_0 (start from 1) as well as ρ_1 (start from 0) for these two parameters are plotted. The differences between the atom-cavity and atom-only simulations can be ignored for both (a) and (b). (c) Mean-field evolution for the cavity photon number with the same parameters for the red and blue curves as in (b).

Then we can simplify the equations above with $\left[\hat{c}_m, \sum_{p,q} J_{p,q} \hat{c}_p^\dagger \hat{c}_q\right] = \sum_n J_{m,n} \hat{c}_n$:

$$\begin{aligned} i\dot{\hat{c}}_m &= m\omega_B \hat{c}_m - \frac{VN}{\beta}\left\{-\frac{\beta}{N}\left[\hat{c}_m, \hat{N}_{\text{eff}}\right] + (\frac{\beta}{N})^2\left[\hat{c}_m, \hat{N}_{\text{eff}}^2\right] - (\frac{\beta}{N})^3\left[\hat{c}_m, \hat{N}_{\text{eff}}^3\right] + \cdots\right]\right\} \\ &= m\omega_B \hat{c}_m - \frac{VN}{\beta}\left\{-\frac{\beta}{N}\sum_n J_{mn}\hat{c}_n + (\frac{\beta}{N})^2(\sum_n J_{mn}\hat{c}_n \hat{N}_{\text{eff}} + \hat{N}_{\text{eff}}\sum_n J_{mn}\hat{c}_n) + \cdots\right]\right\}. \end{aligned} \tag{4.94}$$

Finally, we apply the mean-field approximation to the operators $\left\langle \sum_n J_{mn}\hat{c}_n \hat{N}_{\text{eff}} \right\rangle \approx \langle \sum_n J_{mn}\hat{c}_n \rangle \left\langle \hat{N}_{\text{eff}} \right\rangle$, and obtain the following equations of motion:

$$i\left\langle \dot{\hat{c}}_m \right\rangle = m\omega_B \langle \hat{c}_m \rangle + \frac{V}{\left(1 + \beta \left\langle \hat{N}_{\text{eff}} \right\rangle / N\right)^2} \sum_{m,n} J_{m,n} \langle \hat{c}_n \rangle , \tag{4.95}$$

All the results in the main text were obtained by solving the mean-field equations of motion written above.

Meanwhile, the mean-field equations for the atom-cavity Hamiltonian [Eq. (4.86)] is given

by,

$$
\begin{aligned}
i\dot{\alpha} &= -\left(\Delta_c + i\frac{\kappa}{2} - \frac{\mathcal{G}_0^2\left\langle \hat{N}_{\text{eff}}\right\rangle}{\Delta_0}\right)\alpha + \eta_p \\
i\left\langle \dot{\hat{c}}_m\right\rangle &= m\omega_B\left\langle \hat{c}_m\right\rangle + \frac{\mathcal{G}_0^2}{\Delta_0}|\alpha|^2\sum_{m,n} J_{m,n}\left\langle \hat{c}_n\right\rangle,
\end{aligned}
\tag{4.96}
$$

with $\alpha = \langle \hat{a}\rangle$. We compare the mean-field dynamics Eq. (4.95) and Eq. (4.96) in Fig. 4.24(b). In the simulation, we choose reasonable experimental parameters $N = 2\times 10^4$ atoms, $\Delta_c = 2\pi\times 2$ MHz, $\kappa = \Delta_c/20$, $\eta_p = 3\Delta_c$ as well as $\mathcal{G}_0^2/\Delta_0 = -2\pi\times 100$ Hz in the atom-cavity simulation [Eq. (4.96)], which corresponds to $V = \mathcal{G}_0^2|\eta_p|^2/(\Delta_c^2\Delta_0) = 1.57\omega_B$ and $\beta = -N\mathcal{G}_0^2/(\Delta_0\Delta_c) = 1$ in the atom-only simulation [Eq. (4.95)]. Still, the simulations for both normal regime and amplification regime match with each other pretty well with the difference can be ignored, which again verifies the validation of the effective atom-only Hamiltonian. In Fig. 4.24(c), we plot the evolution of cavity photon number $|\alpha|^2$ which follows the atomic motion adiabatically.

4.4.8 Supplemental Materials: Dynamical phase transition with Wannier-Stark states

In this part, we consider the deep lattice regime and discuss how to map the atom-only Hamiltonian to a spin model. As discussed in the main text, for a deep lattice $V_0 = 20E_R$, the WS states approach the Wannier orbitals which are localized. The overlap integral $J_{m,n}$ for $V_0 = 20E_R$ is shown in the left panel of Fig. 4.23 with $J_{0,0}\approx 0 \ll J_{1,1}\approx J_{-1,-1}$ and $J_{1,0}\approx -J_{0,-1}\approx 0$. As a result non-trivial dynamics happens only for $V(J_{n,n} - J_{0,0}) + n\omega_B \approx 0$ when starting from $|\phi_0\rangle$. Here we consider $V > 0$ and deal with two bosonic modes $\hat{c}_0$, $\hat{c}_{-1}$. For simplicity, we define $\Omega_n = J_{n,n+1}$ as well as $\Delta_n = (J_{n,n} - J_{0,0})/2$. The spin operators are defined as follows,

$$
\begin{aligned}
\hat{S}_x &= \frac{1}{2}(\hat{c}_{-1}^\dagger\hat{c}_0 + \hat{c}_0^\dagger\hat{c}_{-1}) \\
\hat{S}_y &= -\frac{i}{2}(\hat{c}_{-1}^\dagger\hat{c}_0 - \hat{c}_0^\dagger\hat{c}_{-1}) \\
\hat{S}_z &= \frac{1}{2}(\hat{c}_{-1}^\dagger\hat{c}_{-1} - \hat{c}_0^\dagger\hat{c}_0),
\end{aligned}
\tag{4.97}
$$

and the total particle number $\hat{N} = \hat{c}_{-1}^{\dagger}\hat{c}_{-1} + \hat{c}_{0}^{\dagger}\hat{c}_{0}$. Such pseudospin operators satisfy the SU(2) algebra and we can rewrite the effective number operator as ($\bar{\omega} = (J_{-1,-1} + J_{0,0})/2$):

$$\hat{N}_{\text{eff}} = 2\Omega_{-1}\hat{S}_x + 2\Delta_{-1}\hat{S}_z + \bar{\omega}N, \tag{4.98}$$

as well as the effective spin model from Eq. (4.86) in terms only of $\hat{c}_{-1}$ and $\hat{c}_0$:

$$\hat{H}_{\text{eff}}/\hbar = -\omega_B\hat{S}_z + \hat{V}_{\text{cav}}(\hat{N}_{\text{eff}}) \tag{4.99}$$

Similar in Eq. (4.93), we can derive Heisenberg equations of motion for the collective spin operator $\hat{S}_{x,y,z}$. Using the mean-field approximation which neglects the quantum correlation between different spins we obtain,

$$\begin{aligned}
\left\langle \dot{\hat{S}}_x \right\rangle &= (\omega_B - 2\Delta_{-1}\tilde{V}) \left\langle \hat{S}_y \right\rangle \\
\left\langle \dot{\hat{S}}_y \right\rangle &= (2\Delta_{-1}\tilde{V} - \omega_B) \left\langle \hat{S}_x \right\rangle - 2\Omega_{-1}\tilde{V} \left\langle \hat{S}_z \right\rangle \\
\left\langle \dot{\hat{S}}_z \right\rangle &= 2\Omega_{-1}\tilde{V} \left\langle \hat{S}_y \right\rangle .
\end{aligned} \tag{4.100}$$

Moreover, if we introduce the mean-field real variable $s_\alpha = 2\left\langle \hat{S}_\alpha \right\rangle /N, \alpha \in \{x, y, z\}$, the above equations become:

$$\begin{aligned}
\dot{s}_x &= (\omega_B - 2\Delta_{-1}\tilde{V})s_y \\
\dot{s}_y &= (2\Delta_{-1}\tilde{V} - \omega_B)s_x - 2\Omega_{-1}\tilde{V}s_z \\
\dot{s}_z &= 2\Omega_{-1}\tilde{V}s_y,
\end{aligned} \tag{4.101}$$

with

$$\tilde{V} = \frac{V}{(1 + \beta N_{\text{eff}}(t)/N)^2}, \tag{4.102}$$

here $N_{\text{eff}}(t) = N(\Omega_{-1}s_x + \Delta_{-1}s_z + \bar{\omega})$. Later we will use the symbol $n_{\text{eff}} \equiv \Omega_{-1}s_x + \Delta_{-1}s_z + \bar{\omega}$ for convenience. We compare the results from Eq. (4.95) and Eq. (4.101) to numerical simulations of the full Hamiltonian and they match with each other, which means the two-mode approximation works in this case. Now, we discuss the dynamical phase transition predicted by Eq. (4.101). Using both energy conservation as well as the identity $(\hat{S}^x)^2 + (\hat{S}^y)^2 + (\hat{S}^z)^2 = (\frac{N}{2} + 1)\frac{N}{2}$ in the large N limit, the real variable (s_x, s_y, s_z) with initial condition $s_z = -1, s_x = s_y = 0$ satisfy the following

two conservation laws:

$$s_x^2 + s_y^2 + s_z^2 = 1 \tag{4.103}$$

$$-\omega_B s_z - \frac{2V/\beta}{1+\beta n_{\text{eff}}} = \omega_B - \frac{2V/\beta}{1+\beta(\bar{\omega}-\Delta_{-1})}, \tag{4.104}$$

then we can express $s_{x,y,z}$ all as a function of n_{eff}:

$$\begin{aligned} s_z(n_{\text{eff}}) &= \frac{F(\bar{\omega}-\Delta_{-1}) - F(n_{\text{eff}})}{\omega_B} - 1 \\ s_x(n_{\text{eff}}) &= \frac{n_{\text{eff}} - \Delta_{-1} s_z(n_{\text{eff}}) - \bar{\omega}}{\Omega_{-1}} \\ s_y^2(n_{\text{eff}}) &= 1 - s_x^2(n_{\text{eff}}) - s_z^2(n_{\text{eff}}), \end{aligned} \tag{4.105}$$

also we define a function,

$$F(x) = \frac{2V/\beta}{1+\beta x}. \tag{4.106}$$

The dynamics correspond to a classical particle moving in the external potential from Eq. (4.101):

$$(\dot{n}_{\text{eff}})^2 + f(n_{\text{eff}}) = 0, \tag{4.107}$$

with the potential $f(n_{\text{eff}}) = -(\omega_B\Omega_{-1})^2 s_y^2(n_{\text{eff}})$. The condition $f(n_{\text{eff}}) = 0$ determines the roots and we find $n_{\text{eff}}^0 = \bar{\omega} - \Delta_{-1}$ is one of such root. The effective potential can have either two or four solutions within the region $n_{\text{eff}} \in [\bar{\omega} - \sqrt{\Omega_{-1}^2 - \Delta_{-1}^2}, \bar{\omega} + \sqrt{\Omega_{-1}^2 + \Delta_{-1}^2}]$ shown in Fig. 4.25, and the dynamics of n_{neff} can be understood as the oscillations between n_{eff}^0 and the nearest root n_{eff}^*. Begin with a function $f(n_{\text{eff}})$ with two roots, and continuously tune the parameters of $f(n_{\text{eff}})$ so that two new roots appear in between, then a jump of the nearest root n_{eff}^* should occur during this process. The dynamical paramagnetic phase corresponds to four roots, while the dynamical ferromagnetic phase corresponds to two roots. Deep in the dynamical paramagnetic phase, one can access the whole Bloch sphere ($n_{\text{eff}}^* \approx \bar{\omega} + \sqrt{\Omega_{-1}^2 + \Delta_{-1}^2}$), while deep in the dynamical ferromagnetic phase, the Bloch vector only cycles around the south pole ($n_{\text{eff}}^* \approx n_{\text{eff}}^0$). By numerically varying β and V, we compute the number of roots to produce the phase diagram featured in the main text. If $\beta < 0.32$, $f(n_{\text{eff}})$ can only possess two roots, resulting in a smooth crossover rather than a phase transition.

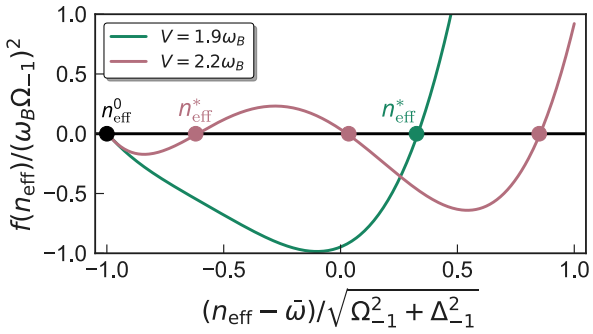

Figure 4.25: Number of roots for the effective potential $f(n_{\rm eff})$. In the case of $V = 1.9\omega_B$, $\beta = 0.5$ (green), $f(n_{\rm eff})$ has two roots; In the case of $V = 2.1\omega_B$, $\beta = 0.5$ (red), $f(n_{\rm eff})$ has four roots. The nearest root is labelled by $n^*_{\rm eff}$ and the jump of $n^*_{\rm eff}$ indicate DPTs.

The LMG model [34, 107] supports a dynamical phase transition with Hamiltonian:

$$\hat{H}_{\rm LMG} = \chi \hat{S}_z^2 + \Omega \hat{S}_x - \delta \hat{S}_z. \tag{4.108}$$

To gain more insights on how our model related to the LMG model, we can expand Eq. (4.86) to first order and second order in $(2\Omega_{-1}\hat{S}_x + 2\Delta_{-1}\hat{S}_z)$. To the first order:

$$\hat{H}_{\rm eff} = -\omega_B \hat{S}_z + V(2\Omega_{-1}\hat{S}_x + 2\Delta_{-1}\hat{S}_z) - \frac{V\beta}{N}(2\Omega_{-1}\hat{S}_x + 2\Delta_{-1}\hat{S}_z)^2, \tag{4.109}$$

If we perform a rotation along y-axis with angle $\theta = \arctan \Omega_{-1}/\Delta_{-1}$, then the Hamiltonian become:

$$\begin{aligned}\hat{H}_{\rm eff} &= -\omega_B \frac{\Delta_{-1}\hat{S}_z - \Omega_{-1}\hat{S}_x}{\sqrt{\Omega^2_{-1} + \Delta^2_{-1}}} + 2V\sqrt{\Omega^2_{-1} + \Delta^2_{-1}}\hat{S}_z - 4\frac{V\beta}{N}(\Omega^2_{-1} + \Delta^2_{-1})\hat{S}_z^2 \\ &= -4\frac{V\beta}{N}(\Omega^2_{-1} + \Delta^2_{-1})\hat{S}_z^2 + \frac{\omega_B\Omega_{-1}}{\sqrt{\Omega^2_{-1} + \Delta^2_{-1}}}\hat{S}_x - \Big(\frac{\omega_B\Delta_{-1}}{\sqrt{\Omega^2_{-1} + \Delta^2_{-1}}} - 2V_1\sqrt{\Omega^2_{-1} + \Delta^2_{-1}}\Big)\hat{S}_z,\end{aligned} \tag{4.110}$$

which takes the form of the LMG model and gives $\tilde{\chi}$, $\tilde{\Omega}$, $\tilde{\delta}$ defined in the main text.

4.4.9 Supplemental Materials: Schwinger bosons and undepleted pump approximation

In this part, we start with the effective Hamiltonian [Eq. (4.92)], but consider the shallow lattice region around $6E_R$. The associated $J_{m,n}$ coumplings are plotted in the right panel of Fig.

4.23. Instead of being localized in a single lattice site, the WS states can extend over a few adjacent lattice sites in a shallow lattice. This can lead to significant suppression of differential AC Stark shifts (homogeneous $J_{n,n}$) at the so-called magic lattice depth ($V_0 = 6E_R$ in our case). Note that the energy difference between nearest-neighbour WS states is rough ω_B, which allows us to study Bloch oscillations under cavity-mediated interaction. We consider the WS states with index $m, n \in \{-1, 0, 1\}$ and use undepleted pump approximation (UPA) $\hat{c}_0 \approx \sqrt{N}$ which is valid at short times when starting from $|\phi_0\rangle$,

$$\hat{N}_{\text{eff}} \approx 2\Delta_1 \hat{c}_1^\dagger \hat{c}_1 + 2\Delta_{-1}\hat{c}_{-1}^\dagger \hat{c}_{-1} + \sqrt{N}[\Omega_1(\hat{c}_1^\dagger + \hat{c}_1) - \Omega_{-1}(\hat{c}_{-1}^\dagger + \hat{c}_{-1})] + NJ_{0,0} \tag{4.111}$$

$$\equiv \hat{O} + NJ_{0,0}. \tag{4.112}$$

Since $\hat{O}$ is small under UPA that assumes the $\hat{c}_{\pm 1}$ modes remain almost unoccupied, we can expand the effective Hamiltonian [Eq. (4.92)] up to second order in $\hat{O}$, and ignore the higher-order terms. The term $\hat{O}^2$ we can be approximated to be:

$$\hat{O}^2 \approx N[\Omega_1(\hat{c}_1^\dagger + \hat{c}_1) - \Omega_{-1}(\hat{c}_{-1}^\dagger + \hat{c}_{-1})]^2, \tag{4.113}$$

and then the effective Hamiltonian becomes:

$$\hat{H}_{\text{eff}}/\hbar = \omega_B(\hat{c}_1^\dagger \hat{c}_1 - \hat{c}_{-1}^\dagger \hat{c}_{-1}) - \frac{VN/\beta}{1 + \beta J_{0,0} + \beta\hat{O}/N} \tag{4.114}$$

$$\approx \omega_B(\hat{c}_1^\dagger \hat{c}_1 - \hat{c}_{-1}^\dagger \hat{c}_{-1}) + V_1\hat{O} + V_2\hat{O}^2 \tag{4.115}$$

$$= \omega_B(\hat{c}_1^\dagger \hat{c}_1 - \hat{c}_{-1}^\dagger \hat{c}_{-1}) + V_1\sqrt{N}[\Omega_1(\hat{c}_1^\dagger + \hat{c}_1) - \Omega_{-1}(\hat{c}_{-1}^\dagger + \hat{c}_{-1})] \tag{4.116}$$

$$+ V_1(\Delta_1 \hat{c}_1^\dagger \hat{c}_1 + \Delta_{-1}\hat{c}_{-1}^\dagger \hat{c}_{-1}) + V_2 N[\Omega_1(\hat{c}_1^\dagger + \hat{c}_1) - \Omega_{-1}(\hat{c}_{-1}^\dagger + \hat{c}_{-1})]^2, \tag{4.117}$$

here

$$V_1 = \frac{2V}{(1 + \beta J_{0,0})^2}, \quad V_2 = -\frac{V\beta/N}{(1 + \beta J_{0,0})^3}. \tag{4.118}$$

Moreover, we can absorb the linear term generated by single-particle tunneling via a displacement of a coherent state, $\hat{c}_{\pm 1} = \alpha_{\pm 1} + \hat{c}'_{\pm 1}$ to obtain,

$$\hat{H}_{\text{eff}}/\hbar \approx \omega_B(\hat{c}_1'^\dagger \hat{c}'_1 - \hat{c}_{-1}'^\dagger \hat{c}'_{-1}) + V_1\Delta(\hat{c}_1'^\dagger \hat{c}'_1 + \hat{c}_{-1}'^\dagger \hat{c}'_{-1}) + V_2 N\Omega^2(\hat{c}_1'^\dagger + \hat{c}'_1 - \hat{c}_{-1}'^\dagger - \hat{c}'_{-1})^2. \tag{4.119}$$

Here we have made the approximation $\Omega_1 \equiv \Omega \approx -\Omega_{-1}$ as well as $\Delta_1 \equiv \Delta = \Delta_{-1}$. The displacements then become,

$$\alpha_1 = \frac{V_1\sqrt{N}\Omega(V_1\Delta - \omega_B)}{(V_1\Delta)^2 - \omega_B^2 - 8\Omega^2 V_2 N\omega_B}, \quad \alpha_{-1} = \frac{V_1\sqrt{N}\Omega(V_1\Delta + \omega_B)}{(V_1\Delta)^2 - \omega_B^2 - 8\Omega^2 V_2 N\omega_B}. \tag{4.120}$$

The short-time dynamics [Eq. (4.117)] can be calculated analytically for the quadratic Hamiltonian in terms of $\hat{c}'_{\pm1}, \hat{c}'^{\dagger}_{\pm1}$ with $\hat{c}'_{\pm1} = i[\hat{H}_{\text{eff}}/\hbar, \hat{c}_{\pm1}]$ and $\hat{c}'^{\dagger}_{\pm1} = i[\hat{H}_{\text{eff}}/\hbar, \hat{c}'^{\dagger}_{\pm1}]$. In this limit the dynamics is given by the equation:

$$i\frac{d}{dt}\begin{pmatrix} \hat{c}'_1 \\ \hat{c}'_{-1} \\ \hat{c}'^{\dagger}_1 \\ \hat{c}'^{\dagger}_{-1} \end{pmatrix} = \mathcal{H}_{\text{BdG}} \begin{pmatrix} \hat{c}'_1 \\ \hat{c}'_{-1} \\ \hat{c}'^{\dagger}_1 \\ \hat{c}'^{\dagger}_{-1} \end{pmatrix}, \tag{4.121}$$

with the coupling matrix S:

$$\mathcal{H}_{\text{BdG}} = \begin{pmatrix} \omega_B + V_1\Delta + 2V_2\Omega^2 & 2V_2\Omega^2 & -2V_2\Omega^2 & -2V_2\Omega^2 \\ -2V_2\Omega^2 & -2V_2\Omega^2 & -\omega_B + V_1\Delta + 2V_2\Omega^2 & 2V_2\Omega^2 \\ -2V_2\Omega^2 & -\omega_B - V_1\Delta - 2V_2\Omega^2 & 2V_2\Omega^2 & 2V_2\Omega^2 \\ 2V_2\Omega^2 & 2V_2\Omega^2 & -2V_2\Omega^2 & \omega_B - V_1\Delta - 2V_2\Omega^2 \end{pmatrix}. \tag{4.122}$$

The matrix $\mathcal{H}_{\text{BdG}}$ can have either real or complex eigenvalues, which leads to distinct dynamical behaviors as shown in the main text. When all the eigenvalues are real, the populations $\rho_{\pm1}$, with $\rho_n = \langle \hat{c}_n^{\dagger}\hat{c}_n \rangle$, feature stable small amplitude oscillations; on the other hand when all the eigenvalues are complex, then $\rho_{\pm1}$ feature an exponential growth associated with the correlated pair production of atoms at WS centered at $n = \pm1$, which leads to the amplification of the Bloch oscillation signal until the UPA breaks down.

4.4.10 Supplemental Materials: Experimental considerations

Single-particle Bloch oscillations

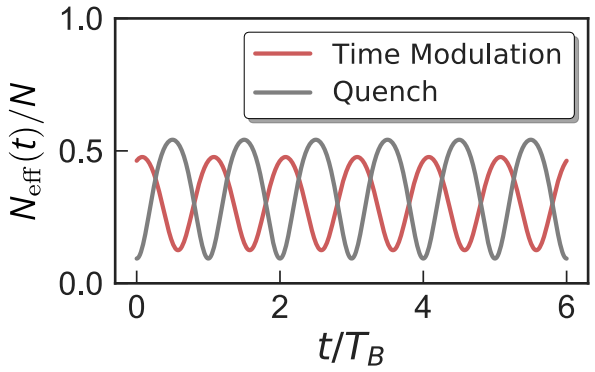

Figure 4.26: Single particle Bloch oscillation with amplitude modulation scheme (pink curve, $V_0 = 8E_R$ and $V_1 = 0.4E_R$) and Quench scheme (grey curve, quench from $V_0 = 15E_R$ to $V_0 = 8E_R$ as main text).

In this section, we discuss the protocols to observe single-particle Bloch oscillations in the experiment. The main idea is to prepare a superposition of different WS states which accumulate different phases under $\hat{H}_0$. In the main text, we discussed the quench scheme where the initial localized WS state ϕ_0 becomes a superposition of delocalized WS states. An alternative way to probe Bloch oscillations is to amplitude modulate the lattice depth as:

$$\begin{aligned} H_1(t)/\hbar &= V_1 \sin^2 k_l z \cos(\omega t + \phi) \\ &= \sum_{m,n=-\infty}^{\infty} t_m \cos(\omega t + \phi)(\hat{c}^\dagger_{m+n}\hat{c}_n + \hat{c}^\dagger_n \hat{c}_{m+n}), \end{aligned} \tag{4.123}$$

which has been demonstrated in [283]. Here we define the tunnelling rate between ϕ_{m+n} and ϕ_n as:

$$t_m = V_1 \int dz \sin^2(k_l z)\phi_{m+n}(z)\phi_n(z). \tag{4.124}$$

Moreover, we can choose $\omega \approx m\omega_B, m \in \mathbb{Z}$ to drive the mth sideband (between ϕ_{m+n} and ϕ_n) and ignore the fast rotating terms:

$$\begin{aligned} H_1(t)/\hbar &= \sum_{m,n=-\infty}^{\infty} t_m \cos(\omega t + \phi)(e^{im\omega_B t}\hat{c}^\dagger_{m+n}\hat{c}_n + e^{-im\omega_B t}\hat{c}^\dagger_n \hat{c}_{m+n}) \\ &\approx \sum_{n=-\infty}^{\infty} \frac{t_m}{2}(e^{-i\phi}\hat{c}^\dagger_{m+n}\hat{c}_n + e^{i\phi}\hat{c}^\dagger_n \hat{c}_{m+n}). \end{aligned} \tag{4.125}$$

As a result, starting from ϕ_0 and performing the amplitude modulation for time τ, we obtain the initial state to be a superposition of WS states $\{\phi_{n\times m}\}$. In Fig. 4.26 (pink curve), we simulate

the case with lattice depth $V_0 = 8E_R$ and modulation strength $V_1 = 0.4E_R$, also the first sideband transition ($\omega = \omega_B$). Different from the quench scheme (grey curve), after the modulation the single particle wavefunction can have a non-zero coupling to the cavity field ($N_{\text{eff}}/N \neq 0$).

In the experiment, there may be higher bands populated in the quench protocol we discussed in the main text. In other words, the WS basis describing the ground band for the shallow lattice (after quench) is not necessarily complete to describe the initial localized state. Higher bands population will inevitably introduce other frequency components to $N_{\text{eff}}(t)$ disrupting the BO signal. However, in the simulations we performed for the main text (quench from $V_0 = 15E_R$ to $V_0 = 8E_R$), 98% atoms remained in the ground band and the higher band population can be ignored. Similarly, in the amplitude modulation schemes, we also choose V_1 to be much smaller than the band gap to avoid higher bands population.

Experimental parameters

Here we discuss the parameters for the specific case of ^{87}Rb with incommensurate lattice wavelength ($\lambda_l = 532$ nm, $\omega_B = 2\pi \times 557$ Hz) and cavity wavelength (D_2 transition with $\lambda_c = 780$ nm). We are interested in the parameter regime with $V \sim \omega_B$ and $\beta \sim O(1)$, where the dynamics is mostly unitary and the dissipative processes can be ignored as we explain below. Another requirement is that the band gap ($27\omega_B$ for $\lambda_l = 532$ nm and $V_0 = 6E_R$) should be much larger than V if we want to only work with the ground band WS states. Moreover, the cavity decay rate $\kappa \sim 2\pi \times 0.1$ MHz, the atom-light coupling strength $\mathcal{G}_0 \sim 2\pi \times 0.3$ MHz, and atomic transition decay rate $\gamma \sim 2\pi \times 10$ MHz give the cavity cooperativity $C = 4\mathcal{G}_0^2/\gamma\kappa \sim 0.36$, which can be tuned even larger for larger $\mathcal{G}_0$ and smaller κ, γ. The cavity loss generates collective dephasing processes at a rate $V\beta\kappa/\Delta_c$, while spontaneous emission generates off-resonant photon scattering processes at a rate $V\gamma/\Delta_0$ as mentioned in the main text. Under $\kappa/\Delta_c \sim 0.05$ and $\gamma/\Delta_0 \sim 0.01$, one obtains negligible dissipation within the experimentally relevant time scales and $\beta \sim O(1)$. For the maximum AC Stark shift, we first find that $\mathcal{G}_0^2/\Delta_0 \sim 2\pi \times 100$ Hz with the parameters listed above, then $|\eta_p|^2/\Delta_c^2$ can be tuned between 1 to 10 for $V \sim \omega_B$.

Our proposal works with a single internal level in the ground state manifold for atoms hopping

between motional states (WS states here). Since interactions are mediated by photons, quantum statistics are not important in our scheme. As a result, even though above we considered the case of Rb, our model can be realized with other species of alkali atoms (D_2 transition) and alkaline earth atoms ($^1S_0 \rightarrow {}^3P_1$ transition) i.e. ^{87}Sr (boson), ^{88}Sr (fermion), ^{171}Yb (fermion) with appropriate choices of lattice wavelength and magic lattice depth summarized in table 4.2. Note that both ^{88}Sr, ^{171}Yb have very small scattering lengths in the ground states.

The single particle Bloch oscillations and dynamical phase transition in the deep lattice doesn't set too much limit on the choice of λ_l and λ_c. We only want the near-neighbour coupling coefficient $J_{m,m+1}$ to be larger, while the overlaps between $\phi_m(z)$, $\phi_{m+1}(z)$ and $\sin^2(k_c z)$ become tiny when $\lambda_l \approx \lambda_c$, so we want to choose different λ_l and λ_c. While for the amplification of BOs in the shallow lattice region, we need to perform the experiment around magic lattice depth thus too shallow magic depth (such as ^{171}Yb) isn't favorable.

Atomic species	λ_l (nm)	λ_c (nm)	Magic lattice depth (E_R)
^{87}Rb (boson)	532	780	$6E_R$
^{87}Sr (fermion)	532	689	$5E_R$
^{88}Sr (boson)	532	689	$5E_R$
^{171}Yb (fermion)	413	556	$3.2E_R$

Table 4.2: Summarized lattice, cavity wavelength and magic lattice depth for different atomic species.

Radial mode thermal distribution

In this section, we discuss the effect of the Radial thermal motion following Ref. [38]. The Gaussian geometry of the laser beams in experiments inevitably couples the vertical and radial wave functions. The Gaussian profile of the lattice and cavity beams causes atoms in different radial modes to have different tunneling rate, resulting in a slightly different overlap integral $J_{m,n}$ for atoms in different radial modes. This effect can also be understood as fluctuations of the lattice potential V_0 due to radial thermal excitation.

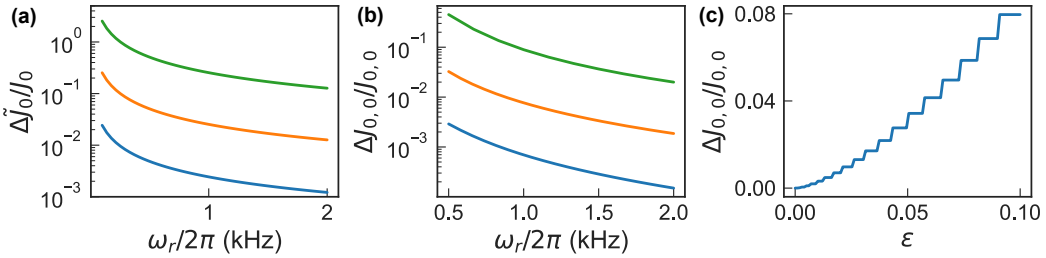

Figure 4.27: The standard deviations of (a) the ground band tunneling rates, (b) the coupling coefficient $J_{0,0}$ as a function of radial trapping ω_r with fixed $T = 0.1$ μK (blue curve), $T = 1$ μK (orange curve) as well as $T = 10$ μK (green curve). We use the beam width $w_l = 50\mu$m and lattice potential $V_0 = 6E_R$ in the calculation. (c) The standard deviations of $J_{0,0}$ as a function of loading error rate ϵ.

First, we focus on the Gaussian beam profile of a 1D lattice, which leads to the following trapping potential:

$$V_0(r,z) = V_0 \sin^2(k_l z) \exp\left(-2r^2/w_l^2\right), \tag{4.126}$$

where w_l is the beam width. In the presence of additional radial trapping potential $V_r(r,z) = M\omega_r^2 r^2/2$ [292] we can expand the total trapping potential $V(r,z) = V_0(r,z) + V_r(r,z)$ to second order of r and obtain:

$$V(r,z) \approx V_0 \sin^2(k_l z) + \frac{1}{2}M\omega_r^2 r^2 - \frac{\omega_{r0}^2}{\omega_r^2}\frac{1}{2}M\omega_r^2 r^2 \sin^2(k_l z), \tag{4.127}$$

here $\omega_{r0} = \sqrt{4V_0/Mw_l^2}$.

The first term describes the lattice potential along the axial direction with the characteristic Bloch functions as eigenstates. The second term describes the radial harmonic trapping with eigenstate $\phi_{n_x,n_y}(r) = \phi_{n_x}(x)\phi_{n_y}(y)$ and eigenenergies $E_{n_x,n_y} = \hbar\omega_r(n_x + n_y + 1/2)$. The third term describes the coupling between axial and radial degrees of freedom. The correction of J_0 is given by [38]:

$$\tilde{J}_0(n_x,n_y) = J_0 + \frac{1}{8}\frac{\omega_{r0}^2}{\omega_r^2}E_{n_x,n_y}[\frac{\partial}{\partial v_0}f(\tilde{q}=0,v_0/4) - \frac{\partial}{\partial v_0}f(\tilde{q}=\pm 1,v_0/4)]. \tag{4.128}$$

Here the function f is the characteristic Mathieu value of type A for $q \in (-\hbar k_l, \hbar k_l)$, and the characteristic Mathieu value of type B for $q = \pm k_l$. We define $\tilde{q} = q/\hbar k_l$ and $v_0 = V_0/E_R$. One

can take such $\tilde{J}_0$ into Eq. (4.85) to calculate $\phi_n(z)$, which causes inhomogeneity for the coupling matrix $J_{m,n}$. We can estimate the contribution from different radial eigenmode with Boltzmann distribution $p_{n_x,n_y} = \exp[-(n_x+n_y)\omega_r\hbar/k_BT]/Z$, in which the partition function $Z \approx (k_BT/\hbar\omega_r)^2$. Then we can calculate the variance of the $\tilde{J}_0$ as:

$$\begin{aligned}\Delta\tilde{J}_0^2 &= \sum_{n_x,n_y} p_{n_x,n_y}[\tilde{J}_0(n_x,n_y) - J_0]^2 \\ &= \{\frac{\hbar}{8}\frac{\omega_{r0}^2}{\omega_r}[\frac{\partial}{\partial v_0}f(\tilde{q}=0,v_0/4) - \frac{\partial}{\partial v_0}f(\tilde{q}=\pm 1,v_0/4)]\}^2\frac{2(e^{\hbar\omega_r/k_BT}+2)}{(e^{\hbar\omega_r/k_BT}-1)^2}.\end{aligned} \tag{4.129}$$

In Fig. 4.27(a), we plot the standard deviation of the tunneling rate J_0 as a function of ω_r and different temperature T. In Fig. 4.27(b), we plot the standard deviation of the coupling coefficient $J_{0,0}$ due to the correction of the tunneling rate. Similar behavior for other coupling coefficients $J_{m,n}$. As a result, one can suppress the effect of the radial modes occupation by increasing the total radial trapping frequency ω_r or lowering the temperature. The standard deviation $\Delta J_{0,0} \approx 0.01 J_{0,0}$ up to temperature $T \sim 1$ μK as well as $\omega_r = 2\pi \times 1$ kHz, thus the radial thermal noise only has a tiny effect on many-body dynamics we predict.

Atoms loading

In this section, we discuss the real process of atoms loading in the experiment. In the main text, we mention first loading atoms at position $k_cz/\pi = r, r \in \mathbb{Z}$ which atoms-cavity coupling becomes perfect zero. However one can only set a threshold for the atom-cavity coupling during the loading process i.e. load all the atoms with $\sin^2 k_cz < \epsilon$ in the real experiment. Such loading error makes $J_{m,n}$ deviate from expected values, which brings additional inhomogeneity. In Fig. 4.27(c), we plot the standard deviation of the coupling coefficient $J_{0,0}$ as a function of error ϵ. We consider the total lattice length to be 1 mm and assume atoms load into all the sites n which satisfy $\sin^2(k_cna_l) < \epsilon$ uniformly. These imperfect sites cause tiny inhomogeneity in the coupling coefficient $J_{m,n}$ up to $\epsilon \sim 5\%$.

4.5 Observing dynamical phases of BCS superconductors in a cavity QED simulator

This section is adapted from: Dylan J. Young*, **Anjun Chu***, Eric Yilun Song, Diego Barberena, David Wellnitz, Zhijing Niu, Vera M. Schäfer, Robert J. Lewis-Swan, Ana Maria Rey, James K. Thompson, Observing dynamical phases of BCS superconductors in a cavity QED simulator, Nature 625, 679 (2024).

4.5.1 Introduction

In conventional Bardeen-Cooper-Schrieffer (BCS) superconductors [293], electrons with opposite momenta bind into Cooper pairs due to an attractive interaction mediated by phonons in the material. While superconductivity naturally emerges at thermal equilibrium, it can also emerge out of equilibrium when the system's parameters are abruptly changed [294–300]. The resulting out-of-equilibrium phases are predicted to occur in real materials and ultracold fermionic atoms but have not yet all been directly observed. Here we realise an alternate way to generate the proposed dynamical phases using cavity quantum electrodynamics (cavity QED). Our system encodes the presence or absence of a Cooper pair in a long-lived electronic transition in ^{88}Sr atoms coupled to an optical cavity and represents interactions between electrons as photon-mediated interactions through the cavity [301, 302]. To fully explore the phase diagram, we manipulate the ratio between the single-particle dispersion and the interactions after a quench and perform real-time tracking of subsequent dynamics of the superconducting order parameter using non-destructive measurements. We observe regimes where the order parameter decays to zero (phase I) [295, 296], assumes a non-equilibrium steady-state value (phase II) [294, 295], or exhibits persistent oscillations (phase III) [294, 295]. This opens up exciting prospects for quantum simulation, including the potential to engineer unconventional superconductors and to probe beyond mean-field effects like the spectral form factor [303, 304], and for increasing coherence time for quantum sensing.

Quantum simulation offers a path to understand a broad range of phenomena, from high-

temperature superconductivity and correlated quantum magnetism in condensed matter physics [305] to quarks and gluons in nuclei and matter under extreme conditions [306], as well as the black hole information paradox in gravitational physics [307]. A fascinating and promising case is the prethermal dynamical phases [193] predicted to emerge from quenches of superconductors and superfluids [294–300, 308–313], systems that feature Cooper pairing of electrons or neutral fermions. While there has been great progress in pump-probe experiments of superconductors to induce such fast quenches using THz technology, and signs of phases I and II have been observed, the intense pulses couple nonlinearly to the Cooper pairs in the superconductor and complicate a clean observation of the dynamical phases [314–316]. For these reasons, the realisation of fermionic superfluids in ultracold atomic gases [317] has generated great excitement [294–300]; however, to date observations have been limited to spectroscopic signatures rather than the full time dynamics [318]. In neither system has a systematic scan of the dynamical phase diagram been performed, and in fact phase III has not been observed.

Here, we take a step forward towards this challenge by using internal electronic states to encode effective Cooper pairs. At the heart of this implementation is the Anderson pseudospin mapping [319] by which the presence or absence of Cooper pairs in a momentum mode is encoded in a pseudo spin-1/2 system. We simulate Anderson pseudospins using a long-lived electronic transition in ^{88}Sr with interactions between the spins mediated by a high finesse optical cavity. As proposed in Refs. [301, 302], the scattering between Cooper pairs in condensed matter systems can be engineered in our system via the exchange of photons through the cavity (see Fig. 4.28**d**). In this way, the dynamics of a collection of interacting spin-1/2 systems maps onto the low-energy physics of a superconductor or superfluid.

We probe all three dynamical phases (phases I, II, and III) predicted to exist in BCS superconductors by utilising the high degree of control and flexibility in state initialisation, interaction control, and non-destructive measurements available when coupling long-lived atoms to an optical cavity. Behaviours intrinsic to phase I (normal phase) and phase II (finite steady-state superconductivity) have previously been observed in spin systems realized in optical cavities [186, 189] and

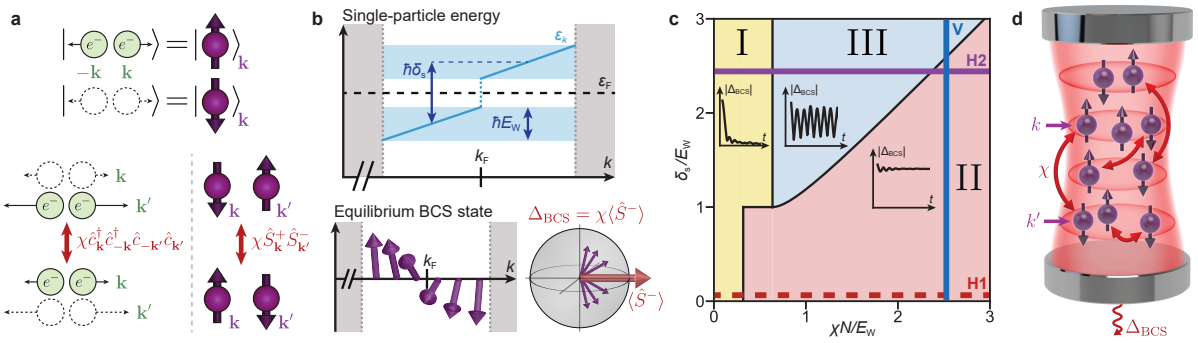

Figure 4.28: **Engineering BCS dynamical phases.** **a**, The Anderson pseudospin mapping encodes the presence and absence of a Cooper pair as the up and down states of a spin-1/2 system, respectively. Under this mapping, the attractive interaction $\chi\hat{c}^\dagger_{\mathbf{k}}\hat{c}^\dagger_{-\mathbf{k}'}\hat{c}_{-\mathbf{k}'}\hat{c}_{\mathbf{k}'}$ between electrons is equivalent to an all-to-all exchange interaction $\chi\hat{S}^+_{\mathbf{k}}\hat{S}^-_{\mathbf{k}'}$ between pseudospins. **b**, Model parameters. The top plot shows the effective dispersion relation near the Fermi surface engineered in our system as a function of parameters δ_s and E_W, controlled using AC Stark shifts. The bottom plot visualises the ground state of a BCS superconductor using Anderson pseudospins. Near the Fermi momentum, the pseudospins develop a phase-coherent superposition at a scale set by a nonzero BCS pairing gap Δ_{BCS}. This gap is self-consistently defined from the spin coherence as shown on the Bloch sphere. **c**, Dynamical phase diagram. The three dynamical phases can be realised by varying parameters χN, δ_s, and E_W. Representative dynamics of the BCS order parameter $|\Delta_{BCS}|$ for each phase are shown as insets. We explore cut H1 (dashed line) in Fig. 4.29 using a single ensemble of atoms and cuts V and H2 (solid lines) in Figs. 4.30 and 4.31 using two separately controlled sub-ensembles. **d**, Cavity QED implementation of the BCS interaction. Coupling many strontium atoms to a detuned optical cavity generates infinite-range spin-exchange interactions mediated by a virtual exchange of cavity photons. This interaction also causes a field proportional to Δ_{BCS} to leak out of the cavity, providing a real-time probe of the dynamics.

in two-level atoms interacting via collisions [108,187,188,320]. We build on this work by clarifying the connection between these dynamical phases from the BCS model and the physics of many-body gap protection in spin systems. Our results also provide the first demonstration of phase III (a self-generated Floquet phase featuring persistent oscillations of the order parameter), which is predicted to dynamically emerge in superconductors via quenches from weak to strong interactions [295,300]. In our system, we instead engineer this phase using flexible control of the single-particle dispersion [301,313], dynamically resembling the low-energy condition of a BCS superconductor. For all experiments, we perform real-time tracking of the superconducting order parameter, enabling fast readout of the dynamics.

4.5.2 Experimental setup and model system

To realise dynamical phases of the BCS model, we laser cool an ensemble of $N = 10^5 - 10^6$ ^{88}Sr atoms and trap them inside a $\lambda_{\mathrm{L}} = 813$ nm 1D optical lattice supported by a high-finesse optical cavity. A spin-1/2 system is encoded in the electronic ground state $|\downarrow\rangle = |^1\mathrm{S}_0, m_J = 0\rangle$ and a long-lived optical excited state $|\uparrow\rangle = |^3\mathrm{P}_1, m_J = 0\rangle$. Along this transition, we define spin operators $\hat{S}_k^- = |\downarrow\rangle\langle\uparrow|_k$ and $\hat{S}_k^z = (|\uparrow\rangle\langle\uparrow|_k - |\downarrow\rangle\langle\downarrow|_k)/2$ for single atoms with labels $k \in \{1, ..., N\}$, as well as the collective lowering operator $\hat{S}^- = \sum_k \hat{S}_k^-$ and raising operator $\hat{S}^+ = (\hat{S}^-)^\dagger$.

Assuming homogeneous atom-light coupling in the cavity and unitary dynamics, our system can be described by the Hamiltonian

$$\hat{H} = \hbar\chi\hat{S}^+\hat{S}^- + \sum_k \varepsilon_k \hat{S}_k^z. \tag{4.130}$$

The first term represents an infinite-range spin-exchange interaction described by a frequency scale χ [186], realised using the collective coupling between the atomic ensemble and a detuned optical cavity mode. Inhomogeneous atom-light coupling and dissipative processes (including, foremost, single-particle spontaneous decay) are present in the current implementation but do not largely change the qualitative behaviour of the targeted dynamical phases under our experimental conditions (see Methods). Previously, we have characterised this interaction [186] and studied collective

dynamics by applying an external drive [107]. In this work, we go beyond the fully collective manifold by engineering a spread in single-particle energies $\varepsilon_k = \hbar\omega_k$ using applied AC Stark shifts ω_k [321, 322]. These shifts form the second term in the Hamiltonian and compete with the spin-exchange interaction.

Equation (4.130) is the so-called Richardson-Gaudin spin model [323, 324], which describes the low-energy physics of Bardeen-Cooper-Schrieffer (BCS) superfluids and superconductors using the Anderson pseudospin mapping [319]. This mapping relates the presence (or absence) of a Cooper pair formed by a pair of electrons with momenta $\pm\mathbf{k}$ to a spin-up (or down) at momentum $\mathbf{k}$, as shown in Fig. 4.28**a**. Correspondingly, annihilating a Cooper pair maps to a spin lowering operator by the relation $\hat{S}^-_{\mathbf{k}} \coloneqq \hat{c}_{\mathbf{k}}\hat{c}_{-\mathbf{k}}$, where $\hat{c}_{\pm\mathbf{k}}$ are fermionic annihilation operators. Similarly, the spin operator $2\hat{S}^z_{\mathbf{k}} + 1 \coloneqq \hat{c}^\dagger_{\mathbf{k}}\hat{c}_{\mathbf{k}} + \hat{c}^\dagger_{-\mathbf{k}}\hat{c}_{-\mathbf{k}}$ counts the number of electrons with momentum $\mathbf{k}$ or $-\mathbf{k}$. Our cavity system therefore manifestly implements a BCS superconductor if one identifies the label k of an atom in the cavity with the momentum $\mathbf{k}$ of the electrons in a Cooper pair. In this way, the first term in Eq. (4.130) is equivalent to the attractive interaction between electrons in the superconductor, and the second term can be associated with the kinetic energy or dispersion relation of the electrons. Note that the BCS model, described by Eq. (4.130), only accounts for the zero momentum collective excitations present in conventional superfluids and superconductors [319].

The BCS order parameter in the Anderson mapping is defined by $\Delta_{\mathrm{BCS}} = \chi\langle\sum_{\mathbf{k}}\hat{c}_{\mathbf{k}}\hat{c}_{-\mathbf{k}}\rangle = \chi\langle\hat{S}^-\rangle$, as depicted in Fig. 4.28**b**. In equilibrium, it plays the role of the BCS pairing gap, which energetically favours many-body states where the electrons arrange in a coherent superposition between Cooper pairs and holes for states close to the Fermi energy. Away from equilibrium, Δ_{BCS} is also predicted to characterise the three dynamical phases (I, II, and III) that arise after quenches in superconductors and superfluids [193]. Such dynamical phases represent distinct regimes of dynamical behaviour that arise after a sudden perturbation of a control parameter in a closed many-body system. They are described using a time-averaged or steady-state order parameter that demonstrates non-analytic behaviour at the boundary between phases. In particular, the BCS model is predicted to exhibit second-order dynamical phase transitions.

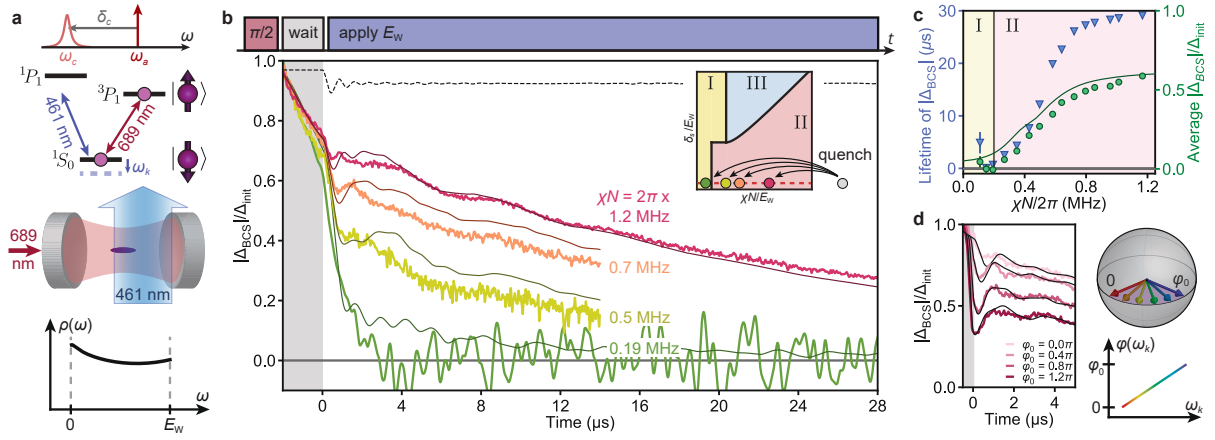

Figure 4.29: **Phase I to phase II transition. a**, Tuning the single-particle dispersion. We shine an off-resonant 461 nm beam onto the atoms from outside the cavity. This generates a distribution of AC Stark shifts representing a roughly uniform density of states $\rho(\omega)$ (bottom plot). **b**, Probing phase I and phase II. We perform a rapid $\pi/2$ pulse to prepare a highly coherent initial state, wait for 2 μs, quench to a variable $\chi N/E_W$ with $\delta_s = 0$, and then let the system evolve. The inset shows the explored parameter cut and identifies post-quench $\chi N/E_W$ values with coloured dots. The main plot shows experimental time traces of $|\Delta_{BCS}|$ (coloured curves) accompanied by numerical simulations (darker lines). Two curves are extended to demonstrate long-time coherence protection, with the $\chi N/2\pi = 0.19$ MHz trace smoothed for clarity. For $\chi N/2\pi = 1.2$ MHz, we show an ideal simulation neglecting dissipation and motional effects (dashed line), which exhibits transient Higgs oscillations. Hints of these oscillations are present in experimental data with additional damping. **c**, Characterising the phase transition. Blue triangles show the fitted coherence time of $|\Delta_{BCS}|$ from $t = 1$ μs to 30 μs. Green circles show the time-averaged $|\Delta_{BCS}|$ between $t = 3$ μs and 8 μs, with the dark green line representing numerical simulations. In all cases, we identify a phase transition at $\chi N/2\pi = 0.2$ MHz. Error bars in all plots represent the s.e.m. of boostrap resamplings on experimental shots. **d**, Varying initial conditions. Before $t = 0$, we shine a high-intensity 461 nm beam within 300 ns, engineering an initial phase spread $\varphi(\omega_k) \in [0, \varphi_0]$ depicted on the Bloch sphere. The phase $\varphi(\omega_k)$ applied to atom k is proportional to the post-quench frequency shift ω_k. Traces represent different φ_0 and show enhanced oscillations with increasing φ_0.

Phase I is characterised by a steady state with a vanishing order parameter $|\Delta_{\mathrm{BCS}}(t)|\to 0$ at long times. Phase II exhibits a steady state with a constant nonzero order parameter $\Delta_\infty \coloneqq \lim_{t\to\infty}|\Delta_{\mathrm{BCS}}(t)|> 0$. Finally, phase III features oscillations in $|\Delta_{\mathrm{BCS}}(t)|$ that persist to long times, realising a Floquet superfluid despite not being periodically driven [298–300, 312]. The long-time behaviour of these dynamical phases admits a simpler description in terms of the Lax-reduced Hamiltonian, which is an effective Hamiltonian taking the same form of Eq. (4.130) but with rescaled parameters and a reduced number of spins [193, 300]. Under this formulation, phases I, II, and III emerge when the Lax-reduced Hamiltonian describes effective zero-spin, one-spin, and two-spin systems respectively.

Inspired by the Lax-reduced Hamiltonian, and in order to explore all three dynamical phases, we engineer two sub-ensembles of atoms with separate control over energy shifts within each sub-ensemble. For practical convenience, we introduce experimental control in the form of an overall frequency splitting δ_{s} between two sub-ensembles and an effective frequency width E_{W} of each sub-ensemble to engineer a tunable dispersion relation ε_k as in Fig. 4.28**b**. Phase I and phase II can also be observed using a single ensemble of atoms as shown in Fig. 4.29. Both experimental setups can nonetheless be described by a common phase diagram as shown in Fig. 4.28**c**.

We initialise all the atoms in the $|\downarrow\rangle$ state and then apply a coherent $\pi/2$ pulse through the cavity in 100 ns such that $\Omega \gg \chi N$, where Ω is the pulse Rabi frequency and χN is the characteristic interaction strength for an ensemble of N atoms. This establishes a large BCS order parameter Δ_{BCS} on a timescale faster than any other relevant dynamics, mimicking the ground state of a Hamiltonian with an infinite interaction strength χ. We then quench the system by rapidly turning on ε_k, which sets a finite ratio $\chi N/E_{\mathrm{W}}$ and a variable $\delta_{\mathrm{s}}/E_{\mathrm{W}}$, allowing us to explore the dynamical phase diagram shown in Fig. 4.28**c**.

We measure both the pre- and post-quench dynamics of $|\Delta_{\mathrm{BCS}}|$ by monitoring light emitted by the atoms into the cavity as a function of time (see Fig. 4.28**d**). This light arises from a superradiance process which is suppressed when the cavity resonance is detuned from the atomic transition frequency by much more than κ, the cavity power decay linewidth [325–327]. In this limit,

the established cavity field adiabatically follows $\langle \hat{S}^- \rangle$, which is proportional to Δ_{BCS}. By measuring the leakage of light from the cavity in heterodyne with a local oscillator, we therefore obtain a real-time probe of Δ_{BCS}. Importantly, at the chosen detuning this probe is quasi-nondestructive, since only a small fraction of the atoms emit light over relevant timescales. In plots of $|\Delta_{\mathrm{BCS}}|$ over time, we normalise traces to the initial gap size Δ_{init} measured right after the $\pi/2$ pulse.

4.5.3 Phase I to phase II

We probe the phase I to phase II transition by varying the ratio $\chi N/E_{\mathrm{W}}$ between the interaction strength and the width of the single-particle energy distribution. As shown in Fig. 4.29**a**, we shine an off-resonant 461 nm beam onto a single atomic ensemble from the side of the cavity that generates a distribution of AC Stark shifts with a spread E_{W}. Careful shaping of the 461 nm beam allows us to realise a roughly flat density of states (see Methods), resulting in a setup consistent with the $\delta_{\mathrm{s}} = 0$ line in Fig. 4.28**c** (see SOM). After the initial $\pi/2$ pulse, we wait for 2 μs to let transient dynamics settle and then turn on the 461 nm beam to quench on $E_{\mathrm{W}}/2\pi = 0.83$ MHz from an initial value $E_{\mathrm{W}}^{(0)}/2\pi \ll 0.1$ MHz. The beam exhibits a rise time of roughly 50 ns, much faster than the relevant dynamics. To scan across the phase diagram in the inset of Fig. 4.29**b**, we vary the interaction strength χN between shots by changing the atom number N.

As shown in Fig. 4.29**b** and **c**, we observe two distinct dynamical behaviours corresponding to phases I and II, signalled by the decay rate of $|\Delta_{\mathrm{BCS}}|$. For experiments with sufficiently small χN, such as $\chi N/2\pi = 0.19$ MHz, $|\Delta_{\mathrm{BCS}}|$ decays with a $1/e$ coherence time of 0.9 ± 0.1 μs. This coherence time is consistent with single-particle dephasing of $\langle \hat{S}^- \rangle$ set by the energy spread $\hbar E_{\mathrm{W}}$ and is nearly constant throughout this regime. We identify the fast decay of $|\Delta_{\mathrm{BCS}}|$ as an experimental signature of phase I. For larger interaction strengths, we observe a rapid increase in coherence time up to a maximum of 29 μs when $\chi N/2\pi = 1.2$ MHz; this constitutes an improvement of more than a factor of 30. We identify this extended coherence time regime as phase II. The residual decay of $|\Delta_{\mathrm{BCS}}|$ in this regime can be attributed to intrinsic dissipative processes including spontaneous emission, off-resonant superradiant emission, and scattering of 461 nm light [186,327], which set a maximum

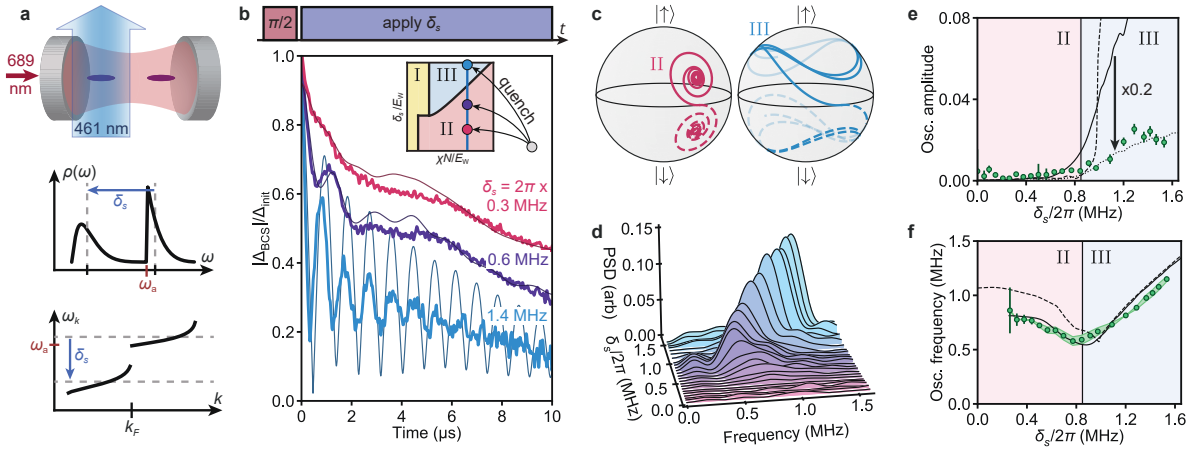

Figure 4.30: **Phase II to phase III transition.** **a**, Engineering a bimodal energy distribution. We prepare two atomic clouds with centres separated by 3 mm and shine an off-resonant 461 nm beam centred on one cloud. This generates a density of states $\rho(\omega)$ (middle plot), equivalent to a dispersion relation $\varepsilon_k = \hbar\omega_k$ (bottom plot). **b**, Probing phase II and phase III. We prepare the same initial state as in Fig. 4.29**b** with a $\pi/2$ pulse, quench to a finite $\delta_\mathrm{s}/E_\mathrm{W}$, and then let the system evolve. The inset shows the explored parameter cut and identifies post-quench $\delta_\mathrm{s}/E_\mathrm{W}$ values with coloured dots. As before, coloured traces represent experimental time traces of $|\Delta_\mathrm{BCS}|$, and darker lines represent numerical simulations. **c**, Ideal simulations of mean-field trajectories for the two sub-ensembles (solid and dashed curves) in phase II (magenta) and phase III (blue). The trajectories are projected onto the surface of the Bloch sphere for visual clarity. **d**, Fourier response of $|\Delta_\mathrm{BCS}|^2$ for different δ_s, plotted as power spectra of the dynamics from $t = 0.5$ μs to 4 μs after subtracting slow-moving behaviour. **e**, Average oscillation amplitude between $t = 3$ μs and 8 μs. For the remaining plots, dashed lines represent ideal simulations (ignoring dissipation or motional effects), and solid dark lines correspond to full simulations. The additional dotted line represents numerical simulations rescaled by $\times 0.2$, plotted to show similar trend behaviour between experimental data and simulations. We identify a phase transition around $\delta_\mathrm{s}/2\pi = 0.85$ MHz. **f**, Oscillation frequency of $|\Delta_\mathrm{BCS}|$, measured using power spectra calculated in (**d**). We correct for systematics inferred from our data analysis and assume this correction has an uncertainty of 100%, shown by the green band. The phase transition point observed in data in panels (**e**) and (**f**) agrees well with simulations.

predicted coherence time of 29 μs (see Methods). All experimental observations (coloured traces) are in good agreement with numerical simulations based on experimental conditions (dark lines—see Methods).

Due to the separation of timescales in the decay of $|\Delta_{\mathrm{BCS}}|$, we are able to determine the boundary between phase I and phase II in our experiment by calculating the average $|\Delta_{\mathrm{BCS}}|$ in a time window from 3 μs to 8 μs as a function of χN (see Fig. 4.29**c**). In this analysis, phase I features a vanishing average $|\Delta_{\mathrm{BCS}}|$, while phase II sees a nonzero $|\Delta_{\mathrm{BCS}}|$ that increases with χN. The sharp rise of average $|\Delta_{\mathrm{BCS}}|$ around $\chi N/2\pi = 0.2$ MHz indicates a dynamical phase transition, which agrees with the point predicted by numerical simulations. In a spin-model picture, the BCS pairing gap corresponds to the energy gap between collective angular momentum states, which exists due to the spin-exchange interaction $\chi \hat{S}^{+}\hat{S}^{-}$ [328]. Phase II corresponds to the parameter region where such interactions are sufficiently strong to protect against single-particle dephasing. As a result, the observed transition directly relates to previous experiments exploring coherence protection in other systems [108, 186–189, 320].

In BCS superconductors, the excitation of a Higgs mode is predicted to occur in phase II. This mode can be characterised by a collective damped oscillation of the order parameter $|\Delta_{\mathrm{BCS}}|$ with a characteristic frequency of $2\Delta_{\infty}$ [300]. We observe hints of Higgs oscillations by comparing the experimental trace of $|\Delta_{\mathrm{BCS}}|$ at $\chi N/2\pi = 1.2$ MHz (red curve in Fig. 4.29**b**) with the dissipation-free simulation (dashed line in Fig. 4.29**b**) and noticing that the first dip in the experimental trace coincides with the first cycle of Higgs oscillations (see Methods). The size of this feature can be increased experimentally by engineering an initial phase spread $\varphi(\omega_k) \in [0, \varphi_0]$ between atoms which is correlated with the post-quench frequency shifts ω_k of the atoms, as shown in Fig. 4.29**d**. The initial state with a nonzero opening angle φ_0 shares qualitative features with the BCS ground state at finite χ up to a $\pi/2$ rotation on the Bloch sphere [301], in contrast to the initial state mimicking the BCS ground state with infinite χ in Fig. 4.29**b**.

4.5.4 Phase II to phase III

We probe the phase II to phase III transition using a vertical cut through the dynamical phase diagram. To realise this, we introduce an energy splitting $\hbar\delta_{\mathrm{s}}$ between two individually addressable clouds of atoms along the cavity axis using AC Stark shifts from our 461 nm beam, as shown in Fig. 4.30**a**. In combination with a background energy spread $\hbar E_{\mathrm{W}}$ associated with lattice shifts (see Methods), this produces a bimodal density of states and a dispersion relation similar to the one proposed in Fig. 4.28**b**. As before, we begin the experiment with a highly coherent state and with $\delta_{\mathrm{s}} = 0$. Then, we quench on a nonzero δ_{s} and let the system evolve. Between shots, we scan δ_{s} while fixing $\chi N/2\pi = 0.9$ MHz and $E_{\mathrm{W}}/2\pi \approx 0.34$ MHz to explore the vertical cut.

The resulting dynamics show a marked change in the dynamical evolution of $|\Delta_{\mathrm{BCS}}|$ over the scan as shown in Fig. 4.30**b**, which we attribute to a transition between phase II and phase III dynamics. For small δ_{s}, we either see Higgs-like oscillations which are damped after 3 μs (the trace where $\delta_{\mathrm{s}}/2\pi = 0.6$ MHz) or, for very small splittings, no oscillations resolvable above the noise floor ($\delta_{\mathrm{s}}/2\pi = 0.3$ MHz). We associate this regime with phase II since it overlaps with the previously observed phase II dynamics in parameter space. For larger δ_{s}, curves instead show large-amplitude oscillations that persist for more than 5 μs ($\delta_{\mathrm{s}}/2\pi = 1.4$ MHz). We identify the long-lived oscillations in this parameter regime as an experimental signature of phase III.

Intuitively, we can understand the difference between the two phases by identifying the two sub-ensembles of atoms with two Bloch vectors (see Fig. 4.30**c**). In phase II, a finite δ_{s} causes the Bloch vectors to precess in different directions, but the dominant scale χN locks them together to form the solid and dashed magenta orbits. In the presence of a finite E_{W}, the orbits decay, but the Bloch vectors maintain phase coherence. On the other hand, in phase III δ_{s} is large enough that the two Bloch vectors accrue an unbounded relative phase, as in the blue orbits. The presence of interactions locks each sub-ensemble separately against a finite E_{W}, leading to persistent oscillations. This effective beating of two large spins in a macroscopic array of spin-1/2 particles is truly an interaction-driven effect since the interactions are strong enough to lock the

spins within each sub-ensemble but not strong enough to lock both sub-ensembles together. In our implementation of phase III, the bimodal distribution allows us to dynamically separate the Bloch vectors of the two sub-ensembles, instead of starting with an already split distribution like in weakly interacting BCS ground states featuring a sharp Fermi edge. Despite their qualitative differences, these two situations can be dynamically connected (see Methods).

We can experimentally define a boundary between phase II and phase III using the separation of timescales observed for oscillations in $|\Delta_{\mathrm{BCS}}|$. Fig. 4.30**e** shows the average oscillation amplitude in a time window from $t = 3$ μs to 8 μs. In this analysis, we observe a sharp rise in oscillation amplitude at $\delta_{\mathrm{s}}/2\pi = 0.85$ MHz $\approx \chi N/2\pi$ as we increase δ_{s}, which we identify as a dynamical phase transition. Numerical simulations plotted in Fig. 4.30**e** agree fairly well with data in capturing trend behaviour and estimating the phase transition point. However, we see a discrepancy in the absolute size of the observed and predicted oscillation amplitudes. We attribute this to an extra dephasing mechanism (likely residual motional effects) in our system or other imperfections in the experimental sequence not captured by the theory model.

We verify the location of the phase II to phase III transition using the short-time oscillation frequency (from $t = 0.5$ μs to 4 μs) as an additional experimental signature. As can be seen in the Fourier responses in Fig. 4.30**d** and quantified in Fig. 4.30**f**, the oscillation frequency exhibits a dip vs. δ_{s} at the previously-identified phase boundary. This dip is present in roughly the same location for experiment and theory and is expected to coincide with the phase II to phase III transition (see SOM).

4.5.5 Scan across three dynamical phases

Finally, we observe all three dynamical phases in a single cut through parameter space, as shown in Fig. 4.31**a**. We run the same experimental sequence described in Fig. 4.30, but instead scan χN between shots with $\delta_{\mathrm{s}}/2\pi = 1.1$ MHz and $E_{\mathrm{W}}/2\pi = 0.46$ MHz fixed. This allows us to probe phase I, phase III and then phase II by increasing atom number N. Using order parameters established in Figs. 4.29 and 4.30, we determine boundaries between the three phases. As shown in

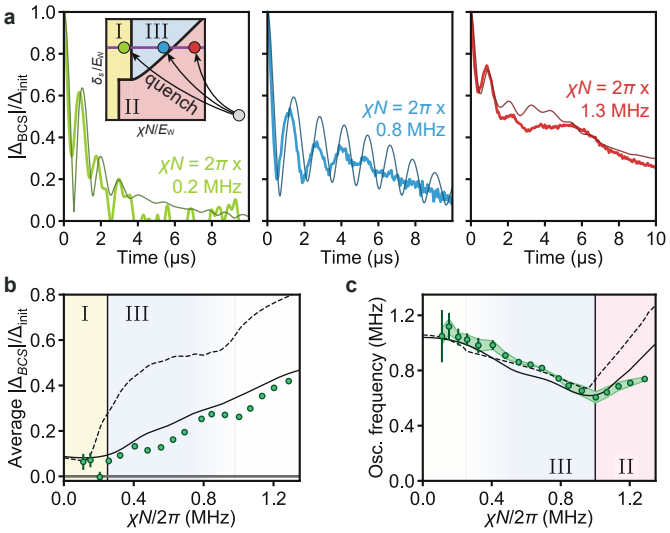

Figure 4.31: **Scan across three dynamical phases.** **a**, Probing phase I, II and III dynamics using time traces of $|\Delta_{\mathrm{BCS}}|$. Quenches are performed in the same manner as in Fig. 4.30**b**, except between shots we hold post-quench values of δ_{s} fixed and vary χN instead. The inset shows the explored cut through the phase diagram and identifies final $\chi N/E_{\mathrm{W}}$ values with green (phase I), blue (phase III), and red (phase II) dots. The $\chi N/2\pi = 0.2$ MHz trace is smoothed for clarity. **b**, Time average of $|\Delta_{\mathrm{BCS}}|$ in a bin from $t = 3$ μs to 8 μs vs. interaction strength. The experimental data shows signatures of a phase I to phase III transition at $\chi N/2\pi = 0.25$ MHz. **c**, Oscillation frequency of $|\Delta_{\mathrm{BCS}}|$ vs. interaction strength in a bin from $t = 0.5$ μs to 4 μs. Again, we correct for systematics inferred from our data analysis and assume this correction has an uncertainty of 100%, shown by the green band. This data identifies a phase III to phase II transition at $\chi N/2\pi = 1.0$ MHz. Experimental data and transitions in both plots are consistent with numerical simulations.

Fig. 4.31**b**, the long-time average of $|\Delta_{\mathrm{BCS}}|$ rises suddenly around $\chi N/2\pi = 0.25$ MHz in both data and simulations. This transition marks the boundary between phase I and phase III. Additionally, at $\chi N/2\pi = 1.0$ MHz we observe a dip in the short-time oscillation frequency of $|\Delta_{\mathrm{BCS}}|$ (Fig. 4.31**c**), marking a transition between phase III and phase II. For this scan, we do not use the long-time oscillation amplitude as an order parameter due to poor signal-to-noise for smaller values of χN.

4.5.6 Conclusion

The demonstrated capability to emulate dynamical phases of superconductors in optical cavities opens exciting prospects for quantum simulation. For example, it will be interesting to see if our cavity simulator can engineer and probe topological superfluid phases [299, 329–334] and understand competing superconducting orders [335, 336] in a single system, or else enable simulation of superfluidity in phenomena relevant to high energy physics [337, 338].

4.5.7 Methods: Experimental setup

Phase I to phase II transition

To explore the phase diagram cut in Fig. 4.29, we first load $10^5 - 10^6$ ^{88}Sr atoms from a magneto-optical trap into an 813 nm optical lattice supported by a high-finesse optical cavity, similar to previous experiments [107, 186, 263, 327]. The resulting atomic cloud has a temperature of roughly 15 μK, resulting in a Gaussian distribution transverse to the cavity axis with standard deviation $\sigma_y = \sigma_z = 16$ μm (coordinates defined in Fig. 4.32**a**). Further, the cloud is extended over thousands of lattice sites, forming a distribution along the cavity axis with a standard deviation $\sigma_x = 430$ μm. We measure an axial trapping frequency of $\omega_x/2\pi = 165$ kHz, giving a Lamb-Dicke parameter of $\eta = 0.17$ for excitation with 689 nm light. At the measured temperature, $\eta^2(2\bar{n}+1) = 0.11 \ll 1$, placing the atoms in the Lamb-Dicke regime. We set a quantisation axis along $\hat{y}$ with a 2.4 G magnetic field and tune the lattice polarisation to a "magic angle" relative to this axis, such that the differential lattice shift between ground ($|^1S_0\rangle$) and excited ($|^3P_1, m_J = 0\rangle$) states vanishes [107]. Using piezoelectric actuators, we stabilise the cavity length to set the closest

TEM_{00} resonance to be 51 MHz red-detuned from the atomic transition.

After loading into the lattice, we initialise the atoms with a $\hat{y}$-polarised drive through the cavity which is nominally resonant with the atomic transition. Because the drive is far off-resonance from the cavity (which has linewidth $\kappa/2\pi = 153$ kHz at 689 nm), the induced Rabi frequency is somewhat suppressed. Nonetheless, we find that roughly 5 mW of power before the cavity is sufficient to drive the atoms with a $\pi/2$ pulse in 100 ns. We allow the atoms to settle for 2 μs in order to distinguish the desired physics from transient dynamics observed after state initialisation, which we attribute to undesired excitation of sideband transitions. We then shine a 461 nm beam from the side of the cavity along the $\hat{y}$ direction, detuned from the $|^1S_0\rangle - |^1P_1\rangle$ transition by more than 10 GHz, in order to induce AC Stark shifts on the ground state. The beam has waists $(w_x, w_z) = (1030\ \mu\mathrm{m}, 75\ \mu\mathrm{m})$ along the $\hat{x}$ and $\hat{z}$ directions at the plane of the atoms, and its centre is displaced from the centre of the atomic cloud by $x_0 = 580\ \mu$m along the cavity axis. From these dimensions, we calculate an atomic density of states $\rho(\omega)$ as a function of frequency shift which is roughly uniform between 0 and a maximum shift $\hbar E_{\mathrm{W}}$. We estimate that for the power and detuning used in this cut, the 461 nm beam scatters off the atoms with an average rate of $R_{\mathrm{sc}}/2\pi = 1.3$ kHz, roughly a factor of six smaller than $\gamma/2\pi = 7.5$ kHz, the spontaneous emission rate. Combined with collective emission from the atoms as described in the Readout section of the Methods, these dissipation processes set a maximum predicted coherence time in the system of 29 μs.

Cuts through phase III

For the two cuts through phase III described in Figs. 4.30 and 4.31, we load the atoms in two clouds separated by 3 mm, as shown in Fig. 4.32**b**. The left cloud has an extent described by standard deviations $(\sigma_x, \sigma_z) = (200\ \mu\mathrm{m}, 16\ \mu\mathrm{m})$. The right cloud has a similar extent along σ_z but is broader along the cavity axis. We tune the lattice polarisation to point along $\hat{z}$, which breaks the magic angle condition and introduces a differential trap depth between ground and excited states of 0.47 MHz for atoms experiencing peak lattice intensity. Due to their finite temperature, the atoms experience a spread in lattice intensities which leads to an inhomogeneous trap depth. We estimate

the induced distribution of energy shifts by assuming the atoms occupy a 2D Gaussian distribution radially with standard deviation $\sigma_y = \sigma_z = 16\ \mu$m, compared to the lattice waist $w_y = w_z = 80\ \mu$m. This produces a peaked distribution equivalent to the narrow peak in Fig. 4.30**a**.

In these experiments, we perform a $\pi/2$ pulse as before and then immediately shine a 461 nm beam centred on the left ("bright") atomic cloud. Unlike in the previous cut, we do not wait for transient dynamics to settle after state initialisation, for the sake of simplicity. We do not see major differences between observed and expected behaviour when omitting the wait period. The beam has waists $(w_x, w_z) = (1700\ \mu\text{m}, 80\ \mu\text{m})$. We install a beam block just before the chamber that clips the beam tail that would otherwise hit the right ("dark") atomic cloud. The 3 mm separation between clouds is sufficiently large to ensure the beam does not significantly diffract around the beam block. The beam shifts the mean energy of the bright cloud away from that of the dark cloud, introducing a tunable δ_s. While nominally, we hold E_W fixed while scanning δ_s to explore the phase II to phase III transition, in reality the finite size of the blue beam introduces an additional contribution to E_W on the bright cloud. As δ_s increases, therefore, both the size and shape of the single-particle energy distribution changes. We calculate E_W in a consistent manner by estimating the standard deviation of the bright cloud distribution and matching the result to a uniform distribution with the same standard deviation (see SOM). In the main text, we report the value of E_W obtained at the phase transition point for the phase II to phase III transition. As we increase the 461 nm beam power, the atoms also scatter more blue photons. At the largest applied AC Stark shift, we estimate that the bright cloud experiences a scattering rate of $R_\text{sc}/2\pi = 3.4$ kHz, resulting in lower coherence times for traces with large δ_s. However, this excess decoherence does not bias our measurements of oscillation amplitude and frequency at times $t \leq 8\ \mu$s.

Readout

After initialisation in all experiments, the atomic ensemble establishes a small electric field inside the cavity which adiabatically follows $\langle \hat{S}^- \rangle$ [186]. Assuming homogeneous atom-light coupling (see next section for modifications due to inhomogeneous coupling), the complex amplitude of the

electric field leaking out of the cavity is given by

$$\alpha_{\text{out}}(t) = -\frac{g}{\delta_c}\sqrt{\kappa_m}\langle\hat{S}^-(t)\rangle, \tag{4.131}$$

where α_{out} has units of $\sqrt{\text{photons/s}}$. Here, $2g/2\pi = 10.6$ kHz is the single-photon Rabi frequency for an atom maximally coupled to the cavity, $\delta_c/2\pi = (\omega_c - \omega_a)/2\pi = -51$ MHz is the detuning between the cavity resonance frequency ω_c and the atomic transition frequency ω_a, and $\kappa_m/2\pi = 41$ kHz is the rate at which photons incident on the cavity mirror are transmitted. α_{out} is a form of dissipation in the system equivalent to superradiance in a detuned cavity limit. Over the region of parameter space explored in this work, we estimate that the dissipation rate never exceeds $\gamma_{\text{SR}}/2\pi = 2.3$ kHz. We measure the detuned superradiant light as it leaks out of the cavity using balanced heterodyne detection, providing us with a real-time probe of $\langle\hat{S}^-\rangle \propto \Delta_{\text{BCS}}$. In plots of $|\Delta_{\text{BCS}}|$ in the main text, we calculate the square magnitude of this quantity and average over 400-1600 shots of the experiment, taken within 2-10 minutes. We then perform background subtraction to remove vacuum noise power from the heterodyne signal. Finally, we take a signed square root of the result to return an estimate of $|\Delta_{\text{BCS}}|$ which averages to zero in the absence of a real signal. This explains why some traces dip below zero despite representing a nonnegative quantity.

Additionally, the cavity experiences a (dispersive) shift in its resonance frequency proportional to the number of atoms. We use this fact to measure atom number by sending a pulsed probe tone through the cavity and measuring the frequency shift using the transmitted light. Since this light is spectrally resolved from the light emitted by the atoms, we are able to measure both signals independently on our heterodyne detector. The different optical frequencies involved in the heterodyne beat are compared in Fig. 4.32**c**.

4.5.8 Methods: Dynamical phase diagram

The unitary dynamics of our system is modelled by an effective atom-only Hamiltonian, given by

$$\hat{H} = \hbar\chi\sum_{jk}\zeta_j\zeta_k\hat{S}_j^+\hat{S}_k^- + \sum_k \varepsilon_k\hat{S}_k^z, \tag{4.132}$$

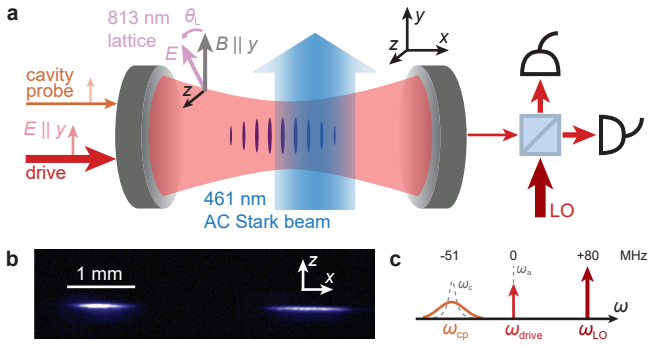

Figure 4.32: **Experimental configuration.** **a**, Detailed diagram of the cavity and all relevant beams. A magnetic field along $\hat{y}$ sets the quantisation axis. The 813 nm optical lattice supported by the cavity has a tunable linear polarisation. We drive a $\pi/2$ pulse with a beam polarised along $\hat{y}$ through the cavity, and during the experiment we probe the cavity resonance frequency using a second $\hat{y}$-polarised beam to measure atom number. A 461 nm beam far-detuned from the $|^1S_0\rangle - |^1P_1\rangle$ transition shines on the atoms from the side of the cavity, inducing AC Stark shifts. We probe signals transmitted through the cavity using a balanced heterodyne detector. **b**, Fluorescence image of the two atomic clouds used when scanning through phase III in Figs. 4.30 and 4.31. **c**, Frequency landscape of 689 nm beams. The atomic drive frequency ω_{drive} is resonant with the atomic transition. The cavity probe frequency ω_{cp} is nominally centred with the cavity resonance frequency, 51 MHz red-detuned from the atomic transition. The local oscillator used in heterodyne detection has frequency ω_{LO} and is 80 MHz blue-detuned from the atomic transition.

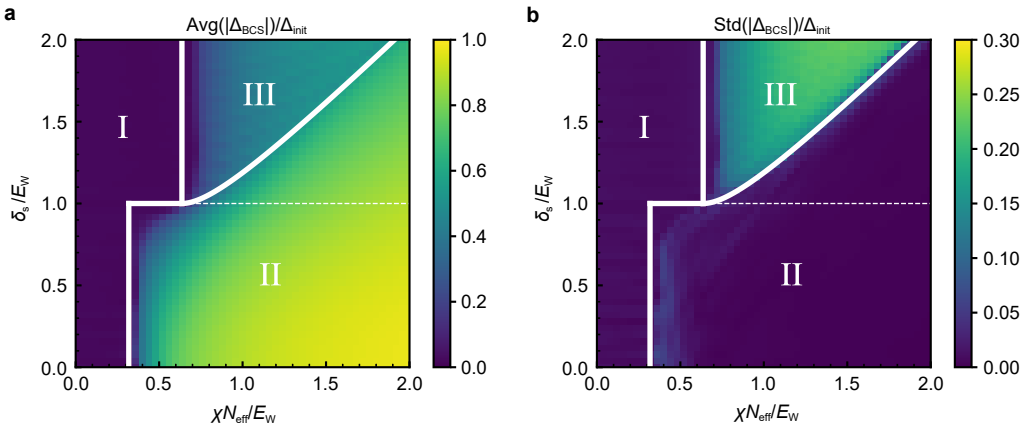

Figure 4.33: **Numerical simulation of the dynamical phase diagram based on Eq. (4.132).** We identify the dynamical phases based on the long-time average (**a**) and the long-time standard deviation (**b**) of $|\Delta_{\mathrm{BCS}}(t)|$, normalised by its initial value $\Delta_{\mathrm{init}} \equiv |\Delta_{\mathrm{BCS}}(0)|$. The white solid lines mark the corresponding dynamical phase boundaries, analytically derived from Eq. (4.130), which agree with the numerical results based on Eq. (4.132). The white dashed lines mark an extra dynamical phase transition that only exists for Eq. (4.130).

where $\hat{S}_k^{+,-}, \hat{S}_k^{x,y,z}$ are the standard spin-1/2 operators on atom k. We define $\chi = -g^2\delta_c/(\delta_c^2+\kappa^2/4)$, where g and δ_c are as defined in the previous section, and κ is the cavity linewidth. The spatial dependence of the interaction term is characterised by $\zeta_j = \cos(j\phi)$ with $\phi = \pi\lambda_L/\lambda_c$, which arises because the lattice wavelength $\lambda_L = 813$ nm is incommensurate with the cavity wavelength $\lambda_c = 689$ nm. In contrast to Eq. (4.130), Eq. (4.132) becomes non-integrable due to the inhomogeneity in the interaction term. Nevertheless, as shown in Fig. 4.33, Eq. (4.132) leads to a similar dynamical phase diagram as Eq. (4.130) if we

i) Use a generalised superconducting order parameter $\Delta_{\mathrm{BCS}} = \chi \sum_k \zeta_k \langle \hat{S}_k^- \rangle$;

ii) Interpret the $\pi/2$-pulse as a pulse along the cavity axis under the Hamiltonian $\hat{H}_{\mathrm{drive}} = \hbar\Omega \sum_k \zeta_k S_k^y$ that generates the maximum possible $|\Delta_{\mathrm{BCS}}|$, which occurs when $\Omega t = 0.586\pi$;

iii) Replace the atomic number N by an effective atom number $N_{\mathrm{eff}} = N/2$, such that χN_{eff} represents the averaged interaction strength of Eq. (4.132).

We can still measure the generalised order parameter Δ_{BCS} using the field leaking out of the cavity as in the previous section, since with inhomogeneous coupling the transmitted field takes the form $\alpha_{\mathrm{out}}(t) = -\frac{g}{\delta_c}\sqrt{\kappa_m}\sum_k \zeta_k \langle \hat{S}_k^-(t) \rangle \propto \Delta_{\mathrm{BCS}}$. The dynamical phase diagram in Fig. 4.33 is numerically calculated based on unitary evolution under Eq. (4.132), with a single-particle dispersion $\varepsilon_k/\hbar$ sampled from a uniform distribution in the frequency range $[-\delta_{\mathrm{s}}/2 - E_{\mathrm{W}}/2, -\delta_{\mathrm{s}}/2 + E_{\mathrm{W}}/2]$ and $[\delta_{\mathrm{s}}/2 - E_{\mathrm{W}}/2, \delta_{\mathrm{s}}/2 + E_{\mathrm{W}}/2]$. There χN corresponds to the averaged interaction strength of Eq. (4.132). We identify the dynamical phases based on the long-time average of $|\Delta_{\mathrm{BCS}}|$, given by

$$\mathrm{Avg}(|\Delta_{\mathrm{BCS}}|) = \lim_{T\to\infty} \frac{1}{T} \int_0^T |\Delta_{\mathrm{BCS}}(t)| dt, \tag{4.133}$$

as well as the long-time oscillation amplitude of $|\Delta_{\mathrm{BCS}}|$. Since the oscillations in $|\Delta_{\mathrm{BCS}}|$ might deviate from a sinusoidal form, for theoretical simulations it is easier to use the standard deviation as a measure of the oscillation amplitude:

$$\mathrm{Std}(|\Delta_{\mathrm{BCS}}|) = \left[\lim_{T\to\infty} \frac{1}{T} \int_0^T \Big(|\Delta_{\mathrm{BCS}}(t)| - \mathrm{Avg}(|\Delta_{\mathrm{BCS}}|) \Big)^2 dt \right]^{1/2}. \tag{4.134}$$

When comparing to experimental data, we measure oscillation amplitude using the Fourier spectrum because technical noise in the experiment contributes to the standard deviation of the time traces (see Fig. 4.30**d**). The dynamical phases can be characterised in theoretical simulations by

- Phase I: $\mathrm{Avg}(|\Delta_{\mathrm{BCS}}|) = 0$, $\mathrm{Std}(|\Delta_{\mathrm{BCS}}|) = 0$.
- Phase II: $\mathrm{Avg}(|\Delta_{\mathrm{BCS}}|) > 0$, $\mathrm{Std}(|\Delta_{\mathrm{BCS}}|) = 0$.
- Phase III: $\mathrm{Avg}(|\Delta_{\mathrm{BCS}}|) > 0$, $\mathrm{Std}(|\Delta_{\mathrm{BCS}}|) > 0$.

The dynamical phase boundaries (white solid lines) in Fig. 4.33 are analytically calculated using a Lax analysis applied to Eq. (4.130), similar to the one discussed in [193,301], and take the following form (see SOM for a detailed derivation):

- Phase I to phase II:

$$\begin{aligned} &\frac{\chi N}{E_{\mathrm{W}}} = \frac{1}{\pi} \quad \text{with} \quad \frac{\delta_{\mathrm{s}}}{E_{\mathrm{W}}} \in [0,1], \\ &\frac{\delta_{\mathrm{s}}}{E_{\mathrm{W}}} = 1 \quad \text{with} \quad \frac{\chi N}{E_{\mathrm{W}}} \in \left[\frac{1}{\pi}, \frac{2}{\pi}\right]. \end{aligned} \tag{4.135}$$

- Phase I to phase III:

$$\frac{\chi N}{E_{\mathrm{W}}} = \frac{2}{\pi} \quad \text{with} \quad \frac{\delta_{\mathrm{s}}}{E_{\mathrm{W}}} > 1. \tag{4.136}$$

- Phase II to phase III:

$$\frac{\delta_s}{E_{\mathrm{W}}} = \csc\left(\frac{E_{\mathrm{W}}}{\chi N}\right) \quad \text{with} \quad \frac{\chi N}{E_{\mathrm{W}}} > \frac{2}{\pi}. \tag{4.137}$$

The analytical results agree with the numerical simulations for Eq. (4.132). The only difference is that Eq. (4.130) predicts an extra dynamical phase transition marked by the white dashed line. The dynamical phase boundaries shown in Fig. 4.28**c** are constructed by the analytical formulas above.

4.5.9 Methods: Phase III dynamics in the case of a continuous single-particle dispersion

In this work, we generate phase III using a bimodal single-particle dispersion, represented with idealized assumptions by Fig. 4.28**b** and with actual experimental conditions by Fig. 4.30**a**.

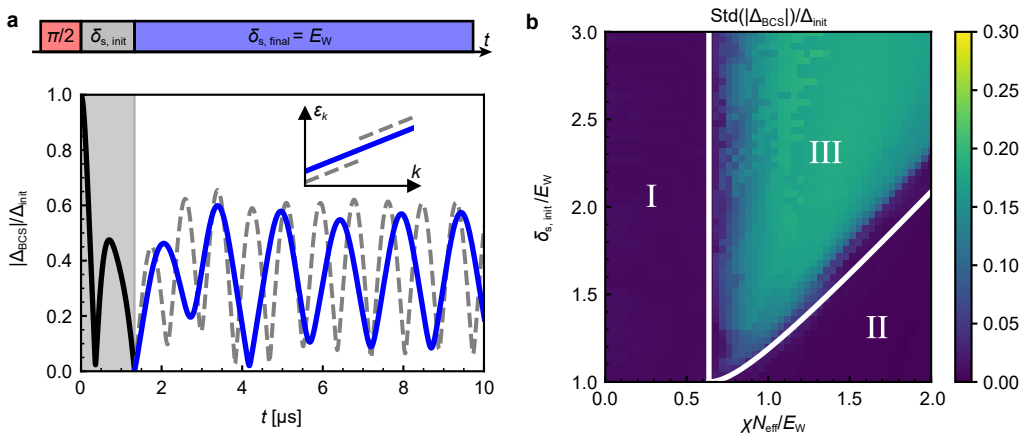

Figure 4.34: **Alternative approach for phase III. a**, Simulation of an alternative experimental sequence. As described by the timing sequence at the top, we simulate an experiment that prepares the initial state using a $\pi/2$ pulse, lets the system evolve under a bimodal distribution of single-particle energy (see the inset) until $|\Delta_{\mathrm{BCS}}|$ reaches its minimum value, and then quenches the system back to a continuous distribution of single-particle energies (see the inset). The theoretically predicted time trace of $|\Delta_{\mathrm{BCS}}|$ with $\chi N/E_{\mathrm{W}} = 1.0$ and $\delta_{\mathrm{s,init}}/E_{\mathrm{W}} = 1.6$ is shown at the bottom. The blue (grey dashed) line shows phase III dynamics under a continuous (bimodal) distribution. **b**, Long-time standard deviation of $|\Delta_{\mathrm{BCS}}(t)|$ after quenching to the continuous distribution shown in **a**. The white lines are dynamical phase boundaries for bimodal distributions (see Fig. 4.33). Nearly all the choices of parameter for phase III using bimodal distributions can lead to phase III behaviours after quenching to the continuous distribution.

Here we show that this experimentally convenient approach generates similar phase III dynamics to the one obtained in the case of a continuous dispersion but with different initial conditions.

This is done by the protocol shown in Fig. 4.34**a**, which uses a bimodal distribution ($\delta_{\mathrm{s,init}} > E_{\mathrm{W}}$) just to generate a state with minimum $|\Delta_{\mathrm{BCS}}|$. At this point the system's dispersion is restored to be continuous by setting $\delta_{\mathrm{s,final}} = E_{\mathrm{W}}$. This approach more closely resembles the phase III quench discussed in actual BCS superconductors, where phase III is observed by quenching from a state with weak BCS paring gap $|\Delta_{\mathrm{BCS}}|$ to one with a strong pairing gap [300]. Numerical simulations based on Eq. (4.132) show that nearly all choices of parameters that lead to phase III using a bimodal distribution also lead to phase III dynamics when quenching to a continuous distribution. The only exception is a small parameter regime close to the boundary between phase III and phase II (see Fig. 4.34**b**). Note that here we use definitions for Δ_{BCS}, the $\pi/2$ pulse, and χN which correspond to Eq. (4.132), as explained in the previous section.

4.5.10 Methods: Numerical simulations

The black dashed lines in Figs. 4.29, 4.30, and 4.31 are computed from unitary evolution under Eq. (4.132) using a single-particle dispersion ε_k, sampled from the experimentally engineered distribution.

The black solid lines in the same figures are obtained by adding dissipative processes and axial motion to Eq. (4.132). The system dynamics is described by the following master equation for the density matrix $\hat{\rho}$:

$$\frac{d\hat{\rho}}{dt} = -\frac{i}{\hbar}[\hat{H}, \hat{\rho}] + \mathcal{L}(\hat{L}_c)[\hat{\rho}] + \sum_k \mathcal{L}(\hat{L}_{s,k})[\hat{\rho}] + \sum_k \mathcal{L}(\hat{L}_{\mathrm{el},k})[\hat{\rho}]. \tag{4.138}$$

The Lindblad superoperator takes the form $\mathcal{L}(\hat{L})[\hat{\rho}] = \hat{L}\hat{\rho}\hat{L}^\dagger - \frac{1}{2}(\hat{L}^\dagger\hat{L}\hat{\rho} + \hat{\rho}\hat{L}^\dagger\hat{L})$. Superradiance through the cavity is described by the jump operator

$$\hat{L}_c = \sqrt{\Gamma}\sum_k \zeta_k \hat{S}_k^-, \tag{4.139}$$

where $\Gamma = \chi\kappa/\delta_c$. Spontaneous emission from the atomic excited state is described by the jump

operator

$$\hat{L}_{s,k} = \sqrt{\gamma}\hat{S}_k^-, \tag{4.140}$$

where $\gamma/2\pi = 7.5$ kHz is the spontaneous emission rate out of $^3P_1$. Single-particle decoherence is described by the jump operator

$$\hat{L}_{\mathrm{el},k} = \sqrt{2\gamma_{\mathrm{el}}}\hat{S}_k^z, \tag{4.141}$$

where γ_{el} is a fitting parameter taking into account free space scattering from the AC Stark shift beam, as well as other decoherence processes in the experiment (see Supplemental Online Material). These are the dominant dissipative processes in our system.

The axial trapping frequency of the lattice is 165 kHz and is therefore smaller than the spin-exchange interaction rate χN for most of the experiments. As a consequence, in contrast to the idealised model where atoms are assumed to be frozen, motional processes need to be accounted for, even though they are suppressed in the Lamb-Dicke regime. As shown in the SOM, axial motion can lead to a faster damping rate of $|\Delta_{\mathrm{BCS}}|$ oscillations. The predicted dynamical phase boundaries are nevertheless unaffected by the axial motion.

All the numerical simulations are computed using the mean-field approximation, which replaces the operators $\hat{S}_k^{x,y,z}$ by their expectation values $\langle \hat{S}_k^{x,y,z} \rangle$ in the Heisenberg equation of motion. The mean-field treatment of the BCS model is predicted to be exact in the thermodynamic limit due to the infinite-range nature of the interactions [300]. The atom number for numerical simulation is set to 5000 for the ideal conditions and 2000 for actual experimental conditions. We rescale χ to match χN with experimental values.

4.5.11 Methods: Higgs-like behaviour in short-time phase II dynamics

When quenching into phase II, we observe highly damped oscillations in $|\Delta_{\mathrm{BCS}}|$, reminiscent of the Higgs oscillations predicted to arise in this regime of the BCS model. Here, we analyse traces from Fig. 4.29**d**, in which we engineer a variable phase spread $\varphi(\omega_k) \in [0, \varphi_0]$ before quenching into phase II, to study this potential connection.

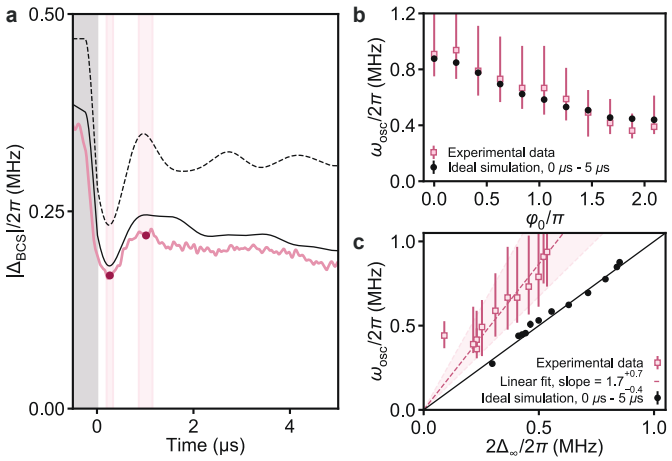

Figure 4.35: **Collective scaling in damped phase II oscillations.** **a**, Time dynamics of $|\Delta_{\mathrm{BCS}}|$ measured after engineering an initial phase spread over $[0, \varphi_0]$ where $\varphi_0 = 0.8\pi$ as in Fig. 2**d**, plotted in absolute frequency units (pink trace). The solid black curve represents a numerical simulation of the full system, whereas the dashed curve represents an ideal simulation neglecting dissipation and motional effects. We obtain a crude estimate of oscillation frequency in the experimental data by fitting a trough and peak to smoothed data (after subtracting slow-moving behaviour) within the first couple μs (magenta points), using these points to infer a half period of oscillation, and with uncertainties determined using a 90% amplitude threshold (pink bands). **b**, Comparing oscillation frequency estimates of experimental data (pink squares) with those of ideal simulations (black dots) for different φ_0. Theory oscillation frequencies are calculated using a Fourier transform from $t = 0$ μs to $t = 5$ μs. Error bars for experimental data are set by the minimum and maximum frequencies implied by uncertainties in the half period shown in **a**. The two frequency estimates agree within error bars. **c**, Collective scaling of oscillation frequency. For each φ_0 measured in the experiment, we plot the oscillation frequency against the long-time BCS gap Δ_∞, calculated at $t = 18$ μs for ideal simulations and at $t = 3$ μs for experimental data. The solid black line is defined by $\omega_{\mathrm{osc}} = 2\Delta_\infty$, demonstrating the expected scaling for Higgs oscillations. The dashed pink line represents a linear fit to the experimental data. The pink band shows the uncertainty in the slope assuming correlated error in ω_{osc}, such that its bounds are defined by linear fits to the data assuming maximum and minimum values for ω_{osc} as defined by the error bars.

In the BCS model, Higgs oscillations can be characterised by their frequency, which should scale with the long-time BCS order parameter Δ_∞ as $\omega_{\rm osc} = 2\Delta_\infty$ [300]. We confirm this scaling in theory by measuring the oscillation frequency from $t = 0$ μs to $t = 5$ μs in idealised numerical simulations ignoring dissipation and motional effects (black dashed line in Fig. 4.35**a**). For different values of the phase spread extent φ_0, the system reaches its steady state at a different long-time BCS gap Δ_∞. By parametrically plotting the oscillation frequency vs. $2\Delta_\infty$ as a function of φ_0 in panel **c**, we observe the expected scaling.

As discussed in the main text, oscillations in $|\Delta_{\rm BCS}|$ are consistently smaller and decay more quickly in experiment than in theory. Nonetheless, we obtain a crude estimate of the experimental oscillation frequency by measuring a half period from the first trough and peak of $|\Delta_{\rm BCS}(t)|$, as shown in panel **a**. In panel **b**, we compare the frequency in experimental data to that of ideal simulations for different φ_0 and show that the frequencies agree within error bars. This suggests that the transient dynamics observed in $|\Delta_{\rm BCS}|$ are related to the Higgs oscillations present in theory.

Although the experimental oscillation frequency agrees with simulations, the steady-state order parameter Δ_∞ is much smaller, as can be seen in Fig. 4.35**a**. As a result, the measured frequencies scale linearly with Δ_∞ but with a different prefactor. In panel **c**, we fit a linear relation of $\omega_{\rm osc} = (1.7^{+0.7}_{-0.4}) \times 2\Delta_\infty$ to the data, where the slope uncertainty bounds are calculated assuming errors in $\omega_{\rm osc}$ are perfectly correlated. Most of the reduction in Δ_∞ can be captured in theory by considering dissipation and motional effects (solid black trace). We see an additional small difference in $|\Delta_{\rm BCS}|$ between full numerical simulations and experimental data, which we attribute to drifts in experimental alignments and calibration factors over time. This difference is not apparent in Fig. 4.29**d** because we plot $|\Delta_{\rm BCS}|$ in normalised units.

4.5.12 Supplemental Materials: Dynamical phase diagram

Here we perform detailed analysis of the dynamical phase diagram shown in Fig. 4.28. We start from analytic calculation in the case of homogeneous couplings, and then generalize to the

case of inhomogeneous couplings. Finally we discuss the application of our findings to experimental conditions.

Homogeneous model

First we discuss the dynamical phases for the BCS Hamiltonian with homogeneous couplings,

$$\hat{H} = \hbar\chi \hat{S}^+ \hat{S}^- + \sum_k \varepsilon_k \hat{S}^z_k. \tag{4.142}$$

We will set $\hbar = 1$. As shown in Ref. [300, 301], the dynamical phases can be determined using a mean-field Lax vector analysis. The Lax vector is defined as $\vec{L}(u) = L^x(u)\hat{x} + L^y(u)\hat{y} + L^z(u)\hat{z}$ with components,

$$L^x(u) = \sum_k \frac{S^x_k(0)}{u - \varepsilon_k/2}, \quad L^y(u) = \sum_k \frac{S^y_k(0)}{u - \varepsilon_k/2}, \quad L^z(u) = -\frac{1}{\chi} - \sum_i \frac{S^z_k(0)}{u - \varepsilon_k/2}, \tag{4.143}$$

where $S^{x,y,z}_k(0)$ are the expectation value of operators $\hat{S}^{x,y,z}_k$ in the initial state.

Here we consider the initial state as $S^x_k(0) = 1/2$, $S^y_k(0) = S^z_k(0) = 0$, and ε_k is chosen from a uniform distribution in the frequency range $[-\delta_s/2 - E_W/2, -\delta_s/2 + E_W/2]$ and $[\delta_s/2 - E_W/2, \delta_s/2 + E_W/2]$. In this case, the mean-field Lax vector takes the following form:

$$\begin{aligned}
\chi L^x(u) &\approx \frac{\chi N}{2}\left[\frac{1}{2E_W}\int_{-\delta_s/2-E_W/2}^{-\delta_s/2+E_W/2} \frac{dx}{u - x/2} + \frac{1}{2E_W}\int_{\delta_s/2-E_W/2}^{\delta_s/2+E_W/2} \frac{dx}{u - x/2}\right] \\
&= \frac{\chi N}{2E_W}\left[\ln\left(u + \frac{\delta_s}{4} + \frac{E_W}{4}\right) - \ln\left(u + \frac{\delta_s}{4} - \frac{E_W}{4}\right) + \ln\left(u - \frac{\delta_s}{4} + \frac{E_W}{4}\right)\right. \\
&\left. - \ln\left(u - \frac{\delta_s}{4} - \frac{E_W}{4}\right)\right],
\end{aligned} \tag{4.144}$$

$$\chi L^y(u) = 0,$$

$$\chi L^z(u) = -1.$$

Note that $\ln z$ in the complex plane is a multivalued function. Here we take the principal value $\ln z = \ln|z| + i\mathrm{Arg}(z)$, where $\mathrm{Arg}(z)$ is the argument of z restricted in the interval $(-\pi, \pi]$. Directly combining the logarithm functions might lead to moving out of the principal branch.

One can define the dynamical phases based on the number of complex roots of equation $\vec{L}(u) \cdot \vec{L}(u) = 0$: Phase I has zero complex roots, phase II has a pair of complex roots, phase III has two pairs of complex roots. Whether the complex roots have non-zero or vanishing real parts

could be used for further separation of the phases. In our case, the equation $\vec{L}(u)\cdot\vec{L}(u)=0$ takes the following form,

$$\frac{\chi N}{2E_{\rm W}}\left[\ln\left(u+\frac{\delta_{\rm s}}{4}+\frac{E_{\rm W}}{4}\right)-\ln\left(u+\frac{\delta_{\rm s}}{4}-\frac{E_{\rm W}}{4}\right)+\ln\left(u-\frac{\delta_{\rm s}}{4}+\frac{E_{\rm W}}{4}\right)-\ln\left(u-\frac{\delta_{\rm s}}{4}-\frac{E_{\rm W}}{4}\right)\right]=\pm i. \quad (4.145)$$

We find four dynamical phases based on analyzing the roots of Eq. (4.145):

- Phase I: No complex roots, which exist in the regime

$$\frac{\delta_{\rm s}}{E_{\rm W}}<1,\quad \frac{\chi N}{E_{\rm W}}<\frac{1}{\pi}\qquad\text{or}\qquad \frac{\delta_{\rm s}}{E_{\rm W}}>1,\quad \frac{\chi N}{E_{\rm W}}<\frac{2}{\pi}. \quad (4.146)$$

- Phase II: A pair of complex roots,

$$\frac{u}{E_{\rm W}}=\pm\frac{i}{4}\left[\cot\left(\frac{E_{\rm W}}{\chi N}\right)+\sqrt{\csc^2\left(\frac{E_{\rm W}}{\chi N}\right)-\frac{\delta_{\rm s}^2}{E_{\rm W}^2}}\right], \quad (4.147)$$

  which exist in the regime

$$\frac{\delta_{\rm s}}{E_{\rm W}}<1,\quad \frac{\chi N}{E_{\rm W}}>\frac{1}{\pi}. \quad (4.148)$$

- Phase IIIa: Two pairs of complex roots with vanishing real parts,

$$\begin{aligned}\frac{u_1}{E_{\rm W}}&=\pm\frac{i}{4}\left[\cot\left(\frac{E_{\rm W}}{\chi N}\right)+\sqrt{\csc^2\left(\frac{E_{\rm W}}{\chi N}\right)-\frac{\delta_{\rm s}^2}{E_{\rm W}^2}}\right],\\ \frac{u_2}{E_{\rm W}}&=\pm\frac{i}{4}\left[\cot\left(\frac{E_{\rm W}}{\chi N}\right)-\sqrt{\csc^2\left(\frac{E_{\rm W}}{\chi N}\right)-\frac{\delta_{\rm s}^2}{E_{\rm W}^2}}\right],\end{aligned} \quad (4.149)$$

  which exist in the regime

$$\frac{\delta_{\rm s}}{E_{\rm W}}>1,\quad \frac{\chi N}{E_{\rm W}}>\frac{2}{\pi},\quad \frac{\delta_{\rm s}}{E_{\rm W}}<\csc\left(\frac{E_{\rm W}}{\chi N}\right). \quad (4.150)$$

  In phase IIIa, the order parameter, $\Delta_{\rm BCS}$ oscillates around a non-zero value (non-ZOPA) as pointed out in Ref. [301, 313].

- Phase IIIb: Two pairs of complex roots with non-zero real parts,

$$\begin{aligned}\frac{u_1}{E_{\rm W}}&=\frac{1}{4}\left[\sqrt{\delta_{\rm s}^2-\csc^2\left(\frac{1}{\chi N}\right)}\pm i\cot\left(\frac{1}{\chi N}\right)\right],\\ \frac{u_2}{E_{\rm W}}&=\frac{1}{4}\left[-\sqrt{\delta_{\rm s}^2-\csc^2\left(\frac{1}{\chi N}\right)}\pm i\cot\left(\frac{1}{\chi N}\right)\right],\end{aligned} \quad (4.151)$$

which exist in the regime

$$\frac{\delta_{\rm s}}{E_{\rm W}} > 1, \quad \frac{\chi N}{E_{\rm W}} > \frac{2}{\pi}, \quad \frac{\delta_{\rm s}}{E_{\rm W}} > \csc\left(\frac{E_{\rm W}}{\chi N}\right). \tag{4.152}$$

In phase IIIb, $\Delta_{\rm BCS}$ oscillates with zero order parameter average (ZOPA) as explained in Ref. [301, 313].

The dynamical phases derived from the Lax analysis above are supported by numerical evidences, as shown in Fig. 4.36**a** and Fig. 4.36**b**. We numerically solve the dynamics of $\Delta_{\rm BCS} = \chi\langle\hat{S}^-\rangle$ under Eq. (4.142) based on mean field approximation, and then identify dynamical phases based on long-time average of $|\Delta_{\rm BCS}|$,

$$\mathrm{Avg}(|\Delta_{\rm BCS}|) = \lim_{T\to\infty}\frac{1}{T}\int_0^T |\Delta_{\rm BCS}(t)|dt, \tag{4.153}$$

and long-time oscillation amplitude of $|\Delta_{\rm BCS}|$. Since the oscillations in $|\Delta_{\rm BCS}|$ might deviates from a sinusoidal form, it is easier to use the standard deviation as a measure of the oscillation amplitude,

$$\mathrm{Std}(|\Delta_{\rm BCS}|) = \left[\lim_{T\to\infty}\frac{1}{T}\int_0^T \Big(|\Delta_{\rm BCS}(t)| - \mathrm{Avg}(|\Delta_{\rm BCS}|)\Big)^2 dt\right]^{1/2}, \tag{4.154}$$

although experimentally it's better to use the peak of Fourier spectrum to suppress the noise (see Fig. 3**d** in the main text). The dynamical phases can be characterized by

- Phase I: $\mathrm{Avg}(|\Delta_{\rm BCS}|) = 0$, $\mathrm{Std}(|\Delta_{\rm BCS}|) = 0$.
- Phase II: $\mathrm{Avg}(|\Delta_{\rm BCS}|) > 0$, $\mathrm{Std}(|\Delta_{\rm BCS}|) = 0$.
- Phase III: $\mathrm{Avg}(|\Delta_{\rm BCS}|) > 0$, $\mathrm{Std}(|\Delta_{\rm BCS}|) > 0$.

Since ε_k is chosen from a distribution with particle-hole symmetry (symmetric about 0), $\Delta_{\rm BCS}$ becomes a real number in this case. One can further separate phase IIIa and phase IIIb by the behavior of $\Delta_{\rm BCS}$ shown in Fig. 4.36**e** and Fig. 4.36**f**.

Inhomogeneous model

Here we discuss the dynamical phases for the BCS Hamiltonian with inhomogeneous coupling,

$$\hat{H} = \hbar\chi\sum_{jk}\zeta_j\zeta_k\hat{S}_j^+\hat{S}_k^- + \sum_k \varepsilon_k\hat{S}_k^z, \tag{4.155}$$

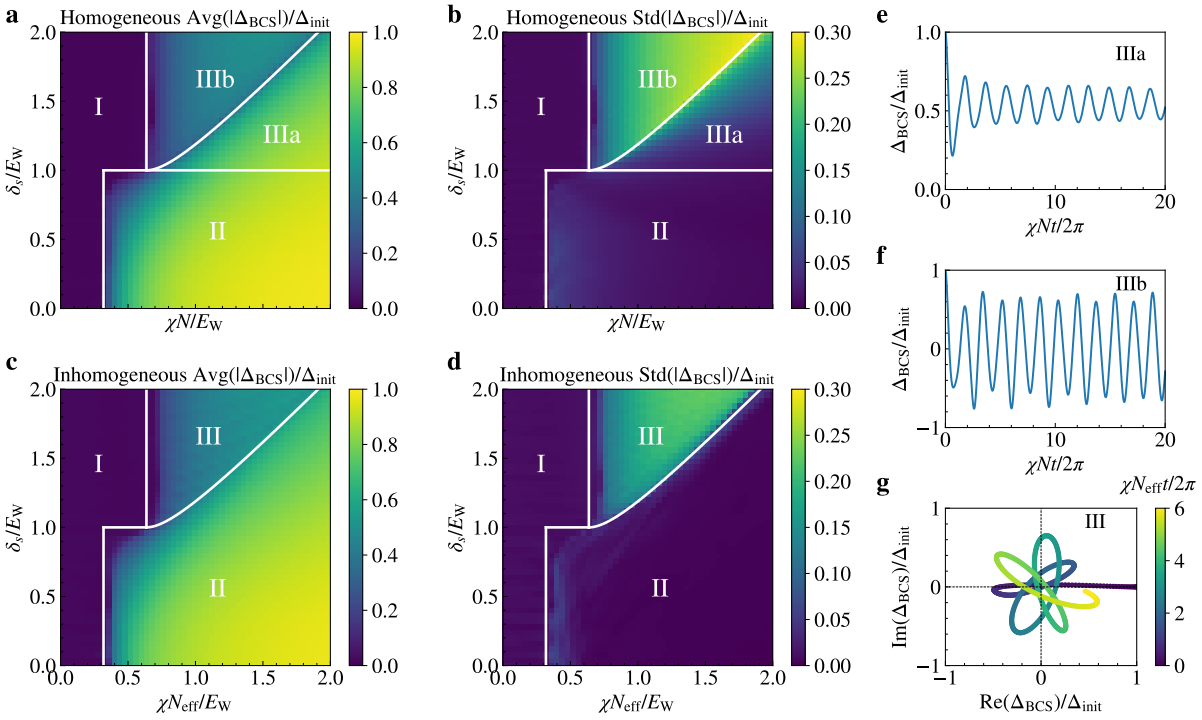

Figure 4.36: **Dynamical phase diagrams.** **a** and **b**, Dynamical phase diagram of the homogeneous model normalized by $\Delta_{\text{init}}/\chi N = 1/2$, where Δ_{init} is the initial value of $|\Delta_{\text{BCS}}|$. The white lines are the dynamical critical points derived from the Lax analysis. **c** and **d**, Dynamical phase diagram of the inhomogeneous model normalized by $\Delta_{\text{init}}/\chi N_{\text{eff}} = \mathcal{J}_1(\Omega\tau)$. The white lines are the same as the homogeneous model. **e**, Time evolution of Δ_{BCS} at $\delta_{\text{s}}/E_{\text{W}} = 1.1$, $\chi N/E_{\text{W}} = 1.0$ under the homogeneous model (phase IIIa). **f**, Time evolution of Δ_{BCS} at $\delta_{\text{s}}/E_{\text{W}} = 1.6$, $\chi N/E_{\text{W}} = 1.0$ under the homogeneous model (phase IIIb). **g**, Time evolution of Δ_{BCS} at $\delta_{\text{s}}/E_{\text{W}} = 1.6$, $\chi N/E_{\text{W}} = 1.0$ under the inhomogeneous model (phase III).

where ζ_k is generated by random sampling of $\cos(x)$, with x chosen from a uniform distribution in the interval $[0, 2\pi)$. Similar to the homogeneous model, $\varepsilon_k/\hbar$ is still chosen from a uniform distribution in the frequency range $[-\delta_s/2 - E_W/2, -\delta_s/2 + E_W/2]$ and $[\delta_s/2 - E_W/2, \delta_s/2 + E_W/2]$. In this case, we explore the dynamical phases numerically since the Lax analysis is not applicable. As shown in Fig. 4.38**c** and Fig. 4.38**d**, one can obtain similar dynamical phases as the homogeneous model: Phase I remains the same, Phase IIIa merges into Phase II, and Phase IIIb becomes the new Phase III. The phase boundary can be roughly captured by the analytical solution of the homogeneous model. Note that χN_{eff} is the averaged interaction strength in the inhomogeneous case, where $N_{\text{eff}} = N/2$. The superconducting order parameter is defined as $\Delta_{\text{BCS}} = \chi \sum_k \zeta_k \langle \hat{S}_k^- \rangle$. The initial condition is chosen as the maximum $|\Delta_{\text{BCS}}|$ one can achieved by an external drive along the cavity axis, $\hat{H}_{\text{drive}} = \Omega \sum_k \zeta_k \hat{S}_k^y$. Assuming the initial state can be prepared by applying $\hat{H}_{\text{drive}}$ for a time τ, we have

$$\frac{\Delta_{\text{init}}}{\chi N_{\text{eff}}} \approx \frac{1}{2\pi} \int_0^{2\pi} dx \cos(x) \sin(\Omega\tau \cos(x)) = \mathcal{J}_1(\Omega\tau), \tag{4.156}$$

where $\mathcal{J}_n$ is the Bessel function of the first-kind, and the maximum of $\mathcal{J}_1(\Omega\tau)$ can be achieved at $\Omega\tau = 0.586\pi$. It is worth to mention that Δ_{BCS} is a real number initially, but it becomes a complex number during the time evolution, as shown in Fig. 4.38**g**.

Experimental control of dynamical phases

Here we elaborate on the experimental implementation of the Hamiltonian Eq. (4.155). As discussed in the previous section, we would like to approximately engineer single-particle energies $\varepsilon_k/\hbar$ sampled from a uniform distribution in the frequency range $[-\delta_s/2 - E_W/2, -\delta_s/2 + E_W/2]$ and $[\delta_s/2 - E_W/2, \delta_s/2 + E_W/2]$. The two different experimental schemes used in the main text to explore the energy distribution are summarized in the following table:

	Description	Approx. $\varepsilon_k/\hbar$
Scheme I (Fig. 4.29)	1) Single atomic cloud 2) AC Stark shift	$[-\tilde{E}_W/2, \tilde{E}_W/2]$
Scheme II (Figs. 4.30, 4.31)	1) Two atomic clouds 2) AC Stark shift to cloud 1	Cloud 1: $[-\delta_s/2 - E_W/2, -\delta_s/2 + E_W/2]$ Cloud 2: $[+\delta_s/2 - E_W/2, +\delta_s/2 + E_W/2]$

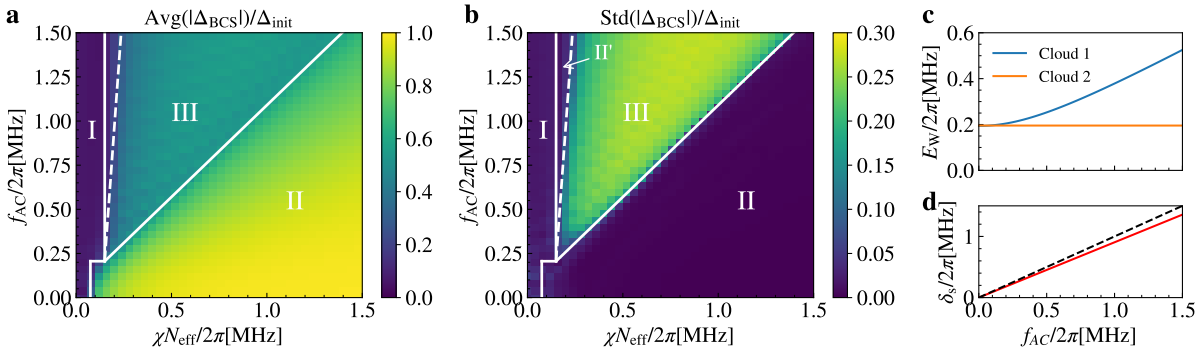

Figure 4.37: **Experimental control of dynamical phases.** **a** and **b**, Dynamical phase diagram for the experiment with two atomic ensembles, in terms of averaged spin-exchange interaction strength $\chi N_{\rm eff}$ and peak AC Stark shift $f_{\rm AC}$. The white lines show the predicted dynamical phase boundaries to guide the eye. The white dashed line marks a small region of phase II' due to the imbalance of $E_{\rm W}$ for the two atomic ensembles. **c**, $E_{\rm W}$ as a function of peak AC Stark shift $f_{\rm AC}$, with AC Stark shift applying to atomic cloud 1. **d**, $\delta_{\rm s}$ as a function of peak AC Stark shift $f_{\rm AC}$ (red line). The dashed line marks the place where $\delta_{\rm s} = f_{\rm AC}$.

The first scheme is used to probe the phase I to phase II transition. We use a single atomic ensemble and apply an AC Stark shift beam with a gradient to approximately engineer $\varepsilon_k/\hbar$ from a uniform distribution $[-\tilde{E}_{\rm W}/2, \tilde{E}_{\rm W}/2]$, as discussed in the Methods. As shown in Fig. 4.29**a**, the distribution of atomic frequencies is not exactly uniform, so we calculate the variance of the frequency distribution experimentally. Theoretically we assign a spread $\tilde{E}_{\rm W}$ such that the uniform distibution over $[-\tilde{E}_{\rm W}/2, \tilde{E}_{\rm W}/2]$ matches the measured experimental variance. We use this scheme to probe the dynamical phase diagram at $\delta_{\rm s} = 0$ (see Fig. 1**c** in the main text).

It is worth mentioning that the uniform distribution $[-\tilde{E}_{\rm W}/2, \tilde{E}_{\rm W}/2]$ can be interpreted in two different ways: 1) $\delta_{\rm s} = 0$ and $E_{\rm W} = \tilde{E}_{\rm W}$; 2) $\delta_{\rm s} = E_{\rm W} = \tilde{E}_{\rm W}/2$. Here we prefer the first interpretation $\delta_{\rm s} = 0$ because in this scheme we only have a single control parameter (the strength of AC Stark shift beam). Additionally, the line $\delta_{\rm s} = E_{\rm W}$ in the dynamical phase diagram has an implication that a small perturbation of $\delta_{\rm s}$ can generate a gap in atomic frequency, which is prohibited under this mapping between experimental controls and the model parameters.

In the second scheme that probes transitions into phase III, we use two atomic ensembles and apply an AC Stark shift beam (peak AC Stark shift $f_{\rm AC}$) to the first ensemble to generate a

frequency splitting δ_s between the two ensembles. In contrast to the first scheme, as discussed in the Methods, here we instead use the differential lattice light shifts to engineer a frequency spread E_W for each ensemble. As shown in Fig. 4.30**a**, in this case we define δ_s as the mean frequency difference between the two ensembles, and E_W as the width of a uniform distribution generating the same variance.

It is worth mentioning that the Gaussian profile of the AC Stark shift beam leads to an increase in E_W for the first atomic ensemble, as well as a reduction of the expected splitting of the two ensembles $\delta_s < f_{AC}$, as shown in Fig. 4.37**c** and **d**. Using experimental parameters, we get the dynamical phase diagram as depicted in Fig. 4.37**a** and **b**. The imbalance of E_W for the two atomic ensembles can lead to a small region of phase II' marked by the white dashed line. This occurs because the spin-exchange interaction is able to lock the ensemble with smaller E_W, while the ensemble with larger E_W remains unlocked, which leads to $|\Delta_{BCS}|$ approaching a small but nonzero constant value. In the experiment, due to other dissipative processes and reduced signal-to-noise ratio for small χN, we do not observe a difference between phase I and phase II'. This is the cause of a small discrepancy between theory and experiment in Fig. 4**b** in the main text in identifying the position of the phase transition.

4.5.13 Supplemental Materials: Short-time signatures of dynamical phases

Here we discuss the properties of the dynamical phases using short-time observables, since dissipative processes and noise in the experiment lead to difficulties in measuring long-time observables. In the following, we show that phase I can be characterized by the fast decay of $|\Delta_{BCS}|$, phase II can be characterized by Higgs oscillations. We further show that the phase II to phase III transition can be captured by the dip in the short-time oscillation frequency of $|\Delta_{BCS}|$. Finally, we provide an explanation of the frequency dip using an analytical solution of the two-spin BCS model.

Phase I: fast decay

In phase I, the single-particle energy term $\sum_k \varepsilon_k \hat{S}_k^z$ dominates over the spin-exchange inter-

action. To leading order, one can calculate $|\Delta_{\mathrm{BCS}}|$ in the homogeneous model by dropping the interaction term, which gives

$$\begin{aligned}\frac{|\Delta_{\mathrm{BCS}}|}{\chi N} &\approx \frac{1}{2N}\left|\sum_k e^{-i\varepsilon_k t/\hbar}\right| = \frac{1}{2}\left|\frac{1}{2E_{\mathrm{W}}}\int_{-\delta_{\mathrm{s}}/2-E_{\mathrm{W}}/2}^{-\delta_{\mathrm{s}}/2+E_{\mathrm{W}}/2} e^{-ixt}dx + \frac{1}{2E_{\mathrm{W}}}\int_{\delta_{\mathrm{s}}/2-E_{\mathrm{W}}/2}^{\delta_{\mathrm{s}}/2+E_{\mathrm{W}}/2} e^{-ixt}dx\right| \\ &= \frac{1}{2}\left|\cos\left(\frac{\delta_{\mathrm{s}}}{2}\right)\right| \cdot \left|\frac{\sin(E_{\mathrm{W}}t/2)}{E_{\mathrm{W}}t/2}\right|.\end{aligned} \tag{4.157}$$

The decay profile of $|\Delta_{\mathrm{BCS}}|$ is set by a sinc function with a $1/e$ coherence time t satisfying $E_{\mathrm{W}}t/2\pi \approx 0.7$. For the inhomogeneous model a similar fast decay time scale of the order of $E_{\mathrm{W}}t/2\pi \sim 1$ can be derived. As shown in Fig. 2**b** in the main text, we observe fast decay of $|\Delta_{\mathrm{BCS}}|$ within 1 μs in phase I. The decay time scale for the other dynamical phases can be more than 10 times longer.

Phase II: Higgs oscillation

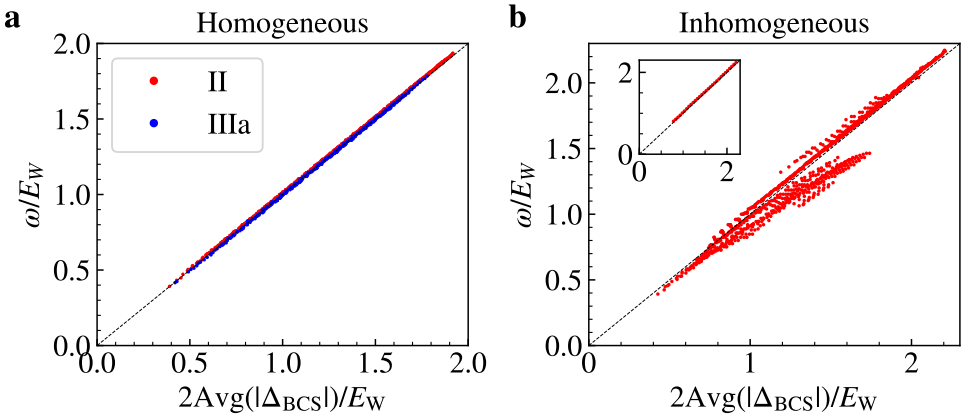

Figure 4.38: **Relation between oscillation frequency and averaged order parameter in Higgs oscillations.** **a**, Homogeneous model where each point is a choice of $(\chi N, \delta_{\mathrm{s}})$ in phase II (red) and phase IIIa (blue). The dashed line represents $\omega = 2\mathrm{Avg}(|\Delta_{\mathrm{BCS}}|)$. **b**, Inhomogeneous model where each point is a choice of $(\chi N_{\mathrm{eff}}, \delta_{\mathrm{s}})$ in phase II. The inset shows the points with $\delta_{\mathrm{s}} = 0$.

Higgs oscillation, generated by collective excitation of the Higgs mode in BCS superconductor, is characterized by the oscillation of $|\Delta_{\mathrm{BCS}}|$ at frequency $\omega = 2\mathrm{Avg}(|\Delta_{\mathrm{BCS}}|)$ [300]. For the homogeneous model (see Fig. 4.38**a**), we numerically confirmed this relation for all the points in phase II and phase IIIa. For the inhomogeneous model (see Fig. 4.38**b**), this relation is approximately satisfied in phase II. In experiment, we observe hints of Higgs oscillation (see Fig. 4.29), which can be ideally described by the inhomogeneous model with $\delta_{\mathrm{s}} = 0$ (see the inset in Fig. 4.38**b**).

Transition to phase III: frequency dip

In the main text, we discuss a way to understand the phase II to phase III transition by visualising the two atomic ensembles as two large spins. For the inhomogeneous model, phase II exists in the small $\delta_{\rm s}$ regime, where the two spins lock to each other and form a single large spin through spin-exchange interactions. In this case the many-body gap protection leads to the damped oscillations observed in phase II. Increasing $\delta_{\rm s}$ in phase II leads to the reduction of the many-body gap, and hence to a decrease of the corresponding oscillation frequency. Phase III exists in the large $\delta_{\rm s}$ regime, where the spin locking occurs separately in each ensemble, and the two large spin are instead precessing around each other, with a rate set by the splitting $\delta_{\rm s}$ and the spin-exchange interaction. Increasing $\delta_{\rm s}$ in phase III leads to a speed up of the oscillation frequency. Therefore one expects the existence of a frequency dip separating between phase II and phase III. Indeed as shown in Fig. 4.39**c** and **d**, we find good agreement between the frequency dip and the corresponding dynamical critical point. For small $\delta_{\rm s}$, the oscillation frequency approaches the Higgs oscillation frequency discussed in the previous subsection. For large $\delta_{\rm s}$, the oscillation frequency approaches $\delta_{\rm s}$. The reduction of oscillation frequency compared to $\delta_{\rm s}$ indicates many-body effects in phase III. It's worth to mention that in contrast to the inhomogeneous model, the frequency dip indicates the phase IIIa to phase IIIb transition for the homogeneous model.

Frequency dip in the two-spin BCS model

Here we use the analytical mean field solution of the BCS Hamiltonian with two large spins ($S = N/4$ for each spin) to understand the frequency dip discussed above. In this case, the Hamiltonian simplifies to

$$\hat{H}/\hbar = \chi \hat{S}^+ \hat{S}^- + \frac{\delta_{\rm s}}{2}\hat{S}_1^z - \frac{\delta_{\rm s}}{2}\hat{S}_2^z, \tag{4.158}$$

where $\hat{S}^\pm = \hat{S}_1^\pm + \hat{S}_2^\pm$. The mean field equations of motion for the Hamiltonian above can then be written as

$$\begin{aligned}
&\frac{d}{dt}S_1^x = 2\chi S^y S_1^z - \frac{\delta_{\rm s}}{2}S_1^y, \quad \frac{d}{dt}S_1^y = -2\chi S^x S_1^z + \frac{\delta_{\rm s}}{2}S_1^x, \quad \frac{d}{dt}S_1^z = -2\chi(S_2^y S_1^x - S_2^x S_1^y),\\
&\frac{d}{dt}S_2^x = 2\chi S^y S_2^z + \frac{\delta_{\rm s}}{2}S_2^y, \quad \frac{d}{dt}S_2^y = -2\chi S^x S_2^z - \frac{\delta_{\rm s}}{2}S_2^x, \quad \frac{d}{dt}S_2^z = -2\chi(S_1^y S_2^x - S_1^x S_2^y).
\end{aligned} \tag{4.159}$$

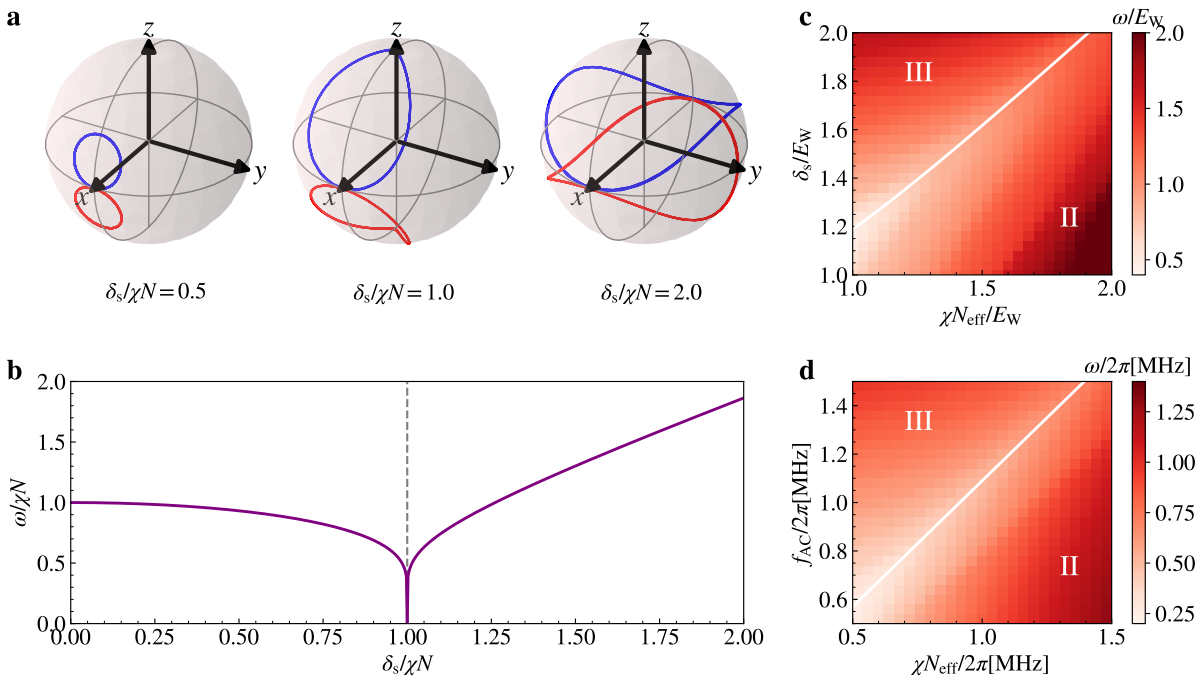

Figure 4.39: **Frequency dip as a signature of the phase II to phase III transition.** **a**, Mean field trajectories of the two large spin model evolving under Eq. (4.158). From left to right, Bloch spheres display trajectories with $\delta_s/(\chi N) = 0.5, 1$, and 2 respectively. **b**, Oscillation frequency of $|\Delta_{BCS}|$ in the two-spin BCS model Eq. (4.158) as a function of $\delta_s/\chi N$. The frequency dip at $\delta_s/\chi N = 1$ marks the dynamical phase transition point. **c**, Short-time frequency ω of the dynamics under inhomogneous atom-light coupling (see Eq. (3) in the Methods). The white line marks the phase II to phase III transition, the same boundary as shown in Extended Data Fig. 2 from the Methods. **d**, Short-time frequency ω of the dynamics using experimental control parameters. The white line marks the phase II to phase III transition and represents the same boundary as in Fig. 4.37. The frequency dips match the dynamical critical points for both cases.

The spin components without the hat represent the expectation value of the corresponding spin operators.

In the following, we assume an initial state satisfying $S_1^x = S_2^x = N/4$, $S_1^y = S_2^y = S_1^z = S_2^z = 0$. The conserved quantities of the two-spin BCS model are the total magnetisation

$$S^z = S_1^z + S_2^z = 0, \tag{4.160}$$

the total energy

$$E/\hbar = \chi S^+ S^- + \frac{\delta_s}{2} S_1^z - \frac{\delta_s}{2} S_2^z = \chi \left(\frac{N}{2}\right)^2, \tag{4.161}$$

as well as the spin length of each of the large spins, $(S_1^x)^2 + (S_1^y)^2 + (S_1^z)^2 = (N/4)^2$, $(S_2^x)^2 + (S_2^y)^2 + (S_2^z)^2 = (N/4)^2$. Using these conserved quantities, one can derive from the mean field equations in Eq. (4.159) an equation of motion for the BCS order parameter, $\Delta_{\rm BCS} = \chi S^-$. To simplify the notation, we define $\Delta \equiv |\Delta_{\rm BCS}|/\chi N$, i.e. $\Delta^2 = S^+ S^-/N^2$. From Eq. (4.160) and Eq. (4.161), we obtain

$$\frac{d}{dt}\Delta^2 = -\frac{\delta_s}{\chi N^2}\frac{d}{dt} S_1^z = \frac{2\delta_s}{N^2}(S_2^y S_1^x - S_2^x S_1^y), \tag{4.162}$$

which leads to

$$\begin{aligned} \frac{d^2}{dt^2}\Delta^2 &= \frac{2\delta_s}{N^2}\left(S_1^x \frac{d}{dt} S_2^y + S_2^y \frac{d}{dt} S_1^x - S_1^y \frac{d}{dt} S_2^x - S_2^x \frac{d}{dt} S_1^y\right) \\ &= 4\delta_s \chi \Delta^2 S_1^z - \frac{2\delta_s^2}{N^2}(S_1^x S_2^x + S_1^y S_2^y). \end{aligned} \tag{4.163}$$

From the above conserved quantities, we can create the equivalent expressions $\delta_s S_1^z = -\chi N^2(\Delta^2 - 1/4)$, $2(S_1^x S_2^x + S_1^y S_2^y) = N^2\Delta^2 - 2 \times (N/4)^2 + 2(S_1^z)^2$. Plugging these into the equation of motion gives

$$\frac{d^2}{dt^2}\Delta^2 = -6(\chi N)^2(\Delta^2)^2 + \Big(2(\chi N)^2 - \delta_s^2\Big)\Delta^2 + \frac{\delta_s^2 - (\chi N)^2}{8}. \tag{4.164}$$

The equation above can be further simplified to

$$\frac{1}{2}\left(\frac{d}{dt}\Delta\right)^2 + V(\Delta) = 0, \tag{4.165}$$

where

$$V(\Delta) = \frac{1}{2}(\chi N)^2\left(\Delta^2 - \frac{1}{4}\right)\left(\Delta^2 - \frac{1 - (\delta_s/\chi N)^2}{4}\right), \tag{4.166}$$

with an initial condition $\Delta = 1/2$. Eq. (4.165) can be understood as a classical particle with position Δ oscillating in the potential $V(\Delta)$. For $\delta_s < \chi N$, we find Δ oscillating between $\Delta_{\max} = 1/2$ and $\Delta_{\min} = \sqrt{1-(\delta_s/\chi N)^2}/2$. This is equivalent to phase II in the cases of many spins with inhomogeneous atom-light couplings, because all the oscillations damp in the large χN limit. For $\delta_s > \chi N$, we find Δ oscillating between $\Delta_{\max} = 1/2$ and $\Delta_{\min} = 0$, since the definition of Δ requires $\Delta \geq 0$. This is equivalent to phase III in the cases of many spins because the phase connects to single-particle oscillations in the large δ_s limit. Therefore, a dynamical phase transition occurs at $\delta_s/\chi N = 1$, which is equivalent to the phase II to phase III transition in the many-spin system.

The analytical solution of Eq. (4.165) can be written in terms of Jacobian elliptic funtions dn and cn:

$$\Delta(t) = \begin{cases} \frac{1}{2}\mathrm{dn}\left(\frac{1}{2}\chi N t \middle| (\delta_s/\chi N)^2\right) & \text{if } \delta_s < \chi N \\ \\ \frac{1}{2}\left|\mathrm{cn}\left(\frac{1}{2}\delta_s t \middle| (\chi N/\delta_s)^2\right)\right| & \text{if } \delta_s > \chi N \end{cases} . \tag{4.167}$$

The frequency of $\Delta(t)$ can be written in terms of the complete elliptic integral of the first kind $K(k^2)$:

$$\frac{\omega}{\chi N} = \begin{cases} \dfrac{\pi}{2K\left((\delta_s/\chi N)^2\right)} & \text{if } \delta_s < \chi N \\ \\ \dfrac{\delta_s}{\chi N}\dfrac{\pi}{2K\left((\chi N/\delta_s)^2\right)} & \text{if } \delta_s > \chi N \end{cases} . \tag{4.168}$$

The mean-field trajectories on the Bloch sphere are shown in Fig. 4.39**a**, and the oscillation frequency Eq. (4.168) is shown in Fig. 4.39**b**. The dynamical phase transition can also be understood from the mean field trajectories. For $\delta_s < \chi N$, the two large spins lock to each other and oscillate near the x axis of the Bloch sphere. For $\delta_s > \chi N$, the two large spins are unlocked and precess around the whole Bloch sphere. Near the dynamical critical point, the mean field trajectories are close to the north pole or south pole of the Bloch sphere, which leads to a slow down of the oscillations because they approach stable fixed points of the Hamiltonian.

4.5.14 Supplemental Materials: Axial motion

In this section, we elaborate on how to take into account axial motion present in the experimental system. Similar discussions can be found in Ref. [107]. We start with the one-dimensional Hamiltonian of our cavity QED system with two internal atomic levels ($|\uparrow\rangle$ and $|\downarrow\rangle$), given by

$$\begin{aligned}\hat{H} = &\sum_{\sigma=\{\uparrow,\downarrow\}} \int dx\ \hat{\psi}^\dagger_\sigma(x)\left[\frac{\hat{p}^2}{2M} + V_0\sin^2(k_L x)\right]\hat{\psi}_\sigma(x) + \int dx\ \hat{\psi}^\dagger_\uparrow(x)\left[\hbar\omega_0 + U_{ac}(x)\right]\hat{\psi}_\uparrow(x) \\ &+ \hbar g_c \int dx\ \cos(k_c x)\left[\hat{\psi}^\dagger_\uparrow(x)\hat{\psi}_\downarrow(x)\hat{a} + \hat{a}^\dagger\hat{\psi}^\dagger_\downarrow(x)\hat{\psi}_\uparrow(x)\right] + \hbar\omega_c\hat{a}^\dagger\hat{a},\end{aligned} \tag{4.169}$$

where $k_L = 2\pi/\lambda_L$ is the wavenumber of the lattice beams ($\lambda_L = 813$nm), k_c is the wavenumber of the cavity mode ($\lambda_c = 689$nm), ω_0 is the atomic transition frequency between $|\uparrow\rangle$ and $|\downarrow\rangle$ states, $U_{ac}(x)$ is the AC Stark shift applied to the atoms (including the differential light shift from the lattice beams and the transverse AC Stark shift beam), and ω_c is the frequency of cavity resonance.

Since the atoms are trapped in an optical lattice with lattice depth on the order of $10^3 E_R$, we can approximate each lattice site as an harmonic trap with axial trapping frequency $\hbar\omega_T = \sqrt{4V_0 E_R}$, where $E_R = \hbar^2 k_L^2/2M$ is the lattice recoil energy. We also ignore tunnelling processes between lattice sites. In this case, one can expand the atomic field operator in terms of lattice site index j and harmonic oscillator levels n:

$$\hat{\psi}_\sigma(x) = \sum_{jn} \hat{c}_{jn,\sigma}\phi_n(x - ja_L). \tag{4.170}$$

Here, $a_L = \lambda_L/2$ is the lattice spacing, and ϕ_n is the harmonic oscillator wave function for mode n, given by

$$\phi_n(x) = \frac{1}{\sqrt{2^n n!}}\left(\frac{M\omega_T}{\pi\hbar}\right)^{1/4} \mathrm{e}^{-M\omega_T x^2/2\hbar} H_n\left(\sqrt{\frac{M\omega_T}{\hbar}}x\right) \tag{4.171}$$

where $H_n(x)$ are the Hermite polynomials. Plugging this expansion into the Hamiltonian and transforming to the rotating frame of the atoms, we obtain

$$\hat{H}/\hbar = \sum_{jn\sigma} n\omega_T \hat{c}^\dagger_{jn,\sigma}\hat{c}_{jn,\sigma} + \sum_{jn}\varepsilon_{jn}\hat{c}^\dagger_{jn,\uparrow}\hat{c}_{jn,\uparrow} + g_c\sum_{jnm}\zeta^{nm}_j(\hat{c}^\dagger_{jn,\uparrow}\hat{c}_{jm,\downarrow}\hat{a} + \hat{a}^\dagger\hat{c}^\dagger_{jm,\downarrow}\hat{c}_{jn,\uparrow}) + \delta_c\hat{a}^\dagger\hat{a} \tag{4.172}$$

where $\delta_c = \omega_c - \omega_a$. For simplicity, we assume $U_{ac}(x)$ is either small or slowly varying in space and thus does not change the trap geometry. This term gives rise to an inhomogeneous transition

frequency $\varepsilon_{jn} = \int dx U_{ac}(x)[\phi_n(x - ja_L)]^2/\hbar$. We calculate ζ_j^{nm} in the following way:

$$\begin{aligned}\zeta_j^{nm} &= \int dx\ \cos(k_c x)\phi_n(x - ja_L)\phi_m(x - ja_L) = \int dx\ \cos(k_c x + k_c j a_L)\phi_n(x)\phi_m(x) \\ &= \cos(j\varphi)\int dx\ \cos(k_c x)\phi_n(x)\phi_m(x) - \sin(j\varphi)\int dx\ \sin(k_c x)\phi_n(x)\phi_m(x) \\ &= \cos(j\varphi)\,\mathrm{Re}\left[(i\eta)^s e^{-\eta^2/2}\sqrt{\frac{n_<!}{n_>!}}L^s_{n_<}(\eta^2)\right] - \sin(j\varphi)\,\mathrm{Im}\left[(i\eta)^s e^{-\eta^2/2}\sqrt{\frac{n_<!}{n_>!}}L^s_{n_<}(\eta^2)\right].\end{aligned} \tag{4.173}$$

where $\varphi = \pi k_L/k_c$, $s = |n - m|$, $n_< = \min(n, m)$, $n_> = \max(n, m)$, $L_n^\alpha(x)$ are the generalised Laguerre polynomials, and $\eta = k_c\sqrt{\hbar/2M\omega_T}$ is the Lamb-Dicke parameter. In our case $\omega_T/2\pi =$ 165 kHz, implying that $\eta = 0.17$. This places us in the Lamb-Dicke regime where ζ_j^{nm} is negligible for $|n - m| > 1$. It can be convenient to rewrite the Hamiltonian in terms of operators $\hat{S}^j_{n\sigma,m\sigma'} = \hat{c}^\dagger_{jn,\sigma}\hat{c}_{jm,\sigma'}$, resulting in the following form:

$$\hat{H}/\hbar = \sum_{jn\sigma} n\omega_T \hat{S}^j_{n\sigma,n\sigma} + \sum_{jn}\varepsilon_{jn}\hat{S}^j_{n\uparrow,n\uparrow} + g_c\sum_{jnm}\zeta_j^{nm}(\hat{S}^j_{n\uparrow,m\downarrow}\hat{a} + \hat{a}^\dagger\hat{S}^j_{m\downarrow,n\uparrow}) + \delta_c\hat{a}^\dagger\hat{a}. \tag{4.174}$$

In addition to the Hamiltonian dynamics, we also consider dissipation processes such as cavity loss with a rate $\kappa/2\pi = 153$ kHz, as well as spontaneous emission with a rate $\gamma/2\pi = 7.5$ kHz. The full dynamics of this open system can be described by the following Lindblad master equation:

$$\frac{\mathrm{d}}{\mathrm{d}t}\hat{\rho} = -\frac{i}{\hbar}[\hat{H}, \hat{\rho}] + \left[\hat{L}_{\mathrm{cav}}\hat{\rho}\hat{L}^\dagger_{\mathrm{cav}} - \frac{1}{2}\{\hat{L}^\dagger_{\mathrm{cav}}\hat{L}_{\mathrm{cav}}, \hat{\rho}\}\right] + \sum_{jn}\left[\hat{L}_{j,n}\hat{\rho}\hat{L}^\dagger_{j,n} - \frac{1}{2}\{\hat{L}^\dagger_{j,n}\hat{L}_{j,n}, \hat{\rho}\}\right], \tag{4.175}$$

where the jump operator for cavity loss is given by $\hat{L}_{\mathrm{cav}} = \sqrt{\kappa}\hat{a}$, and the single-particle jump operators for spontaneous emission are given by $\hat{L}_{j,n} = \sqrt{\gamma}\hat{S}^j_{n\downarrow,n\uparrow}$. Here, we assume that spontaneous emission is in the Lamb-Dicke regime.

In the experiment, δ_c is the largest frequency scale ($\delta_c \gg g_c\sqrt{N}, \kappa$), so we can adiabatically eliminate the cavity photons [339] and obtain the following effective atom-only master equation:

$$\frac{\mathrm{d}}{\mathrm{d}t}\hat{\rho} = -\frac{i}{\hbar}[\hat{H}_{\mathrm{eff}}, \hat{\rho}] + \left[\hat{L}_{\mathrm{col}}\hat{\rho}\hat{L}^\dagger_{\mathrm{col}} - \frac{1}{2}\{\hat{L}^\dagger_{\mathrm{col}}\hat{L}_{\mathrm{col}}, \hat{\rho}\}\right] + \sum_{jn}\left[\hat{L}_{j,n}\hat{\rho}\hat{L}^\dagger_{j,n} - \frac{1}{2}\{\hat{L}^\dagger_{j,n}\hat{L}_{j,n}, \hat{\rho}\}\right]. \tag{4.176}$$

Here, the effective Hamiltonian is given by

$$\hat{H}_{\mathrm{eff}}/\hbar = \sum_{jn\sigma} n\omega_T\hat{S}^j_{n\sigma,n\sigma} + \sum_{jn}\varepsilon_{jn}\hat{S}^j_{n\uparrow,n\uparrow} + \chi\sum_{jnm}\sum_{kpq}\zeta_j^{nm}\zeta_k^{pq}\hat{S}^j_{n\uparrow,m\downarrow}\hat{S}^k_{p\downarrow,q\uparrow}, \tag{4.177}$$

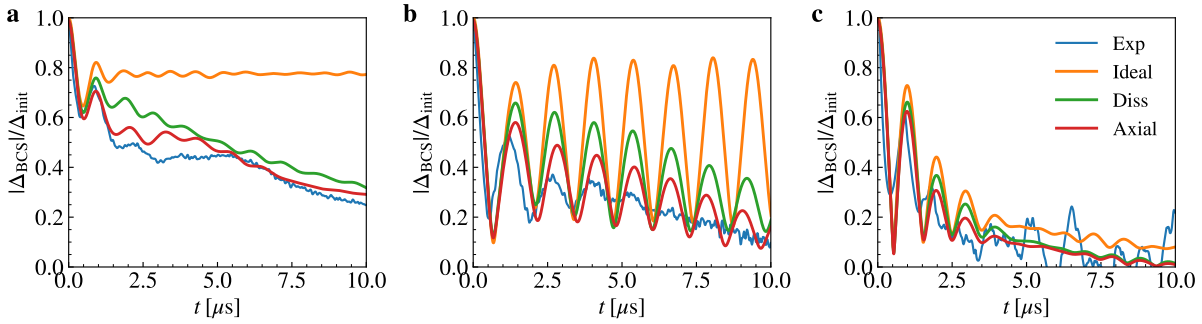

Figure 4.40: **Understanding experimental results with axial motion effects.** **a** Example phase II traces with $\chi N/2\pi = 1.29$MHz, $f_{AC}/2\pi = 1.1$MHz. **b** Example phase III traces with $\chi N/2\pi = 0.79$MHz, $f_{AC}/2\pi = 1.1$MHz. **c** Example phase I traces with $\chi N/2\pi = 0.15$MHz, $f_{AC}/2\pi = 1.1$MHz. The blue points are experimental data, the orange lines represent numerical simulations under ideal conditions (see Eq. (3) in the Methods), the green lines include dissipative processes on top of the ideal simulations, and the red lines consider both dissipative processes and axial motion effects.

and effective collective jump operator generating superradiant decay takes the form

$$\hat{L}_{\text{col}} = \sqrt{\Gamma} \sum_{jnm} \zeta_j^{nm} \hat{S}^j_{m\downarrow,n\uparrow}, \tag{4.178}$$

where $\chi = -g_c^2 \delta_c/(\delta_c^2 + \kappa^2/4)$ and $\Gamma = g_c^2 \kappa/(\delta_c^2 + \kappa^2/4)$. The equivalent superconducting order parameter takes the following form:

$$\Delta_{\text{BCS}} = \chi \sum_{kpq} \zeta_k^{pq} \langle \hat{S}^k_{p\downarrow,q\uparrow} \rangle. \tag{4.179}$$

One can recover the inhomogeneous model discussed in the previous section by removing the axial harmonic oscillator level labels.

Similarly, the Hamiltonian for initial state preparation takes the form

$$\hat{H}_{\text{drive}}/\hbar = \sum_{jn\sigma} n\omega_T \hat{S}^j_{n\sigma,n\sigma} + \frac{1}{2} \sum_{jnm} \zeta_j^{nm} (\Omega \hat{S}^j_{n\uparrow,m\downarrow} + \Omega^* \hat{S}^j_{m\downarrow,n\uparrow}). \tag{4.180}$$

In numerical simulations, we perform a mean-field approximation, which replaces the operators $\hat{S}^j_{p\sigma,q\sigma'}$ by their expectation values $\langle \hat{S}^j_{p\sigma,q\sigma'} \rangle$ in the Heisenberg equation of motion. We perform a random sampling of the axial harmonic oscillator mode n for each atom based on a thermal distribution of 15 μK, and we only include the modes n and $n\pm1$ into our calculation due to the Lamb-Dicke parameter. The atom number in our simulations is set to 2000; to match χN to experimental values,

we rescale χ accordingly. We also empirically take into account two additional dissipation processes to quantitatively capture the behavior of $|\Delta_{\mathrm{BCS}}|$ at longer time scales. The first is a single-particle decoherence between electronic states, described by the jump operators $\hat{L}^{\mathrm{el}}_{j,\sigma} = \sqrt{\gamma_{\mathrm{el}}} \sum_n \hat{S}^j_{n\sigma,n\sigma}$ with $\gamma_{\mathrm{el}}/2\pi < 1\mathrm{kHz}$ for Fig. 2 starting from $t = 0\mu\mathrm{s}$, and by $\gamma_{\mathrm{el}}/2\pi = 0.0036(f_{\mathrm{AC}}/2\pi) + 4\mathrm{kHz}$ for Fig. 3 and Fig. 4 in the main text. The second is a single-particle decoherence between motional states, described by the jump operators $\hat{L}^{\mathrm{mo}}_{j,n} = \sqrt{\gamma_{\mathrm{mo}}} \sum_\sigma \hat{S}^j_{n\sigma,n\sigma}$ with $\gamma_{\mathrm{mo}}/2\pi = 15\mathrm{kHz}$.

Some example traces including axial motion effects are depicted in Fig. 4.40. Generally speaking, accounting for these effects allows us to more accurately predict features present in the experimentally measured evolution of $|\Delta_{\mathrm{BCS}}|$, at the same time leaving the predicted dynamical phase boundaries unchanged. As shown in Fig. 4.40a, including axial motion effects in phase II traces allows us to capture the faster damping rate of the Higgs oscillations, as well as a slow oscillation in $|\Delta_{\mathrm{BCS}}|$ at the axial trapping frequency. Likewise, as shown in Fig. 4.40b, including axial motion effects in phase III traces allows us to capture the faster damping rate of the oscillations in $|\Delta_{\mathrm{BCS}}|$, although the observed damping rate is still faster than the rate predicted by theory. Finally, as shown in Fig. 4.40c, all the theory simulations of phase I dynamics are similar to the simulation under ideal conditions, indicating that axial motion does not play an significant role in this regime.

Chapter 5

Entanglement generation via photon-mediated interactions and measurements

5.1 Overview

Utilizing quantum entanglement in practical sensing problems is a milestone for quantum science. For example, the use of squeezed light in LIGO and Virgo [10, 11] has helped to boost the sensitivity of the gravitational waves. In the field of cold atom experiments, proof of principle experiments in optical clocks and atom interferometers has been engineered [14–16], nevertheless the goal of surpassing the sensitivity of state-of-the-art atomic sensors via quantum entanglement still needs to be accomplished. Due to the all-to-all connectivity of photon-mediated interactions, cavity QED systems are becoming one of the most promising platforms for engineering large-scale entangled states [7]. In this chapter, we focus on entanglement generation via photon-mediated interactions and measurements. Our efforts can be divided into two thrusts: 1) Protocols to generate homogeneous spin squeezed states useful for practical sensing applications in atom interferometers; 2) Optimal schemes for spin squeezing generation in a cavity QED setup.

5.2 Quantum enhanced cavity QED interferometer with partially delocalized atoms in lattices

This section is adapted from: **Anjun Chu**, Peiru He, James K. Thompson, Ana Maria Rey, *Quantum enhanced cavity QED interferometer with partially delocalized atoms in lattices*, Physical Review Letters 127, 210401 (2021).

5.2.1 Introduction

Ultracold atomic systems offer tremendous potential for quantum sensing applications including time keeping [20] and gravimetry [95], and thus provide opportunities for searching or constraining new physics in outstandingly precise and compact experiments. Despite the great advances in quantum sensing accomplished by cold atom experiments, one of the most important milestones that needs to be accomplished is to introduce quantum entanglement to enhance the sensitivity of real-world sensors beyond the so-called standard quantum limit (SQL) attainable with uncorrelated particles [10–13].

Important steps towards this goal have been accomplished such as the generation of up to 19 dB spin squeezing in cavities [14, 340–342]. Nevertheless, the use of entangled states in state-of-the-art inertial sensors has yet to be achieved. Limitations include the spatial mismatch between the lattice potential and the cavity mode which degrades the utility of spin squeezing after releasing the atomic cloud to free space [343]. Conventional free-falling experiments also lack spatial resolution and suffer from limited interrogation time [344]. Theoretical and experimental progresses to overcome these challenges have been reported in recent years although in different setups. For example, homogeneous atom-cavity couplings have been engineered by the use of commensurate lattices [340, 345, 346], ring cavities [347–350], or via time averaging as atoms free fall along the cavity axis [292]. In parallel, lattice-based interferometers enjoying compact spatial volumes [96, 270, 344, 351, 352] have reported capabilities to trap atoms near surfaces, and have achieved up to 20 s holding time using uncorrelated atoms [96].

Here we propose a quantum enhanced lattice-based protocol that uses the motional eigenstates of the combined lattice plus gravity potential, the so-called Wannier-Stark (WS) states, to overcome relevant limitations faced by current atomic sensors. The key idea is the use of delocalized WS states over a few lattice sites, which enables averaging out the inhomegeneities of atom-cavity couplings at specific lattice depths. This allows for the generation of uniform spin squeezed states via dynamical one-axis twisting (OAT) evolution [30, 74], or via homogeneous quantum nonde-

molition (QND) measurements [353, 354], even in incommensurate lattice-cavity geometries. The uniformly generated spin squeezing are not only useful for quantum enhanced measurements of gravity [346], but also ideal for fundamental tests of short-ranged forces [96, 344] which require loading small atomic clouds close to a surface or a source mass, such as dark energy [152], Casimir-Polder forces [355], and non-Newtonian corrections of gravity [356,357]. Furthermore, the ability to tune the inhomogeneities of couplings to a bosonic mode that mediates interactions or introduces disorder opens new possibilities in quantum many-body simulators [26].

Our work focuses on the dynamical generation of spin squeezing and the interferometric sequence to transfer the atoms to WS orbitals separated by several lattice sites to improve phase accumulation. Moreover, the interferometric phase can be mapped into a magnified rotation of the atomic internal state by reversing the squeezing protocol, which can be measured without the need of below-SQL detection resolution [358–360]. After accounting for primary sources of decoherence, we show that applying our scheme to arrays of 10^4 atoms, it should be possible to detect short-range forces acting at μm-scale distances, with an averaging time reduced by a factor of 10 compared to unentangled lattice-based interferometers [344,351].

5.2.2 Engineering homogeneous couplings

We consider an ensemble of N ultracold atoms, with mass M trapped in a vertical standing-wave optical cavity, as depicted in Fig. 5.1. The atoms are confined in the lowest band of a one dimensional (1D) optical lattice oriented along the vertical direction $\vec{z}$. The gravitational potential with local acceleration g generates a differential energy shift Mgz between two atoms separated by a vertical distance z. Two long-lived internal levels of the atoms, with energy splitting $\hbar\omega_0$, are used to encode a spin-1/2 degree of freedom with states labeled as $|\uparrow\rangle$ and $|\downarrow\rangle$. A single cavity mode with frequency ω_c and wavelength λ_c couples the $|\uparrow\rangle$ and $|\downarrow\rangle$ states to an optically excited state $|e\rangle$ of the atoms separated by a frequency ω_e from the $|\downarrow\rangle$ state. The atom-cavity coupling has a spatial profile $\mathcal{G}_{\uparrow,\downarrow}(z) = \mathcal{G}^0_{\uparrow,\downarrow}\cos(k_c z)$, where $k_c = 2\pi/\lambda_c$. The cavity mode is coherently pumped by an external field detuned from the cavity resonance by $\Delta_c = \omega_p - \omega_c$.

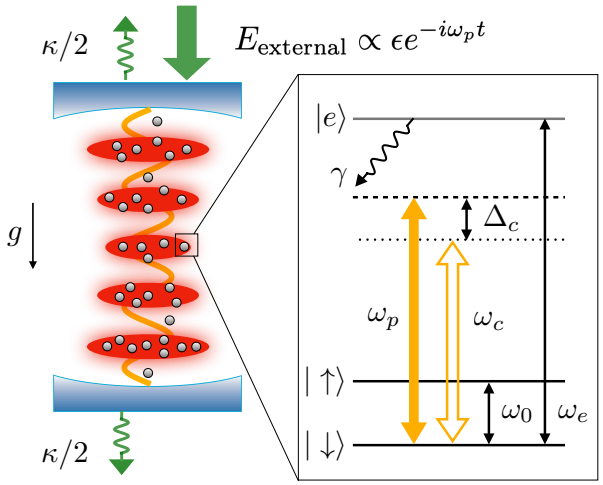

Figure 5.1: Protocol schematics: An ensemble of ultracold atoms are trapped in the lowest band of a lattice supported by a standing-wave optical cavity oriented along the direction of the gravitational acceleration g. The cavity decay rate is $\kappa/2$ on each side. The two long-lived internal levels of an atom with energy splitting $\hbar\omega_0$ act as a spin-1/2 degree of freedom labeled as $|\uparrow\rangle$ and $|\downarrow\rangle$. These two states are coupled through a single cavity mode to the excited state $|e\rangle$, with energy $\hbar\omega_e$ and spontaneous emission rate γ. The cavity mode is coherently pumped by an external light field with detuning $\Delta_c = \omega_p - \omega_c$ from the cavity resonance which generates a net injected field in the cavity with amplitude ϵ.

We are focusing on the system operating in the dispersive regime of atom-light interaction, where both the pump and cavity mode are far-detuned from the atomic resonances, i.e. $\Delta_{\uparrow,\downarrow} \gg \mathcal{G}^0_{\uparrow,\downarrow}\sqrt{\langle \hat{a}^\dagger \hat{a}\rangle}$, with $\Delta_\uparrow = \omega_p - \omega_e + \omega_0$ and $\Delta_\downarrow = \omega_p - \omega_e$. In this limit, the atomic excited state $|e\rangle$ can be adiabatically eliminated (see SOM), leading to the following Hamiltonian written in second quantized form in the rotating frame of the external optical pumping field,

$$\hat{H} = \sum_{\beta=\uparrow,\downarrow} \int dz \hat{\psi}^\dagger_\beta(z) \left[\frac{\hat{p}^2}{2M} + V_0 \sin^2(k_l z) + Mgz + \frac{\hbar |\mathcal{G}_\beta(z)|^2}{\Delta_\beta} \hat{a}^\dagger \hat{a} \right] \hat{\psi}_\beta(z) + \hat{H}_{\text{cav}} + \hat{H}_{\text{drive}}. \quad (5.1)$$

Here, V_0 is the lattice depth, $k_l = 2\pi/\lambda_l$ is the wave number of lattice beams that sets the atomic recoil energy $E_R = \hbar^2 k_l^2/2M$ and the lattice spacing $a_l = \lambda_l/2$, where λ_l is the wavelength of the lattice. The operator $\hat{a}$ is the annihilation field operator for cavity photons, and the operator $\hat{\psi}_\beta(z)$ annihilates an atom of spin β at position z. The cavity Hamiltonian is given by $\hat{H}_{\text{cav}}/\hbar = -\Delta_c \hat{a}^\dagger \hat{a} + \varepsilon \hat{a}^\dagger + \varepsilon^* \hat{a}$, where ε is the amplitude of the injected field. The drive Hamiltonian $\hat{H}_{\text{drive}}/\hbar = \int dz [\Omega \hat{\psi}^\dagger_\uparrow(z) \hat{\psi}_\downarrow(z) + \text{h.c.}] - \delta \hat{\psi}^\dagger_\uparrow(z) \hat{\psi}_\uparrow(z)$ describes a switchable external microwave drive, with Rabi frequency Ω, drive detuning δ that uniformly couples the spin-1/2 degree of freedom when applied.

We expand the atom field operators $\hat{\psi}_\beta(z)$ in terms of the Wannier-Stark (WS) orbitals: $\hat{\psi}_\beta(z) = \sum_n \hat{c}_{n\beta}\phi_n(z)$, where $\hat{c}_{n\beta}$ annihilates an atom of spin β in the WS state $|\phi_n\rangle$ centered at site n. In the tight-binding limit, the wave function of the WS state $|\phi_n\rangle$ takes the form $\phi_n(z) = \sum_m \mathcal{J}_{m-n}(2J_0/Mga_l)w(z-ma_l)$ [290], where $\mathcal{J}_n(x)$ is the Bessel function of the first kind, $J_0/\hbar$ is the nearest-neighbor tunneling rate, and $w(x)$ is the ground band Wannier function. If we assume the cavity-induced AC Stark shifts $\hbar|\mathcal{G}^0_{\uparrow,\downarrow}|^2\langle\hat{a}^\dagger\hat{a}\rangle/\Delta_{\uparrow,\downarrow}$ are smaller than Mga_l (see SOM), so transitions between WS orbitals are suppressed, the atom-cavity dynamics can be simplified into the following Hamiltonian,

$$\hat{H} = \hbar\sum_n \Big(-\delta + \eta_n\hat{a}^\dagger\hat{a}\Big)\hat{S}^z_n + H_{\text{cav}} + \hbar\sum_n \Omega\hat{S}^x_n. \tag{5.2}$$

Here, the spin operators are defined in terms of atomic creation and annihilation operators for $|\uparrow_n\rangle \equiv |\uparrow;\phi_n\rangle$ and $|\downarrow_n\rangle \equiv |\downarrow;\phi_n\rangle$ states, $\hat{S}^{x,y,z}_n = \sum_{\beta,\beta'}\hat{c}^\dagger_{n\beta}\sigma^{x,y,z}_{\beta\beta'}\hat{c}_{n\beta'}$, where $\sigma^{x,y,z}_{\beta\beta'}$ are the matrix elements of the corresponding Pauli matrices and $\beta,\beta' \in \{\uparrow,\downarrow\}$. It is also convenient to define the collective spin operators $\hat{S}^{x,y,z} = \sum_n \hat{S}^{x,y,z}_n$ for later discussions. The dispersive atom-light coupling $\eta_n = \eta^\uparrow_n - \eta^\downarrow_n$, with $\eta^{\uparrow,\downarrow}_n = \int dz|\mathcal{G}_{\uparrow,\downarrow}(z)\phi_n(z)|^2/\Delta_{\uparrow,\downarrow}$, can be evaluated analytically,

$$\eta_n = \eta\left[1 + \mathcal{C}\mathcal{J}_0\left(\frac{4J_0}{Mga_l}\sin(\varphi/2)\right)\cos(n\varphi)\right], \tag{5.3}$$

where $\eta = \frac{1}{2}(|\mathcal{G}^0_\uparrow|^2/\Delta_\uparrow - |\mathcal{G}^0_\downarrow|^2/\Delta_\downarrow)$ is the mean value of η_n over all possible n, $\varphi = 2\pi\lambda_l/\lambda_c$, and $\mathcal{C}$ is a constant of order one (see SOM). We also replace Δ_c by an effective cavity detuning $\tilde{\Delta}_c = \Delta_c - \sum_n N_n(\eta^\uparrow_n + \eta^\downarrow_n)/2$ in $\hat{H}_{\text{cav}}$, where N_n is the total atom number in $|\uparrow_n\rangle$ and $|\downarrow_n\rangle$ states.

The last step is to adiabatically eliminate the injected light field and intracavity fluctuations, possible in the limits $\tilde{\Delta}_c \gg \eta\alpha\sqrt{N}, \kappa$ (see SOM), where $\alpha = \varepsilon/(\tilde{\Delta}_c + i\kappa/2)$ is the steady-state value of the cavity field, and κ is the cavity intensity decay rate. With these reasonable approximations, the system can well described by an effective Hamiltonian involving only the spins,

$$\hat{H}_{\text{eff}}/\hbar = -\sum_n(\delta - \eta_n|\alpha|^2)\hat{S}^z_n + \sum_{nm}\chi_{nm}\hat{S}^z_n\hat{S}^z_m + \Omega\sum_n \hat{S}^x_n. \tag{5.4}$$

When the microwave drive is off, the Hamiltonian above is the so-called one-axis twisting (OAT) model, with $\chi_{nm} = \eta_n\eta_m|\alpha|^2\tilde{\Delta}_c/(\tilde{\Delta}^2_c + \kappa^2/4)$ the OAT interaction strength, which is an iconic

model for the generation of spin squeezed states [30, 74].

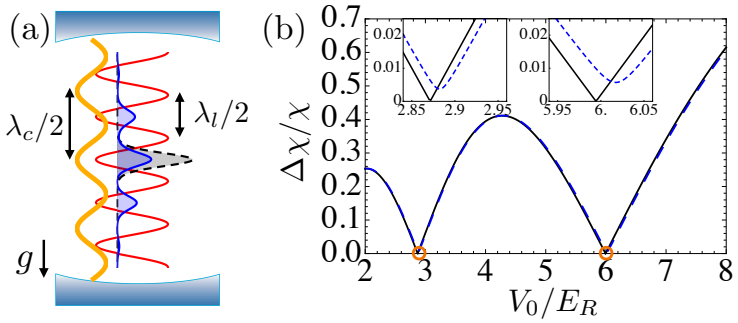

Figure 5.2: (a) Inhomogeneous atom-light couplings arise due to the incommensurate wavelengths of the lattice beams (red curve) and the cavity mode (yellow curve), when atoms are frozen in Wannier states (black dashed curve) for deep lattice limit. The inhomogeneities can be cancelled out in a relatively shallow lattice since Wannier-Stark states (blue curve) can extend over a few lattice sites. (b) Standard deviation of the OAT coupling strengths $\Delta\chi = (\sum_{nm}(\chi_{nm} - \chi)^2/N)^{1/2}$ as a function of lattice depth V_0/E_R assuming ^{87}Rb atoms trapped in a $\lambda_l = 532$ nm lattice. The black curve shows the magic lattice depths ($\Delta\chi = 0$) can be achieved around $6.0E_R$ or $2.9E_R$ under ideal conditions, indicated by the orange circles. The blue dashed curve shows the imperfect cancellation of inhomogeneities in χ_{nm} with radial temperature $T = 1\mu$K and radial trapping frequency $\omega_r/2\pi = 1$kHz. The two insets show the zoomed $\Delta\chi$ near the magic lattice depths.

One limitation of spin squeezing generation protocols with frozen atoms in deep lattices ($J_0 \approx 0$) is the inhomogeneous couplings arising from incommensurate lattice and cavity mode wavelengths ($\varphi \neq \pi j$ with j an integer). However, in a relatively shallow lattice ($V_0 < 10E_R$) where $J_0 \sim Mga_l$, the wave function of WS states can extend over a few adjacent lattice sites [see Fig. 5.2(a)] due to non-negligible nearest-neighbor tunnel couplings, instead of being localized in a single site. The lattice depth can thus be used as a control knob to vary the extension of the WS and for tuning the inhomogeneitiy of the spin coupling parameters [see Fig. 5.2(b)]. In particular, at the magic lattice condition,

$$\mathcal{J}_0\left(\frac{4J_0}{Mga_l}\sin(\varphi/2)\right) = 0, \tag{5.5}$$

we can completely average out the inhomogeneities and obtain uniform couplings in Eq. (5.4) with $\eta_n = \eta$ and $\chi_{nm} = \chi = \eta^2|\alpha|^2\tilde{\Delta}_c/(\tilde{\Delta}_c^2 + \kappa^2/4)$. This technique is relevant not only for the generation of homogeneous spin squeezing but also for quantum simulation of long-range spin models with tunable inhomgeneity [26]. In practice, the thermal distribution of atoms in the radial direction

and the undesirable couplings between axial and radial confinement of the Gaussian beam profile can lead to an imperfect cancellation [see the insets in Fig. 5.2(b)], which can be highly suppressed by operating at low radial temperature or large radial confinement (see SOM). For ^{87}Rb atoms with $\lambda_c = 780$ nm (D_2 transition) and $\lambda_l = 532$ nm, the magic lattice depths are around $6.0E_R$ and $2.9E_R$ [see Fig. 5.2(b)]. For ^{171}Yb atoms with $\lambda_c = 556$ nm ($^1S_0 \rightarrow {}^3P_1$ transition) and $\lambda_l = 413$ nm [361], the magic lattice depth is around $3.2E_R$. The negligible scattering length of ^{171}Yb atoms [362] and their insensitivity to magnetic and electric fields make them ideal for inertial sensing. For the cases above, at the smallest magic lattice depth the WS state spreads within three lattice sites.

5.2.3 Quantum enhanced interferometric protocol

Since the energy splitting of WS states is proportional to the gravitational acceleration g, our system can be directly used for quantum enhanced gravimetry. The protocol consists of the following steps, as illustrated in Fig. 5.3. After the application of a short $\pi/2$ pulse with the microwave drive in an empty cavity [see Eq. (5.4) with $\alpha = 0$] that prepares a spin coherent state along x direction, the system is let to evolve for a time t_0 under the OAT interaction mediated by the optical cavity [see Eq. (5.4) with $\Omega = 0$ using an additional spin echo π pulse at $t_0/2$ to cancel additional $\hat{S}^z$ rotations], which results in the generation of a uniform spin squeezed state [see Fig. 5.3(a)]. The reduced noise quadrature of the state makes it highly sensitive to small rotations about the y axis, $\tilde{R}_y^{\phi} = \mathrm{e}^{-i\phi\hat{S}^y}$.

To perform precise measurement of a phase ϕ arising from gravitational energy shifts, Raman sideband transitions to WS states separated by a few lattice sites are used. Explicitly, the rotation about the y axis is implemented as $\tilde{R}_y^{\phi} = \tilde{R}_x^{-\pi/2}\bar{R}_z^{\phi}\tilde{R}_x^{\pi/2}$, with $\bar{R}_z^{\phi} = (\mathcal{R}^{\dagger})^{m_R}R_z^{\phi}\mathcal{R}^{m_R}$, where m_R is the number of imposed compound pulses, and $\mathcal{R} = \tilde{R}_y^{\pi}R_y^{\pi}$ is a compound pulse to separate the atoms in $|\uparrow\rangle$ and $|\downarrow\rangle$ states by $2r$ lattice sites: $|\uparrow_n\rangle \rightarrow |\uparrow_{n+r}\rangle$ and $|\downarrow_n\rangle \rightarrow |\downarrow_{n-r}\rangle$. It consists of a π Raman pulse R_y^{π} with appropriate momentum kick and frequency ω_{R} to perform the desired r-site transfer in the lattice (apply from side to ensure homogeneity for all atoms), followed by a π pulse

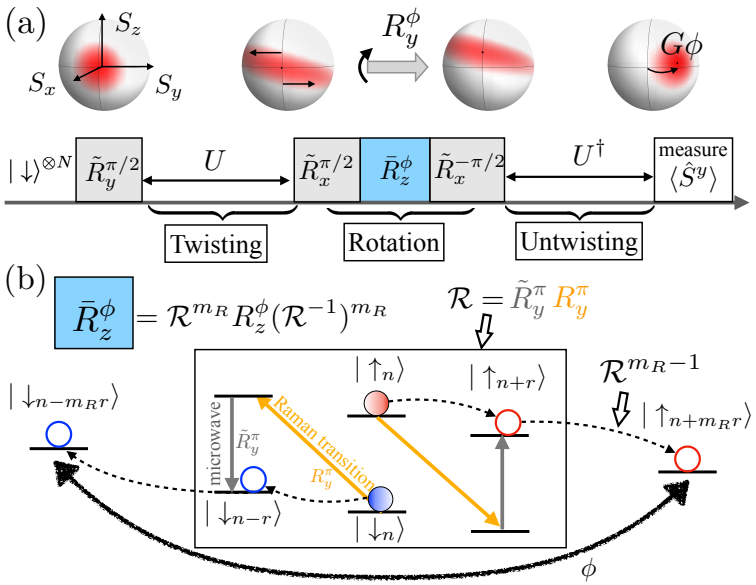

Figure 5.3: Schematic of the quantum-enhanced gravimetry using Wannier-Stark (WS) states. (a) After the preparation of a coherent spin state along x direction in the carrier transition, we apply the twisting Hamiltonian for a time t_0 as $U = \exp\left(-i\chi \hat{S}^z \hat{S}^z t_0\right)$, and the system becomes a squeezed state sensitive to small rotations about the y axis ($\tilde{R}_y^\phi$). By applying the untwisting sequence $U^\dagger$ for the same amount of time t_0, the quantum noise returns to the SQL level and the small rotation angle ϕ is amplified into a larger angle $G\phi$ around z axis, which can be detected by measuring $\langle\hat{S}^y\rangle$. (b) The phase accumulation due to gravitational energy difference is achieved through a compound pulse sequence that separates the atoms in the corresponding WS states by $2m_R r$ lattice sites. A single compound pulse $\mathcal{R}$, as shown in the box, is a combination of a microwave pulse in the carrier transition and a Raman pulse for the r-th WS sidebands, which generates spin-dependent spatial transfer of the atoms (indicated by red/blue circles) from $|\uparrow_n\rangle/|\downarrow_n\rangle$ to $|\uparrow_{n+r}\rangle/|\downarrow_{n-r}\rangle$.

on the carrier transition to flip back the spin using a microwave drive ($\tilde{R}_y^{\pi}$) with frequency ω_{MW} [see Fig. 5.3(b)]. Such type of compound pulse sequences have been already successfully demonstrated in ^{87}Rb atoms [363]. The R_z^{ϕ} operator describes the free evolution for a time τ of the atoms separated by $2m_R r$ lattice sites when they accumulate a phase $\phi = (\omega_{\mathrm{R}} - \omega_{\mathrm{MW}} - Mga_l r/\hbar) \times 2m_R\tau$. Note that one can apply an additional microwave pulse $\tilde{R}_y^{\pi}$ at $\tau/2$ to remove the undesirable hyperfine energy splitting $\hbar\omega_0$.

Finally, one can perform a time reversal of OAT dynamics by changing the frequency of pump laser such that $\tilde{\Delta}_c \to -\tilde{\Delta}_c$, followed by a measurement of $\langle \hat{S}^y \rangle$ [358]. Under this untwisting sequence, the accumulated phase ϕ is amplified by a factor of $G = (\partial_\phi \langle \hat{S}^y \rangle / S)_{\phi\to 0}$, and the quantum noise for phase measurement $\sigma_p = (\Delta S^y/S)_{\phi\to 0}$ returns to the SQL level, $(\sigma_p)_{\mathrm{SQL}} = 1/\sqrt{N}$, which leads to a phase sensitivity $\Delta\phi = \sigma_p/G$ achievable with detection resolution at the atom shot noise level. So we estimate a sensitivity of gravimetry by $\Delta g/g = \xi/(\phi_g\sqrt{N}) \times \sqrt{\tau/T}$, where $\phi_g = 2Mga_l r m_R \tau/\hbar$, $\xi^{-2} = 1/[N(\Delta\phi)^2]$ is the metrological gain over the SQL, and T is the averaging time. The optimal sensitivity approaches the Heisenberg limit $\Delta g/g \propto 1/N$ under pure Hamiltonian dynamics [see the red curve in Fig. 5.4].

Our protocol could be also ideal for sensing weak short-range forces generated by an object placed close to the atoms [152,355–357], which introduces new possibilities in exploring new physics beyond the Standard Model. Such forces will generate an additional potential $\mathcal{U}(z)$ that will mainly modify the phase accumulated by an atom in the WS state centered at site n to $\tilde{\phi}_n = \phi + (\mathcal{U}_{n+m_R r} - \mathcal{U}_{n-m_R r})\tau/\hbar$, where $\mathcal{U}_n = \int dz\, \mathcal{U}(z)|\phi_n(z)|^2$. Given the dependence of the phase on initial WS states, which will dephase the atomic sample if spreading over multiple WS states, the use of atomic clouds with small spatial extension to reduce the number of occupied WS states can be crucial. For these situations, since the inhomogeneities in atom-light couplings do not average out in a single realization, one needs to account for important systematic errors in the amplification factor G, in contrast to the subdominant suppression of G when the atomic array is fully spread across the lattice (see SOM). Therefore, the magic lattice condition can lead to significant improvements if the atoms are restricted to local regions of the lattice.

5.2.4 Experimental considerations

Experimental imperfections such as cavity loss and spontaneous emission of the excited state during the spin squeezing generation and other dephasing mechanisms during the interrogation will degrade the ideal sensitivity in practical implementations as we now discuss. Cavity loss induces phase fluctuations of the collective spin with collective dephasing rate $\Gamma_z = \chi\kappa/\tilde{\Delta}_c$, which lead an increase in the variance of $\hat{S}^y$. Spontaneous emission from the excited state $|e\rangle$, at a rate γ, generates off-resonant photon scattering processes with a total rate $\Gamma \propto \gamma|\mathcal{G}^0_{\uparrow,\downarrow}|^2|\alpha|^2/\Delta^2_{\uparrow,\downarrow}$, including single-particle spin flips and dephasing. Here we focus on the case with balanced spin flip rates, $\gamma_r = P_f\Gamma$ with P_f the spin flip probability, which can be achieved by choosing appropriate energy levels and detunings, so the spontaneous emission generates no biases on the accumulated phase ϕ. The noise induced by the γ_r terms is amplified during the untwisting protocol, making them the dominant single-particle noise source for measuring $\langle\hat{S}^y\rangle$. The combination of cavity loss and spontaneous emission limits the metrological gain ξ^{-2} to (see SOM),

$$\xi^2 \approx \frac{1 + 2N\Gamma_z t_0}{(N\chi t_0)^2} + \frac{8}{3}\gamma_r t_0, \tag{5.6}$$

leading to an optimal value $\xi^{-2}_{\text{opt}} \propto \sqrt{NC'}$, where $C' = \chi^2/\Gamma_z\Gamma$ is related to the single-atom cooperativity (see SOM). This result translates into the sensitivity for gravimetry as $\Delta g/g \propto N^{-3/4}$ [see the blue curve in Fig. 5.4]. Higher sensitivity can be reached by choosing specific schemes (e.g. cycling transitions) to suppress spin flip processes [see the purple curve in Fig. 5.4].

Technical noise in experiment such as mechanical vibrations and local oscillator dephasing, as well as single particle decoherence due to interatomic interactions also impose a constraint on the interrogation time. In particular, single-particle decoherence imposes even more severe restrictions when operating with entangled states given their fragility to it (see SOM). For ^{87}Rb assuming a 5.32 μm atom separation achieved by $r = 5$, $m_R = 2$ in a $\lambda_l = 532$ nm lattice, phase accumulation time $\tau = 1$ s, $C' = 2$, and spin flip probability $P_f = 1/2$, one can achieve $\Delta g/g \sim 6 \times 10^{-9}/\sqrt{\text{Hz}}$ with about 5×10^4 atoms, which is 20 dB enhancement beyond SQL. If we compare this sensitivity with SQL for $\tau = 10$ s, still a 10 dB enhancement is possible, meaning that even after accounting

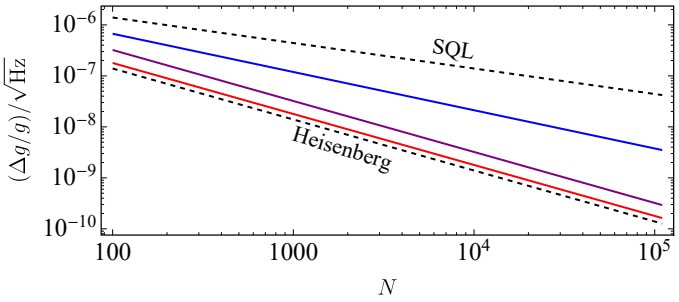

Figure 5.4: Interferometer sensitivity $\Delta g/g$ as a function of atom number N, assuming 5.32 μm separation for ^{87}Rb atoms via compound pulse sequence, 1 s phase accumulation time, and $C' = 2$. The red curve indicates the ideal implementation without decoherence, while the blue curve and purple curve take account the effect of cavity loss and spontaneous emission with spin flip probability $P_f = 1/2$ and $P_f = 0$ respectively.

for the fragility of the spin squeezed states, our protocol can not only reduce the required averaging time by a factor of 10, but also increase the measurement bandwidth of time-varying signal by a factor of 10, compared to unentangled lattice-based interferometers [344, 351].

5.2.5 Conclusion and outlook

We proposed a quantum enhanced interferometric protocol using Wannier-Stark states in standing-wave cavity QED system, which allows for homogeneous spin squeezing generation and micrometric spatial resolution for gravimetry and force sensing. The many-body entanglement in our scheme leads to an order of magnitude reduction of the required averaging time compared to unentangled lattice-based interferometers. Our work opens new possibilities for quantum enhanced interferometry in versatile compact atomic sensors, as well as novel Hamiltonian engineering in quantum many-body simulators.

5.2.6 Supplemental Materials: Cavity QED on Wannier-Stark states

In the main text, we consider an ensemble of three-level atoms trapped in a standing-wave cavity along the vertical direction. A 1D optical lattice with lattice depth V_0 and wave vector $k_l = 2\pi/\lambda_l$ along the cavity axis is used to confine the atoms. Along this direction gravity imposes an additional linear potential of the form Mgz. We assume that the spin-1/2 degree of freedom

($|\uparrow\rangle$, $|\downarrow\rangle$) is encoded in two long-lived internal states of the atoms with single particle energies $\{\hbar\omega_\uparrow, \hbar\omega_\downarrow\} \equiv \{\hbar\omega_0, 0\}$ respectively. They are coupled to an electronic excited state $|e\rangle$ (frequency ω_e) by a single cavity mode with coupling strength $\mathcal{G}_{\uparrow,\downarrow}(z) = \mathcal{G}^0_{\uparrow,\downarrow}\cos(k_c z)$. This cavity mode with resonant frequency ω_c is coherently pumped by an external field with intracavity intensity ε and frequency ω_p. We also include a homogeneous drive in the spin-1/2 degree of freedom with frequency ω_d and Rabi frequency Ω. The Hamiltonian of the system can be written as the following second quantized form,

$$\begin{aligned}\hat{H} = &\sum_{\tau=\uparrow,\downarrow,e}\int \mathrm{d}z\hat{\psi}^\dagger_\tau(z)\left[\frac{\hat{p}^2}{2M} + V_0\sin^2(k_l z) + Mgz + \hbar\omega_\tau\right]\hat{\psi}_\tau(z) + \int dz\Big[\hbar\mathcal{G}_\uparrow(z)\hat{a}\hat{\psi}^\dagger_e(z)\hat{\psi}_\uparrow(z)\\ &+ \hbar\mathcal{G}_\downarrow(z)\hat{a}\hat{\psi}^\dagger_e(z)\hat{\psi}_\downarrow(z) + \mathrm{h.c.}\Big] + \int dz\left[\frac{\hbar\Omega}{2}\hat{\psi}^\dagger_\uparrow(z)\hat{\psi}_\downarrow(z)\mathrm{e}^{-i\omega_d t} + \mathrm{h.c.}\right] + \hbar\omega_c\hat{a}^\dagger\hat{a}\\ &+ \hbar(\varepsilon\mathrm{e}^{-i\omega_p t}\hat{a}^\dagger + \varepsilon^*\mathrm{e}^{i\omega_p t}\hat{a}).\end{aligned} \tag{5.7}$$

It's convenient to transform the Hamiltonian into a frame rotating with the pump laser via the following unitary transformation,

$$\hat{U} = \exp\left\{-it\left[\int dz\Big((\omega_p+\omega_\downarrow)\hat{\psi}^\dagger_e(z)\hat{\psi}_e(z) + (\omega_\uparrow+\delta)\hat{\psi}^\dagger_\uparrow(z)\hat{\psi}_\uparrow(z) + \omega_\downarrow\hat{\psi}^\dagger_\downarrow(z)\hat{\psi}_\downarrow(z)\Big) + \omega_p\hat{a}^\dagger\hat{a}\right]\right\}, \tag{5.8}$$

where $\delta = \omega_d - \omega_0$ is the detuning of the drive to the spin-1/2 transition. After carrying out the unitary transformation described above, the Hamiltonian takes the following form,

$$\begin{aligned}\hat{H} \approx &-\int \mathrm{d}z(\hbar\Delta_\downarrow)\hat{\psi}^\dagger_e(z)\hat{\psi}_e(z) + \sum_{\sigma=\uparrow,\downarrow,e}\int \mathrm{d}z\hat{\psi}^\dagger_\sigma(z)\left[\frac{\hat{p}^2}{2M} + V_0\sin^2(k_l z) + Mgz\right]\hat{\psi}_\sigma(z)\\ &+ \int dz\left[\hbar\mathcal{G}_\uparrow(z)\hat{a}\hat{\psi}^\dagger_e(z)\hat{\psi}_\uparrow(z)\mathrm{e}^{-i(\omega_0+\delta)t} + \hbar\mathcal{G}_\downarrow(z)\hat{a}\hat{\psi}^\dagger_e(z)\hat{\psi}_\downarrow(z) + \mathrm{h.c.}\right]\\ &+ \int dz\left[\frac{\hbar\Omega}{2}\hat{\psi}^\dagger_\uparrow(z)\hat{\psi}_\downarrow(z) + \mathrm{h.c.}\right] - \int dz(\hbar\delta)\hat{\psi}^\dagger_\uparrow(z)\hat{\psi}_\uparrow(z) - \hbar\Delta_c\hat{a}^\dagger\hat{a} + \hbar(\varepsilon\hat{a}^\dagger + \varepsilon^*\hat{a}),\end{aligned} \tag{5.9}$$

where $\Delta_c = \omega_p - \omega_c$ is the cavity detuning, $\Delta_{\uparrow,\downarrow} = \omega_p - \omega_e + \omega_{\uparrow,\downarrow}$ are the detunings of the pump from the corresponding electronic excited state to ground transitions. We assume $\hbar\Delta_{\uparrow,\downarrow}$ are much larger than the motional energy of the atoms. Here we focus on the case that $\Delta_{\uparrow,\downarrow} \gg \mathcal{G}^0_{\uparrow,\downarrow}\sqrt{\langle\hat{a}^\dagger\hat{a}\rangle}$ and $\Delta_{\uparrow,\downarrow} \gg \gamma$, which means the excited state population and the decoherence induced by atomic spontaneous emission are negligible. In this limit we can adiabatically eliminate the atomic excited

state $|e\rangle$ by averaging out the largest frequency scale $\Delta_{\uparrow,\downarrow}$ and ω_0 in this system (see Ref. [364]). This leads to the following effective Hamiltonian acting in the ground state manifold [273, 365],

$$\begin{aligned}\hat{H} = &\sum_{\sigma=\uparrow,\downarrow}\int dz\hat{\psi}_\sigma^\dagger(z)\left[\frac{\hat{p}^2}{2M}+V_0\sin^2(k_l z)+Mgz+\frac{\hbar|\mathcal{G}_\sigma(z)|^2}{\Delta_\sigma}\hat{a}^\dagger\hat{a}\right]\hat{\psi}_\sigma(z)\\ &+\int dz\left[\frac{\hbar\Omega}{2}\hat{\psi}_\uparrow^\dagger(z)\hat{\psi}_\downarrow(z)+\text{h.c.}\right]-\int dz(\hbar\delta)\hat{\psi}_\uparrow^\dagger(z)\hat{\psi}_\uparrow(z)-\hbar\Delta_c\hat{a}^\dagger\hat{a}+\hbar(\varepsilon\hat{a}^\dagger+\varepsilon^*\hat{a}).\end{aligned} \tag{5.10}$$

It's worth to mention that for simplicity we take only one atomic excited state into account in this derivation. For practical experimental system, one might need to sum over the contributions from all relevant excited states.

Assuming all the atoms are located in the ground band of the lattice, in tight-binding limit the single-particle eigenstates of the system can be described by Wannier-Stark states $|\phi_n\rangle$ ($n\in\mathbb{Z}$) [290]:

$$E_n = Mga_l n,\quad \phi_n(z)=\sum_m \mathcal{J}_{m-n}\left(\frac{2J_0}{Mga_l}\right)w(z-ma_l). \tag{5.11}$$

Here, $\mathcal{J}_n(x)$ is the Bessel function of the first kind, $J_0\approx(4/\sqrt{\pi})E_R^{1/4}V_0^{3/4}\exp\left[-2\sqrt{V_0/E_R}\right]$ is the nearest-neighbor tunneling couplings, $a_l=\lambda_l/2$ is the lattice spacing, and $w(x)$ is the ground band Wannier function. Here $E_R=\hbar^2k_l^2/2M$ is the atomic recoil energy. Then we expand the atomic field operators $\hat{\psi}_\sigma(z)$ in terms of Wannier-Stark states,

$$\hat{\psi}_\sigma(z)=\sum_n \hat{c}_{n\sigma}\phi_n(z), \tag{5.12}$$

where $\hat{c}_{n\sigma}$ annihilates an atom of spin σ in the state $|\phi_n\rangle$. We consider the case that $Mga_l \gg \hbar|\mathcal{G}^0_{\uparrow,\downarrow}|^2\langle\hat{a}^\dagger\hat{a}\rangle/\Delta_{\uparrow,\downarrow}$, which means cavity-induced AC Stark shifts in atomic ground state are smaller than Mga_l, the energy difference between adjacent Wannier-Stark ladder states. This implies all the atoms are frozen in their initial Wannier-Stark states (see a later subsection for validity of this approximation), and we only need to consider the dynamics in the carrier transition $|\downarrow;\phi_n\rangle\leftrightarrow|\uparrow;\phi_n\rangle$. Turning off the Rabi drive Ω after initial state preparation, the Hamiltonian can be simplified into the following form,

$$\hat{\tilde{H}} = -\hbar\tilde{\Delta}_c\hat{a}^\dagger\hat{a}+\hbar(\varepsilon\hat{a}^\dagger+\varepsilon^*\hat{a})+\sum_n\Big(-\hbar\delta+\hbar\eta_n\hat{a}^\dagger\hat{a}\Big)\hat{S}_n^z, \tag{5.13}$$

and

$$\begin{aligned}\tilde{\Delta}_c &= \Delta_c - \sum_n \frac{N_n}{2}\left(\frac{|\mathcal{G}^0_\uparrow|^2}{\Delta_\uparrow} + \frac{|\mathcal{G}^0_\downarrow|^2}{\Delta_\downarrow}\right)\int dz \cos^2(k_c z)\phi_n(z)\phi_n(z),\\ \eta_n &= \left(\frac{|\mathcal{G}^0_\uparrow|^2}{\Delta_\uparrow} - \frac{|\mathcal{G}^0_\downarrow|^2}{\Delta_\downarrow}\right)\int dz \cos^2(k_c z)\phi_n(z)\phi_n(z).\end{aligned} \tag{5.14}$$

And the spin operators are defined as follows,

$$\begin{aligned}\hat{S}^x_n &= \frac{1}{2}(\hat{c}^\dagger_{n\uparrow}\hat{c}_{n\downarrow} + \hat{c}^\dagger_{n\downarrow}\hat{c}_{n\uparrow}), \quad \hat{S}^y_n = -\frac{i}{2}(\hat{c}^\dagger_{n\uparrow}\hat{c}_{n\downarrow} - \hat{c}^\dagger_{n\downarrow}\hat{c}_{n\uparrow}),\\ \hat{S}^z_n &= \frac{1}{2}(\hat{c}^\dagger_{n\uparrow}\hat{c}_{n\uparrow} - \hat{c}^\dagger_{n\downarrow}\hat{c}_{n\downarrow}), \quad \hat{N}_n = \hat{c}^\dagger_{n\uparrow}\hat{c}_{n\uparrow} + \hat{c}^\dagger_{n\downarrow}\hat{c}_{n\downarrow}.\end{aligned} \tag{5.15}$$

Assuming the ground band Wannier function $w(x)$ are localized on a single lattice site, the integral in η_n can be evaluated analytically,

$$\int dz \cos^2(k_c z)\phi_n(z)\phi_m(z) \approx \frac{1}{2}\left[\delta_{nm} + \mathcal{C}\mathcal{J}_{n-m}\left(\frac{4J_0}{Mga_l}\sin(\varphi/2)\right)\cos\left(\frac{(n+m)\varphi}{2} + \frac{(n-m)\pi}{2}\right)\right], \tag{5.16}$$

where $\varphi = 2k_c a_l$, and $\mathcal{C} = \int dz\, \mathrm{e}^{2ik_c z}|w(z)|^2$. Thus the analytic expression for η_n is

$$\eta_n = \frac{1}{2}\left[\frac{|\mathcal{G}^0_\uparrow|^2}{\Delta_\uparrow} - \frac{|\mathcal{G}^0_\downarrow|^2}{\Delta_\downarrow}\right]\left[1 + \mathcal{C}\mathcal{J}_0\left(\frac{4J_0}{Mga_l}\sin(\varphi/2)\right)\cos(n\varphi)\right]. \tag{5.17}$$

which leads to the magic lattice condition to achieve uniform η_n,

$$\mathcal{J}_0\left(\frac{4J_0}{Mga_l}\sin(\varphi/2)\right) = 0. \tag{5.18}$$

Under this magic lattice condition, we can replace η_n by η, which is given by

$$\eta = \frac{1}{2}\left[\frac{|\mathcal{G}^0_\uparrow|^2}{\Delta_\uparrow} - \frac{|\mathcal{G}^0_\downarrow|^2}{\Delta_\downarrow}\right]. \tag{5.19}$$

We consider the cavity mode has decay rate κ, so the dynamics of this system can be described by the following master equation,

$$\begin{aligned}\frac{d}{dt}\hat{\rho} &= -\frac{i}{\hbar}[\hat{\tilde{H}}, \hat{\rho}] + \hat{L}\hat{\rho}\hat{L}^\dagger - \frac{1}{2}\{\hat{L}^\dagger\hat{L}, \hat{\rho}\},\\ \hat{\tilde{H}}/\hbar &= -\tilde{\Delta}_c\hat{a}^\dagger\hat{a} + \varepsilon\hat{a}^\dagger + \varepsilon^*\hat{a} + \sum_n\Big(-\delta + \eta_n\hat{a}^\dagger\hat{a}\Big)\hat{S}^z_n,\\ \hat{L} &= \sqrt{\kappa}\,\hat{a}.\end{aligned} \tag{5.20}$$

If the cavity detuning $\tilde{\Delta}_c$ is now the largest frequency scale, we can proceed to adiabatically eliminate the cavity mode. For that first we expand the cavity field operator $\hat{a}$ as a sum of its steady state value $\alpha = \langle \hat{a} \rangle$ and quantum fluctuation $\hat{b}$,

$$\hat{a} = \alpha + \hat{b}, \quad \alpha = \frac{\varepsilon}{\tilde{\Delta}_c + i\kappa/2}. \tag{5.21}$$

Assuming $\tilde{\Delta}_c \gg \sum_n \eta_n \langle \hat{S}_n^z \rangle$, the Hamiltonian and jump operators become

$$\begin{aligned} \hat{\tilde{H}}/\hbar &\approx -\tilde{\Delta}_c \hat{b}^\dagger \hat{b} + \sum_n \Big(-\delta + \eta_n |\alpha|^2 + \eta_n \alpha^* \hat{b} + \eta_n \hat{b}^\dagger \alpha \Big) \hat{S}_n^z, \\ \hat{L} &= \sqrt{\kappa}\, \hat{b}. \end{aligned} \tag{5.22}$$

Now we focus on the initial condition where the collective spin is aligned along the equator, and the fluctuation of $\hat{S}^z$ is given by $\sqrt{N}/2$. In this case if $\tilde{\Delta}_c \gg \eta\alpha\sqrt{N}$ then $\langle \hat{b} \rangle \ll 1$, and therefore we can adiabatically eliminate the photon excitation (see Ref. [339]) and obtain an effective master equation in zero-photon subspace,

$$\begin{aligned} \frac{d}{dt}\hat{\rho} &= -\frac{i}{\hbar}[\hat{H}_{\text{eff}}, \hat{\rho}] + \hat{L}_{\text{eff}} \hat{\rho} \hat{L}_{\text{eff}}^\dagger - \frac{1}{2}\{\hat{L}_{\text{eff}}^\dagger \hat{L}_{\text{eff}}, \hat{\rho}\}, \\ \hat{H}_{\text{eff}}/\hbar &= -\sum_n (\delta_k - \eta_n |\alpha|^2) \hat{S}_n^z + \sum_{nm} \frac{\eta_n \eta_m |\alpha|^2 \tilde{\Delta}_c}{\tilde{\Delta}_c^2 + \kappa^2/4} \hat{S}_n^z \hat{S}_m^z, \\ \hat{L}_{\text{eff}} &= \sqrt{\kappa} \sum_n \frac{\eta_n \alpha}{\tilde{\Delta}_c + i\kappa/2} \hat{S}_n^z. \end{aligned} \tag{5.23}$$

5.2.7 Supplemental Materials: Validity of spin model and homogeneous couplings

Here we would like to discuss the validity of our results discussed in the main text, considering the effects of experimental imperfections and the validity of the approximations in the theory model.

Effects of thermal distribution on magic lattice condition

In the main text, we discuss the magic lattice condition to achieve uniform one-axis twisting,

$$\mathcal{J}_0\left(\frac{4J_0}{Mga_l} \sin(\varphi/2) \right) = 0, \tag{5.24}$$

assuming a separable confinement potential and tunneling only along the gravity direction. For practical experimental system, the Gaussian geometry of the laser beams inevitably couple the vertical and radial wave-functions. In this case therefore we have to consider the thermal distribution

of atoms in the transverse direction, which leads to an imperfect cancellation of the inhomogeneity. The Gaussian profile of the lattice and cavity beams leads to the following imperfections:

(1) Atoms in different radial modes have a slightly different nearest-neighbor tunneling rate.

(2) Atoms in different radial modes feel a differential AC-Stark shifts and thus extra inhomogeneities.

First we focus on the Gaussian beam profile of a 1D lattice, which leads to the following trapping potential,

$$V_0(\mathbf{r},z)=\begin{cases} V_0-V_0\cos^2(k_l z)\exp\left(-2r^2/w_l^2\right) & \text{(red-detuned lattice)} \\ V_0\sin^2(k_l z)\exp\left(-2r^2/w_l^2\right) & \text{(blue-detuned lattice)} \end{cases}, \tag{5.25}$$

where $k_l=2\pi/\lambda_l$ is the lattice wave number, w_l is the beam waist, and $V_0>0$ is the lattice depth. Using a technique similar to the one used in Ref. [292], one can also introduce an additional radial trapping potential $V_r(\mathbf{r},z)=M\omega_{r1}^2r^2/2$ from the optical cavity. Expanding the total trapping potential $V(\mathbf{r},z)=V_0(\mathbf{r},z)+V_r(\mathbf{r},z)$ to second order of r, we have

$$V(\mathbf{r},z)\approx V_0\sin^2(k_l z)+\frac{1}{2}M\omega_r^2r^2-\frac{\omega_{r0}^2}{\omega_r^2}\cdot\frac{1}{2}M\omega_r^2r^2\sin^2(k_l z). \tag{5.26}$$

Here, the total radial trapping frequency is given by $\omega_r=\sqrt{\omega_{r0}^2+\omega_{r1}^2}$ for red-detuned lattice, and $\omega_r=\omega_{r1}$ for blue-detuned lattice. Here $\omega_{r0}=\sqrt{4V_0/Mw_l^2}$.

In the expression above, the first term describes the lattice potential along the axial direction. The corresponding axial eigenfunctions are Bloch functions $\phi_q(z)$ in the ground band with a band structure $E(q)/E_R=f(q/\hbar k_l,V_0/4E_R)+V_0/2E_R$, where $q\in[-\hbar k_l,\hbar k_l]$ is the quasimomentum, and the function f is the characteristic Mathieu value of type A for $q\in(-\hbar k_l,\hbar k_l)$, and the characteristic Mathieu value of type B for $q=\pm\hbar k_l$. The second term describes the radial trapping potential as a harmonic oscillator with eigenfunctions $\phi_{n_x,n_y}(\mathbf{r})=\phi_{n_x}(x)\phi_{n_y}(y)$ and eigenenergies $E_{n_x,n_y}=\hbar\omega_r(n_x+n_y+1)/2$. The third term is the anharmonicity in the Gaussian beam profile, which couples the axial and radial degrees of freedom. Similar to Ref. [102], we use first-order

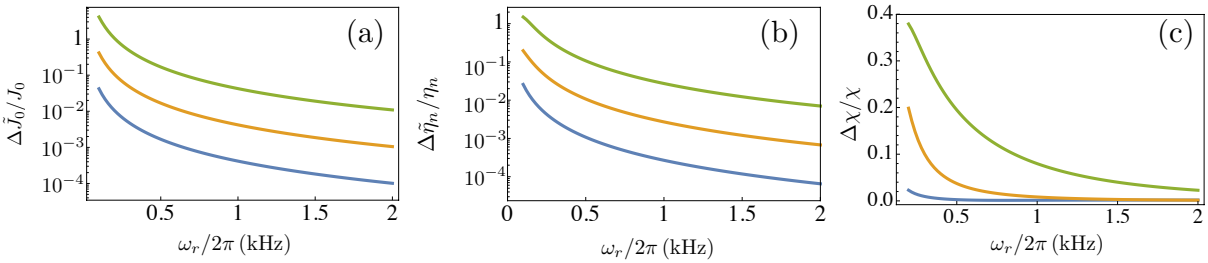

Figure 5.5: The standard deviations of (a) the tunneling rates, (b) the AC-Stark shifts and (c) the interaction strength as a function of the total radial trapping potential ω_r for fixed $T = 0.1\mu$K (blue curves), $T = 1.0\mu$K (yellow curves) and $T = 10\mu$K (green curves). Here we assume the beam waists are $w_c \approx w_l = 50\mu$m and the trapping depth is $V_0 = 6E_r$. We find the corrections can be suppressed by increasing the radial trapping frequency or lowering the temperature.

perturbation theory to calculate the energy corrections from the anharmonicity,

$$E_{n_x,n_y}(q) = E_{n_x,n_y} + E(q) - \frac{1}{2}\frac{\omega_{r0}^2}{\omega_r^2}E_{n_x,n_y}\langle q|\sin^2(k_l z)|q\rangle. \tag{5.27}$$

Based on Feynman–Hellman theorem, we have

$$\langle q|\sin^2(k_l z)|q\rangle = \frac{1}{2} + \frac{\partial}{\partial v_0}f(\tilde{q}, v_0/4), \tag{5.28}$$

in which we define $\tilde{q} = q/\hbar k_l$, and $v_0 = V_0/E_R$. Notice that in the tight-binding limit, we can calculate the nearest-neighbor tunneling by $J_0 = [E(q = \pm\hbar k_l) - E(q = 0)]/4$, so the correction of J_0 is given by

$$\tilde{J}_0(n_x, n_y) = J_0 + \frac{1}{8}\frac{\omega_{r0}^2}{\omega_r^2}E_{n_x,n_y}\left[\frac{\partial}{\partial v_0}f(\tilde{q} = 0, v_0/4) - \frac{\partial}{\partial v_0}f(\tilde{q} = \pm 1, v_0/4)\right], \tag{5.29}$$

where $J_0 \approx (4/\sqrt{\pi})E_R^{1/4}V_0^{3/4}\exp\left[-2\sqrt{V_0/E_R}\right]$. As depicted in Fig. 5.5(a), one can suppress the correction of J_0 by increasing the total radial trapping frequency ω_r, or lowering the temperature.

With respect to the cavity mode we used to mediate one-axis twisting interaction, and this cavity mode has the finite beam waist w_c. Notice that since the 1D lattice is also injected into the cavity, it's reasonable to assume $w_c \approx w_l$. In this case we can estimate the differential AC-Stark shifts by

$$\tilde{\eta}_n(n_x, n_y) = \eta_n \int dxdy \exp\left(-\frac{2r^2}{w_c^2}\right)[\phi_{n_x}(x)\phi_{n_y}(y)]^2, \tag{5.30}$$

where

$$\phi_m(x) = \frac{1}{\sqrt{2^m m!}}\left(\frac{M\omega_r}{\pi\hbar}\right)^{1/4} \mathrm{e}^{-M\omega_r x^2/2\hbar} H_m\left(\sqrt{\frac{M\omega_r}{\hbar}}x\right). \tag{5.31}$$

Using the following identity of Hermite polynomials,

$$\int dx\, \mathrm{e}^{-2\alpha^2 x^2}[H_m(x)]^2 = 2^{m-1/2}\alpha^{-(2m+1)}(1-2\alpha^2)^m \Gamma\left(m+\frac{1}{2}\right) {}_2F_1\left(-m,-m;\frac{1}{2}-m;\frac{\alpha^2}{2\alpha^2-1}\right), \tag{5.32}$$

where ${}_2F_1(a,b;c;x)$ is hypergeometric function, we get

$$\tilde{\eta}_n(n_x,n_y) = \eta_n h(n_x)h(n_y), \tag{5.33}$$

where

$$h(m) = \frac{1}{\sqrt{2\pi}}\frac{1}{m!}\alpha^{-(2m+1)}(1-2\alpha^2)^m \Gamma\left(m+\frac{1}{2}\right) {}_2F_1\left(-m,-m;\frac{1}{2}-m;\frac{\alpha^2}{2\alpha^2-1}\right), \tag{5.34}$$

$$\alpha = \sqrt{\frac{1}{2}+\frac{\hbar}{M\omega_r w_c^2}}. \tag{5.35}$$

As depicted in Fig. 5.5(b), one can suppress the the differential AC-Stark shifts by increasing the total radial trapping frequency ω_r, or lowering the temperature. Finally, we calculate the inhomogeneties in the OAT interaction strength [Fig. 5.5(c)] combining the corrections in tunneling rates and differential AC Stark shifts.

Tight-binding approximation

Our protocol in the main text works in relatively shallow lattices. However, all the discussions above were based on the tight-binding approximation which neglects the next nearest neighbor and higher order tunneling processes. It's therefore important to check the validity of the tight-binding approximation for typical lattice depths in our protocol. We denote the tunneling rate between site n and site $n+m$ in the ground band as $J_{0,m}/\hbar$, which can be calculated by

$$\frac{J_{0,m}}{E_R} = -\frac{1}{2}\int_{-1}^{1} d\tilde{q}\, \mathrm{e}^{-im\pi\tilde{q}} f(\tilde{q}, v_0/4). \tag{5.36}$$

in which the function f related to characteristic Mathieu value is defined in the previous section. For ^{87}Rb atoms and 532nm lattice, we have $|J_{0,2}|/|J_{0,1}| = 0.038$ at $V_0 = 6.0E_R$, and $|J_{0,2}|/|J_{0,1}| =$

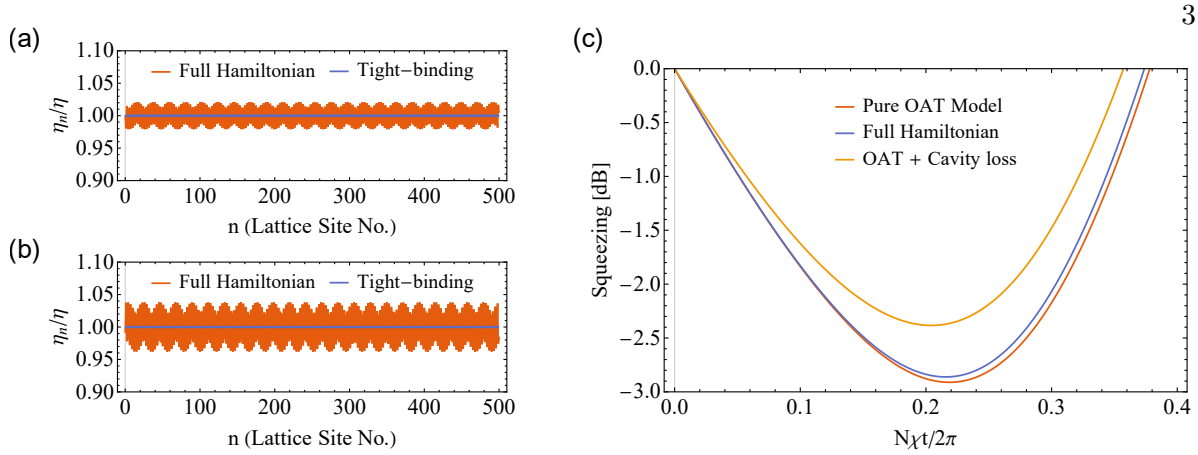

Figure 5.6: (a,b) Beyond tight-binding model effects on the dispersive atom-light coupling η_n for lattice depth (a) $V_0 = 6.0E_R$ and (b) $V_0 = 2.9E_R$. (c) Modifications on the achievable spin squeezing by cavity induced WS couplings for 4 particles in a 4-site lattice. The orange curve shows the spin squeezing generated by pure one-axis twisting (OAT) model, the blue curve includes the effect of correction terms $\hat{\tilde{H}}_{\rm corr}$ with $\eta|\alpha|^2 = 0.2Mga_l/\hbar$, while the yellow curve includes the effect of cavity loss with $\Gamma_z/\chi = 0.1$.

0.105 at $V_0 = 2.9E_R$. This result shows that the nearest neighbor tunneling rate is dominant for the typical lattice depths in our discussion, which agrees with the key idea of tight-binding approximation. And we can also numerically check that the cancellation of inhomogeneities under magic lattice condition is still approximately valid even if we include all the possible tunneling processes [see Fig. 5.6(a,b)].

Hopping between Wannier-Stark states

In the main text, we consider an approximation that all the atoms are frozen in the Wannier-Stark (WS) states from Eq. (1) to Eq. (2), assuming the cavity-induced AC Stark shifts are smaller than the energy gap Mga_l between WS states. Here we provide the justifications of this approximation in detail. We denote the corrections to Eq. (2) in the main text by $\hat{H}_{\rm corr}$, which takes the following form,

$$\hat{H}_{\rm corr} = \sum_{n\sigma}(Mga_l n)\hat{c}^\dagger_{n\sigma}\hat{c}_{n\sigma} + \sum_{m\neq n,\sigma} K^{nm}_\sigma \hat{a}^\dagger\hat{a}\hat{c}^\dagger_{n\sigma}\hat{c}_{m\sigma}, \tag{5.37}$$

where K^{nm}_σ with $m \neq n$ is given by

$$K^{nm}_\sigma = \frac{1}{2}\frac{\hbar|\mathcal{G}^0|^2}{\Delta_\sigma}\mathcal{C}\mathcal{J}_{n-m}\left(\frac{4J_0}{Mga_l}\sin(\varphi/2)\right)\cos\left(\frac{(n+m)\varphi}{2} + \frac{(n-m)\pi}{2}\right). \tag{5.38}$$

If we replace the cavity field operator $\hat{a}$ by its steady state value α, $\hat{H}_{\rm corr}$ takes the similar form as the single-particle Hamiltonian in lattice oriented in vertical direction, but here we are considering hopping between WS states instead of Wannier states. And our approximation is mainly based on the fact that hopping between WS states is highly suppressed by the large energy gap Mga_l. To estimate the suppression, we would like to neglect the terms beyond nearest neighbor hopping, as these terms will eventually be suppressed by the Bessel function $\mathcal{J}_{n-m}$, and then we also replace the inhomogeneous K_σ^{nm} by its peak value K. If we initialize an atom at the WS state $|\phi_{n=0}\rangle$, the probability in find this atom at WS state $|\phi_n\rangle$ is given by

$$P_n(t) = \mathcal{J}_n\left[\frac{4K|\alpha|^2}{Mga_l}\left|\sin\left(\frac{Mga_l t}{2\hbar}\right)\right|\right]^2. \tag{5.39}$$

Average over the fast frequency scale $Mga_l/\hbar$, we can estimate the probability in WS state $|\phi_{n=1}\rangle$ by $\overline{P}_1 \approx 2K^2|\alpha|^4/(Mga_l)^2$. For ^{87}Rb atoms and 532nm lattice, if we choose the magic lattice condition $V_0 = 6.0E_R$, and set the cavity-induced AC Stark shift $\eta|\alpha|^2 = 0.2Mga_l/\hbar$ (assuming $\mathcal{G}_\uparrow^0 = \mathcal{G}_\downarrow^0$ and $\Delta_\uparrow = -\Delta_\downarrow$ to estimate K), we have $\overline{P}_1 \approx 0.5\%$. And this is why we can assume all the atoms are frozen in the initial WS states.

One can also step further to analyze the quantum fluctuations of cavity field a in $H_{\rm corr}$. If we add $H_{\rm corr}$ back to Eq. (2) in the main text, and then adiabatically eliminate the cavity field based on section S2, the corrections to Eq. (3) in the main text would be

$$\hat{\tilde{H}}_{\rm corr} = \sum_{n\sigma}(Mga_l n)\hat{c}_{n\sigma}^\dagger\hat{c}_{n\sigma} + \sum_{m\neq n,\sigma} K_\sigma^{nm}|\alpha|^2\hat{c}_{n\sigma}^\dagger\hat{c}_{m\sigma} + {\sum_{nmpq}}' \sum_{\sigma\sigma'} \frac{K_\sigma^{nm}K_{\sigma'}^{pq}|\alpha|^2}{\tilde{\Delta}_c}(\hat{c}_{n\sigma}^\dagger\hat{c}_{m\sigma})(\hat{c}_{p\sigma'}^\dagger\hat{c}_{q\sigma'}), \tag{5.40}$$

where $\sum'_{nmpq}$ means neglecting the terms with $n = m$ and $p = q$. Similar to the discussions above, the terms violate the energy conservation are highly suppressed by the large energy gap Mga_l. And one may only need to consider the effect of some resonant terms like $(\hat{c}_{n+1,\sigma}^\dagger\hat{c}_{n\sigma})(\hat{c}_{p-1,\sigma'}^\dagger\hat{c}_{p\sigma'})$, which play a role similar to dephasing because there are no spin flip processes in these correction terms. As depicted in Fig. 5.6(c), we compare the spin squeezing achieved in the ideal one-axis twisting model (see Eq. (3) in the main text) with exact diagonalization of the full Hamiltonian (add back $\hat{\tilde{H}}_{\rm corr}$) for 4 particles in a 4-site lattice with magic lattice condition. The effect of all

these corrections turns out to be negligible for the spin squeezing generation, as it is much smaller than the effect of collective dephasing with $\Gamma_z/\chi = 0.1$ due to cavity loss.

5.2.8 Supplemental Materials: Analytic results of OAT model with time reversal

Here we would like to discuss the analytic results of OAT model with time reversal under different sources of dissipation and experimental imperfection in state preparation and interrogation.

Cavity loss

We already include cavity loss in the derivation of Eq. (5.23). Now we discuss the effect of cavity loss in our scheme for quantum-enhanced gravimetry. For simplicity, we focus on pure OAT interaction with homogeneous couplings, which can be achieved with the magic lattice condition and spin echo pulses. In this case the effective master equation takes the following form,

$$\frac{\mathrm{d}}{\mathrm{d}t}\hat{\rho} = -i[\chi\hat{S}^z\hat{S}^z, \hat{\rho}] + \Gamma_z\left[\hat{S}^z\hat{\rho}\hat{S}^z - \frac{1}{2}\{\hat{S}^z\hat{S}^z, \hat{\rho}\}\right], \tag{5.41}$$

where

$$\chi = \frac{\eta^2|\alpha|^2\tilde{\Delta}_c}{\tilde{\Delta}_c^2 + \kappa^2/4}, \quad \Gamma_z = \frac{\kappa}{\tilde{\Delta}_c}\chi = \frac{\eta^2|\alpha|^2\kappa}{\tilde{\Delta}_c^2 + \kappa^2/4}. \tag{5.42}$$

Similar to Ref. [366], it is convenient to expand the density matrix in the collective spin basis $|S, m\rangle\langle S, n|$,

$$\hat{\rho} = \sum_{mn}\rho_{mn}|S, m\rangle\langle S, n|, \tag{5.43}$$

and Eq. (5.41) becomes

$$\frac{\mathrm{d}}{\mathrm{d}t}\rho_{mn} = \left[-i\chi(m^2 - n^2) - \frac{\Gamma_z}{2}(m-n)^2\right]\rho_{mn}. \tag{5.44}$$

First, we calculate the quantum noise for phase measurement $\sigma_p = (\Delta S^y/S)_{\phi\to 0}$. Starting from the initial state $|S^x = N/2\rangle$, we let the system evolve on OAT interaction for time t_0, then accumulate a phase in the rotation about y axis, $\hat{\tilde{R}}_y^{\phi} = \mathrm{e}^{-i\phi\hat{S}^y}$, and finally perform time reversal on the OAT interaction part. The twisting echo above leads to the following density matrix,

$$\rho_{mn}(2t_0)|_{\phi\to 0} = \rho_{mn}(0)\exp\left[-(m-n)^2\Gamma_z t_0\right], \tag{5.45}$$

where $\rho_{mn}(0) = c_m c_n^*$ with

$$c_m = \frac{1}{2^S}\sqrt{\frac{(2S)!}{(S+m)!\,(S-m)!}}. \tag{5.46}$$

So we have

$$\begin{aligned}(\Delta S^y)^2_{\phi\to 0} = \mathrm{Tr}[\hat{S}^y\hat{S}^y\hat{\rho}_{\phi\to 0}] &= \frac{1}{2}\left[S\left(S+\frac{1}{2}\right) - S\left(S-\frac{1}{2}\right)\mathrm{e}^{-4\Gamma_z t_0}\right] \\ &\approx \frac{S}{2}\Big(1+4S\Gamma_z t_0\Big),\end{aligned} \tag{5.47}$$

in which the approximation is valid if $\Gamma_z t_0 \ll 1$ and $S \gg 1$. Here we also used the fact that $\langle\hat{S}^y\rangle_{\phi\to 0} = 0$.

Then, we calculate the amplification factor $G = (\partial_\phi\langle\hat{S}^y\rangle/S)_{\phi\to 0}$. It's convenient to rewrite Eq. (5.41) using the Lindblad superoperator $\mathcal{L}_\chi$, $\partial_t\hat{\rho} = \mathcal{L}_\chi(\hat{\rho})$. Notice that $\langle\hat{S}^y\rangle_{\phi\to 0} = 0$, for small ϕ we have

$$\begin{aligned}\langle\hat{S}^y\rangle &= \mathrm{Tr}\left[\hat{S}^y\mathrm{e}^{\mathcal{L}_{-\chi}t_0}\Big(\mathrm{e}^{-i\phi\hat{S}^y}\mathrm{e}^{\mathcal{L}_\chi t_0}(\hat{\rho})\mathrm{e}^{i\phi\hat{S}^y}\Big)\right] \\ &\approx i\phi\Big\{\mathrm{Tr}\left[\hat{S}^y\mathrm{e}^{\mathcal{L}_{-\chi}t_0}\Big(\mathrm{e}^{\mathcal{L}_\chi t_0}(\hat{\rho})\hat{S}^y\Big)\right] - \mathrm{Tr}\left[\hat{S}^y\mathrm{e}^{\mathcal{L}_{-\chi}t_0}\Big(\hat{S}^y\mathrm{e}^{\mathcal{L}_\chi t_0}(\hat{\rho})\Big)\right]\Big\},\end{aligned} \tag{5.48}$$

This yields

$$(\partial_\phi\langle\hat{S}^y\rangle)_{\phi\to 0} = S(2S-1)\sin(\chi t_0)\cos^{2S-2}(\chi t_0)\cosh(\Gamma_z t_0)\mathrm{e}^{-3\Gamma_z t_0/2}. \tag{5.49}$$

The metrological gain $\xi^{-2} = 1/[N(\Delta\phi)^2]$ can be calculated based on Eq. (5.47) and Eq. (5.49) as:

$$\xi^2 \approx \frac{1+2N\Gamma_z t_0}{(N\chi t_0)^2} + \frac{1}{N} + \frac{1}{2}(\chi t_0)^2. \tag{5.50}$$

Spontaneous emission

Here we discuss the effect of spontaneous emission on our gravimetry protocol focusing again on the pure OAT model with homogeneous couplings, which leads single-particle decoherence in contrast to the collective dephasing described in the previous subsection. Single-particle decoherence mechanisms for atoms off-resonantly coupled to excited states include spin flip or dephasing processes emerging from Raman or Rayleigh scattering into free space respectively, which effectively transfer the atomic spin states outside the collective Dicke manifold. These processes can be

described by the following master equation acting on the spin degrees of freedom,

$$\begin{aligned}\frac{\mathrm{d}}{\mathrm{d}t}\hat{\rho} = -i\Big[\frac{\chi}{2}\sum_{j<k}\hat{\sigma}_j^z\hat{\sigma}_k^z,\hat{\rho}\Big] + \gamma_+\sum_j\Big[\hat{\sigma}_j^+\hat{\rho}\hat{\sigma}_j^- - \frac{1}{2}\{\hat{\sigma}_j^-\hat{\sigma}_j^+,\hat{\rho}\}\Big] \\ + \gamma_-\sum_j\Big[\hat{\sigma}_j^-\hat{\rho}\hat{\sigma}_j^+ - \frac{1}{2}\{\hat{\sigma}_j^+\hat{\sigma}_j^-,\hat{\rho}\}\Big] + \frac{\gamma_z}{4}\sum_j\Big[\hat{\sigma}_j^z\hat{\rho}\hat{\sigma}_j^z - \hat{\rho}\Big].\end{aligned} \tag{5.51}$$

The analytic solution of Eq. (5.51) has been reported in Ref. [367] by summing over all possible quantum trajectories. Here we present an alternative way by solving Heisenberg equations of motion to all order. Let's first focus on the terms that commute with the Hamiltonian, we have

$$\frac{\mathrm{d}}{\mathrm{d}t}\langle\hat{\sigma}_1^z\rangle = -(\gamma_+ + \gamma_-)\langle\hat{\sigma}_1^z\rangle + (\gamma_+ - \gamma_-) \quad \Rightarrow \quad \langle\hat{\sigma}_1^z\rangle = \frac{\gamma_+ - \gamma_-}{\gamma_+ + \gamma_-}\Big[1 - \mathrm{e}^{-(\gamma_+ + \gamma_-)t}\Big], \tag{5.52}$$

$$\frac{\mathrm{d}}{\mathrm{d}t}\langle\hat{\sigma}_1^z\hat{\sigma}_2^z\rangle = -2(\gamma_+ + \gamma_-)\langle\hat{\sigma}_1^z\hat{\sigma}_2^z\rangle + 2(\gamma_+ - \gamma_-)\langle\hat{\sigma}_1^z\rangle \quad \Rightarrow \quad \langle\hat{\sigma}_1^z\hat{\sigma}_2^z\rangle = \langle\hat{\sigma}_1^z\rangle^2, \tag{5.53}$$

$$\frac{\mathrm{d}}{\mathrm{d}t}\langle\hat{\sigma}_1^+\hat{\sigma}_2^-\rangle = -2\Gamma\langle\hat{\sigma}_1^+\hat{\sigma}_2^-\rangle \quad \Rightarrow \quad \langle\hat{\sigma}_1^+\hat{\sigma}_2^-\rangle = \frac{1}{4}\mathrm{e}^{-2\Gamma t}, \tag{5.54}$$

where $\Gamma = (\gamma_+ + \gamma_- + \gamma_z)/2$, and we consider the initial state as $|S^x = N/2\rangle$. Then we consider $\langle\hat{\sigma}_1^+\rangle$ and the higher order correlators generated in the Heisenberg equations of motion,

$$\frac{\mathrm{d}}{\mathrm{d}t}\begin{pmatrix}\langle\hat{\sigma}_1^+\rangle\\ \langle\hat{\sigma}_1^+\hat{\sigma}_2^z\rangle\\ \langle\hat{\sigma}_1^+\hat{\sigma}_2^z\hat{\sigma}_3^z\rangle\\ \vdots\\ \langle\hat{\sigma}_1^+\hat{\sigma}_2^z\cdots\hat{\sigma}_N^z\rangle\end{pmatrix} = \begin{pmatrix}-\Gamma & i\chi(N-1) & 0 & 0 & \cdots & 0 & 0\\ J & -\Gamma-\Gamma_r & i\chi(N-2) & 0 & \cdots & 0 & 0\\ 0 & 2J & -\Gamma-2\Gamma_r & i\chi(N-3) & \cdots & 0 & 0\\ \vdots & \vdots & \vdots & \vdots & & \vdots & \vdots\\ 0 & 0 & 0 & 0 & \cdots & (N-1)J & -\Gamma-(N-1)\Gamma_r\end{pmatrix}\begin{pmatrix}\langle\hat{\sigma}_1^+\rangle\\ \langle\hat{\sigma}_1^+\hat{\sigma}_2^z\rangle\\ \langle\hat{\sigma}_1^+\hat{\sigma}_2^z\hat{\sigma}_3^z\rangle\\ \vdots\\ \langle\hat{\sigma}_1^+\hat{\sigma}_2^z\cdots\hat{\sigma}_N^z\rangle\end{pmatrix}, \tag{5.55}$$

where we define $J = \gamma_+ - \gamma_- + i\chi$, and $\Gamma_r = \gamma_+ + \gamma_-$. We can solve the differential equations above via a trial solution of the form,

$$\begin{aligned}\langle\hat{\sigma}_1^+\rangle = \frac{1}{2}[f(t)]^{N-1}\mathrm{e}^{-\Gamma t}, \quad \langle\hat{\sigma}_1^+\hat{\sigma}_2^z\rangle = \frac{1}{2}[f(t)]^{N-2}\frac{f'(t)}{i\chi}\mathrm{e}^{-\Gamma t}, \\ \langle\hat{\sigma}_1^+\hat{\sigma}_2^z\hat{\sigma}_3^z\rangle = \frac{1}{2}[f(t)]^{N-3}\left(\frac{f'(t)}{i\chi}\right)^2\mathrm{e}^{-\Gamma t}, \quad \cdots, \quad \langle\hat{\sigma}_1^+\hat{\sigma}_2^z\cdots\hat{\sigma}_N^z\rangle = \frac{1}{2}\left(\frac{f'(t)}{i\chi}\right)^{N-1}\mathrm{e}^{-\Gamma t}.\end{aligned} \tag{5.56}$$

This trial solution simplifies the coupled differential equations above into a single equation of the form,

$$f''(t) + \Gamma_r f'(t) - i\chi J f(t) = 0. \tag{5.57}$$

For an initial state as $|S^x = N/2\rangle$, the initial condition for the differential equation is $f(0) = 1$, $f'(0) = 0$. A similar analysis can also be applied to $\langle\hat{\sigma}_1^+\hat{\sigma}_2^+\rangle$ as follows,

$$\frac{\mathrm{d}}{\mathrm{d}t}\begin{pmatrix} \langle\hat{\sigma}_1^+\hat{\sigma}_2^+\rangle \\ \langle\hat{\sigma}_1^+\hat{\sigma}_2^+\hat{\sigma}_3^z\rangle \\ \vdots \\ \langle\hat{\sigma}_1^+\hat{\sigma}_2^+\hat{\sigma}_3^z\cdots\hat{\sigma}_N^z\rangle \end{pmatrix} = \begin{pmatrix} -2\Gamma & 2i\chi(N-2) & 0 & 0 & \cdots & 0 & 0 \\ J' & -\Gamma-\Gamma_r & 2i\chi(N-3) & 0 & \cdots & 0 & 0 \\ \vdots & \vdots & \vdots & \vdots & & \vdots & \vdots \\ 0 & 0 & 0 & 0 & \cdots & (N-2)J' & -\Gamma-(N-2)\Gamma_r \end{pmatrix} \begin{pmatrix} \langle\hat{\sigma}_1^+\hat{\sigma}_2^+\rangle \\ \langle\hat{\sigma}_1^+\hat{\sigma}_2^+\hat{\sigma}_3^z\rangle \\ \vdots \\ \langle\hat{\sigma}_1^+\hat{\sigma}_2^+\hat{\sigma}_3^z\cdots\hat{\sigma}_N^z\rangle \end{pmatrix}, \tag{5.58}$$

where we define $J' = \gamma_+ - \gamma_- + 2i\chi$. Using the following trial solution,

$$\begin{aligned} \langle\hat{\sigma}_1^+\hat{\sigma}_2^+\rangle &= \frac{1}{4}[g(t)]^{N-2}\mathrm{e}^{-2\Gamma t}, \quad \langle\hat{\sigma}_1^+\hat{\sigma}_2^+\hat{\sigma}_3^z\rangle = \frac{1}{4}[g(t)]^{N-3}\frac{g'(t)}{2i\chi}\mathrm{e}^{-2\Gamma t} \\ \langle\hat{\sigma}_1^+\hat{\sigma}_2^+\hat{\sigma}_3^z\hat{\sigma}_4^z\rangle &= \frac{1}{4}[g(t)]^{N-4}\left(\frac{g'(t)}{2i\chi}\right)^2\mathrm{e}^{-2\Gamma t}, \quad \cdots, \quad \langle\hat{\sigma}_1^+\hat{\sigma}_2^+\hat{\sigma}_3^z\cdots\hat{\sigma}_N^z\rangle = \frac{1}{4}\left(\frac{g'(t)}{2i\chi}\right)^{N-2}\mathrm{e}^{-2\Gamma t}, \end{aligned} \tag{5.59}$$

we simplify the coupled differential equations above to a single one in the following form,

$$g''(t) + \Gamma_r g'(t) - 2i\chi J' g(t) = 0. \tag{5.60}$$

For the initial state $|S^x = N/2\rangle$, the initial condition for the differential equation is $g(0) = 1$, $g'(0) = 0$.

After introducing the analytic solutions for the master equation Eq. (5.51), now we apply them to the twisting echo protocol. First, we calculate the quantum noise for phase measurement $\sigma_p = (\Delta S^y/S)_{\phi\to 0}$. Notice that $\langle\hat{S}^y\rangle_{\phi\to 0} = 0$, we have

$$(\Delta S^y)^2_{\phi\to 0} = \langle\hat{S}^y\hat{S}^y\rangle_{\phi\to 0} = \frac{N}{4} + \frac{N(N-1)}{2}\mathrm{Re}\Big[\langle\hat{\sigma}_1^+\hat{\sigma}_2^-\rangle - \langle\hat{\sigma}_1^+\hat{\sigma}_2^+\rangle\Big], \tag{5.61}$$

so we need to calculate $\langle\hat{\sigma}_1^+\hat{\sigma}_2^-\rangle$ and $\langle\hat{\sigma}_1^+\hat{\sigma}_2^+\rangle$ in the case of $\phi = 0$. It's easy to observe Eq. (5.54) that the dynamics of $\langle\hat{\sigma}_1^+\hat{\sigma}_2^-\rangle$ does not depend on χ. The solution is given by

$$\langle\hat{\sigma}_1^+\hat{\sigma}_2^-\rangle_{t=2t_0} = \frac{1}{4}\mathrm{e}^{-4\Gamma t_0}. \tag{5.62}$$

As for $\langle\hat{\sigma}_1^+\hat{\sigma}_2^+\rangle$, since we focus on the case with balanced spin flip rates, $\gamma_+ = \gamma_- \equiv \gamma_r$, we can rewrite Eq. (5.60) into the following form,

$$g''(t) + 2\gamma_r g'(t) + 4\chi^2 g(t) = 0, \tag{5.63}$$

and applying the initial condition $g(0) = 1$, $g'(0) = 0$ leads to

$$g(t_0) = \left[\cosh(\nu t_0) + \frac{\gamma_r}{\nu}\sinh(\nu t_0)\right]\mathrm{e}^{-\gamma_r t_0}, \quad g'(t_0) = \frac{\nu^2 - \gamma_r^2}{\nu}\sinh(\nu t_0)\mathrm{e}^{-\gamma_r t_0}, \tag{5.64}$$

where $\nu = \gamma_r\sqrt{1 - 4\chi^2/\gamma_r^2}$. For the time reversal of OAT interaction ($\chi \to -\chi$), we can apply a modified version of trial solution as follows,

$$\langle\hat{\sigma}_1^+\hat{\sigma}_2^+\rangle = \frac{1}{4}\mathrm{e}^{-2\Gamma t_0}[\tilde{g}(t)]^{N-2}\mathrm{e}^{-2\Gamma t}, \quad \langle\hat{\sigma}_1^+\hat{\sigma}_2^+\hat{\sigma}_3^z\rangle = \frac{1}{4}\mathrm{e}^{-2\Gamma t_0}[\tilde{g}(t)]^{N-3}\frac{\tilde{g}'(t)}{2i(-\chi)}\mathrm{e}^{-2\Gamma t}, \quad \cdots, \tag{5.65}$$

in which $\tilde{g}(t)$ still satisfying the differential equation Eq. (5.63), with initial condition $\tilde{g}(0) = g(t_0)$ and $\tilde{g}'(0) = -g'(t_0)$. So we get

$$\tilde{g}(t_0) = \left[1 - \frac{\gamma_r^2}{\nu^2} + \frac{\gamma_r^2}{\nu^2}\cosh(2\nu t_0) + \frac{\gamma_r}{\nu}\sinh(2\nu t_0)\right]\mathrm{e}^{-2\gamma_r t_0}, \tag{5.66}$$

which leads to

$$\langle\hat{\sigma}_1^+\hat{\sigma}_2^+\rangle_{t=2t_0} = \frac{1}{4}\mathrm{e}^{-4\Gamma t_0}[\tilde{g}(t_0)]^{N-2} \approx \frac{1}{4}\mathrm{e}^{-4\Gamma t_0}\left[1 - \frac{16}{3}(N-2)\gamma_r\chi^2 t_0^3\right], \tag{5.67}$$

in which the approximation is valid if $\gamma_r t_0 \ll 1$. So we have

$$(\Delta S^y)^2_{\phi\to 0} \approx \frac{N}{4}\left[1 + \frac{8}{3}(N\chi)^2\gamma_r t_0^3\right]. \tag{5.68}$$

Then, we calculate the amplification factor $G = (\partial_\phi\langle\hat{S}^y\rangle/S)_{\phi\to 0}$. Similarly we can rewrite Eq. (5.57) into the following form,

$$f''(t) + 2\gamma_r f'(t) + \chi^2 f(t) = 0. \tag{5.69}$$

and then apply the initial condition $f(0) = 1$, $f'(0) = 0$ to calculate $f(t_0)$ and $f'(t_0)$. The next step is to apply the rotation about y axis, $\hat{\tilde{R}}_y^\phi = \mathrm{e}^{-i\phi\hat{S}^y}$, which leads to

$$\begin{aligned}
\langle(\hat{\tilde{R}}_y^\phi)^\dagger\hat{\sigma}_1^+\hat{\tilde{R}}_y^\phi\rangle &= \langle\hat{\sigma}_1^+\rangle_{t=t_0}\cos\phi, \\
\langle(\hat{\tilde{R}}_y^\phi)^\dagger\hat{\sigma}_1^+\hat{\sigma}_2^z\hat{\tilde{R}}_y^\phi\rangle &= \langle\hat{\sigma}_1^+\hat{\sigma}_2^z\rangle_{t=t_0}\cos\phi - 2\Big(\langle\hat{\sigma}_1^+\hat{\sigma}_2^-\rangle_{t=t_0} + \langle\hat{\sigma}_1^+\hat{\sigma}_2^+\rangle_{t=t_0}\Big)\cos\phi\sin\phi,
\end{aligned} \tag{5.70}$$

where we use the fact that $\langle\hat{\sigma}_1^y\rangle_{t=t_0} = \langle\hat{\sigma}_1^z\rangle_{t=t_0} = \langle\hat{\sigma}_1^x\hat{\sigma}_2^z\rangle_{t=t_0} = \langle\hat{\sigma}_1^x\hat{\sigma}_2^y\rangle_{t=t_0} = 0$. Then we apply a modified version of trial solution, similar to Eq. (5.65), to take account of the time reversal of OAT

interaction. And we can similarly define $\tilde{f}(t)$ still satisfying Eq. (5.69), with the following initial condition for small ϕ limit,

$$\tilde{f}(0) \approx f(t_0), \quad \tilde{f}'(0) \approx -\Big[f'(t_0) - i\chi\phi\Big(1-(N-2)\chi^2 t_0^2\Big)\mathrm{e}^{-\Gamma t_0}\Big], \tag{5.71}$$

which leads to

$$\mathrm{Re}[\tilde{f}(t_0)] \approx 1 - \frac{4}{3}\gamma_r\chi^2 t_0^3, \quad \mathrm{Im}[\tilde{f}(t_0)] \approx \phi\Big(1-(N-2)\chi^2 t_0^2\Big)(\chi t_0)\mathrm{e}^{-\Gamma t_0}\mathrm{e}^{-\gamma_r t_0}. \tag{5.72}$$

So we have

$$(\partial_\phi\langle\hat{S}^y\rangle)_{\phi\to 0} \approx \frac{N(N-1)}{2}\mathrm{Re}[\tilde{f}(t_0)]^{N-2}\mathrm{Im}[\tilde{f}(t_0)]\mathrm{e}^{-2\Gamma t_0} \approx \frac{N(N-1)}{2}(\chi t_0)\mathrm{e}^{-4\gamma_r t_0}\mathrm{e}^{-3\gamma_z t_0/2}. \tag{5.73}$$

And the metrological gain $\xi^{-2} = 1/[N(\Delta\phi)^2]$ can be calculated based on Eq. (5.68) and Eq. (5.73),

$$\xi^2 \approx \frac{1+(8\gamma_r+3\gamma_z)t_0}{(N\chi t_0)^2} + \frac{8}{3}\gamma_r t_0. \tag{5.74}$$

Joint effects of cavity loss and spontaneous emission

Now we discuss the joint effects of cavity loss and spontaneous emission, and we can show that optimal sensitivity of gravimetry only depends on the atom number N and single atom cooperativity $C = 4|\mathcal{G}^0|^2/\kappa\gamma$. Here, $\mathcal{G}^0$ relates to $\mathcal{G}^0_{\uparrow,\downarrow}$ defined in the main text up to Clebsch-Gordan coefficients, κ is the cavity decay rate, and γ is the spontaneous emission rate of the relevant electronic state coupled to the cavity. The dipole matrix element in $|\mathcal{G}^0|^2$ and γ will eventually cancel in such a way that C only depends on the details of the cavity. In our case, it is convenient to rewrite C in terms of the parameters in the effective master equation in previous subsections. Notice that we can express $\Gamma = \gamma_r + \gamma_z/2$ defined in the previous subsection by $\Gamma \propto \gamma|\mathcal{G}^0_{\uparrow,\downarrow}|^2|\alpha|^2/\Delta^2_{\uparrow,\downarrow}$, and the photon-mediated interaction strength χ, Γ_z [see Eq. (5.42)] by $\chi \propto |\mathcal{G}^0_{\uparrow,\downarrow}|^4|\alpha|^2/\Delta^2_{\uparrow,\downarrow}\tilde{\Delta}_c$ and $\Gamma_z \propto |\mathcal{G}^0_{\uparrow,\downarrow}|^4|\alpha|^2\kappa/\Delta^2_{\uparrow,\downarrow}\tilde{\Delta}_c^2$, when $\tilde{\Delta}_c \gg \kappa$ as the case considered here. In this limit we can express the single atom cooperativity C as

$$C = AC', \quad C' = \frac{\chi^2}{\Gamma_z\Gamma}. \tag{5.75}$$

Here, A is a multiplicative constant set by appropriate Clebsch-Gordan coefficients. Based on the discussions above, if we increase $\tilde{\Delta}_c$, the effect of cavity loss decreases, while the effect of

spontaneous emission increases. So we can consider $\tilde{\Delta}_c$ as the tuning parameter for the relative strength of cavity loss and spontaneous emission. For convenience, we also define $d \equiv \Gamma_z/\chi$ in the calculations below.

In the following, we discuss different cases that depend whether spin flip processes are allowed or not. Here it's convenient to define the spin flip probability P_f by $\gamma_r = P_f\Gamma$. Consider $N\Gamma_z \gg \gamma_z$, based on Eq. (5.50) and Eq. (5.74), the metrological gain $\xi^{-2} = 1/[N(\Delta\phi)^2]$ can be calculated as follows,

$$\xi^2 \approx \frac{1 + 2N\Gamma_z t_0}{(N\chi t_0)^2} + \frac{8}{3}\gamma_r t_0. \tag{5.76}$$

Furthermore if we assume $N\Gamma_z t_0 > 1$ to reach optimal metrological gain, we can minimize the last two terms in Eq. (5.76), which leads to $\xi^2_{\text{opt}} = \sqrt{64P_f/3NC'}$ at $(\chi t_0)_{\text{opt}} = \sqrt{3C'd^2/4NP_f}$. This assumption is valid if $(4P_f/3C'N)^{1/4} \ll d \ll 1$, and the optimal metrological gain is independent of the choice of d in this regime. This result agrees with the calculation in Ref. [358]. Therefore, if the spin flip processes are allowed, the optimal sensitivity of gravimetry would be $\Delta g/g \propto N^{-3/4}$.

In the case of $P_f = 0$, the metrological gain ξ^{-2} now becomes

$$\xi^2 \approx \frac{1 + (2N\Gamma_z + 3\gamma_z)t_0}{(N\chi t_0)^2} + \frac{1}{N} + \frac{1}{2}(\chi t_0)^2. \tag{5.77}$$

Based on Eq. (5.75), we can first minimize the sum $2N\Gamma_z + 3\gamma_z$ by $(2N\Gamma_z + 3\gamma_z)_{\min} = 4\chi\sqrt{3N/C'}$. This minimum can be reached by choosing $d = \sqrt{3/NC'}$. Similarly we assume $2N\Gamma_z t_0 + 3\gamma_z t_0 > 1$ to reach optimal metrological gain, so the minimization of Eq. (5.77) leads to $\xi^2_{\text{opt}} = [1+3(6/C')^{1/3}]/N$, which can be achieved at $(\chi t_0)_{\text{opt}} = (48/C')^{1/6}/\sqrt{N}$. This assumption is valid if $C' \ll 48$. For large C', the effect of decoherence would be negligible, and one will get the optimal metrological gain for ideal implementation $\xi^2_{\text{ideal}} = e/N$ [358], where e is the base of natural logarithm. Therefore, if the spin flip processes are forbidden, the optimal sensitivity of gravimetry would be $\Delta g/g \propto 1/N$.

Inhomogeneous atom-light couplings

Now we discuss the inhomogeneous OAT interactions, which are described by the following Hamiltonian,

$$\hat{H} = \sum_{nm} \chi_{nm} \hat{S}^z_n \hat{S}^z_m, \tag{5.78}$$

where $\chi_{nm} = \chi_{mn}$. Obviously we find $(\Delta S^y)^2_{\phi\to 0} = N/4$, which is not affected by the inhomogeneities. So we only need to focus on the calculation of $(\partial_\phi \langle \hat{S}^y \rangle)_{\phi\to 0}$. Notice that

$$\begin{aligned}(\partial_\phi \langle \hat{S}^y \rangle)_{\phi\to 0} &= -i\langle \tilde{x}|[\hat{S}^y, \hat{U}^\dagger \hat{S}^y \hat{U}]|\tilde{x}\rangle \\ &= \frac{i}{4}\sum_{jk}\Big[\langle \tilde{x}|[\hat{\sigma}_j^+, \hat{U}^\dagger \hat{\sigma}_k^+ \hat{U}]|\tilde{x}\rangle - \langle \tilde{x}|[\hat{\sigma}_j^-, \hat{U}^\dagger \hat{\sigma}_k^+ \hat{U}]|\tilde{x}\rangle \\ &\qquad - \langle \tilde{x}|[\hat{\sigma}_j^+, \hat{U}^\dagger \hat{\sigma}_k^- \hat{U}]|\tilde{x}\rangle + \langle \tilde{x}|[\hat{\sigma}_j^-, \hat{U}^\dagger \hat{\sigma}_k^- \hat{U}]|\tilde{x}\rangle\Big],\end{aligned} \tag{5.79}$$

where $|\tilde{x}\rangle$ is a shorthand notation for the state $|S^x = N/2\rangle$, and $\hat{U} = \exp\Big[-it\sum_{nm}\chi_{nm}\hat{S}_n^z\hat{S}_m^z\Big]$ is the time evolution operator of inhomogeneous OAT interactions. Here we elaborate the calculation of the first term $\langle \tilde{x}|[\hat{\sigma}_j^+, U^\dagger \hat{\sigma}_k^+ U]|\tilde{x}\rangle$. Using the fact that the $|\tilde{x}\rangle$ state can be expressed in the following form,

$$|\tilde{x}\rangle = \frac{1}{\sqrt{2^N}}\sum_{\sigma_1,\cdots,\sigma_N=\pm 1}|\sigma_1,\cdots,\sigma_N\rangle, \tag{5.80}$$

where $\sigma_j = 1/-1$ means the j-th atom in $|\uparrow\rangle/|\downarrow\rangle$ state, we have

$$\begin{aligned}
&\hat{\sigma}_k^+\hat{U}|\tilde{x}\rangle = \frac{1}{\sqrt{2^N}}\times \\
&\sum_{\substack{\sigma_1,\cdots,\sigma_{k-1},\\ \sigma_{k+1},\cdots,\sigma_N=\pm 1}}\exp\Big[-i\frac{t}{4}\sum_{mn}^{(k)}\chi_{mn}\sigma_m\sigma_n - i\frac{t}{4}\chi_{kk} + i\frac{t}{2}\sum_m^{(k)}\chi_{mk}\sigma_m\Big]|\sigma_1,\cdots,\sigma_k=+1,\cdots,\sigma_N\rangle, \\
&\hat{U}\hat{\sigma}_j^-|\tilde{x}\rangle = \frac{1}{\sqrt{2^N}}\times \\
&\sum_{\substack{\sigma_1,\cdots,\sigma_{j-1},\\ \sigma_{j+1},\cdots,\sigma_N=\pm 1}}\exp\Big[-i\frac{t}{4}\sum_{mn}^{(j)}\chi_{mn}\sigma_m\sigma_n - i\frac{t}{4}\chi_{jj} + i\frac{t}{2}\sum_m^{(j)}\chi_{mj}\sigma_m\Big]|\sigma_1,\cdots,\sigma_j=-1,\cdots,\sigma_N\rangle, \\
&\hat{U}\hat{\sigma}_j^+|\tilde{x}\rangle = \frac{1}{\sqrt{2^N}}\times \\
&\sum_{\substack{\sigma_1,\cdots,\sigma_{j-1},\\ \sigma_{j+1},\cdots,\sigma_N=\pm 1}}\exp\Big[-i\frac{t}{4}\sum_{mn}^{(j)}\chi_{mn}\sigma_m\sigma_n - i\frac{t}{4}\chi_{jj} - i\frac{t}{2}\sum_m^{(j)}\chi_{mj}\sigma_m\Big]|\sigma_1,\cdots,\sigma_j=+1,\cdots,\sigma_N\rangle, \\
&\hat{\sigma}_k^-\hat{U}|\tilde{x}\rangle = \frac{1}{\sqrt{2^N}}\times \\
&\sum_{\substack{\sigma_1,\cdots,\sigma_{k-1},\\ \sigma_{k+1},\cdots,\sigma_N=\pm 1}}\exp\Big[-i\frac{t}{4}\sum_{mn}^{(k)}\chi_{mn}\sigma_m\sigma_n - i\frac{t}{4}\chi_{kk} - i\frac{t}{2}\sum_m^{(k)}\chi_{mk}\sigma_m\Big]|\sigma_1,\cdots,\sigma_k=-1,\cdots,\sigma_N\rangle,
\end{aligned} \tag{5.81}$$

where $\sum_m^{(k)}$ means summation without the term $m = k$. Based on Eq. (5.81), we get (assuming $j \neq k$)

$$\begin{aligned}\langle\tilde{x}|[\hat{\sigma}_j^+, \hat{U}^\dagger\hat{\sigma}_k^+\hat{U}]|\tilde{x}\rangle &= \langle\tilde{x}|\hat{\sigma}_j^+\hat{U}^\dagger\hat{\sigma}_k^+\hat{U}|\tilde{x}\rangle - \langle\tilde{x}|\hat{U}^\dagger\hat{\sigma}_k^+\hat{U}\hat{\sigma}_j^+|\tilde{x}\rangle \\ &= \frac{1}{4}\mathrm{e}^{-it\chi_{jk}}\prod_l^{(j,k)}\cos(\chi_{kl}t) - \frac{1}{4}\mathrm{e}^{it\chi_{jk}}\prod_l^{(j,k)}\cos(\chi_{kl}t) \\ &= -\frac{i}{2}\sin(\chi_{jk}t)\prod_l^{(j,k)}\cos(\chi_{kl}t).\end{aligned} \tag{5.82}$$

It is easy to check that $\langle\tilde{x}|[\hat{\sigma}_j^+, \hat{U}^\dagger\hat{\sigma}_k^+\hat{U}]|\tilde{x}\rangle = 0$ for $j = k$. Similar analysis can also apply to the other three terms based on Eq. (5.81) and finally arrive to the following expression:

$$(\partial_\phi\langle\hat{S}^y\rangle)_{\phi\to 0} = \frac{1}{2}\sum_{j<k}\sin(\chi_{jk}t)\Big[\prod_l^{(j,k)}\cos(\chi_{jl}t) + \prod_l^{(j,k)}\cos(\chi_{kl}t)\Big]. \tag{5.83}$$

For the times at which squeezing takes place, to an excellent approximation $\chi_{jk}t_0 \ll 1$ and therefore $(\partial_\phi\langle\hat{S}^y\rangle)_{\phi\to 0} \sim \sum_{j<k}\chi_{jk}t_0$. If the average is carried out over the full lattice array, we have $(\partial_\phi\langle\hat{S}^y\rangle)_{\phi\to 0} \sim \frac{1}{2}N(N-1)\chi t_0$, and therefore inhomogeneities only give small higher order corrections. However, for applications such as measurements of short-range forces, that require the atoms to be placed at local region of the lattice, then in this situation inhomogeneities does not average out in a single realization and can give rise to important systematic errors that will need to be accounted for. In this situation, operating with homogeneous couplings by satisfying the magic lattice condition (5.24) can provide an important measurement advantage.

Single-particle dephasing during interrogation time

As pointed out by Ref. [17], single-particle dephasing imposes severe restrictions when operating with entangled states given their fragility to it. Here we estimate the longest interrogation time at which our protocol can still give a quantum advantage over uncorrelated states when the system is subjected to single-particle dephasing at a rate $\tilde{\gamma}_z$. To simplify the analysis, instead of direct calculation of the twisting echo, we consider a spin squeezed state generated by OAT Hamiltonian. The master equation for interrogation takes the following form,

$$\frac{\mathrm{d}}{\mathrm{d}t}\hat{\rho} = i\Big[\frac{\tilde{\delta}}{2}\sum_j\hat{\sigma}_j^z, \hat{\rho}\Big] + \frac{\tilde{\gamma}_z}{4}\sum_j\Big[\hat{\sigma}_j^z\hat{\rho}\hat{\sigma}_j^z - \hat{\rho}\Big] \tag{5.84}$$

where $\tilde{\delta} = (\omega_{\mathrm{R}} - \omega_{\mathrm{MW}} - Mga_l r/\hbar) \times 2m_R$ in our case, and the system evolves under the Eq. (5.84) to accumulate a phase $\phi = \tilde{\delta}\tau$, where τ is the interrogation time. The measurement uncertainty on the accumulated phase ϕ is given by

$$\Delta\phi = \left.\frac{\Delta S^y}{|\partial_\phi \langle \hat{S}^y \rangle|}\right|_{\phi\to 0}. \tag{5.85}$$

Therefore, the corresponding sensitivity for gravity measurements, $\Delta g/g$, is given by

$$\frac{\Delta g}{g} = \frac{\Delta\phi}{g|\partial_g \phi|}\sqrt{\frac{\tau}{T}} = \frac{\Delta\phi}{\omega_g\sqrt{\tau T}}, \tag{5.86}$$

where $\omega_g = 2Mga_l r m_R/\hbar$, and T is the total averaging time.

The Heisenberg equation of motion that follow from Eq. (5.84) are the following

$$\begin{aligned}
\frac{\mathrm{d}}{\mathrm{d}t}\langle\hat{\sigma}_1^+\rangle &= (-i\tilde{\delta} - \tilde{\gamma}_z/2)\langle\hat{\sigma}_1^+\rangle, \\
\frac{\mathrm{d}}{\mathrm{d}t}\langle\hat{\sigma}_1^+\hat{\sigma}_2^-\rangle &= -\tilde{\gamma}_z\langle\hat{\sigma}_1^+\hat{\sigma}_2^-\rangle, \\
\frac{\mathrm{d}}{\mathrm{d}t}\langle\hat{\sigma}_1^+\hat{\sigma}_2^+\rangle &= (-2i\tilde{\delta} - \tilde{\gamma}_z)\langle\hat{\sigma}_1^+\hat{\sigma}_2^+\rangle.
\end{aligned} \tag{5.87}$$

For the spin coherent state along x direction, the initial condition for interrogation would be $\langle\hat{\sigma}_1^+\rangle_{t=0} = 1/2$, $\langle\hat{\sigma}_1^+\hat{\sigma}_2^-\rangle_{t=0} = 1/4$, and $\langle\hat{\sigma}_1^+\hat{\sigma}_2^+\rangle_{t=0} = 1/4$, which gives

$$\langle\hat{S}^y\rangle = N\mathrm{Im}\langle\hat{\sigma}_1^+\rangle = -\frac{N}{2}\mathrm{e}^{-\tilde{\gamma}_z\tau/2}\sin\phi, \tag{5.88}$$

$$\begin{aligned}
\langle\hat{S}^y\hat{S}^y\rangle &= \frac{N}{4} + \frac{N(N-1)}{2}\mathrm{Re}\Big[\langle\hat{\sigma}_1^+\hat{\sigma}_2^-\rangle - \langle\hat{\sigma}_1^+\hat{\sigma}_2^+\rangle\Big] \\
&= \frac{N}{4} + \frac{N(N-1)}{8}\mathrm{e}^{-\tilde{\gamma}_z\tau}[1-\cos(2\phi)].
\end{aligned} \tag{5.89}$$

These results lead to the following sensitivity for gravity measurements

$$\frac{\Delta g}{g} = \frac{1}{\omega_g\sqrt{NT}}\sqrt{\frac{\mathrm{e}^{\tilde{\gamma}_z\tau}}{\tau}}. \tag{5.90}$$

If instead a spin squeezed state generated by one-axis twisting Hamiltonian $\hat{H}_{\mathrm{OAT}} = \chi\hat{S}^z\hat{S}^z$, followed by an additional rotation about x direction by an angle φ, is injected, the initial conditions

for phase interrogation are

$$\begin{aligned}
\langle\hat{\sigma}_1^+\rangle_{t=0} &= \frac{1}{2}\cos^{N-1}(\chi t_0),\\
\langle\hat{\sigma}_1^+\hat{\sigma}_2^-\rangle_{t=0} &= \frac{1}{8}\Big(1+\cos^{N-2}(2\chi t_0)\Big)+\frac{1}{8}\cos^2\varphi\Big(1-\cos^{N-2}(2\chi t_0)\Big)\\
&\quad-\frac{1}{2}\cos\varphi\sin\varphi\cos^{N-2}(\chi t_0)\sin(\chi t_0),\\
\langle\hat{\sigma}_1^+\hat{\sigma}_2^+\rangle_{t=0} &= \frac{1}{8}\Big(1+\cos^{N-2}(2\chi t_0)\Big)-\frac{1}{8}\cos^2\varphi\Big(1-\cos^{N-2}(2\chi t_0)\Big)\\
&\quad+\frac{1}{2}\cos\varphi\sin\varphi\cos^{N-2}(\chi t_0)\sin(\chi t_0).
\end{aligned} \tag{5.91}$$

So we get

$$\partial_\phi\langle\hat{S}^y\rangle_{\phi\to0} = -\frac{N}{2}\mathrm{e}^{-\tilde{\gamma}_z\tau/2}\cos^{N-1}(\chi t_0), \tag{5.92}$$

$$\langle\hat{S}^y\hat{S}^y\rangle_{\phi\to0} = \frac{N}{4}+N(N-1)\mathrm{e}^{-\tilde{\gamma}_z\tau}\left[\frac{1}{8}\cos^2\varphi\Big(1-\cos^{N-2}(2\chi t_0)\Big)-\frac{1}{2}\cos\varphi\sin\varphi\cos^{N-2}(\chi t_0)\sin(\chi t_0)\right]. \tag{5.93}$$

Using a Ramsey spin squeezing parameter defined as $\xi^2=\min_\varphi N(\Delta S_\varphi^\perp)^2/|\langle\mathbf{S}\rangle|^2$, after minimizing with respect to rotation angle φ one can calculate the following sensitivity of this state for gravity measurements,

$$\frac{\Delta g}{g}\approx\frac{1}{\omega_g\sqrt{NT}}\sqrt{\frac{\mathrm{e}^{\tilde{\gamma}_z\tau}-1+\xi^2}{\tau}}. \tag{5.94}$$

We will assume that $1/\tilde{\gamma}_z$ can be set to be 100 s in state-of-the-art experiments. In this case for unentangled initial states [see Eq. (5.90)], an interrogation time τ of the order of 10 s is possible, if other technical noises do not impose further constraints at this time scale. For the spin squeezed states [see Eq. (5.94)] with 20 dB metrological gain discussed in the main text, one would need to reduce the interrogation time $\tau\sim1$ s in order to retain the quantum advantage of the initial state. In this case, our protocol not only reduces the required averaging time by a factor of 10, but also increases the measurement bandwidth of time-varying signals by a factor of 10, compared to unentangled lattice-based interferometers.

5.3 Trade-offs between unitary and measurement induced spin squeezing in cavity QED

This section is adapted from: Diego Barberena, **Anjun Chu**, James K. Thompson, Ana Maria Rey, *Trade-offs between unitary and measurement induced spin squeezing in cavity QED*, Physical Review Research, in press (2024) [arXiv:2309.15353]

5.3.1 Introduction

Within the field of quantum metrology [6,7], spin squeezed states [30,31] constitute a concrete example of a quantum-enhanced resource with near-term practical applications. Their ability to measure spin rotations with a sensitivity that surpasses the standard quantum limit (SQL), i.e. the fundamental limit on phase estimation achievable with N uncorrelated particles, provides the opportunity for practical metrological gain in e.g. atomic clocks [14, 16], magnetometers [368–370] and matter-wave interferometers [15, 371, 372]. Consequently, schemes for efficient spin squeezing preparation [30, 354, 373], and experimental demonstrations in a variety of quantum platforms [14, 190, 340–342, 374–376] have attracted considerable attention.

Particularly promising strategies for the scalable generation of squeezing are provided by QED cavities, where a shared light field mediates all-to-all interactions among atoms inside of a cavity. When driven by an external laser, the resulting dispersive atomic response is nonlinear and can be interpreted as an infinite range unitary Ising interaction called one-axis-twising (OAT) [30]. This is known to create spin squeezing [30] and this specific drive-induced mechanism is known as cavity-feedback squeezing [14, 190, 376, 377]. On the other hand, after atoms and light interact, photons leaking out of the cavity carry information about the atomic ensemble [340–342] that can be accessed by continuously monitoring the output light via quantum non-demolition (QND) measurements [353, 354, 378]. Adequate use of this information allows for the estimation of the number of non-excited atoms, which decreases the noise of the state along the magnetization axis, leading to spin squeezing.

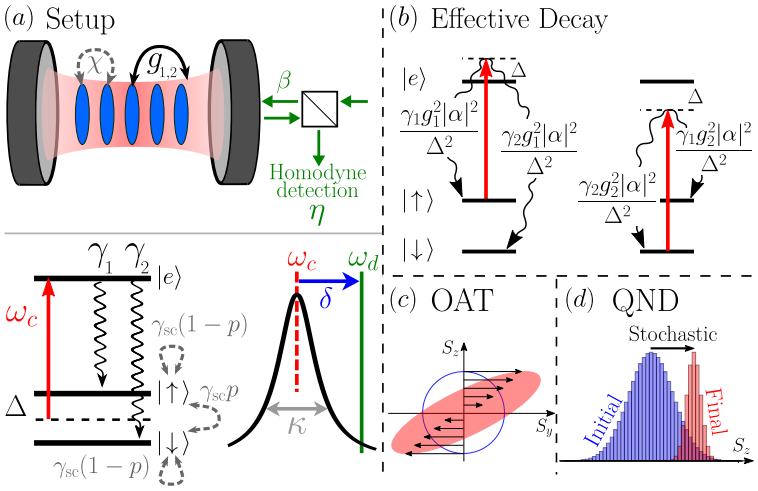

Figure 5.7: (a) Schematic of the model: a three level system interacting with a QED cavity, which is in turn driven by a laser. Output light is measured via homodyne detection with efficiency η. Dashed gray lines represent effective processes (χ, $\gamma_{\rm sc}$). (b) Effective single particle processes in ground manifold. (c) OAT dynamics shears the noise distribution, causing it to get squeezed. (d) Schematic of QND, showing pre (blue) and post (red) measurement distribution in the basis of $\hat{S}_z$.

In this work we examine the possible advantages of combining both methods of preparation. We employ a general analytical framework, analogous but distinct to the one presented in Ref. [379], that considers the effects of finite detection efficiency, and include from the outset fundamental sources of noise and dissipation. Our main result can be stated succinctly: when the detection efficiency of the QND measurement is above 0.19, QND outperforms OAT. Otherwise, the choice between QND or OAT depends on other experimentally relevant parameters such as spin flip probability, cavity cooperativity, and atom number [see Fig. 5.10(c) for details]. We also perform a systematic study of the area of the generated measurement noise, which negatively impacts the dynamical range and utility of the state for quantum-enhanced phase measurements [380].

5.3.2 Model

We begin with a simple model that exemplifies the physics that we are trying to describe [358] [see Fig. 5.7(a)]. We consider an ensemble of N atoms with three-levels: $|\uparrow\rangle$, $|\downarrow\rangle$ and $|e\rangle$ in the level configuration shown in Fig. 5.7(a). The excited state has a finite lifetime, and decays to $|\uparrow\rangle$ and $|\downarrow\rangle$ with rates γ_1 and γ_2, respectively. The atoms interact with a single mode of a single port

QED cavity, with resonance frequency ω_c, which is detuned from resonance with the $|\uparrow\rangle, |\downarrow\rangle \rightarrow |e\rangle$ transitions by $\pm\Delta$, as illustrated in Fig. 5.7(a). The cavity is in turn driven close to resonance by a laser tone at frequency ω_d [detuning $\delta = \omega_d - \omega_c$, see Fig. 5.7(a)] and input flux of $|\beta|^2$ photons per second, and.the transitions $|\uparrow\rangle, |\downarrow\rangle \leftrightarrow |e\rangle$ are coupled to the cavity with single photon Rabi frequencies $2g_1$ and $2g_2$, respectively. The light that comes out of the system can then be measured in a homodyne configuration with detection efficiency η.

Under conditions (to be stated later) that permit adiabatic elimination of the excited state $|e\rangle$ and the cavity degree of freedom, the system evolves under an effective Ito stochastic differential equation (see Ref. [69] and SOM),

$$\begin{aligned} d\hat{\rho} =& \left\{ -i\chi\left[\hat{S}_z^2, \hat{\rho}\right] + \Gamma\mathcal{L}_{\hat{S}_z}(\hat{\rho}) + \frac{\gamma_{sc}}{2}\sum_{k=1}^{N}\frac{(1-p)}{2}\mathcal{L}_{\hat{\sigma}_z^k}(\hat{\rho}) + p\left[\mathcal{L}_{\hat{\sigma}_+^k}(\hat{\rho}) + \mathcal{L}_{\hat{\sigma}_-^k}(\hat{\rho})\right]\right\} dt \\ &+ \sqrt{\Gamma\eta}\left(\hat{S}_z\hat{\rho} + \hat{\rho}\hat{S}_z - 2\langle\hat{S}_z\rangle\hat{\rho}\right) dW, \end{aligned} \tag{5.95}$$

where $\hat{S}_{x,y,z} = \sum_{k=1}^{N}\hat{\sigma}_{x,y,z}^k/2$ are collective spin operators acting on the ground manifold $|\uparrow\rangle, |\downarrow\rangle$, $\hat{\sigma}_{x,y,z}^k$ are Pauli matrices acting on atom k, and $\chi, \Gamma, \gamma_{\rm sc}, p$ are effective parameters related to experimental quantities (we will state their precise definition further on). Unitary dynamics is described by the parameter χ. Incoherent evolution is expressed in terms of Lindbladians $\mathcal{L}_{\hat{L}}(\hat{\rho}) \equiv \hat{L}^\dagger\hat{\rho}\hat{L} - \{\hat{L}^\dagger\hat{L}, \hat{\rho}\}/2$, and includes collective dephasing (Γ) and single particle spin conserving $[\gamma_{\rm sc}(1-p)]$ and spin changing ($\gamma_{\rm sc}p$) incoherent processes. The final line of Eq. (5.95) incorporates continuous measurement of $\hat{S}_z$ via homodyne detection (in an appropriately chosen quadrature) [69, 381] with efficiency η and includes a stochastic Wiener increment dW to model the probabilistic nature of quantum measurements. The output of the measurements is a time-dependent current $i(t) \equiv dq/dt = 2\sqrt{\Gamma\eta}\langle\hat{S}_z\rangle + dW/dt$.

To unpack the content of Eq. (5.95) in detail, we consider an initial condition where all atoms begin in the superposition $|\uparrow\rangle + |\downarrow\rangle$, which is relevant to experimental implementations and corresponds to a Bloch vector entirely polarized along the x direction, i.e. $\langle\hat{S}_x\rangle = N/2$. Furthermore, to obtain a manageable set of equations we use a large N approximation, in which the state remains gaussian, but relax these assumptions later. In this limit the Bloch vector

remains polarized along x but relaxes due to $\gamma_{\rm sc}$ according to $\langle \hat{S}_x \rangle = Ne^{-\gamma_{\rm sc} t/2}/2$. Fluctuations perpendicular to the Bloch vector satisfy (see Ref. [36, 382] and SOM)

$$\begin{aligned}
\dot{v}_{zz} &= -\Gamma\eta N v_{zz}^2 - 2\gamma_{\rm sc} p (v_{zz} - 1) \\
\dot{v}_{yy} &= 2\chi N v_{zy} e^{-\gamma_{\rm sc} t/2} + \Gamma N e^{-\gamma_{\rm sc} t} - \Gamma N \eta v_{zy}^2 - \gamma_{\rm sc}(v_{yy} - 1) \\
\dot{v}_{zy} &= \chi N e^{-\gamma_{\rm sc} t/2} v_{zz} - \Gamma\eta N v_{zz} v_{zy} - \frac{\gamma_{\rm sc}}{2}(2p+1) v_{zy},
\end{aligned} \tag{5.96}$$

where $v_{ab} = (2\langle\{\hat{S}_a, \hat{S}_b\}\rangle - 4\langle \hat{S}_a \rangle \langle \hat{S}_b \rangle)/N$ (for $a, b = z, y$) are (co)variances normalized to the spin projection noise. The equation for v_{zz} ($\propto \hat{S}_z$ variance) evolves under two competing effects: measurements ($\Gamma N \eta$) reveal information about the magnetization and thus reduce v_{zz} [see Fig. 5.7(d)]. On the other hand, spin flips ($\gamma_{\rm sc} p$) restore the variance to its initial uncorrelated value $v_{zz} = 1$. For v_{yy} ($\hat{S}_y$ variance), single particle processes ($\gamma_{\rm sc}$) also restore the variance to its uncorrelated value, but measurement backaction (ΓN) instead increases the variance. Furthermore, coherent interactions (χN) mix v_{yy} with v_{zy} and leave v_{zz} untouched, reflecting the shearing dynamics characteristic of OAT [see Fig. 5.7(c)] that leads to a noise distribution squeezed along an intermediate direction in the $\hat{S}_z/\hat{S}_y$ plane. Note that dW does not appear in these equations, indicating that the dynamics they describe does not depend on the specific measurement outcomes.

Measurements do introduce small stochastic corrections to the orientation of the Bloch vector that manifest as deflections in the yz plane. In a small time interval dt, these deflections satisfy (see SOM)

$$\begin{aligned}
dz &= -\gamma_{\rm sc} p\, z\, dt + \sqrt{\Gamma\eta N} v_{zz}\, dW \\
dy &= (\chi N e^{-\gamma_{\rm sc} t/2} z - \gamma_{\rm sc} y/2)\, dt + \sqrt{\Gamma\eta N} v_{zy}\, dW,
\end{aligned} \tag{5.97}$$

where $z = \langle \hat{S}_z \rangle / \sqrt{N/4}$ and $y = \langle \hat{S}_y \rangle / \sqrt{N/4}$. The measured current evolves according to $dq = \sqrt{\Gamma N \eta}\, z\, dt + dW$ and is connected to y and z through the common increment dW. To take advantage of the measurement process these deflections need to be calculated accurately using $i(t)$, since they are different for each measurement realization. Neglecting this information leads to an average state that is not squeezed in any directions.

The absolute scale for time is set by $\gamma_{\rm sc}$, which is the total scattering rate from the excited state induced by the probe [see Fig. 5.7(b)]:

$$\gamma_{\rm sc} = \frac{\gamma_1 g_1^2 |\alpha|^2}{\Delta^2} + \frac{\gamma_1 g_2^2 |\alpha|^2}{\Delta^2} + \frac{\gamma_2 g_1^2 |\alpha|^2}{\Delta^2} + \frac{\gamma_2 g_2^2 |\alpha|^2}{\Delta^2}, \tag{5.98}$$

where $|\alpha|^2 = \kappa|\beta|^2/(\delta_*^2 + \kappa^2/4)$ is the number of circulating photons in the cavity, found by multiplying the incident photon number, $|\beta|^2$ [See Fig. 1(a)], by the cavity buildup factor $\kappa/(\delta_*^2 + \kappa^2/4)$, and $\delta_* = \delta - (g_1^2 - g_2^2)N/2\Delta$ is the detuning of the drive with respect to the dressed cavity mode (see SOM). The rest of effective parameters can be expressed in terms of $\gamma_{\rm sc}$, $d = 2\delta_*/\kappa$ and $C = 4g_1^2/(\kappa\gamma_1) = 4g_2^2/(\kappa\gamma_2)$, the single particle cooperativity, which is a property of cavity geometry:

$$\chi = \frac{C\gamma_{\rm sc} d/2}{1+d^2}, \quad \Gamma = \frac{C\gamma_{\rm sc}}{1+d^2}, \quad p = \frac{2\gamma_1\gamma_2}{(\gamma_1+\gamma_2)^2} \leq \frac{1}{2}. \tag{5.99}$$

The spin flip probability p measures the relative importance of single particle spin changing processes relative to spin conserving processes, both of which arise through virtual excitation of the excited state and subsequent decay into the ground manifold [see Fig. 5.7(b)].

Cavity feedback squeezing arises when $\delta_* \gg \kappa$. Then $\chi \gg \Gamma$ and OAT dominates until single particle processes disrupt the generation of spin squeezing. QND measurements operate in the opposite regime, with $\delta_* = \chi = 0$ and Γ maximal. In the absence of $\gamma_{\rm sc}$, the resulting evolution continuously projects the system onto an $\hat{S}_z$ eigenstate, reducing the variance of $\hat{S}_z$ even beyond the gaussian limit [see Fig. 5.7(d)]. However, the precise eigenstate onto which the system is projected is stochastic and must be estimated accurately using the measurement record. Adiabatic elimination gives rise to Eq. (5.95) when $\Delta \gg \gamma_{1,2}, 2g_{1,2}|\alpha|, 2g_{1,2}\sqrt{N}$. These conditions guarantee that the excited state is never appreciably populated and that the atom-cavity interaction is dispersive.

5.3.3 Analysis of spin squeezing

Equations (5.96) must be solved with initial conditions $v_{zz}(0) = v_{yy}(0) = 1$ and $v_{zy}(0) = 0$. Within the gaussian regime, the evolution generates a noise distribution on the yz plane in the form of a ellipse whose axes have minimum (maximum) length $v_{\rm min}$ ($v_{\rm max}$) (see SOM), and in terms of

which we define

$$\xi^2 = e^{\gamma_{\rm sc} t} v_{\rm min}, \qquad A = e^{\gamma_{\rm sc} t} \sqrt{v_{\rm min} v_{\rm max}}. \tag{5.100}$$

The Wineland squeezing parameter ξ^2 [74] quantifies the metrological enhancement of phase measurements compared to uncorrelated atoms (SQL) and includes the effects of reduced contrast. The state area A measures the size of the noise distribution, normalized to the length of the Bloch vector squared. Under ideal evolution, ($\gamma_{\rm sc} = 0$ and $\eta = 1$), A remains of order 1, but loss of information leads to an area that can be substantially larger. An increase in A reduces the metrological utility of the generated squeezing since it limits the range of phases that can be measured with some degree of quantum enhancement [380].

Measurement limit: Here $\delta_* = \chi = 0$ and $\Gamma = C\gamma_{\rm sc}$. Assuming that $NC\eta \gg 1$, simple analytic solutions can be written for the fluctuations and the estimator of $\langle \hat{S}_z \rangle$ (see SOM). The minimum-variance axis lies along z, giving rise to a Wineland parameter of

$$\xi_t^2 = v_{zz} = \sqrt{\frac{2p}{NC\eta}}, \tag{5.101}$$

within the timescale $\tau = (NC\eta p)^{-1/2}/(2\gamma_{\rm sc})$, while v_{yy} grows as $1 + NC\gamma_{\rm sc} t$ and $v_{zy} = 0$. The subscript t in ξ_t^2 indicates that ξ^2 has been optimized over time. ξ^2 is depicted as a function of $s = \gamma_{\rm sc} t\sqrt{NC}/2$ for different values of NC in Fig. 5.8(a). Waiting for a few τ times gets ξ^2 closer to ξ_t^2, but waiting for too long leads to uncontrolled growth of v_{yy} and hence of state area. We show this in Fig. 5.8(b), where we plot A vs. ξ^2 parametrically as a function of time. The sharp upward turn in the curve indicates that A is growing without any improvement in ξ^2. Notice also that there are plateaus of constant $A = \eta^{-1/2}$, more visible at larger NC. In these plateaus spin flips are not yet active, so the decrease in $\hat{S}_z$ variance is exactly compensated by the increase in $\hat{S}_y$ variance.

Unitary limit: Here $\eta = 0$ and $\delta_* \gg \kappa$. All the relevant equations are now linear and can be solved exactly, but we consider the effects of $\gamma_{\rm sc} p$ on ξ^2 perturbatively. Assuming $\chi N t \gg 1$, this leads to (see Ref. [38] and SOM)

$$\xi^2 \approx \frac{1}{\chi^2 N^2 t^2} + \frac{\Gamma/\chi}{\chi N t} + \frac{2}{3}\gamma_{\rm sc} p t. \tag{5.102}$$

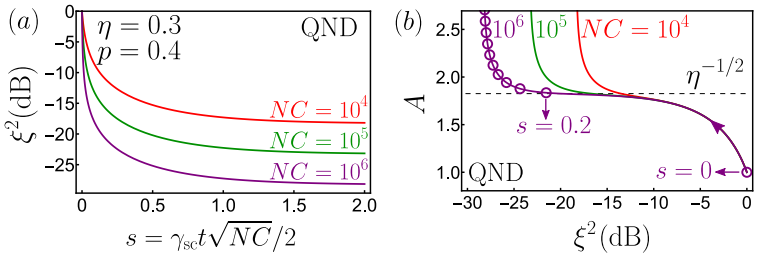

Figure 5.8: (a) Squeezing (ξ^2) as a function of time for various NC in the QND configuration. (b) QND squeezing vs. state area (A) plotted parametrically with time as a parameter. Circles are equally spaced in s intervals of size 0.2.

The first and second terms include the effects of interactions (χ) and collective dephasing (Γ), respectively. The third term is due to spin flips and is the main obstruction for unitary spin squeezing.

The behaviour of ξ_t^2 (time optimized squeezing) with d depends on whether collective dephasing (Γ) is active at the optimal squeezing time or not. If Γ is active, relevant for smaller values of d, then ξ_t^2 arises from the competition between the second and third terms in Eq. (5.102), leading to $\xi_t^2 = \xi_{t,\delta}^2\sqrt{1+1/d^2}$, where

$$\xi_{t,\delta}^2 = \sqrt{\frac{32p}{3NC}}, \tag{5.103}$$

is the best possible squeezing attainable in this region, obtained roughly at $d \geq 1$. This leads to a very broad minimum in ξ_t^2, depicted in Fig. 5.9(a) for various NC. This trend lasts until $d \approx 1.7(CN/p)^{1/4}$, after which Γ is no longer active, and ξ_t^2 now arises from the competition between the first and third terms in Eq. (5.102). Further increase in d worsens $\xi_t^2 \sim [pd/(NC)]^{2/3}$ (independent of κ) because interactions get smaller than the spin flip rate. The optimal squeezing is thus given by Eq. (5.103).

While the region of minimum ξ_t^2 is very broad in Fig. 5.9(a), the state area at each of these points is distinct. We show this in Fig. 5.9(b), where ξ_t^2 vs. A is plotted parametrically using $d = 2\delta_*/\kappa$ as a parameter for various NC. The leftmost vertical sections of the curves indicate the optimal $\xi_{t,\delta}^2$, but the variation in A is quite dramatic. It is preferable to work at larger values of d, potentially sacrificing a few dB of ξ_t^2 in exchange for a substantially smaller area, as has been

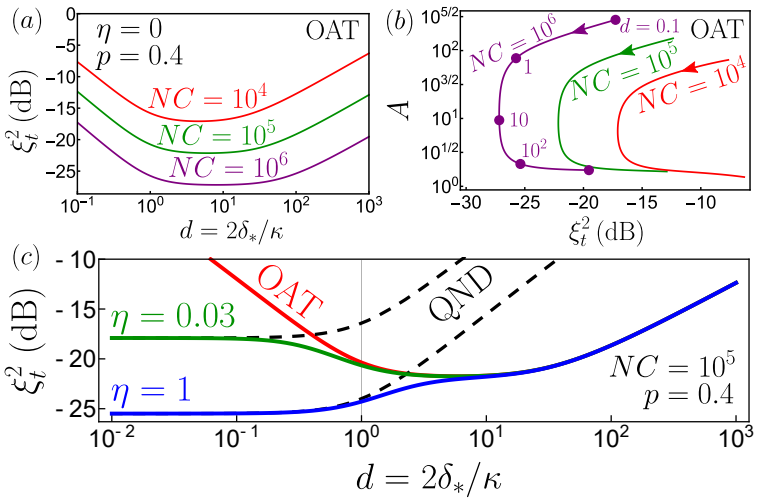

Figure 5.9: (a) Time optimized squeezing (ξ_t^2) as a function of detuning in the OAT configuration for various NC. (b) OAT squeezing vs. state area plotted parametrically with d as a parameter. Each filled circle occurs at a value of d 10 times bigger than the previous one. (c) Squeezing optimized over time as a function of d at fixed $p = 0.4$ and $NC = 10^5$ for different η. Solid red is OAT ($\eta = 0$) and dashed black is pure QND ($\hat{S}_z$ variance).

pointed out before [376, 377].

Measurement and unitary evolution: A natural question to ask is whether a combination of measurements and unitary evolution, operating at some finite value of d for a given $\eta \neq 0$, can improve upon the two limiting situations described in the previous sections.

In Fig. 5.9(c) we show the results of simulating numerically Eqs. (5.96), where at any given detuning d and η, squeezing has been optimized over time within a time window of $s \in [0, 50]$ (this accounts for the fact that at $\delta_* = 0$ the optimal is only reached asymptotically). From the curves shown for different η, it can be observed that ξ_t^2 is obtained either purely through measurement at $\delta_* = 0$ or in the unitary limit, where the value of η is irrelevant. Thus, the decision to use measurements vs. OAT is determined by the comparison between Eq. (5.101) and Eq. (5.103). They are equal when the efficiency η has the value

$$\eta_c \equiv \frac{3}{16} = 0.1875. \tag{5.104}$$

When $\eta > \eta_c$, measurements are efficient enough that operating at $\delta_* = 0$ is preferable. When $\eta < \eta_c$, unitary evolution will lead to a better ξ_t^2.

Absence of spin flips: In cycling transitions p is very close to 0 and the analysis based on Eqs. (5.96) is no longer applicable because the state evolves beyond the gaussian regime and gets distorted, thus introducing corrections (typically called "finite-size" or "curvature" effects) that limit the attainable spin squeezing. In the OAT setting ($\eta = 0$), this is remedied by solving Eqs. (5.96) with $p = 0$ and adding an extra curvature term to the minimum variance [30, 38, 383],

$$\xi^2 \approx e^{\gamma_{\rm sc} t}\left(\frac{e^{\gamma_{\rm sc} t} + \Gamma N t}{\chi^2 N^2 t^2} + \frac{\chi^4 N^4 t^4}{6N^2}\right). \tag{5.105}$$

A comparison with the analytical solution of Eq. (5.95) for $p = 0$ indicates that Eq. (5.105) captures accurately the time optimized ξ^2 (see SOM). Variations of N or C now have different effects on ξ^2, whereas previously they only appeared in the combination NC.

When $p = 0$, the time optimized ξ_t^2 shows three distinct behaviours as a function of detuning, depicted in Fig. 5.10(a). For $d < 2.3N^{1/3}$, collective dephasing is active, competes with the curvature term and leads to $\xi_t^2 \approx 2N^{-2/5}d^{-4/5}$ [383] and $A = 1.76N^{1/5}/d^{3/5}$. When $2.3N^{1/3} < d < 0.4CN^{2/3}$, the optimal squeezing arises from unitary dynamics, leading to the well-known OAT result $\xi_t^2 = 1.04N^{-2/3}$ [30] and $A = \sqrt{1.5}$, independent of d. For $d > 0.4CN^{2/3}$, the exponential prefactors are the main obstruction to squeezing, and lead to $\xi_t^2 \approx 6.8d^2/(N^2C^2)$ and $A \approx \sqrt{e}$. Furthermore, the existence of the OAT minimum imposes a restriction on the cooperativity: $C > 6N^{-1/3}$. Otherwise, the center region in Fig. 5.10(a) disappears.

As p is increased, the dependence of ξ_t^2 on d will switch from the one shown in Fig. 5.10(a) to the one depicted in Fig. 5.9(a). We can estimate this value of spin flip probability, which we denote as p_{c_1}, by equating the exact OAT result and Eq. (5.103):

$$p_{c_1} = \frac{0.1C}{N^{1/3}}. \tag{5.106}$$

In the QND setup ($d = 0$) at $p = 0$, the system will approach a state with no $\hat{S}_z$ variance in a timescale $\sim (\Gamma\eta)^{-1}$, but squeezing will be limited by loss of contrast. This is shown in Fig. 5.10(b), which is obtained by solving semi-analytically Eq. (5.95) (see SOM) for $p = d = 0$, $N = 100$ and averaging ξ^2 over different measurement trajectories. At the optimal time, the average squeezing

is

$$\xi_t^2 \approx \frac{e}{N\eta}\left(1+\frac{1}{C}\right), \tag{5.107}$$

calculated using the model depicted in Fig. 5.10(b) [dashed black, see SOM for derivation], which captures reasonably well the time development of the average ξ^2, though individual measurement trajectories may reach better values of ξ_t^2 when $C \gtrsim 1$ and $\eta \approx 1$ [see Fig 5.10(b), shaded area]. Equating Eq. (5.107) and Eq. (5.101) indicates that this minimum can be reached when $p < p_{c_2} = e^2(C+1)^2/(2NC\eta)$.

5.3.4 Summary and conclusions

These results form a coherent picture, summarized in terms of a few key statements, and shown schematically in Fig. 5.10(c) and (d).

- $\eta > 0.1875$: QND is better than OAT for any value of spin flip probability p.
- $\eta < 0.1875$: OAT dominates over QND for p close to 1/2. As p is reduced OAT saturates to the curvature-limited ideal minimum, but QND continues to improve according to Eq. (5.101). QND will outperform OAT when $p < p_{c_3} = 0.54C\eta/N^{1/3}$ (obtained by equating Eq. (5.101) and the squeezing at the ideal OAT minimum) as long as $\eta > 2.6(1+C^{-1})/N^{1/3}$ (obtained by equating Eq. (5.107) and the ideal OAT minimum). Otherwise OAT ourperforms QND for all p (not depicted in Fig. 5.10).

In SOM we discuss how our results can indeed be used to set bounds on the amount of squeezing achievable in experiments where our analysis applies [190, 340–342, 376, 384]. Our results should also apply to two tone QND schemes [385], which are more favourable for technical reasons but don't change fundamental scalings. Future research will involve the consequences of parking the cavity closer to atomic resonance [36, 376], comparisons with time-reversal based unitary protocols [358, 359, 386, 387] and including more complicated unitary dynamics (e.g. twist-and-turn, two-axis-twisting) [285, 388, 389] using the stochastic Schrödinger equation formalism. During com-

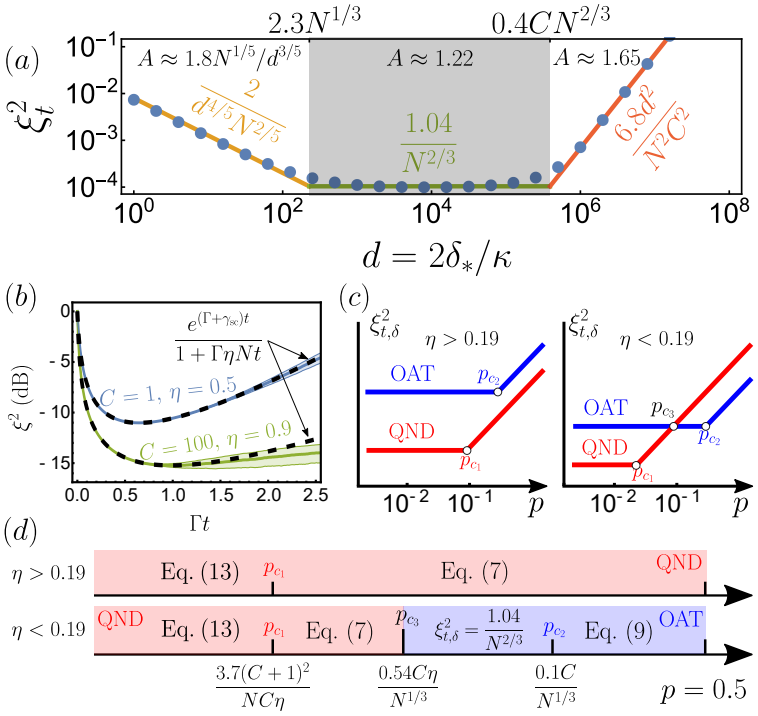

Figure 5.10: (a) Time optimized spin squeezing ξ_t^2 as a function of d when $p = 0$, $\eta = 0$, $C = 10^2$ and $N = 10^6$. (b) Time profile of ξ^2 for two values of (η, C) averaged over measurement realizations. Shaded areas indicate the dispersion of ξ^2 values over different individual measurements. Dashed black is an analytical model, with $\Gamma = C\gamma_{\rm sc}$. (c) Optimal spin squeezing for OAT and QND as a function of p for different η. (d) Summary of results.

pletion of this work we became aware of a related theory work examining the combination of OAT and QND in the context of Bose-Einstein condensates [390].

5.3.5 Supplemental Materials: Effective evolution equation

Here we show how to obtain Eq. (5.95) starting from the fundamental atom-light interaction inside a cavity. We consider N three-level atoms (levels $|e\rangle$, $|\downarrow\rangle$, $|\uparrow\rangle$ with energies ω_e, $\omega_\downarrow$ and $\omega_\uparrow$) in the configuration shown in Fig. 5.7(a). The atoms interact with one cavity mode at frequency ω_c, with single photon Rabi frequencies $2g_1$ and $2g_2$ for the transitions $|e\rangle \leftrightarrow |\uparrow\rangle$ and $|e\rangle \leftrightarrow |\downarrow\rangle$, respectively. The cavity has power decay linewidth κ, and the atoms spontaneously emit from $|e\rangle \rightarrow |\uparrow\rangle$ and from $|e\rangle \rightarrow |\downarrow\rangle$ with rates γ_1 and γ_2, respectively. Furthermore, the cavity is externally driven by a laser at frequency ω_d (close to ω_c) and with a flux of $|\beta|^2$ photons per second. The light escaping the cavity is then collected and subjected to homodyne detection with overall efficiency η. The evolution of the combined atom-light system in the presence of all these processes is described by the following stochastic differential equation

$$
\begin{aligned}
d\hat{\rho} = -i\Big[& \underbrace{\omega_e \hat{N}_e + \omega_\uparrow \hat{N}_\uparrow + \omega_\downarrow \hat{N}_\downarrow + \omega_c \hat{a}^\dagger \hat{a}}_{\hat{H}_{\text{free}}} + \underbrace{g_1(\hat{a}\hat{S}_{e\uparrow} + \text{h.c.}) + g_2(\hat{a}\hat{S}_{e\downarrow} + \text{h.c.})}_{\hat{H}_{\text{int}}} \\
& + \underbrace{\beta\sqrt{\kappa}(\hat{a}e^{i\omega_d t} + \text{h.c.})}_{\hat{H}_{\text{drive}}}, \hat{\rho}\Big]\, dt + \underbrace{\kappa\Big(\hat{a}\hat{\rho}\hat{a}^\dagger - \frac{\{\hat{a}^\dagger\hat{a}, \hat{\rho}\}}{2}\Big)}_{\text{photon leakage}}\, dt \\
& + \underbrace{\gamma_1 \sum_{i=1}^{N} \Big(\hat{\sigma}^i_{\uparrow e}\, \hat{\rho}\, \hat{\sigma}^i_{e\uparrow} - \frac{\{\hat{\sigma}^i_{ee}, \hat{\rho}\}}{2}\Big) dt + \gamma_2 \sum_{i=1}^{N} \Big(\hat{\sigma}^i_{\downarrow e}\, \hat{\rho}\, \hat{\sigma}^i_{e\downarrow} - \frac{\{\hat{\sigma}^i_{ee}, \hat{\rho}\}}{2}\Big) dt}_{\text{spontaneous emission}} \\
& + \underbrace{\sqrt{\kappa\eta}\Big(\hat{a}e^{-i\phi}\hat{\rho} + \hat{\rho}\hat{a}^\dagger e^{i\phi} - \langle \hat{a}e^{-i\phi} + \hat{a}^\dagger e^{i\phi}\rangle\, \hat{\rho}\Big)}_{\text{homodyne detection}}\, dW,
\end{aligned}
\tag{5.108}
$$

where $\hat{\rho}$ is the density matrix of the atom-light system, $\hat{\sigma}^i_{ab} = |a\rangle\langle b|_i$ $(a, b = e, \uparrow, \downarrow)$ is a single particle transition operator for atom i, $\hat{S}_{ab} = \sum_{i=1}^{N} \hat{\sigma}^i_{ab}$ is a collective transition operator, $\hat{N}_a = \hat{S}_{aa}$ is the "number of atoms in level a" operator, $\hat{a}^\dagger$ $(\hat{a})$ are bosonic creation (annihilation) operators for the cavity mode and ϕ is the homodyne detection angle, which is an experimentally adjustable parameter. The first line describes coherent evolution under a Hamiltonian that consists of three parts:

the free uncoupled evolution of atoms and cavity, the atom-light interaction (of Jaynes-Cummings type), and the external laser drive. The second line describes the dissipative processes: photon leakage and spontaneous emission from the excited state. The third line implements homodyne detection [69,381], which is intimately tied to photon leakage since these photons are the ones that are being measured.

Since the cavity is detuned from the $|\downarrow\rangle, |\uparrow\rangle \leftrightarrow |e\rangle$ by an amount $\pm\Delta$, the atom-light interaction becomes dispersive when $|\Delta| \gg g_{1,2}\sqrt{N}, g_{1,2}\sqrt{n_{\text{phot}}}$, where n_{phot} is the number of photons inside the cavity. We implement this mathematically by means of a Schrieffer-Wolff transformation. To be more precise, we define a dressed density matrix $\hat{\rho}_d = e^{\hat{W}}\,\hat{\rho}\,e^{-\hat{W}}$, where

$$\hat{W} = \frac{g_1}{\Delta}(\hat{a}^\dagger \hat{S}_{\uparrow e} - \hat{a}\hat{S}_{e\uparrow}) + \frac{g_2}{\Delta}(\hat{a}\hat{S}_{e\downarrow} - \hat{a}^\dagger \hat{S}_{\downarrow e}) \tag{5.109}$$

is the Schrieffer-Wolff generator (note $e^{\hat{W}}$ is unitary). The conditions $|\Delta| \gg g_{1,2}\sqrt{N}, g_{1,2}\sqrt{n_{\text{phot}}}$ then mean that $\hat{W}$ acts perturbatively in the states of interest. The evolution equation for $\hat{\rho}_d$ can then be written down by considering the following relations:

$$\begin{aligned}
e^{\hat{W}}(\hat{H}_{\text{free}} + \hat{H}_{\text{int}})e^{-\hat{W}} &= \hat{H}_{\text{free}} + \frac{g_1^2}{\Delta}[\hat{a}^\dagger\hat{a}(\hat{S}_{\uparrow\uparrow} - \hat{S}_{ee}) - \hat{S}_{e\uparrow}\hat{S}_{\uparrow e}] \\
&\quad - \frac{g_2^2}{\Delta}[\hat{a}^\dagger\hat{a}(\hat{S}_{\downarrow\downarrow} - \hat{S}_{ee}) - \hat{S}_{e\downarrow}\hat{S}_{\downarrow e}] + O(g_{1,2}^3/\Delta^2) \\
e^{\hat{W}}\,\hat{a}\,e^{-\hat{W}} &= \hat{a} + \frac{1}{\Delta}(g_2\hat{S}_{\downarrow e} - g_1\hat{S}_{\uparrow e}) + O(g_{1,2}^2/\Delta^2) \\
e^{\hat{W}}\,\hat{\sigma}^i_{\uparrow e}\,e^{-\hat{W}} &= \hat{\sigma}^i_{\uparrow e} + \frac{g_1\hat{a}}{\Delta}(\hat{\sigma}^i_{\uparrow\uparrow} - \hat{\sigma}^i_{ee}) - \frac{g_2\hat{a}}{\Delta}\hat{\sigma}^i_{\uparrow\downarrow} + O(g_{1,2}^2/\Delta^2) \\
e^{\hat{W}}\,\hat{\sigma}^i_{\downarrow e}\,e^{-\hat{W}} &= \hat{\sigma}^i_{\uparrow e} + \frac{g_2\hat{a}}{\Delta}(\hat{\sigma}^i_{\downarrow\downarrow} - \hat{\sigma}^i_{ee}) + \frac{g_1\hat{a}}{\Delta}\hat{\sigma}^i_{\downarrow\uparrow} + O(g_{1,2}^2/\Delta^2) \\
e^{\hat{W}}\,\hat{\sigma}^i_{ee}\,e^{-\hat{W}} &= \hat{\sigma}^i_{ee} + \frac{1}{\Delta}\Big[\hat{a}(g_1\hat{\sigma}^i_{e\uparrow} - g_2\hat{\sigma}^i_{e\downarrow}) + \hat{a}^\dagger(g_1\hat{\sigma}^i_{\uparrow e} - g_2\hat{\sigma}^i_{\downarrow e})\Big] \\
&\quad + \frac{\hat{a}^\dagger\hat{a}}{\Delta}\Big[g_1^2(\hat{\sigma}^i_{\uparrow\uparrow} - \hat{\sigma}^i_{ee}) + g_2^2(\hat{\sigma}^i_{\downarrow\downarrow} - \hat{\sigma}^i_{ee}) - g_1g_2(\hat{\sigma}^i_{\uparrow\downarrow} + \hat{\sigma}^i_{\downarrow\uparrow})\Big] \\
&\quad + \frac{1}{2\Delta}\Big[g_1g_2(\hat{\sigma}^i_{e\downarrow}\hat{S}_{\uparrow e} + \hat{\sigma}^i_{e\uparrow}\hat{S}_{\downarrow e}) - g_1^2\hat{\sigma}^i_{e\uparrow}\hat{S}_{\uparrow e} - g_2^2\hat{\sigma}^i_{e\downarrow}\hat{S}_{\downarrow e} + \text{ h.c.}\Big] + O(g_{1,2}^3/\Delta^3)
\end{aligned} \tag{5.110}$$

We have expanded the transformed operators only to the order that will be relevant for the evolution equation of $\hat{\rho}_d$. However, before writing this equation down we will point out a few features that will

allow us to simplify the result. First, single particle decoherence will now include terms of the form $\gamma_{1,2}g_1\hat{\sigma}^i_{e\uparrow}\hat{a}\hat{\rho}_d/\Delta, \gamma_{1,2}g_2\hat{\sigma}^i_{e\downarrow}\hat{a}\hat{\rho}_d/\Delta$ (and complex conjugates), which transfer atoms from the ground manifold to the excited state. However, they oscillate at frequency $\pm\Delta$ (due to $\hat{H}_{\text{free}}$) and can thus be neglected since they will effectively contribute corrections of size $\gamma_{1,2}^2 g^2/\Delta^3$ to the evolution equation. These terms become relevant when $\Delta \leq \gamma$ in which case a more refined treatment is required where both spontaneous emission and $\hat{H}_{\text{free}}$ are included as the zeroth order term of a dissipative Schrieffer-Wolff transformation. We do not attempt this since it is considerably more challenging to implement from a technical standpoint and is outside our regime of interest anyway, but this means that $\Delta \gtrsim \gamma$ is another assumption of our treatment. After neglecting these terms, the resulting equation will preserve the $|\uparrow\rangle, |\downarrow\rangle$ manifold. In the dressed basis, all atoms are in the ground states, and any admixture with $|e\rangle$ is taken care of by the dressing, which allows us to get rid of any term of the form $\hat{\sigma}^i_{\uparrow e}\hat{\rho}$, $\hat{\sigma}^i_{\downarrow e}\hat{\rho}$, $\hat{\sigma}^i_{ee}\hat{\rho}$ (and their complex conjugates). All these simplifications are generic after adiabatic elimination of $|e\rangle$. However, in the specific case we are considering, there is also a large energy difference between $|\uparrow\rangle$ and $|\downarrow\rangle$ of $\pm 2\Delta$. This means that terms of the form $\hat{\sigma}^i_{\uparrow\downarrow}\hat{\rho}_d\hat{\sigma}^i_{\uparrow\uparrow}$, $\hat{\sigma}^i_{\uparrow\downarrow}\hat{\rho}_d$ (and similar), which arise due to interfering decay pathways, oscillate very fast and can be neglected too. Taking all of this into consideration, the resulting equation for $\hat{\rho}_d$ is

$$
\begin{aligned}
d\hat{\rho}_d = -i\Big[&\omega_c\hat{a}^\dagger\hat{a} + \omega_\downarrow\hat{N}_\downarrow + \omega_\uparrow\hat{N}_\uparrow + \frac{(g_1^2-g_2^2)}{2\Delta}\hat{a}^\dagger\hat{a}\,N + \frac{g_1^2+g_2^2}{2\Delta}\hat{a}^\dagger\hat{a}\,(\hat{S}_{\uparrow\uparrow}-\hat{S}_{\downarrow\downarrow}) \\
&+ \beta\sqrt{\kappa}(\hat{a}e^{i\omega_d t} + \text{h.c.}), \hat{\rho}_d\Big]\,dt \\
&+ \frac{\gamma_1 g_1^2}{\Delta^2}\sum_{i=1}^{N}\Big(\hat{\sigma}^i_{\uparrow\uparrow}\hat{a}\,\hat{\rho}_d\,\hat{a}^\dagger\hat{\sigma}^i_{\uparrow\uparrow} - \frac{\{\hat{a}^\dagger\hat{a}\,\hat{\sigma}^i_{\uparrow\uparrow}, \hat{\rho}_d\}}{2}\Big)\,dt + \frac{\gamma_2 g_2^2}{\Delta^2}\sum_{i=1}^{N}\Big(\hat{\sigma}^i_{\downarrow\downarrow}\hat{a}\,\hat{\rho}_d\,\hat{a}^\dagger\hat{\sigma}^i_{\downarrow\downarrow} - \frac{\{\hat{a}^\dagger\hat{a}\,\hat{\sigma}^i_{\downarrow\downarrow}, \hat{\rho}_d\}}{2}\Big)\,dt \\
&+ \frac{\gamma_1 g_2^2}{\Delta^2}\sum_{i=1}^{N}\Big(\hat{\sigma}^i_{\uparrow\downarrow}\hat{a}\,\hat{\rho}_d\,\hat{a}^\dagger\hat{\sigma}^i_{\downarrow\uparrow} - \frac{\{\hat{a}^\dagger\hat{a}\,\hat{\sigma}^i_{\downarrow\downarrow}, \hat{\rho}_d\}}{2}\Big)\,dt + \frac{\gamma_2 g_1^2}{\Delta^2}\sum_{i=1}^{N}\Big(\hat{\sigma}^i_{\downarrow\uparrow}\hat{a}\,\hat{\rho}_d\,\hat{a}^\dagger\hat{\sigma}^i_{\uparrow\downarrow} - \frac{\{\hat{a}^\dagger\hat{a}\,\hat{\sigma}^i_{\uparrow\uparrow}, \hat{\rho}_d\}}{2}\Big)\,dt \\
&+ \kappa\Big(\hat{a}\hat{\rho}_d\hat{a}^\dagger - \frac{\{\hat{a}^\dagger\hat{a}, \hat{\rho}\}}{2}\Big)\,dt + \sqrt{\kappa\eta}\Big(\hat{a}e^{-i\phi}\hat{\rho}_d + \hat{\rho}_d\hat{a}^\dagger e^{i\phi} - \langle\hat{a}e^{-i\phi} + \hat{a}^\dagger e^{i\phi}\rangle\,\hat{\rho}_d\Big)\,dW.
\end{aligned}
\tag{5.111}
$$

Note that in the photon leakage, laser drive and homodyne detection terms, the leading order contribution is zeroth order in g/Δ. The single particle decoherence terms, which are $O(g^2/\Delta^2)$, describe off-resonant scattering of cavity light (hence the presence of the operators $\hat{a}$ and $\hat{a}^\dagger$) and

involve both spin flip and spin conserving processes. We also now define $\hat{S}_z = (\hat{S}_{\uparrow\uparrow} - \hat{S}_{\downarrow\downarrow})/2$ and $\hat{N}_g = \hat{S}_{\uparrow\uparrow} + \hat{S}_{\downarrow\downarrow}$ for notational simplicity. Furthermore, since we are considering only the ground manifold, we will now write $\hat{\sigma}^i_{\uparrow\uparrow} + \hat{\sigma}^i_{\downarrow\downarrow} = 1$.

The drive will establish a field inside the cavity that will depend on the drive-cavity detuning. However, the frequency of the cavity now depends on the state of the atoms, through the $\hat{a}^\dagger\hat{a}\,\hat{S}_z$ term, and will create an effective nonlinear atom-atom interaction. We take this into account perturbatively by analyzing fluctuations about the cavity field that would be established at the mean field level, taking into account that the average inversion is $\langle\hat{S}_z\rangle = 0$ for the initial conditions we want to consider [and it will remain so, as per Eq. (5.111)]. We thus define the fluctuation $\hat{b} = \hat{a} - \alpha e^{-i\omega_d t}$, where

$$\alpha = -\frac{i\sqrt{\kappa}\beta}{-i\delta_* + \kappa/2}, \tag{5.112}$$

and $\delta_* = \omega_d - \omega_c - (g_1^2 - g_2^2)N/(2\Delta)$. At this point it is convenient to move into the rotating frame of the drive. In this frame, and in terms of the fluctuation field $\hat{b}$, we approximately get

$$\begin{aligned}
d\hat{\rho}_d = &-i\Big[-\delta_*\hat{b}^\dagger\hat{b} + \frac{(\omega_\downarrow + \omega_\uparrow)}{2}\hat{N}_g + \Big(2\Delta + \frac{(g_1^2+g_2^2)|\alpha|^2}{\Delta}\Big)\hat{S}_z + \frac{(g_1^2+g_2^2)(\alpha\hat{b}^\dagger + \alpha^*\hat{b})\hat{S}_z}{\Delta}, \hat{\rho}_d\Big]\,dt \\
&+ \kappa\Big(\hat{b}\hat{\rho}_d\hat{b}^\dagger - \frac{\{\hat{b}^\dagger\hat{b}, \hat{\rho}\}}{2}\Big)\,dt + \frac{(\gamma_1 g_1^2 + \gamma_2 g_2^2)|\alpha|^2}{2\Delta^2}\sum_{i=1}^{N}\Big(\hat{\sigma}^i_{\uparrow\uparrow}\,\hat{\rho}_d\,\hat{\sigma}^i_{\uparrow\uparrow} + \hat{\sigma}^i_{\downarrow\downarrow}\,\hat{\rho}_d\,\hat{\sigma}^i_{\downarrow\downarrow} - \hat{\rho}_d\Big)\,dt \\
&+ \frac{\gamma_1 g_2^2|\alpha|^2}{\Delta^2}\sum_{i=1}^{N}\Big(\hat{\sigma}^i_{\uparrow\downarrow}\,\hat{\rho}_d\,\hat{\sigma}^i_{\downarrow\uparrow} - \frac{\{\hat{\sigma}^i_{\downarrow\downarrow}, \hat{\rho}_d\}}{2}\Big)\,dt + \frac{\gamma_2 g_1^2|\alpha|^2}{\Delta^2}\sum_{i=1}^{N}\Big(\hat{\sigma}^i_{\downarrow\uparrow}\,\hat{\rho}_d\,\hat{\sigma}^i_{\uparrow\downarrow} - \frac{\{\hat{\sigma}^i_{\uparrow\uparrow}, \hat{\rho}_d\}}{2}\Big)\,dt \\
&+ \sqrt{\kappa\eta}\Big(\hat{b}e^{-i\phi}\hat{\rho}_d + \hat{\rho}_d\hat{b}^\dagger e^{i\phi} - \langle\hat{b}e^{-i\phi} + \hat{b}^\dagger e^{i\phi}\rangle\,\hat{\rho}_d\Big)\,dW.
\end{aligned} \tag{5.113}$$

In the previous equation we have symmetrized the spin conserving single particle processes by using the relation $\hat{\sigma}^i_{\uparrow\uparrow} + \hat{\sigma}^i_{\downarrow\downarrow} = 1$, kept only the leading order terms (in $|\alpha|$) in the single particle decoherence contributions, and we have neglected $(g_1^2+g_2^2)\hat{b}^\dagger\hat{b}\,\hat{S}_z/\Delta$ in the Hamiltonian part, which is a nonlinear fluctuation term. It amounts to assuming that the quantum fluctuations in $\hat{b}$ that arise because of $\hat{S}_z$ are smaller than $|\alpha|$. We now adiabatically eliminate the cavity degree of freedom. This can be done by means of a dissipative Schrieffer-Wolff transformation (since κ and

δ may be comparable now), but the fastest way to obtain the result is by doing the replacement

$$\hat{b} \to -\frac{i(g_1^2+g_2^2)\alpha\hat{S}_z/\Delta}{-i\delta_* + \kappa/2}, \tag{5.114}$$

which is what a mean field treatment suggests will be the steady state intracavity field, on average. This leads to

$$\begin{aligned}
d\hat{\rho}_d = &-i\Big[\frac{(\omega_\downarrow+\omega_\uparrow)}{2}\hat{N}_g + \Big(2\Delta + \frac{(g_1^2+g_2^2)|\beta|^2}{\Delta}\Big)\hat{S}_z + \Big(\frac{(g_1^2+g_2^2)|\alpha|}{\Delta}\Big)^2\frac{\delta_*\,\hat{S}_z^2}{\delta_*^2+(\kappa/2)^2}, \hat{\rho}_d\Big]\,dt \\
&+ \Big(\frac{(g_1^2+g_2^2)|\alpha|}{\Delta}\Big)^2\frac{\kappa}{\delta_*^2+(\kappa/2)^2}\Big(\hat{S}_z\hat{\rho}_d\hat{S}_z - \frac{\{\hat{S}_z^2,\hat{\rho}\}}{2}\Big)\,dt \\
&+ \frac{\gamma_1 g_2^2|\alpha|^2}{\Delta^2}\sum_{i=1}^{N}\Big(\hat{\sigma}^i_{\uparrow\downarrow}\,\hat{\rho}_d\,\hat{\sigma}^i_{\downarrow\uparrow} - \frac{\{\hat{\sigma}^i_{\downarrow\downarrow},\hat{\rho}_d\}}{2}\Big)\,dt + \frac{\gamma_2 g_1^2|\alpha|^2}{\Delta^2}\sum_{i=1}^{N}\Big(\hat{\sigma}^i_{\downarrow\uparrow}\,\hat{\rho}_d\,\hat{\sigma}^i_{\uparrow\downarrow} - \frac{\{\hat{\sigma}^i_{\uparrow\uparrow},\hat{\rho}_d\}}{2}\Big)\,dt \\
&+ \frac{(\gamma_1 g_1^2+\gamma_2 g_2^2)|\alpha|^2}{2\Delta^2}\sum_{i=1}^{N}\Big(\hat{\sigma}^i_{\uparrow\uparrow}\,\hat{\rho}_d\,\hat{\sigma}^i_{\uparrow\uparrow} + \hat{\sigma}^i_{\downarrow\downarrow}\,\hat{\rho}_d\,\hat{\sigma}^i_{\downarrow\downarrow} - \hat{\rho}_d\Big)\,dt \\
&+ \sqrt{\Big(\frac{(g_1^2+g_2^2)|\alpha|}{\Delta}\Big)^2\frac{\kappa\eta}{\delta_*^2+(\kappa/2)^2}}\Big(\hat{S}_z\hat{\rho}_d + \hat{\rho}_d\hat{S}_z - 2\,\langle\hat{S}_z\rangle\,\hat{\rho}_d\Big)\,dW.
\end{aligned} \tag{5.115}$$

At this point it is convenient to introduce the parameters

$$\begin{aligned}
C &= \frac{4g_1^2}{\kappa\gamma_1} = \frac{4g_2^2}{\kappa\gamma_2} \\
\gamma_{\rm sc} &= \frac{\gamma_1 g_1^2|\alpha|^2}{\Delta^2} + \frac{\gamma_1 g_2^2|\alpha|^2}{\Delta^2} + \frac{\gamma_2 g_1^2|\alpha|^2}{\Delta^2} + \frac{\gamma_2 g_2^2|\alpha|^2}{\Delta^2} = \frac{(\gamma_1+\gamma_2)(g_1^2+g_2^2)|\alpha|^2}{\Delta} \\
p &= \frac{\gamma_1 g_2^2+\gamma_2 g_1^2}{(\gamma_1+\gamma_2)(g_1^2+g_2^2)} = \frac{2\gamma_1\gamma_2}{(\gamma_1+\gamma_2)^2}.
\end{aligned} \tag{5.116}$$

The cooperativity C is a property of cavity geometry. Its existence implies that $g_2^2/\gamma_2 = g_1^2/\gamma_1$ and hence that the rates of the $\hat{\sigma}^i_{\uparrow\downarrow}$ and $\hat{\sigma}^i_{\downarrow\uparrow}$ processes are equal. The parameter $\gamma_{\rm sc}$ is the total scattering rate of photons off the drive and is the sum of the rates of all single particle processes, and p is the spin flip probability, which is defined as the ratio between the sum of the rates of the $\hat{\sigma}^i_{\uparrow\downarrow}$ and $\hat{\sigma}^i_{\downarrow\uparrow}$ processes and $\gamma_{\rm sc}$. We have also made a specific choice of homodyne angle, $\phi = 2\arctan(2\delta/\kappa) - \pi$, to guarantee maximum measurement strength. To simplify notation, we define

$$\chi = \Big(\frac{(g_1^2+g_2^2)|\alpha|}{\Delta}\Big)^2\frac{\delta_*}{\delta_*^2+(\kappa/2)^2} = \frac{C\gamma_{\rm sc}d/2}{d^2+1}, \qquad \Gamma = \Big(\frac{(g_1^2+g_2^2)|\alpha|}{\Delta}\Big)^2\frac{\kappa}{\delta_*^2+(\kappa/2)^2} = \frac{C\gamma_{\rm sc}}{1+d^2}, \tag{5.117}$$

and we have decided to express the effective parameters χ and Γ in terms of C, $\gamma_{\rm sc}$ and $d = 2\delta_*/\kappa$. Omitting single particle rotation terms, we can thus express the evolution of the system in terms of the effective equation

$$d\hat{\rho}_d = -i\Big[\chi\hat{S}_z^2, \hat{\rho}_d\Big]\,dt + \Gamma\Big(\hat{S}_z\hat{\rho}_d\hat{S}_z - \frac{\{\hat{S}_z^2, \hat{\rho}\}}{2}\Big)\,dt + \frac{\gamma_{\rm sc}p}{2}\sum_{i=1}^{N}\Big(\hat{\sigma}^i_{\uparrow\downarrow}\,\hat{\rho}_d\,\hat{\sigma}^i_{\downarrow\uparrow} + \hat{\sigma}^i_{\downarrow\uparrow}\,\hat{\rho}_d\,\hat{\sigma}^i_{\uparrow\downarrow} - \hat{\rho}_d\Big)\,dt$$
$$+ \frac{\gamma_{\rm sc}(1-p)}{2}\sum_{i=1}^{N}\Big(\hat{\sigma}^i_{\uparrow\uparrow}\,\hat{\rho}_d\,\hat{\sigma}^i_{\uparrow\uparrow} + \hat{\sigma}^i_{\downarrow\downarrow}\,\hat{\rho}_d\,\hat{\sigma}^i_{\downarrow\downarrow} - \hat{\rho}_d\Big)\,dt + \sqrt{\Gamma\eta}\Big(\hat{S}_z\hat{\rho}_d + \hat{\rho}_d\hat{S}_z - 2\,\langle\hat{S}_z\rangle\,\hat{\rho}_d\Big)\,dW. \tag{5.118}$$

Equations (5.118) and (5.117) are the same as Eq. (5.95) and Eq. (5.99) in the main text once we replace $\hat{\sigma}_{\uparrow\downarrow} = \hat{\sigma}^+$, $\hat{\sigma}_{\downarrow\uparrow} = \hat{\sigma}^-$, $\hat{\sigma}_{\uparrow\uparrow} = (1+\hat{\sigma}_z)/2$ and $\hat{\sigma}_{\downarrow\downarrow} = (1-\hat{\sigma}_z)/2$.

We also summarize here the assumptions that went into this derivation. First $\Delta \gg \gamma, g_{1,2}\sqrt{N}$, $g_{1,2}|\alpha|$ ($|\alpha|^2$ is the number of photons in the cavity) for the elimination of the the excited state. Then $|\alpha|^2 \gg \langle\hat{b}^\dagger\hat{b}\rangle$ to treat the resulting dispersive atom-light interaction perturbatively during adiabatic elimination of the cavity. This translates into

$$\frac{(g_1^2+g_2^2)\sqrt{\langle\hat{S}_z^2\rangle}}{\Delta\sqrt{\delta_*^2+(\kappa/2)^2}} < \frac{2(g_1^2+g_2^2)\sqrt{\langle\hat{S}_z^2\rangle}}{\Delta\kappa} \ll 1 \to C\sqrt{\langle\hat{S}_z^2\rangle} \ll \frac{\Delta}{(\gamma_1+\gamma_2)/2}. \tag{5.119}$$

We have considered the worst case scenario with $\delta_* = 0$ since this is relevant for QND measurements. For the initial conditions we are considering, $\langle\hat{S}_z^2\rangle \sim N$, so this assumption becomes $NC \ll \Delta\sqrt{N}/(\gamma_1+\gamma_2)$. A violation of this condition indicates that quantum fluctuations are strong enough that the relation between the adiabatically eliminated $\hat{b}$ and $\hat{S}_z$ can no longer be captured by the simple linear relation Eq. (5.114) and a nonlinear approximation is required [358].

5.3.6 Supplemental Materials: Large N equations for first and second order correlators

Here we compute the evolution equations for relevant observables. We calculate things exactly as much as possible, and apply approximations only in the end. The equations for linear observables are obtained by multiplying Eq. (5.95) with the appropriate operator and tracing the result. First

we do averages of $\hat{S}_{x,y,z}$,

$$
\begin{aligned}
d\langle\hat{S}_x\rangle &= \Big[-\chi\langle\{\hat{S}_z,\hat{S}_y\}\rangle - \frac{\Gamma}{2}\langle\hat{S}_x\rangle - \frac{\gamma_{\rm sc}}{2}\langle\hat{S}_x\rangle\Big]dt + \sqrt{\Gamma\eta}\Big[\langle\{\hat{S}_x,\hat{S}_z\}\rangle - 2\langle\hat{S}_x\rangle\langle\hat{S}_z\rangle\Big]dW \\
d\langle\hat{S}_y\rangle &= \Big[\chi\langle\{\hat{S}_z,\hat{S}_x\}\rangle - \frac{\Gamma}{2}\langle\hat{S}_y\rangle - \frac{\gamma_{\rm sc}}{2}\langle\hat{S}_y\rangle\Big]dt + \sqrt{\Gamma\eta}\Big[\langle\{\hat{S}_y,\hat{S}_z\}\rangle - 2\langle\hat{S}_y\rangle\langle\hat{S}_z\rangle\Big]dW \\
d\langle\hat{S}_z\rangle &= -\gamma_{\rm sc}p\langle\hat{S}_z\rangle\,dt + 2\sqrt{\Gamma\eta}\Big[\langle\hat{S}_z^2\rangle - \langle\hat{S}_z\rangle\langle\hat{S}_z\rangle\Big]dW,
\end{aligned}
\tag{5.120}
$$

where $\{\}$ is the anticommutator. Relevant two-point correlators are

$$
\begin{aligned}
d\langle\hat{S}_z^2\rangle &= -2\gamma_{\rm sc}p\Big[\langle\hat{S}_z\rangle^2 - \frac{N}{4}\Big]dt + 2\sqrt{\Gamma\eta}\Big[\langle\hat{S}_z^3\rangle - \langle\hat{S}_z^2\rangle\langle\hat{S}_z\rangle\Big]dW, \\
d\langle\{\hat{S}_z,\hat{S}_y\}\rangle &= \Big[2\chi\langle\{\hat{S}_z,\{\hat{S}_z,\hat{S}_x\}\}\rangle - \frac{\Gamma}{2}\langle\{\hat{S}_z,\hat{S}_y\}\rangle - \gamma_{\rm sc}(p+1/2)\langle\{\hat{S}_z,\hat{S}_y\}\rangle\Big]dt \\
&\qquad + \sqrt{\Gamma\eta}\Big[\langle\{\hat{S}_z,\{\hat{S}_z,\hat{S}_y\}\}\rangle - 2\langle\{\hat{S}_z,\hat{S}_y\}\rangle\langle\hat{S}_z\rangle\Big]dW \\
d\langle\hat{S}_y^2\rangle &= \Big[\chi\langle\{\hat{S}_y,\{\hat{S}_z,\hat{S}_x\}\}\rangle + \Gamma\langle\hat{S}_x^2\rangle - \Gamma\langle\hat{S}_y^2\rangle - \gamma_{\rm sc}\Big(\langle\hat{S}_y^2\rangle - N/4\Big)\Big]dt \\
&\qquad + \sqrt{\Gamma\eta}\Big[\langle\{\hat{S}_z,\hat{S}_y^2\}\rangle - 2\langle\hat{S}_z\rangle\langle\hat{S}_y^2\rangle\Big]dW
\end{aligned}
\tag{5.121}
$$

We can obtain exact equations for variances and covariances, keeping in mind the product rule $d(ab) = adb + bda + da\,db$ and the Ito rules $dW^2 = dt$, $dtdW = dt^2 = 0$ to get the right stochastic equations. Thus

$$
\begin{aligned}
d\,{\rm Var}(\hat{S}_z) &= \Big[-4\Gamma\eta\,{\rm Var}(\hat{S}_z)^2 - 2\gamma_{\rm sc}p\Big({\rm Var}(\hat{S}_z) - \frac{N}{4}\Big)\Big]dt \\
&\qquad + 2\sqrt{\Gamma\eta}\Big[\langle\hat{S}_z^3\rangle - 3\langle\hat{S}_z^2\rangle\langle\hat{S}_z\rangle + 2\langle\hat{S}_z\rangle^3\Big]dW \\
d\,{\rm Cov} &= \Big(\frac{\chi}{2}\Big[\langle\{\{\hat{S}_x,\hat{S}_z\},\hat{S}_z\}\rangle - 2\langle\hat{S}_z\rangle\langle\{\hat{S}_x,\hat{S}_z\}\rangle\Big] - 4\Gamma\eta{\rm Var}(\hat{S}_z)\,{\rm Cov} \\
&\qquad - \Big[\frac{\Gamma}{2} + \gamma_{\rm sc}(p+1/2)\Big]{\rm Cov}\Big)dt + \frac{\sqrt{\Gamma\eta}}{2}\Big[\langle\{\hat{S}_z,\{\hat{S}_y,\hat{S}_z\}\}\rangle - 4\langle\{\hat{S}_z,\hat{S}_y\}\rangle\langle\hat{S}_z\rangle \\
&\qquad - 4\langle\hat{S}_y\rangle\langle\hat{S}_z^2\rangle + 8\langle\hat{S}_y\rangle\langle\hat{S}_z\rangle^2\Big]dW \\
d\,{\rm Var}(\hat{S}_y) &= \Big(\chi\Big[\langle\{\hat{S}_y,\{\hat{S}_z,\hat{S}_x\}\}\rangle - 2\langle\hat{S}_y\rangle\langle\{\hat{S}_z,\hat{S}_x\}\rangle\Big] + \Gamma\Big[\langle\hat{S}_x^2\rangle - {\rm Var}(\hat{S}_y)\Big] - \gamma_{\rm sc}\Big[{\rm Var}(\hat{S}_y) - N/4\Big] \\
&\qquad - 4\Gamma\eta\,{\rm Cov}^2\Big)dt + \sqrt{\Gamma\eta}\Big[\langle\{\hat{S}_y^2,\hat{S}_z\}\rangle - 2\langle\hat{S}_z\rangle\langle\hat{S}_y^2\rangle - 2\langle\hat{S}_y\rangle\langle\{\hat{S}_y,\hat{S}_z\}\rangle \\
&\qquad + 4\langle\hat{S}_y\rangle^2\langle\hat{S}_z\rangle\Big]dW,
\end{aligned}
\tag{5.122}
$$

where Var and Cov $= \langle\{\hat{S}_z, \hat{S}_y\}\rangle/2 - \langle\hat{S}_y\rangle\langle\hat{S}_z\rangle$ are short-hands for variance and the YZ covariance, respectively. We now begin with the large N approximation. To apply it, we define the mean field equations of motion, obtained by replacing $(\langle\hat{S}_x\rangle, \langle\hat{S}_y\rangle, \langle\hat{S}_z\rangle) \to N(X,Y,Z)/2$ and $(\langle\hat{S}_z^2\rangle, \langle\{\hat{S}_z, \hat{S}_y\}\rangle, \langle\{\hat{S}_z, \hat{S}_x\}\rangle) \to N^2(Z^2, 2YZ, 2XZ)/4$ (factorization), where X, Y, Z are functions of time. This results in

$$\dot{X} = -\chi NYZ - \frac{\gamma_{\rm sc}}{2}X, \qquad \dot{Y} = \chi NXZ - \frac{\gamma_{\rm sc}}{2}Y, \qquad \dot{Z} = -\gamma_{\rm sc}pZ, \tag{5.123}$$

where we have further neglected $\Gamma \ll \Gamma N$, since it is of higher order in the $1/N$ expansion. By keeping $\gamma_{\rm sc}$ we are implicitly assuming that $\gamma_{\rm sc} > \Gamma$. This is not necessarily always the case, especially when the single particle cooperativity $C \sim 1$. However, in all cases $\gamma_{\rm sc}$ is the obstruction to squeezing, and so we will always keep it. The mean field equations, together with initial conditions $X(0) = 1, Y(0) = Z(0) = 0$ result in $X = e^{-\gamma_{\rm sc}t/2}, Y = Z = 0$. We define the deviations from mean field $(\delta\hat{S}_x, \delta\hat{S}_y, \delta\hat{S}_z) = (\hat{S}_x - Ne^{-\gamma_{\rm sc}t}/2, \hat{S}_y, \hat{S}_z)$. In the large N limit, fluctuations and standard deviations are typically of size $\sqrt{N}$, so we further define $[v_{zz}, v_{zy}, v_{yy}] = 4[\mathrm{Var}(\hat{S}_z), \mathrm{Cov}, \mathrm{Var}(\hat{S}_y)]/N$ and $(\hat{x}, \hat{y}, \hat{z}) = 2(\delta\hat{S}_x, \delta\hat{S}_y, \delta\hat{S}_z)/\sqrt{N}$. Initially, all of these quantities are ~ 1, so we expect that this will remain so for some time. In terms of these definitions (but still working exactly),

$$\begin{aligned}
d\langle\hat{x}\rangle &= \Big[-\frac{\chi\sqrt{N}}{2}\langle\{\hat{z}, \hat{y}\}\rangle - \frac{\Gamma\sqrt{N}e^{-\gamma_{\rm sc}t/2}}{2} - \frac{\Gamma}{2}\langle\hat{x}\rangle - \frac{\gamma_{\rm sc}}{2}\langle\hat{x}\rangle\Big]\,dt + \frac{\sqrt{\Gamma N\eta}}{2}\Big[\langle\{\hat{x}, \hat{z}\}\rangle - 2\langle\hat{x}\rangle\langle\hat{z}\rangle\Big] \\
d\langle\hat{y}\rangle &= \Big[\chi Ne^{-\gamma_{\rm sc}t/2}\langle\hat{z}\rangle - \frac{\gamma_{\rm sc}}{2}\langle\hat{y}\rangle + \frac{\chi\sqrt{N}}{2}\langle\{\hat{z}, \hat{x}\}\rangle - \frac{\Gamma}{2}\langle\hat{y}\rangle\Big]\,dt + \sqrt{\Gamma N\eta}\,v_{zy}\,dW \\
d\langle\hat{z}\rangle &= -\gamma_{\rm sc}p\,\langle\hat{z}\rangle\,dt + \sqrt{\Gamma N\eta}\,v_{zz}\,dW
\end{aligned} \tag{5.124}$$

and

$$
\begin{aligned}
dv_{zz} &= \Big[-\Gamma N\eta v_{zz}^2 - 2\gamma_{\rm sc} p(v_{zz}-1)\Big]\, dt + \sqrt{\Gamma N\eta}\Big[\langle \hat{z}^3\rangle - 3\langle \hat{z}^2\rangle \langle \hat{z}\rangle + 2\langle \hat{z}\rangle^3 \Big]\, dW \\
dv_{zy} &= \Big(\chi N e^{-\gamma_{\rm sc} t/2} v_{zz} - \Gamma N v_{zz} v_{zy} - \gamma_{\rm sc}(p+1/2) v_{zy} + \frac{\chi\sqrt{N}}{4}\Big[\langle\{\{\hat{x},\hat{z}\},\hat{z}\}\rangle - 2\langle \hat{z}\rangle \langle\{\hat{x},\hat{z}\}\rangle \Big] \\
&\qquad - \frac{\Gamma}{2} v_{zy}\Big)\, dt + \frac{\sqrt{\Gamma\eta N}}{4}\Big[\langle\{\hat{z},\{\hat{y},\hat{z}\}\}\rangle - 4\langle\{\hat{z},\hat{y}\}\rangle\langle\hat{z}\rangle - 4\langle\hat{y}\rangle\langle\hat{z}^2\rangle + 8\langle\hat{y}\rangle\langle\hat{z}\rangle^2 \Big]\, dW \\
dv_{yy} &= \Big(2\chi N e^{-\gamma_{\rm sc} t/2} v_{zy} + \Gamma N e^{-\gamma_{\rm sc} t} - \gamma_{\rm sc}(v_{yy}-1) - \Gamma N\eta v_{zy}^2 \\
&\quad + \frac{\chi\sqrt{N}}{2}\Big[\langle\{\hat{y},\{\hat{z},\hat{x}\}\}\rangle - 2\langle\hat{y}\rangle\langle\{\hat{z},\hat{x}\}\rangle \Big] + 2\Gamma\sqrt{N} e^{-\gamma_{\rm sc} t/2}\langle\hat{x}\rangle + \Gamma\langle\hat{x}\rangle^2 - \Gamma\langle\hat{y}^2\rangle + \Gamma\langle\hat{y}\rangle^2 \Big)\, dt \\
&\quad + \frac{\sqrt{\Gamma\eta N}}{2}\Big[\langle\{\hat{y}^2,\hat{z}\}\rangle - 2\langle\hat{z}\rangle\langle\hat{y}^2\rangle - 2\langle\hat{y}\rangle\langle\{\hat{y},\hat{z}\}\rangle + 4\langle\hat{y}\rangle^2\langle\hat{z}\rangle \Big]\, dW
\end{aligned}
\tag{5.125}
$$

Note that $\langle\hat{z}\rangle$ and $\langle\hat{y}\rangle$ are not zero since they are fluctuations with respect to the mean field values, not with respect to the true mean values of $\hat{z},\hat{y}$. The reason for this choice is that it makes the relative N-dependent size of various quantities more transparent. So far Eq. (5.124) and Eq. (5.125) are exact given that they are just rewritings. In the large N limit we omit terms $\propto \chi\sqrt{N}, \Gamma\sqrt{N}, \Gamma \ll \chi N, \Gamma N$. The resulting evolution equations preserve gaussianity. Since the initial state is gaussian, the stochastic terms in the equations for v_{zz}, v_{zy}, v_{yy} drop out. We are thus led to

$$
\begin{aligned}
\dot{v}_{zz} &= -\Gamma N\eta v_{zz}^2 - 2\gamma_{\rm sc} p(v_{zz}-1), \quad dz = -\gamma_{\rm sc} pz dt + \sqrt{\Gamma N\eta} v_{zz}\, dW \\
\dot{v}_{yz} &= \chi N e^{-\gamma_{\rm sc} t/2} - \Gamma N v_{zz} v_{zy} - \gamma_{\rm sc}(p+1/2) v_{zy}, \quad dy = \Big(\chi N e^{-\gamma_{\rm sc} t/2} z - \frac{\gamma_{\rm sc}}{2} y\Big)\, dt + \sqrt{\Gamma N\eta} v_{zy}\, dW \\
\dot{v}_{yy} &= 2\chi N e^{-\gamma_{\rm sc} t/2} v_{zy} + \Gamma N e^{-\gamma_{\rm sc} t} - \Gamma N\eta v_{zy}^2 - \gamma_{\rm sc}(v_{yy}-1),
\end{aligned}
\tag{5.126}
$$

which are Eq. (5.96) and Eq. (5.97) in the main text, with $z = \langle\hat{z}\rangle$, $y = \langle\hat{y}\rangle$ and $\langle\hat{S}_x\rangle = \frac{N}{2} e^{-\gamma_{\rm sc} t/2}$. At the same time, the measurement record becomes

$$
dq = 2\sqrt{\Gamma\eta}\,\langle\hat{S}_z\rangle\, dt + dW = \sqrt{\Gamma N\eta}\, z\, dt + dW. \tag{5.127}
$$

5.3.7 Supplemental Materials: Spin squeezing from second order correlators

To leading order in N, the Bloch vector is pointing along $+x$ with length $Ne^{-\gamma_{\rm sc} t/2}/2$. We thus need to consider fluctuations along the y and z directions. To be more specific, we define the

matrix

$$\begin{pmatrix} v_{zz} & v_{zy} \\ v_{zy} & v_{yy} \end{pmatrix}. \tag{5.128}$$

The minimal and maximal variances are, respectively, the smallest and largest eigenvalues of this matrix:

$$v_{\min} = \frac{v_{zz}+v_{yy}}{2} - \sqrt{\frac{(v_{zz}-v_{yy})^2}{4} + v_{zy}^2}, \quad v_{\max} = \frac{v_{zz}+v_{yy}}{2} + \sqrt{\frac{(v_{zz}-v_{yy})^2}{4} + v_{zy}^2}, \tag{5.129}$$

and the normalization we have chosen for v_{zz}, v_{yy}, v_{zy} ensures that a spin coherent state has $v_{\min} = v_{\max} = 1$. The naive state area is defined as the square root of the product of minimum and maximum variances. Thus

$$A^* = \sqrt{v_{\min} \times v_{\max}} = \sqrt{v_{zz}v_{yy} - v_{zy}^2}. \tag{5.130}$$

The Wineland squeezing parameter and normalized state area are defined by dividing by the Bloch vector length (normalized by $N/2$) squared. Thus

$$\xi^2 = \frac{v_{\min}}{e^{-\gamma_{\rm sc}t}} = e^{\gamma_{\rm sc}t}\left[\frac{v_{zz}+v_{yy}}{2} - \sqrt{\frac{(v_{zz}-v_{yy})^2}{4} + v_{zy}^2}\right], \quad A = \frac{\sqrt{v_{\min}\times v_{\max}}}{e^{-\gamma_{\rm sc}t}} = e^{\gamma_{\rm sc}t}\sqrt{v_{zz}v_{yy} - v_{zy}^2}, \tag{5.131}$$

which is Eq. (5.100).

QND with spin flips

The equations for v_{zz} and z are decoupled from the rest and can be solved exactly. We write the solution in the limit that $\Gamma N\eta \gg \gamma_{\rm sc}p$. Then

$$\begin{aligned}\dot{v}_{zz} &= -\Gamma N\eta\left(v_{zz} + \frac{\gamma_{\rm sc}p}{\Gamma N\eta} + 2\sqrt{\frac{\gamma_{\rm sc}p}{2\Gamma N\eta}}\sqrt{1-\frac{\gamma_{\rm sc}p}{2\Gamma N\eta}}\right)\left(v_{zz} + \frac{\gamma_{\rm sc}p}{\Gamma N\eta} - 2\sqrt{\frac{\gamma_{\rm sc}p}{2\Gamma N\eta}}\sqrt{1-\frac{\gamma_{\rm sc}p}{2\Gamma N\eta}}\right) \\ &\approx -\Gamma N\eta\left(v_{zz} + \sqrt{2\frac{\gamma_{\rm sc}p}{\Gamma N\eta}}\right)\left(v_{zz} - \sqrt{\frac{2\gamma_{\rm sc}p}{\Gamma N\eta}}\right).\end{aligned} \tag{5.132}$$

We want to solve z in terms of the measurement record, which is the accessible information, not in terms of dW so we rewrite its equation as $dz = -(\Gamma\eta N v_{zz} + \gamma_{\rm sc}p)z\,dt + \sqrt{\Gamma N\eta}\,v_{zz}\,dq$. The solutions for v_{zz} and z (with $v_{zz}(0) = 1$ and $z(0) = 0$) are then

$$v_{zz}(t) \approx \epsilon\coth\left(\frac{\Gamma N\eta t + 1}{\Gamma N\eta\tau}\right), \qquad z(t) \approx \frac{\sqrt{2\gamma_{\rm sc}p}}{\sinh\left[\frac{\Gamma N\eta t+1}{\Gamma N\eta\tau}\right]}\int_0^t \cosh\left[\frac{\Gamma N\eta s+1}{\Gamma N\eta\tau}\right]dq(s), \tag{5.133}$$

where $\epsilon = \sqrt{2\gamma_{\rm sc}p/(\Gamma N\eta)}$ and $\tau^{-1} = 2\sqrt{\gamma_{\rm sc}\Gamma N\eta\gamma_{\rm sc}p}$. Note that $\Gamma N\eta\tau = 1/\epsilon \gg 1$. When $t \ll \tau$ spin flips are not active, and the solutions reduce to $v_{zz}(t) = (1+\Gamma N\eta t)^{-1}$ and $z(t) \approx \sqrt{\Gamma N\eta}(1+\Gamma N\eta t)^{-1}\int_0^t dq(s)$, which is the time-averaged measurement record, in accordance with well-known results. In the opposite limit, when $t \gtrsim \tau$ and spin flips are active, we get $v_{zz}(t) \approx \sqrt{\epsilon}(1+2e^{-2t/\tau})$ and $z(t) \approx \sqrt{2\gamma_{\rm sc}p}\int_0^t e^{-(t-s)/\tau}\,dq(s)$. Thus, the z deflection of the Bloch vector is determined by the measurement record only within a time-window of size τ. Spin flips have effectively introduced a memory time.

QND without spin flips

In this case ($p = 0$), Eq. (5.95) can be solved exactly (they can also be solved exactly for nonzero χ, but this is not relevant for the QND analysis). The first thing to notice is that when $p = 0$ the single particle dephasing terms commute (in the superoperator sense) with the rest of the evolution equation. We thus define $\hat{v} = e^{-\mathcal{L}_{\rm deph}t}\hat{\rho}$, where $\mathcal{L}_{\rm deph} = \sum_i(\mathcal{L}_{\hat{\sigma}^i_{\uparrow\uparrow}} + \mathcal{L}_{\hat{\sigma}^i_{\downarrow\downarrow}})$ so that

$$\mathrm{Tr}(\hat{S}_z\hat{\rho}) = \mathrm{Tr}(\hat{S}_z\hat{v}), \quad \mathrm{Tr}(\hat{S}_z^2\hat{\rho}) = \mathrm{Tr}(\hat{S}_z^2\hat{v}), \quad \mathrm{Tr}(\hat{S}_x\hat{\rho}) = e^{-\gamma_{\rm sc}t/2}\mathrm{Tr}(\hat{S}_x\hat{v}), \tag{5.134}$$

and $\hat{v}$ satisfies

$$d\hat{v} = \Gamma\Big(\hat{S}_z\hat{v}\hat{S}_z - \frac{\{\hat{S}_z^2,\hat{v}\}}{2}\Big)\,dt + \sqrt{\Gamma\eta}\Big(\hat{S}_z\hat{v} + \hat{v}\hat{S}_z - 2\,\langle\hat{S}_z\rangle\Big)\,dW, \tag{5.135}$$

and the expectation value is now taken with respect to $\hat{v}$. The matrix element $\langle m|\hat{v}|n\rangle$ satisfies the equation

$$d\,\langle m|\hat{v}|n\rangle = -\frac{\Gamma(m-n)^2}{2}\,\langle m|\hat{v}|n\rangle\,dt + \sqrt{\Gamma\eta}(m+n)\,\langle m|\hat{v}|n\rangle\,dW - 2\sqrt{\Gamma\eta}\,\langle\hat{S}_z\rangle\,\langle m|\hat{v}|n\rangle\,dW, \tag{5.136}$$

which can be integrated taking into account the Ito rule. Up to m and n independent prefactors, this yields

$$\begin{aligned}\langle m|\hat{v}|n\rangle\,(t) \propto\; & e^{-\Gamma t(m-n)^2/2}\,e^{-\Gamma\eta t(n+m)^2/2}\,e^{\sqrt{\Gamma\eta}(m+n)\left(W_t + 2\sqrt{\Gamma\eta}\int_0^t\langle\hat{S}_z\rangle\,dt'\right)} \\ & \times e^{-2\sqrt{\Gamma\eta}\int_0^t\langle\hat{S}_z\rangle\,dW_{t'}}\,\underbrace{e^{-(m^2+n^2)/N}}_{\langle m|\hat{v}|n\rangle(0)},\end{aligned} \tag{5.137}$$

where we have approximated $\langle m|\hat{v}|n\rangle\,(0)$ and $W_t = \int_0^t dW$ is a Brownian process. With this explicit

form for the matrix elements, we can calculate the relevant expectation values

$$\mathcal{C} = \sum_{n=-\infty}^{\infty} e^{-2\left(\frac{1}{N}+\Gamma\eta t\right)(n-n^*)^2}, \qquad \mathrm{Tr}(\hat{\rho}\hat{S}_x) = \frac{Ne^{-\frac{\Gamma t}{2}-\gamma_{\mathrm{sc}}t/2}}{2\mathcal{C}} \sum_{n=-\infty}^{\infty} e^{-2\left(\frac{1}{N}+\Gamma\eta t\right)(n-n^*+\frac{1}{2})^2}$$
$$\mathrm{Tr}(\hat{\rho}\hat{S}_z) = \frac{1}{\mathcal{C}} \sum_{n=-\infty}^{\infty} e^{-2\left(\frac{1}{N}+\Gamma\eta t\right)(n-n^*)^2} n, \qquad \mathrm{Tr}(\hat{\rho}\hat{S}_z^2) = \frac{1}{\mathcal{C}} \sum_{n=-\infty}^{\infty} e^{-2\left(\frac{1}{N}+\Gamma\eta t\right)(n-n^*)^2} n^2 \tag{5.138}$$

where we have extended the sums to $\pm\infty$ and

$$n^* \equiv \frac{\sqrt{\Gamma\eta}/2}{\Gamma\eta t + 1/N}\left(W_t + 2\sqrt{\Gamma\eta}\int_0^t \langle \hat{S}_z\rangle \, dt'\right) \tag{5.139}$$

sets the average $\langle \hat{S}_z\rangle$ and thus satisfies the consistency requirement

$$dn^* = \frac{\Gamma\eta}{\Gamma\eta t + \frac{1}{N}}\left[\frac{\sum_{n=-\infty}^{\infty} e^{-2\left(\frac{1}{N}+\Gamma\eta t\right)(n-n^*)^2}(n-n^*)}{\sum_{n=-\infty}^{\infty} e^{-2\left(\frac{1}{N}+\Gamma\eta t\right)(n-n^*)^2}}\right] dt + \frac{\sqrt{\Gamma\eta}}{2\left(\Gamma\eta t + \frac{1}{N}\right)} dW_t. \tag{5.140}$$

Average quantities are then computed by first calculating them at fixed n^* and then sampling n^* from the previous stochastic equation. When $\Gamma\eta\, t \lesssim 1$, the arguments of the sums vary slowly and can be approximated by integrals, leading to

$$\xi^2 = \frac{e^{(\Gamma+\gamma_{\mathrm{sc}})t}}{1+\Gamma N\eta t} \longrightarrow \Gamma t_{\mathrm{opt}} = \frac{1}{1+\frac{\gamma_{\mathrm{sc}}}{\Gamma}} = \frac{C}{C+1}, \quad \xi^2_{\mathrm{opt}} = \frac{e}{\eta N}\left(1+\frac{1}{C}\right). \tag{5.141}$$

Note that $\Gamma t_{\mathrm{opt}} < 1$ always so that $\Gamma\eta t_{\mathrm{opt}}$ satisfies $\Gamma\eta t_{\mathrm{opt}} \lesssim 1$ quite generically, except when $\eta = 1$ and $C \gg 1$. Note also that squeezing is independent of n^* within this approximation. Beyond this regime, which is a situation relevant only when $C \gtrsim 1$ and $\eta \approx 1$, the result does depend on n^*. In this scenario, squeezing can reach $\xi^2 = 2/N$ on specific trajectories (when n^* is even) but the average over trajectories is still captured relatively well by Eq. (5.141).

OAT with spin flips

When $\eta = 0$, Eqs. (5.126) become linear. The solutions are $y = z = 0$ (no stochastic terms),

$v_{zz} = 1$, and

$$\begin{aligned}
v_{zy} &= \frac{\chi N}{\gamma_{\rm sc} p} e^{-\gamma_{\rm sc} t}(1 - e^{-\gamma_{\rm sc} p t}) \\
v_{yy} &= 1 + \Gamma N t e^{-\gamma_{\rm sc} t} + \frac{2(\chi N)^2}{(\gamma_{\rm sc} p)^2} e^{-\gamma_{\rm sc} t}(\gamma_{\rm sc} p t - 1 + e^{-\gamma_{\rm sc} p t}) \\
A^2 &= e^{2\gamma_{\rm sc} t}(v_{yy} v_{zz} - v_{zy}^2) = e^{2\gamma_{\rm sc} t}\left[1 + \Gamma N t e^{-\gamma_{\rm sc} t} + \frac{2(\chi N)^2}{(\gamma_{\rm sc} p)^2}\left(\gamma_{\rm sc} p t - \frac{3}{2} + 2e^{-\gamma_{\rm sc} p t} - \frac{e^{-2\gamma_{\rm sc} p t}}{2}\right)\right], \\
\xi^2 &= \frac{e^{\gamma_{\rm sc} t}(v_{zz} v_{yy} - v_{zy}^2)}{\frac{1+v_{yy}}{2} + \sqrt{\left(\frac{1-v_{yy}}{2}\right)^2 + v_{zy}^2}}
\end{aligned} \tag{5.142}$$

where A is the state area and ξ^2 is the squeezing parameter.

We expect the optimal squeezing to occur for $\gamma_{\rm sc} t \ll 1$, so we calculate things perturbatively in $\gamma_{\rm sc}$. This leads to $v_{zy} \approx \chi N t$, $v_{yy} \approx 1 + \Gamma N t + \chi^2 N^2 t^2 \approx \chi^2 N^2 t^2$ ($\chi N t \gg 1$ since we would not have any squeezing otherwise). Then

$$\begin{aligned}
A^2 &\approx v_{zz} v_{yy} - v_{zy}^2 \approx 1 + \Gamma N t + \frac{2(\chi N)^2 \gamma_{\rm sc} t^3}{3} \\
\xi^2 &\approx \frac{A^2}{v_{yy}} = \frac{1 + \Gamma N t}{(\chi N t)^2} + \frac{2}{3}\gamma_{\rm sc} p t,
\end{aligned} \tag{5.143}$$

in agreement with the exact treatment presented in Ref. [38]. For smaller detunings $d = 2\delta_*/\kappa$, the collective dephasing term is active and the minimum squeezing is the result of the minimization of

$$\xi^2 \approx \frac{\Gamma/\chi}{\chi N t} + \frac{2}{3}\gamma_{\rm sc} p t \longrightarrow \xi_t^2 = \sqrt{\frac{32p}{3NC}}\sqrt{1 + \frac{1}{d^2}}, \quad \gamma_{\rm sc} p\, t_{\rm opt} = \frac{3\xi_t^2}{4}, \quad A^2 = 2\sqrt{6}\sqrt{\frac{NC}{pd^2(d^2+1)}} \tag{5.144}$$

where we have used Eq. (5.99). This expression for squeezing leads to Eq. (5.103) for $d \gtrsim 1$. Note also that, assuming p is not too small, the optimal time $t_{\rm opt}$ satisfies $\gamma_{\rm sc} t_{\rm opt} \ll 1$, as promised. Even if ξ_t^2 is relatively insensitive to d at large values of d, the area A gets smaller at larger detunings, which is desirable. As d is further increased, Γ gets small very quickly, and the optimal squeezing is then the result of minimizing (assuming $d \gg 1$)

$$\xi^2 = \frac{1}{(\chi N t)^2} + \frac{2}{3}\gamma_{\rm sc} p t \longrightarrow \xi_t^2 = 3^{1/3}\left(\frac{2pd}{NC}\right)^{2/3}, \quad \gamma_{\rm sc} p t_{\rm opt} = \xi_t^2, \quad A^2 \approx 3 \tag{5.145}$$

Squeezing gets worse as d increases, but the area is reasonably small, so it's a good idea to operate at the crossover between these two regimes. We estimate the detuning value at which this happens

by equating the expressions for squeezing on both sides. This leads to

$$d_{\text{crossover}} \approx \frac{8}{3^{5/4}}\left[\frac{NC}{2p}\right]^{1/4} \approx 2\left[\frac{NC}{2p}\right]^{1/4}. \tag{5.146}$$

OAT without spin flips

We set $p = 0$ here, but do not assume $\gamma_{\text{sc}}t \ll 1$ necessarily. Then $v_{yy} \approx (\chi Nt)^2 e^{-\gamma_{\text{sc}}t}$, $(A^*)^2 \approx v_{yy} \times v_{\min}$ and

$$v_{\min} \approx \frac{e^{\gamma_{\text{sc}}t} + \Gamma Nt}{(\chi Nt)^2} + \underbrace{\frac{(\chi Nt)^4}{6N^2}}_{\text{curvature}}, \tag{5.147}$$

where the extra curvature term is a correction that is not captured by Eq. (5.126) since it is of next to leading order in $1/N$. Furthermore, loss of contrast due to γ_{sc} may be relevant. With $\langle \hat{S}_x \rangle \approx N e^{-\gamma_{\text{sc}}t}/2$, the squeezing parameter is

$$\xi^2 = e^{\gamma_{\text{sc}}t}\left[\frac{e^{\gamma_{\text{sc}}t} + \Gamma Nt}{(\chi Nt)^2} + \frac{(\chi Nt)^4}{6N^2}\right]. \tag{5.148}$$

In fact, for $p = 0$ and $\eta = 0$, Eq. (5.95) can be solved exactly since all the terms in the master equation commute (in the superoperator sense). The exact values for relevant observables are

$$\begin{aligned}
\langle \hat{S}_z^2 \rangle &= \frac{N}{4} \\
\langle \{\hat{S}_z, \hat{S}_y\} \rangle &= \frac{N(N-1)}{2} e^{-(\gamma_{\text{sc}}+\Gamma)t/2} \cos(\chi t)^{N-2} \sin(\chi t) \\
\langle \hat{S}_y^2 \rangle &= \frac{N}{4}(1 - e^{-\gamma_{\text{sc}}t}) + \frac{N(N+1)e^{-\gamma_{\text{sc}}t}}{8} + \frac{N(1-N)e^{-\gamma_{\text{sc}}t - 2\Gamma t}}{8} \cos(2\chi t)^{N-2} \\
\langle \hat{S}_x \rangle &= e^{-(\gamma_{\text{sc}}+\Gamma)t/2} \cos(\chi t)^{N-1}.
\end{aligned} \tag{5.149}$$

A comparison of squeezing (optimized over time) obtained with the exact equations and with Eq. (5.148) is shown in Fig. 5.11(a) for $N = 10^6$ and $C = 10^2$. Since the agreement is almost perfect, we keep working with Eq. (5.148) for analytical insight.

As Fig. 5.11(a) demonstrates, there can be three regimes. At smaller detunings (but still $d \gtrsim 1$), collective dephasing is active but single particle dephasing is not. The optimal squeezing is then limited by curvature and is obtained by minimizing

$$\xi^2 \approx \frac{\Gamma/\chi}{\chi Nt} + \frac{(\chi Nt)^4}{6N} \longrightarrow \xi_t^2 \approx \frac{5/2}{3^{1/5} d^{4/5} N^{2/5}}, \quad \chi N t_{\text{opt}} = \left(\frac{3N^2}{d}\right)^{1/5}, \quad A \approx \sqrt{1 + \frac{3.1 N^{4/5}}{d^{6/5}}}. \tag{5.150}$$

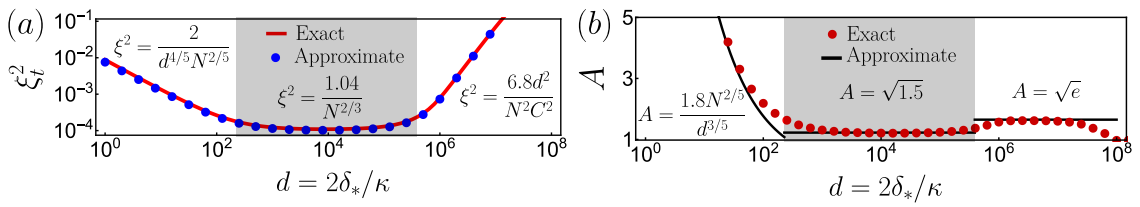

Figure 5.11: (a) Comparison of time optimized ξ_t^2 using the exact Eqs. (5.149) (solid red) and approximate Eq. (5.148) (blue dots) as a function of detuning $d = 2\delta_*/\kappa$ for $N = 10^6$ and $C = 10^2$. Boundary between different shaded regions are given by $d_{c1} = 2.3N^{1/3}$ and $d_{c2} = 0.4CN^{2/3}$. (b) Area at the optimal squeezing time as a function of detuning. Red dots are calculated using Eqs. (5.149), while black lines are the approximations for each of the regions described in section.

As the detuning is increased, both the optimal squeezing and the area improve. Eventually neither collective nor single particle dephasing will be active but the optimal squeezing will still be limited by curvature and is obtained by minimizing

$$\xi^2 \approx \frac{1}{(\chi N t)^2} + \frac{(\chi N t)^4}{6N^2} \longrightarrow \xi_t^2 \approx \frac{3^{2/3}/2}{N^{2/3}}, \quad \chi N t_{\rm opt} = (3N^2)^{1/6}, \quad A \approx \sqrt{1.5}. \tag{5.151}$$

This is the well-known OAT result. Finally, at much larger detunings χ is small enough that curvature is irrelevant, and the main limitations are now single particle dephasing and contrast decay. Hence, the optimal squeezing is obtained by minimizing

$$\xi^2 = \frac{e^{2\gamma_{\rm sc} t}}{(\chi N t)^2} \longrightarrow \xi_t^2 \approx \left(\frac{ed}{NC}\right)^2, \quad \gamma_{\rm sc} t_{\rm opt} = 1, \quad A \approx \sqrt{e}. \tag{5.152}$$

We can estimate the detunings at which the behaviour of ξ_t^2 changes by equating the values of the time optimized squeezing on both sides of a crossover. We find these detuning values to be

$$d_{c1} = \frac{5^{5/4}}{3^{13/12}} N^{1/3} \approx 2.3N^{1/3}, \qquad d_{c2} = \frac{3^{1/3}N^{2/3}C}{e\sqrt{2}} \approx 0.4CN^{2/3}. \tag{5.153}$$

For the unitary region in the middle to exist, we need $d_{c1} < d_{c2}$, which requires that $C \gtrsim 6N^{-1/3}$. Otherwise, the two outer regions in Fig. merge, and the detuning optimized squeezing will be worse than the OAT result. We show the results for the area A in Fig. 5.11(b).

5.3.8 Supplemental Materials: Examples of experimental system

We illustrate our results using examples that are related to the experimental system we analyzed in the main text. We will consider various QND and OAT implementations, including

systems that are not directly described by Eq. (5.95).

- We first analyze Ref. [190], which implemented OAT using the same level scheme as the one in Fig. 5.7. Using $p = 1/2$, $C = 0.14$ and $N = 3 \times 10^4$ (see second column of page 2 of Ref. [190], where single atom cooperativity is denoted η instead of C) leads to 14.5 dB of noise reduction according to Eq. (5.103). The experiment reports 10(1) dB of inferred noise reduction (after subtraction of detection noise, see first column of page 4) and is further affected by fluctuations in intracavity probe power and dephasing effects that reduce the effective radius of the Bloch vector. Importantly, a theoretical analysis of this experiment was presented in Refs. [383] and Eq. (5.103) is the same as the equation reported in Ref. [383] in the presence of free space scattering.

- Next, we analyze Ref. [342], which implemented QND measurements in the same level structure as Ref. [190]. Using $p = 1/2$, $\eta = 0.4$ (quantum efficiency, see second column of page 2 of Ref. [342]), and $NC = 3100 \times 3/2$ (see second column of page 3, the factor $3/2$ comes from discrepancies in the definition of our C and the effective cooperativity in Ref. [342]) leads to a noise reduction of 16 dB, according to Eq. (5.101) and 18 dB if $\eta = 1$, in agreement with the fundamental limit provided in Eq. (20) of the Supplementary Material of Ref. [342]. Technical noise modifies this value to 9 dB of noise reduction and 3 dB of metrological enhancement when including contrast decay. As discussed in the Supplementary Material of Ref. [342], in the ideal scenario the fundamental limit of 18 dB is not modified by the presence of contrast decay.

- Now we analyze Ref. [341], which implemented QND measurements in the same level structure as Ref. [342], but in a configuration where the cavity is closer to resonance with $|\uparrow\rangle$ than $|\downarrow\rangle$ and with different hyperfine levels. The different choice of levels means that $p \to 0$. In this QND setup, application of Eq. (5.107) with $\eta = 0.37$, $N = 4 \times 10^5$ and $C = 0.044$ leads to 34 dB of squeezing (without taking into account inhomogeneous couplings of the atoms to the cavity mode), compared to the 19 dB of noise reduction and 17 dB of metro-

logical enhancement reported in Ref. [341]. As discussed in the cited reference, detection noise (25 dB below quantum projection noise) and optomechanical effects were the main technical limitations.

- Then we analyze Ref. [340], which does QND measurements in the same level structure and also the same levels as Ref. [342]. Using $p = 1/2$, $\eta = 0.16$ and $NC = (5 \times 10^5)(0.78) \times 3/2$ (the factor of $3/2$ arises because of discrepancies with our definition of cooperativity) leads, via Eq. (5.101), to 25 dB of squeezing. The cited reference reports 20 dB of metrological enhancement and predicts 24 dB. The difference of this prediction with our calculation originates from the broadening of the cavity linewidth due to free space scattering, a effect that we neglect and that arises as a higher order term in the adiabatic elimination of the excited state.

- Let us now study the QND implementation of Ref. [384]. The setup involves $N \approx 10^{11}$ atoms in a vapour cell but has no cavity. To establish a comparison to our results, we thus need to find the quantity in Ref. [384] analogous to the collective cooperativity C in terms of which we express all of our findings. In this case, it will be the optical depth of the atomic sample. We relate both by using the definition of C

$$NC = \frac{4g_1^2 N}{\kappa \gamma_1}, \tag{5.154}$$

and expressing γ_1, g_1 and κ in terms of atomic and cavity properties. We use the Wigner-Weisskopf expression for γ_1, Eq. (2) of Ref. [391] for g_1 and express κ in terms of the cavity's free spectral range and finesse $\mathcal{F}$:

$$\gamma_1 = \frac{\omega_1^3 \mu^2}{3\pi\hbar\epsilon_0 c^3} \qquad g_1 = \left(\frac{\mu^2 \omega_1}{2\hbar\epsilon_0 V_m}\right)^{1/2} \qquad \kappa = \frac{\pi c}{L\mathcal{F}}, \tag{5.155}$$

where ω_1 is the transition frequency from $|\uparrow\rangle$ to $|e\rangle$, μ is the transition dipole moment, L is the cavity length and V_m is the mode volume. Putting all these together we have that

$$NC = \frac{6c^2}{\omega_1^2} \times \frac{N}{V_m} \times L \times \mathcal{F}. \tag{5.156}$$

The resonant scattering cross section is $\sigma_1 = 4\pi c^2/\omega_1^2$, and we can take N/V_m as a representative of the average atom density n. Then

$$NC = \frac{3}{2\pi} n\sigma_1 L\mathcal{F} = \frac{3}{2\pi}(OD)\mathcal{F}, \tag{5.157}$$

where $OD = n\sigma_1 L$ is the optical depth of the sample. The experiment in Ref. [384] works at an optical depth of 70 and uses no cavity, so we set $\mathcal{F} = 1$. Using these numbers to obtain a representative NC and using Eq. (5.101) with $\eta = 1$ (perfect detection efficiency) and $p = 1/2$ we obtain 7.5 dB as the limit to squeezing caused by scattering from the excited state. The experiment predicts 5.3 dB and reports 3.4 dB of noise reduction (see last paragraph of Supplementary Information of Ref. [384] for a detailed discussion), which are close to our bound, and at the level where the differences in implementation (which may introduce factors of order 1) matter. Furthermore, at these smaller values of "NC" contrast decay modifies the attainable metrological enhancement by amounts that are sizeable relative to the noise reduction, and Ref. [384] reports 2.3 dB of actual squeezing. Finally, Ref. [384] uses an experimental scheme put forward in Ref. [392]. The Supplementary Material of Ref. [392] also includes the limitations to squeezing coming from probe-induced scattering and arrive at Eq. (S40). Up to factors of order 1 this is the same as Eq. (5.101) in our paper, once the equivalence between NC, optical depth and finesse is made.

- The last experiment we analyze is the OAT implementation of Ref. [376]. In this experiment, the cavity is parked close to resonance with one of the atomic transition frequencies and $p = 0$, similar to Ref. [341], albeit using a different atom. For technical reasons, the experiment employs a two-tone scheme for the generation of squeezing. The first, blue-detuned, tone operates with an atom-drive detuning that falls in the center region of Fig. 5.10(a) while the second, red-detuned, tone is in the left region of Fig. 5.10(a) (numerical values for κ and the atom-drive detunings are given in sections I and V of the Supplementary Material of Ref. [376]). For simplicity, we use the bound in the center region, which is the Kitagawa-Ueda limit. With $N = 1000$ this leads to 20 dB of squeezing,

but inhomogeneous couplings of the atoms to the cavity mode lead to 16 dB, as discussed in section VIII of the Supplementary Material of Ref. [376]. The experiment reports 16 dB of noise reduction, very much in agreement with the theoretical bound, and 12 dB of inferred metrological enhancement.

These considerations are summarized in Table 5.1.

Table 5.1: Squeezing in experiments

Experiment	Inferred noise reduction	Estimation by Ref.	Our prediction
Ref. [190] (OAT)	10 dB	-	14.5 dB
Ref. [342] (QND)	9 dB	18 dB	18 dB
Ref. [341] (QND)	19 dB	-	34 dB
Ref. [340] (QND)	20 dB	24 dB	25 dB
Ref. [384] (QND)	3.4 dB	5.3 dB	7.5 dB
Ref. [376] (OAT)	16 dB	16 dB	20 dB

Chapter 6

Conclusion and outlook

In this thesis I presented a summary of the theoretical research that I carried out during my PhD that aims to advance the frontier of quantum simulation and metrology via contact and photon-mediated interactions. In Chapter 3, I illustrated how Hamiltonian engineering can help improve state-of-the-art optical lattice clocks and how the new records of sensitivity in clocks are openning new possibilities for the exploration of general relativistic effects. In Chapter 4, I presented studies which explored different types of emergent collective behaviors and dynamical phases in interacting arrays. In Chapter 5, I studied entanglement generation via photon-mediated interactions and measurements. Here I would like to conclude by providing an outlook of new directions that we are currently working on or research avenues I would like to pursue in the future.

In Wannier-Stark optical lattice clocks, we have shown that the partially delocalized Wannier-Stark wave functions allows Rabi drive in carrier transitions and Wannier-Stark sidebands. So far we have mainly focused on the tunability of the carrier transition (see Chapter 3.2, 3.3). However, more possibilities can emerge by interrogating the Wannier-Stark sidebands. For example, in an ongoing research we are considering the simultaneous application of both a carrier and a sideband drive, which we have shown can allow us to engineer the Su–Schrieffer–Heeger (SSH) model and the Rice-Mele (RM) model. These models feature unique topological properties and the implementation of these models in an optical lattice clock setup can be very helpful for exploring topologically protected quantum sensing. Another direction is the exploration of GR effects in optical lattice clocks. Our research of the interplay between mass-energy equivalence and photon-mediated inter-

actions is a just first step (see Chapter 3.4). Possible future research includes exploring the use of interactions to magnify GR effects, the use of itinerant particles to understand the role of GR on motional degrees of freedom, as well as GR corrections on many-body interactions.

With respect to the exploration of emergent collective behaviors and dynamical phases, we have shown that all-to-all spin exchange interactions in cavity QED systems can lead to simulations of the Bardeen–Cooper–Schrieffer (BCS) model, an iconic model for s-wave superconductors and superfluids (see Chapter 4.5). An ongoing project in this direction is to extend this idea to simulate topological superconductors with p-wave or d-wave pairings, and the competition of these superconducting orders in cavity QED systems. Another possibility is to engineer protocols to capable to explore other missing ingredients in the current s-wave BCS simulation. So far we have only focused on the dynamical phases and superconducting order parameters. Possible future research includes the simulation of the BCS-BEC crossover and exploration of the different dynamical relaxation rates in the BCS and the BEC regimes, as well as the simulation of the Meissner effect and flux quantization via additional spin-orbit coupling. Moreover, one can also consider the use of multilevel atoms to explore new possibilities in cavity QED simulators. For example, in an ongoing collaboration with Professor James Thompson's group, we want to include a third level as an alternative resource for the implementation of the analog of radio frequency spectroscopy intensively studied in fermionic superfluids. The use of multilevel atoms can also enable the possibility to simulate pair breaking terms and neutrino oscillations.

So far for entanglement generation, we have mainly focused on one-axis twisting (OAT) interactions and quantum nondemolition measurement (QND). In cavity QED systems, there could be many other possibilities for engineering an entangled state. One approach we are actively working on is developing protocols for two-axis counter twisting (TACT) as well as n-body interactions. We have already shown the capabilities for observing mean-field effects (see Ref. [41]), while there is still plenty of room to explore optimal protocols for quantum enhancement. Another relevant approach is to consider the use of dissipation for entanglement generation in steady states. In principle this is a relatively robust way of entanglement generation against environmental noise.

It would be very intriguing to explore feasible protocols for engineering the desire Lindblad jump operators. Apart from entanglement generation, it is equally important to discuss the utility of entanglement when applying to practical sensors such as optical clocks and atom interferometers. We have shown the tunability of spatial inhomogeneities of an OAT-induced spin squeezed state and its potential application in gravimetry and short-range force sensing (see Chapter 5.2). It would be really fascinating to explore quantum enhanced protocol tailored for a practical sensing task.

I hope that the theory I have developed in this thesis is continuously shedding light on all these exciting directions in quantum simulation and metrology.

Bibliography

[1] R. P. Feynman, *Simulating physics with computers*, International Journal of Theoretical Physics **21**, 467 (1982).

[2] I. Georgescu, S. Ashhab, and F. Nori, *Quantum simulation*, Reviews of Modern Physics **86**, 153 (2014).

[3] C. Gross and I. Bloch, *Quantum simulations with ultracold atoms in optical lattices*, Science **357**, 995 (2017).

[4] J. Preskill, *Quantum Computing in the NISQ era and beyond*, Quantum **2**, 79 (2018).

[5] K. Bharti, A. Cervera-Lierta, T. H. Kyaw, T. Haug, S. Alperin-Lea, A. Anand, M. Degroote, H. Heimonen, J. S. Kottmann, T. Menke, W.-K. Mok, S. Sim, L.-C. Kwek, and A. Aspuru-Guzik, *Noisy intermediate-scale quantum algorithms*, Reviews of Modern Physics **94**, 015004 (2022).

[6] C. Degen, F. Reinhard, and P. Cappellaro, *Quantum sensing*, Reviews of Modern Physics **89**, 035002 (2017).

[7] L. Pezzè, A. Smerzi, M. K. Oberthaler, R. Schmied, and P. Treutlein, *Quantum metrology with nonclassical states of atomic ensembles*, Reviews of Modern Physics **90**, 035005 (2018).

[8] K. Azuma, S. E. Economou, D. Elkouss, P. Hilaire, L. Jiang, H.-K. Lo, and I. Tzitrin, *Quantum repeaters: From quantum networks to the quantum internet*, Reviews of Modern Physics **95**, 045006 (2023).

[9] M. Safronova, D. Budker, D. DeMille, D. F. J. Kimball, A. Derevianko, and C. W. Clark, *Search for new physics with atoms and molecules*, Reviews of Modern Physics **90**, 025008 (2018).

[10] M. Tse et al., *Quantum-Enhanced Advanced LIGO Detectors in the Era of Gravitational-Wave Astronomy*, Physical Review Letters **123**, 231107 (2019).

[11] F. Acernese et al., *Increasing the Astrophysical Reach of the Advanced Virgo Detector via the Application of Squeezed Vacuum States of Light*, Physical Review Letters **123**, 231108 (2019).

[12] M. Malnou, D. Palken, B. Brubaker, L. R. Vale, G. C. Hilton, and K. Lehnert, *Squeezed Vacuum Used to Accelerate the Search for a Weak Classical Signal*, Physical Review X **9**, 021023 (2019).

[13] K. M. Backes et al., *A quantum enhanced search for dark matter axions*, Nature **590**, 238 (2021).

[14] E. Pedrozo-Peñafiel, S. Colombo, C. Shu, A. F. Adiyatullin, Z. Li, E. Mendez, B. Braverman, A. Kawasaki, D. Akamatsu, Y. Xiao, and V. Vuletić, *Entanglement on an optical atomic-clock transition*, Nature **588**, 414 (2020).

[15] G. P. Greve, C. Luo, B. Wu, and J. K. Thompson, *Entanglement-enhanced matter-wave interferometry in a high-finesse cavity*, Nature **610**, 472 (2022).

[16] J. M. Robinson, M. Miklos, Y. M. Tso, C. J. Kennedy, T. Bothwell, D. Kedar, J. K. Thompson, and J. Ye, *Direct comparison of two spin-squeezed optical clock ensembles at the 10^{-17} level*, Nature Physics **20**, 208 (2024).

[17] S. F. Huelga, C. Macchiavello, T. Pellizzari, A. K. Ekert, M. B. Plenio, and J. I. Cirac, *Improvement of Frequency Standards with Quantum Entanglement*, Physical Review Letters **79**, 3865 (1997).

[18] R. P. Feynman, *There's plenty of room at the bottom [data storage]*, Journal of Microelectromechanical Systems **1**, 60 (1992).

[19] H. J. Metcalf and P. Van der Straten, *Laser cooling and trapping*Graduate texts in contemporary physics (Springer, New York, 1999).

[20] A. D. Ludlow, M. M. Boyd, J. Ye, E. Peik, and P. O. Schmidt, *Optical atomic clocks*, Reviews of Modern Physics **87**, 637 (2015).

[21] A. Derevianko and H. Katori, *Colloquium: Physics of optical lattice clocks*, Reviews of Modern Physics **83**, 331 (2011).

[22] D. B. Newell and E. Tiesinga, National Institute of Standards and Technology Report No. NIST SP 330-2019, 2019.

[23] T. Bothwell, C. J. Kennedy, A. Aeppli, D. Kedar, J. M. Robinson, E. Oelker, A. Staron, and J. Ye, *Resolving the gravitational redshift across a millimetre-scale atomic sample*, Nature **602**, 420 (2022).

[24] A. Aeppli, K. Kim, W. Warfield, M. S. Safronova, and J. Ye, A clock with 8×10^{-19} systematic uncertainty, 2024, arXiv:2403.10664 [physics].

[25] A. Aeppli, A. Chu, T. Bothwell, C. J. Kennedy, D. Kedar, P. He, A. M. Rey, and J. Ye, *Hamiltonian engineering of spin-orbit–coupled fermions in a Wannier-Stark optical lattice clock*, Science Advances **8**, eadc9242 (2022).

[26] H. Ritsch, P. Domokos, F. Brennecke, and T. Esslinger, *Cold atoms in cavity-generated dynamical optical potentials*, Reviews of Modern Physics **85**, 553 (2013).

[27] A. Reiserer and G. Rempe, *Cavity-based quantum networks with single atoms and optical photons*, Reviews of Modern Physics **87**, 1379 (2015).

[28] F. Mivehvar, F. Piazza, T. Donner, and H. Ritsch, *Cavity QED with quantum gases: new paradigms in many-body physics*, Advances in Physics **70**, 1 (2021).

[29] The Nobel Prize in Physics 2012.

[30] M. Kitagawa and M. Ueda, *Squeezed spin states*, Physical Review A **47**, 5138 (1993).

[31] J. Ma, X. Wang, C. Sun, and F. Nori, *Quantum spin squeezing*, Physics Reports **509**, 89 (2011).

[32] W. R. Milner, S. Lannig, M. Mamaev, L. Yan, A. Chu, B. Lewis, M. N. Frankel, R. B. Hutson, A. M. Rey, and J. Ye, Coherent evolution of superexchange interaction in seconds long optical clock spectroscopy, 2024, arXiv:2402.13398 [cond-mat, physics:physics].

[33] A. Chu, V. J. Martínez-Lahuerta, M. Miklos, K. Kim, P. Zoller, K. Hammerer, J. Ye, and A. M. Rey, Exploring the interplay between mass-energy equivalence, interactions and entanglement in an optical lattice clock, 2024, arXiv:2406.03804 [cond-mat, physics:gr-qc, physics:physics, physics:quant-ph].

[34] A. Chu, J. Will, J. Arlt, C. Klempt, and A. M. Rey, *Simulation of XXZ Spin Models Using Sideband Transitions in Trapped Bosonic Gases*, Physical Review Letters **125**, 240504 (2020).

[35] A. Chu, A. P. Orioli, D. Barberena, J. K. Thompson, and A. M. Rey, *Photon-mediated correlated hopping in a synthetic ladder*, Physical Review Research **5**, L022034 (2023).

[36] H. Zhang, A. Chu, C. Luo, J. K. Thompson, and A. M. Rey, *Control and amplification of Bloch oscillations via photon-mediated interactions*, Physical Review Research **5**, L032039 (2023).

[37] D. J. Young, A. Chu, E. Y. Song, D. Barberena, D. Wellnitz, Z. Niu, V. M. Schäfer, R. J. Lewis-Swan, A. M. Rey, and J. K. Thompson, *Observing dynamical phases of BCS superconductors in a cavity QED simulator*, Nature **625**, 679 (2024).

[38] A. Chu, P. He, J. K. Thompson, and A. M. Rey, *Quantum Enhanced Cavity QED Interferometer with Partially Delocalized Atoms in Lattices*, Physical Review Letters **127**, 210401 (2021).

[39] D. Barberena, A. Chu, J. K. Thompson, and A. M. Rey, Trade-offs between unitary and measurement induced spin squeezing in cavity QED, 2023, arXiv:2309.15353 [quant-ph].

[40] B. Sundar, D. Barberena, A. P. Orioli, A. Chu, J. K. Thompson, A. M. Rey, and R. J. Lewis-Swan, *Bosonic Pair Production and Squeezing for Optical Phase Measurements in Long-Lived Dipoles Coupled to a Cavity*, Physical Review Letters **130**, 113202 (2023).

[41] C. Luo, H. Zhang, A. Chu, C. Maruko, A. M. Rey, and J. K. Thompson, Hamiltonian Engineering of collective XYZ spin models in an optical cavity: From one-axis twisting to two-axis counter twisting models, 2024, arXiv:2402.19429 [physics, physics:quant-ph].

[42] C. Luo, H. Zhang, V. P. W. Koh, J. D. Wilson, A. Chu, M. J. Holland, A. M. Rey, and J. K. Thompson, *Momentum-exchange interactions in a Bragg atom interferometer suppress Doppler dephasing*, Science **384**, 551 (2024).

[43] J. D. Wilson, J. T. Reilly, H. Zhang, C. Luo, A. Chu, J. K. Thompson, A. M. Rey, and M. J. Holland, Entangled Matter-waves for Quantum Enhanced Sensing, 2024, arXiv:2406.13616 [physics, physics:quant-ph].

[44] F. Le Kien, P. Schneeweiss, and A. Rauschenbeutel, *Dynamical polarizability of atoms in arbitrary light fields: general theory and application to cesium*, The European Physical Journal D **67**, 92 (2013).

[45] F. W. J. Olver, editor, *NIST handbook of mathematical functions* (Cambridge University Press, 2010).

[46] M. S. Safronova, S. G. Porsev, U. I. Safronova, M. G. Kozlov, and C. W. Clark, *Blackbody-radiation shift in the Sr optical atomic clock*, Physical Review A **87**, 012509 (2013).

[47] C. Shi, J.-L. Robyr, U. Eismann, M. Zawada, L. Lorini, R. Le Targat, and J. Lodewyck, *Polarizabilities of the 87Sr clock transition*, Physical Review A **92**, 012516 (2015).

[48] N. Marzari, A. A. Mostofi, J. R. Yates, I. Souza, and D. Vanderbilt, *Maximally localized Wannier functions: Theory and applications*, Reviews of Modern Physics **84**, 1419 (2012).

[49] W. Kohn, *Analytic Properties of Bloch Waves and Wannier Functions*, Physical Review **115**, 809 (1959).

[50] K. Beloy, W. F. McGrew, X. Zhang, D. Nicolodi, R. J. Fasano, Y. S. Hassan, R. C. Brown, and A. D. Ludlow, *Modeling motional energy spectra and lattice light shifts in optical lattice clocks*, Physical Review A **101**, 053416 (2020).

[51] T. Hartmann, F. Keck, H. J. Korsch, and S. Mossmann, *Dynamics of Bloch oscillations*, New Journal of Physics **6**, 2 (2004).

[52] L. D. Landau and E. M. Lifshitz, *Quantum mechanics: non-relativistic theory*, Course of Theoretical Physics Vol. 3, 3rd, rev. and enl., authorized engl. reprint ed. (Elsevier, 2007).

[53] K. Huang and C. N. Yang, *Quantum-Mechanical Many-Body Problem with Hard-Sphere Interaction*, Physical Review **105**, 767 (1957).

[54] A. Derevianko, *Anisotropic pseudopotential for polarized dilute quantum gases*, Physical Review A **67**, 033607 (2003).

[55] A. Derevianko, *Revised Huang-Yang multipolar pseudopotential*, Physical Review A **72**, 044701 (2005).

[56] Z. Idziaszek and T. Calarco, *Pseudopotential Method for Higher Partial Wave Scattering*, Physical Review Letters **96**, 013201 (2006).

[57] Z. Idziaszek, *Analytical solutions for two atoms in a harmonic trap: p-wave interactions*, Physical Review A **79**, 062701 (2009).

[58] H. Zhai, *Ultracold atomic physics* (Cambridge University Press, 2021).

[59] G. F. Gribakin and V. V. Flambaum, *Calculation of the scattering length in atomic collisions using the semiclassical approximation*, Physical Review A **48**, 546 (1993).

[60] Z. Idziaszek and P. S. Julienne, *Universal Rate Constants for Reactive Collisions of Ultracold Molecules*, Physical Review Letters **104**, 113202 (2010).

[61] A. V. Gorshkov, M. Hermele, V. Gurarie, C. Xu, P. S. Julienne, J. Ye, P. Zoller, E. Demler, M. D. Lukin, and A. M. Rey, *Two-orbital SU(N) magnetism with ultracold alkaline-earth atoms*, Nature Physics **6**, 289 (2010).

[62] X. Zhang, M. Bishof, S. L. Bromley, C. V. Kraus, M. S. Safronova, P. Zoller, A. M. Rey, and J. Ye, *Spectroscopic observation of SU(N)-symmetric interactions in Sr orbital magnetism*, Science **345**, 1467 (2014).

[63] A. Auerbach, *Interacting electrons and quantum magnetism* (Springer-Verlag, 1994).

[64] G. S. Agarwal, *Relation between atomic coherent-state representation, state multipoles, and generalized phase-space distributions*, Physical Review A **24**, 2889 (1981).

[65] D. F. Bailey, *Counting Arrangements of 1's and -1's*, Mathematics Magazine **69**, 128 (1996).

[66] M. D. Swallows, M. Bishof, Y. Lin, S. Blatt, M. J. Martin, A. M. Rey, and J. Ye, *Suppression of Collisional Shifts in a Strongly Interacting Lattice Clock*, Science **331**, 1043 (2011).

[67] J. Preskill, Physics 219 Course Information.

[68] M. O. Scully and M. S. Zubairy, *Quantum optics* (Cambridge University Press, Cambridge ; New York, 1997).

[69] H. M. Wiseman and G. J. Milburn, *Quantum measurement and control* (Cambridge University Press, Cambridge, UK ; New York, 2010), OCLC: ocn434744599.

[70] M. G. A. Paris, *Quantum Estimation for Quantum Technology*, International Journal of Quantum Information **07**, 125 (2009).

[71] L. J. Fiderer, T. Tufarelli, S. Piano, and G. Adesso, *General Expressions for the Quantum Fisher Information Matrix with Applications to Discrete Quantum Imaging*, PRX Quantum **2**, 020308 (2021).

[72] J. Liu, H. Yuan, X.-M. Lu, and X. Wang, *Quantum Fisher information matrix and multiparameter estimation*, Journal of Physics A: Mathematical and Theoretical **53**, 023001 (2020).

[73] L. Pezzé and A. Smerzi, *Entanglement, Nonlinear Dynamics, and the Heisenberg Limit*, Physical Review Letters **102**, 100401 (2009).

[74] D. J. Wineland, J. J. Bollinger, W. M. Itano, F. L. Moore, and D. J. Heinzen, *Spin squeezing and reduced quantum noise in spectroscopy*, Physical Review A **46**, R6797 (1992).

[75] K. Kim, A. Aeppli, T. Bothwell, and J. Ye, *Evaluation of Lattice Light Shift at Low 10^{-19} Uncertainty for a Shallow Lattice Sr Optical Clock*, Physical Review Letters **130**, 113203 (2023).

[76] S. L. Campbell, R. B. Hutson, G. E. Marti, A. Goban, N. Darkwah Oppong, R. L. McNally, L. Sonderhouse, J. M. Robinson, W. Zhang, B. J. Bloom, and J. Ye, *A Fermi-degenerate three-dimensional optical lattice clock*, Science **358**, 90 (2017).

[77] E. Oelker, R. B. Hutson, C. J. Kennedy, L. Sonderhouse, T. Bothwell, A. Goban, D. Kedar, C. Sanner, J. M. Robinson, G. E. Marti, D. G. Matei, T. Legero, M. Giunta, R. Holzwarth, F. Riehle, U. Sterr, and J. Ye, *Demonstration of 4.8×10^{-17} stability at 1 s for two independent optical clocks*, Nature Photonics **13**, 714 (2019).

[78] T. Nicholson, S. Campbell, R. Hutson, G. Marti, B. Bloom, R. McNally, W. Zhang, M. Barrett, M. Safronova, G. Strouse, W. Tew, and J. Ye, *Systematic evaluation of an atomic clock at 2×10^{-18} total uncertainty*, Nature Communications **6**, 6896 (2015).

[79] W. F. McGrew, X. Zhang, R. J. Fasano, S. A. Schäffer, K. Beloy, D. Nicolodi, R. C. Brown, N. Hinkley, G. Milani, M. Schioppo, T. H. Yoon, and A. D. Ludlow, *Atomic clock performance enabling geodesy below the centimetre level*, Nature **564**, 87 (2018).

[80] X. Zheng, J. Dolde, V. Lochab, B. N. Merriman, H. Li, and S. Kolkowitz, *Differential clock comparisons with a multiplexed optical lattice clock*, Nature **602**, 425 (2022).

[81] P. Lemonde and P. Wolf, *Optical lattice clock with atoms confined in a shallow trap*, Physical Review A **72**, 033409 (2005).

[82] I. Dimitrova, N. Jepsen, A. Buyskikh, A. Venegas-Gomez, J. Amato-Grill, A. Daley, and W. Ketterle, *Enhanced Superexchange in a Tilted Mott Insulator*, Physical Review Letters **124**, 043204 (2020).

[83] R. C. Brown, R. Wyllie, S. B. Koller, E. A. Goldschmidt, M. Foss-Feig, and J. V. Porto, *Two-dimensional superexchange-mediated magnetization dynamics in an optical lattice*, Science **348**, 540 (2015).

[84] S. Trotzky, P. Cheinet, S. Fölling, M. Feld, U. Schnorrberger, A. M. Rey, A. Polkovnikov, E. A. Demler, M. D. Lukin, and I. Bloch, *Time-Resolved Observation and Control of Superexchange Interactions with Ultracold Atoms in Optical Lattices*, Science **319**, 295 (2008).

[85] H. Miyake, G. A. Siviloglou, C. J. Kennedy, W. C. Burton, and W. Ketterle, *Realizing the Harper Hamiltonian with Laser-Assisted Tunneling in Optical Lattices*, Physical Review Letters **111**, 185302 (2013).

[86] M. Aidelsburger, M. Atala, M. Lohse, J. T. Barreiro, B. Paredes, and I. Bloch, *Realization of the Hofstadter Hamiltonian with Ultracold Atoms in Optical Lattices*, Physical Review Letters **111**, 185301 (2013).

[87] M. Aidelsburger, M. Lohse, C. Schweizer, M. Atala, J. Barreiro, S. Nascimbène, N. Cooper, I. Bloch, and N. Goldman, *Measuring the Chern number of Hofstadter bands with ultracold bosonic atoms*, Nature Physics **11**, 162 (2015).

[88] C. J. Kennedy, W. C. Burton, W. C. Chung, and W. Ketterle, *Observation of Bose–Einstein condensation in a strong synthetic magnetic field*, Nature Physics **11**, 859 (2015).

[89] J. Simon, W. S. Bakr, R. Ma, M. E. Tai, P. M. Preiss, and M. Greiner, *Quantum simulation of antiferromagnetic spin chains in an optical lattice*, Nature **472**, 307 (2011).

[90] F. Meinert, M. J. Mark, E. Kirilov, K. Lauber, P. Weinmann, A. J. Daley, and H.-C. Nägerl, *Quantum Quench in an Atomic One-Dimensional Ising Chain*, Physical Review Letters **111**, 053003 (2013).

[91] S. Scherg, T. Kohlert, P. Sala, F. Pollmann, B. Hebbe Madhusudhana, I. Bloch, and M. Aidelsburger, *Observing non-ergodicity due to kinetic constraints in tilted Fermi-Hubbard chains*, Nature Communications **12**, 4490 (2021).

[92] E. Guardado-Sanchez, A. Morningstar, B. M. Spar, P. T. Brown, D. A. Huse, and W. S. Bakr, *Subdiffusion and Heat Transport in a Tilted Two-Dimensional Fermi-Hubbard System*, Physical Review X **10**, 011042 (2020).

[93] W. Morong, F. Liu, P. Becker, K. S. Collins, L. Feng, A. Kyprianidis, G. Pagano, T. You, A. V. Gorshkov, and C. Monroe, *Observation of Stark many-body localization without disorder*, Nature **599**, 393 (2021).

[94] Q. Beaufils, G. Tackmann, X. Wang, B. Pelle, S. Pelisson, P. Wolf, and F. P. Dos Santos, *Laser Controlled Tunneling in a Vertical Optical Lattice*, Physical Review Letters **106**, 213002 (2011).

[95] G. M. Tino, *Testing gravity with cold atom interferometry: results and prospects*, Quantum Science and Technology **6**, 024014 (2021).

[96] V. Xu, M. Jaffe, C. D. Panda, S. L. Kristensen, L. W. Clark, and H. Müller, *Probing gravity by holding atoms for 20 seconds*, Science **366**, 745 (2019).

[97] G. K. Campbell, M. M. Boyd, J. W. Thomsen, M. J. Martin, S. Blatt, M. D. Swallows, T. L. Nicholson, T. Fortier, C. W. Oates, S. A. Diddams, N. D. Lemke, P. Naidon, P. Julienne, J. Ye, and A. D. Ludlow, *Probing Interactions Between Ultracold Fermions*, Science **324**, 360 (2009).

[98] A. D. Ludlow, N. D. Lemke, J. A. Sherman, C. W. Oates, G. Quéméner, J. Von Stecher, and A. M. Rey, *Cold-collision-shift cancellation and inelastic scattering in a Yb optical lattice clock*, Physical Review A **84**, 052724 (2011).

[99] N. D. Lemke, J. von Stecher, J. A. Sherman, A. M. Rey, C. W. Oates, and A. D. Ludlow, *p-Wave Cold Collisions in an Optical Lattice Clock*, Physical Review Letters **107**, 103902 (2011).

[100] M. J. Martin, M. Bishof, M. D. Swallows, X. Zhang, C. Benko, J. von Stecher, A. V. Gorshkov, A. M. Rey, and J. Ye, *A Quantum Many-Body Spin System in an Optical Lattice Clock*, Science **341**, 632 (2013).

[101] A. Rey, A. Gorshkov, C. Kraus, M. Martin, M. Bishof, M. Swallows, X. Zhang, C. Benko, J. Ye, N. Lemke, and A. Ludlow, *Probing many-body interactions in an optical lattice clock*, Annals of Physics **340**, 311 (2014).

[102] S. Kolkowitz, S. L. Bromley, T. Bothwell, M. L. Wall, G. E. Marti, A. P. Koller, X. Zhang, A. M. Rey, and J. Ye, *Spin–orbit-coupled fermions in an optical lattice clock*, Nature **542**, 66 (2017).

[103] S. L. Bromley, S. Kolkowitz, T. Bothwell, D. Kedar, A. Safavi-Naini, M. L. Wall, C. Salomon, A. M. Rey, and J. Ye, *Dynamics of interacting fermions under spin–orbit coupling in an optical lattice clock*, Nature Physics **14**, 399 (2018).

[104] M. L. Wall, A. P. Koller, S. Li, X. Zhang, N. R. Cooper, J. Ye, and A. M. Rey, *Synthetic Spin-Orbit Coupling in an Optical Lattice Clock*, Physical Review Letters **116**, 035301 (2016).

[105] J. Zhang, G. Pagano, P. W. Hess, A. Kyprianidis, P. Becker, H. Kaplan, A. V. Gorshkov, Z.-X. Gong, and C. Monroe, *Observation of a many-body dynamical phase transition with a 53-qubit quantum simulator*, Nature **551**, 601 (2017).

[106] K. Xu, Z.-H. Sun, W. Liu, Y.-R. Zhang, H. Li, H. Dong, W. Ren, P. Zhang, F. Nori, D. Zheng, H. Fan, and H. Wang, *Probing dynamical phase transitions with a superconducting quantum simulator*, Science Advances **6**, eaba4935 (2020).

[107] J. A. Muniz, D. Barberena, R. J. Lewis-Swan, D. J. Young, J. R. K. Cline, A. M. Rey, and J. K. Thompson, *Exploring dynamical phase transitions with cold atoms in an optical cavity*, Nature **580**, 602 (2020).

[108] S. Smale, P. He, B. A. Olsen, K. G. Jackson, H. Sharum, S. Trotzky, J. Marino, A. M. Rey, and J. H. Thywissen, *Observation of a transition between dynamical phases in a quantum degenerate Fermi gas*, Science Advances **5**, eaax1568 (2019).

[109] A. Goban, R. B. Hutson, G. E. Marti, S. L. Campbell, M. A. Perlin, P. S. Julienne, J. P. D'Incao, A. M. Rey, and J. Ye, *Emergence of multi-body interactions in a fermionic lattice clock*, Nature **563**, 369 (2018).

[110] S. Kolkowitz, I. Pikovski, N. Langellier, M. Lukin, R. Walsworth, and J. Ye, *Gravitational wave detection with optical lattice atomic clocks*, Physical Review D **94**, 124043 (2016).

[111] R. B. Hutson, W. R. Milner, L. Yan, J. Ye, and C. Sanner, *Observation of millihertz-level cooperative Lamb shifts in an optical atomic clock*, Science **383**, 384 (2024).

[112] Boulder Atomic Clock Optical Network (BACON) Collaboration* et al., *Frequency ratio measurements at 18-digit accuracy using an optical clock network*, Nature **591**, 564 (2021).

[113] N. Nemitz, T. Ohkubo, M. Takamoto, I. Ushijima, M. Das, N. Ohmae, and H. Katori, *Frequency ratio of Yb and Sr clocks with 5×10^{-17} uncertainty at 150 seconds averaging time*, Nature Photonics **10**, 258 (2016).

[114] W. M. Itano, J. C. Bergquist, J. J. Bollinger, J. M. Gilligan, D. J. Heinzen, F. L. Moore, M. G. Raizen, and D. J. Wineland, *Quantum projection noise: Population fluctuations in two-level systems*, Physical Review A **47**, 3554 (1993).

[115] W. J. Eckner, N. Darkwah Oppong, A. Cao, A. W. Young, W. R. Milner, J. M. Robinson, J. Ye, and A. M. Kaufman, *Realizing spin squeezing with Rydberg interactions in an optical clock*, Nature **621**, 734 (2023).

[116] J. Franke, S. R. Muleady, R. Kaubruegger, F. Kranzl, R. Blatt, A. M. Rey, M. K. Joshi, and C. F. Roos, *Quantum-enhanced sensing on optical transitions through finite-range interactions*, Nature **621**, 740 (2023).

[117] L. Sonderhouse, C. Sanner, R. B. Hutson, A. Goban, T. Bilitewski, L. Yan, W. R. Milner, A. M. Rey, and J. Ye, *Thermodynamics of a deeply degenerate SU(N)-symmetric Fermi gas*, Nature Physics **16**, 1216 (2020), Publisher: Nature Publishing Group.

[118] L.-M. Duan, E. Demler, and M. D. Lukin, *Controlling Spin Exchange Interactions of Ultracold Atoms in Optical Lattices*, Physical Review Letters **91**, 090402 (2003).

[119] M. Lewenstein, A. Sanpera, V. Ahufinger, B. Damski, A. Sen(De), and U. Sen, *Ultracold atomic gases in optical lattices: mimicking condensed matter physics and beyond*, Advances in Physics **56**, 243 (2007).

[120] E. Manousakis, *The spin-1/2 Heisenberg antiferromagnet on a square lattice and its application to the cuprous oxides*, Reviews of Modern Physics **63**, 1 (1991).

[121] P. A. Lee, N. Nagaosa, and X.-G. Wen, *Doping a Mott insulator: Physics of high-temperature superconductivity*, Reviews of Modern Physics **78**, 17 (2006).

[122] D. Greif, T. Uehlinger, G. Jotzu, L. Tarruell, and T. Esslinger, *Short-Range Quantum Magnetism of Ultracold Fermions in an Optical Lattice*, Science **340**, 1307 (2013).

[123] R. A. Hart, P. M. Duarte, T.-L. Yang, X. Liu, T. Paiva, E. Khatami, R. T. Scalettar, N. Trivedi, D. A. Huse, and R. G. Hulet, *Observation of antiferromagnetic correlations in the Hubbard model with ultracold atoms*, Nature **519**, 211 (2015).

[124] M. Boll, T. A. Hilker, G. Salomon, A. Omran, J. Nespolo, L. Pollet, I. Bloch, and C. Gross, *Spin- and density-resolved microscopy of antiferromagnetic correlations in Fermi-Hubbard chains*, Science **353**, 1257 (2016).

[125] L. W. Cheuk, M. A. Nichols, K. R. Lawrence, M. Okan, H. Zhang, E. Khatami, N. Trivedi, T. Paiva, M. Rigol, and M. W. Zwierlein, *Observation of spatial charge and spin correlations in the 2D Fermi-Hubbard model*, Science **353**, 1260 (2016).

[126] A. Mazurenko, C. S. Chiu, G. Ji, M. F. Parsons, M. Kanász-Nagy, R. Schmidt, F. Grusdt, E. Demler, D. Greif, and M. Greiner, *A cold-atom Fermi–Hubbard antiferromagnet*, Nature **545**, 462 (2017).

[127] M. Takahashi, *Thermodynamics of One-Dimensional Solvable Models* (Cambridge University Press, Cambridge, 1999).

[128] S. Taie, E. Ibarra-García-Padilla, N. Nishizawa, Y. Takasu, Y. Kuno, H.-T. Wei, R. T. Scalettar, K. R. A. Hazzard, and Y. Takahashi, *Observation of antiferromagnetic correlations in an ultracold SU(N) Hubbard model*, Nature Physics **18**, 1356 (2022).

[129] M. Gall, N. Wurz, J. Samland, C. F. Chan, and M. Köhl, *Competing magnetic orders in a bilayer Hubbard model with ultracold atoms*, Nature **589**, 40 (2021).

[130] P. N. Jepsen, J. Amato-Grill, I. Dimitrova, W. W. Ho, E. Demler, and W. Ketterle, *Spin transport in a tunable Heisenberg model realized with ultracold atoms*, Nature **588**, 403 (2020).

[131] H. Sun, B. Yang, H.-Y. Wang, Z.-Y. Zhou, G.-X. Su, H.-N. Dai, Z.-S. Yuan, and J.-W. Pan, *Realization of a bosonic antiferromagnet*, Nature Physics **17**, 990 (2021).

[132] M. Mamaev, I. Kimchi, R. M. Nandkishore, and A. M. Rey, *Tunable-spin-model generation with spin-orbit-coupled fermions in optical lattices*, Physical Review Research **3**, 013178 (2021).

[133] P. N. Jepsen, Y. K. E. Lee, H. Lin, I. Dimitrova, Y. Margalit, W. W. Ho, and W. Ketterle, *Long-lived phantom helix states in Heisenberg quantum magnets*, Nature Physics **18**, 899 (2022).

[134] B. Bertini, F. Heidrich-Meisner, C. Karrasch, T. Prosen, R. Steinigeweg, and M. Žnidarič, *Finite-temperature transport in one-dimensional quantum lattice models*, Reviews of Modern Physics **93**, 025003 (2021).

[135] P. He, M. A. Perlin, S. R. Muleady, R. J. Lewis-Swan, R. B. Hutson, J. Ye, and A. M. Rey, *Engineering spin squeezing in a 3D optical lattice with interacting spin-orbit-coupled fermions*, Physical Review Research **1**, 033075 (2019).

[136] T. Hernández Yanes, M. Płodzień, M. Mackoit Sinkevičienė, G. Žlabys, G. Juzeliūnas, and E. Witkowska, *One- and Two-Axis Squeezing via Laser Coupling in an Atomic Fermi-Hubbard Model*, Physical Review Letters **129**, 090403 (2022).

[137] M. Mamaev, D. Barberena, and A. M. Rey, *Spin squeezing in mixed-dimensional anisotropic lattice models*, Physical Review A **109**, 023326 (2024).

[138] G. E. Marti, R. B. Hutson, A. Goban, S. L. Campbell, N. Poli, and J. Ye, *Imaging Optical Frequencies with \$100\mu\mathrm{Hz}\$ Precision and \$1.1\mu\mathrm{m}\$ Resolution*, Physical Review Letters **120**, 103201 (2018), Publisher: American Physical Society.

[139] W. R. Milner, L. Yan, R. B. Hutson, C. Sanner, and J. Ye, *High-fidelity imaging of a band insulator in a three-dimensional optical lattice clock*, Physical Review A **107**, 063313 (2023).

[140] D. Matei, T. Legero, S. Häfner, C. Grebing, R. Weyrich, W. Zhang, L. Sonderhouse, J. Robinson, J. Ye, F. Riehle, and U. Sterr, *\$1.5\mu\mathrm{m}\$ Lasers with Sub-10 mHz Linewidth*, Physical Review Letters **118**, 263202 (2017).

[141] S. Murmann, A. Bergschneider, V. M. Klinkhamer, G. Zürn, T. Lompe, and S. Jochim, *Two Fermions in a Double Well: Exploring a Fundamental Building Block of the Hubbard Model*, Physical Review Letters **114**, 080402 (2015).

[142] R. B. Hutson, A. Goban, G. E. Marti, L. Sonderhouse, C. Sanner, and J. Ye, *Engineering Quantum States of Matter for Atomic Clocks in Shallow Optical Lattices*, Physical Review Letters **123**, 123401 (2019).

[143] T. Gullion, D. B. Baker, and M. S. Conradi, *New, compensated Carr-Purcell sequences*, Journal of Magnetic Resonance (1969) **89**, 479 (1990).

[144] J.-R. Li, K. Matsuda, C. Miller, A. N. Carroll, W. G. Tobias, J. S. Higgins, and J. Ye, *Tunable itinerant spin dynamics with polar molecules*, Nature **614**, 70 (2023).

[145] M. A. Perlin, C. Qu, and A. M. Rey, *Spin Squeezing with Short-Range Spin-Exchange Interactions*, Physical Review Letters **125**, 223401 (2020).

[146] A. L. Gaunt, T. F. Schmidutz, I. Gotlibovych, R. P. Smith, and Z. Hadzibabic, *Bose-Einstein Condensation of Atoms in a Uniform Potential*, Physical Review Letters **110**, 200406 (2013).

[147] D.-S. Lühmann, O. Jürgensen, and K. Sengstock, *Multi-orbital and density-induced tunneling of bosons in optical lattices*, New Journal of Physics **14**, 033021 (2012).

[148] A. Polkovnikov, *Phase space representation of quantum dynamics*, Annals of Physics **325**, 1790 (2010).

[149] S. Fray, C. A. Diez, T. W. Hänsch, and M. Weitz, *Atomic Interferometer with Amplitude Gratings of Light and Its Applications to Atom Based Tests of the Equivalence Principle*, Physical Review Letters **93**, 240404 (2004).

[150] H. Müller, A. Peters, and S. Chu, *A precision measurement of the gravitational redshift by the interference of matter waves*, Nature **463**, 926 (2010).

[151] S.-Y. Lan, P.-C. Kuan, B. Estey, D. English, J. M. Brown, M. A. Hohensee, and H. Müller, *A Clock Directly Linking Time to a Particle's Mass*, Science **339**, 554 (2013).

[152] M. Jaffe, P. Haslinger, V. Xu, P. Hamilton, A. Upadhye, B. Elder, J. Khoury, and H. Müller, *Testing sub-gravitational forces on atoms from a miniature in-vacuum source mass*, Nature Physics **13**, 938 (2017).

[153] G. Rosi, G. D'Amico, L. Cacciapuoti, F. Sorrentino, M. Prevedelli, M. Zych, C. Brukner, and G. M. Tino, *Quantum test of the equivalence principle for atoms in coherent superposition of internal energy states*, Nature Communications **8**, 15529 (2017).

[154] P. Asenbaum, C. Overstreet, M. Kim, J. Curti, and M. A. Kasevich, *Atom-Interferometric Test of the Equivalence Principle at the 10^{-12} Level*, Physical Review Letters **125**, 191101 (2020).

[155] C. W. Chou, D. B. Hume, T. Rosenband, and D. J. Wineland, *Optical Clocks and Relativity*, Science **329**, 1630 (2010).

[156] M. Takamoto, I. Ushijima, N. Ohmae, T. Yahagi, K. Kokado, H. Shinkai, and H. Katori, *Test of general relativity by a pair of transportable optical lattice clocks*, Nature Photonics **14**, 411 (2020).

[157] X. Zheng, J. Dolde, M. C. Cambria, H. M. Lim, and S. Kolkowitz, *A lab-based test of the gravitational redshift with a miniature clock network*, Nature Communications **14**, 4886 (2023).

[158] F. E. Close and H. Osborn, *Relativistic Center-of-Mass Motion and the Electromagnetic Interaction of Systems of Charged Particles*, Physical Review D **2**, 2127 (1970).

[159] K.-P. Marzlin, *Dipole coupling of atoms and light in gravitational fields*, Physical Review A **51**, 625 (1995).

[160] S. Dimopoulos, P. W. Graham, J. M. Hogan, and M. A. Kasevich, *General relativistic effects in atom interferometry*, Physical Review D **78**, 042003 (2008).

[161] M. Sonnleitner and S. M. Barnett, *Mass-energy and anomalous friction in quantum optics*, Physical Review A **98**, 042106 (2018).

[162] V. Yudin and A. Taichenachev, *Mass defect effects in atomic clocks*, Laser Physics Letters **15**, 035703 (2018).

[163] P. K. Schwartz and D. Giulini, *Post-Newtonian Hamiltonian description of an atom in a weak gravitational field*, Physical Review A **100**, 052116 (2019).

[164] R. Haustein, G. J. Milburn, and M. Zych, Mass-energy equivalence in harmonically trapped particles, 2019, arXiv:1906.03980 [cond-mat, physics:quant-ph].

[165] S. Khandelwal, M. P. Lock, and M. P. Woods, *Universal quantum modifications to general relativistic time dilation in delocalised clocks*, Quantum **4**, 309 (2020).

[166] F. Di Pumpo, C. Ufrecht, A. Friedrich, E. Giese, W. P. Schleich, and W. G. Unruh, *Gravitational Redshift Tests with Atomic Clocks and Atom Interferometers*, PRX Quantum **2**, 040333 (2021).

[167] P. T. Grochowski, A. R. H. Smith, A. Dragan, and K. Debski, *Quantum time dilation in atomic spectra*, Physical Review Research **3**, 023053 (2021).

[168] V. J. Martínez-Lahuerta, S. Eilers, T. E. Mehlstäubler, P. O. Schmidt, and K. Hammerer, *Ab initio quantum theory of mass defect and time dilation in trapped-ion optical clocks*, Physical Review A **106**, 032803 (2022).

[169] F. Di Pumpo, A. Friedrich, A. Geyer, C. Ufrecht, and E. Giese, *Light propagation and atom interferometry in gravity and dilaton fields*, Physical Review D **105**, 084065 (2022).

[170] A. Alibabaei, P. K. Schwartz, and D. Giulini, *Geometric post-Newtonian description of massive spin-half particles in curved spacetime*, Classical and Quantum Gravity **40**, 235014 (2023).

[171] M. Werner, P. K. Schwartz, J.-N. Kirsten-Siemß, N. Gaaloul, D. Giulini, and K. Hammerer, *Atom interferometers in weakly curved spacetimes using Bragg diffraction and Bloch oscillations*, Physical Review D **109**, 022008 (2024).

[172] M. Zych, F. Costa, I. Pikovski, and C. Brukner, *Quantum interferometric visibility as a witness of general relativistic proper time*, Nature Communications **2**, 505 (2011).

[173] I. Pikovski, M. Zych, F. Costa, and C. Brukner, *Universal decoherence due to gravitational time dilation*, Nature Physics **11**, 668 (2015).

[174] I. Pikovski, M. Zych, F. Costa, and C. Brukner, *Time dilation in quantum systems and decoherence*, New Journal of Physics **19**, 025011 (2017).

[175] M. Zych and C. Brukner, *Quantum formulation of the Einstein equivalence principle*, Nature Physics **14**, 1027 (2018).

[176] A. Roura, *Gravitational Redshift in Quantum-Clock Interferometry*, Physical Review X **10**, 021014 (2020).

[177] A. R. H. Smith and M. Ahmadi, *Quantum clocks observe classical and quantum time dilation*, Nature Communications **11**, 5360 (2020).

[178] C. Marletto and V. Vedral, *Gravitationally Induced Entanglement between Two Massive Particles is Sufficient Evidence of Quantum Effects in Gravity*, Physical Review Letters **119**, 240402 (2017).

[179] S. Bose, A. Mazumdar, G. W. Morley, H. Ulbricht, M. Toroš, M. Paternostro, A. A. Geraci, P. F. Barker, M. Kim, and G. Milburn, *Spin Entanglement Witness for Quantum Gravity*, Physical Review Letters **119**, 240401 (2017).

[180] M. Zych, L. Rudnicki, and I. Pikovski, *Gravitational mass of composite systems*, Physical Review D **99**, 104029 (2019).

[181] A. Paige, A. Plato, and M. Kim, *Classical and Nonclassical Time Dilation for Quantum Clocks*, Physical Review Letters **124**, 160602 (2020).

[182] D. Carney, H. Müller, and J. M. Taylor, *Using an Atom Interferometer to Infer Gravitational Entanglement Generation*, PRX Quantum **2**, 030330 (2021).

[183] J. S. Pedernales, K. Streltsov, and M. B. Plenio, *Enhancing Gravitational Interaction between Quantum Systems by a Massive Mediator*, Physical Review Letters **128**, 110401 (2022).

[184] M. Christodoulou, A. Di Biagio, M. Aspelmeyer, C. Brukner, C. Rovelli, and R. Howl, *Locally Mediated Entanglement in Linearized Quantum Gravity*, Physical Review Letters **130**, 100202 (2023).

[185] C. M. Will, *Theory and Experiment in Gravitational Physics*, 2nd ed. (Cambridge University Press, 2018).

[186] M. A. Norcia, R. J. Lewis-Swan, J. R. K. Cline, B. Zhu, A. M. Rey, and J. K. Thompson, *Cavity-mediated collective spin-exchange interactions in a strontium superradiant laser*, Science **361**, 259 (2018).

[187] J. C. Allred, R. N. Lyman, T. W. Kornack, and M. V. Romalis, *High-Sensitivity Atomic Magnetometer Unaffected by Spin-Exchange Relaxation*, Physical Review Letters **89**, 130801 (2002).

[188] C. Deutsch, F. Ramirez-Martinez, C. Lacroûte, F. Reinhard, T. Schneider, J. N. Fuchs, F. Piéchon, F. Laloë, J. Reichel, and P. Rosenbusch, *Spin Self-Rephasing and Very Long Coherence Times in a Trapped Atomic Ensemble*, Physical Review Letters **105**, 020401 (2010).

[189] E. J. Davis, A. Periwal, E. S. Cooper, G. Bentsen, S. J. Evered, K. Van Kirk, and M. H. Schleier-Smith, *Protecting Spin Coherence in a Tunable Heisenberg Model*, Physical Review Letters **125**, 060402 (2020).

[190] I. D. Leroux, M. H. Schleier-Smith, and V. Vuletić, *Implementation of Cavity Squeezing of a Collective Atomic Spin*, Physical Review Letters **104**, 073602 (2010).

[191] M. A. Perlin and A. M. Rey, *Effective multi-body SU(N)-symmetric interactions of ultracold fermionic atoms on a 3D lattice*, New Journal of Physics **21**, 043039 (2019).

[192] A. Piñeiro Orioli, J. Thompson, and A. Rey, *Emergent Dark States from Superradiant Dynamics in Multilevel Atoms in a Cavity*, Physical Review X **12**, 011054 (2022).

[193] J. Marino, M. Eckstein, M. S. Foster, and A. M. Rey, *Dynamical phase transitions in the collisionless pre-thermal states of isolated quantum systems: theory and experiments*, Reports on Progress in Physics **85**, 116001 (2022).

[194] M. Heyl, *Dynamical quantum phase transitions: a review*, Reports on Progress in Physics **81**, 054001 (2018).

[195] M. Heyl, A. Polkovnikov, and S. Kehrein, *Dynamical Quantum Phase Transitions in the Transverse-Field Ising Model*, Physical Review Letters **110**, 135704 (2013).

[196] B. Žunkovič, M. Heyl, M. Knap, and A. Silva, *Dynamical Quantum Phase Transitions in Spin Chains with Long-Range Interactions: Merging Different Concepts of Nonequilibrium Criticality*, Physical Review Letters **120**, 130601 (2018).

[197] R. Nandkishore and D. A. Huse, *Many-Body Localization and Thermalization in Quantum Statistical Mechanics*, Annual Review of Condensed Matter Physics **6**, 15 (2015).

[198] D. A. Abanin, E. Altman, I. Bloch, and M. Serbyn, *Colloquium : Many-body localization, thermalization, and entanglement*, Reviews of Modern Physics **91**, 021001 (2019).

[199] P. Sierant, M. Lewenstein, A. Scardicchio, L. Vidmar, and J. Zakrzewski, Many-Body Localization in the Age of Classical Computing, 2024, arXiv:2403.07111 [cond-mat, physics:quant-ph].

[200] R. J. Lewis-Swan, A. Safavi-Naini, A. M. Kaufman, and A. M. Rey, *Dynamics of quantum information*, Nature Reviews Physics **1**, 627 (2019).

[201] S. Xu and B. Swingle, *Scrambling Dynamics and Out-of-Time-Ordered Correlators in Quantum Many-Body Systems*, PRX Quantum **5**, 010201 (2024).

[202] M. K. Joshi, F. Kranzl, A. Schuckert, I. Lovas, C. Maier, R. Blatt, M. Knap, and C. F. Roos, *Observing emergent hydrodynamics in a long-range quantum magnet*, Science **376**, 720 (2022).

[203] D. Wei, A. Rubio-Abadal, B. Ye, F. Machado, J. Kemp, K. Srakaew, S. Hollerith, J. Rui, S. Gopalakrishnan, N. Y. Yao, I. Bloch, and J. Zeiher, *Quantum gas microscopy of Kardar-Parisi-Zhang superdiffusion*, Science **376**, 716 (2022).

[204] H. Bernien, S. Schwartz, A. Keesling, H. Levine, A. Omran, H. Pichler, S. Choi, A. S. Zibrov, M. Endres, M. Greiner, V. Vuletić, and M. D. Lukin, *Probing many-body dynamics on a 51-atom quantum simulator*, Nature **551**, 579 (2017).

[205] P. Jurcevic, H. Shen, P. Hauke, C. Maier, T. Brydges, C. Hempel, B. P. Lanyon, M. Heyl, R. Blatt, and C. F. Roos, *Direct Observation of Dynamical Quantum Phase Transitions in an Interacting Many-Body System*, Physical Review Letters **119**, 080501 (2017).

[206] H.-X. Yang, T. Tian, Y.-B. Yang, L.-Y. Qiu, H.-Y. Liang, A.-J. Chu, C. B. Dağ, Y. Xu, Y. Liu, and L.-M. Duan, *Observation of dynamical quantum phase transitions in a spinor condensate*, Physical Review A **100**, 013622 (2019).

[207] J. L. Bohn, A. M. Rey, and J. Ye, *Cold molecules: Progress in quantum engineering of chemistry and quantum matter*, Science **357**, 1002 (2017).

[208] N. Q. Burdick, Y. Tang, and B. L. Lev, *Long-Lived Spin-Orbit-Coupled Degenerate Dipolar Fermi Gas*, Physical Review X **6**, 031022 (2016).

[209] S. Baier, M. J. Mark, D. Petter, K. Aikawa, L. Chomaz, Z. Cai, M. Baranov, P. Zoller, and F. Ferlaino, *Extended Bose-Hubbard models with ultracold magnetic atoms*, Science **352**, 201 (2016).

[210] S. Lepoutre, J. Schachenmayer, L. Gabardos, B. Zhu, B. Naylor, E. Maréchal, O. Gorceix, A. M. Rey, L. Vernac, and B. Laburthe-Tolra, *Out-of-equilibrium quantum magnetism and thermalization in a spin-3 many-body dipolar lattice system*, Nature Communications **10**, 1714 (2019).

[211] C. S. Adams, J. D. Pritchard, and J. P. Shaffer, *Rydberg atom quantum technologies*, Journal of Physics B: Atomic, Molecular and Optical Physics **53**, 012002 (2020).

[212] C. D. Bruzewicz, J. Chiaverini, R. McConnell, and J. M. Sage, *Trapped-ion quantum computing: Progress and challenges*, Applied Physics Reviews **6**, 021314 (2019).

[213] R. Mottl, F. Brennecke, K. Baumann, R. Landig, T. Donner, and T. Esslinger, *Roton-Type Mode Softening in a Quantum Gas with Cavity-Mediated Long-Range Interactions*, Science **336**, 1570 (2012).

[214] E. J. Davis, G. Bentsen, L. Homeier, T. Li, and M. H. Schleier-Smith, *Photon-Mediated Spin-Exchange Dynamics of Spin-1 Atoms*, Physical Review Letters **122**, 010405 (2019).

[215] Y. Guo, R. M. Kroeze, V. D. Vaidya, J. Keeling, and B. L. Lev, *Sign-Changing Photon-Mediated Atom Interactions in Multimode Cavity Quantum Electrodynamics*, Physical Review Letters **122**, 193601 (2019).

[216] A. M. Rey, A. V. Gorshkov, and C. Rubbo, *Many-Body Treatment of the Collisional Frequency Shift in Fermionic Atoms*, Physical Review Letters **103**, 260402 (2009).

[217] A. P. Koller, M. L. Wall, J. Mundinger, and A. M. Rey, *Dynamics of Interacting Fermions in Spin-Dependent Potentials*, Physical Review Letters **117**, 195302 (2016).

[218] G. Kleine Büning, J. Will, W. Ertmer, E. Rasel, J. Arlt, C. Klempt, F. Ramirez-Martinez, F. Piéchon, and P. Rosenbusch, *Extended Coherence Time on the Clock Transition of Optically Trapped Rubidium*, Physical Review Letters **106**, 240801 (2011).

[219] C. Solaro, A. Bonnin, F. Combes, M. Lopez, X. Alauze, J.-N. Fuchs, F. Piéchon, and F. Pereira Dos Santos, *Competition between Spin Echo and Spin Self-Rephasing in a Trapped Atom Interferometer*, Physical Review Letters **117**, 163003 (2016).

[220] A. Widera, S. Trotzky, P. Cheinet, S. Fölling, F. Gerbier, I. Bloch, V. Gritsev, M. D. Lukin, and E. Demler, *Quantum Spin Dynamics of Mode-Squeezed Luttinger Liquids in Two-Component Atomic Gases*, Physical Review Letters **100**, 140401 (2008).

[221] H. Lipkin, N. Meshkov, and A. Glick, *Validity of many-body approximation methods for a solvable model*, Nuclear Physics **62**, 188 (1965).

[222] V. Borish, O. Marković, J. A. Hines, S. V. Rajagopal, and M. Schleier-Smith, *Transverse-Field Ising Dynamics in a Rydberg-Dressed Atomic Gas*, Physical Review Letters **124**, 063601 (2020).

[223] B. Allard, M. Fadel, R. Schmied, and P. Treutlein, *Sideband Rabi spectroscopy of finite-temperature trapped Bose gases*, Physical Review A **93**, 043624 (2016).

[224] A. Sørensen, L.-M. Duan, J. I. Cirac, and P. Zoller, *Many-particle entanglement with Bose–Einstein condensates*, Nature **409**, 63 (2001).

[225] A. Micheli, D. Jaksch, J. I. Cirac, and P. Zoller, *Many-particle entanglement in two-component Bose-Einstein condensates*, Physical Review A **67**, 013607 (2003).

[226] E. G. M. Van Kempen, S. J. J. M. F. Kokkelmans, D. J. Heinzen, and B. J. Verhaar, *Interisotope Determination of Ultracold Rubidium Interactions from Three High-Precision Experiments*, Physical Review Letters **88**, 093201 (2002).

[227] Y.-J. Lin, A. R. Perry, R. L. Compton, I. B. Spielman, and J. V. Porto, *Rapid production of 87Rb Bose-Einstein condensates in a combined magnetic and optical potential*, Physical Review A **79**, 063631 (2009).

[228] A. Kaplan, M. Fredslund Andersen, and N. Davidson, *Suppression of inhomogeneous broadening in rf spectroscopy of optically trapped atoms*, Physical Review A **66**, 045401 (2002).

[229] W. Maineult, C. Deutsch, K. Gibble, J. Reichel, and P. Rosenbusch, *Spin Waves and Collisional Frequency Shifts of a Trapped-Atom Clock*, Physical Review Letters **109**, 020407 (2012).

[230] G. Reinaudi, T. Lahaye, Z. Wang, and D. Guéry-Odelin, *Strong saturation absorption imaging of dense clouds of ultracold atoms*, Optics Letters **32**, 3143 (2007).

[231] J. Schachenmayer, A. Pikovski, and A. M. Rey, *Many-Body Quantum Spin Dynamics with Monte Carlo Trajectories on a Discrete Phase Space*, Physical Review X **5**, 011022 (2015).

[232] O. Dutta, M. Gajda, P. Hauke, M. Lewenstein, D.-S. Lühmann, B. A. Malomed, T. Sowiński, and J. Zakrzewski, *Non-standard Hubbard models in optical lattices: a review*, Reports on Progress in Physics **78**, 066001 (2015).

[233] G. I. Japaridze and A. P. Kampf, *Weak-coupling phase diagram of the extended Hubbard model with correlated-hopping interaction*, Physical Review B **59**, 12822 (1999).

[234] T. J. Elliott and I. B. Mekhov, *Engineering many-body dynamics with quantum light potentials and measurements*, Physical Review A **94**, 013614 (2016).

[235] F. Görg, K. Sandholzer, J. Minguzzi, R. Desbuquois, M. Messer, and T. Esslinger, *Realization of density-dependent Peierls phases to engineer quantized gauge fields coupled to ultracold matter*, Nature Physics **15**, 1161 (2019).

[236] C. Schweizer, F. Grusdt, M. Berngruber, L. Barbiero, E. Demler, N. Goldman, I. Bloch, and M. Aidelsburger, *Floquet approach to Z2 lattice gauge theories with ultracold atoms in optical lattices*, Nature Physics **15**, 1168 (2019).

[237] C. V. Kraus, M. Dalmonte, M. A. Baranov, A. M. Läuchli, and P. Zoller, *Majorana Edge States in Atomic Wires Coupled by Pair Hopping*, Physical Review Letters **111**, 173004 (2013).

[238] T. Chanda, R. Kraus, G. Morigi, and J. Zakrzewski, *Self-organized topological insulator due to cavity-mediated correlated tunneling*, Quantum **5**, 501 (2021).

[239] R. Ma, M. E. Tai, P. M. Preiss, W. S. Bakr, J. Simon, and M. Greiner, *Photon-Assisted Tunneling in a Biased Strongly Correlated Bose Gas*, Physical Review Letters **107**, 095301 (2011).

[240] F. Meinert, M. Mark, K. Lauber, A. Daley, and H.-C. Nägerl, *Floquet Engineering of Correlated Tunneling in the Bose-Hubbard Model with Ultracold Atoms*, Physical Review Letters **116**, 205301 (2016).

[241] W. Xu, W. Morong, H.-Y. Hui, V. W. Scarola, and B. DeMarco, *Correlated spin-flip tunneling in a Fermi lattice gas*, Physical Review A **98**, 023623 (2018).

[242] L. W. Clark, B. M. Anderson, L. Feng, A. Gaj, K. Levin, and C. Chin, *Observation of Density-Dependent Gauge Fields in a Bose-Einstein Condensate Based on Micromotion Control in a Shaken Two-Dimensional Lattice*, Physical Review Letters **121**, 030402 (2018).

[243] K. Baumann, C. Guerlin, F. Brennecke, and T. Esslinger, *Dicke quantum phase transition with a superfluid gas in an optical cavity*, Nature **464**, 1301 (2010).

[244] J. Klinder, H. Keßler, M. R. Bakhtiari, M. Thorwart, and A. Hemmerich, *Observation of a Superradiant Mott Insulator in the Dicke-Hubbard Model*, Physical Review Letters **115**, 230403 (2015).

[245] S. Schuster, P. Wolf, S. Ostermann, S. Slama, and C. Zimmermann, *Supersolid Properties of a Bose-Einstein Condensate in a Ring Resonator*, Physical Review Letters **124**, 143602 (2020).

[246] X. Zhang, Y. Chen, Z. Wu, J. Wang, J. Fan, S. Deng, and H. Wu, *Observation of a superradiant quantum phase transition in an intracavity degenerate Fermi gas*, Science **373**, 1359 (2021).

[247] Y. Guo, R. M. Kroeze, B. P. Marsh, S. Gopalakrishnan, J. Keeling, and B. L. Lev, *An optical lattice with sound*, Nature **599**, 211 (2021).

[248] A. Periwal, E. S. Cooper, P. Kunkel, J. F. Wienand, E. J. Davis, and M. Schleier-Smith, *Programmable interactions and emergent geometry in an array of atom clouds*, Nature **600**, 630 (2021).

[249] H. Konishi, K. Roux, V. Helson, and J.-P. Brantut, *Universal pair polaritons in a strongly interacting Fermi gas*, Nature **596**, 509 (2021).

[250] R. Rosa-Medina, F. Ferri, F. Finger, N. Dogra, K. Kroeger, R. Lin, R. Chitra, T. Donner, and T. Esslinger, *Observing Dynamical Currents in a Non-Hermitian Momentum Lattice*, Physical Review Letters **128**, 143602 (2022).

[251] A. S. Sørensen and K. Mølmer, *Entangling atoms in bad cavities*, Physical Review A **66**, 022314 (2002).

[252] A. Celi, P. Massignan, J. Ruseckas, N. Goldman, I. Spielman, G. Juzeliūnas, and M. Lewenstein, *Synthetic Gauge Fields in Synthetic Dimensions*, Physical Review Letters **112**, 043001 (2014).

[253] T. Ozawa and H. M. Price, *Topological quantum matter in synthetic dimensions*, Nature Reviews Physics **1**, 349 (2019).

[254] M. Mancini, G. Pagano, G. Cappellini, L. Livi, M. Rider, J. Catani, C. Sias, P. Zoller, M. Inguscio, M. Dalmonte, and L. Fallani, *Observation of chiral edge states with neutral fermions in synthetic Hall ribbons*, Science **349**, 1510 (2015).

[255] B. K. Stuhl, H.-I. Lu, L. M. Aycock, D. Genkina, and I. B. Spielman, *Visualizing edge states with an atomic Bose gas in the quantum Hall regime*, Science **349**, 1514 (2015).

[256] T. Chalopin, T. Satoor, A. Evrard, V. Makhalov, J. Dalibard, R. Lopes, and S. Nascimbene, *Probing chiral edge dynamics and bulk topology of a synthetic Hall system*, Nature Physics **16**, 1017 (2020).

[257] T.-W. Zhou, G. Cappellini, D. Tusi, L. Franchi, J. Parravicini, C. Repellin, S. Greschner, M. Inguscio, T. Giamarchi, M. Filippone, J. Catani, and L. Fallani, *Observation of universal Hall response in strongly interacting Fermions*, Science **381**, 427 (2023).

[258] O. Katz, M. Cetina, and C. Monroe, *N -Body Interactions between Trapped Ion Qubits via Spin-Dependent Squeezing*, Physical Review Letters **129**, 063603 (2022).

[259] J. Kitzinger, M. Chaudhary, M. Kondappan, V. Ivannikov, and T. Byrnes, *Two-axis two-spin squeezed states*, Physical Review Research **2**, 033504 (2020).

[260] M. Cheneau, P. Barmettler, D. Poletti, M. Endres, P. Schauß, T. Fukuhara, C. Gross, I. Bloch, C. Kollath, and S. Kuhr, *Light-cone-like spreading of correlations in a quantum many-body system*, Nature **481**, 484 (2012).

[261] P. Jurcevic, B. P. Lanyon, P. Hauke, C. Hempel, P. Zoller, R. Blatt, and C. F. Roos, *Quasiparticle engineering and entanglement propagation in a quantum many-body system*, Nature **511**, 202 (2014).

[262] P. Richerme, Z.-X. Gong, A. Lee, C. Senko, J. Smith, M. Foss-Feig, S. Michalakis, A. V. Gorshkov, and C. Monroe, *Non-local propagation of correlations in quantum systems with long-range interactions*, Nature **511**, 198 (2014).

[263] M. A. Norcia, J. R. Cline, J. A. Muniz, J. M. Robinson, R. B. Hutson, A. Goban, G. E. Marti, J. Ye, and J. K. Thompson, *Frequency Measurements of Superradiance from the Strontium Clock Transition*, Physical Review X **8**, 021036 (2018).

[264] R. Belyansky, P. Bienias, Y. A. Kharkov, A. V. Gorshkov, and B. Swingle, *Minimal Model for Fast Scrambling*, Physical Review Letters **125**, 130601 (2020).

[265] M. M. Boyd, T. Zelevinsky, A. D. Ludlow, S. Blatt, T. Zanon-Willette, S. M. Foreman, and J. Ye, *Nuclear spin effects in optical lattice clocks*, Physical Review A **76**, 022510 (2007).

[266] F. Bloch, *Über die Quantenmechanik der Elektronen in Kristallgittern*, Zeitschrift für Physik **52**, 555 (1929).

[267] C. Waschke, H. G. Roskos, R. Schwedler, K. Leo, H. Kurz, and K. Köhler, *Coherent submillimeter-wave emission from Bloch oscillations in a semiconductor superlattice*, Physical Review Letters **70**, 3319 (1993).

[268] M. Ben Dahan, E. Peik, J. Reichel, Y. Castin, and C. Salomon, *Bloch Oscillations of Atoms in an Optical Potential*, Physical Review Letters **76**, 4508 (1996).

[269] B. P. Anderson and M. A. Kasevich, *Macroscopic Quantum Interference from Atomic Tunnel Arrays*, Science **282**, 1686 (1998).

[270] H. Keßler, J. Klinder, B. P. Venkatesh, C. Georges, and A. Hemmerich, *In situ observation of optomechanical Bloch oscillations in an optical cavity*, New Journal of Physics **18**, 102001 (2016).

[271] C. Georges, J. Vargas, H. Keßler, J. Klinder, and A. Hemmerich, *Bloch oscillations of a Bose-Einstein condensate in a cavity-induced optical lattice*, Physical Review A **96**, 063615 (2017).

[272] B. M. Peden, D. Meiser, M. L. Chiofalo, and M. J. Holland, *Nondestructive cavity QED probe of Bloch oscillations in a gas of ultracold atoms*, Physical Review A **80**, 043803 (2009).

[273] B. Prasanna Venkatesh, M. Trupke, E. A. Hinds, and D. H. J. O'Dell, *Atomic Bloch-Zener oscillations for sensitive force measurements in a cavity*, Physical Review A **80**, 063834 (2009).

[274] B. P. Venkatesh and D. H. J. O'Dell, *Bloch oscillations of cold atoms in a cavity: Effects of quantum noise*, Physical Review A **88**, 013848 (2013).

[275] B. Wu, G. P. Greve, C. Luo, and J. K. Thompson, Site-dependent selection of atoms for homogeneous atom-cavity coupling, 2021.

[276] R. D. Niederriter, C. Schlupf, and P. Hamilton, *Cavity probe for real-time detection of atom dynamics in an optical lattice*, Physical Review A **102**, 051301 (2020).

[277] A. Buchleitner and A. R. Kolovsky, *Interaction-Induced Decoherence of Atomic Bloch Oscillations*, Physical Review Letters **91**, 253002 (2003).

[278] A. R. Kolovsky, *New Bloch Period for Interacting Cold Atoms in 1D Optical Lattices*, Physical Review Letters **90**, 213002 (2003).

[279] D. Witthaut, M. Werder, S. Mossmann, and H. J. Korsch, *Bloch oscillations of Bose-Einstein condensates: Breakdown and revival*, Physical Review E **71**, 036625 (2005).

[280] T. Schulte, S. Drenkelforth, G. K. Büning, W. Ertmer, J. Arlt, M. Lewenstein, and L. Santos, *Dynamics of Bloch oscillations in disordered lattice potentials*, Physical Review A **77**, 023610 (2008).

[281] S. Walter, D. Schneble, and A. C. Durst, *Bloch oscillations in lattice potentials with controlled aperiodicity*, Physical Review A **81**, 033623 (2010).

[282] F. Meinert, M. Mark, E. Kirilov, K. Lauber, P. Weinmann, M. Gröbner, and H.-C. Nägerl, *Interaction-Induced Quantum Phase Revivals and Evidence for the Transition to the Quantum Chaotic Regime in 1D Atomic Bloch Oscillations*, Physical Review Letters **112**, 193003 (2014).

[283] A. Alberti, G. Ferrari, V. V. Ivanov, M. L. Chiofalo, and G. M. Tino, *Atomic wave packets in amplitude-modulated vertical optical lattices*, New Journal of Physics **12**, 065037 (2010).

[284] L. Masi, T. Petrucciani, G. Ferioli, G. Semeghini, G. Modugno, M. Inguscio, and M. Fattori, *Spatial Bloch Oscillations of a Quantum Gas in a "Beat-Note" Superlattice*, Physical Review Letters **127**, 020601 (2021).

[285] Z. Li, S. Colombo, C. Shu, G. Velez, S. Pilatowsky-Cameo, R. Schmied, S. Choi, M. Lukin, E. Pedrozo-Peñafiel, and V. Vuletić, *Improving metrology with quantum scrambling*, Science **380**, 1381 (2023).

[286] C. Gross, H. Strobel, E. Nicklas, T. Zibold, N. Bar-Gill, G. Kurizki, and M. K. Oberthaler, *Atomic homodyne detection of continuous-variable entangled twin-atom states*, Nature **480**, 219 (2011).

[287] B. Lücke, M. Scherer, J. Kruse, L. Pezzé, F. Deuretzbacher, P. Hyllus, O. Topic, J. Peise, W. Ertmer, J. Arlt, L. Santos, A. Smerzi, and C. Klempt, *Twin Matter Waves for Interferometry Beyond the Classical Limit*, Science **334**, 773 (2011).

[288] F. Finger, R. Rosa-Medina, N. Reiter, P. Christodoulou, T. Donner, and T. Esslinger, *Spin- and Momentum-Correlated Atom Pairs Mediated by Photon Exchange and Seeded by Vacuum Fluctuations*, Physical Review Letters **132**, 093402 (2024).

[289] C. D. Panda, M. Tao, J. Egelhoff, M. Ceja, V. Xu, and H. Müller, Minute-scale gravimetry using a coherent atomic spatial superposition, 2023, arXiv:2210.07289 [gr-qc, physics:physics, physics:quant-ph].

[290] M. Glück, *Wannier–Stark resonances in optical and semiconductor superlattices*, Physics Reports **366**, 103 (2002).

[291] E. Colella, A. Kosior, F. Mivehvar, and H. Ritsch, *Open Quantum System Simulation of Faraday's Induction Law via Dynamical Instabilities*, Physical Review Letters **128**, 070603 (2022).

[292] K. C. Cox, G. P. Greve, B. Wu, and J. K. Thompson, *Spatially homogeneous entanglement for matter-wave interferometry created with time-averaged measurements*, Physical Review A **94**, 061601 (2016).

[293] J. Bardeen, L. N. Cooper, and J. R. Schrieffer, *Theory of Superconductivity*, Physical Review **108**, 1175 (1957).

[294] E. A. Yuzbashyan, O. Tsyplyatyev, and B. L. Altshuler, *Relaxation and Persistent Oscillations of the Order Parameter in Fermionic Condensates*, Physical Review Letters **96**, 097005 (2006).

[295] R. A. Barankov and L. S. Levitov, *Synchronization in the BCS Pairing Dynamics as a Critical Phenomenon*, Physical Review Letters **96**, 230403 (2006).

[296] E. A. Yuzbashyan and M. Dzero, *Dynamical Vanishing of the Order Parameter in a Fermionic Condensate*, Physical Review Letters **96**, 230404 (2006).

[297] V. Gurarie and L. Radzihovsky, *Resonantly paired fermionic superfluids*, Annals of Physics **322**, 2 (2007).

[298] V. Gurarie, *Nonequilibrium Dynamics of Weakly and Strongly Paired Superconductors*, Physical Review Letters **103**, 075301 (2009).

[299] M. S. Foster, M. Dzero, V. Gurarie, and E. A. Yuzbashyan, *Quantum quench in a $p + i\,p$ superfluid: Winding numbers and topological states far from equilibrium*, Physical Review B **88**, 104511 (2013).

[300] E. A. Yuzbashyan, M. Dzero, V. Gurarie, and M. S. Foster, *Quantum quench phase diagrams of an s -wave BCS-BEC condensate*, Physical Review A **91**, 033628 (2015).

[301] R. J. Lewis-Swan, D. Barberena, J. R. Cline, D. J. Young, J. K. Thompson, and A. M. Rey, *Cavity-QED Quantum Simulator of Dynamical Phases of a Bardeen-Cooper-Schrieffer Superconductor*, Physical Review Letters **126**, 173601 (2021).

[302] S. P. Kelly, J. K. Thompson, A. M. Rey, and J. Marino, *Resonant light enhances phase coherence in a cavity QED simulator of fermionic superfluidity*, Physical Review Research **4**, L042032 (2022).

[303] G. R. Stewart, *Unconventional superconductivity*, Advances in Physics **66**, 75 (2017).

[304] M. Sato and Y. Ando, *Topological superconductors: a review*, Reports on Progress in Physics **80**, 076501 (2017).

[305] X. Zhou, W.-S. Lee, M. Imada, N. Trivedi, P. Phillips, H.-Y. Kee, P. Törmä, and M. Eremets, *High-temperature superconductivity*, Nature Reviews Physics **3**, 462 (2021).

[306] E. Shuryak, *Strongly coupled quark-gluon plasma in heavy ion collisions*, Reviews of Modern Physics **89**, 035001 (2017).

[307] D. Harlow, *Jerusalem lectures on black holes and quantum information*, Reviews of Modern Physics **88**, 015002 (2016).

[308] A. F. Volkov and S. M. Kogan, *Collisionless relaxation of the energy gap in superconductors*, Journal of Experimental and Theoretical Physics **38**, 1018 (1974).

[309] E. A. Yuzbashyan, B. L. Altshuler, V. B. Kuznetsov, and V. Z. Enolskii, *Solution for the dynamics of the BCS and central spin problems*, Journal of Physics A: Mathematical and General **38**, 7831 (2005).

[310] R. A. Barankov, L. S. Levitov, and B. Z. Spivak, *Collective Rabi Oscillations and Solitons in a Time-Dependent BCS Pairing Problem*, Physical Review Letters **93**, 160401 (2004).

[311] E. A. Yuzbashyan, *Normal and anomalous solitons in the theory of dynamical Cooper pairing*, Physical Review B **78**, 184507 (2008).

[312] M. S. Foster, V. Gurarie, M. Dzero, and E. A. Yuzbashyan, *Quench-Induced Floquet Topological p -Wave Superfluids*, Physical Review Letters **113**, 076403 (2014).

[313] H. P. O. Collado, N. Defenu, and J. Lorenzana, *Engineering Higgs dynamics by spectral singularities*, Physical Review Research **5**, 023011 (2023).

[314] B. Mansart, J. Lorenzana, A. Mann, A. Odeh, M. Scarongella, M. Chergui, and F. Carbone, *Coupling of a high-energy excitation to superconducting quasiparticles in a cuprate from coherent charge fluctuation spectroscopy*, Proceedings of the National Academy of Sciences **110**, 4539 (2013).

[315] R. Matsunaga, Y. I. Hamada, K. Makise, Y. Uzawa, H. Terai, Z. Wang, and R. Shimano, *Higgs Amplitude Mode in the BCS Superconductors Nb 1-x Ti x N Induced by Terahertz Pulse Excitation*, Physical Review Letters **111**, 057002 (2013).

[316] R. Matsunaga, N. Tsuji, H. Fujita, A. Sugioka, K. Makise, Y. Uzawa, H. Terai, Z. Wang, H. Aoki, and R. Shimano, *Light-induced collective pseudospin precession resonating with Higgs mode in a superconductor*, Science **345**, 1145 (2014).

[317] M. Randeria and E. Taylor, *Crossover from Bardeen-Cooper-Schrieffer to Bose-Einstein Condensation and the Unitary Fermi Gas*, Annual Review of Condensed Matter Physics **5**, 209 (2014).

[318] A. Behrle, T. Harrison, J. Kombe, K. Gao, M. Link, J.-S. Bernier, C. Kollath, and M. Köhl, *Higgs mode in a strongly interacting fermionic superfluid*, Nature Physics **14**, 781 (2018).

[319] P. W. Anderson, *Random-Phase Approximation in the Theory of Superconductivity*, Physical Review **112**, 1900 (1958).

[320] A. Kleine, C. Kollath, I. P. McCulloch, T. Giamarchi, and U. Schollwöck, *Excitations in two-component Bose gases*, New Journal of Physics **10**, 045025 (2008).

[321] M. Baghdad, P.-A. Bourdel, S. Schwartz, F. Ferri, J. Reichel, and R. Long, *Spectral engineering of cavity-protected polaritons in an atomic ensemble*, Nature Physics **19**, 1104 (2023).

[322] N. Sauerwein, F. Orsi, P. Uhrich, S. Bandyopadhyay, F. Mattiotti, T. Cantat-Moltrecht, G. Pupillo, P. Hauke, and J.-P. Brantut, *Engineering random spin models with atoms in a high-finesse cavity*, Nature Physics **19**, 1128 (2023).

[323] R. Richardson and N. Sherman, *Exact eigenstates of the pairing-force Hamiltonian*, Nuclear Physics **52**, 221 (1964).

[324] M. Gaudin, *Diagonalisation d'une classe d'hamiltoniens de spin*, Journal de Physique **37**, 1087 (1976).

[325] J. M. Weiner, K. C. Cox, J. G. Bohnet, Z. Chen, and J. K. Thompson, *Superradiant Raman laser magnetometer*, Applied Physics Letters **101**, 261107 (2012).

[326] J. G. Bohnet, Z. Chen, J. M. Weiner, K. C. Cox, and J. K. Thompson, *Active and passive sensing of collective atomic coherence in a superradiant laser*, Physical Review A **88**, 013826 (2013).

[327] M. A. Norcia, M. N. Winchester, J. R. K. Cline, and J. K. Thompson, *Superradiance on the millihertz linewidth strontium clock transition*, Science Advances **2**, e1601231 (2016).

[328] A. M. Rey, L. Jiang, M. Fleischhauer, E. Demler, and M. D. Lukin, *Many-body protected entanglement generation in interacting spin systems*, Physical Review A **77**, 052305 (2008).

[329] A. M. Black-Schaffer, *Edge Properties and Majorana Fermions in the Proposed Chiral d - Wave Superconducting State of Doped Graphene*, Physical Review Letters **109**, 197001 (2012).

[330] R. Nandkishore, L. S. Levitov, and A. V. Chubukov, *Chiral superconductivity from repulsive interactions in doped graphene*, Nature Physics **8**, 158 (2012).

[331] M. L. Kiesel, C. Platt, W. Hanke, D. A. Abanin, and R. Thomale, *Competing many-body instabilities and unconventional superconductivity in graphene*, Physical Review B **86**, 020507 (2012).

[332] M. L. Kiesel, C. Platt, W. Hanke, and R. Thomale, *Model Evidence of an Anisotropic Chiral d + i d -Wave Pairing State for the Water-Intercalated Na x CoO 2 · y H 2 O Superconductor*, Physical Review Letters **111**, 097001 (2013).

[333] M. H. Fischer, T. Neupert, C. Platt, A. P. Schnyder, W. Hanke, J. Goryo, R. Thomale, and M. Sigrist, *Chiral d -wave superconductivity in SrPtAs*, Physical Review B **89**, 020509 (2014).

[334] A. Shankar, E. A. Yuzbashyan, V. Gurarie, P. Zoller, J. J. Bollinger, and A. M. Rey, *Simulating Dynamical Phases of Chiral p + i p Superconductors with a Trapped ion Magnet*, PRX Quantum **3**, 040324 (2022).

[335] R. B. Laughlin, *Magnetic Induction of dx2-y2 + id xy Order in High-Tc Superconductors*, Physical Review Letters **80**, 5188 (1998).

[336] A. V. Balatsky, I. Vekhter, and J.-X. Zhu, *Impurity-induced states in conventional and unconventional superconductors*, Reviews of Modern Physics **78**, 373 (2006).

[337] T. Schäfer and D. Teaney, *Nearly perfect fluidity: from cold atomic gases to hot quark gluon plasmas*, Reports on Progress in Physics **72**, 126001 (2009).

[338] Y. Pehlivan, A. B. Balantekin, T. Kajino, and T. Yoshida, *Invariants of collective neutrino oscillations*, Physical Review D **84**, 065008 (2011).

[339] F. Reiter and A. S. Sørensen, *Effective operator formalism for open quantum systems*, Physical Review A **85**, 032111 (2012).

[340] O. Hosten, N. J. Engelsen, R. Krishnakumar, and M. A. Kasevich, *Measurement noise 100 times lower than the quantum-projection limit using entangled atoms*, Nature **529**, 505 (2016).

[341] K. C. Cox, G. P. Greve, J. M. Weiner, and J. K. Thompson, *Deterministic Squeezed States with Collective Measurements and Feedback*, Physical Review Letters **116**, 093602 (2016).

[342] M. H. Schleier-Smith, I. D. Leroux, and V. Vuletić, *States of an Ensemble of Two-Level Atoms with Reduced Quantum Uncertainty*, Physical Review Letters **104**, 073604 (2010).

[343] J. Hu, W. Chen, Z. Vendeiro, H. Zhang, and V. Vuletić, *Entangled collective-spin states of atomic ensembles under nonuniform atom-light interaction*, Physical Review A **92**, 063816 (2015).

[344] X. Alauze, A. Bonnin, C. Solaro, and F. P. D. Santos, *A trapped ultracold atom force sensor with a μm-scale spatial resolution*, New Journal of Physics **20**, 083014 (2018).

[345] J. Lee, G. Vrijsen, I. Teper, O. Hosten, and M. A. Kasevich, *Many-atom–cavity QED system with homogeneous atom–cavity coupling*, Optics Letters **39**, 4005 (2014).

[346] Y. Wu, R. Krishnakumar, J. Martínez-Rincón, B. K. Malia, O. Hosten, and M. A. Kasevich, *Retrieval of cavity-generated atomic spin squeezing after free-space release*, Physical Review A **102**, 012224 (2020).

[347] S. Bernon, T. Vanderbruggen, R. Kohlhaas, A. Bertoldi, A. Landragin, and P. Bouyer, *Heterodyne non-demolition measurements on cold atomic samples: towards the preparation of non-classical states for atom interferometry*, New Journal of Physics **13**, 065021 (2011).

[348] L. Salvi, N. Poli, V. Vuletić, and G. M. Tino, *Squeezing on Momentum States for Atom Interferometry*, Physical Review Letters **120**, 033601 (2018).

[349] A. Shankar, L. Salvi, M. L. Chiofalo, N. Poli, and M. J. Holland, *Squeezed state metrology with Bragg interferometers operating in a cavity*, Quantum Science and Technology **4**, 045010 (2019).

[350] K. Gietka, F. Mivehvar, and H. Ritsch, *Supersolid-Based Gravimeter in a Ring Cavity*, Physical Review Letters **122**, 190801 (2019).

[351] M. Tarallo, T. Mazzoni, N. Poli, D. Sutyrin, X. Zhang, and G. Tino, *Test of Einstein Equivalence Principle for 0-Spin and Half-Integer-Spin Atoms: Search for Spin-Gravity Coupling Effects*, Physical Review Letters **113**, 023005 (2014).

[352] L. Morel, Z. Yao, P. Cladé, and S. Guellati-Khélifa, *Determination of the fine-structure constant with an accuracy of 81 parts per trillion*, Nature **588**, 61 (2020).

[353] V. B. Braginsky and F. Y. Khalili, *Quantum nondemolition measurements: the route from toys to tools*, Reviews of Modern Physics **68**, 1 (1996).

[354] A. Kuzmich, N. P. Bigelow, and L. Mandel, *Atomic quantum non-demolition measurements and squeezing*, Europhysics Letters (EPL) **42**, 481 (1998).

[355] D. M. Harber, J. M. Obrecht, J. M. McGuirk, and E. A. Cornell, *Measurement of the Casimir-Polder force through center-of-mass oscillations of a Bose-Einstein condensate*, Physical Review A **72**, 033610 (2005).

[356] D. J. Kapner, T. S. Cook, E. G. Adelberger, J. H. Gundlach, B. R. Heckel, C. D. Hoyle, and H. E. Swanson, *Tests of the Gravitational Inverse-Square Law below the Dark-Energy Length Scale*, Physical Review Letters **98**, 021101 (2007).

[357] A. O. Sushkov, W. J. Kim, D. A. R. Dalvit, and S. K. Lamoreaux, *New Experimental Limits on Non-Newtonian Forces in the Micrometer Range*, Physical Review Letters **107**, 171101 (2011).

[358] E. Davis, G. Bentsen, and M. Schleier-Smith, *Approaching the Heisenberg Limit without Single-Particle Detection*, Physical Review Letters **116**, 053601 (2016).

[359] O. Hosten, R. Krishnakumar, N. J. Engelsen, and M. A. Kasevich, *Quantum phase magnification*, Science **352**, 1552 (2016).

[360] M. Schulte, V. J. Martínez-Lahuerta, M. S. Scharnagl, and K. Hammerer, *Ramsey interferometry with generalized one-axis twisting echoes*, Quantum **4**, 268 (2020).

[361] V. A. Dzuba and A. Derevianko, *Dynamic polarizabilities and related properties of clock states of the ytterbium atom*, Journal of Physics B: Atomic, Molecular and Optical Physics **43**, 074011 (2010).

[362] M. A. Cazalilla and A. M. Rey, *Ultracold Fermi gases with emergent SU(N) symmetry*, Reports on Progress in Physics **77**, 124401 (2014).

[363] B. Pelle, A. Hilico, G. Tackmann, Q. Beaufils, and F. Pereira Dos Santos, *State-labeling Wannier-Stark atomic interferometers*, Physical Review A **87**, 023601 (2013).

[364] D. F. James and J. Jerke, *Effective Hamiltonian theory and its applications in quantum information*, Canadian Journal of Physics **85**, 625 (2007).

[365] C. Maschler and H. Ritsch, *Cold Atom Dynamics in a Quantum Optical Lattice Potential*, Physical Review Letters **95**, 260401 (2005).

[366] C.-G. Ji, Y.-C. Liu, and G.-R. Jin, *Spin squeezing of one-axis twisting model in the presence of phase dephasing*, Quantum Information & Computation **13**, 266 (2013).

[367] M. Foss-Feig, K. R. A. Hazzard, J. J. Bollinger, and A. M. Rey, *Nonequilibrium dynamics of arbitrary-range Ising models with decoherence: An exact analytic solution*, Physical Review A **87**, 042101 (2013).

[368] D. Budker and M. Romalis, *Optical magnetometry*, Nature Physics **3**, 227 (2007).

[369] T. Thiele, Y. Lin, M. Brown, and C. Regal, *Self-Calibrating Vector Atomic Magnetometry through Microwave Polarization Reconstruction*, Physical Review Letters **121**, 153202 (2018).

[370] H. Zheng, Z. Sun, G. Chatzidrosos, C. Zhang, K. Nakamura, H. Sumiya, T. Ohshima, J. Isoya, J. Wrachtrup, A. Wickenbrock, and D. Budker, *Microwave-Free Vector Magnetometry with Nitrogen-Vacancy Centers along a Single Axis in Diamond*, Physical Review Applied **13**, 044023 (2020).

[371] M. Kasevich and S. Chu, *Atomic interferometry using stimulated Raman transitions*, Physical Review Letters **67**, 181 (1991).

[372] A. D. Cronin, J. Schmiedmayer, and D. E. Pritchard, *Optics and interferometry with atoms and molecules*, Reviews of Modern Physics **81**, 1051 (2009).

[373] W. Qin, Y.-H. Chen, X. Wang, A. Miranowicz, and F. Nori, *Strong spin squeezing induced by weak squeezing of light inside a cavity*, Nanophotonics **9**, 4853 (2020).

[374] W. Muessel, H. Strobel, D. Linnemann, D. Hume, and M. Oberthaler, *Scalable Spin Squeezing for Quantum-Enhanced Magnetometry with Bose-Einstein Condensates*, Physical Review Letters **113**, 103004 (2014).

[375] J. G. Bohnet, B. C. Sawyer, J. W. Britton, M. L. Wall, A. M. Rey, M. Foss-Feig, and J. J. Bollinger, *Quantum spin dynamics and entanglement generation with hundreds of trapped ions*, Science **352**, 1297 (2016).

[376] B. Braverman, A. Kawasaki, E. Pedrozo-Peñafiel, S. Colombo, C. Shu, Z. Li, E. Mendez, M. Yamoah, L. Salvi, D. Akamatsu, Y. Xiao, and V. Vuletić, *Near-Unitary Spin Squeezing in Yb 171*, Physical Review Letters **122**, 223203 (2019).

[377] Y.-L. Zhang, C.-L. Zou, X.-B. Zou, L. Jiang, and G.-C. Guo, *Detuning-enhanced cavity spin squeezing*, Physical Review A **91**, 033625 (2015).

[378] V. B. Braginsky, Y. I. Vorontsov, and K. S. Thorne, *Quantum Nondemolition Measurements*, Science **209**, 547 (1980).

[379] Z. Li, B. Braverman, S. Colombo, C. Shu, A. Kawasaki, A. F. Adiyatullin, E. Pedrozo-Peñafiel, E. Mendez, and V. Vuletić, *Collective Spin-Light and Light-Mediated Spin-Spin Interactions in an Optical Cavity*, PRX Quantum **3**, 020308 (2022).

[380] B. Braverman, A. Kawasaki, and V. Vuletić, *Impact of non-unitary spin squeezing on atomic clock performance*, New Journal of Physics **20**, 103019 (2018).

[381] K. Jacobs and D. A. Steck, *A straightforward introduction to continuous quantum measurement*, Contemporary Physics **47**, 279 (2006).

[382] L. B. Madsen and K. Mølmer, *Spin squeezing and precision probing with light and samples of atoms in the Gaussian description*, Physical Review A **70**, 052324 (2004).

[383] M. H. Schleier-Smith, I. D. Leroux, and V. Vuletić, *Squeezing the collective spin of a dilute atomic ensemble by cavity feedback*, Physical Review A **81**, 021804 (2010).

[384] H. Bao, J. Duan, S. Jin, X. Lu, P. Li, W. Qu, M. Wang, I. Novikova, E. E. Mikhailov, K.-F. Zhao, K. Mølmer, H. Shen, and Y. Xiao, *Spin squeezing of 1011 atoms by prediction and retrodiction measurements*, Nature **581**, 159 (2020).

[385] Z. Chen, J. G. Bohnet, S. R. Sankar, J. Dai, and J. K. Thompson, *Conditional Spin Squeezing of a Large Ensemble via the Vacuum Rabi Splitting*, Physical Review Letters **106**, 133601 (2011).

[386] D. Linnemann, H. Strobel, W. Muessel, J. Schulz, R. Lewis-Swan, K. Kheruntsyan, and M. Oberthaler, *Quantum-Enhanced Sensing Based on Time Reversal of Nonlinear Dynamics*, Physical Review Letters **117**, 013001 (2016).

[387] S. Colombo, E. Pedrozo-Peñafiel, A. F. Adiyatullin, Z. Li, E. Mendez, C. Shu, and V. Vuletić, *Time-reversal-based quantum metrology with many-body entangled states*, Nature Physics **18**, 925 (2022).

[388] J. Borregaard, E. J. Davis, G. S. Bentsen, M. H. Schleier-Smith, and A. S. Sørensen, *One- and two-axis squeezing of atomic ensembles in optical cavities*, New Journal of Physics **19**, 093021 (2017).

[389] J. Hu, W. Chen, Z. Vendeiro, A. Urvoy, B. Braverman, and V. Vuletić, *Vacuum spin squeezing*, Physical Review A **96**, 050301 (2017).

[390] L. A. Fuderer, J. J. Hope, and S. A. Haine, *Hybrid method of generating spin-squeezed states for quantum-enhanced atom interferometry*, Physical Review A **108**, 043722 (2023).

[391] H. J. Kimble, *Strong Interactions of Single Atoms and Photons in CavityQED*, Physica Scripta **T76**, 127 (1998).

[392] G. Vasilakis, H. Shen, K. Jensen, M. Balabas, D. Salart, B. Chen, and E. S. Polzik, *Generation of a squeezed state of an oscillator by stroboscopic back-action-evading measurement*, Nature Physics **11**, 389 (2015).

[393] J. J. Sakurai and J. Napolitano, *Modern quantum mechanics*, 2nd ed. (Addison-Wesley, 2011).

[394] G. S. Agarwal and E. Wolf, *Calculus for Functions of Noncommuting Operators and General Phase-Space Methods in Quantum Mechanics. I. Mapping Theorems and Ordering of Functions of Noncommuting Operators*, Physical Review D **2**, 2161 (1970).

Appendix A

Second order perturbation theory

We consider second order perturbation theory for Lindblad master equation as follows,

$$\frac{d}{dt}\hat{\rho} = -i[\hat{H}, \hat{\rho}] + \sum_k \left(\hat{L}_k \hat{\rho} \hat{L}_k^\dagger - \frac{1}{2}(\hat{L}_k^\dagger \hat{L}_k \hat{\rho} + \hat{\rho} \hat{L}_k^\dagger \hat{L}_k) \right), \tag{A.1}$$

where $\hat{H}$ is the Hamiltonian of the system, and $\hat{L}_k$ are jump operators representing decay processes from excited to ground subspace. If we define the projection operator for ground and excited subspace as $\hat{P}_g$ and $\hat{P}_e$ respectively, we can divide the Hamiltonian into four parts,

$$\hat{H} = \hat{H}_g + \hat{H}_e + \hat{V}_+ + \hat{V}_-, \tag{A.2}$$

where $\hat{H}_g = \hat{P}_g \hat{H} \hat{P}_g$, $\hat{H}_e = \hat{P}_e \hat{H} \hat{P}_e$, $\hat{V}_+ = \hat{P}_e \hat{H} \hat{P}_g$, and $\hat{V}_- = \hat{P}_g \hat{H} \hat{P}_e$. We assume $\hat{V}_+$ and $\hat{V}_-$ are perturbative couplings between the ground and excited subspace. Based on Ref. [339], the effective master equation in ground subspace ($\hat{\tilde{\rho}} = \hat{P}_g \hat{\rho} \hat{P}_g$) takes the following form,

$$\frac{d}{dt}\hat{\tilde{\rho}} = -i[\hat{H}_{\text{eff}}, \hat{\tilde{\rho}}] + \sum_k \left(\hat{L}_{k,\text{eff}} \hat{\tilde{\rho}} \hat{L}_{k,\text{eff}}^\dagger - \frac{1}{2}(\hat{L}_{k,\text{eff}}^\dagger \hat{L}_{k,\text{eff}} \hat{\tilde{\rho}} + \hat{\tilde{\rho}} \hat{L}_{k,\text{eff}}^\dagger \hat{L}_{k,\text{eff}}) \right), \tag{A.3}$$

where the effective Hamiltonian and jump operators are given by

$$\hat{H}_{\text{eff}} = -\frac{1}{2} \hat{V}_- \left(\hat{H}_{\text{NH}}^{-1} + (\hat{H}_{\text{NH}}^{-1})^\dagger \right) \hat{V}_+ + \hat{H}_g, \tag{A.4}$$

$$\hat{L}_{k,\text{eff}} = \hat{L}_k \hat{H}_{\text{NH}}^{-1} \hat{V}_+, \tag{A.5}$$

with $\hat{H}_{\text{NH}}$ the non-Hermitian Hamiltonian,

$$\hat{H}_{\text{NH}} = \hat{H}_e - \frac{i}{2} \sum_k \hat{L}_k^\dagger \hat{L}_k. \tag{A.6}$$

In the formalism above, we typically assume the energy scale of $\hat{H}_g$ are negligible compared to $\hat{H}_{\text{NH}}$, and we stay in an appropriate rotating frame such that the Hamiltonian $\hat{H}$ and jump operators $\hat{L}_k$ are time independent. This formalism can be generalized to the case when ground state energy is comparable with $\hat{H}_{\text{NH}}$, and $\hat{V}_+$ and $\hat{V}_-$ can have multiple frequency components. We assume

$$\hat{H}_g = \sum_l E_l \hat{P}_l, \tag{A.7}$$

where $\hat{P}_l = |l\rangle\langle l|$ is the projection operator in the eigenbasis, and

$$\hat{V}_+(t) = \sum_f \hat{v}_+^f e^{-i\omega_f t} = \sum_{f,l} \hat{V}_+^{(f,l)}(t), \tag{A.8}$$

where $\hat{V}_+^{(f,l)}(t) = \hat{v}_+^f \hat{P}_l e^{-i\omega_f t}$. The effective Hamiltonian and jump operators now become [339]

$$\hat{H}_{\text{eff}} = -\frac{1}{2}\left[\hat{V}_-(t) \sum_{f,l} \left(\hat{H}_{\text{NH}}^{(f,l)}\right)^{-1} \hat{V}_+^{(f,l)}(t) + \text{H.c.}\right] + \hat{H}_g, \tag{A.9}$$

$$\hat{L}_{k,\text{eff}} = \hat{L}_k \sum_{f,l} \left(\hat{H}_{\text{NH}}^{(f,l)}\right)^{-1} \hat{V}_+^{(f,l)}(t), \tag{A.10}$$

where

$$\hat{H}_{\text{NH}}^{(f,l)} = \hat{H}_{\text{NH}} - E_l - \hbar\omega_f. \tag{A.11}$$

Derivation

Here we provide a simplified version of derivation for Eq. (A.4) and Eq. (A.5). Based on Eq. (A.1), we have

$$\frac{d}{dt}(\hat{P}_g\hat{\rho}\hat{P}_g) = -i[\hat{H}_g, (\hat{P}_g\hat{\rho}\hat{P}_g)] - i\hat{V}_-(\hat{P}_e\hat{\rho}\hat{P}_g) + i(\hat{P}_g\hat{\rho}\hat{P}_e)\hat{V}_+ + \sum_k \hat{L}_k(\hat{P}_e\hat{\rho}\hat{P}_e)\hat{L}_k^\dagger, \tag{A.12}$$

$$\frac{d}{dt}(\hat{P}_e\hat{\rho}\hat{P}_g) = -i\hat{H}_{\text{NH}}(\hat{P}_e\hat{\rho}\hat{P}_g) - i\hat{V}_+(\hat{P}_g\hat{\rho}\hat{P}_g) + i(\hat{P}_e\hat{\rho}\hat{P}_g)\hat{H}_g + i(\hat{P}_e\hat{\rho}\hat{P}_e)\hat{V}_+, \tag{A.13}$$

$$\frac{d}{dt}(\hat{P}_e\hat{\rho}\hat{P}_e) = -i\hat{H}_{\text{NH}}(\hat{P}_e\hat{\rho}\hat{P}_e) + i(\hat{P}_e\hat{\rho}\hat{P}_e)\hat{H}_{\text{NH}}^\dagger - i\hat{V}_+(\hat{P}_g\hat{\rho}\hat{P}_e) + i(\hat{P}_e\hat{\rho}\hat{P}_g)\hat{V}_-. \tag{A.14}$$

Now we assume $\hat{P}_g\hat{\rho}\hat{P}_g, \hat{H}_{\text{NH}} \sim O(1)$, $\hat{V}_+, \hat{V}_- \sim O(\epsilon)$, we get $\hat{P}_e\hat{\rho}\hat{P}_g \sim O(\epsilon)$, and $\hat{P}_e\hat{\rho}\hat{P}_e \sim O(\epsilon^2)$. In Eq. (A.13), we only keep the terms up to $O(\epsilon)$, and we also assume the energy scale of $\hat{H}_g$ are

negligible compared to $\hat{H}_{\mathrm{NH}}$, which gives

$$\frac{d}{dt}(\hat{P}_e\hat{\rho}\hat{P}_g) \approx -i\hat{H}_{\mathrm{NH}}(\hat{P}_e\hat{\rho}\hat{P}_g) - i\hat{V}_+(\hat{P}_g\hat{\rho}\hat{P}_g). \tag{A.15}$$

Assuming the time scale of excited state dynamics are much faster than ground state dynamics, $\hat{P}_e\hat{\rho}\hat{P}_g$ and $\hat{P}_e\hat{\rho}\hat{P}_e$ should reach their steady states,

$$\hat{P}_e\hat{\rho}\hat{P}_g \to -\hat{H}_{\mathrm{NH}}^{-1}\hat{V}_+(\hat{P}_g\hat{\rho}\hat{P}_g), \tag{A.16}$$

$$\hat{P}_e\hat{\rho}\hat{P}_e \to \hat{H}_{\mathrm{NH}}^{-1}\hat{V}_+(\hat{P}_g\hat{\rho}\hat{P}_g)\hat{V}_-(\hat{H}_{\mathrm{NH}}^{-1})^\dagger. \tag{A.17}$$

Plug in Eq. (A.12), we get Eq. (A.4) and Eq. (A.5).

Appendix B

Spherical tensor operators

Spherical tensor operators are discussed in quantum mechanics textbooks such as Ref. [393]. Since the definition of spherical tensor operators and reduced matrix elements varies in different textbooks, here we would like to provide a consistent definition for all the formula within this thesis. Spherical tensor operators of rank k are defined as a set of $2k+1$ operators $\hat{T}_q^{(k)}$ with $q = -k, -k+1, \cdots, k$, which transform among themselves like angular momentum states $|j = k, m = q\rangle$, which gives

$$e^{i\theta\hat{\mathbf{J}}\cdot\mathbf{n}}\hat{T}_q^{(k)}e^{-i\theta\hat{\mathbf{J}}\cdot\mathbf{n}} = \sum_{q'}\langle k, q'|e^{-i\theta\hat{\mathbf{J}}\cdot\mathbf{n}}|k, q\rangle\hat{T}_{q'}^{(k)}. \tag{B.1}$$

Taking infinitesimal rotation of θ, Eq. (B.1) is equivalent to the following commutation relations,

$$[\hat{J}_z, \hat{T}_q^{(k)}] = q\hat{T}_q^{(k)}, \quad [\hat{J}_\pm, \hat{T}_q^{(k)}] = \sqrt{(k \mp q)(k \pm q + 1)}\hat{T}_{q\pm1}^{(k)}. \tag{B.2}$$

Based on the definition of spherical tensor operators, one can obtain the following properties:

- Wigner-Eckart theorem

$$\langle jm|\hat{T}_q^{(k)}|j'm'\rangle = \langle j'm'; kq|jm\rangle\frac{\langle j||\hat{T}^{(k)}||j'\rangle}{\sqrt{2j+1}}, \tag{B.3}$$

  where $\langle j'm'; kq|jm\rangle$ is the Clebsch-Gordan coefficient, and $\langle j||\hat{T}^{(k)}||j'\rangle$ is the reduced matrix element following the normalization convention

$$|\langle j||\hat{T}^{(k)}||j'\rangle|^2 = (2j+1)\sum_{m'q}|\langle jm|\hat{T}_q^{(k)}|j'm'\rangle|^2 = \sum_{mm'q}|\langle jm|\hat{T}_q^{(k)}|j'm'\rangle|^2. \tag{B.4}$$

- Combination of spherical tensors

$$\hat{T}_q^{(k)} = \sum_{q_1 q_2} \langle k_1 q_1; k_2 q_2 | k q \rangle \hat{U}_{q_1}^{(k_1)} \hat{V}_{q_2}^{(k_2)}, \tag{B.5}$$

$$\hat{U}_{q_1}^{(k_1)} \hat{V}_{q_2}^{(k_2)} = \sum_{kq} \langle k_1 q_1; k_2 q_2 | k q \rangle \hat{T}_q^{(k)}, \tag{B.6}$$

  which take the same form as the rules of addition of angular momentum.

Here we list two properties of the reduced matrix elements relevant in chapter 2,

- Conjugates of reduced matrix elements

$$\langle j' || \hat{T}^{(k)} || j \rangle = (-1)^{j'-j} \langle j || \hat{T}^{(k)} || j' \rangle^*. \tag{B.7}$$

- Relation for combination of spherical tensors

$$\langle j || \hat{T}^{(k)} || j' \rangle = (-1)^{k+j+j'} \sqrt{2k+1} \sum_{j''} \begin{Bmatrix} k_1 & k_2 & k \\ j' & j & j'' \end{Bmatrix} \langle j || \hat{U}^{(k_1)} || j'' \rangle \langle j'' || \hat{V}^{(k_2)} || j' \rangle, \tag{B.8}$$

  where the curly bracket marks the Wigner-6j symbol.

Conversion to Cartesian tensor operators

First we focus on rank-1 Cartesian tensor operators (vector operators). A vector operator $\hat{\mathbf{V}}$ is rotated like a classical vector,

$$e^{i\theta \hat{\mathbf{J}} \cdot \mathbf{n}} \hat{\mathbf{V}} e^{-i\theta \hat{\mathbf{J}} \cdot \mathbf{n}} = \sum_j R_{ij} \hat{V}_j, \tag{B.9}$$

where R_{ij} is the classical rotation matrix. Similarly, Eq. (B.9) is equivalent to the following commutation relation,

$$[\hat{V}_i, \hat{J}_j] = i \epsilon_{ijk} \hat{V}_k. \tag{B.10}$$

Compared to Eq. (B.2), we can construct vector operators based on rank-1 spherical tensor operators,

$$\hat{V}_x = \frac{-\hat{V}_1^{(1)} + \hat{V}_{-1}^{(1)}}{\sqrt{2}}, \quad \hat{V}_y = i \frac{\hat{V}_1^{(1)} + \hat{V}_{-1}^{(1)}}{\sqrt{2}}, \quad \hat{V}_z = \hat{V}_0^{(1)}, \tag{B.11}$$

and the inverse formula,

$$\hat{V}_1^{(1)} = -\frac{\hat{V}_x + i\hat{V}_y}{\sqrt{2}}, \quad \hat{V}_0^{(1)} = \hat{V}_z, \quad \hat{V}_{-1}^{(1)} = \frac{\hat{V}_x - i\hat{V}_y}{\sqrt{2}}. \tag{B.12}$$

Then we focus on rank-2 Cartesian tensor operators constructed by $\hat{T}_{ij} = \hat{U}_i\hat{V}_j$, where $\hat{\mathbf{U}}$ and $\hat{\mathbf{V}}$ are vector operators. Based on Eq. (B.6), $\hat{T}_{ij}$ can be decomposed into scalar (rank-0 spherical tensor), vector (rank-1 spherical tensor) and tensor (rank-2 spherical tensor) parts. Here we only list the formula for relevant calculation in chapter 2,

$$\hat{T}_{xx} = \frac{1}{2}\Big(\hat{U}_1^{(1)}\hat{V}_1^{(1)} + \hat{U}_{-1}^{(1)}\hat{V}_{-1}^{(1)} - \hat{U}_1^{(1)}\hat{V}_{-1}^{(1)} - \hat{U}_{-1}^{(1)}\hat{V}_1^{(1)}\Big) = -\frac{1}{\sqrt{3}}\hat{T}_0^{(0)} - \frac{1}{\sqrt{6}}\hat{T}_0^{(2)} + \frac{1}{2}(\hat{T}_2^{(2)} + \hat{T}_{-2}^{(2)}), \tag{B.13}$$

$$\hat{T}_{yy} = -\frac{1}{2}\Big(\hat{U}_1^{(1)}\hat{V}_1^{(1)} + \hat{U}_{-1}^{(1)}\hat{V}_{-1}^{(1)} + \hat{U}_1^{(1)}\hat{V}_{-1}^{(1)} + \hat{U}_{-1}^{(1)}\hat{V}_1^{(1)}\Big) = -\frac{1}{\sqrt{3}}\hat{T}_0^{(0)} - \frac{1}{\sqrt{6}}\hat{T}_0^{(2)} - \frac{1}{2}(\hat{T}_2^{(2)} + \hat{T}_{-2}^{(2)}), \tag{B.14}$$

$$\hat{T}_{zz} = \hat{U}_0^{(1)}\hat{V}_0^{(1)} = -\frac{1}{\sqrt{3}}\hat{T}_0^{(0)} + \sqrt{\frac{2}{3}}\hat{T}_0^{(2)}, \tag{B.15}$$

$$\hat{T}_{xy} = \frac{i}{2}\Big(-\hat{U}_1^{(1)}\hat{V}_1^{(1)} + \hat{U}_{-1}^{(1)}\hat{V}_{-1}^{(1)} - \hat{U}_1^{(1)}\hat{V}_{-1}^{(1)} + \hat{U}_{-1}^{(1)}\hat{V}_1^{(1)}\Big) = -\frac{i}{\sqrt{2}}\hat{T}_0^{(1)} + \frac{i}{2}(-\hat{T}_2^{(2)} + \hat{T}_{-2}^{(2)}), \tag{B.16}$$

$$\hat{T}_{yx} = \frac{i}{2}\Big(-\hat{U}_1^{(1)}\hat{V}_1^{(1)} + \hat{U}_{-1}^{(1)}\hat{V}_{-1}^{(1)} + \hat{U}_1^{(1)}\hat{V}_{-1}^{(1)} - \hat{U}_{-1}^{(1)}\hat{V}_1^{(1)}\Big) = \frac{i}{\sqrt{2}}\hat{T}_0^{(1)} + \frac{i}{2}(-\hat{T}_2^{(2)} + \hat{T}_{-2}^{(2)}). \tag{B.17}$$

as well as their inverse formula,

$$\hat{T}_0^{(0)} = -\frac{1}{\sqrt{3}}\Big(\hat{U}_1^{(1)}\hat{V}_{-1}^{(1)} + \hat{U}_0^{(1)}\hat{V}_0^{(1)} + \hat{U}_{-1}^{(1)}\hat{V}_1^{(1)}\Big) = -\frac{1}{\sqrt{3}}(\hat{T}_{xx} + \hat{T}_{yy} + \hat{T}_{zz}), \tag{B.18}$$

$$\hat{T}_0^{(1)} = \frac{1}{\sqrt{2}}\Big(\hat{U}_1^{(1)}\hat{V}_{-1}^{(1)} - \hat{U}_{-1}^{(1)}\hat{V}_1^{(1)}\Big) = \frac{i}{\sqrt{2}}(\hat{T}_{xy} - \hat{T}_{yx}), \tag{B.19}$$

$$\hat{T}_0^{(2)} = \frac{1}{\sqrt{6}}\Big(\hat{U}_1^{(1)}\hat{V}_{-1}^{(1)} + 2\hat{U}_0^{(1)}\hat{V}_0^{(1)} + \hat{U}_{-1}^{(1)}\hat{V}_1^{(1)}\Big) = \frac{1}{\sqrt{6}}(2\hat{T}_{zz} - \hat{T}_{xx} - \hat{T}_{yy}). \tag{B.20}$$

The other sets of formula can be obtained in a similar way.

Appendix C

Mathieu function

The discussion of Mathieu function can be found in most of the handbooks for mathematical functions, e.g. Ref. [45]. Since it is closely related to the theory of optical lattice in this thesis, we would like to provide a short review of Mathieu function. We consider the Mathieu's differential equation as follow,

$$\frac{\mathrm{d}^2\phi}{\mathrm{d}\xi^2} + \Big(\lambda - 2q\cos(2\xi)\Big)\phi = 0. \tag{C.1}$$

The eigenfunctions of this equation is denoted by Mathieu function $\mathrm{me}_\nu(\xi, q)$ with eigenvalues $\lambda = \lambda_\nu(q)$, where ν can be any real numbers (the case with integer ν is treated separately). Here we list the relevant properties of Mathieu function below:

$$\mathrm{me}_\nu(\xi + \pi, q) = \mathrm{e}^{i\pi\nu}\mathrm{me}_\nu(\xi, q), \tag{C.2}$$

$$\mathrm{me}_{-\nu}(\xi, q) = \mathrm{me}_\nu(-\xi, q) = \Big(\mathrm{me}_\nu(\xi, q)\Big)^*, \quad \lambda_\nu(q) = \lambda_{-\nu}(q), \tag{C.3}$$

$$\int_0^\pi d\xi\ |\mathrm{me}_\nu(\xi, q)|^2 = \pi. \tag{C.4}$$

The real-valued Mathieu functions are the real and imaginary part of $\mathrm{me}_\nu(\xi, q)$,

$$\mathrm{ce}_\nu(\xi, q) = \mathrm{Re}\Big(\mathrm{me}_\nu(\xi, q)\Big), \quad \mathrm{se}_\nu(\xi, q) = \mathrm{Im}\Big(\mathrm{me}_\nu(\xi, q)\Big), \tag{C.5}$$

where $\mathrm{ce}_\nu(\xi, q)$ has even parity, and $\mathrm{se}_\nu(\xi, q)$ has odd parity. For the special case that ν is an integer, we have

$$\mathrm{me}_m(\xi, q) = \sqrt{2}\,\mathrm{ce}_m(\xi, q), \quad \lambda_m(q) = a_m(q), \quad m = 0, 1, 2, \cdots, \tag{C.6}$$

$$\mathrm{me}_{-m}(\xi,q) = -\sqrt{2}i\ \mathrm{se}_m(\xi,q), \quad \lambda_{-m}(q) = b_m(q), \quad m = 1,2,\cdots. \tag{C.7}$$

Here $a_m(q)$ and $b_m(q)$ are the Mathieu characteristic values. The asymptotic expansion of the Mathieu characteristic values at large q is given by

$$a_m(q), b_{m+1}(q) \sim -2q + 2(2m+1)\sqrt{q} - \frac{1+(2m+1)^2}{8} + O\left(\frac{1}{\sqrt{q}}\right), \tag{C.8}$$

$$b_{m+1}(q) - a_m(q) = \frac{2^{4m+5}}{m!}\left(\frac{2}{\pi}\right)^{1/2}(\sqrt{q})^{m+3/2}\mathrm{e}^{-4\sqrt{q}}\left[1 + O\left(\frac{1}{\sqrt{q}}\right)\right]. \tag{C.9}$$

We then consider the Fourier series of the Mathieu function. If we define $\mathrm{me}_\nu(\xi,q) = f_\nu(\xi,q)e^{i\nu\xi}$, we get $f_\nu(\xi,q)$ is a periodic function for ξ with period π. Therefore, the Fourier series of $\mathrm{me}_\nu(\xi,q)$ can be written as

$$\mathrm{me}_\nu(\xi,q) = \sum_{m=-\infty}^{\infty} c_{2m}^{\nu}(q)e^{i(\nu+2m)\xi}, \tag{C.10}$$

with real coefficients $c_{2m}^{\nu}(q)$. Plug in Eq. (C.1), we get the following recurrence relation,

$$q\ c_{2m+2}^{\nu}(q) - \left(\lambda_\nu(q) - (\nu+2m)^2\right)\ c_{2m}^{\nu}(q) + q\ c_{2m-2}^{\nu}(q). \tag{C.11}$$

Appendix D

Phase space representation of bosons

Here we would like to have a short review of the phase space representation of bosons, which provides useful intuitions for defining the phase space representation of spins. The bosonic coherent state is defined as the eigenstate of the bosonic annihilation operator $\hat{a}$ with an eigenvalue α,

$$\hat{a}|\alpha\rangle = \alpha|\alpha\rangle, \tag{D.1}$$

where

$$|\alpha\rangle = \hat{D}(\alpha)|0\rangle = e^{-|\alpha|^2/2}\sum_{n=0}^{\infty}\frac{\alpha^n}{\sqrt{n!}}|n\rangle, \tag{D.2}$$

with $\hat{D}(\alpha) = \exp\big(\alpha\hat{a}^\dagger - \alpha^*\hat{a}\big)$ the displacement operator and $|n\rangle$ the Fock states. Note that different bosonic coherent states are not orthogonal,

$$\langle\alpha|\alpha'\rangle = \exp\bigg(-\frac{1}{2}|\alpha|^2 + \alpha'\alpha^* - \frac{1}{2}|\alpha'|^2\bigg), \tag{D.3}$$

and thus form an overcomplete basis,

$$\frac{1}{\pi}\int|\alpha\rangle\langle\alpha|d^2\alpha = \hat{I}. \tag{D.4}$$

Here $\int d^2\alpha$ means integration over the complex plane. In the coherent state basis, the trace of an operator $\hat{O}$ can be expressed as

$$\mathrm{Tr}[\hat{O}] = \frac{1}{\pi}\int\langle\alpha|\hat{O}|\alpha\rangle d^2\alpha. \tag{D.5}$$

Since any operator acting on the Fock space can be written in polynomials of $\hat{a}$ and $\hat{a}^\dagger$, so we typically express an operator $\hat{O}$ by the corresponding polynomial function, $\hat{O} \equiv O(\hat{a}, \hat{a}^\dagger)$. As

discussed in Ref. [394], one can define the kernel operator

$$\hat{\Delta}^{(\Omega)}(\alpha,\alpha^*)=\frac{1}{\pi^2}\int\Omega(\beta,\beta^*)\hat{D}(\beta)\exp\Big(-(\beta\alpha^*-\beta^*\alpha)\Big)d^2\beta, \tag{D.6}$$

as well as the inverse kernel operator

$$\hat{\Delta}^{(\tilde{\Omega})}(\alpha,\alpha^*)=\frac{1}{\pi^2}\int\tilde{\Omega}(\beta,\beta^*)\hat{D}(\beta)\exp\Big(-(\beta\alpha^*-\beta^*\alpha)\Big)d^2\beta, \tag{D.7}$$

where $\tilde{\Omega}(\beta,\beta^*)=[\Omega(-\beta,-\beta^*)]^{-1}$ and $\Omega(0,0)=1$. Different choice of filter function $\Omega(\beta,\beta^*)$ leads to different types of phase space representation as we discussed later. Based on $\mathrm{Tr}[\hat{D}(\beta)\hat{D}(\beta')]=\pi\delta^{(2)}(\beta+\beta')$, where $\delta^{(2)}$ represents 2D Dirac δ-function, one can prove that

$$\mathrm{Tr}[\hat{\Delta}^{(\Omega)}(\alpha_1,\alpha_1^*)\hat{\Delta}^{(\tilde{\Omega})}(\alpha_2,\alpha_2^*)]=\frac{1}{\pi}\delta^{(2)}(\alpha_1-\alpha_2). \tag{D.8}$$

Based on Eq. (D.8), one can establish a mapping between the operator function $O(\hat{a},\hat{a}^\dagger)$ and the c-number function $F^{(\Omega)}(\alpha,\alpha^*)$ using the kernel operators,

$$O(\hat{a},\hat{a}^\dagger)=\pi\int F^{(\Omega)}(\alpha,\alpha^*)\hat{\Delta}^{(\Omega)}(\alpha,\alpha^*)d^2\alpha, \tag{D.9}$$

$$F^{(\Omega)}(\alpha,\alpha^*)=\mathrm{Tr}[O(\hat{a},\hat{a}^\dagger)\hat{\Delta}^{(\tilde{\Omega})}(\alpha,\alpha^*)]. \tag{D.10}$$

We call the c-number function $F^{(\Omega)}(\alpha,\alpha^*)$ as phase space representation of operator $\hat{O}$. A special case is that the operator $\hat{O}$ is the density matrix $\hat{\rho}$, and in this case the c-number function $F_\rho^{(\Omega)}(\alpha,\alpha^*)$ is called phase space representation of a quantum state. Since $\mathrm{Tr}[\hat{\rho}]=1$, we have

$$\int F_\rho^{(\Omega)}(\alpha,\alpha^*)d^2\alpha=1. \tag{D.11}$$

So one can interpret $F_\rho^{(\Omega)}(\alpha,\alpha^*)$ as a quasi-probability distribution in phase space. Also based on Eq. (D.8), it is clear that

$$\mathrm{Tr}[\hat{O}_1\hat{O}_2]=\pi\int F_1^{(\Omega)}(\alpha,\alpha^*)F_2^{(\tilde{\Omega})}(\alpha,\alpha^*)d^2\alpha. \tag{D.12}$$

Here we introduce some examples of the filter function $\Omega(\beta,\beta^*)$:

- $\Omega(\beta,\beta^*)=\tilde{\Omega}(\beta,\beta^*)=1$ (Wigner representation)

  Here we use $W(\alpha,\alpha^*)$ to represent the c-number function $F_\rho^{(W)}(\alpha,\alpha^*)$ for density matrix $\hat{\rho}$. In this case we have

$$\hat{\Delta}^{(W)}(\alpha,\alpha^*)=\frac{1}{\pi^2}\int \hat{D}(\beta)\exp\Big(-(\beta\alpha^*-\beta^*\alpha)\Big)d^2\beta, \tag{D.13}$$

$$\begin{aligned} W(\alpha,\alpha^*)&=\frac{1}{\pi^2}\int \mathrm{Tr}[\hat{\rho}\hat{D}(\beta)]\exp\Big(-(\beta\alpha^*-\beta^*\alpha)\Big)d^2\beta \\ &=\frac{2}{\pi^2}\exp\big(2|\alpha|^2\big)\int\langle-\beta|\hat{\rho}|\beta\rangle\exp\Big(-2(\beta\alpha^*-\beta^*\alpha)\Big)d^2\beta. \end{aligned} \tag{D.14}$$

  One can refer to Ref. [68] for the proof of Eq. (D.14).

- $\Omega(\beta,\beta^*)=\exp\big(-|\beta|^2/2\big)$ (Glauber P-representation), $\tilde{\Omega}(\beta,\beta^*)=\exp\big(|\beta|^2/2\big)$ (Husimi Q-representation)

  Here we use $P(\alpha,\alpha^*)$ to represent the c-number function $F_\rho^{(P)}(\alpha,\alpha^*)$, and $Q(\alpha,\alpha^*)$ to represent the c-number function $F_\rho^{(Q)}(\alpha,\alpha^*)$. In this case we have

$$\hat{\Delta}^{(P)}(\alpha,\alpha^*)=\frac{1}{\pi^2}\int\exp\Big(\beta^*(\alpha-\hat{a})\Big)\exp\Big(-\beta(\alpha^*-\hat{a}^\dagger)\Big)d^2\beta=\frac{1}{\pi}|\alpha\rangle\langle\alpha|, \tag{D.15}$$

  which gives

$$\hat{\rho}=\int P(\alpha,\alpha^*)|\alpha\rangle\langle\alpha|d^2\alpha. \tag{D.16}$$

  On the other hand,

$$\begin{aligned} &\hat{\Delta}^{(Q)}(\alpha,\alpha^*)=\frac{1}{\pi^2}\int\exp\Big(-\beta(\alpha^*-\hat{a}^\dagger)\Big)\exp\Big(\beta^*(\alpha-\hat{a})\Big)d^2\beta \\ \Rightarrow\quad &\langle\alpha'|\hat{\Delta}^{(Q)}(\alpha,\alpha^*)|\alpha'\rangle=\delta^{(2)}(\alpha-\alpha'), \end{aligned} \tag{D.17}$$

  which gives

$$Q(\alpha,\alpha^*)=\frac{1}{\pi}\langle\alpha|\hat{\rho}|\alpha\rangle. \tag{D.18}$$